Springer Geophysics

Dapeng Zhao

Multiscale Seismic Tomography

Springer

Springer Geophysics

For further volumes:
http://www.springer.com/series/10173

Dapeng Zhao

Multiscale Seismic Tomography

Springer

Dapeng Zhao
Tohoku University
Sendai
Japan

Springer Geophysics
ISBN 978-4-431-55359-5 ISBN 978-4-431-55360-1 (eBook)
DOI 10.1007/978-4-431-55360-1

Library of Congress Control Number: 2015932775

Springer Tokyo Heidelberg New York Dordrecht London

Printed on acid-free paper

Springer is part of Springer Science+Business Media (www.springer.com)

Preface

In this book, I would like to share my research experiences in the field of earthquake seismology; in particular, using seismic tomography to study seismotectonics, volcanism, and the interior structure and dynamics of the Earth and Moon. To date, I have been fortunate to have studied and worked at eight universities in China, Japan, and the USA, and so I have had opportunities to become acquainted with many outstanding scientists working in various fields of the Earth sciences, and to collaborate with some of them in studying seismic structure and geodynamics of many different regions and tectonic settings.

As an undergraduate student, I studied in the Department of Geological Sciences, Peking University, from 1980 to 1984, where I acquired a basic knowledge of Earth sciences and participated in the 2–8 week field geology course every year in northern China. This helped me realize that geological structures and processes are very complicated and can hardly be described precisely using mathematical and physical methods. Between November 1984 and September 1985, I joined an intensive course for learning Japanese at the Dalian University of Foreign Languages, where I met 99 students from different universities in China, selected from various fields including natural sciences, social sciences, engineering, agriculture, and medical sciences. From these classmates, I learned the main concepts, issues, and research approaches of their respective fields. In October 1985, we 100 Chinese students went to study at the Japanese national universities. Five years later, most obtained a Ph.D. degree in Japan, and now many of them are distinguished experts in their fields.

In the period April 1986 to March 1991, I was a graduate student in the Department of Geophysics, Tohoku University, and my advisors were Profs. Akio Takagi, Akira Hasegawa, and Shigeki Horiuchi, who introduced me to the field of earthquake seismology. With their kind and helpful guidance, I studied the Conrad and Moho discontinuities beneath NE Japan (Tohoku) for my Master's thesis, and worked on the seismic tomography of the Japan subduction zone for my Ph.D. thesis. From April 1991, I spent one year in the Geophysical Institute (GI), University of Alaska Fairbanks as a post-doctoral fellow, and I worked with Prof. Douglas Christensen on the tomographic imaging of the Alaska subduction zone. I was impressed by the then GI director Prof. Syun-Ichi Akasofu's aurora study. During May 1992 to

April 1995, I was a Texaco post-doc fellow at the Seismological Laboratory of the California Institute of Technology (Caltech), and Prof. Hiroo Kanamori was my advisor. I learned the basic facts of earthquake source studies from Prof. Kanamori, and I worked with him on the high-resolution tomographic imaging of the source zones of large crustal earthquakes, including the 1992 Landers (M 7.3), the 1994 Northridge (M 6.7). and the 1995 Kobe (M 7.2) earthquakes. I was impressed by Prof. Kanamori's earthquake source studies, Prof. Don Anderson's global seismology, and Prof. Don Helmberger's waveform modeling studies. In my first year at Caltech, I was supported by a fellowship from the Southern California Earthquake Center (SCEC), and so I had opportunities to report my works to the then SCEC director Prof. Keiiti Aki, who was at the University of Southern California. Prof. Aki kindly gave me thoughtful comments and suggestions on my tomographic studies.

During May 1995 to June 1997, I worked in the Department of Earth and Planetary Sciences, Washington University in St. Louis, as a research scientist, where I worked with Prof. Douglas Wiens on the tomographic imaging of the Tonga subduction zone. At the weekly seminars, I was impressed by Prof. Julie Morris's geochemical study of arc magmatism and Prof. Michael Wysession's study of the deep Earth structure. In St. Louis, I also worked on the stress tensor inversion for the 1994 Northridge earthquake area. In July 1997, I moved to the Department of Earth Sciences, University of Southern California (USC), as a research scientist, where I continued my study of local and regional tomography. At USC, I was impressed by the fault-zone trapped-wave study by Dr. Yong-Gang Li and Prof. K. Aki.

Beginning in February 1998, I spent nine years at Ehime University, Japan, as an associate professor, and then as a full professor from January 2003. I established my laboratory where I worked with my graduate students, post-docs, and visiting scholars to make extensive studies of multiscale seismic tomography. I started my study of global seismic tomography in 1999 and used global tomography to study hotspots, mantle plumes, and deep subducting slabs. I also invited many able researchers and students from India, China, the USA, Spain, Egypt, Taiwan, Korea, and South Africa to study in my lab, and we collaborated to study the 3-D crustal and mantle structure, seismotectonics, and volcanism in different regions and tectonic settings. We developed the off-network tomography method to study the 3-D velocity structure beneath oceanic regions. We proposed the big mantle wedge (BMW) model to explain the intraplate magmatism and mantle dynamics in East Asia. I had the idea to study seismic tomography of the Moon and we obtained a good result.

In April 2007, I moved back to my alma mater, Tohoku University, as a professor of geophysics. I worked with my colleagues and students on the global tomography, the East Asia mantle tomography, and the detailed structure of the Japan subduction zone. We presented tomographic images of the source area of the great 2011 Tohoku-oki earthquake (Mw 9.0) soon after its occurrence. We also worked on P-wave anisotropy tomography, and applied the new method to study the seismic anisotropy and structural heterogeneity of many subduction zones and continental regions. Recently, we worked on the 3-D attenuation (Qp and Qs) structure of the Japan subduction zone.

The main results of these multiscale tomographic studies are summarized in the present book, especially the results obtained during the past decade. To date, several nice books on seismic tomography have been published. The first one, *Seismic Tomography: With Applications in Global Seismology and Exploration Geophysics,* edited by Nolet (1987) and written by 17 authors, summarized the early theoretical developments of seismic tomography and its applications in exploration geophysics and global seismology. The second book is *Seismic Tomography: Theory and Practice,* which was edited by Iyer and Hirahara (1993) with contributions by 49 authors. Except for a few chapters which focused on the technical aspects of seismic tomography, most of the chapters in Iyer and Hirahara (1993) introduced applications of seismic tomography to various regions and tectonic settings, from local to global scales. The third book, *A Breviary of Seismic Tomography: Imaging the Interior of the Earth and Sun,* written by Nolet (2008), focused on the theoretical aspects of seismic tomography and contained many mathematical equations. The present book describes the state-of-the-art in seismic tomography, with an emphasis on the tomographic results, rather than on the methods. All the tomographic images are shown in color in this book, which are clearly visible and easy to understand. In contrast, no color figures were included in the previous three books.

As mentioned above, I have become acquainted with many researchers working in various fields of the Earth sciences. My experiences have taught me that seismology is an important, but small, field in the Earth sciences. Most non-seismologists have no interest in the technical details of seismological studies; instead they are much more interested in the seismological results and need seismologists to provide them with useful information and constraints on the geological phenomena they are working on, such as earthquake fault zones, active volcanoes, basins, mountain building, subduction zones, hotspots, mantle plumes, large igneous provinces, etc. Some seismologists enjoy developing new and mathematically sophisticated techniques, which may look advanced and profound and so may frighten most geoscientists who are generally not good at advanced mathematics. Concerning methods for solving the very complicated geoscience problems, I like the Chinese proverb, *Dadao Zhijian*, which means "the simplest way is the best way!" Occam's razor expresses the same principle for solving problems. A sophisticated new technique is certainly fine, but it must produce better results which can better explain the geological, geophysical, and geochemical observations. I think that body-wave travel-time tomography based on ray theory is the most straightforward, robust, and mature tool that has produced many more credible and geologically reasonable results than any other tomographic methods, and now it is time to summarize these reliable and nice results obtained with travel-time tomography in a monograph. As Prof. Peter Shearer (2009) argued in his book *Introduction to Seismology*, a large fraction of current seismological research continues to rely on travel times, and ray theory is still good enough for most seismological applications. Therefore, in this book I have perhaps included more results from ray theory based travel-time tomography and less on surface waves, normal modes, and other methods than a truly balanced book would require. Any book, to some extent, reflects the prejudices of its author (Shearer, 2009). Hence, this book is not written for professional seismologists but

for undergraduate and graduate students, researchers, and professionals in the broad fields of Earth and planetary sciences, who need to broaden their horizons about the crustal and upper mantle structure beneath various geological features and tectonic settings, seismotectonics, volcanism, and the deep structure and dynamics of the Earth and Moon. I hope this book may help to foster more communications among seismologists, geologists, geochemists, mineral physicists, and planetary scientists.

I have tried to keep each chapter concise but not economize on references which provide more detail. However, it is a huge job to review all related publications, and I confess that a complete review of seismic tomography was not possible. For example, when I began to write Chap. 3, "Subduction Zone Tomography", I tried to review the related publications region to region. However, after a few months of hard work, I found it was impossible to do it that way, because there are thousands of related publications, which require a grand tome to summarize. Hence, I had to change my mind and to summarize the subduction-zone tomographic studies according to the three seismic-structural parameters: seismic velocity, attenuation, and anisotropy. Thus, in the text I had to introduce only some representative publications for every subduction zone, and had to give up many other important papers which are worth mentioning, although I have tried to include them in the list of references as much as possible. Now I know there are so many diligent tomographers working on subduction zones! Similarly, in the whole book, I have cited publications in English, Chinese, and Japanese but had to omit related publications in other languages which I cannot read. This is unfortunate, and I apologize for this to the authors of those papers.

Springer Japan asked me to write each chapter independently with a complete list of references. Although this has resulted in some references appearing in different chapters, every chapter has become self-consistent and independent, and so the reader may feel free to pick up any chapter to read without having to refer to the other chapters. The mathematical equations are kept to a minimum in all chapters except for Chap. 2 on the tomographic methodology, so that the non-seismologists can read and understand them easily. Even in Chap. 2, simpler equations and formulas are adopted, so that undergraduate students will also understand them. Those readers who are interested in the technical details of tomographic methods are referred to Nolet (1987, 2008).

In this book, each chapter focuses on the tomographic studies of one type of tectonic setting. However, not all tectonic settings are covered by this book. For example, an important tectonic setting, the mid-ocean ridges, is not reviewed by this book, simply because the author has not worked on this topic and is not very familiar with it. The interested reader may refer to a nice review article written by R. Dunn and D. Forsyth (2007), "Crust and Lithospheric Structure—Seismic Structure of Mid-Ocean Ridges", Vol. 1.12 in *Treatise on Geophysics* edited by G. Schubert.

Department of Geophysics, Prof. Dapeng Zhao
Tohoku University, Sendai, Japan

Acknowledgments

Many of my mentors, colleagues, graduate students, and post-doctoral fellows have collaborated with me in studies of multiscale seismic tomography, helping me to learn more than I knew. Some of them are mentioned in the preface, while the following is a more complete list, roughly in the time order of their research collaboration with me: Akio Takagi, Akira Hasegawa, Shigeki Horiuchi, Norihito Umino, Toru Matsuzawa, Akira Yamamoto, Sadato Ueki, Hiroo Kanamori, Douglas Christensen, Hans Pulpan, Kuo-Fong Ma, Eugene Humphreys, Douglas Wiens, Eric Roth, LeRoy Dorman, John Hildebrand, Spahr Webb, Hiroaki Negishi, Inma Serrano, Jose Morales, J.R. Kayal, Guangwei Fan, Terry Wallace, Alex Gorbatov, Takashi Mizuno, Hikaru Iwamori, Tetsuo Irifune, Toru Inoue, Koichi Asamori, Fumiko Ochi, Junichi Nakajima, Tetsuzo Seno, Kelin Wang, Garry Rogers, Simon Peacock, O.P. Mishra, D.D. Singh, Jinli Huang, Jianshe Lei, Ryohei Sanda, Aya Kurogi, Takeshi Ono, Toshiyuki Nishino, Keiji Yamamoto, Yoshihiko Tamura, Yoshiyuki Tatsumi, Hiroki Sato, Masaki Nakamura, Mohamed Salah, Hideto Tani, Andrew Martin, Biao Guo, Qiyuan Liu, Reiji Kobayashi, Mohamed Abdelwahed, Zhi Wang, Yigang Zhang, Masanori Matsui, Yingshuang Ai, Sachiko Todo, Honn Kao, Sagarika Mukhopadhyay, Michiharu Ikeda, Akira Yamada, Tomofumi Inoue, Stephen S. Gao, Han-Chiang Chou, Ban-Yuan Kuo, Ling-Yun Chiao, Shigenori Maruyama, Soichi Omori, Tomomi Okada, M. Santosh, Guust Nolet, Richard Allen, Koki Idehara, Cheng Qi, Baoshan Wang, Shaohong Xia, Guoming Jiang, You Tian, Anhui Sun, Rizheng He, Hongwei Zheng, Peifen Xu, Eiji Ohtani, Rei Shiraishi, Jian Wang, Yonghong Duan, Sandeep Gupta, Yoshihiro Yamamoto, Takahiro Yanada, Wei Wei, Zhouchuan Huang, Xiaobo Tian, Tatsuya Sakamaki, Bin Cheng, Simanchal Padhy, Yukihisa Nishizono, Hirohito Inakura, Madoka Tanaka, Takuma Sasaki, Ping Tong, Heng Zhang, Tomoko Arai, Andrew Lloyd, Xin Liu, Chuanxu Chen, Genti Toyokuni, Hiroki Kitagawa, Moeto Fujisawa, and Tatsuya Torimoto.

I was fortunate to have obtained the steady support of science foundations in the USA and Japan, including the U.S. National Science Foundation, the U.S. Geological Survey, the Japan Society for the Promotion of Science, special financial support from the Ehime University President, Global COE (Center of Excellence) Program of Earth and Planetary Sciences of Tohoku University, as well as some funds from private companies in Japan via research collaborations. I have greatly benefitted

from the excellent research environment in Japan. All of my colleagues, students, technicians, and secretaries are very friendly and cooperative, enabling me to concentrate on teaching students and doing research. In our Research Center for Prediction of Earthquakes and Volcanic Eruptions, Tohoku University, the technicians Yukihiko Chiba, Satoshi Hirahara, Tomotsugu Demachi, Takashi Nakayama, and Toshiaki Kaida as well as the secretaries Yuko Sasaki, Yuko Daikoku, and Mika Iibuchi are all very helpful in supporting my research. In particular, my secretary, Ms. Yuko Sasaki, has kindly provided much help during the preparation of this book.

I am very grateful to Mr. Ken Kimlicka and Ms. Mihoko Kumazawa of Springer Japan for stimulating me to write this book and for kindly answering my questions related to its preparation.

I would like to thank my family, especially my wife, Lucy, for many forms of support without which this book would never have been finished. I can never forget my father, Mr. Fulin Zhao (1937–1990), for his love, care, guidance, and encouragement to me all the times before he suddenly passed away in China when I was studying in Japan preparing my Ph.D. thesis. I dedicate this book to him.

Contents

About the Author

Prof. Dapeng Zhao is a professor at the Department of Geophysics, Tohoku University, Sendai, Japan. He received his B.Sc. (1984) from Peking University, and his M.Sc. (1988) and Ph.D. (1991) from Tohoku University. He was a post-doctoral fellow at the California Institute of Technology during 1992–1995, and associate professor during 1998–2002 and professor during 2003–2007 at Ehime University. In April 2007, he moved to Tohoku University as a professor. His research interests include earthquake seismology, seismic tomography, Earth structure and dynamics from local to global scales, subduction zones, hotspots, mantle plumes, moonquakes, and lunar interior structure. He has published more than 200 research papers in refereed international journals with his coworkers, which have been cited over 9000 times (H-index = 50). According to his SCI publications during 2000 to 2010, Prof. D. Zhao was selected to be one of the world Top-10 earthquake researchers by Thomson-Reuters (http://archive.sciencewatch.com/ana/st/earthquakes2/authors/). He has been awarded the 2014 Island Arc Award by the Geological Society of Japan. To date, Prof. D. Zhao has advised more than 40 graduate students and post-doctoral researchers. Now he is an editor of the *Journal of Asian Earth Sciences*.

Chapter 1
Introduction

Abstract In this chapter, we first introduce the basic principles of seismic tomography and discuss the common features and differences between seismic tomography and the medical CT-scan. Considering the fact that many different kinds of tomographic studies have been made and a large number of tomography-related technical terms are used in the literature, we present a classification of seismic tomography. Then we explain the meaning of multiscale seismic tomography, and discuss how to interpret the obtained tomographic images. Finally, the scope and contents of this book are outlined.

Keywords Multiscale seismic tomography · Subduction zones · Slabs · Hotspots · Mantle plumes · Volcanoes

Once a seismic event, such as a natural earthquake or a seismic explosion, takes place, seismic waves are generated which pass through the Earth's interior and finally reach the Earth's surface where they are recorded by seismometers installed at seismic stations in different parts of the world (Fig. 1.1a, b). By analyzing the observed seismic wave records, seismologists can obtain information on the causal mechanism of earthquakes, as well as the physical properties of materials along the trajectories of the seismic waves. These are the basic research targets of seismology—a branch of solid-Earth geophysics. Since the advent of seismology nearly 130 years ago (e.g., Howell 1990), classical studies of seismic waves have enabled seismologists to make a number of important discoveries which have had far-reaching and profound impacts on the Earth sciences, such as the establishment of the layered structure of the Earth's interior (i.e., the one-dimensional (1-D) Earth structure) and the discovery of deep-focus earthquakes (Aki 1988).

Since the mid 1970s, benefitting from increasing computer power and a greater quality and quantity of seismic data, seismologists have established a new field of seismology—*seismic tomography*—starting with the pioneering works of Aki and Lee (1976), Aki et al. 1977, and Dziewonski et al. (1977). By definition, seismic tomography has two meanings: it is a seismological method to determine three-dimensional (3-D) images of the Earth's interior by combining information from a large number of crisscrossing seismic waves triggered by natural

D. Zhao, *Multiscale Seismic Tomography,* Springer Geophysics,
DOI 10.1007/978-4-431-55360-1_1

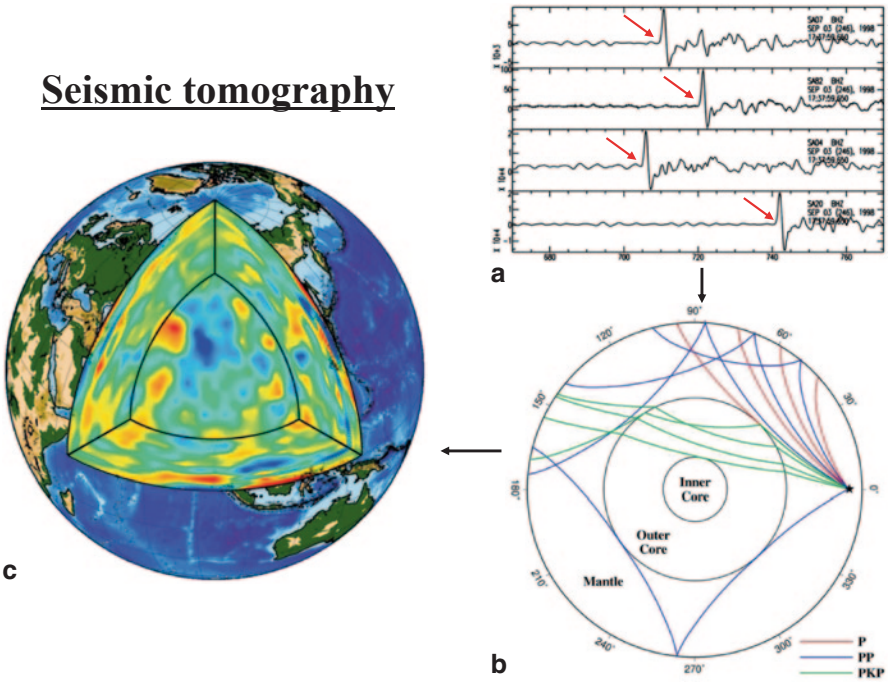

Fig. 1.1 A conceptual diagram of seismic tomography (Zhao 2007). A large number of arrival-time data are collected from observed seismograms (**a**), then the theoretical travel times and ray paths of seismic waves in the Earth's interior are calculated (**b**). Inverting travel-time residuals (i.e., differences between the measured and theoretical travel times) results in a three-dimensional distribution of seismic velocity in the Earth's interior (**c**). The tomographic images in (**c**) show *three vertical* cross-sections of P-wave tomography from the surface to the core-mantle boundary and that of the lowermost mantle (the *central triangle*)

earthquakes or artificial seismic sources (Fig. 1.1); it also means the obtained result of a 3-D inversion, or *tomogram*. During the past four decades, seismologists have been using seismic tomography to study the 3-D structure of the Earth's interior at local to global scales. These 3-D models of the Earth's structure promise to answer some basic questions of geodynamics, and they signify a revolution in the Earth sciences (Dziewonski and Anderson 1984). Seismic tomography is a powerful tool that seismologists have provided the geoscience community with and it has greatly influenced developments in the Earth sciences. With its vast scope for understanding the Earth's structure and processes, its influence will continue for a long time to come (Aki 1988; Zhao and Kayal 2000). A quarter of a century ago, Iyer wrote "at present, seismic tomography is still developing at an accelerated pace and it is expected to be an active field of seismological research for several decades to come" (Iyer 1989). His insightful comment and prediction are still valid today!

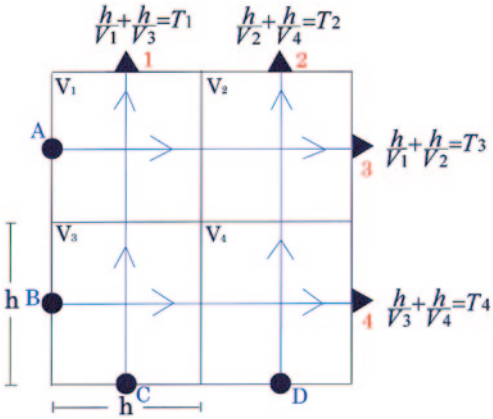

Fig. 1.2 A simple example of body-wave travel-time tomography. Four seismic waves are generated from four earthquakes (*black dots*) to four seismic stations (*black triangles*), leading to four equations relating the travel times (T1–T4) to seismic velocities (V1–V4) of the four blocks

1.1 Basic Principle of Seismic Tomography

The most important prerequisite which makes seismic tomography possible is that seismic waves can pass through the Earth's interior. It is this important property of seismic waves that seismologists have exploited to study the 1-D and 3-D structures of the Earth's interior (Fig. 1.1).

Figure 1.2 shows a simple example of the tomographic problem. A square is divided into four blocks of the same size (h). Seismic wave (P or S) velocities of the four blocks, V1–V4, are the unknown parameters to be determined. Suppose that four seismometers (Nos. 1–4) are installed at one edge of each block to record P (or S) waves from four seismic events (earthquakes or explosions) that occur at another edge of each block (A–D). Then we will have at least four data that can be measured from the observed seismograms, which are the travel times from event C to seismometer 1 (T1), from event D to seismometer 2 (T2), from event A to seismometer 3 (T3), and from event B to seismometer 4 (T4). Thus, we can establish four simple equations relating the travel times to the seismic velocities of the four blocks, as shown in Fig. 1.2. Unfortunately, the four equations are not independent, but we can measure and add one more datum, e.g., the travel time from event C to seismometer 2 (T5; Fig. 1.3). We then have a system of four independent equations which can be solved to obtain V1–V4. In the same way, we can further divide the square into many more smaller blocks, and add more seismometers and seismic events, which will result in a more detailed distribution of seismic velocity within the square, i.e., a higher-resolution tomographic image of the study area.

The principle of seismic tomography is similar to that of a medical CT-scanner (Fig. 1.4). Here, CT means *computerized tomography* (Herman 1980). In the CT-scan, X-rays radiated from a source can pass through the human body, and the intensity of the X-rays is measured at receivers. The X-ray source is rotated through 360° enabling a number of X-ray intensity data to be measured. The data are used to construct a two-dimensional density image of the human body (Fig. 1.4a). In seismic

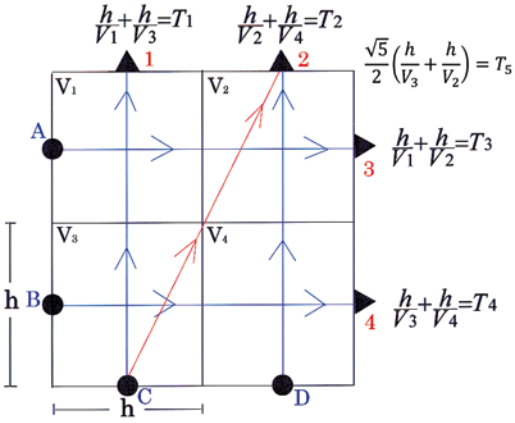

Fig. 1.3 The same as Fig. 1.2 but one more seismic ray from event C to station 2 is added, because the four equations in Fig. 1.2 are not independent. The four unknown parameters (V1–V4) of the tomographic problem can be determined by solving the system of linear equations

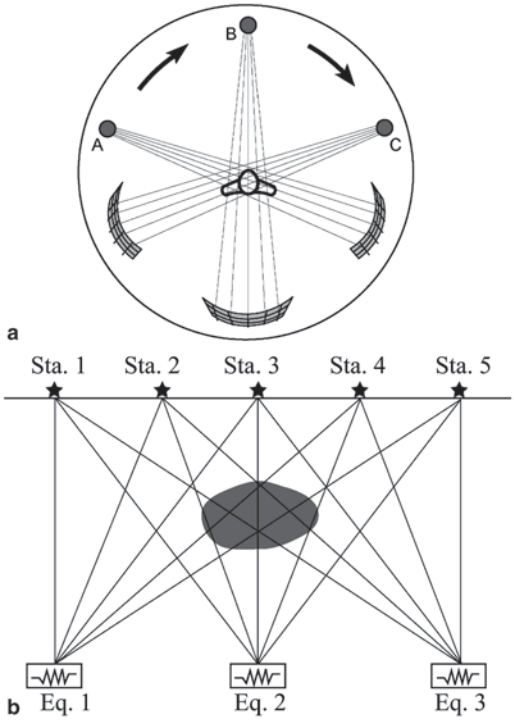

Fig. 1.4 Schematic diagram of medical CT-scan (**a**), and seismic tomography (**b**). After Zhao (2009)

tomography (ST), instead of X rays, *seismic rays* are involved which represent the propagating trajectories of seismic waves (Fig. 1.4b). This approach is called *ray theory* (or *ray approximation*), which is valid for short-period surface waves and most body waves which have a sufficiently high frequency (for details, see Cerveny 2001). The sources of energy in ST are natural earthquakes, or artificial explosions,

which are powerful enough to generate seismic waves reaching areas far from the sources, and even to the antipode of the sources, whereas X rays cannot propagate far enough in the Earth's interior, and so they cannot be used to image the Earth's structure, although X-rays can be used to study the fine structure of rock samples (e.g., Carlson 2006; Cnudde and Boone 2013), as is the case with the medical CT-scan. Of course, the receivers in ST are seismometers installed at seismic stations on the Earth's surface, or at some depths beneath the surface such as boreholes.

The most widely-used data in ST are the travel-time delays of P- and S-waves; hence ST determines the image of the seismic velocity of the Earth's interior instead of its density. The travel times of seismic waves (rays) passing through an anomalous body such as a hot magma chamber (or a cold subducting slab) can be delayed (or advanced), whereas rays propagating through the normal portions of the Earth exhibit no difference in travel time from that calculated for an average 1-D velocity model of the Earth's interior. The location, geometry and velocity deviation of the anomalous body can be estimated from the ray paths and travel-time data using an inverse calculation (called *inversion*).

Although the basic principles of the medical CT and ST are the same, there are many differences in their technical details. In the CT-scan, both sources and receivers can be controlled and so a large number of data can be measured easily to obtain a high-resolution image of the human body or a rock sample (e.g., Carlson 2006; Cnudde and Boone 2013). In contrast, for ST of the Earth's interior, both the sources and receivers are hard to control, because earthquakes have a certain distribution in the crust and upper mantle associated with plate tectonics, and seismic stations are expensive to install and maintain. Therefore the images of the Earth's interior cannot be determined as precisely and accurately as the CT-scan of the human body or rock samples (Zhao 2009).

1.2 Classification of Seismic Tomography

In the past four decades, ST has evolved from a small field of seismology into an important aspect of Solid Earth Sciences, and a large number of researchers are working on different kinds of tomographic problems. In the literature there are many technical terms related to tomography, which can be classified and summarized as follows.

1. Depending on the seismic data used, we refer to *body-wave tomography* and *surface-wave tomography*. The most widely used body-wave data are P- and S-wave travel times, leading to *travel-time tomography* which includes *P-wave tomography* and *S-wave tomography*. Surface-wave tomography usually uses Rayleigh wave or Love wave dispersion data to first estimate 2-D distributions (map views) of the phase velocity or group velocity at different periods, then determine a 3-D distribution of S-wave velocity in the crust and upper mantle. Waveforms of body waves and/or surface waves can be used directly to conduct

waveform tomography after the sophisticated processing of seismograms (e.g., Fichtner et al. 2013).

2. Depending on the lateral scale of the study areas, one has *local tomography*, *regional tomography*, and *global tomography*. There is actually no clear distinction between local and regional tomography. Usually the study area of local tomography is smaller than a few hundred kilometers wide, whereas that of a regional tomography is one to a few thousand kilometers wide, such as the Japan Islands or a continental region (e.g., North America, or East Asia, etc.).
3. According to the depth range of the modeling space, we distinguish between *crustal tomography*, *mantle tomography, and core tomography*. Crustal tomography ranges from the surface to a depth above the Moho discontinuity, or to the uppermost mantle directly beneath the Moho when Pn- or Sn-wave data are used. Mantle tomography ranges from the surface to a depth in the mantle, usually including the crust. Because the diving depth of a direct P- or S-wave depends on the epicentral distance (i.e., the distance between the epicenter and a given seismic station), local tomography under a local seismic array is usually crustal tomography or crustal and upper mantle tomography, whereas regional tomography is usually *upper mantle tomography* above the 670 km discontinuity (i.e., the boundary between the upper and lower mantles) or mantle tomography down to a depth in the lower mantle, or even down to the bottom of the mantle at the core-mantle boundary (2889 km depth).

In global tomography, if many core phase data are used, the core tomography can be determined (e.g., Lei and Zhao 2006). Because the outer core is composed of liquid iron where active convection is taking place, the outer core is essentially homogeneous. Thus core tomography is actually *inner core tomography* for which there is still no reliable model yet. Deep Earth studies have revealed strong seismic anisotropy in the inner core where lateral heterogeneities may also exist.

4. According to the relative distance between the seismic array (or seismic network) and the seismic events used, one has *local earthquake tomography* (LET) and *teleseismic tomography* (TET). In LET (Figs. 1.5a and 1.6a), all the seismic stations and events considered (local earthquakes or seismic explosions) are located in the study area, and all the local earthquakes used are relocated in the inversion process using P- and/or S-wave arrival times recorded by the seismic network, so that the events have reliable hypocentral locations enabling a good enough tomography to be obtained.

In contrast, TET determines a 3-D velocity model beneath a seismic array (or a seismic network) using P- or S-wave data from distant earthquakes and/or large seismic explosions, including nuclear tests, which are located far from the seismic array used (Figs. 1.5b and 7.25). Hence these events are called *teleseismic events*. Usually the teleseismic events considered have epicentral distances of 30°–100° (1° = 111.2 km), and thus the deepest points of all the direct P- and S-wave rays are located in the lower mantle outside of the study area (i.e., the seismic array used; see Fig. 7.25). Instead of the raw travel-time residuals used in LET, relative travel-time residuals are used in

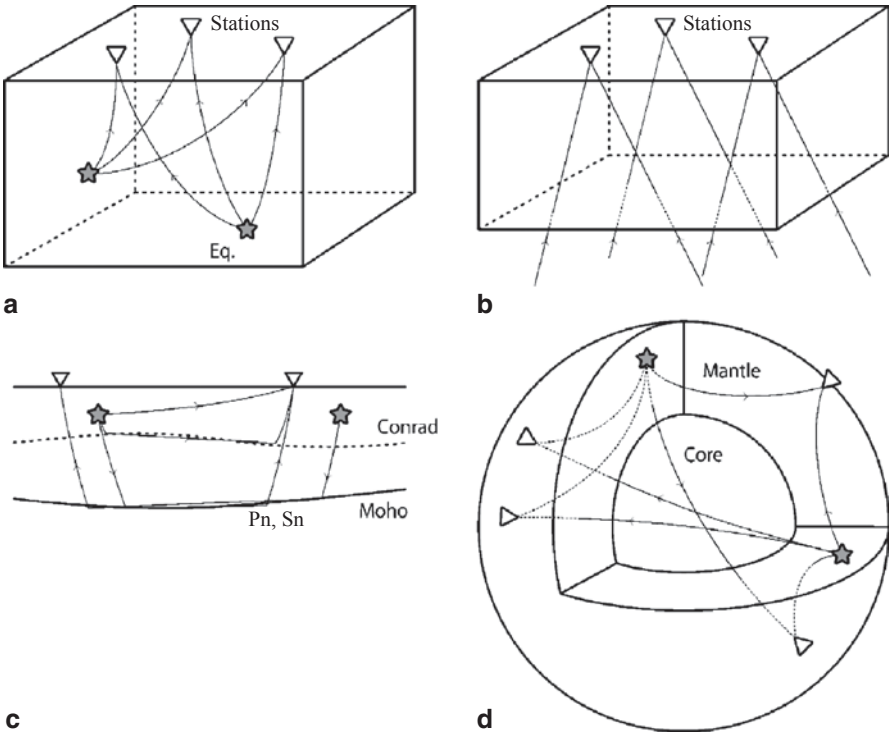

Fig. 1.5. Various approaches of body-wave tomography (Zhao 2009). **a** Local earthquake tomography; **b** teleseismic tomography; **c** determining the Conrad and Moho geometry; and **d** Global tomography. See text for details

TET (see Chap. 7.4). Thus, the effects of hypocentral mislocations of the teleseismic events and structural heterogeneities outside of the study area can be greatly reduced.

Note that LET is different from local tomography. LET can be a regional tomography if the study area is wide enough. Global tomography (Fig. 1.5d) is also a kind of LET because all the events and stations used are located in the study region (the entire Earth). Similarly, a TET can be a local tomography or a regional tomography, depending on the aperture of the seismic array adopted.

5. Depending on the physical parameters to be determined, one has *seismic velocity tomography*, *seismic attenuation tomography*, and *seismic anisotropy tomography*. Most of the tomographic models obtained so far are 3-D P- and S-wave velocity models, mainly because arrival-time data are used which can be measured precisely from a large number of seismograms. In the past decade, many tomographic models of seismic attenuation and anisotropy have been also determined, thanks to the increasing quality and quantity of waveform data recorded

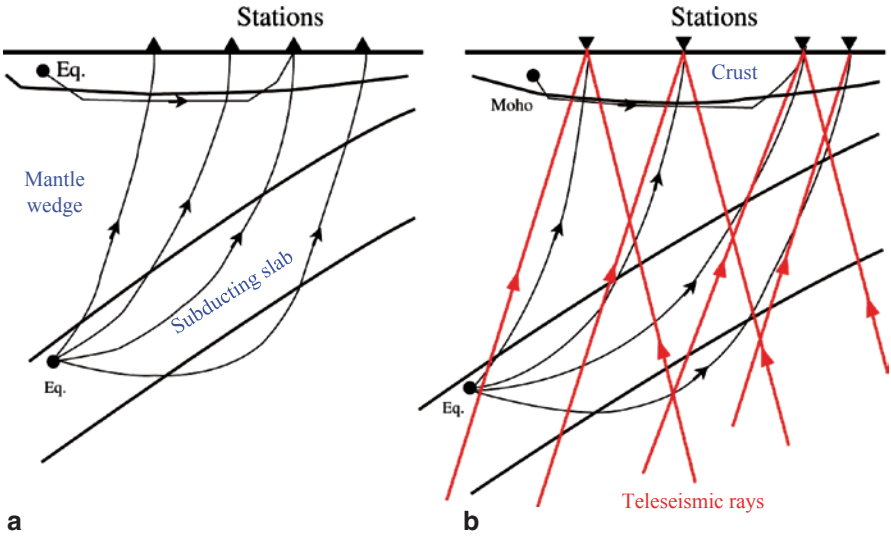

Fig. 1.6 **a** Local earthquake tomography for a subduction zone. **b** Local and teleseismic joint inversion for a subduction zone. The *black* and *red lines* denote ray paths from local earthquakes (*black dots*) and teleseismic events, respectively. (Modified from Zhao 2009)

by permanent and temporary seismic arrays in different parts of the world, as well as technical advances in waveform processing and tomographic inversions.

6. Depending on which heavenly body is being studied, one has *Earth* (*or terrestrial*) *tomography*, *lunar tomography*, and *solar tomography*. Needless to say, so far almost all seismic tomography studies relate to the Earth's interior structure. Only recently has seismic tomography been applied to study the 3-D velocity structure of the lunar interior (Zhao et al. 2008, 2012). In the past two decades, however, solar physicists have been actively investigating the 3-D sound velocity structure of the solar interior using helioseismology methods (e.g., Duvall et al. 1993, 1996; Zhao et al. 2011).

In practical applications, several tomographic terms can be combined, such as teleseismic P-wave velocity tomography of the crust and upper mantle, local earthquake S-wave attenuation tomography, etc.

The pioneering studies of body-wave travel-time tomography are Aki and Lee (1976) and Aki et al. (1977) for the local scale, and Dziewonski et al. (1977) for the global scale. Aki and Lee (1976) initiated LET, while Aki et al. (1977) developed the TET method. Surface-wave tomography was initiated by Nakanishi and Anderson (1982), and Woodhouse and Dziewonski (1984). Generally speaking, surface-wave tomography has a lower spatial resolution because of the long wavelength nature of surface waves, and so it is more appropriate for global and regional-scale studies. In contrast, body-wave tomography can have a much higher spatial resolution because of the short wavelengths of body waves, and can be applied to local, regional and global studies. However, surface-wave tomography is more powerful than body-

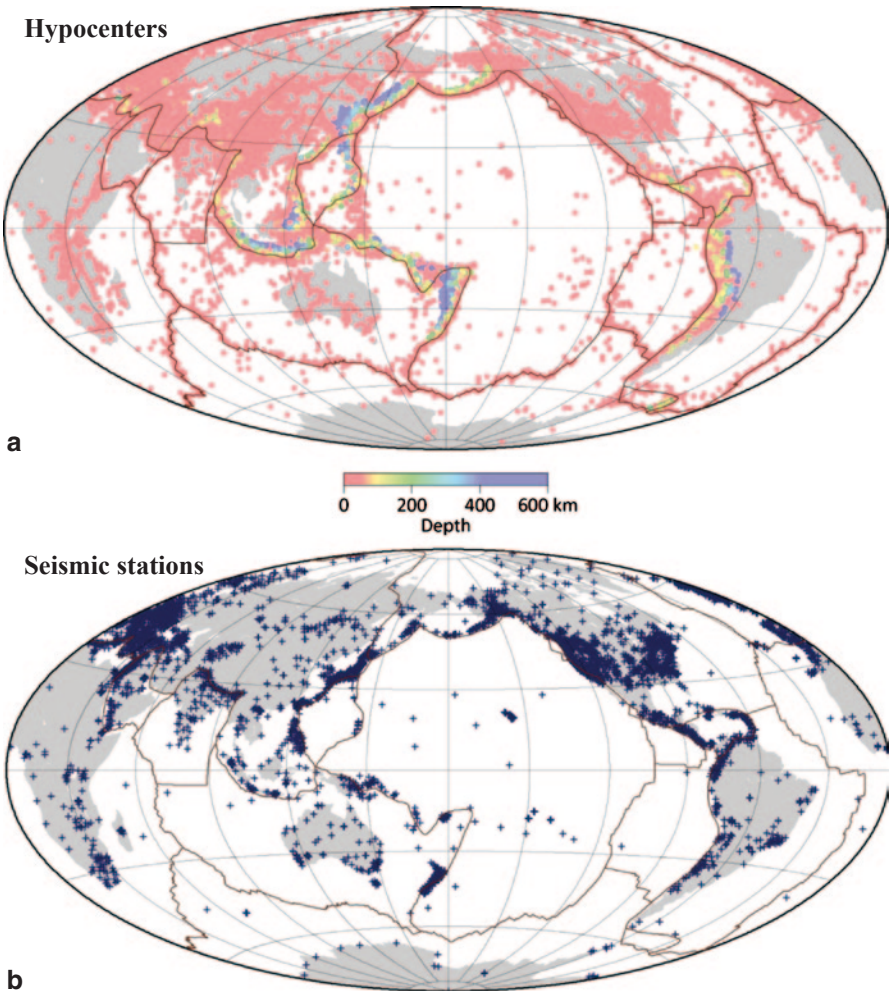

Fig. 1.7 Distribution of earthquakes (**a**) and seismic stations (**b**) which were used for global tomographic inversion by Zhao et al. (2013). The colors in (**a**) denote focal depths. The color scale is shown below (**a**). The *purple lines* denote major plate boundaries

wave tomography for studying the upper mantle structure beneath oceanic regions because there are fewer ocean-bottom-seismometer (OBS) stations. Because of the sparse and uneven distribution of global seismic networks, as well as natural earthquakes (Fig. 1.7), global tomographic models still have a lower resolution (>100 to a few hundred kilometers), but global models contain information on the deep Earth structure. In contrast, local and regional tomographic models for some areas, such as Japan and California, have a much higher resolution (20–30 km), thanks to the dense coverage of seismic stations and the high level of seismicity, but these local tomography models are limited to the crust and/or the upper mantle (e.g., Zhao 2009, 2012).

LET (Fig. 1.5a) and TET (Fig. 1.5b) are the two most widely-used methods employed in local and regional tomographic studies, as introduced in the following chapters of this book. The two methods have inherent advantages and drawbacks (Zhao 2009). LET can determine the shallow structure of an area to a depth above which earthquakes occur or diving rays propagate, but cannot determine the deeper structure. For example, under the Japan Islands, earthquakes occur mainly in the upper crust and in the subducting Pacific and Philippine Sea slabs, and thus we can determine the 3-D velocity structure of the crust, mantle wedge and the upper portion of the subducting slabs, but we cannot determine the mantle structure below the Pacific slab (Fig. 1.6a). In contrast, TET can determine the deep structure of an area (the maximum modeling depth is about 1.5 times the aperture of the seismic array used), but usually cannot determine well the shallow structure, because teleseismic rays travel in a sub-vertical direction and do not crisscross well in the crust. To resolve this problem, local-earthquake arrival times and teleseismic relative residuals can be used jointly (e.g., Zhao et al. 1994) (Fig. 1.6b). This joint inversion approach preserves the advantages of LET and TET, and overcomes their drawbacks. Moreover, the horizontally propagating local rays and vertically traveling teleseismic rays crisscross well in the crust and the upper (or uppermost) mantle, and consequently, the tomography resolution there can be greatly improved (Fig. 1.6b).

1.3 Multiscale Seismic Tomography

Structural heterogeneities in the Earth's interior exist at various scales, which are associated with earthquakes, volcanic eruptions and mountain building near the Earth's surface and convective circulations in the deep mantle. The scales of these heterogeneities range from meters, such as those associated with earthquake fault zones, to thousands of kilometers, such as convecting flows in the mantle. These structural heterogeneities have been investigated by different researchers according to their own interests. The target of research determines the method and approach adopted. Local-scale tomography has been used to study small-scale structures of the crust and uppermost mantle, such as earthquake fault zones and magma chambers under active volcanoes, by workers who are interested in the causal mechanism of earthquakes and volcanic eruptions as well as their predictions; in particular, those who are living in earthquake and volcano countries such as Japan, China and western USA. Regional tomography has been used to study the crust and upper mantle structure beneath subduction zones, collision zones, mountain building, hotspots and mantle plumes, etc. Large-scale regional tomography and global tomography have been used to study the structure and processes of the major elements of plate tectonics and geodynamics, such as the lithosphere, asthenosphere, the mantle transition zone, mantle convection, the D" layer in the lowermost mantle, the fate of subducting slabs, and the origin of mantle plumes, etc.

Ideally, there is no need to divide seismic tomography into different kinds if a perfect high-resolution tomography model could be determined for the entire

Earth's interior. However, the fact is that earthquakes exhibit a very non-uniform distribution in the world, most of which occur in plate boundary regions, in particular, subduction zones, while the seismicity is very low in stable continental regions (Fig. 1.7a). The distribution of existing seismic stations on Earth is even more heterogeneous (Fig. 1.7b). Most of the stations are located in the continental regions, in particular, in developed countries such as Japan, USA and Western Europe, while there are few stations in the broad oceanic regions and the developing countries in Africa, South America and Southeast Asia. There are actually data recorded by many local seismic networks or portable stations, but most of these data are still not accessible to the public, due to cultural and political factors. Therefore, it is really difficult to determine a "perfect" high-resolution tomography of the Earth's interior as, for example, the medical CT-scan. Even the updated global tomography model has large variations in its spatial resolution, both in a lateral direction and in depth. The resolution changes from tens of kilometers in subduction zones to ~1000 km in the mantle beneath the oceans in the southern hemisphere (e.g., Zhao et al. 2013). That is why, so far, multiscale (local, regional, and global) tomographic studies have been made to image the structural heterogeneities of various scales and in different portions of the Earth's interior.

The tomographic images shown in the following chapters of this book will be seen to have different resolution scales and different amplitudes of velocity anomalies, which reflect the current status of multiscale tomographic studies. The resolution scale of a tomographic image is determined by the density of ray path coverage and the degree of ray crisscrossing, which are controlled by the distribution of seismic stations and earthquakes used (Zhao 2012). The amplitude of velocity anomalies retrieved by seismic tomography is affected by damping and smoothing regularizations that are required for stabilizing tomographic inversions because of the uneven distribution of seismic rays in the crust and mantle under a study area (Zhao 2009). Thus, the amplitude of velocity anomalies in the real Earth is hard to recover fully and the degree of recovery depends on the scale of the study area as well as the density and homogeneity of the ray path coverage. In local-scale tomography, seismic stations and earthquakes have a relatively uniform distribution, and so weak damping and smoothing are applied, leading to a better recovery of the amplitude of velocity anomalies amounting to 6–10 % (e.g., Zhao 2012). In contrast, strong damping and smoothing have to be applied in global and large-scale regional tomography because of the very uneven distribution of seismic stations and earthquakes (Fig. 1.7), which leads to a small amplitude of velocity anomalies (1–2 %) (e.g., Wei et al. 2012; Zhao et al. 2013). Therefore, the amplitudes of velocity anomalies in a tomographic image should be interpreted carefully by considering the strength of damping and smoothing applied in the inversion as well as the scale of the tomographic model.

The term *multiscale seismic tomography* has been used by different authors with different meanings (e.g., Chiao and Kuo 2001; Chevrot and Zhao 2007; Zhao 2007, 2009; Pesicek et al. 2014). In some studies, it means a multiscale scheme of model parameterization adopted in a tomographic inversion (e.g., Zhou 1996; Chiao and Kuo 2001; Chevrot and Zhao 2007; Pesicek et al. 2014). In Zhao (2007, 2009) and

this book, it simply means local, regional and global tomographic studies made so far by many different authors to image the structural heterogeneities of various scales in the interior of the Earth and Moon, as mentioned in the last section.

1.4 Interpretation of Tomography

Many tomographic images of different tectonic settings are shown in the following chapters of this book, the interpretations of which are essential to understand the structure and dynamics of the Earth's interior. Here, we introduce and discuss the general way to interpret the obtained tomographic results, following Zhao (2009).

Seismic velocity and attenuation anomalies imaged by seismic tomography may reflect thermal anomalies, compositional variations (including volatiles), and the presence of partial melt, cracks, and/or anisotropy. Hence, the interpretation of a tomographic image under a region is usually not easy and conclusive. It is important to be aware that, first we need to know clearly the resolution scale of the obtained tomographic image and whether a feature of interest is robust or not. Various synthetic resolution tests should be conducted to examine the reliability of the feature. Only after the feature concerned is confirmed to be reliable, can one proceed to interpret it.

To interpret tomographic images of the crust and upper mantle beneath a region, one needs to first become familiar with the tectonic background of the region; for example, is the region a subduction zone, collision zone, hotspot area, or a stable craton? All the available geological, geophysical and geochemical findings of the region should be examined. All the related information on the study region is required, such as seismicity, the He^3/He^4 ratio, electro-magnetic soundings, gravity, as well as the surface geological features such as topography, sedimentary basins, mountains, active volcanoes, and active faults, etc. Anomalies of low-velocity (low-V), high-attenuation (low-Q), high Poisson's ratio and high electric conductivity under active volcanoes may reflect magma-chamber related high-temperature anomalies, while those in active fault zones and large earthquake source areas could be related to fault gauges, cracks, and/or crustal fluids. Sedimentary basins and mountain ranges will show up as low and high velocity anomalies, respectively, in the shallow to middle crust.

As is shown in Chap. 3, subducting slabs in the upper mantle with intermediate-depth and deep earthquakes are generally imaged as a higher seismic velocity (high-V) than that of the surrounding mantle. If the resolution of a tomographic image is high enough, then the subducted oceanic crust may be detected which would be a thin (< 10 km) low-V layer at the top of the high-V subducting slab. In some cases, anomalies of lower velocity are revealed within a subducting slab, which may be associated with large intra-slab earthquakes, slab dehydration, and/or fracture zones in the slab (e.g., Mishra and Zhao 2004). Some studies have revealed a thin low-V feature in the Pacific slab at the mantle transition zone depth (420–670 km), which may reflect the metastable olivine wedge associated with the generation of

deep-focus earthquakes (e.g., Jiang et al. 2008; Jiang and Zhao 2011). However, low-V zones within the subducting slab are still not imaged reliably by tomography, and their causes are still poorly understood. High-resolution tomography is required to image the fine structures within the subducting slabs.

In subduction zones, low-V and low-Q anomalies in the crust and upper mantle wedge under the volcanic front and back-arc areas reflect high-temperature anomalies due to the existence of arc and back-arc magma, which are caused by the joint effects of fluids from shallow and deep slab dehydration and corner flow in the mantle wedge, which is a well-established feature (e.g., Zhao 2009, 2012). In the fore-arc area, there is no volcano and the surface heat flow is lower, hence hot magma should not exist there. However, low-V, low-Q and anisotropic bodies are often revealed in the mantle wedge under the fore-arc, especially above the young and warm slabs, which reflect serpentinization associated with fluids from slab dehydration (Hyndman and Peacock 2003; Liu et al. 2013).

Some high-resolution crustal tomography has detected low-V and high-Poisson's ratio anomalies in the source areas of large crustal earthquakes, which may reflect aqueous fluids (e.g., Zhao et al. 1996, 2010; Tong et al. 2012). However, it is difficult to clarify where the fluids come from. The He^3/He^4 ratio is a powerful geochemical indicator for the origin of crustal fluids. It is found that the He^3/He^4 ratio is higher in the large earthquake source areas in Japan, suggesting that the fluids come from the dehydration of the subducting slabs (e.g., Horiguchi 2008; Zhao et al. 2002, 2010).

Collision zones, such as Himalaya and Taiwan, exhibit complex tomographic images (e.g., Wang et al. 2006; Zhang et al. 2012). Continuous or intermittent pieces of descending continental or oceanic lithosphere often appear under the collision zones, and they exhibit high seismic velocity. Low-V columns are often imaged in the upper mantle under hotspot volcanoes, which represent high-temperature upwelling flow (or plume) feeding the hotspots (e.g., Gupta et al. 2009; Liu and Zhao 2014). However, the origin and depth extent of the low-V zones are still not very clear because the aperture of the seismic arrays in the hotspot areas is usually not large enough to image the lower mantle structure beneath the hotspots. Low-V zones are generally imaged in the upper mantle under the active rift zones, which reflect the hot mantle upwelling flow (e.g., Zhao et al. 2006). Similar to the hotspot areas, however, the depth and origin of the upwelling causing the active rifting are still a matter of debate.

High-V anomalies are imaged in the upper mantle down to 200–300 km depth under the stable continental regions (cratons), which represent the thick and old cratonic lithosphere. Low-V anomalies and sometimes hotspot volcanoes are visible around the cratons, which may be caused the small-scale convection in the upper mantle associated with the (sudden) change in the thickness of the lithosphere from a craton to the surrounding regions (e.g., King and Ritsema 2000). Some low-V and high-V anomalies are revealed in the asthenosphere and even in the mantle transition zone under the continental orogenic belts and the reactivated craton (such as the North China Craton) (e.g., Tian and Zhao 2011, 2013; Wang et al. 2014). The

high-V anomalies could be due to the detached pieces of the continental lithosphere, whereas the low-V zones may reflect upwelling asthenospheric materials.

For interpreting the tomographic images of the mantle transition zone and lower mantle, the surface geological features mentioned above are less useful, and we need information obtained from other seismological methods (such as receiver functions and waveform modeling) as well as the findings of mineral physics and the numerical modeling of mantle convection. Teleseismic receiver functions and waveform modeling of various seismic waves can be used to estimate the depth variations of the 410- and 670-km discontinuities. According to mineral physics studies, if a cold (high-V) anomaly such as a subducting slab exists in and around the mantle transition zone, then the 410-km discontinuity would be elevated while the 670-km discontinuity will be depressed, resulting in a thicker mantle transition zone (e.g., Helffrich 2000). On the contrary, if a warm (low-V) anomaly like a mantle plume exists in and around the mantle transition zone, the 410-km discontinuity would become deeper while the 670-km discontinuity will become shallower, resulting in a thinner transition zone. This relationship between the transition zone thickness and slab/plume is useful for the interpretation of tomographic results. Early studies tended to attribute the velocity anomalies in the lower mantle to temperature variations alone, while recent studies suggest that the velocity anomalies in the lower mantle could be caused by both temperature and compositional variations.

1.5 The Scope of this Book

So far three books on seismic tomography have been published. The first book, edited by Nolet (1987), comprised 12 chapters written by 17 authors summarizing the early developments of seismic tomography and its applications in exploration geophysics and global seismology. The second book, edited by Iyer and Hirahara (1993), comprised 29 chapters contributed by 49 authors. Except for a few chapters which focused on the technical aspects of seismic tomography, most chapters in Iyer and Hirahara (1993) mainly introduced applications of seismic tomography to various tectonic settings, from local to global scales. The third book, written by Nolet (2008), focused on the theoretical aspects of seismic tomography and contained many mathematical equations.

The present book describes the state-of-the-art in seismic tomography, with an emphasis on the new findings obtained by applying tomographic methods in local, regional and global scales for understanding the causal mechanism of earthquakes and seismotectonics, the 3-D crustal and upper mantle structure and origin of active arc volcanoes and intraplate volcanoes including hotspots, the heterogeneous structure of subduction zones and the fate of subducting slabs, the origin of mantle plumes, mantle convection, and deep Earth dynamics, as well as the first lunar tomography. All the tomographic images in this book are shown in color, which are clearly visible and easy to understand. In contrast, no color figures were included

in the above-mentioned three books. This book is suitable for undergraduate and graduate students, researchers and professionals in Earth and planetary sciences, who need to broaden their horizons about seismotectonics, volcanism, and the interior structure and dynamics of the Earth and Moon.

In Chap. 2, we introduce the main tomographic methods which are widely used to determine 3-D seismic velocity, attenuation and anisotropy structures of the Earth's interior. The fundamental mathematical equations of these methods are presented for a better understanding of the principles of seismic tomography.

In Chap. 3, we introduce tomographic studies of subduction zones and new insights into arc magmatism, seismotectonics and subduction dynamics. Seismic velocity and attenuation tomography has clearly revealed subducting slabs as high-V and high-Q zones where intermediate-depth and deep earthquakes take place. In the crust and upper-mantle wedge, low-V and low-Q anomalies are revealed beneath arc and back-arc volcanoes, and they extend to a deeper portion of the mantle wedge, indicating that the low-V and low-Q anomalies reflect source zones of arc magmatism and volcanism which are caused by the joint effects of corner flow in the mantle wedge and fluids from slab dehydration. P-wave anisotropy tomography and shear-wave splitting measurements have provided important constraints on mantle flows and dynamics in subduction zones.

In Chap. 4, we introduce high-resolution tomographic studies of source zones of large crustal earthquakes, megathrust earthquakes, intraslab earthquakes, and deep earthquakes. It is found that structural heterogeneities in the crust and upper mantle strongly affect or control the generation of large and small earthquakes in various tectonic settings. In particular, fluids and magmas play an important role in the nucleation of large earthquakes. *Fault*, *Force* (stress) and *Fluid* (3F) are three key elements in earthquake generation. These studies indicate that seismic tomography is an important and effective tool for studying earthquakes and seismotectonics.

In Chap. 5, we introduce tomographic studies of hotspots and mantle plumes. Plume-like, continuous low-V anomalies are revealed in the mantle beneath some well-known hotspots (e.g., Hawaii, Tahiti, Louisville, Iceland, Cape Verde, Reunion, Kerguelen, Amsterdam, Afar, Eifel, Hainan, Yellowstone, and Cobb), suggesting that whole-mantle plumes originating from the core-mantle boundary (CMB) may feed those hotspots. These plumes exhibit tilted images, suggesting that plumes are not fixed in the mantle but can be deflected by the mantle flow. Upper-mantle plumes seem to exist beneath Cameroon, Easter, Azores, Vema, East Australia and Erebus hotspots. A mid-mantle plume may exist under the San Felix hotspot. Active intraplate volcanoes in East Asia (e.g., Changbai, Ulleung, Jeju, and Tengchong) are caused by hot and wet upwelling flows in the big mantle wedge above the stagnant slab in the mantle transition zone. The complex images under hotspots reflect strong lateral variations in temperature, viscosity and composition of the mantle, which control the generation and ascent of mantle plumes and the flow pattern of mantle convection.

In Chap. 6, we introduce tomographic studies of the East Asia region and new insights into plate deep subductions, continental seismotectonics, intraplate

magmatism, and mantle dynamics. The subducting Pacific slab is stagnant in the mantle transition zone under the Korean Peninsula and East China, and a big mantle wedge (BMW) has formed above the stagnant slab. Hot and wet upwelling flows in the BMW have caused the intraplate volcanoes in NE Asia, lithospheric thinning and reactivation of the North China Craton, and large earthquakes in and around East China. Deep earthquakes in the Pacific slab may be related to a metastable olivine wedge in the slab. The deepest earthquakes (~600 km depth) under NE Asia may release more fluids preserved in the slab to the overlying BMW, contributing to the Changbai volcanism. The descending Indian plate beneath the Tibetan Plateau is clearly revealed. The Hainan volcano in South China is a hotspot fed by a deep mantle plume associated with plate deep subductions in the east and the west.

In Chap. 7, we introduce global tomography studies which shed new light on the deep structure and fate of subducting slabs and the origin of hotspots and mantle plumes, as well as deep Earth dynamics. It is found that ray paths of direct and reflected P-waves in a 3-D global velocity model deviate up to 100 km from those in a 1-D Earth model, and the differences in their travel times in the 1-D and 3-D velocity models amount to nearly 4.0 s, indicating the necessity of using a 3-D ray tracing technique to calculate ray paths and travel times precisely in global tomographic studies. Ten kinds of later phases transmitted and reflected in the mantle and core are used to conduct global tomographic inversions, and it is found that the later phase data can improve greatly the ray path coverage in the mantle and, hence, the resolution of mantle tomography. Whole-mantle heterogeneities outside the target volume of a regional tomography can cause significant changes (~0.2–0.4 s) to the observed relative travel-time residuals of a teleseismic event. The pattern of regional tomography remains the same even after correcting for the whole-mantle heterogeneity, but there are some changes in the amplitude of velocity anomalies in regional tomography. Hence, it is necessary to correct for mantle heterogeneity outside the target volume in order to obtain a better regional tomography.

In Chap. 8, we introduce seismic tomography of the Moon. P- and S-wave velocity tomography of the lunar crust and mantle under the near-side of the Moon has been obtained using moonquake arrival-time data recorded by the Apollo seismic network operated during 1969–1977 (Zhao et al. 2008, 2012). The results show that significant lateral heterogeneities may exist in the lunar interior. A correlation between S-wave tomography and the thorium abundance distribution is revealed. The area with a high thorium abundance exhibits a distinct low-V anomaly extending down to a depth of ~300 km below the Procellarum KREEP Terrane (PKT), which may reflect a thermal and compositional anomaly under the PKT. Similar to earthquakes, the distribution of deep moonquakes shows a correlation with the tomography in the deep lunar mantle, suggesting that structural heterogeneities in the lunar interior may affect the genesis of moonquakes. The presence of deep moonquakes and seismic-velocity heterogeneity in the mantle implies that the interior of the present Moon may still be thermally and dynamically active. Although the lunar tomography is an experimental work and the results are still preliminary, the indications are that tomographic imaging of the lunar interior is feasible.

References

Aki, K.: Impact of earthquake seismology on the geological community since the Benioff zone. Geol. Soc. Am. Bull. **100,** 625–629 (1988)

Aki, K., Lee, W.: Determination of three-dimensional velocity anomalies under a seismic array using first P arrival times from local earthquakes, 1. A homogeneous initial model. J. Geophys. Res. **81,** 4381–4399 (1976)

Aki, K., Christoffersson, A., Husebye, E.: Determination of the three-dimensional seismic structure of the lithosphere. J. Geophys. Res. **82,** 277–296 (1977)

Carlson, W.: Three-dimensional imaging of earth and planetary materials. Earth Planet. Sci. Lett. **249,** 133–147 (2006)

Cerveny, V.: Seismic Ray Theory, pp 713. Cambridge University Press (2001)

Chevrot, S., Zhao, L.: Multiscale finite-frequency Rayleigh wave tomography of the Kaapvaal craton. Geophys. J. Int. **169,** 201–215 (2007)

Chiao, L., Kuo, B.: Multiscale seismic tomography. Geophys. J. Int. **145,** 517–527 (2001)

Cnudde, V., Boone, M.: High-resolution X-ray computed tomography in geosciences: a review of the current technology and applications. Earth Sci. Rev. **123,** 1–17 (2013)

Duvall, T., Jefferies, S., Harvey, J., Pomerantz, M.: Time-distance helioseismology. Nature **362,** 430–432 (1993)

Duvall, T., D'Silva, S., Jefferies, S., Harvey, J., Schou, J.: Downflows under sunspots detected by helioseismic tomography. Nature **379,** 235–237 (1996)

Dziewonski, A., Anderson, D.: Seismic tomography of the Earth's interior. Am. Sci. **72,** 483–494 (1984)

Dziewonski, A., Hager, B., O'Connell, R.: Large-scale heterogeneities in the lower mantle. J. Geophys. Res. **82,** 239–255 (1977)

Fichtner, A., Trampert, J., Cupillard, P. et al.: Multiscale full waveform inversion. Geophys. J. Int. **194,** 534–556 (2013)

Gupta, S., Zhao, D., Rai, S.: Seismic imaging of the upper mantle under the Erebus hotspot in Antarctica. Gondwana Res. **16,** 109–118 (2009)

Helffrich, G., 2000. Topography of the transition zone seismic discontinuities. Rev. Geophys. **38,** 141–158.

Herman, G.: Image Reconstruction from Projections: the Fundamentals of Computerized Tomography. Academic Press, San Diego (1980)

Horiguchi, S.: Spatial distribution of He^3/He^4 ratio in Northeast Japan. Master's thesis, pp. 123. Tohoku University (2008)

Howell, B.F.: An Introduction to Seismological Research: History and Development, pp 193. Cambridge University Press (1990)

Hyndman, R., Peacock, S.: Serpentinization of the forearc mantle. Earth Planet. Sci. Lett. **212,** 417–432 (2003)

Iyer, H.: Seismic tomography. In James D. (ed.) The Encyclopedia of Solid Earth Geophysics, pp. 1133–1151. Van Nostrand Reinhold, New York (1989)

Iyer, H., Hirahara, K. (eds.): Seismic Tomography: theory and Practice, pp. 842. Chapman & Hall, (1993)

Jiang, G., Zhao, D.: Metastable olivine wedge in the subducting Pacific slab and its relation to deep earthquakes. J. Asian Earth Sci. **42,** 1411–1423 (2011)

Jiang, G., Zhao, D., Zhang, G.: Seismic evidence for a metastable olivine wedge in the subducting Pacific slab under Japan Sea. Earth Planet. Sci. Lett. **270,** 300–307 (2008)

King, S., Ritsema, J.: African hot spot volcanism: small-scale convection in the upper mantle beneath cratons. Science **290,** 1137–1140 (2000)

Lei, J., Zhao, D.: Global P-wave tomography: on the effect of various mantle and core phases. Phys. Earth Planet. Inter. **154,** 44–69 (2006)

Liu, X., Zhao, D.: Seismic evidence for a mantle plume beneath the Cape Verde hotspot. Int. Geol. Rev. **56,** 1213–1225 (2014)

Liu, X., Zhao, D., Li, S.: Seismic imaging of the Southwest Japan arc from the Nankai trough to the Japan Sea. Phys. Earth Planet. Inter. **216,** 59–73 (2013)
Mishra, O.P., Zhao, D.: Seismic evidence for dehydration embrittlement of the subducting Pacific slab. Geophys. Res. Lett. **31,** L09610 (2004)
Nakanishi, I., Anderson, D.: World-wide distribution of group velocity of mantle Rayleigh waves as determined by spherical harmonic inversion. Bull. Seismol. Soc. Am. **72,** 1185–1194 (1982)
Nolet, G. (ed.): Seismic Tomography: With Applications in Global Seismology and Exploration Geophysics, pp. 386. D. Reidel Publishing Company, (1987)
Nolet, G.: A Breviary of Seismic Tomography: Imaging the Interior of the Earth and Sun, pp. 344. Cambridge University Press, (2008)
Pesicek, J., Zhang, H., Thurber, C.: Multiscale seismic tomography and earthquake relocation incorporating differential time data: application to the Maule subduction zone, Chile. Bull. Seismol. Soc. Am. **104,** 1037–1044 (2014)
Tian, Y., Zhao, D.: Destruction mechanism of the North China Craton: insight from P and S wave mantle tomography. J. Asian Earth Sci. **42,** 1132–1145 (2011)
Tian, Y., Zhao, D.: Reactivation and mantle dynamics of North China Craton: insight from P-wave anisotropy tomography. Geophys. J. Int. **195,** 1796–1810 (2013)
Tong, P., Zhao, D., Yang, D.: Tomography of the 2011 Iwaki earthquake (M 7.0) and Fukushima nuclear power plant area. Solid Earth **3,** 43–51 (2012)
Wang, Z., Zhao, D., Wang, J., Kao, H.: Tomographic evidence for the Eurasian lithosphere subducting beneath South Taiwan. Geophys. Res. Lett. **33,** L18306 (2006)
Wang, J., Wu, H., Zhao, D.: P wave radial anisotropy tomography of the upper mantle beneath the North China Craton. Geochem. Geophys. Geosyst. **15,** 2195–2210 (2014)
Wei, W., Xu, J., Zhao, D., Shi, Y.: East Asia mantle tomography: new insight into plate subduction and intraplate volcanism. J. Asian Earth Sci. **60,** 88–103 (2012)
Woodhouse, J., Dziewonski, A.: Mapping the upper mantle: three-dimensional modeling of earth structure by inversion of seismic waveforms. J. Geophys. Res. **89,** 5953–5986 (1984)
Zhang, H., Zhao, D., Zhao, J., Xu, Q.: Convergence of the Indian and Eurasian plates under eastern Tibet revealed by seismic tomography. Geochem. Geophys. Geosyst. **13,** Q06W14 (2012)
Zhou, H.: A high-resolution P wave model for the top 1200 km of the mantle. J. Geophys. Res. **101,** 27791–27810 (1996)
Zhao, D.: Multiscale seismic tomography of mantle plumes and subducting slabs. In: Yuen, D., Maruyama, S., Karato, S., Windley, B. (eds.) Superplumes: Beyond Plate Tectonics, pp. 7–30. Springer, (2007)
Zhao, D.: Multiscale seismic tomography and mantle dynamics. Gondwana Res. **15,** 297–323 (2009)
Zhao, D.: Tomography and dynamics of Western-Pacific subduction zones. Monogr. Environ. Earth Planets **1,** 1–70 (2012)
Zhao, D., Kayal, J.R.: Impact of seismic tomography on earth sciences. Cur. Sci. **79,** 1208–1214 (2000)
Zhao, D., Hasegawa, A., Kanamori, H.: Deep structure of Japan subduction zone as derived from local, regional, and teleseismic events. J. Geophys. Res. **99,** 22313–22329 (1994)
Zhao, D., Kanamori, H., Negishi, H., Wiens, D.: Tomography of the source area of the 1995 Kobe earthquake: evidence for fluids at the hypocenter? Science **274,** 1891–1894 (1996)
Zhao, D., Mishra, O.P., Sanda, R.: Influence of fluids and magma on earthquakes: seismological evidence. Phys. Earth Planet. Inter. **132,** 249–267 (2002)
Zhao, D., Lei, J., Inoue, T., Yamada, A., Gao, S.: Deep structure and origin of the Baikal rift zone. Earth Planet. Sci. Lett. **243,** 681–691 (2006)
Zhao, D., Lei, J., Liu, L.: Seismic tomography of the Moon. Chinese Sci. Bull. **53,** 3897–3907 (2008)
Zhao, D., Santosh, M., Yamada, A.: Dissecting large earthquakes in Japan: role of arc magma and fluids. Island Arc **19,** 4–16 (2010)

Zhao, J.W., Kosovichev, A., Ilonidis, S.: Toward waveform heliotomography: observing interactions of helioseismic waves with a sunspot. Solar Physics **268,** 429–442 (2011)
Zhao, D., Arai, T., Liu, L., Ohtani, E.: Seismic tomography and geochemical evidence for lunar mantle heterogeneity: comparing with Earth. Global Planet. Change **90,** 29–36 (2012)
Zhao, D., Yamamoto, Y., Yanada, T.: Global mantle heterogeneity and its influence on teleseismic regional tomography. Gondwana Res. **23,** 595–616 (2013)

Chapter 2
Methodology of Seismic Tomography

Abstract In this chapter, we introduce the tomographic methods which are widely used to study three-dimensional (3-D) seismic velocity, attenuation and anisotropy structures of the Earth's interior. The fundamental mathematical equations of these methods are presented for a better understanding of the principles of seismic tomography.

Keywords Seismic tomography · Model parameterization · Ray tracing · Inversion · Resolution · Damping parameter

From seismological observations, such as P- and S-wave arrival times, amplitudes, and waveforms, basically three kinds of physical parameters can be determined to characterize the seismological structure of the Earth's interior. These parameters are seismic velocity, attenuation, and anisotropy. Applying tomographic methods to the seismological data, we can estimate the three-dimensional (3-D) distribution of these parameters, i.e., seismic velocity tomography, attenuation tomography, and anisotropy tomography. In this chapter, we introduce the general approaches to conduct the three kinds of tomographic inversions.

In general, a study of seismic tomography includes the following operations: (1) Modeling the Earth's interior structure, i.e., model parameterization; (2) Forward modeling, such as ray tracing in travel-time tomography, earthquake relocation, and the construction of observation equations; (3) Inversion, i.e., solving the large system of observation equations; and (4) Resolution and error analysis, i.e., evaluating the resolution and uncertainty of the obtained tomographic image.

2.1 Seismic Velocity Tomography

Since the advent of seismology, P- and S-wave velocities (Vp, Vs) have been the primary physical parameters to characterize the Earth's structure because they are determined mainly from P- and S-wave arrival-time data which can be measured in high quality and great quantity by the routine processing of seismic networks deployed in many regions. Hence, earthquake arrival times have been the most

D. Zhao, *Multiscale Seismic Tomography,* Springer Geophysics,
DOI 10.1007/978-4-431-55360-1_2

abundant seismological data, and seismic tomography methods have been mainly applied to the arrival-time data to study the 3-D velocity structure of the Earth.

2.1.1 Model Parameterization

In the past four decades, many different approaches have been adopted to tackle the problem of imaging the Earth's interior structure. The major difference between these approaches is in the expression of the Earth's 3-D structure. Aki and Lee (1976) and Aki et al. (1977) used a number of constant-velocity blocks in three-dimensions (Fig. 2.1a); Chou and Booker (1979) adopted a velocity model with variably-sized ideal averaging volumes; Spencer and Gubbins (1980) used a 3-D analytic function defined by a small number of parameters for a velocity model; Horiuchi et al. (1982a, b) chose to use constant-velocity layers with undulating layer boundaries expressed by a power series of latitude and longitude; Thurber (1983)

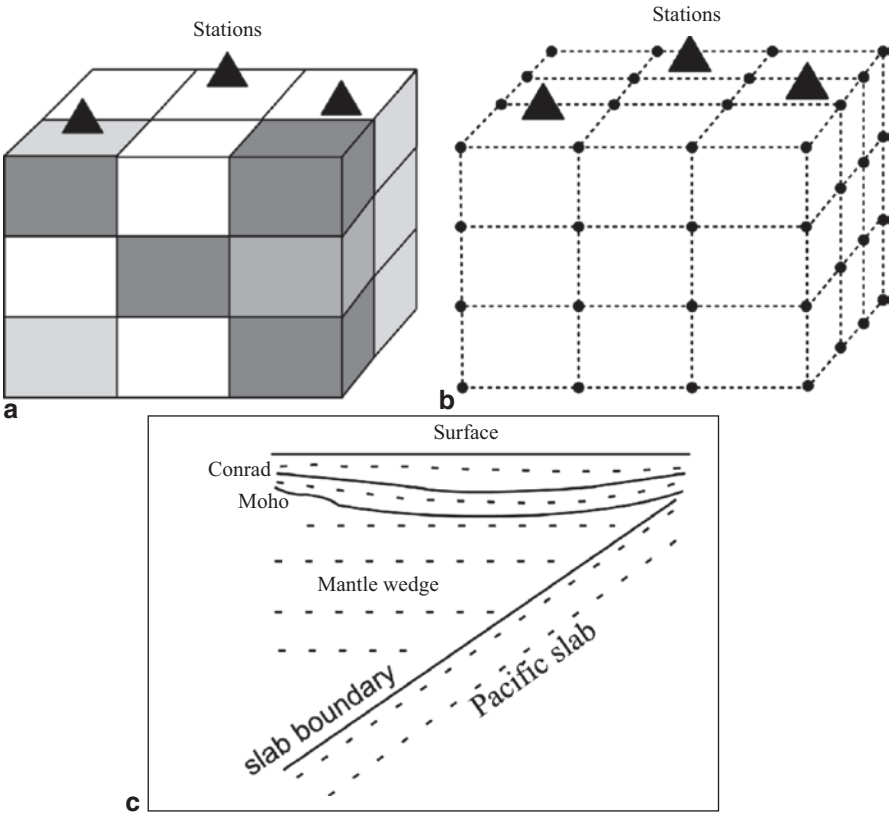

Fig. 2.1 Three ways to express the three-dimensional Earth structure (Zhao 2009). **a** The *block* approach; **b** the *grid* approach; and **c** the *boundary-grid* approach

used a 3-D grid (Fig. 2.1b); and Dziewonski (1984) adopted spherical harmonic expansions. Each of these approaches has pros and cons (for detailed reviews, see Thurber and Aki 1987; Nolet 1987, 2008; Hirahara 1990; Iyer and Hirahara 1993; Zhao 2001a, 2012).

Zhao (1991) and Zhao et al. (1992) adopted a *boundary-grid approach* to express the 3-D Earth's structure in their studies of the Japan subduction zone (Fig. 2.1c). They considered a velocity model which contains several complicated-shaped velocity discontinuities and the velocity changing in three-dimensions everywhere in the model. There are several reasons for their taking this approach. The first is that detailed studies of reflected and converted waves, as well as the first P- and S-waves, revealed the existence of the Conrad and Moho discontinuities and the upper boundary of the subducting Pacific slab beneath NE Japan (Fig. 2.1c), and the three discontinuities exhibit significant lateral depth variations (see the review by Zhao 2012). All the previous tomographic studies prior to 1990 (e.g., Aki and Lee 1976; Thurber 1983) could not handle the complex-shaped velocity discontinuities in the study area. The second reason is that clear later phases (i.e., reflected and converted waves) associated with the three discontinuities were detected in the seismograms of local crustal earthquakes and intermediate-depth earthquakes in the subducting Pacific slab (see Zhao 2012 for the detailed review). These later-phase data contain important information on the Earth's structure, in particular, in and around velocity discontinuities, hence they should be used in tomographic inversion so that local earthquakes can be better located and a better 3-D velocity model can be obtained. For this purpose, the three velocity discontinuities (i.e., the Conrad, the Moho, and the slab upper boundary) should be introduced into the 3-D velocity model. The third reason is that theoretical travel times and ray paths can be calculated much more accurately when the three discontinuities are considered in the model (Zhao 1991). Because the Pacific slab under the Japan Islands is thick (~90 km) and exhibits a higher velocity (4–6% for Vp and 6–10% for Vs) than the surrounding mantle, the slab can deviate the ray paths and travel times significantly. Introducing the Pacific slab into the model can greatly reduce the degree of non-linearity of the tomographic problem, because a better starting velocity model is adopted which is much closer to the true Earth's structure than a simple 1-D velocity model for the subduction zone. The fourth reason is that very small blocks, or grid intervals, are required to express the lateral undulations of the three discontinuities, which are impossible to realize in the actual tomographic inversion, because the available seismic stations and earthquakes are not distributed densely and uniformly enough to allow the use of small blocks, or a grid, for the tomographic inversion. Therefore, it was, and still is, the best choice to take into account the three discontinuities and the Pacific slab in the starting velocity model for the tomographic inversion (e.g., Zhao et al. 1992, 2012; Nakajima et al. 2005; Wagner et al. 2005; Huang et al. 2011a; Tian and Zhao 2012; Liu et al. 2013, 2014).

The depth distribution of a velocity discontinuity is expressed in two ways (Zhao 1991; Zhao et al. 1992). One is a continuous function such as a power series of latitude and longitude, which was used by Horiuchi et al. (1982a, b) and Zhao et al.

(1990) for estimating the Conrad and Moho geometries beneath NE Japan. The depth to the *i*th discontinuity is expressed as:

$$H_i(\phi,\lambda) = \sum\nolimits_K C_{ik} H_{ik}(\phi,\lambda) = C_{i1} + C_{i2}\phi + C_{i3}\lambda + C_{i4}\phi^2 + \cdots, \tag{2.1}$$

where φ and λ are the latitude and longitude, respectively. C_{ik} ($i=1, 2, \ldots$ m; $k=1, 2, \ldots$ n) are coefficients, m is the number of the discontinuities, and n is the number of the coefficients of the power series. Another way to express a discontinuity geometry is to use a two-dimensional (2-D) grid. When the discontinuity depth at each grid node is determined, its depth at any point (φ, λ) in the study area can be determined using a simple interpolation function:

$$Hi(\phi,\lambda) = \sum_{j=1}^{2}\sum_{k=1}^{2} h(\phi_j,\lambda_k)\left[\left(1-\left|\frac{\phi-\phi_j}{\phi_2-\phi_1}\right|\right)\left(1-\left|\frac{\lambda-\lambda_k}{\lambda_2-\lambda_1}\right|\right)\right], \tag{2.2}$$

where ϕ_j and λ_k represent the coordinates of the four grid nodes surrounding that point. The right-hand side of Eq. (2.2) is a continuous function, being a product of linear functions in ϕ and λ.

To express 3-D velocity variations in the study area, Zhao (1991) and Zhao et al. (1992) set 3-D grid nets independently for each layer bounded by two adjacent discontinuities. For each 3-D grid net within one layer, meshes of grid nodes are densely set within the layer, except for the outermost nodes which are set far away from the internal nodes so that all the seismic rays in that layer are completely covered by the grid net. The velocity (or velocity perturbation from a starting model) at each grid node is taken to be an unknown parameter except for those at the outermost nodes. The velocities at the outermost nodes are just used for the interpolation of velocities outside the modelling space. The velocity (or velocity perturbation) at any point in the *m*th layer is expressed using the following interpolation function:

$$V_m(\phi,\lambda,h) = \sum_{i=1}^{2}\sum_{j=1}^{2}\sum_{k=1}^{2} V_m(\phi_i,\lambda_j,h_k)$$

$$\cdot\left[\left(1-\left|\frac{\phi-\phi_i}{\phi_2-\phi_1}\right|\right)\left(1-\left|\frac{\lambda-\lambda_j}{\lambda_2-\lambda_1}\right|\right)\left(1-\left|\frac{h-h_k}{h_2-h_1}\right|\right)\right], \tag{2.3}$$

where h is the depth from the Earth's surface, ϕ_i, λ_j, h_k represent the coordinates of the eight grid nodes surrounding the point (φ, λ, h), and $V_m(\phi_i, \lambda_j, h_k)$ is the velocity at a grid node in the *m*th layer.

If a sufficient number of data, in particular the later-phase data associated with the discontinuities, are available, the discontinuity geometries, i.e., the coefficients C_{ik} in Eq. (2.1) or $h(\phi_j, \lambda_k)$ in Eq. (2.2), can also be taken to be unknown parameters and determined by the tomographic inversion. To obtain a stable solution, however, Zhao (1991) and Zhao et al. (1992) only considered velocities at the 3-D grid nodes in each layer to be unknown parameters, taking into account the limited number and resolution of their data. The geometries of the Conrad, the Moho and the slab upper

boundary under NE Japan obtained by previous studies were adopted, and they were fixed in the inversion process (see Zhao 1991 for details).

2.1.2 Ray Tracing

In a tomographic study, it is very important to perform 3-D ray tracing (i.e., computing travel times and ray paths in a 3-D velocity model) precisely and efficiently, because usually a great number of arrival-time data are used and ray tracing is employed several times for each datum for earthquake relocation and iterative tomographic inversions. Several exact 3-D ray tracing algorithms have been developed (e.g., Jacob 1970; Wesson 1971; Julian and Gubbins 1977; Pereyra et al. 1980), which solve the ray equation exactly and therefore require many complicated computations (CPU). Hence, these algorithms are adaptable for some forward-modeling studies, but inadequate for tomographic problems. Thurber and Ellsworth (1980) and Horie (1980) proposed separately an inexpensive scheme for computing approximate travel times by determining a precise ray path in a 1-D local approximation to the 3-D velocity structure along each ray path. Thurber (1983) introduced another approximate ray tracing technique which adopts a circular arc connecting the hypocenter and receiver to represent the ray path. The two approximate techniques work well when the epicentral distance is <50 km, whereas if the epicentral distance is greater, both the travel time and ray path computed by the two approximate techniques deviate considerably from the true solution (Miyatake 1987). Hence the two techniques are not applicable to most tomographic studies, because the seismic networks used usually have apertures greater than 50 km.

A so-called *pseudo-bending* algorithm was developed by Um and Thurber (1987) for fast 3-D ray tracing, which is described briefly in the following. After some transformations, the ray equation can be written as:

$$-\frac{\mathrm{d}^2\vec{\mathrm{r}}}{\mathrm{ds}^2}=\frac{\left[(\mathrm{grad\ V})-\frac{\mathrm{dv}}{\mathrm{ds}}\cdot\frac{\mathrm{d}\vec{\mathrm{r}}}{\mathrm{ds}}\right]}{\mathrm{V}}, \tag{2.4}$$

where $\vec{\mathrm{r}}$ is the position vector along a ray, and s is the ray length. The first term of the right-hand side of Eq. (2.4) is a velocity gradient, whereas the second term is simply the component of a velocity gradient parallel to the ray vector. Thus, Eq. (2.4) states that the component of a velocity gradient normal to the ray vector is always antiparallel to the ray path curvature. This geometric interpretation of the ray equation was first given by Cerveny et al. (1977), which was used by Um and Thurber (1987) for performing 3-D ray tracing.

Consider three adjacent points along a ray path (Fig. 2.2). Temporarily, we assume that the two end points, X_{k-1} and X_{k+1}, are fixed. A new point X'_k, instead of the previous point X_k, is sought to minimize the travel time along the ray segment from X_{k-1} to X_{k+1}. Two variables are defined for finding the new point X'_k: the

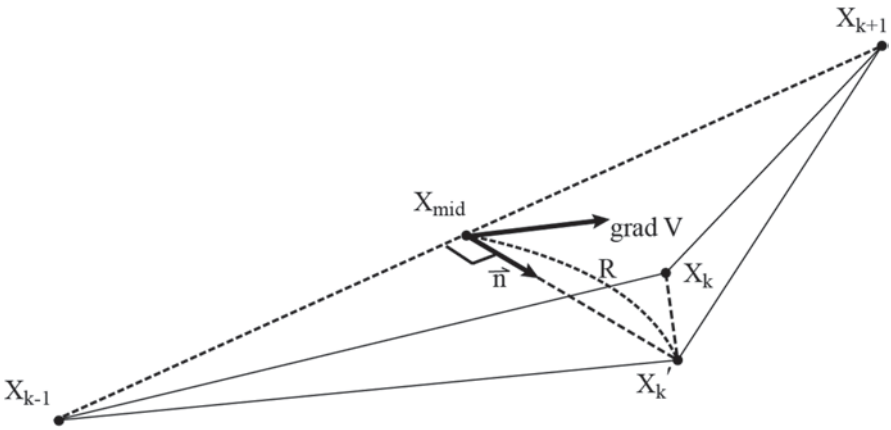

Fig. 2.2 Illustration of a three-point perturbation scheme adopted by the pseudo-bending method (Um and Thurber 1987). See the text for details

direction $\vec{n}$ and the amount R of offset from the mid-point X_{mid}. Because the local ray direction at X'_k, can be approximately expressed by the direction of the line connecting the two end points of the ray segment, X_{k-1} and X_{k-1}, the component of a velocity gradient normal to that direction defines the curvature direction, according to Eq. (2.4). Hence, this direction gives the correct offset direction at the point X'_k, which is as follows:

$$\vec{n} = (\text{grad } V) - \left[(\text{grad } V)\cdot(X_{k+1} - X_{k-1})\right]\cdot\frac{X_{k+1} - X_{k-1}}{\left|X_{k+1} - X_{k-1}\right|^2}. \tag{2.5}$$

We need to estimate the velocity at the new point X'_k, because it is unknown before the perturbation. Using a Taylor expansion of velocity at the mid-point, V_{mid}, the velocity at the new point V'_k is approximated by:

$$V'_k = V_{mid} + \left[\vec{n}\cdot(\text{grad } V)_{mid}\right]R, \tag{2.6}$$

where $(\text{grad } V)_{mid}$ is the velocity gradient at the mid-point X_{mid}. Thus, the amount of perturbation R along the direction $\vec{n}$ can be obtained by minimizing the travel time along the ray segment connecting the three points X_{k-1}, X'_k and X_{k+1}:

$$R = -\frac{CV_{mid} + 1}{4C\vec{n}\cdot(\text{grad } V)_{mid}} + \left[\frac{(CV_{mid} + 1)^2}{\left[4C\vec{n}\cdot(\text{grad } V)_{mid}\right]^2} + \frac{L^2}{2CV_{mid}}\right]^{\frac{1}{2}}, \tag{2.7}$$

where $L = \left|X_{k+1} - X_{k-1}\right|$ and $C = \left(\frac{1}{V_{k+1}} + \frac{1}{V_{k-1}}\right)/2$. For the derivation of Eq. (2.7), see Um and Thurber (1987).

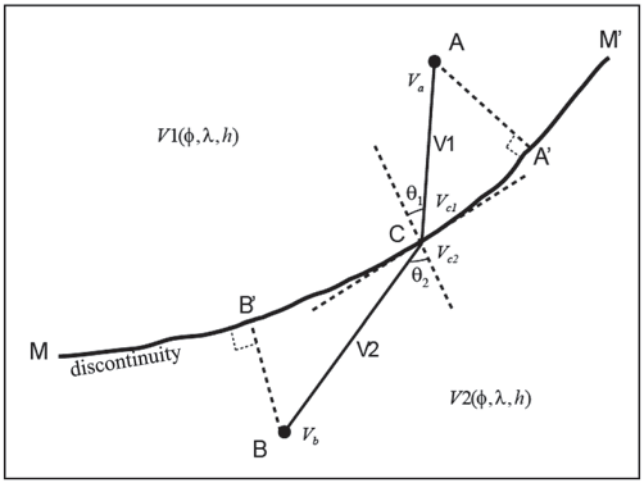

Fig. 2.3 Illustration of a scheme using Snell's law to find the intersection between a ray path A–B and a velocity discontinuity MM' (Zhao 1991; Zhao et al. 1992). See the text for details

This three-point perturbation scheme is successively extended to all the points along a ray path. The perturbation is iteratively performed until the travel time converges to a specified limit. Um and Thurber (1987) showed that the pseudo-bending scheme can find accurate travel times and ray paths in a 3-D velocity model much faster than the exact 3-D ray tracing techniques mentioned above, no matter how long the ray is. However, Um and Thurber (1987) adopted Cartesian coordinates, hence their code mainly works for a local tomography.

The pseudo-bending algorithm adopts a two-point bending approach but does not solve exactly the ray equation, and so it takes a short CPU time. However, its critical drawback is that it fails to work when a velocity discontinuity (e.g., the Moho) exists, and hence, it is applicable only to a continuous velocity model without any velocity discontinuity.

This shortcoming of the pseudo-bending scheme was overcome by Zhao (1991) and Zhao et al. (1992) in their tomographic studies of the Japan subduction zone. They proposed an algorithm that combines the pseudo-bending scheme and Snell's law to perform 3-D ray tracing in a general 3-D velocity model containing complex-shaped velocity discontinuities. Consider the case shown in Fig. 2.3. A complex-shaped velocity discontinuity, MM', exists, and the velocities on its two sides, $V_1(\phi, \lambda, h)$ and $V_2(\phi, \lambda, h)$, are continuous and change in three-dimensions. A and B are two points on different sides of MM'. Velocities at A and B are V_a and V_b, respectively. C is the intersection of a seismic ray AB and MM'. Velocities at C on the two sides of MM' are V_{c1} and V_{c2}, respectively. We take the arithmetic average V_1 of V_a and V_{c1}, and the arithmetic average V_2 of V_b and V_{c2}:

$$V_1 = \frac{V_a + V_{c1}}{2},$$
$$V_2 = \frac{V_b + V_{c2}}{2}, \tag{2.8}$$

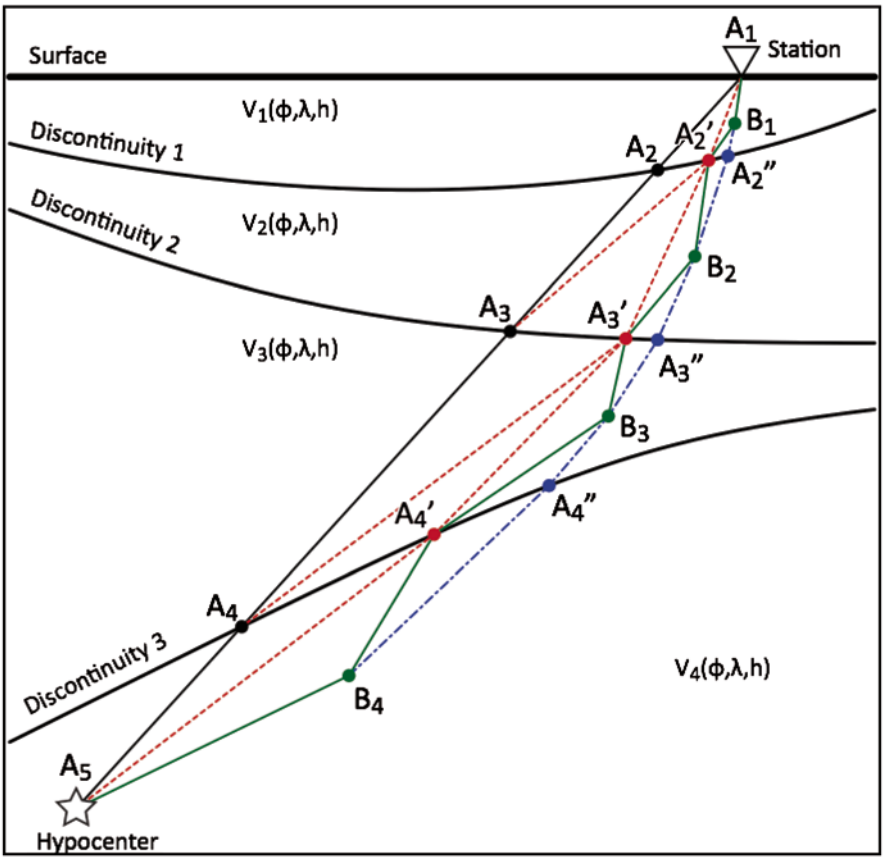

Fig. 2.4 Illustration of the 3-D ray tracing algorithm by Zhao (1991) and Zhao et al. (1992). See the text for details

to represent the mean velocities around AC and BC, respectively. This approximation is poor when A and B are far from MM', but when both A and B are close to MM' the approximation will be good enough. We then iteratively use a bisection method to find the accurate location of point C which satisfies Snell's law:

$$\frac{\sin\theta_1}{V_1} = \frac{\sin\theta_2}{V_2}. \tag{2.9}$$

Figure 2.4 shows schematically the ray tracing algorithm of Zhao (1991) and Zhao et al. (1992). For simplicity, we consider the case that three velocity discontinuities exist. The straight line A_1-A_5 connecting the station and the hypocenter is assumed to be an initial ray path. The intersections (A_2, A_3 and A_4, etc.) of the ray path with the discontinuities are called *discontinuous points* (DPs), whereas the points on the ray path between two adjacent discontinuities are called *continuous points* (CPs). The principle of the algorithm is that Snell's law is used to perturb the DPs as

described above (Fig. 2.3) and the pseudo-bending scheme is adopted to perturb the CPs (Fig. 2.2).

As shown in Fig. 2.4, we first use Snell's law to find new DPs A'_2 from A_1 and A_3, A'_3 from A'_2 and A_4, and A'4 from A'_3 and A_5. Next we use the pseudo-bending scheme to find the new CPs, viz. B_1 from A_1 and A'_2, B_2 from A'_2 and A'_3, B_3 from A'_3 and A'_4, and B_4 from A'_4 and A_5. Then, again using Snell's law, we find A''_2 from B_1 and B_2, A''_3 from B_2 and B_3, and A''_4 from B_3 and B_4, and so on. After a number of iterations the ray path converges gradually to its true location.

Zhao (1991) and Zhao et al. (1992) wrote their ray tracing code in spherical coordinates and tested the algorithm using various 3-D velocity models. They found that their code can always obtain sufficiently accurate ray paths and travel times and shorten the CPU time by one to two orders of magnitude as compared with the exact ray tracing programs. Later, Zhao (2001b, 2004) applied this 3-D ray tracing code to P, pP, PP, PcP and Pdiff phases for conducting whole-mantle tomographic inversions by considering lateral depth variations of the Moho, and the 410 and 670 km discontinuities, at a global scale (Mooney et al. 1998; Flanagen and Shearer 1998). It is found that ray paths in a 3-D global velocity model deviate considerably from those in the average 1-D model such as the iasp91 Earth model (Kennett and Engdahl 1991), and the changes in travel time and ray path amount to as much as 3.9 s and 77 km, respectively (for details, see Zhao and Lei 2004, and Chap. 7 of this book).

Several researchers have examined the algorithm of Zhao (1991) and Zhao et al. (1992) and confirmed that it is a very robust and efficient scheme for conducting ray tracing in general 3-D velocity models from local to global scales (e.g., Koketsu and Sekine 1998; Sadeghi et al. 1999; Ballard et al. 2009; Huang et al. 2013).

All the above-mentioned ray tracing methods are based on the ray theory of seismology, and they may have problems such as determining the global minimum travel-time path when multiple paths exist, and if the structure is very heterogeneous, longer CPU times and a more complex algorithm are required. To overcome these problems, some researchers have proposed wavefront-type methods (e.g., Vidale 1988, 1990; Podvin and Lecomte 1991; Coultrip 1993). In the wavefront approach, a travel-time field is constructed for the entire model space from the hypocenter, no matter how complex the structure is. This feature is an advantage of the wavefront approach, but is also its drawback. In practical applications, there are only a limited number of seismic stations in a study area. We need only travel times and ray paths from the hypocenter to the stations, and it is unnecessary to trace rays to other points in the model (Zhao 2001a). In addition, to achieve a higher accuracy, a denser 3-D grid is needed by the wavefront approach. Therefore, the larger the model is, the greater is the CPU time required.

Moser (1991) applied network theory to seismology and proposed a shortest-path method for ray tracing. Unlike in the wavefront method, Moser (1991) directly used paths between grid nodes to perform ray tracing. Although there are differences in technical details, the principles of the wavefront and the shortest-path methods are similar.

2.1.3 Inversion

Formulation of the Tomographic Problem Starting with the initial hypocenter parameters of a set of earthquakes (events), we estimate correction terms for the hypocentral and velocity structure parameters, in such a way that all the arrival-time data can be best explained in a least-squares sense. The observation equation for an arrival-time datum is written as:

$$\begin{aligned} \mathrm{T}_{ij}^{\mathrm{obs}} = \mathrm{T}_{ij}^{\mathrm{cal}} + \left(\frac{\partial \mathrm{T}}{\partial \phi}\right)_{ij} \Delta\phi_i + \left(\frac{\partial \mathrm{T}}{\partial \lambda}\right)_{ij} \Delta\lambda_i + \left(\frac{\partial \mathrm{T}}{\partial \mathrm{h}}\right)_{ij} \Delta \mathrm{h}_i + \Delta \mathrm{T}_{oi} \\ + \sum_{n=1}^{N} \frac{\partial \mathrm{T}}{\partial \mathrm{V}_n} \Delta \mathrm{V}_n + \mathrm{e}_{ij}, \end{aligned} \tag{2.10}$$

where: $\mathrm{T}_{ij}^{\mathrm{obs}}$ is the observed arrival time for the *i*th event at the *j*th station;

$\mathrm{T}_{ij}^{\mathrm{cal}}$ is the calculated (or theoretical) arrival time;

$\phi_i, \lambda_i, \mathrm{h}_i, \mathrm{T}_{oi}$ are, respectively, the latitude, longitude, focal depth and origin time of the *i*th event;

$\Delta\phi_i, \Delta\lambda_i, \Delta \mathrm{h}_i, \Delta \mathrm{T}_{oi}$ are the perturbations of the four hypocentral parameters;

$\left(\frac{\partial \mathrm{T}}{\partial \phi}\right)_{ij}, \left(\frac{\partial \mathrm{T}}{\partial \lambda}\right)_{ij}, \left(\frac{\partial \mathrm{T}}{\partial \mathrm{h}}\right)_{ij}$ are the partial derivatives of the travel time with respect to the hypocentral location;

$\mathrm{V}_n, \Delta \mathrm{V}_n$ are the velocity and its perturbation at the *n*th node of a 3-D grid arranged in the modeling space;

$\frac{\partial \mathrm{T}}{\partial \mathrm{V}_n}$ is the partial derivative of the travel time with respect to the velocity parameter; and

e_{ij} are higher-order terms of perturbations and error of the datum.

The theoretical travel time in Eq. (2.10) can be calculated using the above-mentioned 3-D ray tracing methods. The partial derivatives in Eq. (2.10) are calculated for the (starting) velocity model and the ray path from the hypocenter to the station determined with the 3-D ray tracing code. The partial derivatives of the travel time with respect to the hypocenter location can be written as:

$$\begin{aligned} \frac{\partial \mathrm{T}}{\partial \phi} &= -(\mathrm{R}_0 - \mathrm{h}) \sin i \cdot \cos \alpha / \mathrm{V}_{\mathrm{e}}, \\ \frac{\partial \mathrm{T}}{\partial \lambda} &= -(\mathrm{R}_0 - \mathrm{h}) \sin i \cdot \cos \phi \cdot \sin \alpha / \mathrm{V}_{\mathrm{e}}, \\ \frac{\partial \mathrm{T}}{\partial \mathrm{h}} &= -\cos i / \mathrm{V}_{\mathrm{e}}, \end{aligned} \tag{2.11}$$

where R_0 is the radius of the Earth, i is the take-off angle at the hypocenter, α is the azimuth from the epicenter to the station, and Ve is the velocity at the hypocenter (see Engdahl and Lee 1976). The partial derivatives with respect to the velocity parameters cannot be calculated analytically, because they involve integrals along the ray path:

$$\frac{\partial T}{\partial V_n} = \int_{source}^{station} -\left[\frac{1}{V(\phi,\lambda,h)}\right]^2 \frac{\partial V(\phi,\lambda,h)}{\partial V_n} ds. \tag{2.12}$$

For computational simplicity, partial derivatives with respect to slowness (1/V) are adopted (Thurber 1983). Instead of Eq. (2.12), we have:

$$\frac{\partial T}{\partial V_n} = \int_{source}^{station} \frac{\partial U(\phi,\lambda,h)}{\partial U_n} ds, \tag{2.13}$$

where $U_n = 1/V_n$ and $U(\phi,\lambda, h) = 1/V(\phi,\lambda, h)$. This ray path integral is approximated by dividing the ray path into M segments:

$$\frac{\partial T}{\partial U_n} = \sum_{m=1}^{M} \frac{\partial U(\phi_m,\lambda_m,h_m)}{\partial U_n} \Delta S_m, \tag{2.14}$$

Where ΔS_m is the step length, and (ϕ_m,λ_m,h_m) is the midpoint of the mth path segment (Thurber, 1983). The partial derivative $\frac{\partial U}{\partial U_n}$ is calculated using the interpolation function in Eq. (2.3).

A travel-time residual is expressed as:

$$t_{ij} = T_{ij}^{obs} - T_{ij}^{cal}. \tag{2.15}$$

All the residuals for a set of data form a column vector **d** of dimension N. The corrections to all the hypocentral and velocity parameters form a column vector $\mathbf{\Delta m}$, which can be arranged as:

$$\mathbf{\Delta m}^T = (\Delta\phi_1, \Delta\lambda_1, \Delta h_1, \Delta T_{o1}, \ldots \Delta\phi_M, \Delta\lambda_M, \Delta h_M, \Delta T_{oM}, \Delta V_1, \Delta V_2, \ldots \Delta V_k),$$

where M, N, and K are the numbers of earthquakes, arrival-time data, and the 3-D grid nodes representing the velocity structure, respectively. The vectors for the data and the unknown parameters are related in the following observation equation:

$$\mathbf{d} = \mathbf{G}\Delta\mathbf{m} + \mathbf{e}, \tag{2.16}$$

where **e** is an error vector, **G** is a matrix with dimension $N \times (4M + K)$ whose elements are the partial derivatives in Eqs. (2.11 and 2.14).

There are several approaches to solve Eq. (2.16). Up to now, most tomographic studies have used the damped least-squares method or iterative inversion methods such as the conjugate-gradient type algorithm LSQR (Paige and Saunders 1982). Hence, in the following, we briefly introduce the two kinds of inversion methods.

Parameter Separation and Damped Least-Squares Methods When many earthquakes are used, the matrix **G** in Eq. (2.16) becomes very large and difficult to handle. To overcome this problem, a so-called *parameter separation* scheme was proposed (Pavlis and Booker 1980; Horiuchi et al. 1982a). Each earthquake results in a set of observation equations such as Eq. (2.10), which can be expressed as (Pavlis and Booker 1980; Thurber 1983):

$$\underset{\mathrm{L}\times 1}{\mathbf{d}_i} = \underset{\mathrm{L}\times 4}{\mathbf{H}_i}\underset{4\times 1}{\Delta\mathbf{h}_i} + \underset{\mathrm{L}\times \mathrm{K}}{\mathbf{M}_i}\underset{\mathrm{K}\times 1}{\Delta m}, \tag{2.17}$$

where $\mathbf{d}_i$ is a vector containing L travel-time residuals of the ith earthquake, $\mathbf{h}_i$ is a vector containing corrections to the four hypocentral parameters of the ith event. $\mathbf{H}_i$ and $\mathbf{M}_i$ are matrices containing partial derivatives of the travel-time with respect to the hypocenter and velocity parameters for the ith event. By applying the parameter separation technique, a matrix **Q** is constructed which satisfies the following relation:

$$\underset{(\mathrm{L}-4)\times \mathrm{L}}{\mathbf{Q}}\,\underset{\mathrm{L}\times 4}{\mathbf{H}_i} = 0. \tag{2.18}$$

Operating on Eq. (2.17) by **Q** leads to:

$$\underset{(\mathrm{L}-4)\times 1}{\mathbf{d}'_i} = \underset{(\mathrm{L}-4)\times \mathrm{K}}{\mathbf{M}'_i}\,\underset{\mathrm{K}\times 1}{\Delta \mathrm{m}}. \tag{2.19}$$

Consider that the matrix $\mathbf{M}'$ is composed of a set of submatrices $\mathbf{M}'_i$ and the vector $\mathbf{d}'$ is composed of a set of subvectors $\mathbf{d}'_i$. As the number of seismic events increases, $\mathbf{M}'$ and $\mathbf{d}'$ become very large, causing difficulties of computer storage. To overcome this problem, $\mathbf{M}'^{\mathrm{T}}\mathbf{M}'$ and $\mathbf{M}'^{\mathrm{T}}\mathbf{d}'$ are accumulated sequentially as each event is processed, resulting in a symmetric matrix and a vector of fixed size:

$$\begin{aligned}\mathbf{M}'^{\mathrm{T}}\mathbf{M}' &= \sum\nolimits_i \mathbf{M}'_i\mathbf{M}'_i,\\ \mathbf{M}'^{\mathrm{T}}\mathbf{d}' &= \sum_i \mathbf{M}'_i\mathbf{d}'_i.\end{aligned} \tag{2.20}$$

Then applying the damped least-squares method, we can have the following *normal equation* (e.g., Aki and Lee 1976; Thurber 1983):

$$\underset{\mathrm{N}\times \mathrm{N}}{(\mathbf{M}'^{\mathrm{T}}\mathbf{M}' + \rho\mathbf{I})}\,\underset{\mathrm{K}\times 1}{\Delta\mathbf{m}} = \underset{\mathrm{N}\times 1}{\mathbf{M}'^{\mathrm{T}}\mathbf{d}'}, \tag{2.21}$$

where **I** is a unit matrix, ρ is a constant called *the damping parameter*.

The resolution matrix defined by Backus and Gilbert (1968) and Wiggins (1972) is given by:

$$\mathbf{R} = (\mathbf{M'}^{\mathrm{T}}\mathbf{M'} + \rho\mathbf{I})^{-1}\mathbf{M'}^{\mathrm{T}}\mathbf{M'}. \tag{2.22}$$

The covariance matrix of $\Delta\mathbf{m}$ can be written as:

$$\mathbf{D} = \sigma^2(\mathbf{M'}^{\mathrm{T}}\mathbf{M'} + \rho\mathbf{I})^{-1}\mathbf{R}, \tag{2.23}$$

where

$$\sigma^2 = \frac{|\mathbf{d'} - \mathbf{M'}\Delta\mathbf{m}|}{\mathrm{N} - \mathrm{K} - 4\,\mathrm{M}}. \tag{2.24}$$

Many researchers have investigated the issue of using the matrix-type damped least-squares method (Eqs. 2.21–2.24) to solve tomographic problems (e.g., Aki and Lee 1976; Aki et al. 1977; Horiuchi et al. 1982a; Thurber 1983). One of the advantages of this method is that the resolution and covariance matrices can be computed simultaneously with the solution. Its drawback is that when there are many unknown parameters, the matrix $\mathbf{M'}^{\mathrm{T}}\mathbf{M'}$ needs great memory storage, and constructing $\mathbf{M'}^{\mathrm{T}}\mathbf{M'}$ requires much CPU time. Therefore, in most tomographic studies using a large amount of data, instead of the matrix-type solver (Eqs. 2.21–2.24), iterative inversion methods are adopted to solve the large and sparse linear system of observation equations (Eq. 2.16), such as the algebraic reconstruction technique (ART) (Herman 1980), the simultaneous iterative reconstruction technique (SIRT) (Humphreys and Clayton 1988), or projection-type methods such as the conjugate-gradient (CG) techniques.

The LSQR Algorithm Among the above-mentioned iterative solvers, the CG-type scheme, the LSQR algorithm by Paige and Saunders (1982), is the most popular one, and it has been applied in most tomographic studies so far. It was first introduced to seismology by Nolet (1985) to solve the tomographic problem. A simple Rational Fortran version of LSQR was given by Nolet (1987). Some workers have compared the operational behaviors of SIRT and LSQR and concluded that LSQR is superior to SIRT (e.g., Nolet 1985; van der Sluis and van der Vorst 1985; Spakman and Nolet 1988). Lees and Crosson (1989), however, showed that LSQR and SIRT gave almost the same result. In realistic analyses, these algorithms may give substantially the same result, but the CG-type solver may be slightly superior from the viewpoint of preferable operation behavior and fast convergence (Hirahara 1990).

Because LSQR seeks a solution from a set of orthogonal vectors, it should theoretically converge in K steps or less (K, dimension of the model space) to find the exact least-squares solution. In practice, because the CPU time is limited, we have to terminate the calculation after p iterations ($p \ll K$), thus the orthogonalization adopted by LSQR results in a faster convergence than the other iterative schemes (e.g., ART and SIRT) which do not adopt the orthogonality properties. Moreover, van der Sluis and van der Vorst (1987) have shown that the LSQR algorithm starts the construction of the solution by neglecting those components belonging to the smaller eigenvalues of $\mathbf{M'}^{\mathrm{T}}\mathbf{M'}$. The contributions of the smaller eigenvalues eventually

enter the solution more and more as iteration proceeds, due to the intrinsic damping properties of LSQR, which is similar to the SVD (singular value decomposition) method with a sharp eigenvalue cut-off.

For more detailed discussions on tomographic inversion problems, see Horiuchi et al. (1982a); Paige and Saunders (1982); Thurber (1983); Nolet (1985, 1987, 2008); van der Sluis and van der Vorst (1987); Hirahara (1990); Zhao (1991); Iyer and Hirahara (1993); Aster et al. (2005); Tarantola (2005) and Menke (2012).

Damping Regularization The damping parameter, ρ, in Eq. (2.21) is very important for obtaining a reliable inversion result. Usually, a beginner in seismic tomography finds it difficult to understand the role of the damping parameter. In a tomographic inversion, if the ray paths are distributed uniformly and all the grid nodes are sampled equally well (e.g., the case shown in Fig. 1.3), then damping regularization is unnecessary and a perfect and unique solution can be obtained. In practice, however, damping regularization is always required, because the distribution of seismic stations and earthquakes available in a study area is usually not uniform, leading to a very heterogeneous distribution of ray paths. The grid nodes in the central part of the study area are well sampled by the rays, whereas the nodes at the edge parts of the study area are much less sampled. For the poorly-sampled nodes, the corresponding diagonal elements of the matrix $\mathbf{M}'^{\mathrm{T}}\mathbf{M}'$ in Eq. (2.21) would be $\ll 1$, being several orders of magnitude smaller than those for the well-sampled nodes (i.e., having diagonal elements $\gg 1$). Thus, if we do not adopt the damping regularization (i.e., $\rho=0$), the solution (i.e., *P*- or *S*-wave velocity perturbations) at the poorly-sampled nodes would become unacceptably large, and the obtained tomographic image would become a mess. To prevent such a situation from happening, we have to add the damping parameter (ρ) to all the diagonal elements of the matrix $\mathbf{M}'^{\mathrm{T}}\mathbf{M}'$ so that a reasonable solution can be obtained (see Eq. 2.21). The effect of the damping parameter is significant to the poorly-sampled grid nodes, but very trivial to the well-sampled nodes, because of the huge differences in the diagonal elements of $\mathbf{M}'^{\mathrm{T}}\mathbf{M}'$ between the poorly- and well-sampled grid nodes. The strength of damping depends on the uniformity of the ray distribution. The more heterogeneous the ray distribution is, the greater is the damping parameter needed.

To determine the damping parameter for a tomographic inversion, a rule of thumb is $\rho=(\mathrm{dT}/\mathrm{dF})^2$, where dT is the standard error of the arrival-time data, dF is the standard level of the fractional velocity variation (i.e., the norm of a 3-D velocity model) expected in the study area (Aki and Lee 1976). For example, if $\mathrm{dT}=0.1$ s and $\mathrm{dF}=5\,\%$, then $\rho=4.0\ \mathrm{s}^2$.

A better way to determine the damping parameter is to use the trade-off curve between the root-mean-square (RMS) travel-time residual and the norm of the 3-D velocity model (see Fig. 2.5), which has been widely used in tomographic studies since Eberhart-Phillips (1986). We need to conduct many tomographic inversions using different values of the damping parameter, to seek its optimal value considering the balance between the reduction of the travel-time residual and the smoothness of the resulting 3-D velocity model. Usually the damping parameter at the corner of the trade-off curve is selected to be the optimal one (see Fig. 2.5). The trade-off

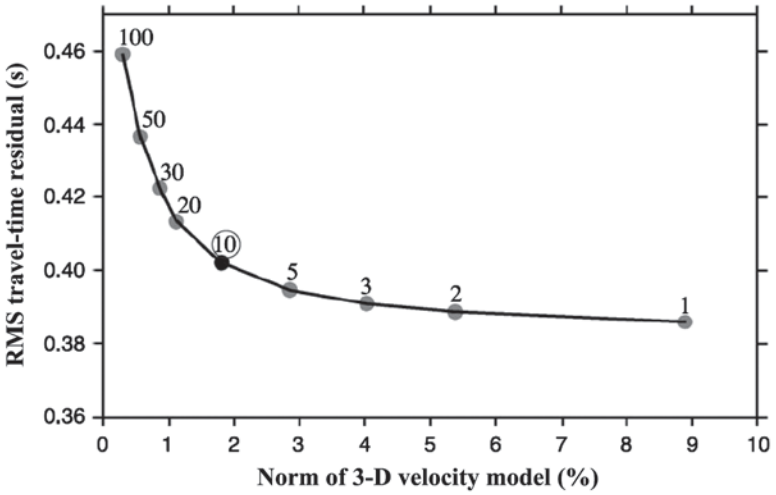

Fig. 2.5 An example of trade-off curve for determining the optimal damping parameter in a tomographic study. The numbers beside the *gray* dots denote the damping parameters adopted in nine tomographic inversions. The *black* dot denotes the optimal damping parameter which leads to the best 3–D velocity model. (Modified from Huang and Zhao 2004)

curve approach has been also adopted to find the optimal value of the smoothing parameter for a tomographic inversion (e.g., Zhao 2001b; Zhao et al. 2013).

2.1.4 Resolution and Error Analysis

Backus and Gilbert (1968) first showed that a solution of an inversion problem must be examined with resolution and error analyses, and the inverted result becomes valuable only after its resolution and error are evaluated properly. Although the formulation of the resolution and covariance matrices (Eqs. 2.22 and 2.23) is well known and applied in tomographic studies, the calculation of the matrices is not an easy task in practice because of the large matrix size when a large data set is used.

By the concept of resolution, we wish to know how the true structure is reconstructed in an inverted tomographic image. The most direct way to estimate the resolution of a tomographic image is to perform the following operations: (1) make a synthetic input model containing assigned velocity anomalies; (2) calculate a set of synthetic travel-time data that result from tracing the rays of an actual set of data for the synthetic model; (3) add random noise to the synthetic data to simulate the picking errors of the observed data; (4) invert the synthetic data using the same method as for the observed data; and (5) compare the inversion result with the synthetic input model and examine how well or poorly the assigned velocity anomalies are recovered.

Two kinds of resolution tests are usually conducted in current tomographic studies. The two tests are basically the same, except for the input synthetic model. The

first is the so-called *checkerboard resolution test* (Humphreys and Clayton 1988; Inoue et al. 1990; Zhao 1991; Zhao et al. 1992). To make a checkerboard model, positive and negative velocity perturbations are assigned alternatively to 3-D grid nodes (or blocks) arranged in a modeling space. The checkerboard image is straightforward and easy to remember. Therefore, by just seeing the result of the synthetic inversion, one can easily understand where the resolution is good and where it is poor in the study area.

The second test is the so-called *restoring resolution test* (Zhao 1991; Zhao et al. 1992). An input synthetic model is constructed which contains the main features of the obtained tomographic image. Synthetic data are generated using a 3-D ray tracing technique to trace the rays in the input synthetic model, because the input model is a heterogeneous 3-D model rather than a simple homogeneous model. Comparing the output result with the input model, one can know whether or not, and how well, the main features of the obtained tomographic image are restored.

The checkerboard test is useful for understanding the degree of recovery in the entire modeling space, but it is not enough to know the resolution and reliability of some complicated structures such as magma chambers and subducting slabs, which can be clarified by conducting the restoring resolution test. Many such synthetic tests should be performed by adopting various input synthetic models with different grid intervals and damping parameters, so that the quality and resolution scale of the obtained tomographic image can be better known.

To estimate the standard errors of the model parameters, some researchers have used statistical techniques such as jackknife and bootstrap (e.g., Lees and Crosson 1989; Tichelaar and Ruff 1989). These kinds of technique involve breaking the data set down into many subsets, performing inversions on the subsets and calculating a standard error from the set of inverted model parameters. Another approach is to assume a distribution of noise for the data and to create artificial data with those noise characteristics. These data are inverted, and the outcome is inspected as a representation of the model uncertainty (e.g., Humphreys and Clayton 1988; Inoue et al. 1990). The advantage of the jackknife type approach is that it is nonparametric, i.e., the data themselves are used to estimate the covariance and no assumption is made about how the data are distributed. Its drawback is that many inversions are required to be conducted with the subsets of data, which is a tedious and time consuming operation (Zhao 2001a). Theoretically, the number of inversions needed for the jackknife or bootstrap is equal to the total number of data used. The jackknife and bootstrap methods are computationally very expensive and are of questionable use for large tomographic problems (Nolet et al. 1999).

Some researchers have attempted to estimate the resolution and covariance matrices using iterative algorithms (e.g., LSQR) without explicitly performing the operations involving the large and complex matrix (e.g., Zhang and McMechan 1995, 1996; Deal and Nolet 1996; Nolet et al. 1999; Yao et al. 1999; Vasco et al. 2003; Zhang and Thurber 2007).

2.1.5 *Velocity Tomography Methods*

In addition to the tomographic methods mentioned above and in Chap. 1, many approaches have been proposed to determine velocity tomography in practical studies. Here, we briefly introduce these approaches. Those readers who are interested in the technical details of these approaches are referred to the related references as follows.

Although most travel-time tomography studies use the first P- and S-wave arrivals, some researchers have used later-phase data (i.e., reflected and converted waves) to determine velocity tomography at both the local scale (e.g., Zhao et al. 1992, 2005; Xia et al. 2007; Gupta et al. 2009) and the global scale (e.g., Vasco et al. 1995, Zhao 2001b, 2004; Zhao et al. 2013). It is found that the later-phase data are very useful in tomographic imaging, because they sample the Earth's structure in areas which are not well sampled by the first P- and S-waves.

A convectional tomography method can determine a 3-D velocity model beneath a seismic network, but cannot determine tomography outside a seismic network. Zhao et al. (2002, 2007) proposed an off-network tomography method to study the 3-D velocity structure beneath oceanic areas adjacent to a land-based seismic network. They have used the method to map the source zone of the great 2011 Tohoku-oki earthquake (Mw 9.0) beneath the Pacific Ocean (for details, see Zhao et al. 2011; Huang and Zhao 2013, and Chap. 4 of this book).

The double-difference (DD) earthquake location algorithm has been developed to relocate seismic events precisely (Waldhauser and Ellsworth 2000). It uses both raw travel-time residuals and differential residuals for a pair of events which are located closely to each other. This DD algorithm has been extended for conducting local earthquake tomography (Zhang and Thurber 2003). One problem of the DD tomography is that those rays adopted for making the DD residuals are used multiple times in constructing the system of observation equations, i.e., those same rays are made to sample the Earth's structure more than once. To avoid this problem, Wang and Zhao (2006) conducted tomography using only the DD scheme of Waldhauser and Ellsworth (2000) to relocate earthquakes, whereas for tomographic inversion they used only the raw residuals but did not use the DD travel-time residuals.

Many researchers have studied the 3-D velocity structure by simultaneously inverting different kinds of seismological and geophysical data, e.g., joint inversions of local and teleseismic travel-time data (e.g., Zhao et al. 1994, 2012; Lei et al. 2009), teleseismic P-wave amplitude and travel-time data (Neele et al. 1993), surface-wave dispersion and receiver functions (e.g., Julia et al. 2000; Shen et al. 2013; Wang et al. 2014), body-wave travel times and surface-wave data (e.g., West et al. 2004), body-wave travel times and Bouguer gravity data (e.g., Lees and VanDecar 1991), receiver functions, surface-wave dispersion and magnetotelluric data (e.g., Moorkamp et al. 2010), and body-wave, surface-wave and higher-mode waveforms (e.g., Megnin and Romanowicz 2000).

The finite-frequency tomography method has been proposed (e.g., Montelli et al. 2004; Hung et al. 2004; Nolet 2008), but many studies have shown that the finite-frequency and ray tomographic methods have produced essentially the same results (e.g., van der Hilst and de Hoop 2005; Boschi et al. 2006; Tong et al. 2011, 2012).

Many workers have used ambient-noise tomography to study shear-wave velocity structure of the crust and shallow mantle (e.g., Campillo and Paul 2003; Shapiro et al. 2005; Lin et al. 2008; Zheng et al. 2011; Kao et al. 2013). This method, however, requires a dense, modern seismic network. The full waveform inversion method has been developed and applied to study regional tomography (e.g., Fichtner et al. 2010, 2013). However, there have been few studies using such a method to determine high-resolution local tomography.

2.2 Seismic Anisotropy Tomography

An important discovery in modern seismological observations is that some features of seismic waves depend on the propagating direction. This phenomenon is called *seismic anisotropy*. Anisotropic media exist widely in the Earth's interior, from the crust and mantle to the inner core, and these have been revealed by a large number of seismological observations and laboratory studies (for detailed reviews, see Silver 1996; Fouch and Rondenay 2006; Long 2013). Studying seismic anisotropy is very important to our understanding of the structure and dynamics of the Earth's interior because anisotropy provides a unique constraint on the character of past and present deformation in the lithosphere and sublithospheric mantle. The major causes of seismic anisotropy are lattice-preferred orientation (LPO) and shape-preferred orientation (SPO) of the materials constituting the Earth. Both body-wave and surface-wave data can be used to study seismic anisotropy. The body-wave methods include shear-wave splitting, receiver functions, and P-wave travel times. Fouch and Rondenay (2006) made a detailed review of the methods for determining seismic anisotropy and their advantages and limitations.

Among the seismic anisotropy studies, P-wave anisotropic tomography is relatively new and has only been developed and applied in the past decade, though Pn anisotropy tomography has a longer history (e.g., Hearn 1996). The Pn-wave tomography can only estimate 2-D P-wave velocity variations and azimuthal anisotropy in the uppermost mantle directly beneath the Moho discontinuity, whereas P-wave anisotropy tomography can determine the 3-D distribution of P-wave anisotropy in the crust and upper mantle beneath a seismic network. Although measuring shear-wave splitting is a popular and useful method to study (detect) seismic anisotropy, it has no depth resolution. This drawback can be overcome by P-wave anisotropy tomography. But one problem of P-wave anisotropy tomography is that there could be a trade-off between velocity heterogeneity and anisotropy, in particular when the ray path coverage is insufficient in different directions. However, recent studies show that the trade-off problem can be resolved when earthquakes and seismic stations used in a tomographic inversion are densely and uniformly distributed in the study area (e.g., Wang and Zhao 2012, 2013).

To fully express an anisotropic medium, 21 independent elastic moduli are required, which is very difficult to deal with in both theory and practice. Fortunately, anisotropy with hexagonal symmetry is a good approximation to the rocks in the Earth and reduces the number of free parameters describing the anisotropy (e.g.,

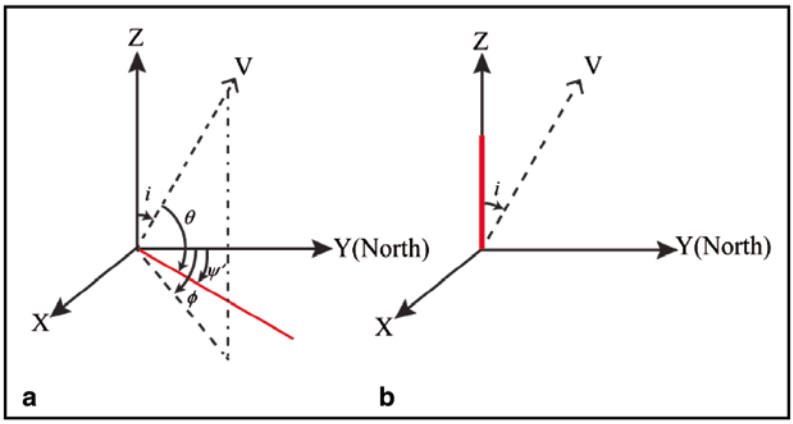

Fig. 2.6 The coordinate system specifying a ray path (the *dashed line*) and the hexagonal symmetry axis (the *red line*) for **a** azimuthal anisotropy and **b** radial anisotropy (Ishise et al. 2012; Wang and Zhao 2013). V is the propagation vector of a ray with incident angle i and azimuthal angle ϕ. θ is the angle between the propagation vector and the symmetry axis. For the azimuthal anisotropy (**a**), the azimuthal angle ψ' of the hexagonal symmetry axis is normal to the fast-velocity direction

Christensen 1984; Park and Yu 1993; Maupin and Park 2007). For a further simplification, the hexagonal symmetry is generally assumed to be horizontal when the azimuthal anisotropy is concerned in shear-wave splitting measurements (e.g., Crampin, 1984; Silver, 1996; Savage 1999; Huang et al. 2011b, c; Long 2013) and P-wave velocity studies (e.g., Hess 1964; Backus 1965; Raitt et al. 1969; Hearn 1996; Eberhart-Phillips and Henderson 2004; Wang and Zhao 2008, 2013); whereas the hexagonal symmetry is generally assumed to be vertical when the radial anisotropy is concerned in the form of a Vsh/Vsv variation (Vsh and Vsv are the velocities of shear waves polarized horizontally and vertically, respectively) in surface-wave studies (e.g., Nettles and Dziewonski 2008; Fichtner et al. 2010; Yuan et al. 2011) and in the form of a Vph/Vpv variation (Vph and Vpv are the velocities of P-waves propagating horizontally and vertically, respectively) in P-wave velocity studies (e.g., Ishise et al. 2012; Wang and Zhao 2013; Wang et al. 2014). Here, we introduce the recent tomographic methods for P-wave azimuthal and radial anisotropy, following Wang and Zhao (2008, 2013).

2.2.1 *P-wave Azimuthal Anisotropy Tomography*

Following the formulation of Barclay et al. (1998) for hexagonal anisotropy, P-wave slowness can be expressed as:

$$S = S_0 + M\cos(2\theta), \tag{2.25}$$

where S is the total slowness, S_0 is the average slowness (i.e., isotropic component), θ is the angle between the propagation vector and the symmetry axis (Fig. 2.6), and M is the parameter for anisotropy. For weak azimuthal anisotropy

with a horizontal hexagonal symmetry axis (Fig. 2.6a), the P-wave slowness can be approximately expressed as (e.g., Backus 1965; Raitt et al. 1969; Hearn 1996; Eberhart-Phillips and Henderson 2004; Wang and Zhao 2008, 2013):

$$S(\phi) = S_0(1 + A_1\cos(2\phi) + B_1\sin(2\phi)), \tag{2.26}$$

where S is the total slowness, S_0 is the azimuthal average slowness, A_1 and B_1 are the azimuthal anisotropy parameters, and ϕ is the ray path azimuth. The fast-velocity direction (FVD) ψ and the amplitude α of the azimuthal anisotropy are expressed as follows:

$$\begin{aligned}
\psi &= \begin{cases}
\dfrac{1}{2}\tan^{-1}\left(\dfrac{B_1}{A_1}\right) + \begin{cases}\dfrac{\pi}{2}, & A_1 > 0\\ 0, & A_1 < 0,\end{cases}\\
-\dfrac{\pi}{4}, A_1 = 0, B_1 > 0,\\
\dfrac{\pi}{4}, A_1 = 0, B_1 < 0,
\end{cases}\\
\alpha &= \frac{V_f - V_s}{2V_0} = \frac{\sqrt{A_1^2 + B_1^2}}{1 - (A_1^2 + B_1^2)},
\end{aligned} \tag{2.27}$$

where V_0 is the average isotropic velocity, and V_f and V_s are the velocities in the fast and slow directions, respectively.

The relation between θ and the propagation vector is as follows (Eberhart-Phillips and Henderson 2004):

$$\cos\theta = \sin i(\sin\phi\sin\psi + \cos\phi\cos\psi), \tag{2.28}$$

where i is the incident angle of a ray path. Thus, for local earthquakes which are located in the modeling space, we have the following observation equation:

$$\begin{aligned}
T_{mn}^{obs} - T_{mn}^{cal} = &\left(\frac{\partial T}{\partial \varphi}\right)_{mn}\Delta\varphi_n + \left(\frac{\partial T}{\partial \lambda}\right)_{mn}\Delta\lambda_n + \left(\frac{\partial T}{\partial h}\right)_{mn}\Delta h_n\\
&+ \Delta T_{0n} + \sum_p\left(\frac{\partial T}{\partial V_p}\Delta V_p\right) + \sum_q\left(\frac{\partial T}{\partial A_{1q}}\Delta A_{1q} + \frac{\partial T}{\partial B_{1q}}\Delta B_{1q}\right) + E_{mn},
\end{aligned} \tag{2.29}$$

where T_{mn}^{obs} and T_{mn}^{cal} are the observed and calculated travel times from the nth event to the mth station, $\varphi_n, \lambda_n, h_n$ and T_{0n} are the latitude, longitude, focal depth and origin time of the nth event, respectively, and Δ denotes the perturbation of a parameter. Two 3-D grid nets are set up in the modeling space, one grid net is for expressing the 3-D isotropic velocity structure, whereas the other grid net is for expressing the 3-D anisotropic structure (Huang et al. 2011a; Wang and Zhao 2013). In Eq. (2.29), V_p is the isotropic velocity at the pth node of the first grid net, whereas A_{1q} and B_{1q} are the azimuthal anisotropy parameters at the qth node of the second grid net. E_{mn} represents higher-order terms of perturbations and data error. The first four terms on the right-hand side of Eq. (2.29) represent contributions of the four hypocentral parameters, which can be obtained using Eq. (2.11).

2.2.2 P-wave Radial Anisotropy Tomography

If the hexagonal symmetry axis is vertical (Fig. 2.6b), Eq. (2.25) can be rewritten as follows (Ishise et al. 2012; Wang and Zhao 2013):

$$S = S_0 + M\cos(2i) = S_0\left(1+\frac{M}{S_0}\cos(2i)\right) = S_0(1+M_1\cos(2i)). \tag{2.30}$$

The amplitude β of radial anisotropy is defined as:

$$\beta = \frac{V_{ph}-V_{pv}}{2V_0} = \frac{M_1}{1-M_1^2}, \tag{2.31}$$

hence, $\beta > 0$ indicates that the horizontally-propagating P-wave travels faster than the vertical one, i.e., $V_{ph}/V_{pv} > 1$.

By using Eq. (2.30), the travel time T_k of the kth ray segment with length d can be written as:

$$\begin{aligned} T_k &= dS = d(1+M_{1k}\cos(2i_k))/V_k, \\ T &= \sum_k T_k, \end{aligned} \tag{2.32}$$

where T is the total travel time of the ray, V_k is the isotropic velocity at the middle point of the kth ray segment, M_{1k} is the parameter for the radial anisotropy at the middle point of the kth ray segment, and i_k is the incident angle of the kth ray segment. Thus, the partial derivatives of the travel time with respect to the velocity and radial anisotropy are expressed as:

$$\begin{aligned} \frac{\partial T}{\partial V_k} &= -d(1+M_{1k}\cos(2i_k))/V_k^2, \\ \frac{\partial T}{\partial M_{1k}} &= \frac{d}{V_k}\cos(2i_k). \end{aligned} \tag{2.33}$$

Similar to the P-wave tomography for azimuthal anisotropy (Wang and Zhao 2008), V_k and M_{1k} at a point are calculated using linear interpolation of the parameters

at the eight grid nodes surrounding that point. Then, the travel-time residual can be written as:

$$T_{mn}^{obs} - T_{mn}^{cal} = \left(\frac{\partial T}{\partial \varphi}\right)_{mn} \Delta\varphi_n + \left(\frac{\partial T}{\partial \lambda}\right)_{mn} \Delta\lambda_n + \left(\frac{\partial T}{\partial h}\right)_{mn} \Delta h_n + \Delta T_{0n} + \sum_p \left(\frac{\partial T}{\partial V_p} \Delta V_p\right) + \sum_q \left(\frac{\partial T}{\partial M_{1q}} \Delta M_{1q}\right) + E_{mn}. \quad (2.34)$$

Similar to the case of isotropic velocity tomography (Zhao et al. 1992, 2009), Eqs. (2.29 and 2.34) are solved using the LSQR algorithm with damping and smoothing regularizations (Wang and Zhao 2008, 2013).

2.3 Seismic Attenuation Tomography

Seismic attenuation (Q) is an important seismological parameter because it provides information on the physical properties and composition of materials in the crust and mantle. Q is sometimes more sensitive to temperature variation and melts than seismic velocity. There are basically three effects which can cause the attenuation of seismic waves (Cormier 1989). The first is geometric spreading, i.e., the reduction of energy density due to the expansion of wavefront with distance. The second is intrinsic attenuation, which is energy lost to heat and internal friction when seismic waves pass through the medium. The third effect is scattering attenuation, when elastic energy is not lost to heat but is redistributed into angular directions away from the receiver or changed to wave types arriving in different time windows at the receiver. Scattering occurs by reflection, refraction, and conversion of elastic energy, by structural heterogeneities which are either discontinuities or rapid changes in seismic velocity and/or density in the Earth's interior (Cormier 1989).

The intrinsic attenuation structure can be determined using amplitudes, or the amplitude spectra, of seismic waves with a method similar to velocity tomography. When seismic waves pass through an attenuating body, their amplitudes are reduced and their spectral contents are altered, just like velocity anomalies change the travel times of seismic waves. The physical parameter adopted to quantify seismic attenuation is the quality factor (Q). Low-Q and high-Q values indicate strong and weak seismic attenuations, respectively. Usually, attenuation (Q) tomography has a lower spatial resolution than velocity tomography in a study area due to at least three reasons. The first is that the amplitude, or amplitude spectrum, data of seismic waves are usually measured by researchers manually or semi-automatically with a complicated procedure. Hence, the attenuation data cannot be measured as much as the arrival-time data. The second is that the amplitudes and spectra are sensitive to the local and surficial structure beneath a seismic station, and so their measurements are usually noisier and hence cannot be measured very accurately as arrival-time pickings. The third reason is that Q has much greater variations than the seismic

velocity. The velocity may vary by 5–10 % from the subducting slab to the overlying mantle wedge, while Q may change by 3000 % (e.g., from 50 to 1500). Because of these reasons, a Q study usually takes much greater effort than a velocity study, and consequently, there have been actually many fewer Q tomography models than 3-D velocity models.

Seismic attenuation tomography has also been estimated using seismic intensity data (e.g., Hashida 1989). The attenuation images thus obtained show some similarity to the Q models determined using amplitudes and the amplitude spectra of seismic waves. However, we cannot expect to obtain high-resolution and accurate Q tomography using intensity data, considering its subjective nature.

Here, we introduce a currently well-used Q tomography method utilizing seismic waveform data, following Liu et al. (2014) who determined high-resolution 3-D P- and S-wave attenuation (Qp and Qs) models of the Tohoku subduction zone. They measured a large number of high-quality t* data precisely from P- and S-wave velocity amplitude spectra of local earthquakes over a frequency range of 0.5–25.0 Hz. t^* is a whole-path attenuation operator, which is expressed as:

$$t^* = \int\limits_{\substack{ray\\path}} \frac{1}{Q(s)V(s)} ds, \tag{2.35}$$

where $Q(s)$ and $V(s)$ are the quality factor and seismic velocity along the ray path s, respectively (e.g., Scherbaum 1990). Thus, the 3-D Q variation can be estimated from t^* for a set of earthquakes and with a 3-D velocity model. The observed velocity amplitude spectrum $A_{ij}(f)$ of event i at station j can be modeled as (Scherbaum 1990):

$$A_{ij}(f) = 2\pi f \cdot S_i(f) \cdot B_{ij}(f) \cdot T_j(f) \cdot I_j(f), \tag{2.36}$$

where f is the frequency, $S_i(f)$ is the source spectrum, $B_{ij}(f)$ is the attenuation spectrum along the ray path from event i to station j, $T_j(f)$ is the site response, and $I_j(f)$ is the instrumental response. According to the ω^2 -source model (Brune, 1970), the source spectrum $S_i(f)$ can be expressed as:

$$S_i(f) = \Omega_{0i} \frac{1}{1+(f/f_{ci})^2}, \tag{2.37}$$

where Ω_{0i} and f_{ci} are the long-period plateau value and the corner frequency for event i, respectively. Assuming whole-path attenuation, the attenuation spectrum $B_{ij}(f)$ can be written as:

$$B_{ij}(f) = \exp(-\pi f^{1-\alpha} t^*), \tag{2.38}$$

where α is a frequency-dependent factor (e.g., Scherbaum 1990; Eberhart-Phillips and Chadwick 2002; Eberhart-Phillips et al. 2008; Ko et al. 2012). Using Eqs. (2.37 and 2.38), Eq. (2.36) can be rewritten as:

$$A_{ij}(f) = 2\pi f \Omega_{0i} \frac{1}{1+(f/f_{ci})^2} \exp(-\pi f^{1-\alpha} t^*), \tag{2.39}$$

if we can remove, or minimize, the effects of the site response $T_j(f)$ and the instrumental response $I_j(f)$.

As shown in Eq. (2.39), the corner frequency f_{ci} is coupled with the whole-path attenuation operator t^*, and so trade-off may occur between them during the spectra-fitting procedure estimating them simultaneously (e.g., Scherbaum 1990; Ko et al. 2012; Liu et al. 2014). To tackle this trade-off problem and obtain high-quality t^* data, the multi-window spectral ratio method (Imanishi and Ellsworth 2006) is used to first estimate the corner frequencies of local earthquakes independently and then to determine the t^* values with the corner frequencies obtained. Following Eq. (2.36), the velocity spectral ratio for a pair of earthquakes (events *l* and *s*) recorded by the same station *j* is:

$$\frac{A_{lj}(f)}{A_{sj}(f)} = \frac{2\pi f \cdot S_l(f) \cdot B_{lj}(f) \cdot T_j(f) \cdot I_j(f)}{2\pi f \cdot S_s(f) \cdot B_{sj}(f) \cdot T_j(f) \cdot I_j(f)}, \tag{2.40}$$

where $B_{lj}(f)$ and $B_{sj}(f)$ can be considered equivalent, when the two events are very close to each other, and hence, share almost the same ray path. Thus, Eq. (2.40) can be rewritten as:

$$\frac{A_{lj}(f)}{A_{sj}(f)} \approx \frac{S_l(f)}{S_s(f)} = \frac{\Omega_{0l}}{\Omega_{0s}} \cdot \frac{1+\left(f/f_{cs}\right)^2}{1+\left(f/f_{cl}\right)^2}, \tag{2.41}$$

where the corner frequencies f_{cl} and f_{cs} can be obtained by fitting the velocity spectral ratio. Equation (2.41) shows that the spectral ratio method can estimate precisely the corner frequencies, largely eliminating the whole-path attenuation (t^*) effect (e.g., Frankel and Wennerberg 1989; Imanishi and Ellsworth 2006; Liu et al. 2014).

Liu et al. (2014) estimated the velocity spectral ratio for a pair of nearby earthquakes recorded at the same station, and did this for all the 316 seismic stations in their study region. All of the spectral ratios for an event pair are stacked if they have a sufficient signal-to-noise (S/N) ratio (>2.0) in the frequency band 0.5–25.0 Hz. A grid search approach is adopted to fit the stacked spectral ratio to determine the corner frequencies of an event pair (Fig. 2.7). For a robust measurement, Liu et al. (2014) not only estimated the corner frequencies of an event pair from P and S direct-wave velocity spectral ratios, but also determined them from P and S coda-wave velocity spectral ratios (Fig. 2.7), because the coda waves could provide more stable spectral ratios which better constrain the source parameters (e.g., Mayeda et al. 2007). They estimated the average velocity spectra from the vertical component for direct P-waves and P-coda waves, and measured them from the transverse and radial components for direct S-waves and S-coda waves (Fig. 2.7). The final P-wave corner frequency of an event is taken to be the weighted average of the values estimated from the direct P and P-coda wave-velocity spectral ratios. Similarly, the weighted average of the values estimated from the direct S and S-coda wave-velocity spectral ratios is taken to be the final S-wave corner frequency of an event.

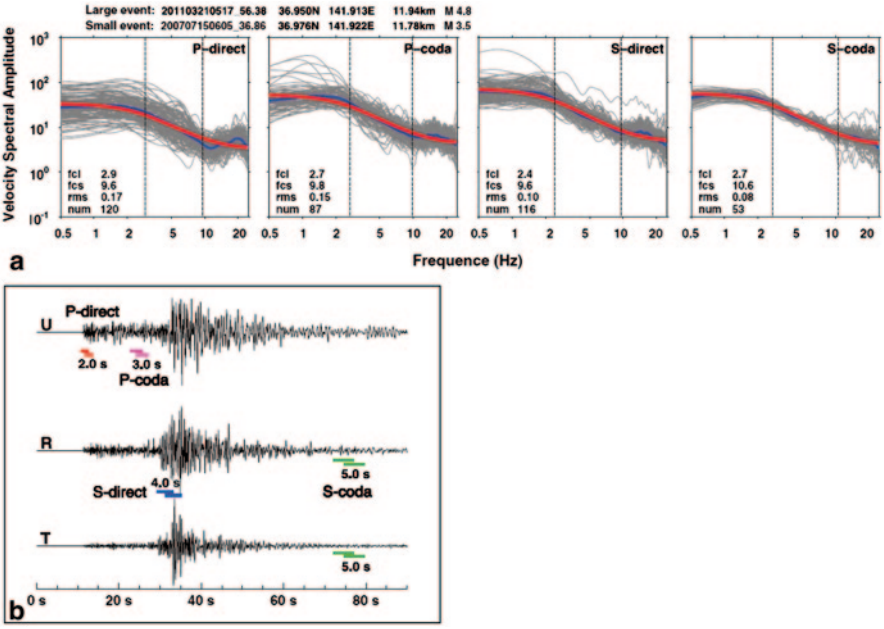

Fig. 2.7 An example of a spectral ratio analysis for a pair of earthquakes. The *gray thin lines* denote spectral ratios for various time windows, components, and stations. The *blue bold lines* show stacked spectral ratios. The *red bold lines* and the *vertical dashed lines* show the theoretical spectral ratios and corner frequencies, respectively. Hypocenter parameters of the event pair are shown at the top and in Fig. 2.8. The durations of time windows of various components are shown at the *bottom*. Corner frequencies of the larger and smaller events (fcl, fcs); root-mean-square of the spectral ratio residual (rms); and the number of spectral ratios (*gray thin lines*) used to calculate the stacked spectral ratio (num). (Modified from Liu et al. 2014)

The obtained P- and S-wave corner frequencies of each event are used to fit P- and S-wave amplitude decay observations from the waveforms for measuring t^*_p and t^*_s, respectively (Fig. 2.8), following the approach of Eberhart-Phillips and Chadwick (2002). The long-period plateau value is estimated by:

$$\Omega_{0i} = \frac{1}{n} \sum_{f<f_{ci}} \frac{A_{ij}^{obs}(f)}{A_{ij(\Omega_{0i}=1)}^{cal}(f)}, \tag{2.42}$$

where $A_{ij(\Omega_{0i}=1)}^{cal}(f)$ is calculated from Eq. (2.39) given an initial estimate of t^*, $A_{ij}^{obs}(f)$ is observed, and n is the number of data points for the velocity amplitude spectrum $A_{ij}(f)$ over the frequency band ($f < f_{ci}$). Then, the estimated Ω_{0i} is used in Eq. (2.43) to get a better-fitting t^*:

$$t^* = \frac{\sum_f \ln[A_{ij(t^*=0)}^{cal}(f)]f - \sum_f \ln[A_{ij}^{obs}(f)]f}{\pi \sum_f f^2}. \tag{2.43}$$

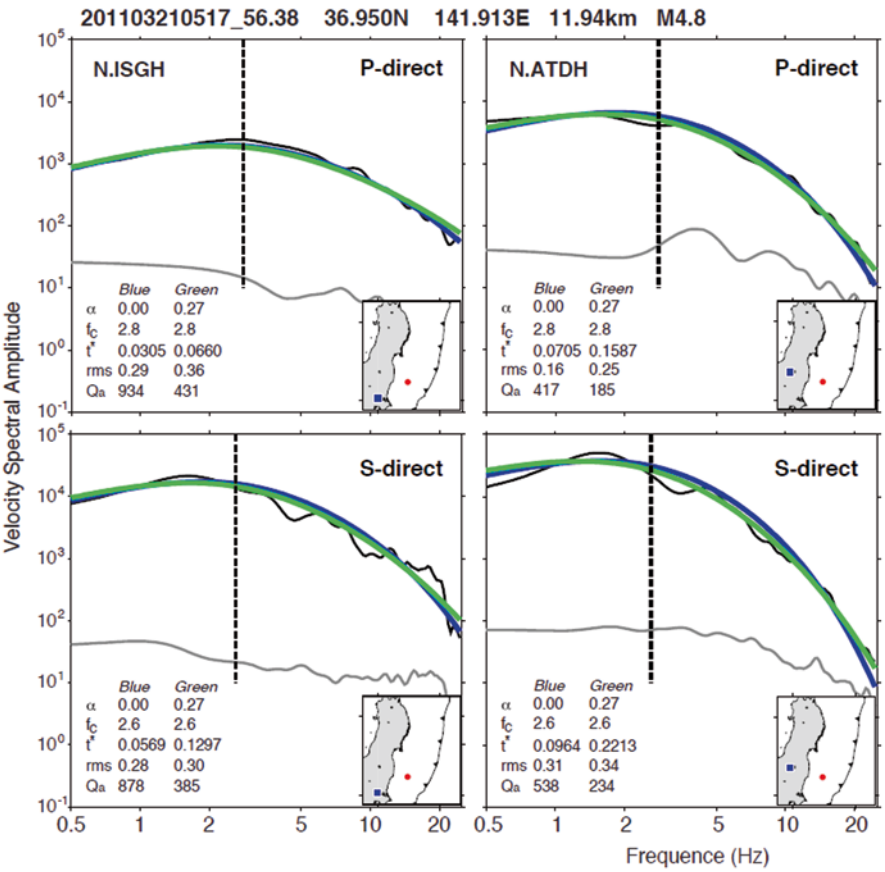

Fig. 2.8 An example of fitting t^* for an earthquake at two stations. In each panel, the *black* and *gray lines* denote the observed velocity and noise spectra, respectively; the *vertical dashed line* shows the corner frequency derived from the observed spectrum; the *blue line* shows the theoretical velocity spectrum with frequency-independent Q and $\alpha = 0$, while the *green line* shows the theoretical velocity spectra with frequency-dependent Q and $\alpha = 0.27$ (see text for details). Hypocenter parameters of the event are shown at the top. The *red dot* and *blue square* in each inset map denote the epicenter and the seismic station, respectively. Durations of the time windows of various components are the same as those shown in Fig. 2.7. *fc*, corner frequency; *rms*, root-mean-square of the velocity spectra residual; *Qa*, path average Q. (Modified from Liu et al. 2014)

The estimated t^* is used in Eq. (2.42) for another iteration of fitting Ω_{0i} which is then used to estimate an improved t^* (Eberhart-Phillips and Chadwick 2002). Liu et al. (2014) made five iterations of this process for measuring t^*, which resulted in a convergent and reliable estimate of t^* (Fig. 2.8). Although the precise calibration does not influence measuring t^*, because the decay is not fitted for the absolute amplitude (Eberhart-Phillips et al. 2008), the effects of the instrumental response and the site response are minimized by the iterative process.

Liu et al. (2014) modified the velocity tomography method of Zhao et al. (1992, 2009) to determine 3-D Qp and Qs models using the measured t^* data. To express the 3-D Q structure, a 3-D grid net is set up in the modeling space. Because the velocity and Q parameters are coupled with each other in Eq. (2.35), the perturbation to the product of velocity and Q (VQ) at each grid node from a starting VQ model is taken to be the unknown parameter. The VQ perturbation at any point in the model is calculated by linearly interpolating the VQ perturbations at the eight grid nodes surrounding that point. The starting VQ model is calculated from a well-constrained 3-D velocity model (Huang and Zhao 2013) and the initial Qp and Qs under the study region. The 3-D ray tracing technique of Zhao et al. (1992) is used to compute theoretical t^* and ray paths. Lateral depth variations of the Conrad and Moho discontinuities and the upper boundary of the subducting Pacific slab (Zhao et al. 1992, 2009) are taken into account in the 3-D ray tracing and the tomographic inversion. A damped least-squares method is used to solve the large and sparse system of observation equations that relate the observed t^* data to the unknown parameters. The 3-D Q model is obtained from the inverted VQ result divided by the 3-D velocity model under the study region (Liu et al. 2014).

2.4 Other Physical Parameters

Poisson's ratio (σ) is the negative ratio of the transverse to axial strain, and it is related to the P- and S-wave velocities (Vp, Vs) as follows:

$$\left(\frac{\mathrm{Vp}}{\mathrm{Vs}}\right)^2 = \frac{2(1-\sigma)}{1-2\sigma}. \tag{2.44}$$

Hence, when 3-D Vp and Vs models are determined for a region by tomographic inversion, images of the Poisson's ratio, or Vp/Vs, can be obtained easily, and they are often used to discuss thermal anomalies in a volcanic area, the melt and fluid content in the crust and mantle, and fore-arc mantle serpentinization, etc. (e.g., Zhao et al. 1996; Christensen 1996, 2004; Kamiya and Kobayashi 2000). In addition, the bulk sound velocity (V_b) can also be derived from Vp and Vs:

$$\mathrm{V_b} = \sqrt{\mathrm{Vp}^2 - \frac{4}{3}\mathrm{Vs}^2}, \tag{2.45}$$

and it can be used to discuss thermal and compositional variations in the mantle (e.g., Kennett et al. 1998; Masters et al. 2000).

Fishwick (2006) proposed the use of velocity gradient maps, because the interpretation of tomographic images may be dependent on the choice of reference models or a particular color scale, whereas gradient maps provide an image that is independent of the reference model.

With some assumptions, a few other parameters can be estimated using Vp and Vs. For example, Zhao and Mizuno (1999) estimated the 3-D distribution of crack

density and saturation rate in the 1995 Kobe earthquake area by applying the crack theory of O'Connell and Budiansky (1974) to values of Vp, Vs and Poisson's ratio obtained from local earthquake tomography (Zhao et al. 1996). Their results show that the Kobe source zone exhibits high values of crack density and saturation rate. Mishra and Zhao (2003) used the same approach to estimate the 3-D distribution of crack density and saturation rate in the source area of the 2000 Bhuj earthquake (M 7.8) in western India. Tian and Liu (2013) discussed the geophysical properties of the interplate megathrust zone beneath the Tohoku fore-arc using 3-D images of six physical parameters: Vp, Vs, Poisson's ratio, crack density, saturation rate, and Vp azimuthal anisotropy. Applying the crack theory of Takei (2002) to 3-D Vp and Vs values obtained by travel-time tomography, Nakajima et al. (2005) discussed the shape and volume fraction of the melt-filled pores in the inclined low-V zone in the mantle wedge beneath NE Japan. In addition, some researchers have used $R = \mathrm{dln}Vs/\mathrm{dln}Vp$, the ratio of the fractional changes in Vs and Vp, to discuss partial melts and thermal anomalies in the upper and lower mantle (e.g., Karato 1993; Masters et al. 2000; Takei 2002).

Shito and Shibutan (2003) estimated temperature, water content and chemical composition effects (concentration of iron) in the upper mantle beneath the northern Philippine Sea using attenuation and velocity tomography results. Yamada et al. (2009) and Suetsugu et al. (2010) estimated lateral variations in temperature and water content in the mantle transition zone under the Japan Islands and the Philippine Sea, respectively, using P-wave velocities and depth variations of the 410 and 660 km discontinuities determined by seismological methods and partial derivatives of velocity and depth variations with respect to temperature and water content determined by mineral physics studies.

References

Aki, K., Lee, W.: Determination of three-dimensional velocity anomalies under a seismic array using first P arrival times from local earthquakes: 1. A homogeneous initial model. J. Geophys. Res. **81,** 4381–4399 (1976)

Aki, K., Christoffersson, A., Husehye, E.: Determination of the three-dimensional seismic structure of the lithosphere. J. Geophys. Res. **82,** 277–296 (1977)

Aster, R., Borchers, B., Thurber, C.: Parameter Estimation and Inverse Problems, p. 301. Elsevier Academic, Burlington (2005)

Backus, G.: Possible forms of seismic anisotropy of uppermost mantle under oceans. J. Geophys. Res. **70,** 3429–3439 (1965)

Backus, G., Gilbert, F.: The resolving power of gross Earth data. Geophys. J.R. Astron. Soc. **16,** 169–205 (1968)

Ballard, S., Hipp, J., Young, C.: Efficient and accurate calculation of ray theory seismic travel time though variable resolution 3D earth models. Seismol. Res. Lett. **80,** 990–1000 (2009)

Barclay, A., Toomey, D., Solomon, S.: Seismic structure and crustal magmatism at the Mid-Atlantic Ridge, 35 degrees N. J. Geophys. Res. **103,** 17827–17844 (1998)

Boschi, L., Becker, T., Soldati, G., Dziewonski, A.: On the relevance of born theory in global seismic tomography. Geophys. Res. Lett. **33,** L06302 (2006)

Brune, J.: Tectonic stress and the spectra of seismic shear waves from earthquakes. J. Geophys. Res. **75,** 4997–5009 (1970)
Campillo, M., Paul, A.: Long-range correlations in the diffuse seismic coda. Science **299,** 547–549 (2003)
Cerveny, V., Molotkov, A., Psencik, I.: Ray Method in Seismology. University of Karlova, Prague (1977)
Chou, W., Booker, R.: A Backus-Gilbert approach to inversion of travel-time data for three-dimensional velocity structure. Geophys. J.R. Astron. Soc. **59,** 325–344 (1979)
Christensen, N.I.: The magnitude, symmetry and origin of upper mantle anisotropy based on fabric analyses of ultramafic tectonites. Geophys. J. R. Astr. Soc. **76,** 89–111 (1984)
Christensen, N.I.: Poisson's ratio and crustal seismology. J. Geophys. Res. **101,** 3139–3156 (1996)
Christensen, N.I.: Serpentinites, peridotites, and seismology. Int. Geol. Rev. **46,** 795–816 (2004)
Cormier, V.: Seismic attenuation: observation and measurement. In: James, D.E. (ed.) The Encyclopedia of Solid Earth Geophysics, pp. 1005–1017. Van Nostrand Reinhold Company, New York (1989)
Coultrip, R.: High-accuracy wavefront tracing traveltime calculation. Geophysics **58,** 284–292 (1993)
Crampin, S.: Effective anisotropic constants for wave-propagation through cracked solids. Geophys. J. R. Astron. Soc. **76,** 135–145 (1984)
Deal, M., Nolet, G.: Comment on "Estimation of resolution and covariance for large matrix inversions" by J. Zhang and G. McMechan. Geophys. J. Int. **127,** 245–250 (1996)
Dziewonski, A.: Mapping the lower mantle: determination of lateral heterogeneity in P velocity up to degree and order 6. J. Geophys. Res. **89,** 5929–5952 (1984)
Eberhart-Phillips, D.: Three-dimensional velocity structure in Northern California Coast Ranges from inversion of local earthquake arrival times. Bull. Seismol. Soc. Am. **76,** 1025–1052 (1986)
Eberhart-Phillips, D., Chadwick, M.: Three-dimensional attenuation model of the shallow Hikurangi subduction zone in the Raukumara Peninsula, New Zealand. J. Geophys. Res. **107,** 2033 (2002)
Eberhart-Phillips, D., Henderson, C.: Including anisotropy in 3-D velocity inversion and application to Marlborough, New Zealand. Geophys. J. Int. **156,** 237–254 (2004)
Eberhart-Phillips, D., Chadwick, M., Bannister, S.: Three-dimensional attenuation structure of central and southern South Island, New Zealand, from local earthquakes. J. Geophys. Res. **113,** B05308 (2008)
Engdahl, E., Lee, W.: Relocation of local earthquakes by seismic ray tracing. J. Geophys. Res. **81,** 4400–4406 (1976)
Fichtner, A., Kennett, B., Igel, H., Bunge, H.: Full waveform tomography for radially anisotropic structure: new insights into present and past states of the Australasian upper mantle. Earth planet. Sci. Lett. **290,** 270–280 (2010)
Fichtner, A., Trampert, J., Cupillard, P. et al.: Multiscale full waveform inversion. Geophys. J. Int. **194,** 534–556 (2013)
Fishwick, S.: Gradient maps: A tool in the interpretation of tomographic images. Phys. Earth Planet. Inter. **156,** 152–157 (2006)
Flanagan, M., Shearer, P.: Global mapping of topography on transition zone velocity discontinuities by stacking SS precursors. J. Geophys. Res. **103,** 2673–2692 (1998)
Fouch, M., Rondenay, S.: Seismic anisotropy beneath stable continental interiors. Phys. Earth Planet. Inter. **158,** 292–320 (2006)
Frankel, A., Wennerberg, L.: Microearthquake spectra from the Anza, California, seismic network: Site response and source scaling. Bull. Seismol. Soc. Am. **79,** 581–609 (1989)
Gupta, S., Zhao, D., Ikeda, M., Ueki, S., Rai, S.: Crustal tomography under the Median Tectonic Line in Southwest Japan using P and PmP data. J. Asian Earth Sci. **35,** 377–390 (2009)
Hashida, T.: Three-dimensional seismic attenuation structure beneath the Japanese Islands and its tectonic and thermal implications. Tectonophysics **159,** 163–180 (1989)
Hearn, T.: Anisotropic Pn tomography in the western United States. J. Geophys. Res. **101,** 8403–8414 (1996)

Herman, G.: Image Reconstruction from Projections: The Fundamentals of Computerized Tomography. Academic Press, San Diego (1980)
Hess, H.: Seismic anisotropy of uppermost mantle under oceans. Nature **203,** 629–631 (1964)
Hirahara, K.: Inversion method of body wave data for three-dimensional Earth structure. J. Seismol. Soc. Japan **43,** 291–306 (1990)
Horie, A.: Three-dimensional seismic velocity structure beneath the Kanto district by inversion of P-wave arrival times. Ph.D. thesis, University of Tokyo (1980)
Horiuchi, S., Ishii, H., Takagi, A.: Two-dimensional depth structure of the crust beneath the Tohoku district, the northeastern Japan arc. I. Method and Conrad discontinuity. J. Phys. Earth **30,** 47–69 (1982a)
Horiuchi, S., Yamamoto, A., Ueki, S.: Two-dimensional depth structure of the crust beneath the Tohoku district, the northeastern Japan arc. II. Moho discontinuity and P-wave velocity. J. Phys. Earth **30,** 71–86 (1982b)
Huang, J., Zhao, D.: Crustal heterogeneity and seismotectonics of the region around Beijing, China. Tectonophysics **385,** 159–180 (2004)
Huang, Z., Zhao, D.: Mechanism of the 2011 Tohoku-oki earthquake (Mw 9.0) and tsunami: insight from seismic tomography. J. Asian Earth Sci. **70,** 160–168 (2013)
Huang, Z., Zhao, D., Wang, L.: Seismic heterogeneity and anisotropy of the Honshu arc from the Japan Trench to the Japan Sea. Geophys. J. Int. **184,** 1428–1444 (2011a)
Huang, Z., Zhao, D., Wang, L.: Shear-wave anisotropy in the crust, mantle wedge and the subducting Pacific slab under Northeast Japan. Geochem. Geophys. Geosyst. **12,** Q01002 (2011b)
Huang, Z., Zhao, D., Wang, L.: Frequency-dependent shear-wave splitting and multilayer anisotropy in Northeast Japan. Geophys. Res. Lett. **38,** L08302 (2011c)
Huang, G., Bai, C., Greenhalgh, S.: Fast and accurate global multiphase arrival tracking: the irregular shortest-path method in a 3-D spherical earth model. Geophys. J. Int. **194,** 1878–1892 (2013)
Humphreys, E., Clayton, R.: Adaptation of back projection tomography to seismic travel time problems. J. Geophys. Res. **93,** 1073–1085 (1988)
Hung, S., Shen, Y., Chiao, L.: Imaging seismic velocity structure beneath the Iceland hotspot: a finite frequency approach. J. Geophys. Res. **109,** B08305 (2004)
Imanishi, K., Ellsworth, W.: Source scaling relationships of microearthquakes at Parkfield, CA, determined using the SAFOD pilot hole seismic array. In: Abercrombie, R. et al. (eds.) Earthquakes: Radiated Energy and the Physics of Earthquake Faulting. AGU, Washington, D.C. (2006) (Geophys. Monogr. Ser., vol. 170, pp. 81–90)
Inoue, H., Fukao, Y., Tanabe, K., Ogata, Y.: Whole mantle P wave travel time tomography. Phys. Earth Planet. Inter. **59,** 294–328 (1990)
Ishise, M., Kawakatsu, K., Shiomi, K.: Anisotropic velocity structure under the Japan Islands using Hi-net arrival-time data. (1) Reexamination of the 3-D anisotropic velocity structure beneath Northeast Japan. Program and Abstracts of the Annual Meeting of Seismological Society of Japan, Hakodate, Japan, B12-02 (2012)
Iyer, H., Hirahara, K. (Eds.): Seismic Tomography: Theory and Practice, p. 842. Chapman & Hall, Boca Raton (1993)
Jacob, K.: Three-dimensional seismic ray tracing in a laterally heterogeneous spherical Earth. J. Geophys. Res. **75,** 6675–6689 (1970)
Julia, J., Ammon, C., Herrmann, R., Correig, A.: Joint inversion of receiver function and surface wave dispersion observations. Geophys. J. Int. **143,** 99–112 (2000)
Julian, B., Gubbins, D.: Three-dimensional seismic ray tracing. J. Geophys. **43,** 95–113 (1977)
Kamiya, S., Kobayashi, Y.: Seismological evidence for the existence of serpentinized wedge mantle. Geophys. Res. Lett. **27,** 819–822 (2000)
Kao, H., Behr, Y., Currie, C. et al.: Ambient seismic noise tomography of Canada and adjacent regions: part I. Crustal structures. J. Geophys. Res. **118,** 5865–5887 (2013)
Karato, S.: Importance of anelasticity in the interpretation of seismic tomography. Geophys. Res. Lett. **20,** 1623–1626 (1993)

Kennett, B., Engdahl, E.: Travel times for global earthquake location and phase identification. Geophys. J. Int. **105,** 426–465 (1991)
Kennett, B., Widiyantoro, S., van der Hilst, R.: Joint seismic tomography for bulk sound and shear wave speed in the Earth's mantle. J. Geophys. Res. **103,** 12469–12493 (1998)
Ko, Y., Kuo, B., Hung, S.: Robust determination of earthquake source parameters and mantle attenuation. J. Geophys. Res. **117,** B04304 (2012)
Koketsu, K., Sekine, S.: Pseudo-bending method for three-dimensional seismic ray tracing in a spherical earth with discontinuities. Geophys. J. Int. **132,** 339–346 (1998)
Lees, J., Crosson, R.: Tomographic inversion for three-dimensional velocity structure at Mount St. Helens using earthquake data. J. Geophys. Res. **94,** 5716–5729 (1989)
Lees, J., VanDecar, J.: Seismic tomography constrained by Bouguer gravity anomalies: applications in Western Washington. Pure Appl. Geophys. **135,** 31–52 (1991)
Lei, J., Zhao, D., Su, Y.: Insight into the origin of the Tengchong intraplate volcano and seismotectonics in southwest China from local and teleseismic data. J. Geophys. Res. **114,** B05302 (2009)
Lin, F., Moschetti, M., Ritzwoller, M.: Surface wave tomography of the western United States from ambient seismic noise: Rayleigh and love wave phase velocity maps. Geophys. J. Int. **173,** 281–298 (2008)
Liu, X., Zhao, D., Li, S.: Seismic heterogeneity and anisotropy of the southern Kuril arc: Insight into megathrust earthquakes. Geophys. J. Int. **194,** 1069–1090 (2013)
Liu, X., Zhao, D., Li, S.: Seismic attenuation tomography of the Northeast Japan arc: Insight into the 2011 Tohoku earthquake (Mw 9.0) and subduction dynamics. J. Geophys. Res. **119,** 1094–1118 (2014)
Long, M.: Constraints on subduction geodynamics from seismic anisotropy. Rev. Geophys. **51,** 76–112 (2013)
Masters, G., Laske, G., Bolton, H., Dziewonski, A.: The relative behavior of shear velocity, bulk sound speed, and compressional velocity in the mantle: implications for chemical and thermal structure. In: Karato, S., Forte, A., Liebermann, R., Master, G., Stixrude, L. (eds.) Earth's Deep Interior: Mineral Physics and Tomography from the Atomic to the Global Scale, pp. 63–87. AGU Monograph, Washington D.C. (2000).
Maupin, V., Park, J.: Theory and Observations-Wave Propagation in Anisotropic Media, in Treatise on Geophysics, pp. 289–321, Schubert, G. (Ed.), Elsevier, Amsterdam (2007)
Mayeda, K., Malagnini, L., Walter, W.: A new spectral ratio method using narrow band coda envelopes: evidence for non-self-similarity in the hector mine sequence. Geophys. Res. Lett. **34,** L11303 (2007)
Megnin, C., Romanowicz, B.: The three-dimensional shear velocity structure of the mantle from the inversion of body, surface and higher-mode waveforms. Geophys. J. Int. **143,** 709–728 (2000)
Menke, W.: Geophysical Data Analysis: Discrete Inverse Theory Third edition. Elsevier (2012)
Mishra, O.P., Zhao, D.: Crack density, saturation rate and porosity at the 2001 Bhuj, India, earthquake hypocenter: a fluid driven earthquake? Earth Planet. Sci. Lett. **212,** 393–405 (2003)
Miyatake, T.: On the travel time calculation by using approximate ray tracing in a laterally heterogeneous velocity structure. J. Seismol. Soc. Japan **40,** 99–110 (1987)
Montelli, R., Nolet, G., Master, G., Dahlen, F., Hung, H.: Global P and PP traveltime tomography: rays versus waves. Geophys. J. Int. **158,** 637–654 (2004)
Mooney, W., Laske, G., Masters, G.: CRUST 5.1: A global crustal model at 5 × 5. J. Geophys. Res. **103,** 727–747 (1998)
Moorkamp, M., Jones, A., Fishwick, S.: Joint inversion of receiver functions, surface wave dispersion, and magnetotelluric data. J. Geophys. Res. **115,** B04318 (2010)
Moser, T.: Shortest path calculation of seismic rays. Geophysics **56,** 59–67 (1991)
Nakajima, J., Takei, Y., Hasegawa, A.: Quantitative analysis of the inclined low-velocity zone in the mantle wedge of northeastern Japan: a systematic change of melt-filled pore shapes with depth and its implications for melt migration. Earth Planet. Sci. Lett. **234,** 59–70 (2005)

Neele, F., VanDecar, J., Snieder, R.: The use of P wave amplitude data in a joint inversion with travel times for upper mantle velocity structure. J. Geophys. Res. **98,** 12033–12054 (1993)
Nettles, M. Dziewonski, A: Radially anisotropic shear velocity structure of the upper mantle globally and beneath North America. J. Geophys. Res. **113,** B02303 (2008)
Nolet, G.: Solving or resolving inadequate and noisy tomographic systems. J. Comput. Phys. **61,** 463–82 (1985)
Nolet, G. (Ed.): Seismic Tomography: With Applications in Global Seismology and Exploration Geophysics, p. 386. D. Reidel Publishing Company (1987)
Nolet, G.: A Breviary of Seismic Tomography: Imaging the Interior of the Earth and Sun, p. 344. Cambridge University Press (2008)
Nolet, G., Montelli, R., Virieux, J.: Explicit, approximate expressions for the resolution and a posteriori covariance of massive tomographic systems. Geophys. J. Int. **138,** 36–44 (1999)
O'Connell, R., Budiansky, B.: Seismic velocities in dry and saturated cracked solids. J. Geophys. Res. **79,** 5412–5426 (1974)
Paige, C., Saunders, M.: LSQR: An algorithm for sparse linear equations and sparse least squares. ACM Trans. Math. Softw. **8,** 43–71 (1982)
Park, J., Yu, Y.: Seismic determination of elastic anisotropy and mantle flow. Science **261,** 1159–1162 (1993)
Pavlis, G., Booker, J.: The mixed discrete continuous inverse problem: application to the simultaneous determination of earthquake hypocenters and velocity structure. J. Geophys. Res. **85,** 4801–4810 (1980)
Pereyra, V., Lee, W., Keller, H.: Solving two-point seismic ray-tracing problems in a heterogeneous medium, 1. A general adaptive finite difference method. Bull. Seismol. Soc. Am. **70,** 79–99 (1980)
Podvin, P., Lecomte, I.: Finite-difference computation of traveltimes in very contrasted velocity models: A massively parallel approach and its associated tools. Geophys. J. Int. **105,** 271–284 (1991)
Raitt, R., Shor, G., Francis, T., Morris, G.: Anisotropy of Pacific upper mantle. J. Geophys. Res. **74,** 3095–3109 (1969)
Sadeghi, H., Suzuki, S., Takenaka, H.: A two-point, three-dimensional seismic ray tracing using genetic algorithms. Phys. Earth Planet. Inter. **113,** 355–365 (1999)
Savage, M.K.: Seismic anisotropy and mantle deformation: what have we learned from shear wave splitting? Rev. Geophys. **37,** 65–106 (1999)
Scherbaum, F.: Combined inversion for the three-dimensional Q structure and source parameters using microearthquake spectra. J. Geophys. Res. **95,** 12423–12438 (1990)
Shapiro, N., Campillo, M., Stehly, L., Ritzwoller, M.: High-resolution surface wave tomography from ambient seismic noise. Science **307,** 1615–1618 (2005)
Shen, W., Ritzwoller, M., Schulte-Pelkum, V., Lin, F.: Joint inversion of surface wave dispersion and receiver functions: a Bayesian Monte-Carlo approach. Geophys. J. Int. **192,** 807–836 (2013)
Shito, A., Shibutan, T.: Nature of heterogeneity of the upper mantle beneath the northern Philippine Sea as inferred from attenuation and velocity tomography. Phys. Earth Planet. Inter. **140,** 331–341 (2003)
Silver, P.G.: Seismic anisotropy beneath the continents: probing the depths of geology. Ann. Rev. Earth Planet. Sci. **24,** 385–432 (1996)
Spakman, W., Nolet, G.: Imaging algorithms, accuracy and resolution in delay time tomography. In Vlaar N. et al. (eds.): Mathematical Geophysics, pp. 155–87. D. Reidel, Norwell (1988)
Spencer, C., Gubbins, D.: Travel-time inversion for simultaneous earthquake location and velocity structure determination in laterally varying media. Geophys. J.R. Astron. Soc. **63,** 95–116 (1980)
Suetsugu, D., Inoue, T., Obayashi, M., Yamada, A. et al.: Depths of the 410 km and 660 km discontinuities in and around the stagnant slab beneath the Philippine Sea: is water stored in the stagnant slab? Phys. Earth Planet. Inter. **183,** 270–279 (2010)

Takei, Y.: Effect of pore geometry on V_P/V_S: from equilibrium geometry to crack. J. Geophys. Res. **107,** doi:10.1029/2001JB000522 (2002)
Tarantola, A.: Inverse Problem Theory and Methods for Model Parameter Estimation. Society for Industrial and Applied Mathematics (2005)
Thurber, C.: Earthquake locations and three-dimensional crustal structure in the Coyote Lake area, central California. J. Geophys. Res. **88,** 8226–8236 (1983)
Thurber, C., Aki, K.: Three-dimensional seismic imaging. Ann. Rev. Earth Planet. Sci. **15,** 115–139 (1987)
Thurber, C., Ellsworth, W.: Rapid solution of ray tracing problems in heterogeneous media. Bull. Seismol. Soc. Am. **70,** 1137–1148 (1980)
Tian, Y., Liu, L.: Geophysical properties and seismotectonics of the Tohoku forearc region. J. Asian Earth Sci. **64,** 235–244 (2013)
Tian, Y., Zhao, D.: Seismic anisotropy and heterogeneity in the Alaska subduction zone. Geophys. J. Int. **190,** 629–649 (2012)
Tichelaar, B., Ruff, L.: How good are our best models? EOS, Trans. Am. Geophys. Un. **70,** 593–606 (1989)
Um, J., Thurber, C.: A fast algorithm for two-point seismic ray tracing. Bull. Seismol. Soc. Am. **77,** 972–986 (1987)
Van der Hilst, R., de Hoop, M.: Banana-doughnut kernels and mantle tomography. Geophys. J. Int. **163,** 956–961 (2005)
van der Sluis, A., van der Vorst, H.: Numerical solution of large, sparse linear algebraic systems arising from tomographic problems. In Nolet, G. (ed.) Seismic Tomography, pp. 49-84. D. Reidel Publishing Company (1987)
Vasco, D., Johnson, L., Pulliam, R.: Lateral variations in mantle velocity structure and discontinuities determined from P, PP, S, SS, and SS-SdS travel time residuals. J. Geophys. Res. **100,** 24037–24059 (1995)
Vasco, D., Johnson, L., Marques, O.: Resolution, uncertainty, and whole Earth tomography. J. Geophys. Res. **108,** 2022 (2003)
Vidale, J. 1988. Finite-difference traveltime calculation. Bull. Seismol. Soc. Am. **78,** 2062–2076.
Vidale, J.: Finite-difference calculation of traveltime in three dimensions. Geophysics **55,** 521–526 (1990)
Wagner, L., Beck, S., Zandt, G.: Upper mantle structure in the south central Chilean subduction zone (30° to 36°S). J. Geophys. Res. **110,** B01308 (2005)
Waldhauser, F., Ellsworth, W.: A double-difference earthquake location algorithm: Method and application to the northern Hayward fault. Bull. Seism. Soc. Am. **90,** 1353–1368 (2000)
Wang, Z., Zhao, D.: Suboceanic earthquake location and seismic structure in the Kanto district, central Japan. Earth Planet. Sci. Lett. **241,** 789–803 (2006)
Wang, J., Zhao, D.: P-wave anisotropic tomography beneath Northeast Japan. Phys. Earth planet. Inter. **170,** 115–133 (2008)
Wang, J., Zhao, D.: P wave anisotropic tomography of the Nankai subduction zone in Southwest Japan. Geochem. Geophys. Geosyst. **13,** Q05017 (2012)
Wang, J., Zhao, D.: P-wave tomography for 3-D radial and azimuthal anisotropy of Tohoku and Kyushu subduction zones. Geophys. J. Int. **193,** 1166–1181 (2013)
Wang, J., Wu, H., Zhao, D.: P wave radial anisotropy tomography of the upper mantle beneath the North China Craton. Geochem. Geophys. Geosyst. **15,** 2195–2210 (2014)
Wesson, R.: Travel-time inversion for laterally inhomogeneous crustal velocity models. Bull. Seismol. Soc. Am. **61,** 729–746 (1971)
West, M., Gao, W., Grand, S.: A simple approach to the joint inversion of seismic body and surface waves applied to the southwest U.S. Geophys. Res. Lett. **31,** L15615 (2004)
Wiggins, R.: The general linear inverse problem: implication of surface waves and free oscillations for Earth structure. Rev. Geophys. Space Phys. **10,** 251–285 (1972)
Xia, S., Zhao, D., Qiu, X. et al.: Mapping the crustal structure under active volcanoes in central Tohoku, Japan using P and PmP data. Geophys. Res. Lett. **34,** L10309 (2007)

Yamada, A., Zhao, D., Inoue, T., Suetsugu, D., Obayashi, M.: Seismological evidence for compositional variations at the base of the mantle transition zone under Japan Islands. Gondwana Res. **16,** 482–490 (2009)

Yao, Z.S., Roberts, R., Tryggvason, A.: Calculating resolution and covariance matrices for seismic tomography with the LSQR method. Geophys. J. Int. **138,** 886–894 (1999)

Yuan, H., Romanowicz, B., Fischer, K., Abt, D.: 3-D shear wave radially and azimuthally anisotropic velocity model of the North American upper mantle. Geophys. J. Int. **184,** 1237–1260 (2011)

Zhang, J., McMechan, G.: Estimation of resolution and covariance for large matrix inversions. Geophys. J. Int. **121,** 409–426 (1995)

Zhang, H., Thurber, C.: Double-difference tomography: the method and its application to the Hayward fault, California. Bull. Seismol. Soc. Am. **93,** 1875–1889 (2003)

Zhang, H., Thurber, C.: Estimating the model resolution matrix for large seismic tomography problems based on Lanczos bidiagonalization with partial reorthogonalization. Geophys. J. Int. **170,** 337–345 (2007)

Zhao, D.: A tomographic study of seismic velocity structure in the Japan Islands. Ph.D. thesis, Tohoku University (1991)

Zhao, D.: New advances of seismic tomography and its applications to subduction zones and earthquake fault zones. Island Arc **10,** 68–84 (2001a)

Zhao, D.: Seismic structure and origin of hotspots and mantle plumes. Earth Planet. Sci. Lett. **192,** 251–265 (2001b)

Zhao, D.: Global tomographic images of mantle plumes and subducting slabs: Insight into deep Earth dynamics. Phys. Earth Planet. Inter. **146**, 3–34 (2004)

Zhao, D.: Multiscale seismic tomography and mantle dynamics. Gondwana Res. **15,** 297–323 (2009)

Zhao, D.: Tomography and dynamics of Western-Pacific subduction zones. Monogr. Environ. Earth Planets **1,** 1–70 (2012)

Zhao, D., Lei, J.: Seismic ray path variations in a 3-D global velocity model. Phys. Earth Planet. Inter. **141,** 153–166 (2004)

Zhao, D., Mizuno, T.: Crack density and saturation rate in the 1995 Kobe earthquake region. Geophys. Res. Lett. **26,** 3213–3216 (1999)

Zhao, D., Horiuchi, S., Hasegawa, A.: 3-D seismic velocity structure of the crust and uppermost mantle in the northeastern Japan arc. Tectonophysics **181,** 135–149 (1990)

Zhao, D., Hasegawa, A., Horiuchi, S.: Tomographic imaging of P and S wave velocity structure beneath northeastern Japan. J. Geophys. Res. **97,** 19909–19928 (1992)

Zhao, D., Kanamori, H., Negishi, H., Wiens, D.: Tomography of the source area of the 1995 Kobe earthquake: Evidence for fluids at the hypocenter? Science **274,** 1891–1894 (1996)

Zhao, D., Mishra, O.P., Sanda, R.: Influence of fluids and magma on earthquakes: seismological evidence. Phys. Earth Planet. Inter. **132,** 249–267 (2002)

Zhao, D., Todo, S., Lei, J.: Local earthquake reflection tomography of the Landers aftershock area. Earth Planet. Sci. Lett. **235,** 623–631 (2005)

Zhao, D., Wang, Z., Umino, N., Hasegawa, A.: Tomographic imaging outside a seismic network: Application to the northeast Japan arc. Bull. Seismol. Soc. Am. **97,** 1121–1132 (2007)

Zhao, D., Wang, Z., Umino, N., Hasegawa, A.: Mapping the mantle wedge and interplate thrust zone of the northeast Japan arc. Tectonophysics **467,** 89–106 (2009)

Zhao, D., Huang, Z., Umino. N., Hasegawa, A., Kanamori, H.: Structural heterogeneity in the megathrust zone and mechanism of the 2011 Tohoku-oki earthquake (Mw 9.0). Geophys. Res. Lett. **38,** L17308 (2011)

Zhao, D., Yanada, T., Hasegawa, A., Umino, N., Wei, W.: Imaging the subducting slabs and mantle upwelling under the Japan Islands. Geophys. J. Int. **190,** 816–828 (2012)

Zhao, D., Yamamoto, Y., Yanada, T.: Global mantle heterogeneity and its influence on teleseismic regional tomography. Gondwana Res. **23,** 595–616 (2013)

Zheng, Y., Shen, W., Zhou, L., Yang, Y., Xie, Z., Ritzwoller, M.: Crust and uppermost mantle beneath the North China Craton, northeastern China, and the Sea of Japan from ambient noise tomography. J. Geophys. Res. **116,** B12312 (2011)

Chapter 3
Subduction Zone Tomography

Abstract In this chapter, we review recent seismic tomography studies of subduction zones and new insights into arc magmatism, seismotectonics and subduction dynamics. Seismic velocity and attenuation tomography clearly reveals subducting slabs as high-velocity and low-attenuation zones, where intermediate-depth and deep earthquakes occur. In the crust and upper-mantle wedge, low-velocity (low-V) and high-attenuation (low-Q) anomalies are revealed beneath arc and back-arc volcanoes, and they extend to a deeper portion of the mantle wedge, indicating that the low-V and low-Q anomalies reflect source zones of arc magmatism and volcanism which are caused by corner flow in the mantle wedge and fluids from slab dehydration. P-wave anisotropy tomography and shear-wave splitting measurements also provide important constraints on mantle flows and dynamics in subduction zones.

Keywords Subduction zones · Arc magmatism · Seismic tomography · Attenuation · Anisotropy

Subduction zones are convergent plate boundaries which are characterized geographically by deep ocean trenches and island arcs or continental margins; seismically by the most abundant and largest earthquakes and the dipping Wadati-Benioff zone of intermediate-depth and deep earthquakes; tectonically by extensive crustal faulting and mountain building; and magmatically by a trench-parallel linear belt of active volcanoes, i.e., the volcanic front (e.g., Zhao 2001a, 2012). Plate subduction is a fundamental and unique process in terrestrial tectonics and geodynamics. Subduction and arc magmatism play a key role in the differentiation and evolution of the Earth. Therefore, the study of subduction zones is one of the most important subjects in geoscience.

Seismic tomography was applied to study the three-dimensional (3-D) velocity structure of subduction zones soon after the method was proposed, e.g., Hirahara (1977, 1981), Horie and Aki (1982), and Takanami (1982), etc. (see Zhao 2012 for a detailed review of the advent of subduction-zone tomography). Compared with other tectonic settings, subduction zones are particularly adaptable to tomographic studies. This is because abundant shallow and deep earthquakes provide crisscrossing seismic rays in a 3-D volume for a tomographic inversion, and the existence of a cold subducting slab and hot magmas in the crust and the mantle wedge leads to

D. Zhao, *Multiscale Seismic Tomography,* Springer Geophysics,
DOI 10.1007/978-4-431-55360-1_3

strong contrasts in seismic velocity and attenuation which can be imaged by seismic tomography. During the past 3 decades, many important tomographic results have been obtained for subduction zones, which have greatly improved our understanding of subduction dynamics. On the other hand, the special tectonic setting and distribution of seismic rays in a subduction zone have also lead to important technical advances in seismic tomography (see the review by Zhao 2012, and Chap. 2 of this book). It is reasonable to submit that, up to the present, subduction zones are the best test field where seismic tomography has been applied and developed most successfully.

To date, a great number of tomographic studies have been reported for subduction zones, and there have been several reviews on subduction-zone geophysics including tomographic studies (e.g., Zhao 2001a, 2012; Stern 2002; Hasegawa et al. 2009). However, these previous reviews focused on the earlier velocity tomography results of subduction zones. During the past decade, thanks both to advances in seismic instrumentation in many regions and seismological methodology, significant progress has been made in the seismic imaging of subduction zones, including not only high-resolution velocity tomography, but also seismic attenuation and anisotropy tomography. The present review covers these recent tomographic findings and the new insights obtained into arc magmatism and subduction dynamics. For this purpose, we focus on high-resolution local-scale tomographic results relating to the crust and upper mantle of subduction zones. The deep structures of subducting slabs in the mantle transition zone and the lower mantle are covered in Chaps. 6 and 8 of this book.

3.1 Seismic Velocity Tomography

So far, velocity tomographic images obtained for most subduction zones have been determined by mainly using two kinds of travel-time tomographic methods. One is local earthquake tomography (Aki and Lee 1976; Thurber 1983; Zhao et al. 1992) which uses the arrival-time data of local earthquakes in the crust and the subducting slab beneath a seismic network, enabling 3-D velocity tomography to be determined for the crust, the upper-mantle wedge and the upper part of the subducting slab (e.g., Horie and Aki 1982; Takanami 1982; Hasemi et al. 1984; Ishida and Hasemi 1988). Zhao et al. (1992) improved the local tomography method, enabling it to handle complex velocity discontinuities in the study area. Their new method was applied to arrival-time data of first P- and S-waves, as well as PS and SP converted waves at the Moho and the upper boundary of the subducting Pacific slab, resulting in high-resolution P- and S-wave velocity (Vp, Vs) tomography down to a depth of 200 km beneath Northeast Japan (Zhao et al. 1992).

The other widely-used method is teleseismic tomography (Aki et al. 1977) which uses relative travel-time residuals of teleseismic events recorded by a local seismic network, enabling the deeper structure of a subduction zone to be determined. Zhao et al. (1994) proposed to use local and teleseismic data simultaneously in

a tomographic inversion. This joint inversion approach preserves the advantages of local earthquake tomography and teleseismic tomography and overcomes their drawbacks. The horizontally-propagating local rays and vertically-traveling teleseismic rays crisscross well in the shallow portion of the model, which can improve the resolution there.

These tomographic methods have become powerful and effective tools for studying the seismic velocity structure and dynamics of subduction zones. The high-resolution tomographic images obtained have shed new light on the detailed structure and processes in different parts of the subduction factory.

3.1.1 Subducting Slabs

To date, three seismological approaches have been adopted to detect a subducting slab and to estimate the slab geometry. The first approach is to map the Wadati-Benioff deep seismic zone which represents the general morphology of a subducting slab (e.g., Fig. 3.1), because all the intermediate-depth and deep earthquakes (60–700 km depths) take place within the subducting slabs (e.g., Umino and Hasegawa 1975; Hasegawa et al. 1978, 2009; Bevis and Isacks 1984; Ishida 1992; Zhao and Hasegawa 1993; Umino et al. 1995; Syracuse and Abers 2006; Gamage et al. 2009; Hayes et al. 2012; McCrory et al. 2012). The second approach is to use reflected and converted waves generated at the slab boundary, or trapped waves within the subducted oceanic crust, to locate the slab boundary (e.g., Okada 1971, 1979; Snoke et al. 1977; Hasegawa et al. 1978; Nakanishi 1980; Hori et al. 1985; Matsuzawa et al. 1986, 1990; Obara 1989; Zhao et al. 1997a; Ohkura 2000; Martin et al. 2003; Abers 2005; Osada et al. 2010; Horleston and Helffrich 2012; Miyoshi et al. 2012; Shiina et al. 2013). Teleseismic receiver functions also belong to this approach because P to S converted waves at the slab boundary are processed (e.g., Yuan et al. 2000; Kind et al. 2002; Ferris et al. 2003; Shiomi et al. 2004; Ai et al. 2005; Kawakatsu and Watada 2007; Igarashi 2009; Iidaka et al. 2009; MacKenzie et al. 2010; Melgar and Perez-Campos 2011; Kim et al. 2012, 2013; Abe et al. 2013; Bostock 2013). The third approach for detecting subducting slabs is tomographic imaging. Subducting slabs are colder than the surrounding mantle and so they always exhibit a faster seismic velocity, which can be imaged by seismic tomography.

Each of the three approaches has advantages and drawbacks. The first approach is straightforward; however, it can only express the seismogenic parts of a subducting slab and cannot show aseismic slabs (e.g., Zhao et al. 2012; Huang et al. 2013). The upper surface of the Wadati-Benioff zone is actually different from the slab upper boundary. Detailed studies of PS and SP converted phases in NE Japan show that the slab upper boundary is actually slightly shallower than the upper surface of the Wadati-Benioff zone (e.g., Matsuzawa et al. 1986, 1990; Zhao et al. 1997a). In addition, poor hypocentral locations of intermediate-depth and deep earthquakes would cause uncertainty of the Wadati-Benioff zone. The second approach can determine the precise location and geometry of the slab boundary for both seismic

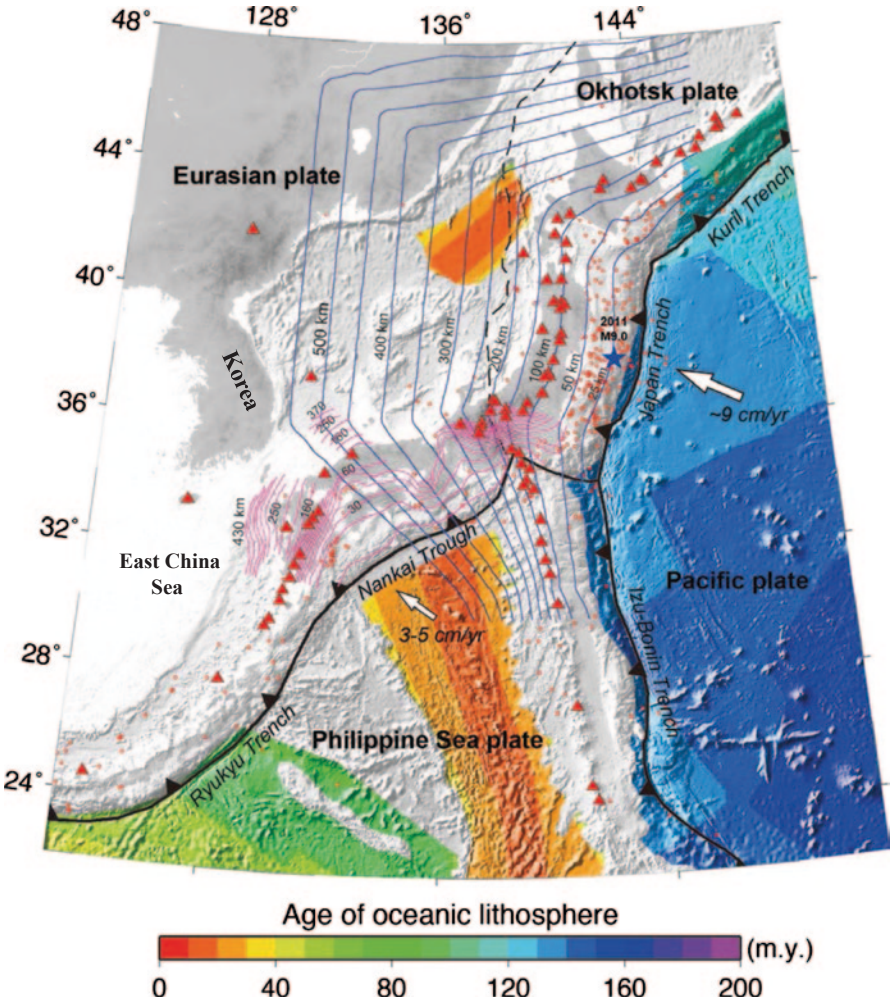

Fig. 3.1 Tectonic settings of the Japan subduction zone. The solid *sawtooth* lines and the *black dashed* line denote the plate boundaries. The *red triangles* denote active volcanoes. The *thin blue* and *pink lines* denote the depth contours to the *upper* boundary of the subducting Pacific slab and that of the subducting Philippine Sea slab, respectively. (Modified from Liu et al. 2013a)

and aseismic slabs. However, a (dense) seismic network is required to detect the slab-related later phases, but such later phases may not be detected easily, even if a dense seismic network is available, because the later phases may not show up if the slab boundary is not sharp enough. Teleseismic receiver-functions can detect the slab boundary, but there are usually large uncertainties in the location of the slab boundary, amounting to 10 km or even greater. The third approach, seismic tomography, can detect a slab-related high-velocity (high-V) anomaly, but it cannot determine the precise location of the slab boundary as do later-phase studies. Because of the limited resolution of a tomographic model, slab-related high-V anomalies are

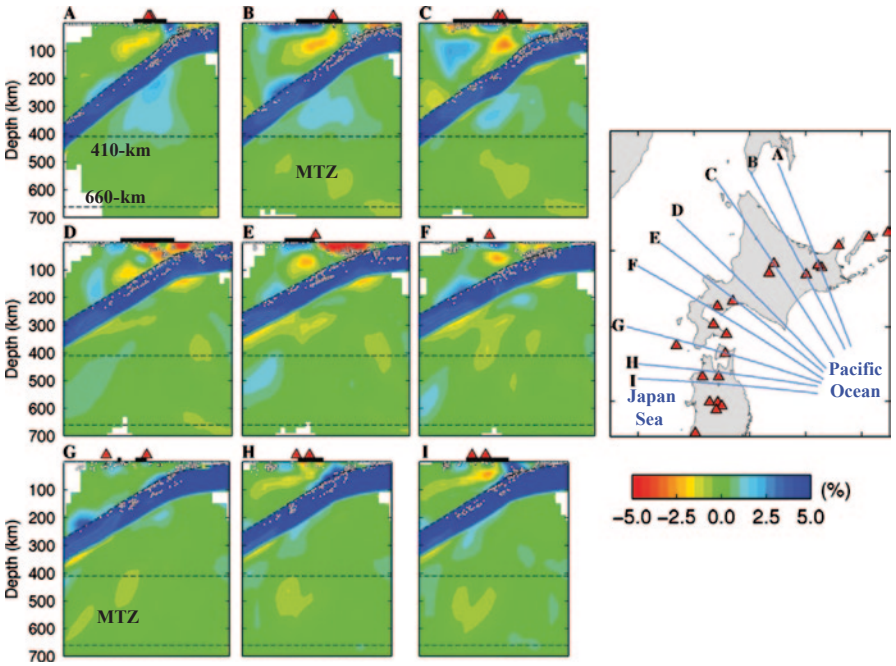

Fig. 3.2 Vertical cross-sections of P-wave tomography along the profiles shown on the inset map. *Red* and *blue* colors denote low and high velocities, respectively. The velocity perturbation (in %) scale is shown below the inset map. The *red triangles* denote the active arc volcanoes. The *black bar* atop each cross-section denotes the land area. The two *dashed lines* in each cross-section represent the 410 and 660 km discontinuities. The *white dots* denote seismicity that occurred within a 20 km width of each profile. MTZ is the mantle transition zone. (Modified from Zhao et al. 2012)

usually blurred, and hence the thickness and geometry of the slab are usually hard to estimate precisely from the tomographic images.

In well-studied subduction zones, such as Japan, the three approaches have been used jointly to study the fine structures of the subducting Pacific and Philippine Sea (PHS) slabs (e.g., Figs. 3.1, 3.2, 3.3, 3.4, 3.5, 3.6, 3.7, 3.8, 3.9 and 3.10). The subducting Pacific slab beneath Japan is clearly imaged as a high-V zone which has a thickness of 85–90 km and a P-wave velocity 4–6 % faster than that of the surrounding mantle (e.g., Zhao et al. 1994, 2012; Hasegawa et al. 2009; Huang et al. 2011a). Intermediate-depth earthquakes form a clear double seismic zone within the Pacific slab down to ~180 km depth under NE Japan (e.g., Umino and Hasegawa 1975; Hasegawa et al. 1978; Gamage et al. 2009). The double seismic zone within a subducting slab has also been found in many other subduction zones in the world (see the reviews by Peacock 2001; Hasegawa et al. 2009). The young PHS slab under SW Japan has a thickness of 30–50 km (e.g., Zhao et al. 2000, 2011a; Wang and Zhao 2006a; Xia et al. 2008). Recently, it has been revealed that the PHS slab has subducted aseismically down to a depth of 430–460 km beneath the back-arc region of the SW Japan arc (Zhao et al. 2012; Huang et al. 2013) (Figs. 3.5 and 3.6).

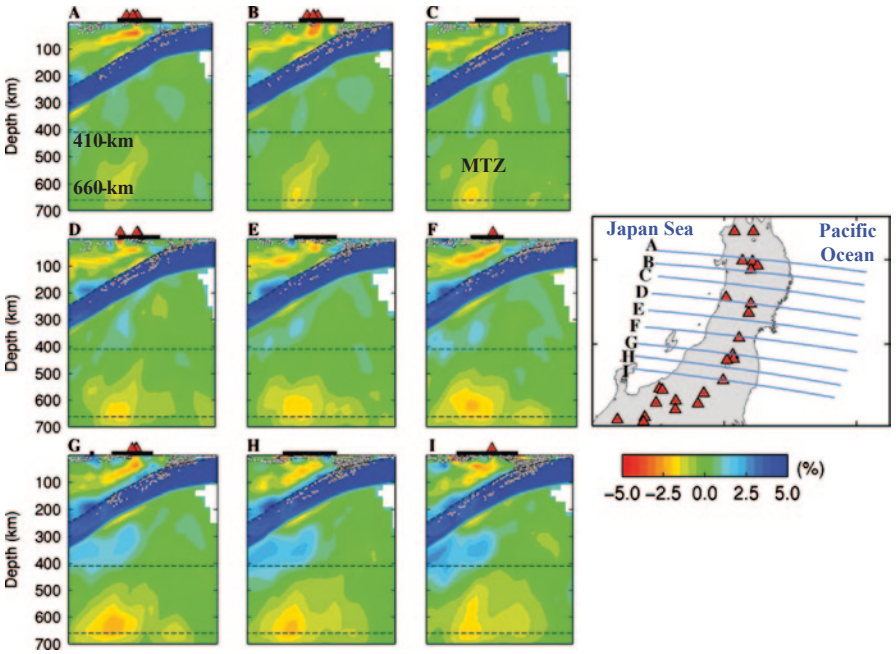

Fig. 3.3 The same as Fig. 3.2 but for vertical cross-sections beneath Tohoku as shown on the inset map. (Modified from Zhao et al. 2012)

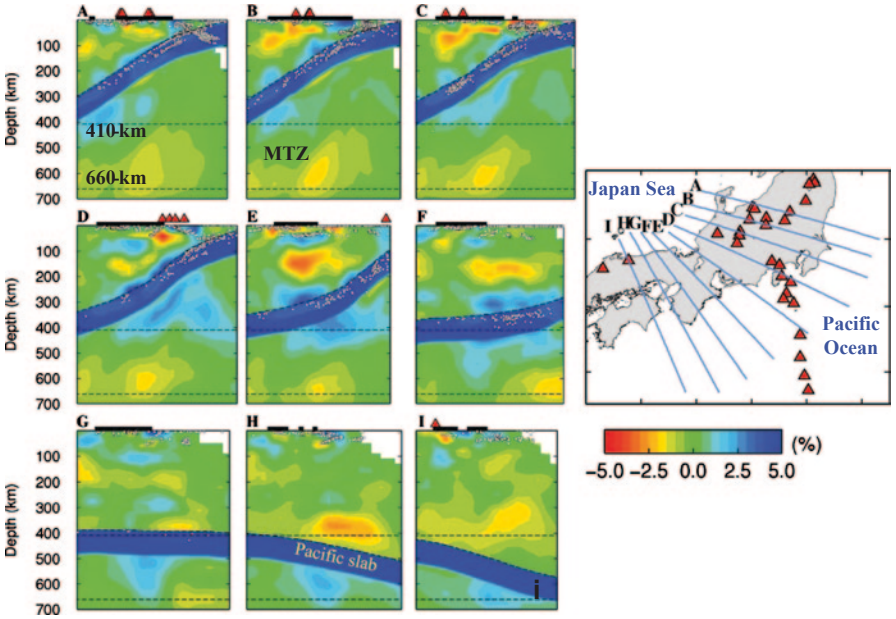

Fig. 3.4 The same as Fig. 3.2 but for different vertical cross-sections as shown on the inset map. (Modified from Zhao et al. 2012)

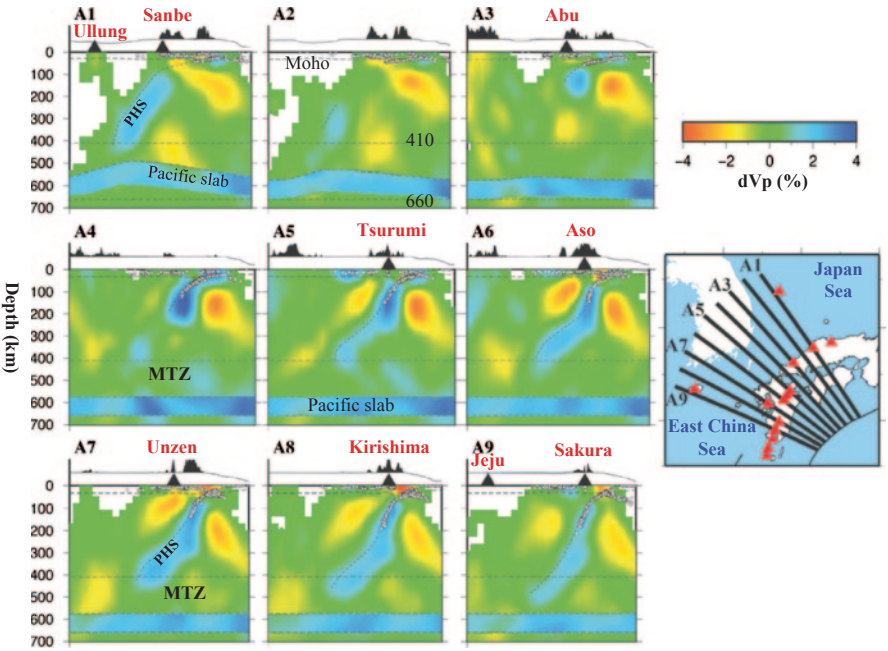

Fig. 3.5 Vertical cross-sections of P-wave tomography along the profiles shown on the inset map. *Red* and *blue* colors denote lower and higher velocities (in %), respectively. The velocity perturbation scale is shown on the *right*. The *red and black triangles* denote active volcanoes. The surface topography is shown atop each cross-section. The three *dashed lines* in each cross-section represent the Moho, 410- and 660 km discontinuities. The *white dots* denote seismicity that occurred within a 20-km width of each profile. The estimated *upper* boundary of the subducting Philippine Sea slab (*PHS*) is shown by a *dashed line*. *MTZ* indicates the mantle transition zone. (Modified from Huang et al. 2013)

The interior structure of subducting slabs appears to be very heterogeneous. The subducted oceanic crust is revealed at the top of subducting slabs under many regions, and has a thickness of < 10 km (e.g., Hori et al. 1985; Matsuzawa et al. 1986; Abers and Sarker 1996; Martin et al. 2003; Abers 2005; Xia et al. 2008; Abe et al. 2013; Shiina et al. 2013). Tomographic images also show velocity variations within the subducting slabs, which may be associated with the inhomogeneous distribution of intraslab earthquakes (e.g., Zhao et al. 1992, 2002; Nakajima et al. 2001; Peacock 2001; Mishra and Zhao 2004; Kita et al. 2006; Hasegawa et al. 2009; Huang et al. 2011a; Abers et al. 2013). Forward-modeling of deep-earthquake travel times and receiver-function studies revealed a thin low-V zone within the subducting Pacific slab in the mantle transition zone (410–660 km depth), which may reflect a metastable olivine wedge probably associated with the generation of deep-focus earthquakes (e.g., Iidaka and Suetsugu 1992; Kaneshima et al. 2007; Jiang et al. 2008; Jiang and Zhao 2011; Kawakatsu and Yoshioka 2011). However, fine structures of

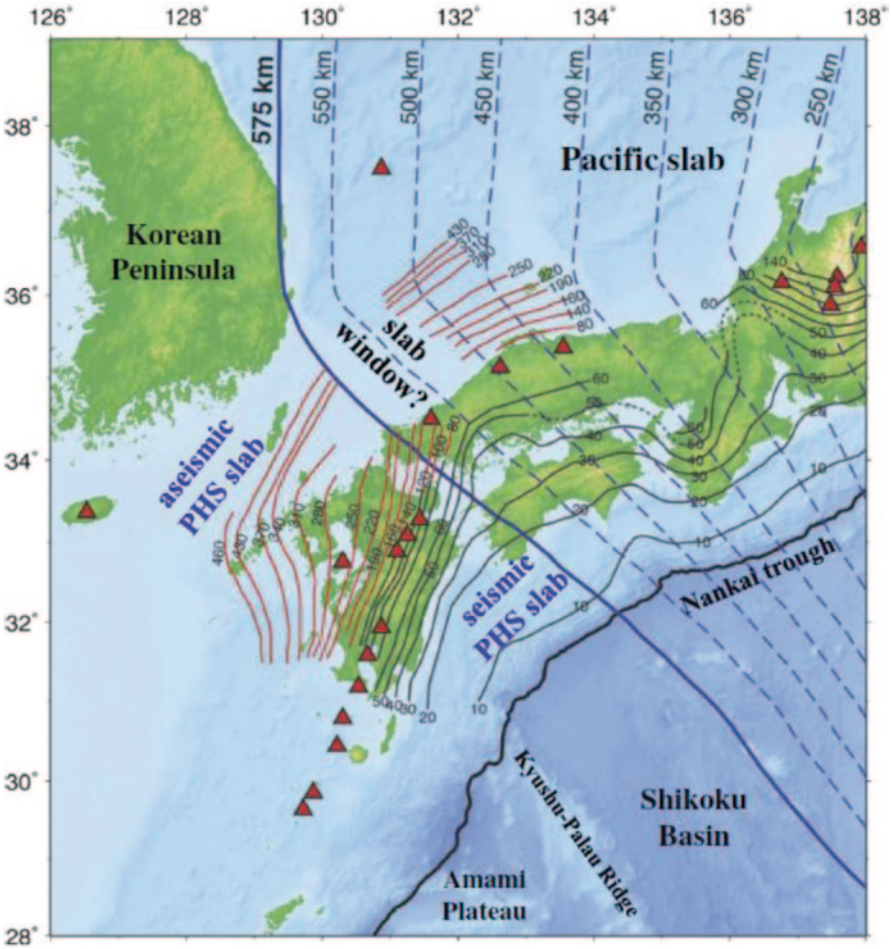

Fig. 3.6 Depth contours to the *upper* boundary of the subducting Pacific slab (*the blue dashed lines*) and that of the subducting Philippine Sea (*PHS*) slab. The *bold blue line* denotes the 575 km depth contour of the Pacific slab which becomes stagnant in the mantle transition zone to the west of the contour line, according to Zhao (2004). The *gray lines* denote the seismic parts of the PHS slab estimated from the seismicity in the PHS slab and local-earthquake tomography (Nakajima et al. 2009). The *red lines* show the upper boundary of the aseismic PHS slab estimated from the teleseismic tomography (Zhao et al. 2012; Huang et al. 2013). The *red triangles* denote active volcanoes. (Modified from Huang et al. 2013)

the subducting slabs are still not yet well resolved, which will be an important subject of future studies when better seismological data become available; in particular, waveform data from ocean-bottom-seismometer (OBS) networks deployed in the marginal seas of the back-arc areas where intermediate-depth and deep earthquakes take place.

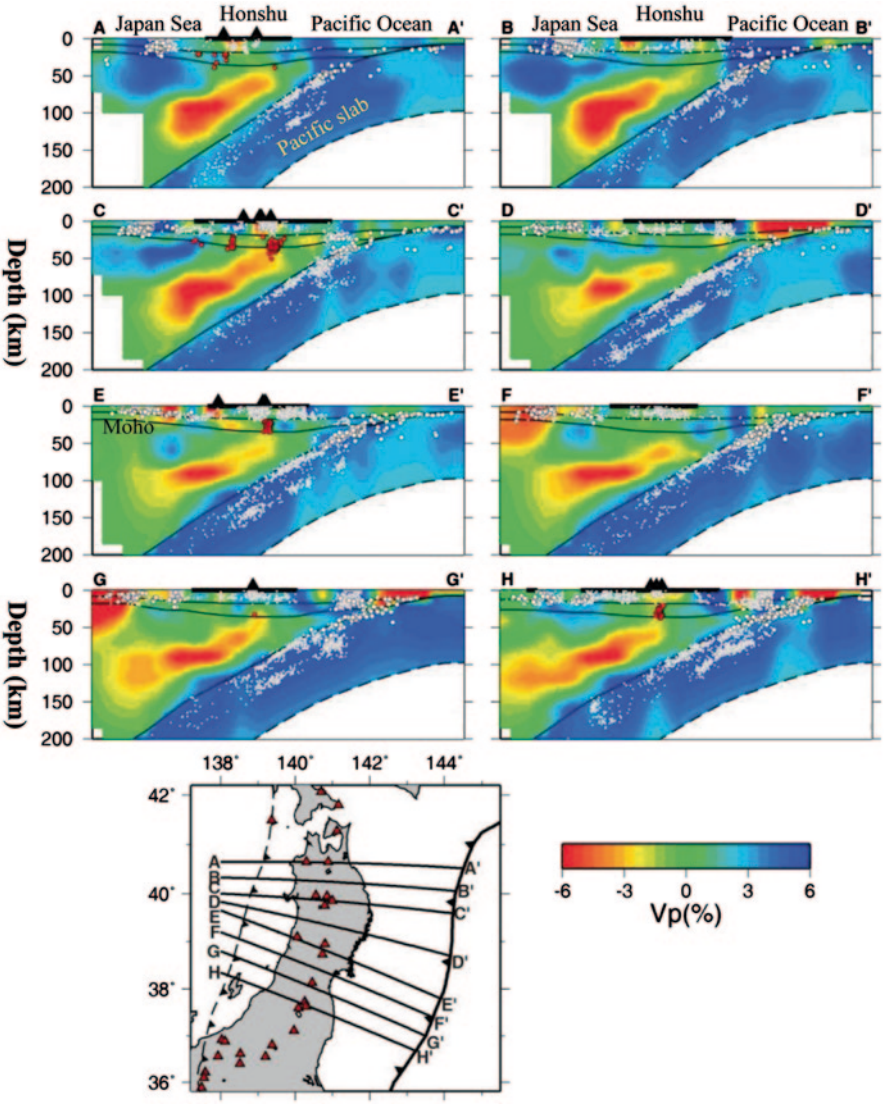

Fig. 3.7 The same as Fig. 3.2 but for P-wave velocity tomography under NE Japan down to a depth of 200 km. The three *black lines* denote the Conrad and Moho discontinuities and the *upper* boundary of the subducting Pacific slab. The *dashed lines* denote the estimated *lower* boundary of the slab. The *red dots* denote low-frequency microearthquakes. (Modified from Huang et al. 2011a)

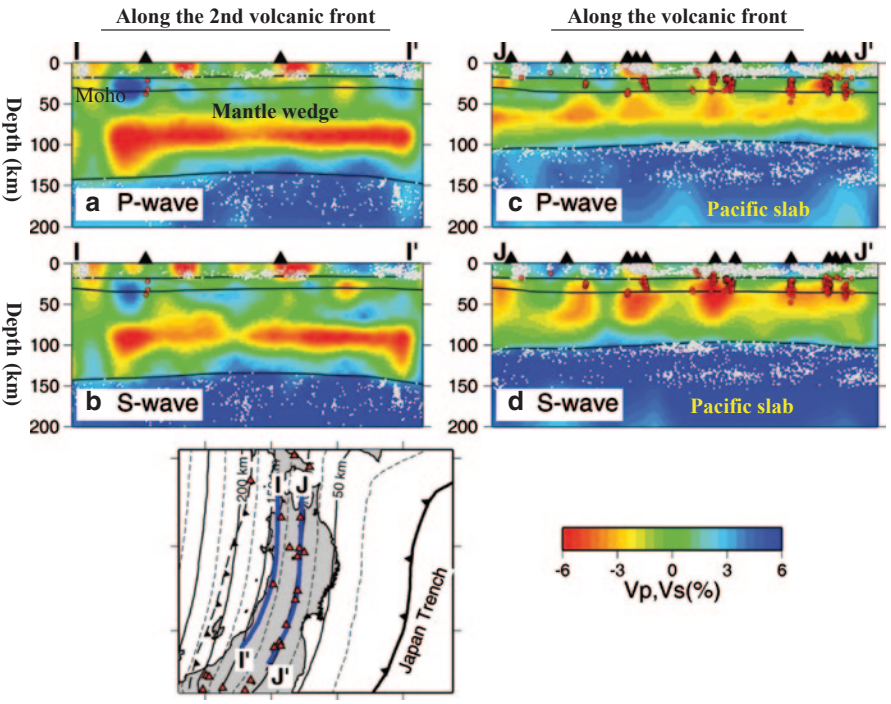

Fig. 3.8 Vertical cross-sections of (**a**, **c**) P- and (**b**, **d**) S-wave tomography along the volcanic front (**c**, **d**) and the Japan Sea coast (**a**, **b**) in NE Japan. Other labeling is the same as that in Fig. 3.7. (Modified from Huang et al. 2011a)

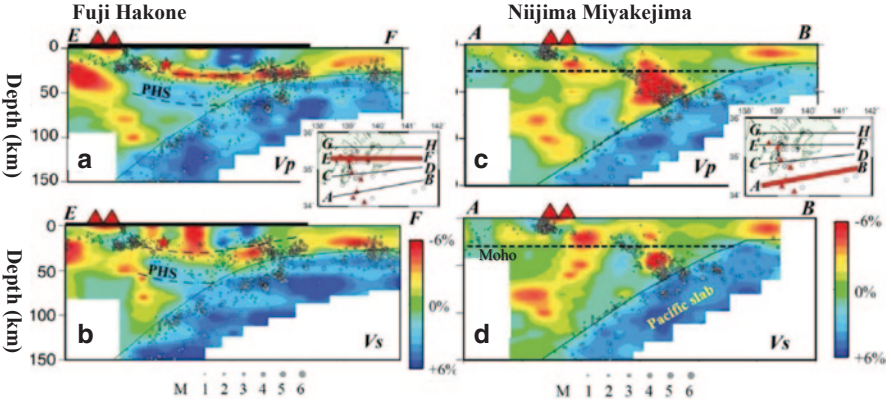

Fig. 3.9 The same as Fig. 3.7 but (**a**, **c**) P- and (**b**, **d**) S-wave tomography under the Kanto-Izu area. In (**a**, **b**), the *dashed lines* denote the estimated *upper* and *lower* boundaries of the Philippine Sea slab, and the *red stars* denote the 1923 Kanto earthquake (*M 7.9*). The *dashed lines* in (**c**, **d**) denote the Moho discontinuity. (Modified from Wang and Zhao 2006b)

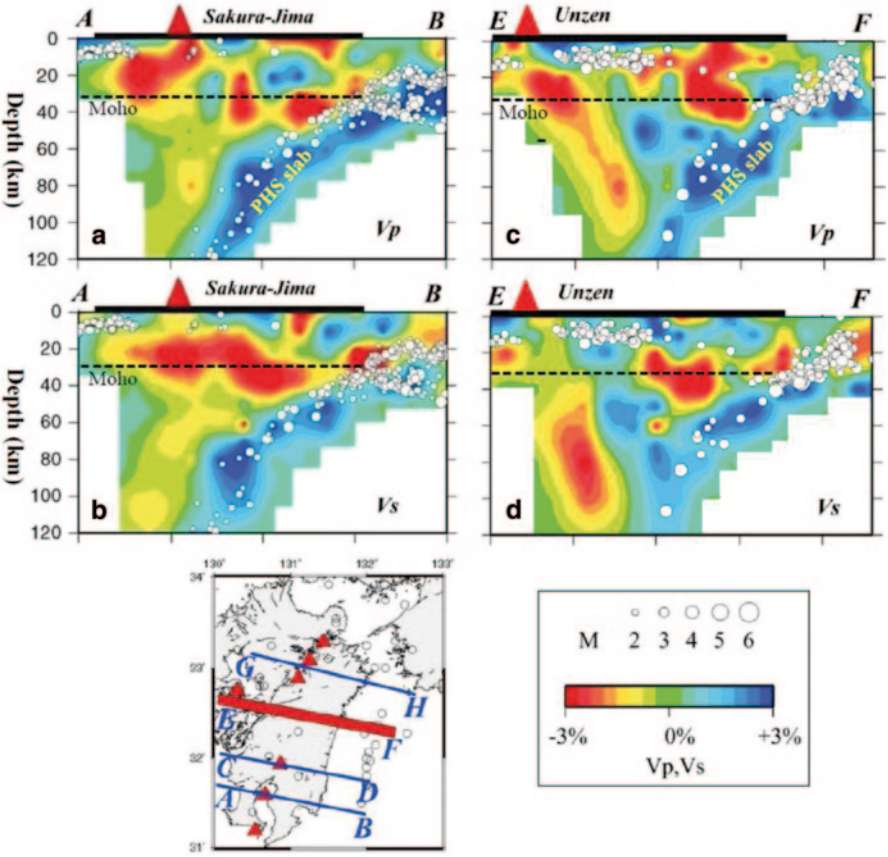

Fig. 3.10 The same as Fig. 3.9 but P- and S-wave tomography under Kyushu. The *dashed lines* denote the Moho discontinuity. (Modified from Wang and Zhao 2006a)

3.1.2 Mantle Wedge and Arc Magmatism

One of the important findings of subduction-zone tomography is the detection of low-V anomalies in the mantle wedge beneath the volcanic front and back-arc areas, which reflect the source zone of arc magmatism and volcanism (e.g., Figs. 3.2, 3.3, 3.4, 3.5, 3.7, 3.8, 3.9, 3.10, 3.11, 3.12 and 3.13). This seismological feature has been found in all subduction zones which have been studied using seismic tomography (e.g., Zhao et al. 1992, 1995, 2000; Hasegawa and Zhao 1994; Ma et al. 1996; Nakajima et al. 2001; McNamara and Pasyanos 2002; Nakamura et al. 2003, 2008; Wagner et al. 2005, 2010; Wang and Zhao 2005, 2006a, b; Katsumata et al. 2006; Matsubara et al. 2008; Wiens et al. 2008; van Stiphout et al. 2009; Schmandt and Humphreys 2010; Huang et al. 2011a; Bianchi et al. 2013; Liu et al. 2013a, b, and many other references mentioned in this and the following sections). This seismic

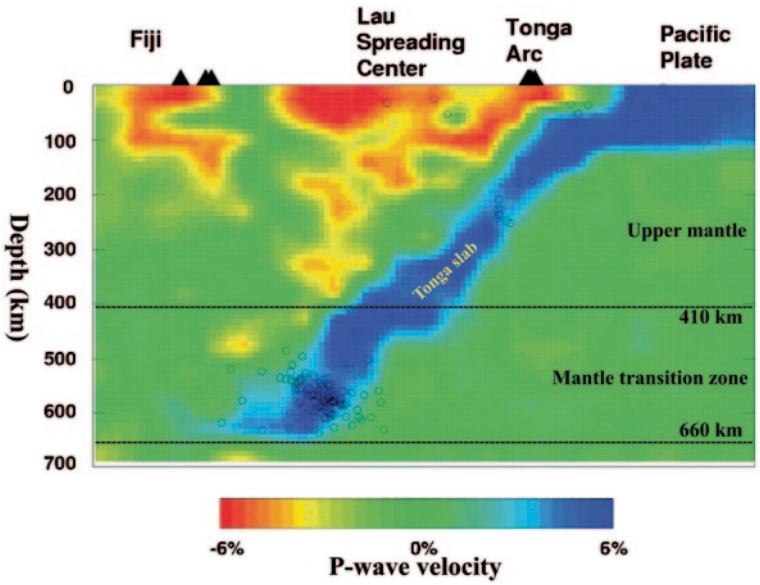

Fig. 3.11 The same as Fig. 3.10 but an *east-west* vertical cross-section of P-wave velocity tomography under the Tonga-Fiji region. (Modified from Zhao et al. 1997b)

feature is also consistent with the petrologic results (e.g., Tatsumi 1989; Peacock 1990; Iwamori and Zhao 2000; Hacker et al. 2003), indicating that arc magmatism and volcanism are caused by the joint effects of fluids from slab dehydration and corner flow in the mantle wedge.

Because of the thermal gradient in the upper mantle, convective circulation can bring heat from the deeper part to the shallower part, and so increase the temperature in the mantle wedge. Fluids from the slab dehydration can reduce the melting point of rocks. Hence, the two effects together lead to partial melting in the mantle wedge beneath the volcanic front and the back-arc area, producing arc magmas which are imaged as low-V and high Poisson's ratio anomalies by seismic tomography. The existence of mantle-wedge low-V zones is a general seismological feature of subduction zones (Zhao et al. 1995; Zhao 2012), which have been revealed in all the subduction regions imaged by seismic tomography.

Beneath the Tohoku arc, the low-V zones in the mantle wedge are continuous under the back-arc area along the Japan Sea coast (Fig. 3.8a, b), whereas they become intermittent under the volcanic front, and localized low-V anomalies are visible beneath each group of active arc volcanoes (Fig. 3.8c, d). Low-frequency microearthquakes are found to occur in or around the low-V zones in the lower crust and uppermost mantle (Figs. 3.7 and 3.8), which are associated with magmatic activity beneath the volcanic front and the back-arc area (e.g., Hasegawa and Yamamoto 1994; Nakamichi et al. 2003). Clear S-wave reflectors are also detected in the upper and lower crust beneath the active volcanoes in NE Japan, which reflect sheets of cracks containing melts or magmatic fluids (e.g., Matsumoto and Hasegawa 1996;

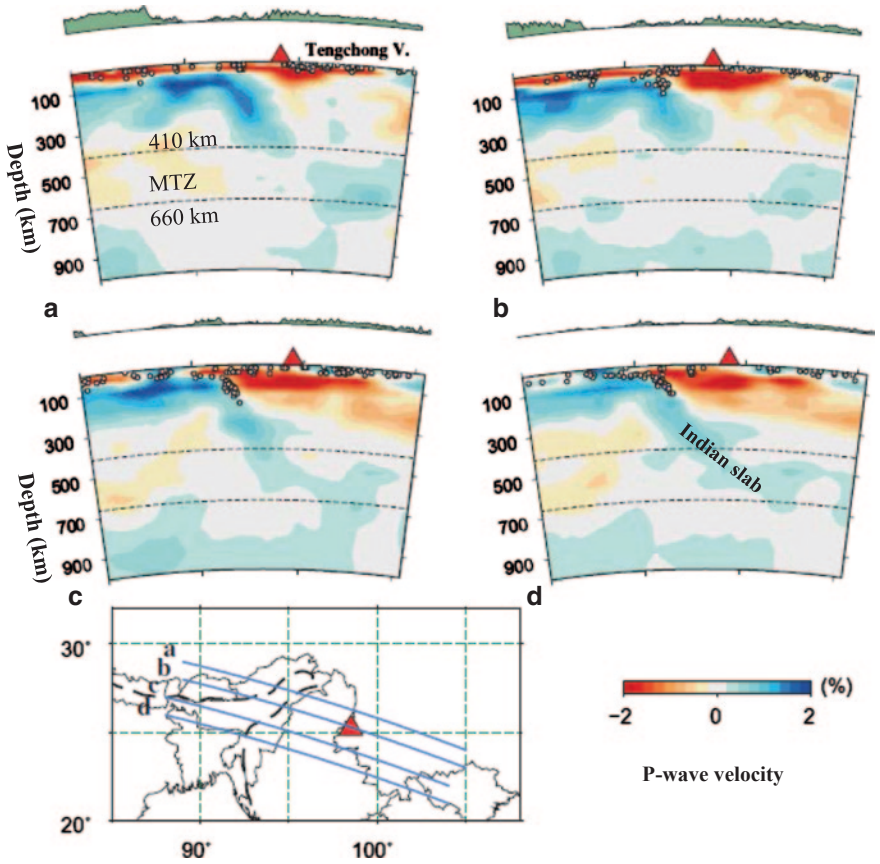

Fig. 3.12 The same as Fig. 3.11 but four vertical cross-sections of P-wave velocity tomography under the active Tengchong volcano in Eastern Tibet and SW China. The surface topography along each profile is shown above each cross-section. (Modified from Wei et al. 2012)

Horiuchi et al. 1997). Magnetotelluric soundings have revealed high-conductivity anomalies in the crust and upper mantle wedge under NE Japan (e.g., Ogawa et al. 2001; Toh et al. 2006; Mishina 2009), consistent with seismological results. The spatial correlation between active volcanoes, low-V zones in the crust and mantle wedge, and low-frequency microearthquakes is also found in SW Japan (e.g., Zhao et al. 2004, 2011a; Liu et al. 2013b).

Based on geological and geophysical findings, including high-resolution tomography (Zhao et al. 1992), Tamura et al. (2002) proposed a hot finger model to explain the along-arc variation in the volcanism in NE Japan. They suggested that the quaternary volcanoes in Tohoku can be grouped into ten volcanic clusters along the arc, which have an average width of 50 km, and are separated by parallel gaps 30–75 km wide. The clustering of volcanoes, topographic profiles, mantle-wedge low-V zones, and local negative gravity anomalies are closely correlated. All these features may be related to locally-developed hot fingers within the mantle wedge.

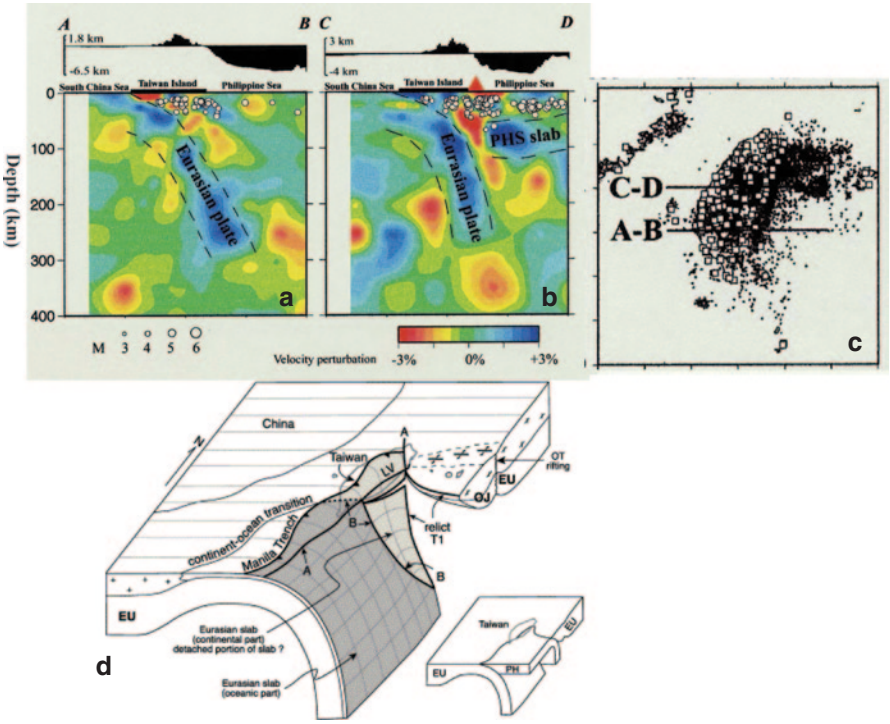

Fig. 3.13 (**a**, **b**) *East-west* vertical cross-sections of P-wave tomography beneath South Taiwan determined by Wang et al. (2006b). Locations of the cross-sections are shown in (**c**). *Red* and *blue* colors denote slow and fast velocities, respectively. The velocity perturbation scale is shown below (**b**). The *red triangle* and the *thick lines* on the top denote a volcano and the land area, respectively. Earthquakes within a 30-km width of each profile are shown with *white dots*. (**d**) Schematic diagram showing the major tectonic features in and around Taiwan (after Lallemand et al. 2001)

Each of the ten fingers extends from ~150 km depth under the back-arc towards the uppermost mantle under the volcanic front. The arc volcanoes are built immediately above the hot fingers. The volcanic basement along the fingers has been uplifted by repeated injection of magmas into the crust, accompanied by quaternary volcanic activity at the surface (Tamura et al. 2002).

It is still not clear whether mantle-wedge hot fingers exist in other subduction zones or not. This is now an interesting and important research subject.

3.1.3 Fore-Arc Processes

Tomographic images of the fore-arc areas from the Japan Trench to the Pacific coast shed new light on the generating mechanism of megathrust earthquakes, such as the great 2011 Tohoku-oki earthquake (Mw 9.0) sequence (Zhao et al. 2011b; Huang and Zhao 2013a, b; Liu et al. 2013a, 2014). Significant lateral velocity variations

are revealed in the interplate megathrust zone, and most of the large megathrust earthquakes ($M \geq 7.0$) which occurred between 1900 and 2013 are situated in or around high-V patches. These high-V zones may represent high-strength asperities at the slab interface where the subducting Pacific plate and the overriding Okhotsk plate are strongly coupled. A shallow high-V zone with large coseismic slip near the Japan Trench may account for the asperity of the 2011 Tohoku-oki main shock (Mw 9.0). Similar features are also found in the fore-arc area of the SW Japan arc (Wang and Zhao 2006a; Liu et al. 2013b). These results indicate that the rupture nucleation of megathrust earthquakes is controlled by structural heterogeneities in the megathrust zone (Zhao et al. 2002, 2011b; Mishra et al. 2003; Wang and Zhao 2005, 2006a; Yamamoto et al. 2011; Collings et al. 2012; Fujie et al. 2013a; Huang and Zhao 2013a, b; Moreno et al. 2014). For details on the mechanism of megathrust earthquakes, see Chap. 4.

Fujie et al. (2013b) conducted a seismic refraction and reflection survey in the outer rise region of the Kuril trench and have revealed systematic changes in Vp, Vs and Vp/Vs. Their results suggest that water content within the Pacific plate increases toward the trench accompanied by the development of bending-related fractures at the top of the oceanic crust, consistent with seawater percolation (e.g., Faccenda et al. 2009). Moreover, their results suggest that plate bending and fracturing during the bending in the outer rise of the trench play an important role in the water cycle of subduction zones.

Significant low-V anomalies have been revealed in the fore-arc mantle wedge beneath Kanto-Tokai and SW Japan (Figs. 3.9 and 3.10), which may reflect the subducting oceanic crust and fore-arc mantle serpentinization (Kamiya and Kobayashi 2000; Zhao et al. 2000, 2011a; Seno et al. 2001; Wang and Zhao 2006a, b; Xia et al. 2008). The significant low-V anomaly in the fore-arc mantle wedge, and even in the upper part of the subducting slab, has also been found in many other subduction zones, in particular, above the young and warm subducting slabs, which indicates the presence of partially-hydrated mantle, most likely serpentinite, as a result of slab dehydration associated with the transformation of metabasalt to eclogite (e.g., Graeber and Asch 1999; Husen et al. 2000; Zhao et al. 2001; Abers et al. 2003; Carlson and Miller 2003; Hacker et al. 2003; Hyndman and Peacock 2003; DeShon and Schwartz 2004; Ramachandran et al. 2005; Rondenay et al. 2008; Syracuse et al. 2008; Tibi et al. 2008; Wada et al. 2008; Nikulin et al. 2009; Kodaira et al. 2010; Obana et al. 2010; Worzewski et al. 2010; Van Avendonk et al. 2011; Collings et al. 2012; Ramachandran and Hyndman 2012; Laigle et al. 2013; Moreno et al. 2014).

Low-frequency microearthquakes are also found in the lower crust beneath the SW Japan fore-arc and non-volcanic areas of the Japan Islands (e.g., Obara 2002; Katsumata and Kamaya 2003; Seno and Yamasaki 2003; Wang et al. 2006a), as well as other subduction zones (see the detailed review by Schwartz and Rokosky 2007; Vidale et al. 2014). The low-frequency events are generally considered to be associated with the slab dehydration reactions. Zhao et al. (2011a) combined seismic tomography and low-frequency events to study fluid and magmatic activity in SW Japan. In the source areas of the 1995 Kobe earthquake (M 7.2) and the 2000 Tottori earthquake (M 7.3), low-frequency events were detected, supporting the early

suggestion that large crustal earthquakes can be triggered by crustal fluids derived from slab dehydration (Zhao et al. 1996, 2004; Salah and Zhao 2003a; Tong et al. 2011, 2012).

Chou et al. (2009) determined the Vp and Vs tomography of the subducting Philippine Sea slab and the fore-arc mantle beneath Northeast Taiwan and the westernmost Ryukyu arc. The subducting Philippine Sea slab exhibits high Vp, high Vs and intermediate to low Vp/Vs. At a depth of 30–80 km in the mantle wedge, significant high Vp/Vs anomalies were revealed. They estimated that the slab is cooled by 200–400℃ relative to the mantle. The serpentinization reaches ~15% at a depth of 50 km in the fore-arc mantle, which is caused by water released from the basalt-eclogite metamorphic reaction in the oceanic crust of the subducting slab (Chou et al. 2009).

3.1.4 Back-Arc Spreading

Back-arc spreading is an important process in subduction zones, but it is still less studied seismologically compared with arc and fore-arc processes, because there are fewer seismic stations available in the marginal seas where back-arc spreading takes place. Geophysical imaging of back-arc spreading centers is important because the width and depth of the hot anomalies below spreading centers provide information on the origin of back-arc spreading, the geochemical source of arc and back-arc magmas, the interaction between the subducting slab and back-arc spreading, whether the mantle upwelling beneath spreading centers is passive or active, and to what depth the upwelling persists (e.g., Zhao et al. 1997b; Volti et al. 2006; Matsuno et al. 2012; Arai and Dunn 2014). The Tonga-Fiji region is an optimal region for clarifying these issues, because it is a subduction zone with an associated back-arc spreading center, and deep earthquakes occur actively beneath the center, providing ideal conditions to image and understand the back-arc spreading processes (Zhao et al. 1997b).

High-resolution tomographic images of the upper mantle beneath the Tonga arc and the Lau back-arc are determined using a large number of arrival-time data recorded by land-based, and ocean-bottom-seismometer (OBS), stations (Zhao et al. 1997b; Conder and Wiens 2006). The subducting Tonga slab is clearly imaged as a high-V zone which is about 100 km thick and has a P-wave velocity 4–6% higher than the normal mantle (Fig. 3.11). Low-V anomalies of up to 6% are revealed beneath the Tonga arc and the Lau back-arc. The low-V zone beneath the Tonga arc dips toward the back-arc side and is located 30–50 km above the Tonga slab, extending from the surface to a depth of ~140 km. This feature is similar to the low-V zones found in the mantle wedge of other subduction zones such as Japan and Alaska (Zhao et al. 1992, 1995; Huang et al. 2011a; Tian and Zhao 2012). Beneath a depth of 100 km, the amplitude of the low-V zone under the back-arc is reduced, but a low-V anomaly (−2–−4%) is still visible down to a depth of at least 400 km. The deep extension of the low-V zones in the mantle wedge has been confirmed

by detailed resolution analyses (Zhao et al. 1997b; Conder and Wiens 2006), and is consistent with the results of seismic attenuation tomography (Roth et al. 1999, 2000) and waveform modeling (Xu and Wiens 1997).

These seismological results suggest that the geodynamic system associated with back-arc spreading is not limited to shallow areas, but is related to deep processes (Zhao et al. 1997b). The low-V zones at a depth of 300–400 km in the mantle wedge (Fig. 3.11) are caused by the joint effects of corner flows in the mantle wedge and fluids from deep dehydration reactions in the subducting Tonga slab (e.g., Nolet 1995; Zhao et al. 1997b; Zhao and Ohtani 2009). The subduction rate of the Tonga slab is very large (16–24 cm/year), and hence, the temperature in the slab is low enough for water to reach the stability depths of dense hydrous magnesian silicate phases (e.g., Parson and Wright 1996; Taylor et al. 1996; Ohtani et al. 2004; Zhao and Ohtani 2009), which allows water penetration down to the mantle transition zone.

The low-V zones under the Tonga arc and the Lau back-arc are separated at depths < 100 km, but they merge in deeper areas (Fig. 3.11). This feature suggests that although the arc and back-arc magma systems are separated at shallow levels, where most of the magma is produced, there may be some interchange between the two magmatic systems at depths > 100 km. Interchange with the slab-derived fluids in the deeper areas may explain some of the unique features of the petrology of back-arc magmas relative to typical mid-ocean ridge basalts, including excess volatiles and large ion lithophile enrichment (e.g., Faul et al. 1994; Zhao et al. 1997b; Conder and Wiens 2006).

Similar low-V anomalies are also revealed in the deep part (400–500 km depths) of the mantle wedge above the Pacific slab under SW Japan (Figs. 3.4 and 3.5) as well as in the big mantle wedge under the active intraplate volcanoes in NE Asia (Zhao et al. 2009, 2012; Huang and Zhao 2006; Duan et al. 2009; Wei et al. 2012; Zhao and Tian 2013). These low-V zones may also reflect the existence of fluids from the deep dehydration of the Pacific slab, because the deep upper mantle under NE China exhibits a high electric conductivity (Ichiki et al. 2006). The subduction rate of the Pacific plate is also fast (7–10 cm/year) at the Japan Trench, and so some hydrous minerals can be brought down to the mantle transition zone depth where dehydration reactions take place to release fluids (Ohtani and Zhao 2009). The frequent generation of large deep earthquakes in the Pacific slab under the NE Asia continental margin may release more fluids preserved within the slab to the overlying mantle wedge, causing additional magmas feeding the active Changbai intraplate volcano (Zhao and Tian 2013).

3.1.5 Sub-Slab Structure

High-resolution teleseismic tomography revealed low-V anomalies in the mantle below the Pacific slab under NE and central Japan (Figs. 3.3 and 3.4). Extensive synthetic tests have been conducted, which have indicated that this is a reliable

feature (Zhao et al. 2012). Being driven by the gravitational force, the subducting Pacific slab continues to sink down to the boundary between the upper and lower mantle—the 660-km discontinuity—where the sudden increase in viscosity will not allow direct slab penetration into the lower mantle (e.g., Turcotte and Schubert 2001). Thus, the Pacific slab becomes stagnant in the mantle transition zone and finally collapses down to the lower mantle as a result of a very large gravitational instability from phase transitions (Maruyama 1994; Fukao et al. 2001; Zhao 2004; Maruyama et al. 2007). This causes turbulence and thermal instability in the mantle transition zone and the lower mantle, and mantle upwelling takes place as a consequence of thermal instability at the thermal boundary layer (Albers and Christensen 1996). The low-V anomalies in the mantle below the Pacific slab may be a result of hot upwelling flow associated with the collapsing of the Pacific slab materials down to the lower mantle (Zhao 2001b, 2004; Abdelwahed and Zhao 2007; Zhao et al. 2012). Another possibility is that the low-V anomalies might be produced in the Pacific superplume region and carried toward the Japan Islands by the horizontal flow associated with the plate movement, and then dragged down by the subducting Pacific slab (Honda et al. 2007).

The deep-subduction related hot mantle upwelling has been also revealed in other regions. For example, recent geophysical and geochemical studies show that a young mantle plume exists under the Hainan hotspot in South China, and that the Hainan plume is caused by thermal instability associated with the Indian plate's deep subduction in the west and the Pacific and PHS slabs' deep subduction in the east down to the lower mantle (Zhao and Liu 2010; Wang et al. 2012).

As mentioned in the last section, low-V zones have also been revealed below the PHS slab under SW Japan (Fig. 3.5), which reflect hot upwelling flows in the big mantle wedge above the Pacific slab, associated with fluids from deep dehydration of the Pacific slab. The hot upwelling from below may change the geometry of the PHS slab, causing a slab window, and elevating the slab temperature, and hence, the PHS slab becomes aseismic at a shallow depth (~100 km) under SW Japan (Zhao et al. 2012; Huang et al. 2013).

3.1.6 Continental Plate Subductions

In most subduction zones, it is an oceanic plate that is subducting beneath a continental plate or a younger oceanic plate. Abundant arc magmas are produced in the mantle wedge, resulting in a clear volcanic front consisting of many arc volcanoes, probably because the oceanic plate contains an abundance of fluids before its subduction.

A continental plate can also subduct into the mantle. A typical example is the Indian lithosphere that is descending beneath the Eurasian plate, resulting in the Tibetan Plateau. The subducting Indian plate is clearly imaged as a high-V zone beneath western, central and eastern parts of Tibet by teleseismic tomography using data recorded by portable seismic stations so far deployed along several profiles in

the Tibetan Plateau (e.g., Zheng et al. 2007; He et al. 2010; Zhang et al. 2012, 2014; Zhao et al. 2014). Low-V anomalies are revealed in the crust and mantle wedge above the subducting Indian slab. In the Tibetan Plateau, there is no prominent volcano, but geothermal anomalies exist there extensively (Liu 1999). Dehydration reactions may also take place in the subducting Indian slab, but the released fluids may not be as much as that of a subducting oceanic plate. In addition, the crust is very thick in Tibet, hence melts in the upper mantle wedge may not reach the surface easily, and so active volcanoes are not produced in the Tibetan Plateau. Other body-wave and surface-wave tomography and receiver-function studies show similar results as the above-mentioned teleseismic tomography (e.g., Huang and Zhao 2006; Kumar et al. 2006; Chen et al. 2009; Nabelek et al. 2009; Fu et al. 2010; Wei et al. 2012).

In the eastern part of the Tibetan Plateau, however, there is a prominent active volcano, Tengchong, which is located at the boundary between China and Burma (Fig. 3.12). Regional tomography shows a clear low-V zone down to a depth of 300 km under the volcano, and the subducting Indian plate (or Burma microplate) is clearly imaged as a high-V zone under Tengchong, and intermediate-depth earthquakes occur down to a depth of 200 km within the high-V zone (Fig. 3.12; Huang and Zhao 2006; Wei et al. 2012). Lei et al. (2009) determined a high-resolution local tomography down to a depth of 650 km under the Tengchong volcano using local and teleseismic data recorded by a local seismic network in SW China. They revealed a narrow low-V zone beneath the Tengchong volcano down to a depth of 410 km, and the low-V zone extends toward the east in the depth range of 250–410 km. These local and regional tomographic results suggest that the origin of the Tengchong volcanism is related to the deep subduction and dehydration of the Burma microplate (or the Indian plate) (Zhao and Liu 2010).

Many researchers have investigated the 3-D seismic structure of the crust and upper mantle under Taiwan using abundant data recorded by the dense local seismic network (e.g., Rau and Wu 1995; Ma et al. 1996; Kim et al. 2005, 2014; Wang et al. 2006b, 2009; Lin et al. 2007; Chou et al. 2009; Kuo-Chen et al. 2012; Koulakov et al. 2014). A high-V zone is imaged from the surface down to a depth of 300 km under South Taiwan, which reflects the subducted Eurasian lithosphere (Fig. 3.13). These tomographic studies suggest that the tectonic framework of Taiwan has changed from subduction in the south to collision in the north, supporting a previous tectonic model proposed by Lallemand et al. (2001) (Fig. 3.13d). The subducted Eurasian lithosphere is colliding with the subducting PHS slab, which may have contributed to mountain building, active seismotectonics, and crustal deformation in and around Taiwan. Significant low-V anomalies appear above the subducted Eurasian lithosphere (Fig. 3.13a) and between the Eurasian lithosphere and the PHS slab down to ~230 km depth (Fig. 3.13b). The low-V zones are overlain by a volcano on the surface (Fig. 3.13b). At least part of the low-V anomalies are caused by fluids from the dehydration of the PHS slab, as well as the subducted Eurasian plate.

These tomographic studies indicate that dehydration reactions also take place after a continental plate subducts into the mantle, which can cause active intraplate volcanoes and geothermal anomalies in those continental areas (Zhao 2012).

Several minerals in the subducting continental plate can transport water into the mantle (Zhao and Ohtani 2009). The dehydration of hydrous minerals in the mafic component of the continental lower crust, such as amphibole, chlorite, zoisite, lawsonite and phengite, occurs in the upper mantle, whereas the hydrous minerals in the acidic component of the continental upper crust, such as phengite, topaz-OH and phase egg, dehydrate in the deep upper mantle and the mantle transition zone (e.g., Ono 1998; Schmidt and Poli 1998; Ohtani et al. 2004). Dehydration of these minerals can cause the low-V anomalies in the upper mantle above the subducting continental plate (Zhao and Ohtani 2009).

3.2 Seismic Attenuation Tomography

It is very important to study the seismic attenuation (Q) structure because it can provide information on the physical properties and composition of materials in the crust and mantle (see Chap. 2 for details). In the earlier stages of seismic tomography, up until the late 1990s, only a few 3-D attenuation (Q) models were determined for subduction zones, most of which focused on the Japan Islands (e.g., Umino and Hasegawa 1984; Furumura and Moriya 1990; Sekiguchi 1991). Since the end of the 1990s, however, there have been rapid advances in Q tomography, and the 3-D Q structure of many subduction zones has been studied, including Tonga (Roth et al. 1999, 2000), New Zealand (Eberhart-Phillips et al. 2008), Japan (Tsumura et al. 2000; Salah and Zhao 2003b; Nakamura et al. 2006; Nakajima et al. 2013; Liu et al. 2014), Alaska (Stachnik et al. 2004; Abers et al. 2006), Izu-Bonin (Shito et al. 2009), Mariana (Pozgay et al. 2009), Taiwan (Wang et al. 2010; Ko et al. 2012; Cheng 2013), Central America (Rychert et al. 2008; Chen and Clayton 2012; Dominguez and Davis 2013), South America (Myers et al. 1998; Haberland and Rietbrock 2001), and Himalaya (Sheehan et al. 2014). According to these studies, the subducting oceanic slabs generally show a very weak attenuation with Q values of up to 1000–1500, whereas the mantle wedge and the crust beneath active arc volcanoes show a very strong attenuation with Q values of 100 or smaller. As a whole, the images of the low-Q zones in the crust and mantle wedge beneath active arc volcanoes and the high-Q zones corresponding to the subducting slab are similar to those of the low-V and high-V zones revealed by travel-time tomography in each of the subduction zones. These 3-D attenuation models have provided additional information on the physical properties of subduction zones, though most of the 3-D Q models have a lower resolution than that of the 3-D velocity models in each of the regions.

Recently, Liu et al. (2014) determined detailed P- and S-wave attenuation (Qp and Qs) tomography of the entire Tohoku arc from the Japan Trench to the Japan Sea using a large number of data measured from P- and S-wave spectra of local crustal and intermediate-depth earthquakes (Fig. 3.14). They used earthquakes under the Pacific Ocean which were relocated precisely with sP depth phases by Huang and Zhao (2013b); hence, Q tomography under the Tohoku fore-arc from

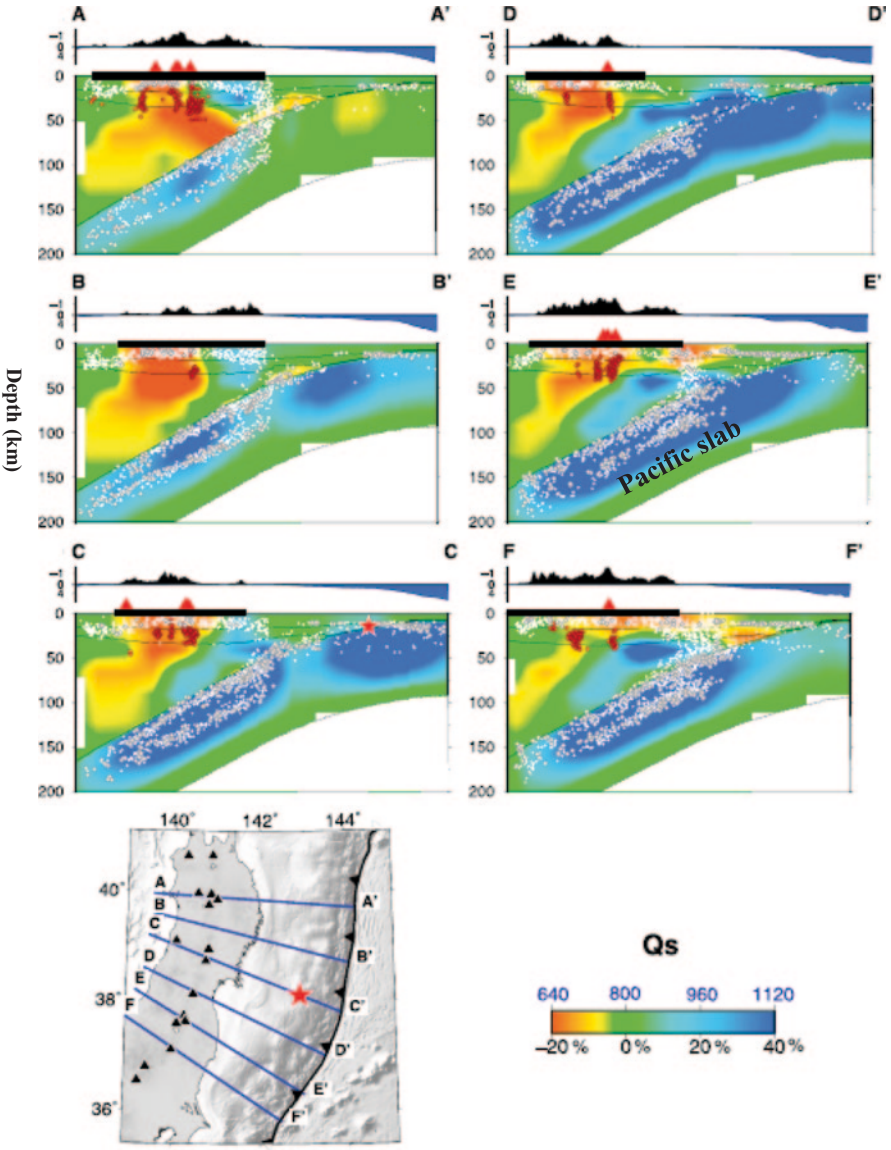

Fig. 3.14 The same as Fig. 3.7 but S-wave attenuation (Q) tomography under NE Japan. The surface topography along each profile is shown above each cross-section. The *red stars* denote the 2011 Tohoku-oki earthquake (Mw 9.0). (Modified from Liu et al. 2014)

the Japan Trench to the Pacific coast was also determined. Beneath the Tohoku land area, the 3-D Q model of Liu et al. (2014) is very similar to those of Tsumura et al. (2000) and Nakajima et al. (2013). The Qp and Qs models are very similar to each other, both of which clearly show the high-Q subducting Pacific slab, a landward dipping intermediate to high Q zone in the mantle wedge between the Pacific coast

and the volcanic front, and significant low-Q anomalies in the crust and mantle wedge between the volcanic front and the Japan Sea coast (Fig. 3.14).

Liu et al. (2014) also revealed prominent high-Q patches, surrounded by low-Q anomalies, in the megathrust zone under the Tohoku fore-arc. The high-Q patches in the megathrust zone generally exhibit large coseismic slips of megathrust earthquakes and a large slip deficit on the slab interface. Similar to the velocity tomography (Zhao et al. 2011b; Huang and Zhao 2013b), the high-Q patches represent asperities in the megathrust zone, whereas the low-Q anomalies reflect weakly-coupled areas. The hypocenters of the great 2011 Tohoku-oki megathrust earthquakes ($M > 7.0$) are located in areas where Qp, Qs and Qp/Qs change abruptly. This Q tomography result also indicates that structural heterogeneities in the megathrust zone control the interplate seismic coupling and nucleation of megathrust earthquakes (Liu et al. 2014).

A ~75 km wide columnar-shaped low-Q anomaly extending from the uppermost mantle to ~100 km depth is revealed beneath the spreading center in the Mariana back-arc (Fig. 3.15a), which reflects a narrow zone of dynamic upwelling and melt production beneath the slow spreading ridge axis (Pozgay et al. 2009). A weaker low-Q zone exists at depths of 50–100 km beneath the volcanic arc, and the low-Q anomalies are connected at depths of 75–125 km. The subducting Pacific plate shows high-Q at depths >100 km, but exhibits low-Q at a depth of 50–100 km. The fore-arc area exhibits low-Q near the volcanic arc and beneath the serpentinite seamounts in the outer fore-arc. The arc and wedge low-Q anomalies may have a high temperature due to hydration and/or melt, whereas the slab and fore-arc anomalies contain slab-derived fluids and/or large-scale serpentinization (Pozgay et al. 2009).

As compared with the velocity tomography (Fig. 3.11), the Q tomography of the Tonga subduction zone (Fig. 3.15b) has a much lower resolution, but low-Q anomalies are revealed down to a depth of ~250 km beneath the Tonga arc and the Lau back-arc spreading center, which is generally consistent with the velocity image.

Ko et al. (2012) has revealed high-Q anomalies in the mantle wedge beneath the SW edge of the Ryukyu arc, suggesting the presence there of a cold and dynamically sluggish edge environment due to a low temperature and probably low water content. These features may result from the coupling of the slab laterally with the thick Eurasian lithosphere, which inhibits back-arc rifting, retards subduction, and reduces the water supply to the mantle wedge. The SW Ryukyu arc represents a subduction-zone edge type distinct from more commonly documented free or warm edges (Ko et al. 2012).

3.3 Seismic Anisotropy Tomography

Seismic anisotropy is a direction-dependent feature of seismic waves propagating in the Earth's interior (see Chap. 2 for details). Long (2013) has made a detailed review of seismic anisotropy studies of subduction zones; in particular, studies using shear-wave splitting measurements and receiver functions. So far, P-wave

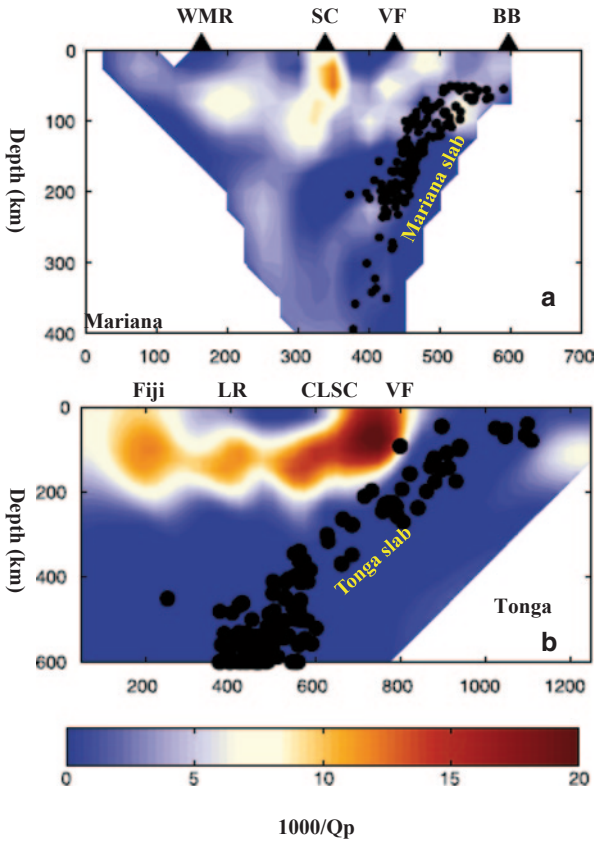

Fig. 3.15 Qp tomography of (**a**) the Mariana and (**b**) Tonga subduction zones. The Mariana result was determined by Pozgay et al. (2009). The Tonga result is from Wiens et al. (2008) but plotted with a new color scale as shown at the bottom. *Black dots* denote earthquakes which occurred in the subducting slabs. Abbreviations are West Mariana Ridge (*WMR*), spreading center (*SC*), volcanic front (*VF*), Big Blue Seamount (*BB*), Lau Ridge (*LR*), and Central Lau Spreading Center (*CLSC*). (Modified from Pozgay et al. 2009)

anisotropy tomography has been applied to investigate the 3-D anisotropic structure in a number of subduction zones, including New Zealand (Eberhart-Philips and Henderson 2004; Eberhart-Philips and Reyners 2009), Northeast Japan (Ishise and Oda 2005; Wang and Zhao 2008, 2010, 2013; Cheng et al. 2011; Huang et al. 2011a; Tian and Liu 2013), Southwest Japan (Ishise and Oda 2008; Wang and Zhao 2012, 2013), South Kuril (Wang and Zhao 2009; Liu et al. 2013a); Java (Koulakov et al. 2009), Central America (Rabbel et al. 2011), Alaska (Tian and Zhao 2012), Eastern Tibet (Wei et al. 2013), North China Craton above the stagnant Pacific slab (Wang et al. 2013, 2014; Tian and Zhao 2013), and western USA (Huang and Zhao 2013c).

Recently, Wang and Zhao (2013) determined a high-resolution P-wave tomography for the 3-D radial and azimuthal anisotropy of the Japan subduction zones using a large number of arrival-time data of local shallow and deep earthquakes

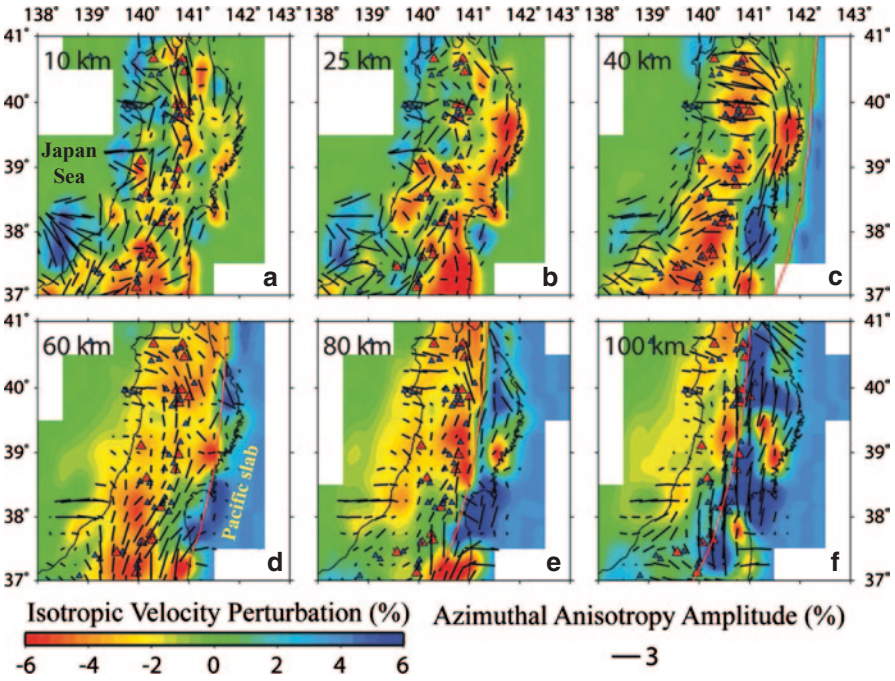

Fig. 3.16 Map views of P-wave anisotropy tomography under NE Japan (Wang and Zhao 2013). *Red* and *blue* colors denote slow and fast isotropic velocities, respectively. The *short lines* denote fast-velocity directions of azimuthal anisotropy. The scales for the isotropic velocity and anisotropic amplitude are shown at the bottom. The *red and black triangles* denote active and quaternary volcanoes, respectively. The *red lines* indicate the *upper* boundary of the Pacific slab.

recorded by the dense seismic network on the Japan Islands (Figs. 3.16, 3.17 and 3.18), which has improved the earlier results (Ishise and Oda 2005, 2008; Wang and Zhao 2008, 2012). They revealed trench-normal fast-velocity directions (FVDs) in the back-arc mantle wedge in both Tohoku and Kyushu (Fig. 3.16), which reflect slab-driven corner flow in the wedge mantle. Trench-parallel FVDs are revealed in the fore-arc mantle wedge under Tohoku and Kyushu, suggesting the existence of a B-type olivine fabric there. Trench-parallel FVDs also appear in the mantle wedge under the volcanic front in Tohoku, but not in Kyushu, suggesting that 3-D flow may exist in the mantle wedge under Tohoku caused by the large subduction rate of the Pacific plate (7–10 cm/year). This FVD pattern of trench-normal in the back-arc and trench-parallel in the fore-arc is very consistent with shear-wave splitting measurements in Tohoku (Okada et al. 1995; Nakajima et al. 2006; Huang et al. 2011b, c) and in Kyushu (e.g., Salah et al. 2008; Terada et al. 2013).

Wang and Zhao (2013) also found negative radial anisotropy (i.e., vertical velocity >horizontal velocity) in the low-V zones in the mantle wedge under the arc volcanoes in Tohoku and Kyushu, as well as in the low-V zones below the Philippine Sea slab under Kyushu (Figs. 3.17 and 3.18), which may reflect hot upwelling flows and transitions of olivine fabrics with the presence of water in the mantle wedge above the

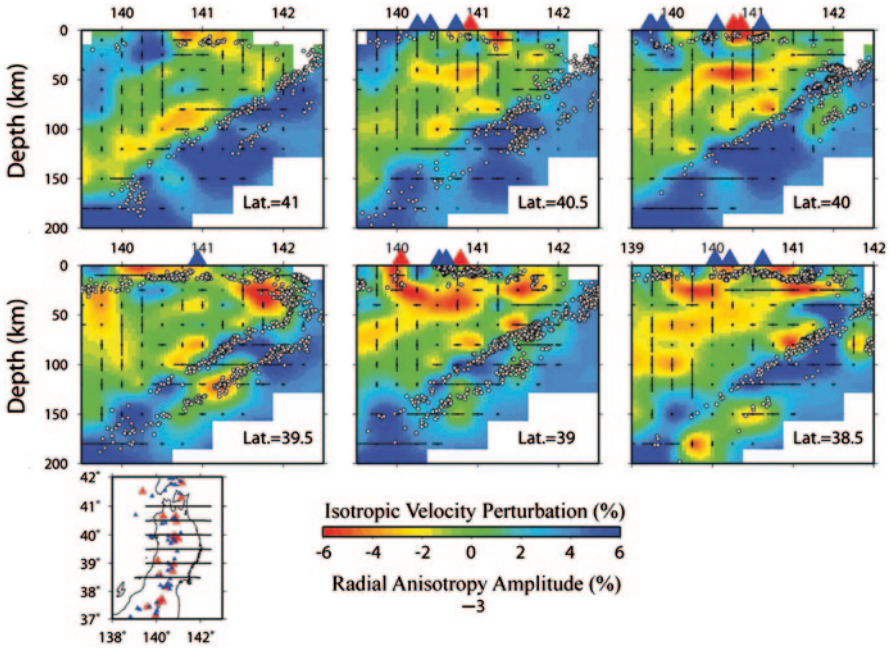

Fig. 3.17 Vertical cross-sections of P-wave radial anisotropy tomography under Tohoku along the profiles as shown on the inset map (Wang and Zhao 2013). The *red* and *blue* colors denote low and high isotropic-velocity anomalies, respectively. The *horizontal bars* denote that horizontal velocity > vertical velocity at each grid node, whereas the *vertical bars* denote that vertical velocity > horizontal velocity at each grid node. The bar length denotes the radial anisotropy amplitude; its scale is shown at the bottom. The *red and blue triangles* denote the active and quaternary volcanoes, respectively. The *white dots* denote the seismicity that occurred within a 10-km width along each profile

Pacific slab, due to the deep dehydration of the Pacific slab (Zhao et al. 2012). Trench-parallel FVDs and positive radial anisotropy (i.e., horizontal velocity >vertical velocity) are revealed in the subducting Pacific slab under Tohoku and the Philippine Sea slab under Kyushu, which may indicate that the two oceanic slabs keep their frozen-in anisotropy formed at the mid-ocean ridge, or that the slab anisotropy is induced by lattice-preferred orientation (LPO) of the B-type olivine (Wang and Zhao 2012, 2013).

Tian and Zhao (2012) determined the Vp and Vs tomography and the 3-D P-wave azimuthal anisotropy of the Alaska subduction zone using the arrival-times of local shallow and intermediate-depth earthquakes recorded by the dense seismic network deployed in South-Central Alaska (Fig. 3.19). They revealed high-V Pacific slab and low-V anomalies in the mantle wedge with significant along-arc variations beneath the active arc volcanoes, which are consistent with previous isotropic Vp tomography under the region (Kissing and Lahr 1991; Zhao et al. 1995; Qi et al. 2007). Significant P-wave anisotropy is revealed, and the predominant FVD is trench-parallel in the shallow part of the mantle wedge (<90 km depth) and in the subslab mantle, whereas the FVD is trench-normal within the subducting Pacific

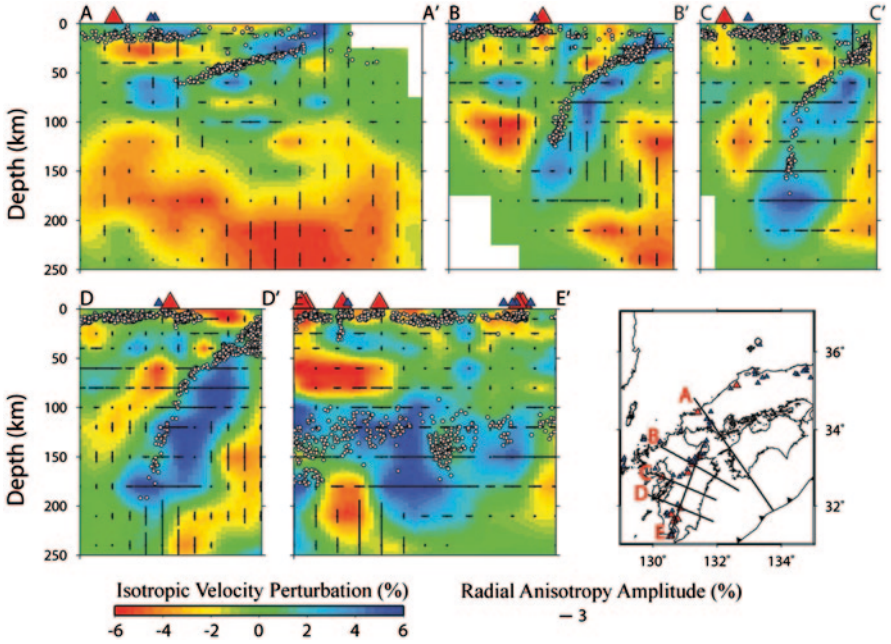

Fig. 3.18 The same as Fig. 3.17 but for P-wave radial anisotropy tomography under SW Japan (Wang and Zhao 2013)

slab (Fig. 3.19). This FVD pattern is consistent with the shear-wave splitting measurements (Christensen and Abers 2010). The trench-parallel FVDs in the mantle wedge and subslab mantle reflect the 3-D mantle flow induced by the complex geometry and strong curvature of the Pacific slab, as well as its flat and oblique subduction under Alaska. The trench-normal FVD within the Pacific slab may reflect the original fossil anisotropy when the Pacific plate was produced at the mid-ocean ridge (Tian and Zhao 2012).

Applying the method of Koulakov et al. (2009) to local earthquake arrival-time data, Rabbel et al. (2011) obtained a 3-D P-wave anisotropy tomography of the Central America subduction zone (Fig. 3.20). In the upper crust beneath Costa Rica, the anisotropy shows strong lateral variations corresponding to the complicated tectonic structure. In the upper mantle, the anisotropy exhibits a more coherent FVD that varies systematically at regional scales. The upper mantle of the incoming Cocos plate exhibits a trench-normal FVD, which may reflect mineral LPO in the transport direction. This pattern changes in the uppermost part of the subduction zone, which may be affected by bending-related trench-parallel faults and serpentinization that can overprint or change the LPO. The overriding Caribbean plate and the mantle wedge show a clear trench-parallel FVD. The anisotropy is stronger in Nicaragua than in southern central Costa Rica, which may be caused by a change in the stress regime from compressional in southern Costa Rica to transpressional in Nicaragua, corresponding to a change from a near-orthogonal subduction in the SE to an

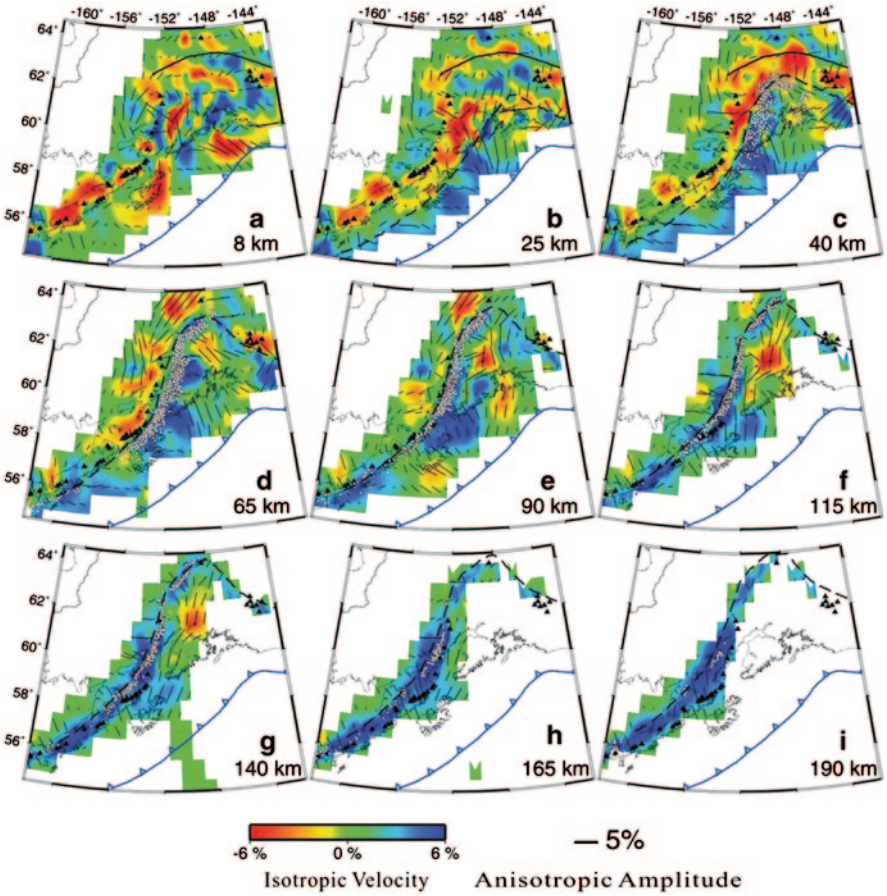

Fig. 3.19 Map views of P-wave anisotropy tomography of the Alaska subduction zone (Tian and Zhao 2012). *Red* and *blue* colors denote slow and fast isotropic velocities, respectively. The *short lines* denote fast-velocity directions of azimuthal anisotropy. The scales for the isotropic velocity and anisotropic amplitude are shown at the *bottom*. The *black triangles* denote active arc volcanoes. The *blue sawtooth* lines denote the trench. The *dashed lines* indicate the *upper* boundary of the Pacific slab. The *grey dots* show the earthquakes occurring in the subducting Pacific slab

oblique subduction and slab retreat in the NW. The obtained P-wave anisotropy in the mantle wedge reflects LPO associated with a trench-parallel shear deformation and/or NW oriented escape flow produced in the compressional zone near the Cocos Ridge collision area (Rabbel et al. 2011).

Applying a surface-wave tomography method to Rayleigh and Love waves recorded by land and seafloor broadband seismometers, Isse et al. (2010) studied isotropic and anisotropic Vs structures in the northern Philippine Sea region. They found that the FVDs of azimuthal anisotropy are parallel to the directions of ancient seafloor spreading in the lithosphere of the Shikoku and West Philippine Basins and the Pacific Ocean, whereas they are parallel to the direction of the present-day

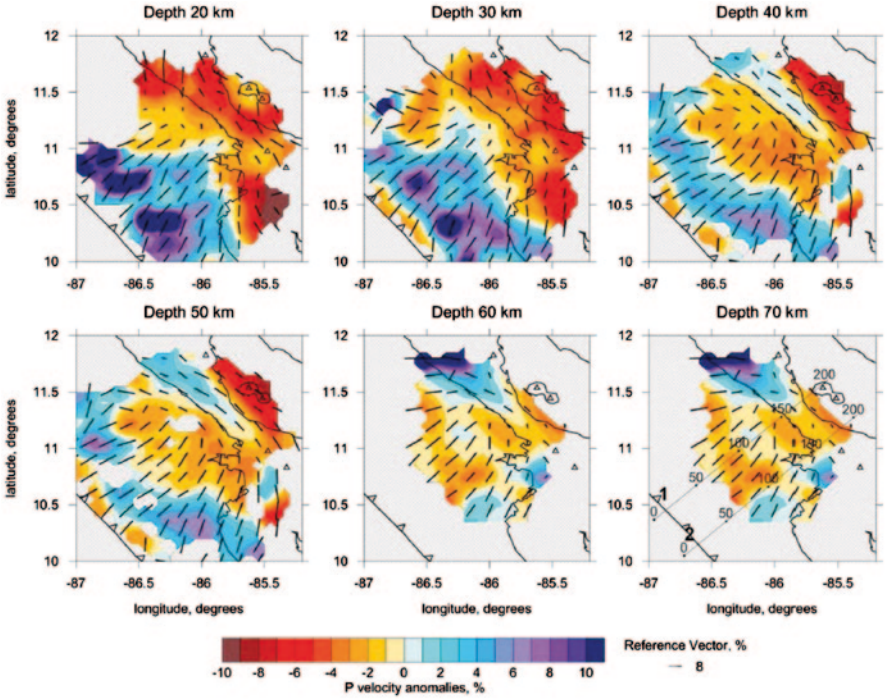

Fig. 3.20 Map views of the P-wave anisotropic tomography of the Central America subduction zone. *Red* and *blue* colors indicate low and high isotropic velocity perturbations with their scale shown at the *bottom*. *Bars* show the directions of maximum horizontal velocities. The *lengths* of the bars show the amplitude of the velocity anisotropy with its scale shown at the *lower-right corner*. The *sawtooth line* denotes the trench axis. (After Rabbel et al. 2011)

absolute plate motion (APM) in the asthenosphere of the Shikoku Basin, and oblique to the APM direction in the Pacific Ocean and in the northern part of the West Philippine Basin. In the subduction zones around the Philippine Sea plate, the FVDs are trench-parallel in the Ryukyu arc, and oriented NW–SE in the Izu–Ogasawara island arc. The Philippine Sea plate shows very large lateral variations in azimuthal and radial anisotropies, compared with the Pacific plate (Isse et al. 2010). In a similar study, Stubailo et al. (2012) determined a 3-D model of S-wave velocity and anisotropy for the Mexico subduction zone using Rayleigh wave phase-velocity dispersion measurements.

McCormack et al. (2013) used receiver functions to study the anisotropic structure of the mantle wedge beneath the entire Ryukyu arc. They detected coherent P-to-SV conversions originating at the top of the subducting slab, and multiple anisotropic layers having a structure which varied significantly along the arc. In the center of the Ryukyu arc there is a ~6 km thick layer with strong anisotropy, most likely serpentinite, directly above the subducting slab. A B-type olivine fabric may exist in the shallow mantle wedge there.

Vavrycuk (2006) has shown differences in P-wave anisotropy between the northern and southern segments of the Tonga slab in the mantle transition zone, which may reflect the difference in the crystallographic preferred orientation pattern of Akimotoite at varying temperatures within the Tonga slab (Zhang et al. 2005; Shiraishi et al. 2008).

Zhang et al. (2007) proposed a 3-D shear-wave splitting tomography method to image the spatial anisotropy distribution by back-projecting shear-wave splitting delay times along ray paths derived from a 3-D Vs model, assuming the delay times are accumulated along the ray paths. Abt and Fischer (2008) presented another method of shear-wave splitting tomography by parameterizing the upper mantle as a 3-D block model of crystallographic orientations with the elastic properties of olivine and orthopyroxene, and both orthorhombic and hexagonal symmetries are tested. The effectiveness of these methods now needs to be confirmed by successful applications in different regions.

3.4 Summary

Recent seismic tomography studies of subduction zones are reviewed. So far seismic velocity tomography has been determined for most subduction zones, and the seismic attenuation and anisotropy tomography of many subduction zones has also been investigated in recent years, which has provided important new insights into arc magmatism, seismotectonics and subduction dynamics. Several common seismological features are revealed in subduction zones, which are summarized as follows.

The subducting slabs are generally imaged clearly as high-V and high-Q zones where intermediate-depth and deep earthquakes take place. Analyses of reflected and converted waves have revealed the fine structure of the upper boundary of the slabs, including the subducted oceanic crust which is imaged as a low-V layer atop the slab. However, detailed structural variations within the slab and their relationship to intraslab earthquakes are still not very clear, and this remains to be an important research subject.

Prominent low-V and low-Q anomalies are revealed in the crust and uppermost mantle beneath active arc and back-arc volcanoes, and the anomalies are visible in the central part of the mantle wedge, subparallel with the subducting slab, suggesting that the low-V and low-Q anomalies reflect the source zone of arc magmatism and volcanism caused by a combination of corner flow in the mantle wedge and fluids from slab dehydration. The corner flow can bring heat from the deeper part of the upper mantle, making the mantle wedge hotter, whereas fluids can reduce the melting temperature of mantle materials. The mantle wedge low-V zones exhibit along-arc variations under NE Japan, which is explained by a hot-finger model. It is still not clear whether such hot fingers exist in the mantle wedge in other subduction zones, which is an interesting subject for future studies.

The fore-arc region exhibits a lower heat flow, and no volcano exists there. Hence, the temperature under the fore-arc is lower than that under the volcanic front and back-arc areas, and partial melting may not occur in the fore-arc. However, a moderate to lower velocity is revealed in the crust and mantle wedge under the fore-arc, and in particular, above young and warm subducting slabs. Slab dehydration may take place in the fore-arc area, which may release a large amount of fluids, causing fore-arc mantle serpentinization. The fluids and serpentine can affect the seismogenesis in the fore-arc, including megathrust earthquakes, intraslab events, and those in the overlying plate.

Seismic velocity variations are also revealed in the mantle below the subducting slabs, which may reflect small-scale convecting flows associated with the collapsing of slab materials down to the lower mantle, or an upwelling flow under an oceanic lithosphere or a subducting slab being dragged down by the slab.

Dehydration reactions also take place after a continental plate subducts into the mantle, which causes low-V anomalies in the mantle wedge, as well as active volcanoes and geothermal anomalies in those continental areas. However, the low-V zones are less prominent than those above the oceanic slabs, and fewer active volcanoes exist above the continental slabs, probably because the continental plate carries much less water than the oceanic lithosphere does.

Shear-wave splitting measurements, surface-wave and receiver-function imaging, and P-wave anisotropy tomography show that seismic anisotropy exists in all parts of subduction zones. These studies have provided important constraints on the mantle flows and dynamics in subduction zones. P-wave anisotropy tomography has become a powerful tool for mapping 3-D variations of azimuthal and radial seismic anisotropy in subduction zones.

References

Abdelwahed, M., Zhao, D.: Deep structure of the Japan subduction zone. Phys. Earth Planet. Inter. **162,** 32–52 (2007)

Abe, Y., Ohkura, T., Hirahara, K., Shibutani, T.: Along-arc variation in water distribution in the uppermost mantle beneath Kyushu, Japan, as derived from receiver function analyses. J. Geophys. Res. **118,** 3540–3556 (2013)

Abers, G.: Seismic low-velocity layer at the top of subducting slabs: observations, predictions, and systematics. Phys. Earth Planet. Inter. **149,** 7–29 (2005)

Abers, G., Sarker, G.: Dispersion of regional body waves at 100–150 km depth beneath Alaska: in situ constraints on metamorphism of subducted crust. Geophys. Res. Lett. **23,** 1171–1174 (1996)

Abers, G., Plank, T., Hacker, B.: The wet Nicaraguan slab. Geophys. Res. Lett. **30,** 1098 (2003)

Abers, G., van Keken, P., Kneller, E., Ferris, A., Stachnik, J.: The thermal structure of subduction zones constrained by seismic imaging: implications for slab dehydration and wedge flow. Earth Planet. Sci. Lett. **241,** 387–397 (2006)

Abers, G., Nakajima, J., van Keken, P., Kita, S., Hacker, B.: Thermal-petrological controls on the location of earthquakes within subducting plates. Earth Planet. Sci. Lett. **369,** 178–187 (2013)

Abt, D., Fisher, K.: Resolving three-dimensional anisotropic structure with shear wave splitting tomography. Geophys. J. Int. **173,** 859–886 (2008)

Ai, Y., Zhao, D., Gao, X., Xu, W.: The crust and upper mantle discontinuity structure beneath Alaska inferred from receiver functions. Phys. Earth Planet. Inter. **150,** 339–350 (2005)
Aki, K., Lee, W.: Determination of three-dimensional velocity anomalies under a seismic array using first P arrival times from local earthquakes, 1. A homogeneous initial model. J. Geophys. Res. **81,** 4381–4399 (1976)
Aki, K., Christoffersson, A., Husebye, E.: Determination of the three-dimensional seismic structure of the lithosphere. J. Geophys. Res. **82,** 277–296 (1977)
Albers, M., Christensen, U.: The excess temperature of plumes rising from the core-mantle boundary. Geophys. Res. Lett. **23,** 3567–3570 (1996)
Arai, R., Dunn, R.: Seismological study of Lau back arc crust: mantle water, magmatic differentiation, and a compositionally zoned basin. Earth Planet. Sci. Lett. **390,** 304–317 (2014)
Bevis, M., Isacks, B.: Hypocentral trend surface analysis: probing the geometry of Benioff zones. J. Geophys. Res. **89,** 6153–6170 (1984)
Bianchi, M., Heit, B., Jakovlev, A., Yuan, X. et al.: Teleseismic tomography of the southern Puna plateau in Argentina and adjacent regions. Tectonophysics. **586,** 65–83 (2013)
Bostock, M.: The Moho in subduction zones. Tectonophysics. **609,** 547–557 (2013)
Carlson, R., Miller, D.: Mantle wedge water contents estimated from seismic velocities in partially serpentinized peridotites. Geophys. Res. Lett. **30,** 1250 (2003)
Chen, T., Clayton, R.: Structure of central and southern Mexico from velocity and attenuation tomography. J. Geophys. Res. **117,** B09302 (2012)
Chen, Y., Badal, J., Zhang, Z.: Radial anisotropy in the crust and upper mantle beneath the Qinghai-Tibet Plateau and surrounding regions. J. Asian Earth Sci. **36,** 289–302 (2009)
Cheng, W.: Three-dimensional seismic attenuation structure beneath the Taiwan region and its tectonic implication. J. Asian Earth Sci. **65,** 86–99 (2013)
Cheng, B., Zhao, D., Zhang, G.: Seismic tomography and anisotropy in the source area of the 2008 Iwate-Miyagi earthquake (M 7.2). Phys. Earth Planet. Inter. **184,** 172–185 (2011)
Chou, H., Kuo, B., Chiao, L., Zhao, D., Hung, S.: Tomography of the westernmost Ryukyu subduction zone and the serpentinization of the forearc mantle. J. Geophys. Res. **114,** B12301 (2009)
Christensen, D., Abers, G.: Seismic anisotropy under central Alaska from SKS splitting observations. J. Geophys. Res. **115,** B04315 (2010)
Collings, R., Lange, D., Rietbrock, A., Tilmann, F. et al.: Structure and seismogenic properties of the Mentawai segment of the Sumatra subduction zone revealed by local earthquake traveltime tomography. J. Geophys. Res. **117,** B01312 (2012)
Conder, J., Wiens, D.: Seismic structure beneath the Tonga arc and Lau back-arc basin determined from joint Vp, Vp/Vs tomography. Geochem. Geophys. Geosyst. **7,** Q03018 (2006)
DeShon, H., Schwartz, S.: Evidence for serpentinization of the forearc mantle wedge along the Nicoya Peninsula, Costa Rica. Geophys. Res. Lett. **31,** L21611 (2004)
Dominguez, L., Davis, P.: Seismic attenuation in the Middle America Region and the frequency dependence of intrinsic Q. J. Geophys. Res. **118,** 2164–2175 (2013)
Duan, Y., Zhao, D., Zhang, X., et al.: Seismic structure and origin of active intraplate volcanoes in Northeast Asia. Tectonophysics. **470,** 257–266 (2009)
Eberhart-Phillips, D., Henderson, C.: Including anisotropy in 3-D velocity inversion and application to Marlborough, New Zealand. Geophys. J. Int. **156,** 237–254 (2004)
Eberhart-Phillips, D., Reyners, M.: Three-dimensional distribution of seismic anisotropy in the Hikurangi subduction zone beneath the central North Island, New Zealand. J. Geophys. Res. **114,** B06301 (2009)
Eberhart-Phillips, D., Chadwick, M., Bannister, S.: Three-dimensional attenuation structure of central and southern South Island, New Zealand, from local earthquakes. J. Geophys. Res. **113,** B05308 (2008)
Faccenda, M., Gerya, T., Burlini, L.: Deep slab hydration induced by bending-related variations in tectonic pressure. Nature Geosci. **2,** 790–793 (2009)
Faul, U., Toomey, D., Waff, H.: Intergranular basaltic melt is distributed in thin, elongated inclusions. Geophys. Res. Lett. **21,** 29–32 (1994)

Ferris, A., Abers, G., Christensen, D., Veenstra, E.: High resolution image of the subducted Pacific (?) plate beneath central Alaska, 50–150 km depth. Earth Planet. Sci. Lett. **214,** 575–588 (2003)
Fu, Y., Li, A., Chen, Y.: Crustal and upper mantle structure of southeast Tibet from Rayleigh wave tomography. J. Geophys. Res. **115,** B12323 (2010)
Fujie, G., Miura, S., Kodaira, S., Kaneda, Y., et al.: Along-trench structural variation and seismic coupling in the northern Japan subduction zone. Earth Planet. Space. **65,** 75–83 (2013a)
Fujie, G., Kodaira, S., Yamashita, M., Sato, T., Takahashi, T., Takahashi, N.: Systematic changes in the incoming plate structure at the Kuril trench. Geophys. Res. Lett. **40,** 88–93 (2013b)
Fukao, Y., Widiyantoro, S., Obayashi, M.: Stagnant slabs in the upper and lower mantle transition region. Rev. Geophys. **39,** 291–323 (2001)
Furumura, T., Moriya, T.: Three-dimensional Q structure in and around the Hidaka mountains, Hokkaido. Japan. J. Seismol. Soc. Japan. **43,** 121–132 (1990)
Gamage, S., Umino, N., Hasegawa, A., Kirby, S.: Offshore double-planed shallow seismic zone in the NE Japan forearc region revealed by sP depth phases recorded by regional networks. Geophys. J. Int. **178,** 195–214 (2009)
Graeber, F., Asch, G.: Three-dimensional models of P wave velocity and P-to-S velocity ratio in the southern central Andes by simultaneous inversion of local earthquake data. J. Geophys. Res. **104,** 20237–20256 (1999)
Haberland, C., Rietbrock, A.: Attenuation tomography in the western central Anders: a detailed insight into the structure of a magmatic arc. J. Geophys. Res. **106,** 11151–11167 (2001)
Hacker, B., Abers, G., Peacock, S.: Subduction factory, 1, theoretical mineralogy, densities, seismic wave speeds, and H2O contents. J. Geophys. Res. **108,** 2029 (2003)
Hasegawa, A., Yamamoto, A.: Deep, low-frequency microearthquakes in or around seismic low-velocity zones beneath active volcanoes in northeastern Japan. Tectonophysics. **233,** 233–252 (1994)
Hasegawa, A., Zhao, D.: Deep structure of island arc magmatic regions as inferred from seismic observations. In: Ryan M.P. (eds.) Magmatic Systems, pp. 179–195. Academic, Waltham (1994)
Hasegawa, A., Umino, N., Takagi, A.: Double-planed deep seismic zone and upper-mantle structure in the northeastern Japan arc. Geophys. J. R. Astron. Soc. **54,** 281–296 (1978)
Hasegawa, A., Nakajima, J., Uchida, N., Okada, T., Zhao, D., Matsuzawa, T., Umino, N.: Plate subduction, and generation of earthquakes and magmas in Japan as inferred from seismic observation: an overview. Gondwana Res. **16,** 370–400 (2009)
Hasemi, A., Ishii, H., Takagi, A.: Fine structure beneath the Tohoku district, northeastern Japan arc, as derived by an inversion of P-wave arrival times from local earthquakes. Tectonophysics. **101,** 245–265 (1984)
Hayes, G., Wald, D., Johnson, R.: Slab 1.0: a three-dimensional model of global subduction zone geometries. J. Geophys. Res. **117,** B01302 (2012)
He, R., Zhao, D., Gao, R., Zheng, H.: Tracing the Indian lithospheric mantle beneath central Tibetan Plateau using teleseismic tomography. Tectonophysics. **491,** 230–243 (2010)
Hirahara, K.: A large-scale three-dimensional seismic structure under the Japan Islands and the Sea of Japan. J. Phys. Earth. **25**, 393–417 (1977)
Hirahara, K.: Three-dimensional seismic structure beneath southwest Japan: the subducting Philippine sea plate. Tectonophysics. **79,** 1–44 (1981)
Honda, S., Morishige, M., Orihashi, Y.: Sinking hot anomaly trapped at the 410 km discontinuity near the Honshu subduction zone, Japan. Earth Planet. Sci. Lett. **261,** 565–577 (2007)
Hori, S., Inoue, H., Fukao, Y., Ukawa, M.: Seismic detection of the untransformed basaltic oceanic crust subducting into the mantle. Geophys. J. R. Astron. Soc. **83,** 169–197 (1985)
Horie, A., Aki, K., K: Three-dimensional velocity structure beneath the Kanto District. Japan. J. Phys. Earth. **30,** 255–281 (1982)
Horiuchi, S., Tsumura, N., Hasegawa, A.: Mapping of a magma reservoir beneath Nikko-Shirane volcano in northern Kanto, Japan, from travel time and seismogram shape anomalies. J. Geophys. Res. **102,** 18071–18090 (1997)

Horleston, A., Helffrich, G.: Constraining sediment subduction: a converted phase study of the Aleutians and Marianas. Earth Planet. Sci. Lett. **359,** 141–151 (2012)
Huang, J., Zhao, D.: High-resolution mantle tomography of China and surrounding regions. J. Geophys. Res. **111,** B09305 (2006)
Huang, Z., Zhao, D.: Relocating the 2011 Tohoku-oki earthquakes (M 6.0–9.0). Tectonophysics. **586,** 35–45 (2013a)
Huang, Z., Zhao, D.: Mechanism of the 2011 Tohoku-oki earthquake (Mw 9.0) and tsunami: insight from seismic tomography. J. Asian Earth Sci. **70,** 160–168 (2013b)
Huang, Z., Zhao, D.: Mapping P-wave azimuthal anisotropy in the crust and upper mantle beneath the United States. Phys. Earth Planet. Inter. **225,** 28–40 (2013c)
Huang, Z., Zhao, D., Wang, L.: Seismic heterogeneity and anisotropy of the Honshu arc from the Japan trench to the Japan Sea. Geophys. J. Int. **184,** 1428–1444 (2011a)
Huang, Z., Zhao, D., Wang, L.: Shear-wave anisotropy in the crust, mantle wedge and the subducting Pacific slab under Northeast Japan. Geochem. Geophys. Geosyst. **12,** Q01002 (2011b)
Huang, Z., Zhao, D., Wang, L.: Frequency-dependent shear-wave splitting and multilayer anisotropy in Northeast Japan. Geophys. Res. Lett. **38,** L08302 (2011c)
Huang, Z., Zhao, D., Hasegawa, A., Umino, N., Park, J., Kang, I.: Aseismic deep subduction of the Philippine Sea plate and slab window. J. Asian Earth Sci. **75,** 82–94 (2013)
Husen, S., Kissling, E., Flueh, E.: Local earthquake tomography of shallow subduction in north Chile: a combined onshore and offshore study. J. Geophys. Res. **105,** 28183–28198 (2000)
Hyndman, R., Peacock, S.: Serpentinization of the forearc mantle. Earth Planet. Sci. Lett. **212,** 417–432 (2003)
Ichiki, M., Baba, K., Obayashi, M., Utada, H.: Water content and geotherm in the upper mantle above the stagnant slab: interpretation of electrical conductivity and seismic P-wave velocity models. Phys. Earth Planet. Inter. **155,** 1–15 (2006)
Igarashi, T.: Seismic velocity discontinuities in the crust and uppermost mantle beneath the Kanto district, central Japan, identified from receiver function imaging and repeating earthquake activity. Gondwana Res. **16,** 491–503 (2009)
Iidaka, T., Suetsugu, D.: Seismological evidence for metastable olivine inside a subducting slab. Nature. **356,** 593–595 (1992)
Iidaka, T., Igarashi, T., Iwasaki, T.: Configuration of the subducting Philippine Sea slab in the eastern part of southwestern Japan with seismic array and Hi-net data. Gondwana Res. **16,** 504–511 (2009)
Ishida, M.: Geometry and relative motion of the Philippine Sea plate and Pacific plate beneath the Kanto-Tokai district. Japan. J. Geophys. Res. **97,** 489–513 (1992)
Ishida, M., Hasemi, A.: The three-dimensional fine velocity structure and hypocentral distribution of earthquakes beneath the Kanto-Tokai District. Japan. J. Geophys. Res. **93,** 2076–2094 (1988)
Ishise, M., Oda, H.: Three-dimensional structure of P-wave anisotropy beneath the Tohoku district, northeast Japan. J. Geophys. Res. **110,** B07304 (2005)
Ishise, M., Oda, H.: Subduction of the Philippine Sea slab in view of P-wave anisotropy. Phys. Earth Planet. Inter. **166,** 83–96 (2008)
Isse, T., Shiobara, H., Montagner, J., et al.: Anisotropic structures of the upper mantle beneath the northern Philippine Sea region from Rayleigh and Love wave tomography. Phys. Earth Planet. Inter. **183,** 33–43 (2010)
Iwamori, H., Zhao, D.: Melting and seismic structure beneath the northeast Japan arc. Geophys. Res. Lett. **27,** 425–428 (2000)
Jiang, G., Zhao, D.: Metastable olivine wedge in the subducting Pacific slab and its relation to deep earthquakes. J. Asian Earth Sci. **42,** 1411–1423 (2011)
Jiang, G., Zhao, D., Zhang, G.: Seismic evidence for a metastable olivine wedge in the subducting Pacific slab under Japan Sea. Earth Planet. Sci. Lett. **270,** 300–307 (2008)
Kamiya, S., Kobayashi, Y.: Seismological evidence for the existence of serpentinized wedge mantle. Geophys. Res. Lett. **27,** 819–822 (2000)

Kaneshima, S., Okamoto, T., Takenaka, H.: Evidence for a metastable olivine wedge inside the subducted Mariana slab. Earth Planet. Sci. Lett. **258,** 219–227 (2007)
Katsumata, A., Kamaya, N.: Low-frequency continuous tremor around the Moho discontinuity away from volcanoes in the southwest Japan. Geophys. Res. Let. **30,** 1020 (2003)
Katsumata, K., Wada, N., Kasahara, M.: Three-dimensional P and S wave velocity structures beneath the Hokkaido corner, Japan-Kurile arc-arc junction. Earth Planet. Space. **58,** e37–40 (2006)
Kawakatsu, H., Watada, S.: Seismic evidence for deep-water transportation in the mantle. Science. **316,** 1468–1471 (2007)
Kawakatsu, H., Yoshioka, S.: Metastable olivine wedge and deep dry cold slab beneath southeast Japan. Earth Planet. Sci. Lett. **303,** 1–10 (2011)
Kim, K., Chiu, J., Pujol, J., Chen, K., Huang, B., Yeh, Y., Shen, P.: Three-dimensional Vp and Vs structural models associated with the active subduction and collision tectonics in the Taiwan region. Geophys. J. Int. **162,** 204–220 (2005)
Kim, Y., Miller, M., Pearce, F., Clayton, R.: Seismic imaging of the Cocos plate subduction zone system in central Mexico. Geochem. Geophys. Geosyst. **13,** Q07001 (2012)
Kim, Y., Clayton, R., Asimow, P., Jackson, J.: Generation of talc in the mantle wedge and its role in subduction dynamics in central Mexico. Earth Planet. Sci. Lett. **384,** 81–87 (2013)
Kim, K., Chen, K., Chiu, J.: Three-dimensional structure of Vp, Vs and Vp/Vs beneath the active collision boundary of eastern Taiwan. Geophys. J. Int. **196,** 78–95 (2014)
Kind, R., et al.: Seismic images of crust and upper mantle beneath Tibet: evidence for Eurasian plate subduction. Science. **298,** 1219–1221 (2002)
Kissling, E., Lahr, J.: Tomographic image of the Pacific Slab under southern Alaska. Eclogae. Geol. Helv. **84,** 297–315 (1991)
Kita, S., Okada, T., Nakajima, J., Matsuzawa, T., Hasegawa, A.: Existence of a seismic belt in the upper plane of the double seismic zone extending in the along-arc direction at depths of 70–100 km beneath NE Japan. Geophys. Res. Lett. **33,** L24310 (2006)
Ko, Y., Kuo, B., Wang, K., Lin, S., Hung, S.: The southwestern edge of the Ryukyu subduction zone: a high Q mantle wedge. Earth Planet. Sci. Lett. **335,** 145–153 (2012)
Kodaira, S., Noguchi, N., Takahashi, N., Ishizuka, O., Kaneda, Y.: Evolution from fore-arc oceanic crust to island arc crust: a seismic study along the Izu - Bonin fore arc. J. Geophys. Res. **115,** B09102 (2010)
Koulakov, I., Jakovlev, A., Luehr, B.: Anisotropic structure beneath central Java from local earthquake tomography. Geochem. Geophys. Geosyst. **10,** Q02011 (2009)
Koulakov, I., Wu, Y., Huang, H., Dobretsov, N., et al.: Slab interactions in the Taiwan region based on the P- and S-velocity distributions in the upper mantle. J. Asian Earth Sci. **79,** 53–64 (2014)
Kumar, P., Yuan, X., Kind, R., J: Ni, J.: Imaging the colliding Indian and Asian lithospheric plates beneath Tibet. J. Geophys. Res. **111,** B06308 (2006)
Kuo-Chen, H., Wu, F., Roecker, S.: Three-dimensional P velocity structures of the lithosphere beneath Taiwan from the analysis of TAIGER and related seismic data sets. J. Geophys. Res. **117,** B06306 (2012)
Laigle, M., Hirn, A., Sapin, M., Becel, A., et al.: Seismic structure and activity of the north-central Lesser Antilles subduction zone from an integrated approach: similarities with the Tohoku forearc. Tectonophysics. **603,** 1–20 (2013)
Lallemand, S., Font, Y., Bijiwaard, H., Kao, H.: New insights on 3-D plates interaction near Taiwan from tomography and tectonic implications. Tectonophysics. **335,** 229–253 (2001)
Lei, J., Zhao, D., Su, Y.: Insight into the origin of the Tengchong intraplate volcano and seismotectonics in southwest China from local and teleseismic data. J. Geophys. Res. **114,** B05302 (2009)
Lin, J.Y., Sibuet, J., Lee, C., Hsu, S., Klingelhoefer, F.: Origin of the southern Okinawa Trough volcanism from detailed seismic tomography. J. Geophys. Res. **112,** B08308 (2007)
Liu, J.: Volcanoes in China, p. 219. Science, Beijing (1999)
Liu, X., Zhao, D., Li, S.: Seismic heterogeneity and anisotropy of the southern Kuril arc: insight into megathrust earthquakes. Geophys. J. Int. **194,** 1069–1090 (2013a)

Liu, X., Zhao, D., Li, S.: Seismic imaging of the Southwest Japan arc from the Nankai trough to the Japan Sea. Phys. Earth Planet. Inter. **216,** 59–73 (2013b)
Liu, X., Zhao, D., Li, S.: Seismic attenuation tomography of the Northeast Japan arc: insight into the 2011 Tohoku earthquake (Mw 9.0) and subduction dynamics. J. Geophys. Res. **119,** 1094–1118 (2014)
Long, M.: Constraints on subduction geodynamics from seismic anisotropy. Rev. Geophys. **51,** 76–112 (2013)
Ma, K., Wang, J., Zhao, D.: Three-dimensional seismic velocity structure of the crust and uppermost mantle beneath Taiwan. J. Phys. Earth. **44,** 85–105 (1996)
MacKenzie, L., Abers, G., Rondenay, S., Fischer, K.: Imaging a steeply dipping subducting slab in Southern Central America. Earth Planet. Sci. Lett. **296,** 459–468 (2010)
Martin, S., Rietbrock, A., Haberland, C., Asch, G.: Guided waves propagating in subducted oceanic crust. J. Geophys. Res. **108,** 2536 (2003)
Maruyama, S.: Plume tectonics. J. Geol. Soc. Japan. **100,** 24–49 (1994)
Maruyama, S., Santosh, M., Zhao, D.: Superplume, supercontinent, and postperovskite: mantle dynamics and anti-plate tectonics on the core-mantle boundary. Gondwana Res. **11,** 7–37 (2007)
Matsubara, M., Obara, K., Kasahara, K.: Three-dimensional P- and S-wave velocity structures beneath the Japan Islands obtained by high-density seismic stations by seismic tomography. Tectonophysics. **454,** 86–103 (2008)
Matsumoto, S., Hasegawa, A.: Distinct S wave reflector in the midcrust beneath Nikko-Shirane volcano in the northeastern Japan arc. J. Geophys. Res. **101,** 3067–3086 (1996)
Matsuno, T., Evans, R., Seama, N., Chave, A.: Electromagnetic constraints on a melt region beneath the central Mariana back-arc spreading ridge. Geochem. Geophys. Geosyst. **13,** Q10017 (2012)
Matsuzawa, T., Umino, N., Hasegawa, A., Takagi, A.: Upper mantle velocity structure estimated from PS-converted wave beneath the northeastern Japan arc. Geophys. J. R. Astron. Soc. **86,** 767–787 (1986)
Matsuzawa, T., Kono, T., Hasegawa, A., Takagi, A.: Subducting plate boundary beneath northeastern Japan arc estimated from SP converted waves. Tectonophysics. **181,** 123–133 (1990)
McCormack, K., Wirth, E., Long, M.: B-type olivine fabric and mantle wedge serpentinization beneath the Ryukyu arc. Geophys. Res. Lett. **40,** 1697–1702 (2013)
McCrory, P., Blair, J., Waldhauser, F., Oppenheimer, D.: Juan de Fuca slab geometry and its relation to Wadati-Benioff zone seismicity. J. Geophys. Res. **117,** B09306 (2012)
McNamara, D., Pasyanos, M.: Seismological evidence for a sub-volcanic arc mantle wedge beneath the Denali volcanic gap. Alaska. Geophys. Res. Let. **29,** 1814 (2002)
Melgar, D., Perez-Campos, X.: Imaging the Moho and subducted oceanic crust at the Isthmus of Tehuantepec, Mexico, from receiver functions. Pure Appl. Geophys. **168,** 1449–1460 (2011)
Mishina, M.: Distribution of crustal fluids in Northeast Japan as inferred from resistivity surveys. Gondwana Res. **16,** 563–571 (2009)
Mishra, O.P., Zhao, D.: Crack density, saturation rate and porosity at the 2001 Bhuj, India, earthquake hypocenter: a fluid driven earthquake? Earth Planet. Sci. Lett. **212,** 393–405 (2003)
Mishra, O.P., Zhao, D.: Seismic evidence for dehydration embrittlement of the subducting Pacific slab. Geophys. Res. Lett. **31,** L09610 (2004)
Mishra, O.P., Zhao, D., Umino, N., Hasegawa, A.: Tomography of Northeast Japan forearc and its implications for interplate seismic coupling. Geophys. Res. Lett. **30,** GL017736 (2003)
Miyoshi, T., Saito, T., Shiomi, K.: Waveguide effects within the Philippine Sea slab beneath southwest Japan inferred from guided SP converted waves. Geophys. J. Int. **189,** 1075–1084 (2012)
Moreno, M., Haberland, C., Oncken, O., Rietbrock, A., Angiboust, S., Heidbach, O.: Locking of the Chile subduction zone controlled by fluid pressure before the 2010 earthquake. Nature Geosci. **7,** 292–296 (2014)
Myers, S., Beck, S., Zandt, G., Wallace, T.: Lithospheric-scale structure across the Bolivian Andes from tomographic images of velocity and attenuation for P and S waves. J. Geophys. Res. **103,** 21233–21252 (1998)

Nabelek, J., Hetenyi, G., Vergne, J., Sapkota, S., Kafle, B., Jiang, M., Su, H. P., Chen, J., Huang, B. S., Team, H.: Underplating in the Himalaya-Tibet collision zone revealed by the Hi-CLIMB Experiment. Science. **325,** 1371–1374 (2009)

Nakajima, J., Matsuzawa, T., Hasegawa, A., Zhao, D.: Three-dimensional structure of Vp, Vs, and Vp/Vs beneath northeastern Japan: implications for arc magmatism and fluids. J. Geophys. Res. **106,** 21843–21858 (2001)

Nakajima, J., Shimizu, J., Hori, S., Hasegawa, A.: Shear-wave splitting beneath the southwestern Kurile arc and northeastern Japan arc: a new insight into mantle return flow. Geophys. Res. Lett. (2006). doi: 10.1029/2005GL025053

Nakajima, J., Hada, S., Hayami, E., Uchida, N., et al.: Seismic attenuation beneath northeastern Japan: constraints on mantle dynamics and arc magmatism. J. Geophys. Res. **118,** 5838–5855 (2013)

Nakamichi, H., Hamaguchi, H., Tanaka, S., Ueki, S., Nishimura, T., Hasegawa, A.: Source mechanisms of deep and intermediate-depth low-frequency earthquakes beneath Iwate volcano, northeastern Japan. Geophys. J. Int. **154,** 811–828 (2003)

Nakamura, M., Yoshida, Y., Zhao, D., Sato, H., Nishimura, S.: Three-dimensional P- and S-wave velocity structures beneath the Ryukyu arc. Tectonophysics. **369,** 121–143 (2003)

Nakamura, R., Satake, K., Toda, S., Uetake, T., Kamiya, S.: Three-dimensional attenuation (Qs) structure beneath the Kanto district, Japan, as inferred from strong motion records. Geophys. Res. Lett. **33,** L21304 (2006)

Nakamura, M., Yoshida, Y., Zhao, D., et al.: Three-dimensional P- and S-wave velocity structures beneath Japan. Phys. Earth Planet. Inter. **168,** 49–70 (2008)

Nakanishi, I.: Precursors to ScS phases and dipping interface in the upper mantle beneath southwestern Japan. Tectonophysics. **69,** 1–35 (1980)

Nikulin, A., Levin, V., Park, J.: Receiver function study of the Cascadia megathrust: evidence for localized serpentinization. Geochem. Geophys. Geosyst. **10,** Q07004 (2009)

Nolet, G.: Deep dehydration of the subducting lithosphere. In: Farley, K. (ed.) Processes of Deep Earth and Planetary Volatiles, pp. 22–32. American Institute of Physics, New York (1995)

Obana, K., Kamiya, S., Kodaira, S., Suetsugu, D., et al.: Along-arc variation in seismic velocity structure related to variable growth of arc crust in northern Izu-Bonin intraoceanic arc. Geochem. Geophys. Geosyst. **11,** Q08012 (2010)

Obara, K.: Regional extent of the S wave reflector beneath the Kanto district. Japan. Geophys. Res. Lett. **16,** 839–842 (1989)

Obara, K.: Nonvolcanic deep tremor associated with subduction in southwest Japan. Science. **296,** 1679–1681 (2002)

Ogawa, Y., Mishina, M., Goto, T., Satoh, H., et al.: Magnetotelluric imaging of fluids in intraplate earthquake zones, NE Japan back arc. Geophys. Res. Lett. **28,** 3741–3744 (2001)

Ohkura, T.: Structure of the upper part of the Philippine Sea plate estimated by later phases of upper mantle earthquakes in and around Shikoku, Japan. Tectonophysics. **321,** 17–36 (2000)

Ohtani, E., Zhao, D.: The role of water in the deep upper mantle and transition zone: dehydration of stagnant slabs and its effects on the big mantle wedge. Russ. Geol. Geophys. **50,** 1073–1078 (2009)

Ohtani, E., Litasov, K., Hosoya, T., Kubo, T., Kondo, T.: Water transport into the deep mantle and formation of a hydrous transition zone. Phys. Earth Planet. Inter. **143,** 255–269 (2004)

Okada, H.: Forerunners of ScS waves from nearby deep earthquakes and upper mantle structure in Hokkaido. J. Seismol. Soc. Japan. **24,** 228–239 (1971)

Okada, H.: New evidence of the discontinuous structure of the descending lithosphere as revealed by ScSp phase. J. Phys. Earth. **27,** S53–S64 (1979)

Okada, T., Matsuzawa, T., Hasegawa, A.: Shear-wave polarization anisotropy beneath the northeastern part of Honshu. Japan. Geophys. J. Int. **123,** 781–797 (1995)

Ono, S.: Stability of hydrous minerals in sediment and mid-oceanic ridge basalt compositions: implications for water transport in subduction zones. J. Geophys. Res. **103,** 18253–18267 (1998)

Osada, K., Yoshizawa, K., Yomogida, K.: Upper boundary of the Pacific plate subducting beneath Hokkaido, Japan, estimated from ScSp phase. Phys. Earth Planet. Inter. **183,** 63–72 (2010)

Parson, L., Wright, I.: The Lau-Havre-Taupo back-arc basin: a southward-propagating, multi-stage evolution from rifting to spreading. Tectonophysics. **263,** 1–22 (1996)
Peacock, S.: Fluid processes in subduction zones. Science. **248,** 329–345 (1990)
Peacock, S.: Are the lower planes of double seismic zones caused by serpentine dehydration in subducting oceanic mantle? Geology. **29,** 299–302 (2001)
Pozgay, S., Wiens, D., Conder, J., Shiobara, H., Sugioka, H.: Seismic attenuation tomography of the Mariana subduction system: implications for thermal structure, volatile distribution, and slow spreading dynamics. Geochem. Geophys. Geosyst. **10,** Q04X05 (2009)
Qi, C., Zhao, D., Chen, Y.: Search for deep slab segments under Alaska. Phys. Earth Planet. Inter. **165,** 68–82 (2007)
Rabbel, W., Koulakov, I., Dinc, A., Jakovlev, A.: Arc-parallel shear deformation and escape flow in the mantle wedge of the Central America subduction zone: evidence from P wave anisotropy. Geochem. Geophys. Geosyst. **12,** Q05S31 (2011)
Ramachandran, K., Hyndman, R.: The fate of fluids released from subducting slab in northern Cascadia. Solid. Earth. **3,** 121–129 (2012)
Ramachandran, K., Dosso, S., Spence, G., Hyndman, R., Brocher, T.: Forearc structure beneath southwestern British Columbia: a three-dimensional tomographic velocity model. J. Geophys. Res. **110,** B02303 (2005)
Rau, R., Wu, F.: Tomographic imaging of lithospheric structures under Taiwan. Earth Planet. Sci. Lett. **133,** 517–532 (1995)
Rondenay, S., Abers, G., van KeKen, P.: Seismic imaging of subduction zone metamorphism. Geology. **36,** 275–278 (2008)
Roth, E., Wiens, D., Dorman, L., Hildebrand, J., Webb, S.: Seismic attenuation tomography of the Tonga-Fiji region using phase pair methods. J. Geophys. Res. **104,** 4795–4810 (1999)
Roth, E., Wiens, D., Zhao, D.: An empirical relationship between seismic attenuation and velocity anomalies in the upper mantle. Geophys. Res. Lett. **27,** 601–604 (2000)
Rychert, C., Fischer, K., Abers, G., et al.: Strong along-arc variations in attenuation in the mantle wedge beneath Costa Rica and Nicaragua. Geochem. Geophys. Geosyst. **9,** Q10S10 (2008)
Salah, M., Zhao, D.: 3-D seismic structure of Kii Peninsula in Southwest Japan: evidence for slab dehydration in the forearc. Tectonophysics. **364,** 191–213 (2003a)
Salah, M., Zhao, D.: Three-dimensional attenuation structure of Southwest Japan estimated from spectra of microearthquakes. Phys. Earth Planet. Inter. **136,** 215–231 (2003b)
Salah, M., Seno, T., Iidaka, T.: Upper mantle anisotropy beneath central and southwest Japan: an insight into subduction-induced mantle flow. J. Geodyn. **46,** 21–37 (2008)
Schmandt, B., Humphreys, E.: Complex subduction and small-scale convection revealed by body-wave tomography of the western United States upper mantle. Earth Planet. Sci. Lett. **297,** 435–445 (2010)
Schmidt, M., Poli, S.: Experimental base water budgets for dehydrating slabs and consequences for arc magma generation. Earth Planet. Sci. Lett. **163,** 361–379 (1998)
Schwartz, S., Rokosky, J.: Slow slip events and seismic tremor at circum-pacific subduction zones. Rev. Geophys. **45,** RG3004 (2007)
Sekiguchi, S.: Three-dimensional Q structure beneath the Kanto-Tokai district, Japan. Tectonophysics. **195,** 83–104 (1991)
Seno, T., Yamasaki, T.: Low-frequency tremors, intraslab and interplate earthquakes in Southwest Japan—from a viewpoint of slab dehydration. Geophys. Res. Lett. **30,** 2171 (2003)
Seno, T., Zhao, D., Kobayashi, Y., Nakamura, M.: Dehydration of serpentinized slab mantle: seismic evidence from southwest Japan. Earth Planet. Space. **53,** 861–871 (2001)
Sheehan, A., de la Torre, T., Monsalve, G., Abers, G., Hacker, B.: Physical state of Himalayan crust and uppermost mantle: constraints from seismic attenuation and velocity tomography. J. Geophys. Res. **119,** 567–580 (2014)
Shiina, T., Nakajima, J., Matsuzawa, T.: Seismic evidence for high pore pressures in the oceanic crust: implications for fluid-related embrittlement. Geophys. Res. Lett. **40,** 2006–2010 (2013)

Shiomi, K., Sato, H., Obara, K., Ohtake, M.: Configuration of subducting Philippine Sea plate beneath southwest Japan revealed from receiver function analysis based on the multivariate autoregressive model. J. Geophys. Res. **109,** B04308 (2004)
Shiraishi, R., Ohtani, E., Kanagawa, K., Shimojuku, A., Zhao, D.: Crystallographic preferred orientation of Akimotoite and seismic anisotropy of the Tonga slab. Nature. **455,** 657–660 (2008)
Shito, A., Shiobara, H., Sugioka, H., Ito, A., et al.: Physical properties of subducted slab and surrounding mantle in the Izu-Bonin subduction zone based on Broadband Ocean Bottom Seismometer data. J. Geophys. Res. **114,** B03308 (2009)
Snoke, J.A., Sacks, I.S., Okada, H.: Determination of the subducting lithosphere boundary by use of converted phases. Bull. Seismol. Soc. Am. **67,** 1051–1060 (1977)
Stachnik, J., Abers, G., Christensen, D.: Seismic attenuation and mantle wedge temperatures in the Alaska subduction zone. J. Geophys. Res. **109,** B10304 (2004)
Stern, R.: Subduction zones. Rev. Geophys. **40,** RG000108 (2002)
Stubailo, I., Beghein, C., Davis, P.: Structure and anisotropy of the Mexico subduction zone based on Rayleigh-wave analysis and implications for the geometry of the Trans-Mexican Volcanic Belt. J. Geophys. Res. **117,** B05303 (2012)
Syracuse, E., Abers, G.: Global compilation of variations in slab depth beneath arc volcanoes and implications. Geochem. Geophys. Geosyst. **7,** Q05017 (2006)
Syracuse, E., Abers, G., Fisher, K., MacKenzie, L., et al.: Seismic tomography and earthquake locations in the Nicaraguan and Costa Rican upper mantle. Geochem. Geophys. Geosyst. **9,** Q07S08 (2008)
Takanami, T.: Three-dimensional seismic structure of the crust and upper mantle beneath the orogenic belts in southern Hokkaido. Japan. J. Phys. Earth. **30,** 87–104 (1982)
Tamura, Y., Tatsumi, Y., Zhao, D., Kido, Y., Shukuno, H.: Hot fingers in the mantle wedge: new insight into magma genesis in subduction zones. Earth Planet. Sci. Lett. **197,** 105–116 (2002)
Tatsumi, Y.: Migration of fluid phases and genesis of basalt magmas in subduction zones. J. Geophys. Res. **94,** 4697–4707 (1989)
Taylor, B., Zellmer, K., Martinez, F., Goodliffe, A.: Sea-floor spreading in the Lau back-arc basin. Earth Planet. Sci. Lett. **144,** 35–40 (1996)
Terada, T., Hiramatsu, Y., Mizukami, T.: Shear wave anisotropy beneath the volcanic front in South Kyushu area, Japan: development of C-type olivine CPO under H2O-rich conditions. J. Geophys. Res. **118,** 4253–4264 (2013)
Thurber, C.: Earthquake locations and three-dimensional crustal structure in the Coyote Lake area, central California. J. Geophys. Res. **88,** 8226–8236 (1983)
Tian, Y., Liu, L.: Geophysical properties and seismotectonics of the Tohoku forearc region. J. Asian Earth Sci. **64,** 235–244 (2013)
Tian, Y., Zhao, D.: Seismic anisotropy and heterogeneity in the Alaska subduction zone. Geophys. J. Int. **190,** 629–649 (2012)
Tian, Y., Zhao, D.: Reactivation and mantle dynamics of North China Craton: insight from P-wave anisotropy tomography. Geophys. J. Int. **195,** 1796–1810 (2013)
Tibi, R., Wiens, D., Yuan, Y.: Seismic evidence for widespread serpentinized forearc mantle along the Mariana convergence margin. Geophys. Res. Lett. **35,** L13303 (2008)
Toh, H., Baba, K., Ichiki, M., Motobayashi, T., Ogawa, Y., Mishina, M., Takahashi, I.: Two-dimensional electrical section beneath the eastern margin of Japan Sea. Geophys. Res. Lett. **33,** L22309 (2006)
Tong, P., Zhao, D., Yang, D.: Tomography of the 1995 Kobe earthquake area: comparison of finite-frequency and ray approaches. Geophys. J. Int. **187,** 278–302 (2011)
Tong, P., Zhao, D., Yang, D.: Tomography of the 2011 Iwaki earthquake (M 7.0) and Fukushima nuclear power plant area. Solid Earth. **3,** 43–51 (2012)
Tsumura, N., Matsumoto, S., Horiuchi, S., Hasegawa, A.: Three-dimensional attenuation structure beneath the northeastern Japan arc estimated from spectra of small earthquakes. Tectonophysics. **319,** 241–260 (2000)
Turcotte, D., Schubert, G.: Geodynamics, 2nd edn. Cambridge University Press, Cambridge (2001)

Umino, N., Hasegawa, A.: On the two-layered structure of deep seismic plane in northeastern Japan arc. J. Seismol. Soc. Japan. **27,** 125–139 (1975)
Umino, N., Hasegawa, A.: Three-dimensional Qs structure in the northeastern Japan arc. J. Seismol. Soc. Japan. **37,** 217–228 (1984)
Umino, N., Hasegawa, A., Matsuzawa, T.: sP depth phase at small epicentral distances and estimated subducting plate boundary. Geophys. J. Int. **120,** 356–366 (1995)
Van Avendonk, H., Holbrook, W., Lizarralde, Denyer, P.: Structure and serpentinization of the subducting Cocos plate offshore Nicaragua and Costa Rica. Geochem. Geophys. Geosyst. **12,** Q06009 (2011)
van Stiphout, T., Kissling, E., Wiemer, S., Ruppert, N.: Magmatic processes in the Alaska subduction zone by combined 3-D b value imaging and targeted seismic tomography. J. Geophys. Res. **114,** B11302 (2009)
Vavrycuk, V.: Spatially dependent seismic anisotropy in the Tonga subduction zone: a possible contributor to the complexity of deep earthquakes. Phys. Earth Planet. Inter. **155,** 63–72 (2006)
Vidale, J., Schmidt, D., Malone, S., Hotovec-Ellis, A., Moran, S., Creager, K., Houston, H.: Deep long-period earthquakes west of the volcanic arc in Oregon: evidence of serpentine dehydration in the fore-arc mantle wedge. Geophys. Res. Lett. **41,** 370–376 (2014)
Volti, T., Gorbatov, A., Shiobara, H., et al.: Shear-wave splitting in the Mariana trough-a relation between back-arc spreading and mantle flow? Earth Planet. Sci. Lett. **244,** 566–575 (2006)
Wada, I., Wang, K., He, J., Hyndman, R.: Weakening of the subduction interface and its effects on surface heat flow, slab dehydration, and mantle wedge serpentinization. J. Geophys. Res. **113,** B04402 (2008)
Wagner, L., Beck, S., Zandt, G.: Upper mantle structure in the south central Chilean subduction zone (30–36°S). J. Geophys. Res. **110,** B01308 (2005)
Wagner, L., Forsyth, D., Fouch, M., James, D.: Detailed three-dimensional shear wave velocity structure of the northwestern United States from Rayleigh wave tomography. Earth Planet. Sci. Lett. **299,** 273–284 (2010)
Wang, J., Zhao, D.: P-wave anisotropic tomography beneath Northeast Japan. Phys. Earth Planet. Inter. **170,** 115–133 (2008)
Wang, J., Zhao, D.: P-wave anisotropic tomography of the crust and upper mantle under Hokkaido, Japan. Tectonophysics. **469,** 137–149 (2009)
Wang, J., Zhao, D.: Mapping P-wave anisotropy of the Honshu arc from Japan trench to the back-arc. J. Asian Earth Sci. **39,** 396–407 (2010)
Wang, J., Zhao, D.: P wave anisotropic tomography of the Nankai subduction zone in Southwest Japan. Geochem. Geophys. Geosyst. **13,** Q05017 (2012)
Wang, J., Zhao, D.: P-wave tomography for 3-D radial and azimuthal anisotropy of Tohoku and Kyushu subduction zones. Geophys. J. Int. **193,** 1166–1181 (2013)
Wang, Z., Zhao, D., Mishra, O.P., Yamada, A.: Structural heterogeneity and its implications for the low-frequency tremors in Southwest Japan. Earth Planet. Sci. Lett. **251,** 66–78 (2006a)
Wang, Z., Zhao, D., Wang, J., Kao, H.: Tomographic evidence for the Eurasian lithosphere subducting beneath South Taiwan. Geophys. Res. Lett. **33,** L18306 (2006b)
Wang, Z., Fukao, Y., Zhao, D., et al.: Structural heterogeneities in the crust and upper mantle beneath Taiwan. Tectonophysics. **476,** 460–477 (2009)
Wang, Y., Ma, K., Mouthereau, F., Eberhard-Phillips, D.: Three-dimensional Qp- and Qs-tomography beneath Taiwan orogenic belt: implications for tectonic and thermal structure. Geophys. J. Int. **180,** 891–910 (2010)
Wang, X., Li, Z., Li, X., Li, J., Liu, Y., Long, W., Zhou, J., Wang, F.: Temperature, pressure, and composition of the mantle source region of Late Cenozoic basalts in Hainan Island, SE Asia: a consequence of a young thermal mantle plume close to subduction zones? J. Petrol. **53,** 177–233 (2012)
Wang, J., Zhao, D., Yao, Z.: Crustal and uppermost mantle structure and seismotectonics of North China Craton. Tectonophysics. **582,** 177–187 (2013)
Wang, J., Wu, H., Zhao, D.: P wave radial anisotropy tomography of the upper mantle beneath the North China Craton. Geochem. Geophys. Geosyst. **15,** 2195–2210 (2014)

Wang, Z., Zhao, D.: Seismic imaging of the entire arc of Tohoku and Hokkaido in Japan using P-wave, S-wave and sP depth-phase data. Phys. Earth Planet. Inter. **152,** 144–162 (2005)
Wang, Z., Zhao, D.: Vp and Vs tomography of Kyushu, Japan new insight into arc magmatism and forearc seismotectonics. Phys. Earth Planet. Inter. **157,** 269–285 (2006a)
Wang, Z., Zhao, D.: Suboceanic earthquake location and seismic structure in the Kanto district, central Japan. Earth Planet. Sci. Lett. **241,** 789–803 (2006b)
Wei, W., Xu, J., Zhao, D., Shi, Y.: East Asia mantle tomography: new insight into plate subduction and intraplate volcanism. J. Asian Earth Sci. **60,** 88–103 (2012)
Wei, W., Zhao, D., Xu, J.: P-wave anisotropic tomography in Southeast Tibet: new insight into the lower crustal flow and seismotectonics. Phys. Earth Planet. Inter. **222,** 47–57 (2013)
Wiens, D., Conder, J., Faul, U.: The seismic structure and dynamics of the mantle wedge. Annu. Rev. Earth Planet. Sci. **36,** 421–455 (2008)
Worzewski, T., Jegen, M., Kopp, H., Brasse, H., Castillo, W.: Magnetotelluric image of the fluid cycle in the Costa Rica subduction zone. Nature Geosci. **4,** 108–111 (2010)
Xia, S., Zhao, D., Qiu, X.: Tomographic evidence for the subducting oceanic crust and forearc mantle serpentinization under Kyushu, Japan. Tectonophysics. **449,** 85–96 (2008)
Xu, Y., Wiens, D.: Upper mantle structure of the southwest Pacific from regional waveform inversion. J. Geophys. Res. **102,** 27439–27451 (1997)
Yamamoto, Y., Hino, R., Shinohara, M.: Mantle wedge structure in the Miyagi Prefecture forearc region, central northeastern Japan arc, and its relation to corner-flow pattern and interplate coupling. J. Geophys. Res. **116,** B10310 (2011)
Yuan, X., Sobolev, S., Kind, R., Oncken, O., et al.: Subduction and collision processes in the Central Andes constrained by converted seismic phases. Nature. **408,** 958–961 (2000)
Zhang, Y., Zhao, D., Matsui, M.: Anisotropy of Akimotoite: a molecular dynamics study. Phys. Earth Planet. Inter. **151,** 309–319 (2005)
Zhang, H.J., Liu, Y., Thurber, C., Roecker, S.: Three-dimensional shear-wave splitting tomography in the Parkfield, California, region. Geophys. Res. Lett. (2007). doi: 10.1029/2007GL031951
Zhang, H., Zhao, D., Zhao, J., Xu, Q.: Convergence of the Indian and Eurasian plates under eastern Tibet revealed by seismic tomography. Geochem. Geophys. Geosyst. **13,** Q06W14 (2012)
Zhang, H., Zhao, D., Zhao, J., Liu, H.: Tomographic imaging of the underthrusting Indian slab and mantle upwelling beneath central Tibet. Gondwana Res., In press (2014).
Zhao, D.: Seismological structure of subduction zones and its implications for arc magmatism and dynamics. Phys. Earth Planet. Inter. **127,** 197–214 (2001a)
Zhao, D.: Seismic structure and origin of hotspots and mantle plumes. Earth Planet. Sci. Lett. **192,** 251–265 (2001b)
Zhao, D.: Global tomographic images of mantle plumes and subducting slabs: insight into deep Earth dynamics. Phys. Earth Planet. Inter. **146,** 3–34 (2004)
Zhao, D.: Tomography and dynamics of Western-Pacific subduction zones. Monogr. Environ. Earth Planet. **1,** 1–70 (2012)
Zhao, D., Hasegawa, A.: P-wave tomographic imaging of the crust and upper mantle beneath the Japan Islands. J. Geophys. Res. **98,** 4333–4353 (1993)
Zhao, D., Ohtani, E.: Deep slab subduction and dehydration and their geodynamic consequences: evidence from seismology and mineral physics. Gondwana Res. **16,** 401–413 (2009)
Zhao, D., Liu, L.: Deep structure and origin of active volcanoes in China. Geosci. Frontiers. **1,** 31–44 (2010)
Zhao, D., Tian, Y.: Changbai intraplate volcanism and deep earthquakes in East Asia: a possible link? Geophys. J. Int. **195,** 706–724 (2013)
Zhao, D., Hasegawa, A., Horiuchi, S.: Tomographic imaging of P and S wave velocity structure beneath northeastern Japan. J. Geophys. Res. **97,** 19909–19928 (1992)
Zhao, D., Hasegawa, A., Kanamori, H.: Deep structure of Japan subduction zone as derived from local, regional and teleseismic events. J. Geophys. Res. **99,** 22313–22329 (1994)
Zhao, D., Christensen, D., Pulpan, H.: Tomographic imaging of the Alaska subduction zone. J. Geophys. Res. **100,** 6487–6504 (1995)

Zhao, D., Kanamori, H., Negishi, H., Wiens, D.: Tomography of the source area of the 1995 Kobe earthquake: evidence for fluids at the hypocenter? Science. **274,** 1891–1894 (1996)
Zhao, D., Matsuzawa, T., Hasegawa, A.: Morphology of the subducting slab boundary in the northeastern Japan arc. Phys. Earth Planet. Inter. **102,** 89–104 (1997a)
Zhao, D., Xu, Y., Wiens, D., Dorman, L., Hildebrand, J., Webb, S.: Depth extent of the Lau backarc spreading center and its relationship to the subduction process. Science. **278,** 254–257 (1997b)
Zhao, D., Asamori, K., Iwamori, H.: Seismic structure and magmatism of the young Kyushu subduction zone. Geophys. Res. Lett. **27,** 2057–2060 (2000)
Zhao, D., Wang, K., Rogers, G., Peacock, S.: Tomographic image of low P velocity anomalies above slab in northern Cascadia subduction zone. Earth Planet. Space. **53,** 285–293 (2001)
Zhao, D., Mishra, O.P., Sanda, R.: Influence of fluids and magma on earthquakes: seismological evidence. Phys. Earth Planet. Inter. **132,** 249–267 (2002)
Zhao, D., Tani, H., Mishra, O.P.: Crustal heterogeneity in the 2000 western Tottori earthquake region: effect of fluids from slab dehydration. Phys. Earth Planet. Inter. **145,** 161–177 (2004)
Zhao, D., Tian, Y., Lei, J., Liu, L., Zheng, S.: Seismic image and origin of the Changbai intraplate volcano in East Asia: role of big mantle wedge above the stagnant Pacific slab. Phys. Earth Planet. Inter. **173,** 197–206 (2009)
Zhao, D., Wei, W., Nishizono, Y., Inakura, H.: Low-frequency earthquakes and tomography in western Japan: insight into fluid and magmatic activity. J. Asian Earth Sci. **42,** 1381–1393 (2011a)
Zhao, D., Huang, Z., Umino. N., Hasegawa, A., Kanamori, H.: Structural heterogeneity in the megathrust zone and mechanism of the 2011 Tohoku-oki earthquake (Mw 9.0). Geophys. Res. Lett. **38,** L17308 (2011b)
Zhao, D., Yanada, T., Hasegawa, A., Umino, N., Wei, W.: Imaging the subducting slabs and mantle upwelling under the Japan Islands. Geophys. J. Int. **190,** 816–828 (2012)
Zhao, J., Zhao, D., Zhang, H., et al.: P-wave tomography and dynamics of the crust and upper mantle beneath western Tibet. Gondwana Res. **25,** 1690–1699 (2014)
Zheng, H., Li, T., Gao, R., Zhao, D., He, R.: Teleseismic P-wave tomography evidence for the Indian lithospheric mantle subducting northward beneath the Qiangtang terrane. Chinese J. Geophys. **50,** 1418–1426 (2007)

Chapter 4
Large Earthquakes and Seismotectonics

Abstract We review seismic tomography studies of source areas of large crustal earthquakes, megathrust earthquakes, intraslab earthquakes, and deep earthquakes to understand the seismogenesis and seismotectonics. It is found that structural heterogeneities in the crust and upper mantle strongly affect or control the generation of large and small earthquakes in various tectonic settings. In particular, fluids and magmas play an important role in the nucleation of large earthquakes. Fault, Force (stress) and Fluid (3F) are three key elements in earthquake generation. These studies indicate that seismic tomography is an important and effective tool for studying earthquakes and seismotectonics.

Keywords Crustal earthquakes · Seismotectonics · Megathrust zone · Subducting slab · Intraslab earthquakes

Earthquakes are a characteristic feature of the planet Earth because it has plate tectonics. A majority of earthquakes take place in the plate boundary regions, i.e., mid-ocean ridges, transform faults, and subduction and collision zones. Shallow earthquakes (< 60 km depth) occur in broad regions on Earth, whereas intermediate-depth (60–300 km) and deep earthquakes (300–680 km depth) occur only in the subducting oceanic or continental lithosphere (slabs). Subduction-zone earthquakes can be classified into three types: crustal earthquakes in the overlying plate, megathrust earthquakes in the interplate boundary zone between the overlying and subducting plates, and intraslab earthquakes within the subducting slab which occur over a wide depth range (0–680 km), including outer-rise earthquakes near the oceanic trench and very deep earthquakes.

Reid (1910) investigated the mechanism of the 1906 San Francisco earthquake (M 7.8) and developed the elastic rebound theory. Since this pioneering work, seismologists have reached a consensus that earthquakes are generated by the (sudden) rupture of active faults in the lithosphere or the subducting slabs. So far, seismic waveforms have been used successfully to estimate the physical parameters and rupture processes of large and small earthquakes (see a recent review by Beroza and Kanamori 2007). Since the late 1970s, seismic tomography has been applied successfully to various tectonic environments on Earth (see recent reviews by Zhao 2009, 2012), however, this method is still not very successful for studying

D. Zhao, *Multiscale Seismic Tomography,* Springer Geophysics,
DOI 10.1007/978-4-431-55360-1_4

earthquake sources and active faults, due to the following reasons. At present, even local-scale tomography has a spatial resolution of ten to tens of kilometers in most cases. Even the best resolution of local tomography is of the order of a few kilometers (e.g., Zhao et al. 1996; Zhao and Negishi 1998; Tong et al. 2011), which is much greater than the width of an active fault zone (~1–100 m). Thus, current seismic tomography can hardly image reliably any earthquake-related structural heterogeneity in a fault zone, such as asperities (Beroza and Kanamori 2007). Seismic tomography is good at detecting three-dimensional (3-D) voluminous variations in the physical properties of the crust and mantle, but not suitable for imaging two-dimensional (2-D) heterogeneity on a plane such as a fault zone (Zhao 2001).

Nevertheless, to date, seismic tomography has been applied with some success in studying the cause of large earthquakes. One crucial condition of successful tomographic studies is that a dense network of permanent or portable seismic stations must be available in or around the target earthquake area so that high-resolution tomographic images can be obtained to detect structural heterogeneities that may be related to the generation of large earthquakes. In practical studies, however, such a crucial condition can hardly be satisfied except for a few well-instrumented regions such as the Japan Islands, California, and the Beijing area, though large earthquakes occur frequently in various regions of the world. Compared with studies of other tectonic environments, such as subduction and collision zones, tomographic studies of earthquake source zones started relatively late, around the early 1990s (e.g., Lees 1990; Michael and Eberhart-Phillips 1991; Zhao and Kanamori 1993). Since then, however, and in particular during the past decade, there has been rapid progress in studying the detailed 3-D crustal structure of large earthquake areas, thanks to the advances in seismic instrumentation technology and the deployment of portable and/or permanent seismic arrays in many seismically active regions. Many high-resolution tomographic images of earthquake source zones have been accumulated, which provide important new insights into the seismotectonics and dynamic processes of not only large crustal earthquakes but also megathrust and intraslab earthquakes.

4.1 Large Crustal Earthquakes

4.1.1 Japan

In 1990, short-period local seismic networks operated by eight Japanese national universities in separate areas of Japan were merged with the nationwide JMA (Japan Meteorological Agency) network to monitor the seismic activity in and around the Japan Islands. In 2000, the high-sensitivity seismic network (Hi-net), consisting of over 600 high-quality short-period stations covering the entire Japan islands, was built by the National Research Institute for Earth Science and Disaster Prevention. All the JMA, university and Hi-net seismic stations have been combined together,

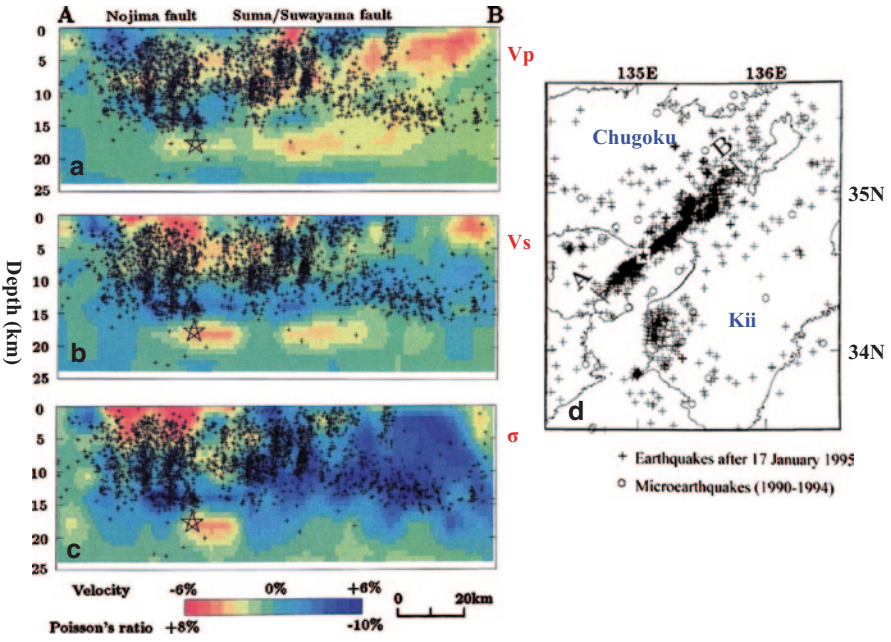

Fig. 4.1 Vertical cross-sections of **a** P-wave velocity, **b** S-wave velocity, and **c** Poisson's ratio, images along the profile AB as shown in d. *Red* color denotes low velocity and high Poisson's ratio; *blue* color denotes high velocity and low Poisson's ratio. The color scale is shown at the *bottom*. The average value of Poisson's ratio is 0.25. The star symbol and crosses denote the mainshock and aftershocks of the 1995 Kobe earthquake (M 7.2). The vertical exaggeration in (**a**–**c**) is 2:1. *Circles* and *crosses* in **d** denote the local crustal earthquakes during 1990–1994 and those after 17 January 1995, respectively. (Modified from Zhao et al. 1996)

forming the Japan Unified Seismic Network which covers the Japan Islands densely and uniformly (Okada et al. 2004). Since 1995, seven damaging crustal earthquakes with magnitudes (M)≥6.8 have occurred in the Japanese land areas which are covered by the dense permanent seismic network, as well as portable seismic stations installed soon after every mainshock. Hence, detailed tomographic images in those source areas have been determined with a high resolution, which shed new light on the relationship between structural heterogeneity and earthquake nucleation in Japan.

The Kobe earthquake (M 7.3), which occurred on 17 January 1995 in SW Japan (Fig. 4.1), was one of the most damaging earthquakes in Japan, killing over 6400 people. Soon after the occurrence of the Kobe mainshock, many portable seismic stations were deployed in the epicenter area to record its aftershocks (Hirata et al. 1996). These portable stations and the permanent network stations formed a dense seismic array covering the Kobe source area, resulting in accurate hypocenter locations of the aftershocks (Fig. 4.1). A large number of arrival-time data from the well-located aftershocks and other local earthquakes in the Kobe area were used to determine high-resolution (4–5 km), 3-D P- and S-wave velocity (Vp, Vs) and Poisson's

ratio (PR) images in the Kobe aftershock area (Zhao et al. 1996). A prominent low-velocity (low-V) and high-PR anomaly was detected at depths of 16–21 km directly beneath the Kobe mainshock hypocenter (under the Akashi strait and Osaka Bay) (Fig. 4.1a–c). The anomaly has a lateral extent of ~15 km. Because there is no active volcano in the Kobe area and the surface heat flow is not very high there, the anomaly in the Kobe hypocenter was interpreted as a fluid-filled, fractured rock matrix that triggered the 1995 Kobe earthquake (Zhao et al. 1996; Zhao and Negishi 1998). Later tomographic studies indicated that the fluids in the Kobe source zone originated from the dehydration of the subducting Philippine Sea (PHS) slab under SW Japan (Zhao et al. 2000, 2002; Salah and Zhao 2003; Ikeda et al. 2006; Gupta et al. 2009). Zhao and Mizuno (1999) estimated the distribution of crack density and saturation rate in the Kobe source area by applying a crack theory (O'Connell and Budiansky 1974) to the values of Vp, Vs and PR determined by seismic tomography. They suggested that seawater in Osaka Bay may have permeated down to the deep crust through the active faults that may have been ruptured many times during every earthquake cycle in the past 2 million years after the formation of Osaka Bay and the active faults there. Tong et al. (2011) used a better data set recorded by the Hi-net and adopted both finite-frequency and ray tomography methods to study the detailed 3-D crustal structure of the Kobe area. Their new results have confirmed the earlier findings of Zhao et al. (1996).

Detailed Vp, Vs and PR images were also determined for the source area of the Western-Tottori earthquake (M 7.3) that occurred on 6 October 2000 in Western Japan (Zhao et al. 2004). The mainshock epicenter is located close to the Daisen volcano, and its hypocenter is located at a depth of 12 km where the tomographic images change drastically (Fig. 4.2). The upper crust exhibits high Vp, slightly low Vs and high PR, indicating a brittle seismogenic layer probably containing fluids. The lower crust beneath the mainshock hypocenter exhibits low Vp and low Vs, which may reflect the presence of high-temperature materials, possibly containing magma, under Daisen that is a potentially active volcano (Zhao et al. 2011a). Later, Shibutani and Katao (2005) used a better data set recorded by portable seismic stations and also found significant velocity variations in the Tottori source area. Low-frequency (LF) microearthquakes were detected at ~30 km depth in this area (Ohmi and Obara 2002). Five LF events occurred within the 3 years before the Tottori mainshock, and more than 60 LF events occurred during 13 months following the mainshock. Waveform analyses show that a single-force source mechanism is preferable to a double-couple mechanism for those LF events (Ohmi and Obara 2002). These results suggest that the LF events were caused by the transport of fluids, such as water or magma. A detailed magnetotelluric imaging detected an anomaly of high electric-conductivity down to a depth of 30 km beneath the western Tottori area, suggesting the existence of fluids in the lower crust (Oshiman 2002). Joint inversions of local and teleseismic data imaged the subducting PHS slab under the Tottori area and offshore under the Japan Sea (Zhao et al. 2004, 2012a; Huang et al. 2013). The PHS slab is located at a depth of ~55 km under the Daisen volcano, and a significant low-V zone has been imaged above the slab and beneath the Daisen volcano. The low-V zone may reflect a magma chamber under the Daisen volcano

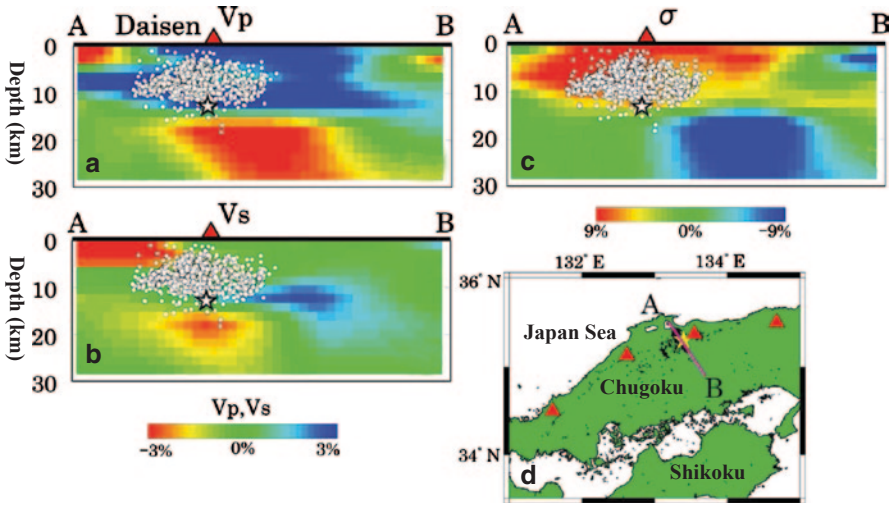

Fig. 4.2 Vertical cross-sections of **a** P-wave velocity, **b** S-wave velocity, and **c** Poisson's ratio, images along the profile AB as shown in **d**. *Red* color denotes low velocity and high Poisson's ratio; *blue* color denotes high velocity and low Poisson's ratio. The scales for velocity and Poisson's ratio are shown below **b** and **c**, respectively. The average value of Poisson's ratio is 0.25. The star symbol and *white* dots denote the mainshock and aftershocks of the 2000 Western Tottori earthquake (M 7.3). The *red triangles* and *yellow* star in **d** show quaternary volcanoes and the Western Tottori earthquake epicenter, respectively. (Modified from Zhao et al. 2004)

associated with the dehydration process of the PHS slab. All these results indicate the existence of arc magma and fluids in the Tottori area and their influence on the generation of the 2000 Western-Tottori earthquake.

The west off-Fukuoka earthquake (M 7.0) took place on 20 March 2005 in the northwestern portion of Kyushu. Most of its aftershocks were located in a NW-SE trending fault offshore under the Tsushima Strait, outside the seismic network in Kyushu. Wang and Zhao (2006a) collected arrival-time data of the sP depth-phase, as well as the first P- and S-waves, to relocate the Fukuoka aftershocks, and then obtained tomographic images in the source area of the Fukuoka earthquake. They found that the Vp and Vs images exhibit similar features in the source area. The mainshock hypocenter is located in a high-V zone, whereas low-V and high-PR zones are revealed in the lower crust under the mainshock hypocenter, similar to the features in the Kobe and Western-Tottori earthquake areas. Hence, it is considered that crustal fluids existed in the Fukuoka earthquake area and affected its nucleation, and that the fluids may be related to a diapiric mantle upwelling off western Kyushu due to the opening of the Okinawa Trough above the subducting PHS slab (Wang and Zhao 2006a).

On 23 October 2004 and 16 July 2007, two crustal earthquakes (M 6.8) took place in the Niigata Prefecture of NE Japan, which caused significant local damage. Detailed tomographic images were determined in the source area of the Niigata earthquakes (e.g., Kato et al., 2005; Wang and Zhao, 2006b; Xia et al., 2008).

Similar to the above-mentioned Kobe, Tottori and Fukuoka earthquakes, significant low-V and high-PR anomalies were detected in the Niigata source areas, and the anomalies in the crust are connected with a low-V zone in the upper mantle wedge above the subducting Pacific slab. Therefore, arc magma and fluids resulting from the Pacific slab dehydration may have played an important role in the nucleation of the two Niigata earthquakes (Wang and Zhao 2006b; Xia et al. 2008; Zhao et al. 2011b).

On 25 March 2007, a damaging crustal earthquake (M 6.9) occurred in the Noto Peninsula in the eastern margin of the Japan Sea. Detailed crustal tomography revealed prominent low-V and high-PR anomalies in the Noto earthquake area, indicating that back-arc magma and fluids resulting from the Pacific slab dehydration and corner flow in the mantle wedge contributed to the nucleation of the 2007 Noto earthquake (Padhy et al. 2011; Zhao et al. 2010, 2011b), very similar to the generation of the Niigata earthquakes.

On 14 June 2008, a damaging crustal earthquake (M 7.2) hit the Iwate-Miyagi area in central Tohoku (Fig. 4.3). Its epicenter was located about 10 km east of the volcanic front and very close to the active Kurikoma volcano. Detailed 3-D Vp, Vs and PR images were obtained for the Iwate-Miyagi source area (Okada et al. 2010; Cheng et al. 2011) (Fig. 4.3). Its mainshock and three large aftershocks occurred in a boundary zone where Vp, Vs and PR all change drastically. A pronounced low-V and high-PR anomaly was revealed in the lower crust and the uppermost mantle under the Kurikoma volcano and the source zone, reflecting arc magma and fluids ascending from the upper-mantle wedge above the Pacific slab, which contributed to the nucleation of the 2008 Iwate-Miyagi earthquake. Wei and Zhao (2013) used irregular-grid tomography to determine detailed 3-D Vp and Vs images in the crust and upper mantle beneath the Iwate-Miyagi earthquake area, and their results are very similar to those of Cheng et al. (2011).

The 11 April 2011 Iwaki earthquake (M 7.0) was one of the major aftershocks of the 11 March 2011 Tohoku-oki earthquake (Mw 9.0) and the strongest one hit the Japan land area (Fig. 4.4). The Iwaki earthquake occurred at a depth of 6.4 km and was located ~200 km southwest of the Tohoku-oki mainshock. It was caused by normal faulting with some strike-slip component along the Idosawa fault. This normal-faulting earthquake is in contrast to the compressional stress regime in NE Japan and may reflect an enhanced extensional stress on the overriding block induced by the Tohoku-oki mainshock (Yoshida et al. 2012). The disabled Fukushima nuclear power plant (FNPP), which suffered major damage from the Tohoku-oki earthquake and the subsequent tsunami, is located ~60 km northeast of the Iwaki earthquake epicenter (Fig. 4.4). Tong et al. (2012) determined high-resolution tomographic images of the crust and upper mantle beneath the Iwaki earthquake and the FNPP area. They found that the Iwaki earthquake and its aftershocks mainly occurred in a boundary zone with strong variations in seismic velocity and Poisson's ratio. Prominent low-V and high-PR anomalies were revealed under the Iwaki source area and the FNPP, which may reflect fluids released from the dehydration of the subducting Pacific slab. These results suggest that the 2011 Iwaki earthquake was triggered by the ascending fluids from the Pacific slab dehydration and the

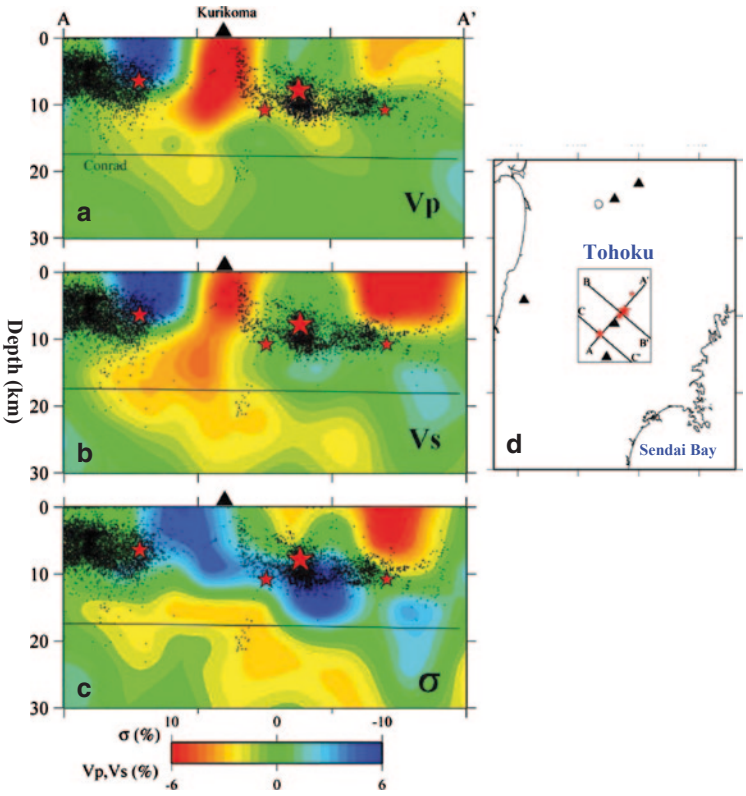

Fig. 4.3 Vertical cross-sections of **a** P-wave velocity, **b** S-wave velocity, and **c** Poisson's ratio, images along the profile A-A' as shown in **d**. *Red* denotes low velocity and high Poisson's ratio; *blue* denotes high velocity and low Poisson's ratio. The color scale is shown at the *bottom*. The *black triangles* denote active arc volcanoes. Small *black* dots show earthquakes which occurred within a 10-km width along the profile A-A'. The thin lines show the Conrad discontinuity. The *red* stars denote the mainshock and large aftershocks of the 2008 Iwate-Miyagi earthquake (M 7.2). (Modified from Cheng et al. 2011)

change of the stress regime induced by the Tohoku-oki megathrust earthquake (Mw 9.0). Similar structures were revealed under the Iwaki source area and the Futaba fault adjacent to the FNPP (Fig. 4.4), suggesting that the security of the FNPP site should be strengthened to withstand potential large earthquakes in the future (Tong et al. 2012). Using aftershock arrival-time data recorded by portable seismic stations deployed in the Iwaki area, Kato et al. (2013) also determined a detailed crustal tomography of the 2011 Iwaki source zone, and suggested that the brittle crust underwent structural failure due to the infiltration of crustal fluids into the seismogenic layer from the upper-mantle wedge, leading to the Iwaki earthquake.

Zhao et al. (2010) compared tomographic images with the distribution of 164 crustal earthquakes (M 5.7–8.0) which occurred under the Japan Islands between 1885 and 2008. They computed P-velocity perturbations (dV/V) in the crust and the

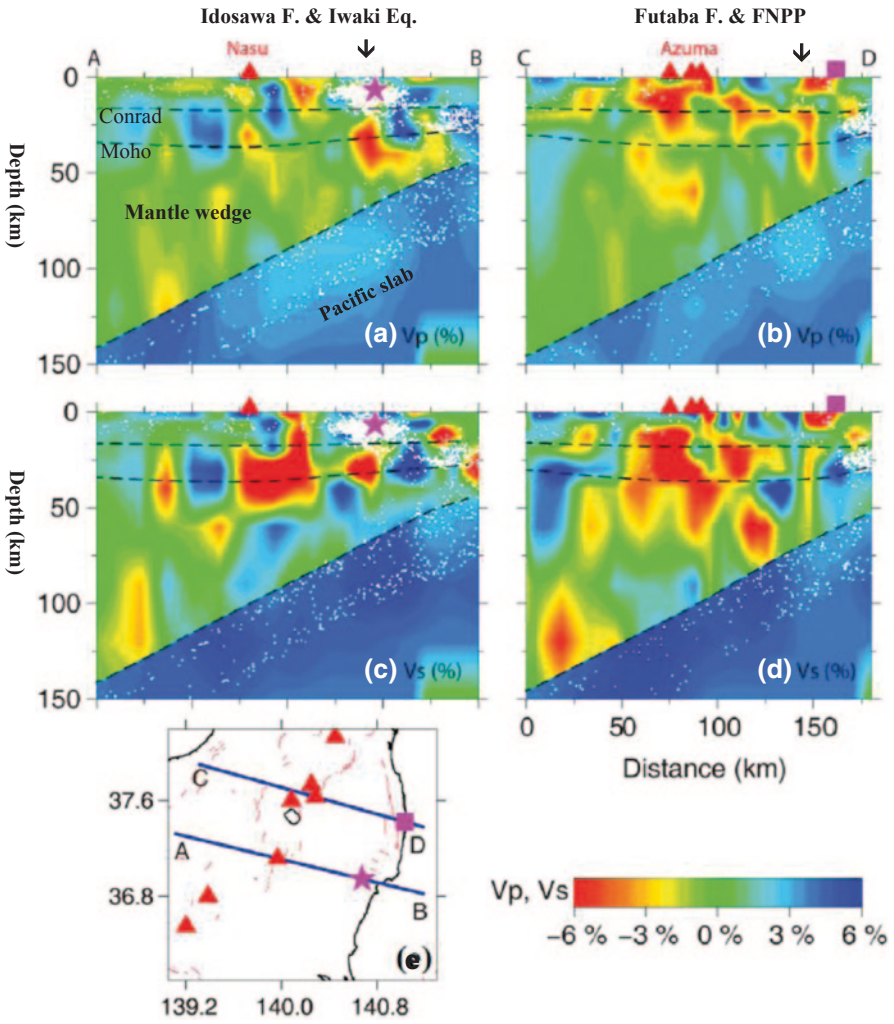

Fig. 4.4 Vertical cross-sections of (**a**, **b**) P-wave and (**c**, **d**) S-wave velocity images along the profiles AB (**a**, **c**) and CD (**b**, **d**) as shown in (**e**). *Red* and *blue* colors denote low and high velocities, respectively. The velocity perturbation (in %) scale is shown at the *bottom*. *Red* triangles denote the active arc volcanoes. Small *white* dots show earthquakes which occurred within a 20-km width along each profile. The *dashed lines* denote the Conrad and the Moho discontinuities and the upper boundary of the subducting Pacific slab. The *purple* stars denote the hypocenter of the 2011 Iwaki earthquake (M 7.0). The *purple square* denotes the location of the Fukushima Nuclear Power Plant (FNPP). The *arrow* above **a** shows the location of the Idosawa fault and the Iwaki epicenter. The *arrow* above **b** shows the location of the Futaba fault. (Modified from Tong et al. 2012)

uppermost mantle at the hypocenters of the 164 large earthquakes and found that for 71 % of these events, −3 % < dV/V < 0 %, and 12 % of them having dV/V < −3 %. For the remaining 17 % of the events, 0 < dV/V < 1.5 %. This result indicates that the large crustal earthquakes in Japan generally take place at the edge portions of low-V

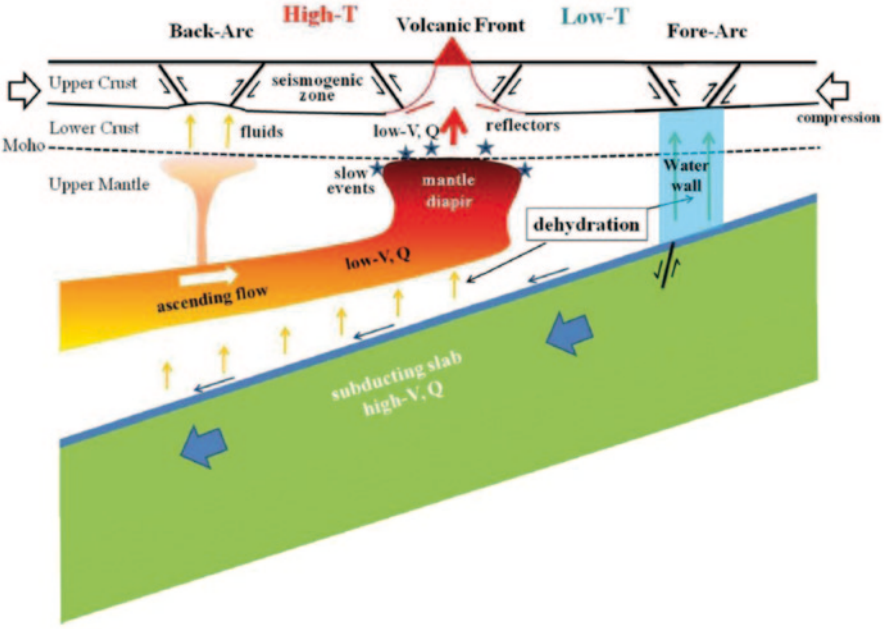

Fig. 4.5 Schematic illustration of across-arc vertical cross-section of the crust and upper mantle under the Japan subduction zone. The generation of large crustal earthquakes is affected by the tectonic background and structural heterogeneities, and in particular, arc magma and fluids (see text for details). (After Zhao et al. 2015)

anomalies, or along the boundary between the low-V and high-V zones. Only some smaller events (M 5.7–5.8) are located within the low-V zones. A few earthquakes have occurred in high-V areas, but they are generally < M 6.0 (Zhao et al. 2010).

The relationship between the crustal seismogenesis and structural heterogeneity in Japan has been investigated by several authors (e.g., Hasegawa and Zhao 1994; Zhao et al. 2000, 2002, 2010; Hasegawa et al. 2005). Two geodynamic processes are considered to be the most important in a subduction zone (Fig. 4.5). One is corner flow, i.e., convection, in the mantle wedge that can carry heat to the mantle wedge from the deeper mantle because of the temperature gradient in the mantle, and thus the mantle wedge becomes hotter beneath the volcanic front and back-arc area. The other is dehydration reactions of the subducting slab. In the forearc area, magma cannot be produced because the temperature there is lower, and fluids from the slab dehydration may migrate directly up to the crust. When the fluids enter an active fault in the crust, pore pressure will increase and fault zone friction will decrease, which can trigger large crustal earthquakes such as the 1995 Kobe and the 2011 Iwaki earthquakes. Under the volcanic front and the back-arc areas, arc magmas are produced because of the hotter mantle wedge and fluids from the slab dehydration. Once magmas ascend up to the surface, arc and back-arc volcanoes can be produced, resulting in strong lateral heterogeneities in the crust and the uppermost mantle. Thus, the seismogenic upper crust becomes weaker and hence, apt to generate large crustal earthquakes, such as the 2000 Western-Tottori, the 2004 and

2007 Niigata, the 2005 west off Fukuoka, and the 2008 Iwate-Miyagi, earthquakes, as mentioned above. The large crustal earthquakes usually do not occur within the weak low-V zones, but at their edges where the mechanical strength of materials is greater than in the low-V zones, but is still smaller than that of the normal sections of the seismogenic layer. Hence, the edge portions of the low-V areas become the optimal sites for large crustal earthquakes to take place, producing faults reaching the Earth's surface, or blind faults within the brittle upper crust (Fig. 4.5). Although the tomographic images obtained are complex and their details change from place to place (Figs. 4.1–4.4), low-V and/or high-PR anomalies are generally visible below or around the mainshock hypocenters. These results indicate the common feature that fluids and arc magma can affect, or even control, the nucleation of large crustal earthquakes in the Japan subduction zone (Hasegawa and Zhao 1994; Zhao et al. 2002, 2010, 2015).

4.1.2 China

In the broad Asian continent, the distribution of permanent seismic stations is very sparse, except in a few areas. One such area is the region in and around Beijing, where a modern digital seismic network consisting of over 100 seismic stations has been in operation since 2000. Huang and Zhao (2004) used a large number of high-quality arrival time data of local crustal earthquakes recorded by the Beijing seismic network to determine a detailed 3-D Vp tomography of the crust and uppermost mantle. They compared their tomographic image with the distribution of large crustal earthquakes in the Beijing region, such as the 1679 Sanhe earthquake (M 8.0), the 1976 Tangshan earthquake (M 7.8) and its two large aftershocks (the M 6.9 Ninghe and the M 7.1 Luanxian earthquakes), and found that these large earthquakes took place in high-V areas in the upper-middle crust, whereas prominent low-V anomalies exist in the lower crust and the uppermost mantle under the hypocenters (Fig. 4.6). These low-V zones also exhibit a high electric conductivity, suggesting that crustal fluids exist there. Later, Qi et al. (2006) determined 3-D Vp, Vs and PR images using more data recorded by the Beijing seismic network. Huang and Zhao (2009) conducted a joint inversion of local and teleseismic data recorded by the Beijing seismic network to determine a 3-D Vp model of the crust and the upper mantle down to a depth of 500 km. Wang et al. (2013) determined a 3-D P-wave anisotropic tomography of the crust and uppermost mantle beneath the North China Craton using the arrival times of local earthquakes. These later studies confirmed the early findings of seismotectonics by Huang and Zhao (2004).

Zhan et al. (2008) determined a 2-D image of electric resistivity across the source area of the 1927 Gulang earthquake (M 8.0) in Western China. Their result shows a significant low-resistivity anomaly existing right beside the Gulang hypocenter, which represents a middle-crust layer containing fluids that affected the nucleation of the Gulang earthquake.

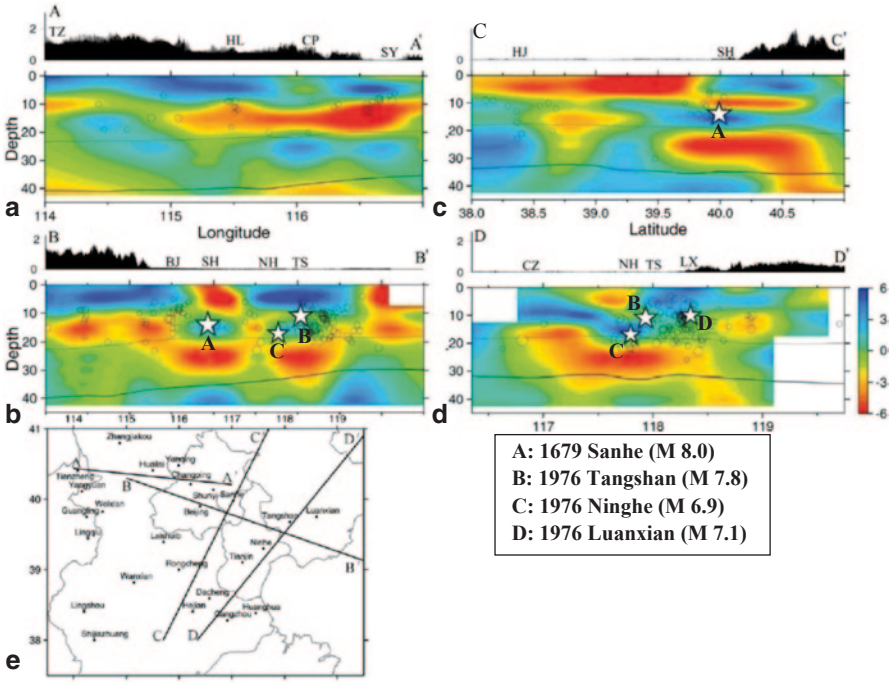

Fig. 4.6 (**a**–**d**) Vertical cross-sections of P-wave tomography along four profiles as shown in (**e**). *Red* and *blue* colors denote low and high velocities, respectively. The velocity perturbation (in %) scale is shown on the *right*. The *thin lines* show the Conrad and Moho discontinuities. The *white stars* denote four large crustal earthquakes in the Beijing region. (Modified from Huang and Zhao 2004)

Fig. 4.7 shows Vp, Vs and PR images in the source area of the 2008 Wenchuan earthquake (M 8.0) that occurred in the Longmenshan (LMS) fault zone in the eastern margin of the Tibetan Plateau (Lei and Zhao 2009). The structure of the LMS fault zone north of the Wenchuan mainshock is very different from that south of the mainshock. The southern section of the LMS fault zone contains a broad zone with low-Vp, low-Vs and high-PR, whereas the northern segment exhibits more scattered heterogeneities, corresponding to most of the aftershocks which occurred there. A prominent anomaly with low-Vp, low-Vs and high-PR appears directly beneath the Wenchuan mainshock hypocenter, suggesting that, in addition to compositional variations, fluid-filled fractured rock matrices may exist in the LMS fault zone, which may have triggered the Wenchuan mainshock and its aftershocks. The tomographic results provide seismic evidence for the hypothesis of the upward intrusion of the lower-crustal flow along the LMS fault zone (Lei and Zhao 2009).

The 20 April 2013 Lushan earthquake (Ms 7.0) occurred in a reverse fault in the eastern margin of the Tibetan Plateau and was located about 50 km southwest of the rupture zone of the 2008 Wenchuan earthquake (Zeng et al. 2013). Li et al. (2013) determined a Vp and Vs tomography of the Lushan source area and found that most

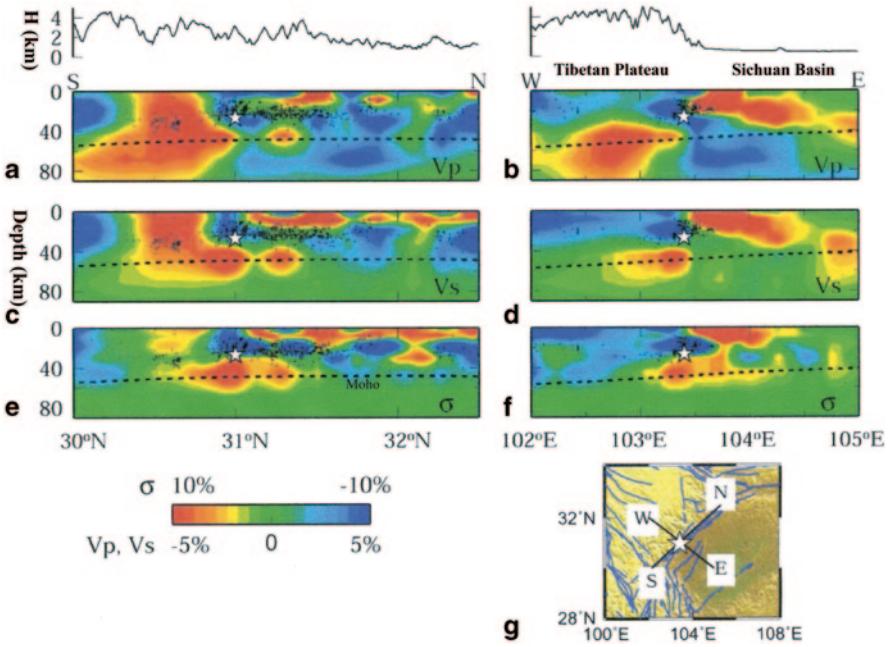

Fig. 4.7 Vertical cross-sections of (**a**, **b**) P-wave velocity, (**c**, **d**) S-wave velocity, and (**e**, **f**) Poisson's ratio, images along two profiles as shown in (**g**). *Red* denotes low velocity and high Poisson's ratio; *blue* denotes high velocity and low Poisson's ratio. The color scale is shown at the *bottom*. The dashed lines show the Moho discontinuity. The *white* stars denote the hypocenter of the 2008 Wenchuan earthquake (M 8.0) in Southwest China. (Modified from Lei and Zhao 2009)

aftershocks occurred in patches of high-Vp, high-Vs and low-Vp/Vs in the fault zone, which may reflect mafic or ultramafic materials thrusting from the mid-lower crust forming an asperity which generated the 2013 Lushan earthquake. A low-Vs anomaly is revealed in the gap between the Wenchuan and Lushan earthquakes, which may reflect ductile rocks (Li et al. 2013).

P-wave anisotropy tomography beneath Southeast Tibet and the adjacent regions was determined using a large number of data from local earthquakes and teleseismic events (Wei et al. 2013). The result shows a low-V layer with a thickness of ~20 km in the lower crust, which may reflect a mechanically weak zone capable of flow on a geological timescale. Most of the large earthquakes in the region, including the 2008 Wenchuan and the 2013 Lushan earthquakes, occurred at the margin of the ductile flow in the lower crust, suggesting that the seismogenesis is controlled by dynamic processes in the crust and upper mantle (Wei et al. 2013).

Cheng et al. (2014) determined a Vp tomography of the crust and uppermost mantle beneath the Helan-Liupan-Ordos western margin tectonic belt in North-Central China using local-earthquake arrival-time data. Their results show that prominent low-V anomalies exist widely in the lower crust and the low-V zones extend to the uppermost mantle in some local areas, suggesting that the lower crust

contains higher-temperature materials and fluids. The major fault zones, especially the large boundary faults of major tectonic blocks, are located at the edge portion of the low-V anomalies, or the transitional zone between the low-V and high-V anomalies in the upper crust, whereas low-V anomalies are revealed in the lower crust under most of the faults. Most large historical earthquakes in the region are located in the boundary zones where Vp changes drastically over a short distance. Beneath the source zones of most of the large historical earthquakes, prominent low-V anomalies are visible in the lower crust. These results shed new light on the seismotectonics and geodynamic processes of the Qinghai-Tibetan Plateau and its northeastern margin.

4.1.3 India

The 26 January 2001 Bhuj earthquake (Mw 7.6) occurred in western India, which was one of the most catastrophic earthquakes to have occurred in India. Kayal et al. (2002) determined 3-D Vp, Vs and PR images of the Bhuj source area using arrival-time data from Bhuj aftershocks recorded by a portable seismic network. Significant velocity and PR variations are revealed in the aftershock area. The mainshock is located in a distinctive zone characterized by high-Vp, low-Vs and high-PR in the depth range 20–30 km and extending 15–30 km laterally. This feature is very similar to that of the 1995 Kobe earthquake (Zhao et al. 1996) and may reflect a fluid-filled, fractured rock matrix which might have contributed to the initiation of the Bhuj earthquake (Kayal et al. 2002). Mishra and Zhao (2003) determined more detailed Vp, Vs and PR images and then estimated the crack density, saturation rate and porosity images in the Bhuj earthquake area (Fig. 4.8), which confirmed the early results of Kayal et al. (2002) and revealed some new features. Mishra (2013) further estimated bulk-sound velocity images in the Bhuj source zone. These results suggested that the earthquake occurrence in Bhuj is closely related to in-situ material heterogeneities in the crust and upper mantle, in addition to tectonic stress concentration.

The 29 September 1993 Latur earthquake (Mw 6.1) was a rare earthquake in a stable continental region, which occurred on a previously unknown blind fault. Mukhopadhyay et al. (2006) determined detailed 3-D Vp, Vs and PR images in the Latur source zone using P- and S-wave arrival-time data from the Latur aftershocks recorded by a network of temporary seismic stations. The Latur source zone exhibits strong lateral heterogeneities in Vp, Vs and PR structures. The mainshock occurred within, but near the boundary, of a low-Vp, high-Vs and low-PR zone. These results suggest that the asperity responsible for the mainshock hypocenter was associated with a partially fluid-saturated fractured rock in a previously unknown source zone with intersecting fault surfaces, which might have triggered the 1993 Latur mainshock and its aftershock sequence. The tomographic results are in good agreement with other geophysical studies revealing high conductivity and high concentration of radiogenic helium gas beneath the Latur source area (Mukhopadhyay et al. 2006).

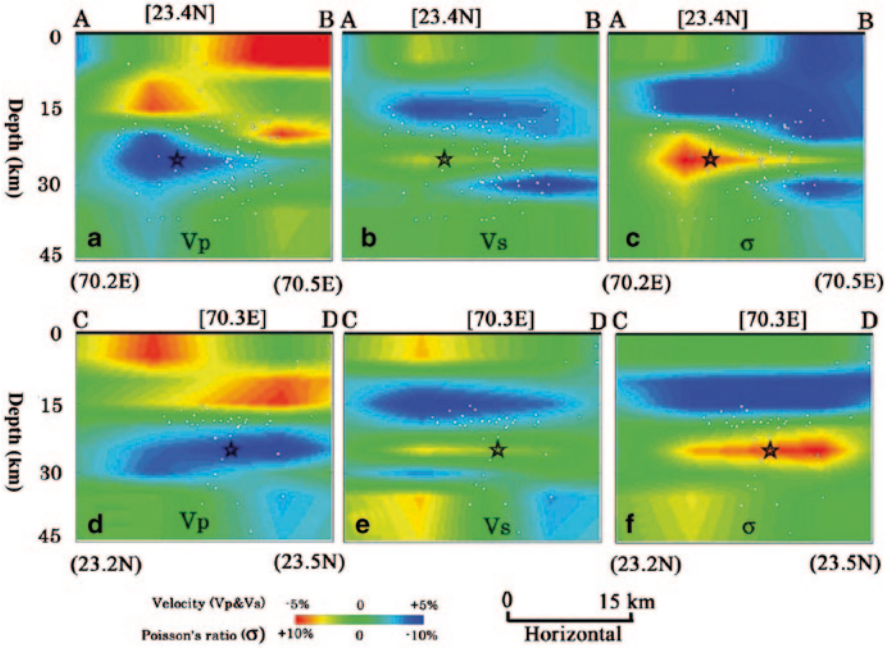

Fig. 4.8 Vertical cross-sections of (**a**, **d**) P-wave velocity, (**b**, **e**) S-wave velocity, and (**c**, **f**) Poisson's ratio, images along an east-west profile AB (**a-c**) and a north-south profile CD (**d-f**) passing through the hypocenter (*star*) of the 2001 Bhuj earthquake (Mw 7.6) in western India. *Red* denotes low velocity and high Poisson's ratio; *blue* denotes high velocity and low Poisson's ratio. The color scale is shown at the bottom. Small *white dots* show the Bhuj aftershocks which occurred within a 9-km width along each profile. (Modified from Mishra and Zhao 2003)

4.1.4 North America

Large earthquakes in North America have mainly occurred in Alaska, western North America and the New Madrid seismic zone in the southern and midwestern USA. High-resolution tomographic studies have been made for source areas of some large crustal earthquakes in North America.

Lees (1990) determined a Vp tomography in the source area of the Loma Prieta earthquake (M 6.9) that took place in Northern California on 17 October 1989. His result shows prominent high-V anomalies near the mainshock hypocenter and prominent low-V anomalies where the dip of the San Andreas fault appears to change significantly. The termination of prominent low-V features existing primarily in the hanging wall to depths of 7–9 km, correlates with the top of the rupture zone. High-V zones along the fault dominate where aftershock activity is high. A high-V anomaly located at depth along the fault is interpreted as imaging the asperity on which the Loma Prieta earthquake occurred. Thurber et al. (1995) determined 3-D Vp and Vp/Vs images along the Loma Prieta rupture zone. Their results

confirmed the early result of Lees (1990) and revealed a significant Vp/Vs increase (equal to a 30 % PR increase) from the middle crust to the upper crust, which may have been responsible for the upward termination of the main shock rupture. They suggested that the deep high-Vp body in the SE portion of the rupture zone consists of two parts, based on model results indicating that the SW part of the body has a relatively high Vp/Vs, whereas the NE part has a relatively low Vp/Vs.

Improved 3-D Vp and Vp/Vs models for the Loma Prieta area were obtained by inverting a large number of local travel-time data from earthquakes, refraction shots and blasts recorded by 1700 stations of the Northern California Seismic Network and numerous portable seismograph deployments (Eberhart-Philipps and Michael 1998). The velocity and density models and seismicity reveal a complex structure that includes a San Andreas fault extending to the base of the seismogenic layer. A high-Vp body extends the length of the rupture and fills the 5-km wide volume between the Loma Prieta mainshock rupture and the San Andreas and Sargent faults. This body may control both the pattern of background seismicity on the San Andreas and Sargent faults and the extent of rupture during the mainshock, thus explaining how the background seismicity outlined the along-strike and depth extent of the mainshock rupture on a different fault plane 5 km away. The subvertical San Andreas fault and the fault surfaces that ruptured in the 1989 Loma Prieta earthquake are both parts of the San Andreas fault zone, and this section of the fault zone does not have a single type of characteristic event (Eberhart-Philipps and Michael 1998).

The 28 June 1992 Landers earthquake (Mw 7.3) occurred in the southeastern Mojave Desert, California. Over 10,000 aftershocks of the earthquake were recorded by the Caltech-USGS Southern California Seismic Network in 1992. Zhao and Kanamori (1993) used a large number of arrival-time data recorded by the permanent and temporary seismic stations to determine a detailed Vp tomography with a spatial resolution of ~5 km, and they relocated the Lander mainshock and aftershocks with the obtained 3-D velocity model. Their results show a correlation between seismicity patterns and velocity patterns, and a tendency for areas rich in seismicity to be associated with higher velocities. The high-V areas are considered to be strong and brittle parts of the fault zone, which are apt to generate earthquakes. In contrast, low-V areas are probably more ductile and weaker, allowing aseismic slippage. If this correlation generally holds, it has the important implication that seismic rupture zones are fixed in space throughout many earthquake cycles (Zhao and Kanamori 1993). Lees and Nicholson (1993) also studied the P-wave crustal tomography of the Landers source area, and their result is similar to that of Zhao and Kanamori (1993).

Zhao et al. (2005) determined a detailed Vs crustal tomography of the Landers earthquake area using first arriving S-waves and reflected S-waves from the Moho discontinuity (SmS, sSmS) generated by the Landers aftershocks (Fig. 4.9). These data were recorded by only two seismic stations (GSC and PFO) which are separated by ~200 km. The tomographic image obtained has a lateral resolution of 25–35 km (i.e., 1/6–1/8 of the station spacing). This work indicates that crustal reflected waves are very useful for improving the spatial resolution of crustal tomography. This Vs tomography is similar to the Vp tomography (Zhao and Kanamori 1993; Lees and Nicholson 1993), suggesting that the Landers earthquake occurrence is closely related to the in-situ structural heterogeneities of the fault zone.

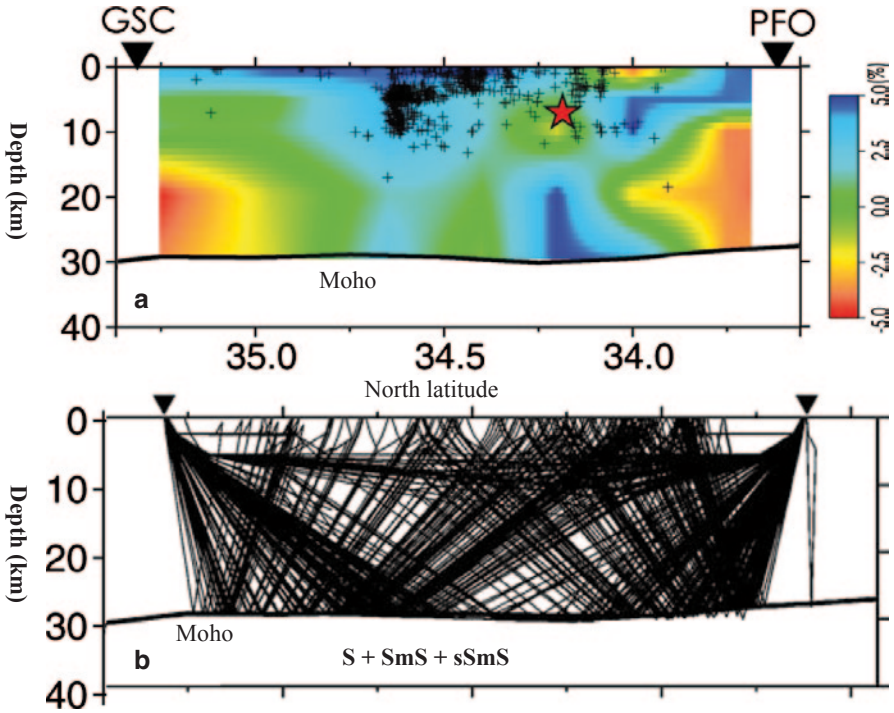

Fig. 4.9 **a** A north-south vertical cross-section of S-wave velocity tomography along a profile passing through the hypocenter (*red star*) of the 1992 Landers earthquake (Mw 7.3) in southern Califonia. *Red* and *blue* colors denote low and high velocities, respectively. The velocity perturbation (in %) scale is shown on the right. The *black triangles* denote two seismic stations GSC and PFO. *Black* crosses show the Landers aftershocks which occurred within a 5-km width along the profile. The *curved line* denotes the Moho discontinuity. **b** Distribution of ray paths of S, SmS and sSmS wave data recorded by GSC and PFO stations, which were used to determine the S-wave tomography in (**a**). (Modified from Zhao et al. 2005)

The 17 January 1994 Northridge earthquake (Mw 6.7) occurred in the San Fernando Valley northwest of Los Angeles, and though of moderate size, caused widespread damage over a large area in the Los Angeles basin. It took place on a south-dipping fault beneath the Transverse Ranges, in striking contrast to the 1971 San Fernando earthquake that occurred on a north-dipping fault. Since the Transverse Ranges involve many active and complex structures formed under a regional N-S compressional stress system, a much larger earthquake could occur if the rupture extended over many segments of the fault system. Zhao and Kanamori (1995) determined a detailed Vp crustal tomography of the Northridge area using a large number of arrival times from Northridge aftershocks and other local events. A test performed using the data from nearby portable stations suggested that the aftershock hypocenters relocated with the obtained 3-D velocity model were accurate to ~2 km. They found that areas with a high aftershock activity were generally associated with a faster P-wave velocity. Vp is high around the main south-dipping fault

of the 1994 Northridge earthquake and the north-dipping fault of the 1971 San Fernando earthquake. A linear distribution of strike-slip aftershocks was found along a NE-SW boundary between high-V and low-V zones. To the west of this boundary, a cluster of large shallow aftershocks with mixed mechanisms occurred in or near the border of a low-V area, whereas to the east, aftershocks with thrust mechanisms occurred in a high-V area. These observations suggest that lateral variations of crustal properties are closely related to the fault segmentation in the Transverse Ranges. A better understanding of these features is important for long-term seismic hazard assessment in the Los Angeles area (Zhao and Kanamori 1995).

The state of tectonic stress in the Northridge earthquake area was investigated by applying a stress inversion method (Horiuchi et al. 1995) to P-wave polarity data from earthquakes in Northridge from July 1981 to January 1994 and from the Northridge aftershocks between January 1994 and December 1995 (Zhao et al. 1997). The 3-D crustal velocity model (Zhao and Kanamori, 1995) was used to trace the rays originating from the hypocenter, which reduced the effect of structural heterogeneities on the determination of the stress tensor. The results suggest that the stress rotated coseismically, then rotated more slowly back to their original orientation. The Northridge aftershocks caused by the mainshock changed the stress distribution in the crust, which showed up as a regional stress change. The stress recovery was completed within 2 years after the mainshock, which is very short compared to the timescale of the earthquake cycle (Zhao et al. 1997).

The enigmatic seismicity in the New Madrid Seismic Zone (NMSZ) has been attributed to some abnormal crustal and lithospheric structures, including the presence of dense mafic intrusions and a low-viscosity lower crust, but the detailed crustal and lithospheric structures in the region remain unclear (Zhang et al. 2009). Powell et al. (2010) determined 3-D Vp and Vs images for a major portion of the NMSZ using local earthquake arrival times recorded by the New Madrid seismic network and some portable stations. Low-Vp and high-Vs anomalies resulted in low Vp/Vs ratios that correspond to the major arms of seismicity north of the intersection of the Cottonwood Grove–Blytheville Arch fault with the Reelfoot fault. The very low Vp/Vs values may reflect the presence of quartz-rich rocks. Two low-V and high-Vp/Vs anomalies are revealed, which cannot be explained by variations in rock composition and may be caused by overpressured fluids. Dunn et al. (2013) determined improved 3-D Vp and Vs crustal models for the NMSZ using a better data set. Their results are compatible with the previous model of Power et al. (2010). A locally high-Vp/Vs anomaly imaged along the central portion of the Reelfoot fault is spatially correlated with a significant change in fault trend and is interpreted as a body containing high pore pressure and/or water-filled microcracks.

Arrival times of local earthquakes and teleseismic events were inverted jointly for a 3-D Vp lithospheric structure beneath the NMSZ (Zhang et al. 2009). The results show that the seismically active zone is associated with a local, NE–SW trending low-V anomaly in the lower crust and upper mantle, instead of high-V intrusive bodies proposed by previous studies. The low-V anomaly is located at the edge of a high-V lithospheric block, consistent with the notion of stress concentration near rheological boundaries. This lithospheric weak zone may shift stress to the upper crust when loaded, thus leading to repeated shallow earthquakes. Chen et al. (2014)

determined an updated 3-D Vp model of the crust and upper mantle down to a depth of 400 km beneath the NMSZ using high-quality arrival times from local earthquakes and teleseismic events recorded by the EarthScope/USArray Transportable Array. Their results show that, beneath the Reelfoot Rift, a significant low-V zone exists in the upper mantle down to a depth of 200 km, which may be related to the passage of the Bermuda hotspot and the stalled ancient Farallon slab materials foundering in the mantle transition zone. This low-V zone may have a lower shear strength and act as a viscously weak zone embedded in the lithosphere, being apt to concentrate tectonic stress and transfer stress to the seismogenic faults in the upper crust, leading to the large intraplate earthquakes in the NMZS (Chen et al. 2014).

4.1.5 Italy

Although many studies have been made, the crustal and upper mantle structures of the Apennines Peninsula, Italy, are still poorly defined, leaving uncertainties concerning the tectonic style (thin or thick-skinned) responsible for the development of the thrust-and-fold belt (Chiarabba et al. 2010). The current active extension, which replaced compression since the early Quaternary, is presumably influenced by the pre-existing structure that yields the location and segmentation of the fault system. To clarify these issues, Chiarabba et al. (2010) determined 3-D Vp and Vs crustal models using local earthquake tomography and teleseismic receiver functions. Their results show strong lateral and vertical heterogeneities that define shallow, imbricate sheets of the Mesozoic cover that overlay very high-Vp and high-Vs anomalies. These anomalies may reflect either dolomitic or, partially hydrated, mafic rocks. The two alternative interpretations respectively imply an ultra-thick deposition of dolomitic rocks in the hanging wall of Triassic normal fault or a deep exhumation of the Pre-Mesozoic basement during the early Mesozoic sin-rift tectonic. In both cases, these bodies must have affected the evolution of the thrust-and-fold belt. Active normal faults, such as those ruptured during the 2009 L'Aquila earthquake (Mw 6.1) sequence, concentrate at the border of these bodies, suggesting that they play an important role in the segmentation of the normal fault system (Chiarabba et al. 2010).

Di Stefano et al. (2011) inverted local-earthquake P- and S-wave arrival times recorded by a dense local seismic network to determine 3-D crustal Vp, Vs and PR images in the source area of the 6 April 2009 L'Aquila earthquake. The initial stages of the mainshock rupture are characterized by an emergent phase followed by an impulsive phase 0.87 s later. The emergent phase is located in a very high-Vp and relatively low-PR zone. The impulsive phase marks the beginning of the large moment release and is located outside the low-PR volume. The comparison between the Vp and PR spatial variations within the mainshock nucleation volume with the rupture history revealed by waveform inversion enables the delayed along-strike propagation to be interpreted in terms of the heterogeneity of the lithology and the material properties (Di Stefano et al. 2011).

4.1.6 Turkey

Turkey is a tectonically very active region and has suffered many large earthquakes to date. Several tomographic studies have been made of the 3-D crustal and uppermost mantle structure and seismotectonics of different parts of Turkey (e.g., Salah et al. 2007, 2011, 2013; Gokalp 2012). These studies indicate that strong lateral heterogeneities exist in the crust and uppermost mantle beneath Turkey. Prominent low-V anomalies are revealed beneath existing volcanoes and active fault segments. Higher Vp/Vs anomalies are widely distributed, which may reflect over-pressurized fluids that may be responsible for triggering large crustal earthquakes in the Anatolian fault zone (Salah et al. 2013).

An earthquake (Mw 7.4) with a focal depth of 15 km occurred in Izmit city, northwestern Turkey on 17 August 1999, causing casualties of more than 15,000 dead and 25,000 injured. It was located at the westernmost part of the active North Anatolian Fault Zone. After the 1939 Erzincan earthquake (M 8.0), a sequence of large earthquakes propagated successively from the east to the west along this fault zone. Nakamura et al. (2002) relocated the aftershocks and determined a Vp crustal tomography in the 1999 Izmit source area. They found that the aftershocks form a 170-km-long narrow zone trending in an east–west direction along the northern branch of the North Anatolian Fault Zone. The aftershocks are not homogeneously distributed but consist of several clusters. Focal mechanism solutions of the aftershocks exhibit different types, whereas they are similar to each other within the same cluster. A distinct low-V zone was revealed to the west of the mainshock hypocenter. The mainshock rupture zone was located in a high-V anomaly sandwiched between two low-V zones. The Anatolian earthquake sequence that had migrated westward during the past 60 years did not propagate into the southern branch of the fault zone, suggesting that the Anatolian earthquake sequence progressed to the west exploiting an area that could break more easily (Nakamura et al. 2002).

4.2 Megathrust Earthquakes

Megathrust earthquakes take place in the interplate megathrust zone where the subducting plate makes contact with the overlying plate. All the huge earthquakes ($M > 8.5$) on Earth occur in the megathrust zones, such as the 1952 Kamchatka earthquake (Mw 9.2), the 1960 Chile earthquake (Mw 9.5), the 1964 Alaska earthquake (Mw 9.2), the 2004 Sumatra earthquake (Mw 9.2), the 2010 Chile earthquake (Mw 8.8), and the 2011 Tohoku-oki earthquake (Mw 9.0). It is important to study the detailed 3-D structure of the interplate megathrust zone so as to clarify the nucleation mechanism of the great megathrust earthquakes. However, because the megathrust zones are located beneath the forearc regions of subduction zones, which are covered by oceans in most cases, few permanent seismic stations are installed there and so usually the forearc earthquakes are poorly located, making

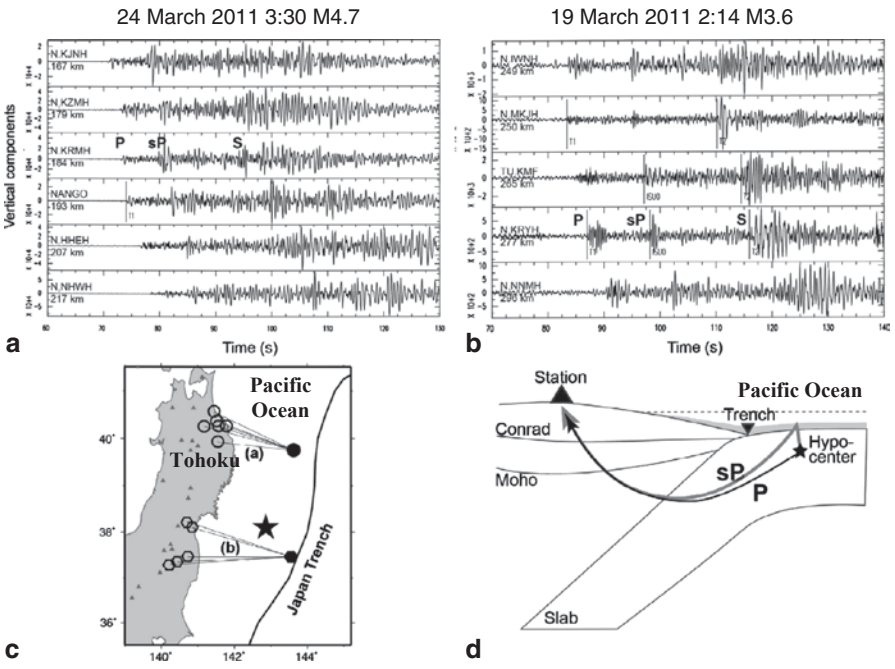

Fig. 4.10 (**a**, **b**) Examples of vertical-component seismograms with the sP depth-phases from two suboceanic earthquakes recorded by the Hi-net seismic stations (*open circles*) on Honshu Island as shown in (**c**). The *star* shows the epicenter of the 2011 Tohoku-oki earthquake (Mw 9.0). The origin time and magnitude of each earthquake are shown above the seismograms. The station code and epicentral distance are shown on the *left* of each seismogram. (**d**) A cartoon showing the ray paths of the sP depth-phase and direct P-wave from a suboceanic earthquake. (Modified from Huang and Zhao 2013b)

it difficult to conduct high-resolution tomographic imaging there. Active-source reflection surveys and ocean-bottom-seismometer (OBS) observations have been conducted in a few forearc regions (e.g., Miura et al. 2003; Hino et al. 2006; Obana et al. 2012), which are very expensive and, hence, limited in both the observation period and area.

An off-network tomography method was developed to study the 3-D seismic velocity structure of the forearc region under the Pacific Ocean (Zhao et al. 2002, 2007). Its principle is to first detect sP depth phases on seismograms of suboceanic earthquakes recorded by the nearby land-based seismic network (e.g., Fig. 4.10) and use arrival times of the sP depth phase as well as the first P- and S-waves to relocate many suboceanic events precisely. Then P- and S-wave arrival times of the relocated suboceanic events are used to conduct tomographic imaging of the forearc region. In the past decade, this approach has been applied successfully to the forearc and back-arc oceanic regions surrounding the Japan Islands (see Zhao 2012 for a review).

In this section, we introduce the tomographic studies carried out for a few subduction-zone forearc regions and the insights obtained into the causal mechanism of megathrust earthquakes.

4.2.1 Northeast Japan Arc

Zhao et al. (2002) determined the first Vp tomography of the Tohoku (NE Japan) forearc region and the interplate megathrust zone under the Pacific Ocean, applying the off-network tomography method to P-wave arrival times of suboceanic events relocated with sP depth phases (Umino et al. 1995). Later, several studies applied this approach to improved data sets to determine 3-D Vp, Vs and PR images of the Tohoku forearc (Mishra et al. 2003; Wang and Zhao 2005; Zhao et al. 2007, 2009; Huang et al. 2011a). This approach was also applied to study the Vp and Vs structures of the Tohoku back-arc region (Huang et al. 2011a; Zhao et al. 2011b). These studies revealed strong lateral heterogeneities in the megathrust zone and their correlation with the distribution of large megathrust earthquakes in the period 1900–2008 (see Zhao 2012 for a review). The pattern of the tomographic images is generally consistent with the results of active-source seismic reflection surveys near the Japan Trench (e.g., Tsuru et al. 2002).

Zhao et al. (2011c) relocated the great 11 March 2011 Tohoku-oki earthquake (Mw 9.0) and its 339 foreshocks and 5609 aftershocks during 9–27 March 2011 using the 3-D velocity model of Huang et al. (2011a) and local P- and S-wave arrival times recorded by the land-based seismic network. They compared the distribution of the relocated hypocenters with the tomographic image of the megathrust zone and found that most of the large megathrust earthquakes during 1900–2011 are located in high-V patches, or at the boundary between the low-V and high-V zones, with only a few situated in the low-V patches (Fig. 4.11a). The low-V patches in the megathrust zone may contain subducted sediments and fluids from slab dehydration. Thus, the subducting Pacific plate and the overriding Okhotsk plate may become weakly coupled or even decoupled in the low-V areas. Large-amplitude reflected waves from the slab boundary were detected in a low-seismicity area under the forearc region off Sanriku (Fujie et al. 2002), as were some slow and ultra-slow thrust earthquakes (Heki et al. 1997; Kawasaki et al. 2001). Both the seismic reflectors and slow thrust earthquakes were caused by fluids at the slab boundary (Fujie et al. 2002; Kawasaki et al. 2001), and they are all located in the off-Sanriku low-V zone (Fig. 4.11a). In contrast, the high-V patches in the megathrust zone (Fig. 4.11a) may result from subducted oceanic ridges, seamounts and other topographic highs, or compositional variations on the seafloor, which become asperities where the subducting Pacific plate and the overriding Okhotsk plate are strongly coupled. Thus, tectonic stress tends to accumulate in these high-V areas for a relatively long time during subduction, leading to the nucleation of the large megathrust earthquakes in those areas (Fig. 4.11a). The off-Miyagi high-V zone where the 2011 Tohoku-oki mainshock and its largest foreshock occurred (Fig. 4.11a) corresponds to the area with a large coseismic slip (>25 m) during the Tohoku-oki mainshock (Fig. 4.11b). This indicates that the off-Miyagi high-V zone is a large asperity (i.e., strongly coupled area) or a cluster of asperities in the megathrust zone that ruptured during the 2011 Tohoku-oki mainshock. The distribution of structural heterogeneities in the megathrust zone and its correlation with the distribution of large thrust earthquakes (Fig. 4.11a) suggest varying degrees of interplate seismic coupling from the north

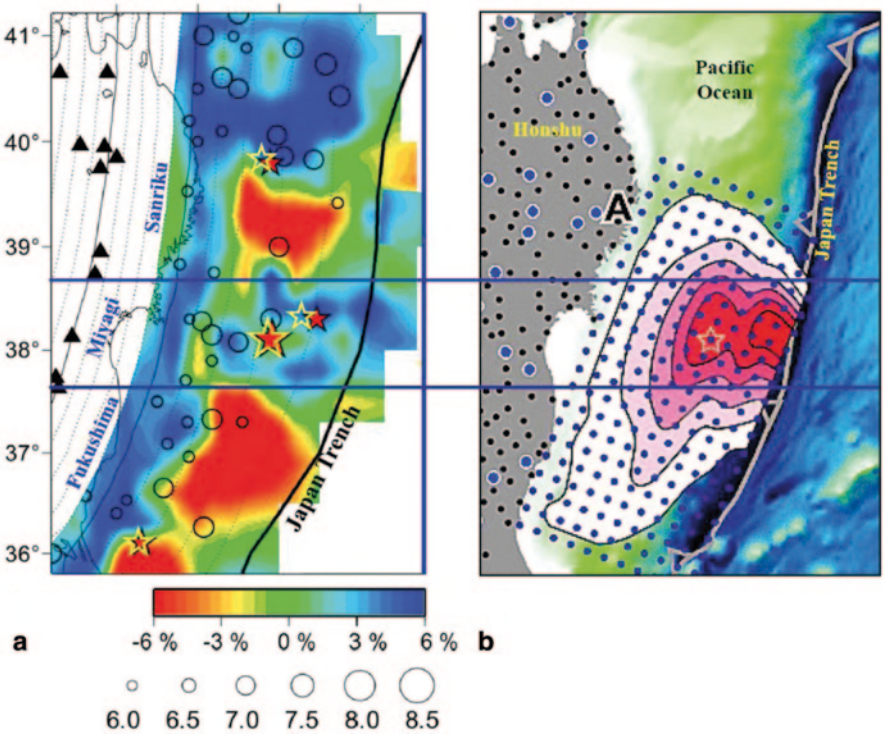

Fig. 4.11 **a** P-wave tomography of the Tohoku megathrust zone (Zhao et al. 2011c). *Red* and *blue* colors denote low and high velocities, respectively. Open circles denote large interplate earthquakes (M≥6.0) that occurred from 1900 to 2010. The velocity perturbation (in %) scale and the earthquake magnitude scale are shown at the *bottom*. *Red* and *yellow* stars denote the JMA (Japan Meteorological Agency) determined epicenters and relocated epicenters of the Tohoku-oki earthquake (Mw 9.0) and its major aftershocks (Mw>7.0) which occurred on 11 March 2011. **b** Coseismic slip distribution of the 2011 Tohoku-oki earthquake (*white star*) estimated by Yue and Lay (2011). The two *blue lines* show the north-south range of the off-Miyagi high-velocity zone in (**a**), where large coseismic slips (>25 m; purple parts) took place

to the south in the Tohoku forearc, possibly controlling the nucleation of the large megathrust earthquakes. The great 2011 Tohoku-oki earthquake sequence is very possibly related to such a process. The differences in interplate seismic coupling may result from variations in the frictional behavior of materials, which may be imaged by the seismic tomography (Fig. 4.11a).

These results also suggest that the distribution pattern of the megathrust earthquakes in the Tohoku forearc (Fig. 4.11a) may not change in the coming 10,000 years, if the seismic velocity variations reflect the structural heterogeneity of the upper boundary of the subducting Pacific plate. The subduction rate of the Pacific plate is 7–10 cm/year at the Japan Trench, and hence, the Pacific slab would not move more than 1 km beneath the Tohoku fore-arc in the coming 10,000 years.

The great Tohoku-oki earthquake was accompanied by nearly 100 large aftershocks (M≥6.0) in the Tohoku forearc by the end of 2011. Huang and Zhao (2013a)

relocated 77 of these large events using three different velocity models. The updated 3-D velocity model (Huang et al. 2011a) significantly reduced the travel-time residuals in the earthquake relocation. They found that, after precise relocation, the large thrust earthquakes are generally located in or around the high-V patches in the megathrust zone, confirming the earlier findings of Zhao et al. (2011c). Many non-thrust large earthquakes are found to take place in the crust of the overriding Okhotsk plate, indicating that the stress field there has been changed by the Tohoku-oki mainshock (Hasegawa et al. 2012; Tong et al. 2012; Yoshida et al. 2012; Huang and Zhao 2013a).

To better understand the generating mechanism of the 2011 Tohoku-oki earthquake and the induced tsunami, Huang and Zhao (2013b) determined improved 3-D Vp and Vs images of the Tohoku forearc using a better data set, including P- and S-wave arrivals of many aftershocks of the 2011 Tohoku-oki earthquake which are relocated precisely with sP depth phases and the 3-D velocity model. They revealed a shallow high-V zone with large coseismic slip near the Japan Trench, which may account for the asperity of the 2011 mainshock. Because it is an isolated asperity surrounded by low-V patches, most of the stress on it could be released in a short time and the plate interface became decoupled following the mainshock. Thus, the overriding Okhotsk plate there was shot out toward the Japan Trench thereby causing the huge tsunami (Ito et al. 2011; Huang and Zhao 2013b). A few other researchers also made tomographic studies of the Tohoku forearc region using different data sets and methods, and obtained more or less similar results (e.g., Wang et al. 2012; Yamamoto et al. 2012; Tian and Liu 2013).

Liu et al. (2014) determined a 3-D attenuation (Qp, Qs) tomography of the crust and upper mantle beneath the entire Tohoku arc from the Japan Trench to the eastern margin of the Japan Sea. They found that most of the large megathrust earthquakes are located in or around the low-attenuation (high-Q) patches of the megathrust zone, very similar to the velocity tomography results mentioned above.

4.2.2 South Kuril Arc

Wang and Zhao (2005) determined the first Vp and Vs tomography in the forearc region of the South Kuril arc off Hokkaido using the off-network tomography method. Liu et al. (2013a) determined more detailed 3-D Vp and Vs images as well as a P-wave anisotropy tomography of the crust and upper mantle beneath the entire South Kuril arc from the Kuril–Japan trench to the eastern margin of the Japan Sea using a large number of high-quality arrival-time data from local earthquakes. The suboceanic earthquakes used in the tomographic inversion are relocated precisely using sP depth phase data, which are collected from three-component seismograms recorded by the dense Japanese seismic network (Figs. 4.12 and 4.13). They revealed three prominent high-V zones separated by low-V anomalies in the megathrust zone beneath the Kuril forearc (Fig. 4.14). Similar to the results for the Tohoku forearc, the high-V zones coincide with areas having large coseismic slips of great megathrust earthquakes, as well as areas with a large slip deficit on the plate

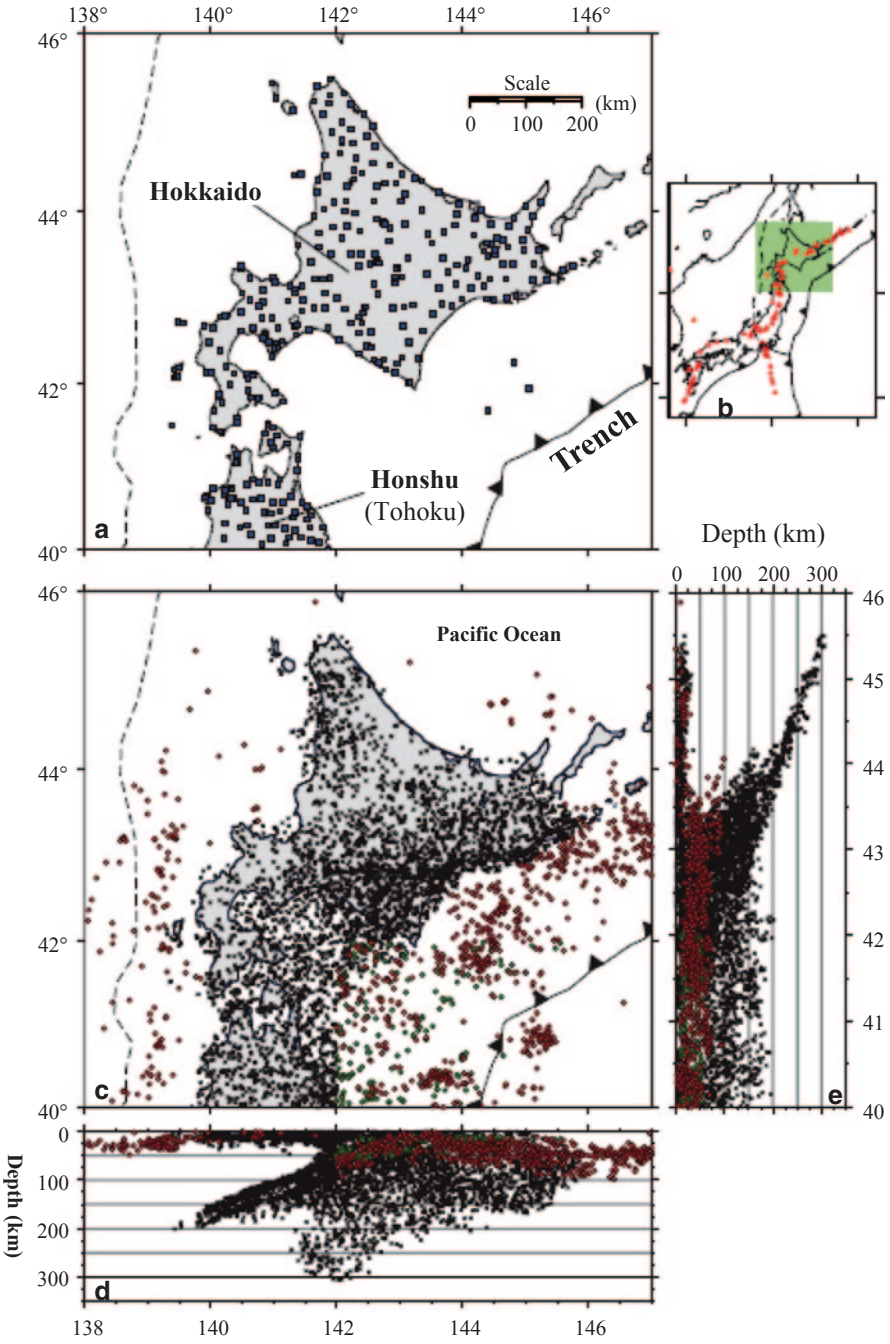

Figure 4.12 **a** Distribution of the 369 seismic stations (*blue squares*) used. **b** Simplified tectonic background of the study area (*green box*). The *sawtooth* and *dashed* lines denote the plate boundaries. The *red triangles* in **b** denote active volcanoes. **c** Distribution of the 4803 earthquakes used. The *black* crosses denote events that occurred under the seismic network. The *green* and *red dots* show suboceanic events which are relocated using sP depth phases. **d** East–west and **e** north–south vertical cross-sections of the earthquakes shown in **c**. (After Liu et al. 2013a)

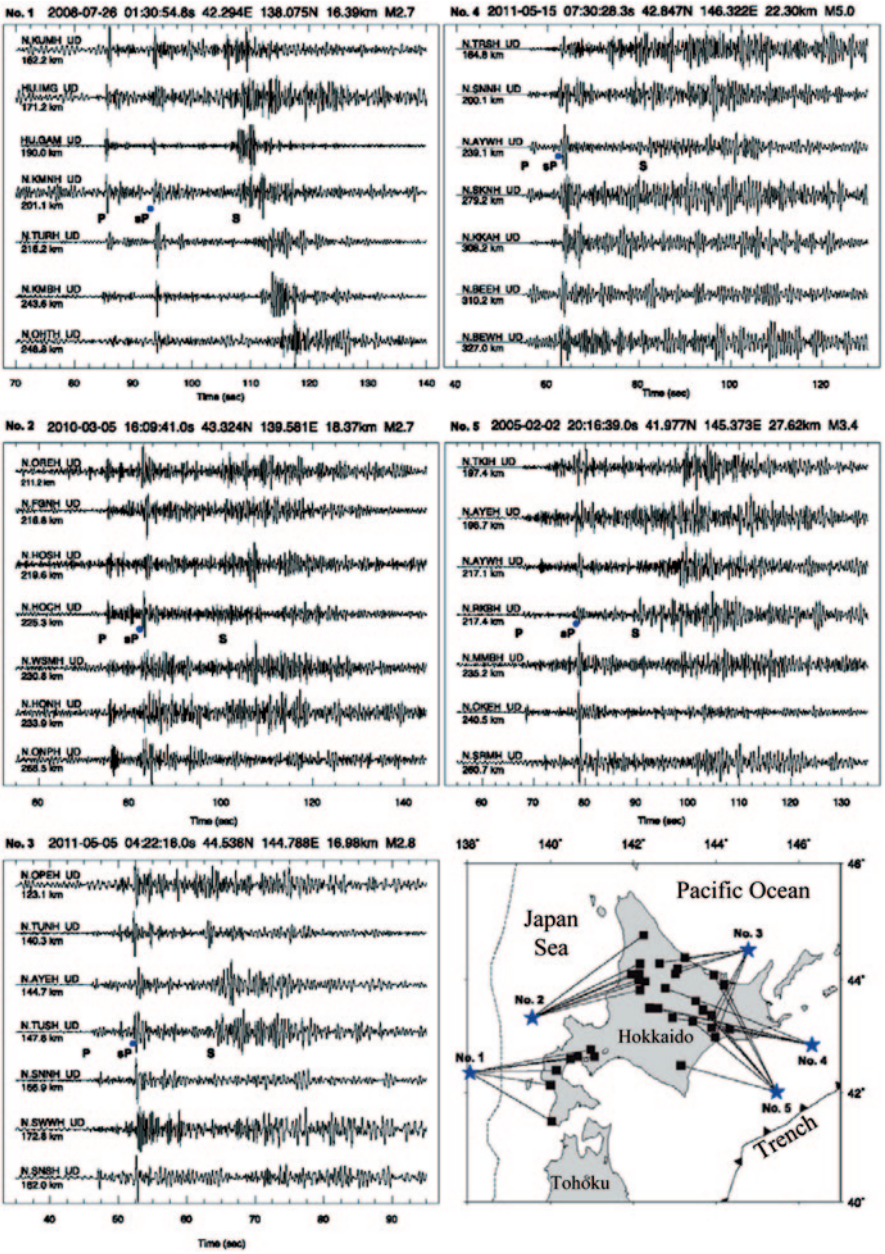

Fig. 4.13 Examples of vertical-component seismograms of five suboceanic earthquakes that occurred beneath the Pacific Ocean, Sea of Okhotsk, and the Japan Sea. Hypocenter parameters of the earthquakes are shown above the seismograms. The station codes and epicentral distances are shown on the *left*. Clear sP depth phases are labelled by *blue dots*. The events (*blue stars*) and seismic stations (*black squares*) are shown on the inset map. (After Liu et al. 2013a)

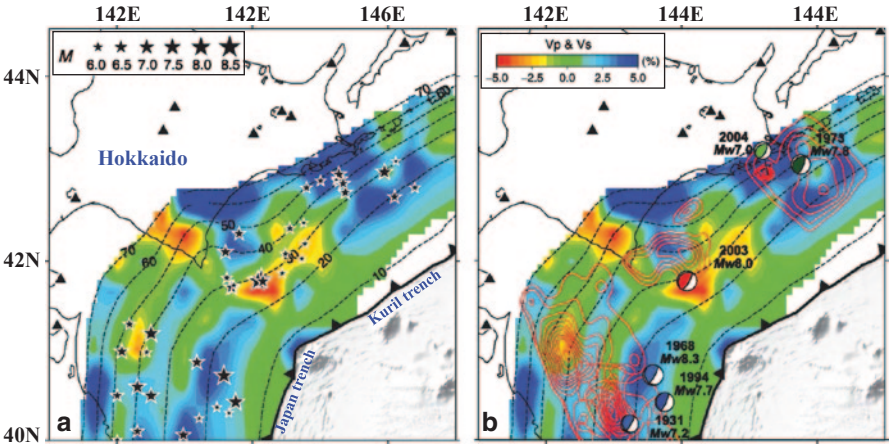

Fig. 4.14 S-wave velocity tomography of the interplate megathrust zone directly above the upper boundary of the subducting Pacific slab (the *black dashed lines*). *Black* stars in **a** denote large earthquakes ($M \geq 6.0$; 1901–2011) that occurred in the forearc region beneath the Pacific Ocean. The earthquake magnitude and velocity perturbation (in %) scales are shown at the *top*. The *red* contour lines in **b** denote coseismic slip distributions of some large megathrust earthquakes estimated by waveform inversion studies. The *inner contour* lines denote larger slips. The *black triangles* denote active arc volcanoes. The sawtooth line indicates the Kuril–Japan Trench. (Modified from Liu et al. 2013a)

interface. In contrast, the low-V patches are generally consistent with the afterslip distribution of the 2003 Tokachi-oki megathrust earthquake (Mw 8.0). These high-V zones probably represent asperities in the megathrust zone, whereas the low-V anomalies around the asperities may contain fluids, which play an important role in the nucleation of the megathrust earthquakes, in addition to the stress concentration. Their results also reveal a boundary in the tomographic images between the Tohoku arc and the Kuril arc, especially at the Hidaka collision zone. This boundary extends southwards to the rupture zones of the 1952 and 2003 Tokachi-oki earthquakes (Mw 8.1 and 8.0), which may have contributed to the formation of the asperity for the two great megathrust events (Liu et al. 2013a).

4.2.3 Southwest Japan Arc

Wang and Zhao (2006c) applied the off-network tomography method to study the 3-D Vp and Vs structure of the forearc region of the Kyushu subduction zone where the young Philippine Sea slab is descending beneath the Eurasian plate. Liu et al. (2013b) determined a Vp and Vs tomography of the entire Southwest Japan arc from the Nankai Trough to the Japan Sea by applying the off-network tomography method to a large number of high-quality arrival-time data of local earthquakes (Figs. 4.15 and 4.16). The suboceanic earthquakes used in the tomographic inversion were relocated precisely using sP depth phase data. The two studies revealed

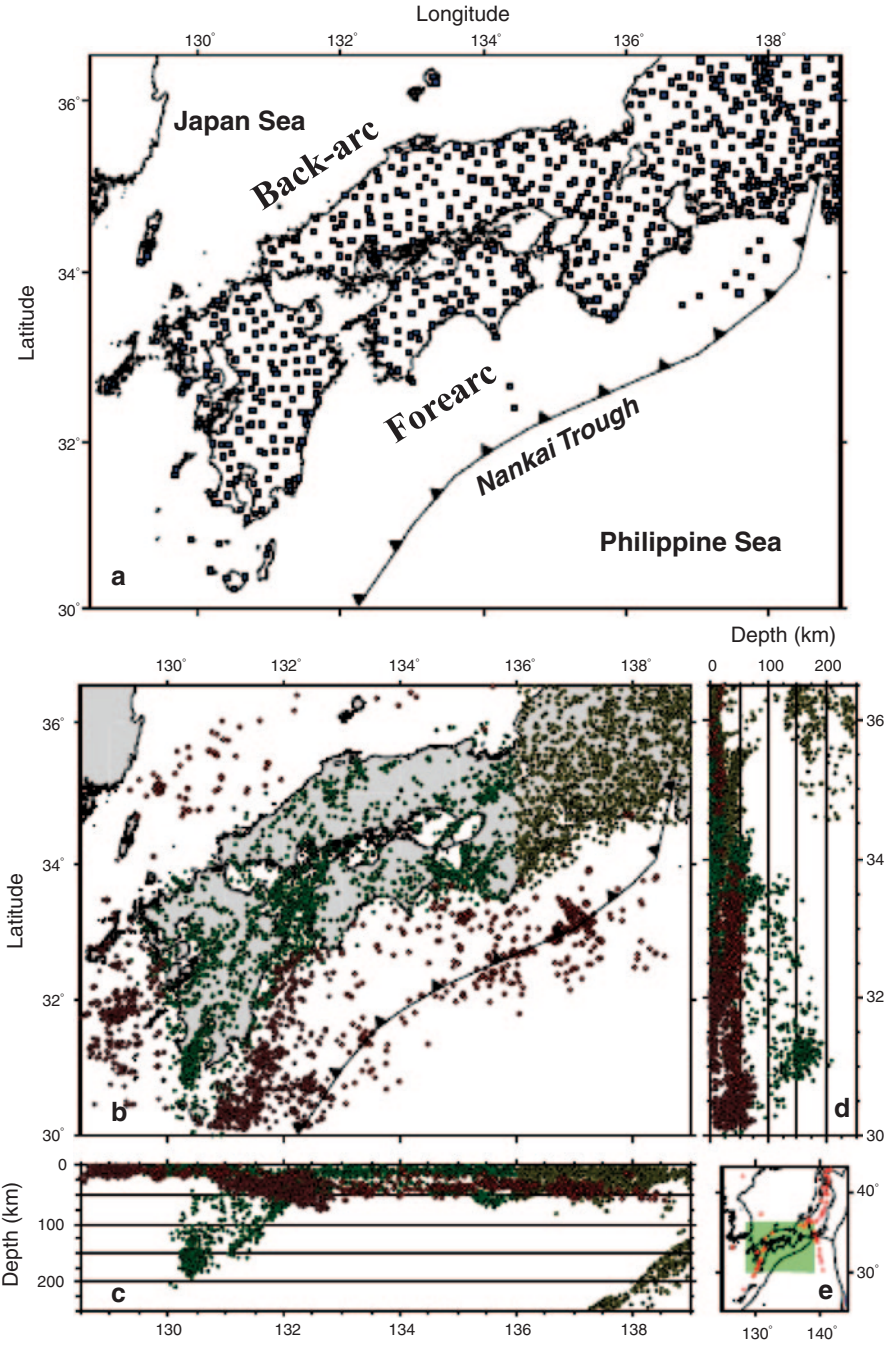

Fig. 4.15 **a** Distribution of the 876 seismic stations (*blue squares*) used. **b** Distribution of the 6622 earthquakes (*dots*) used. *Green* and *yellow dots* denote events that occurred under the seismic network. *Red dots* denote suboceanic events that are relocated using sP depth-phase data. **c** East–west and **d** north–south vertical cross-sections of the earthquakes shown in **b**. **e** Simplified tectonic background of the study area (*green box*). The *black and dashed bold lines* denote the plate boundaries. The *red solid triangles* denote active volcanoes. (After Liu et al. 2013b)

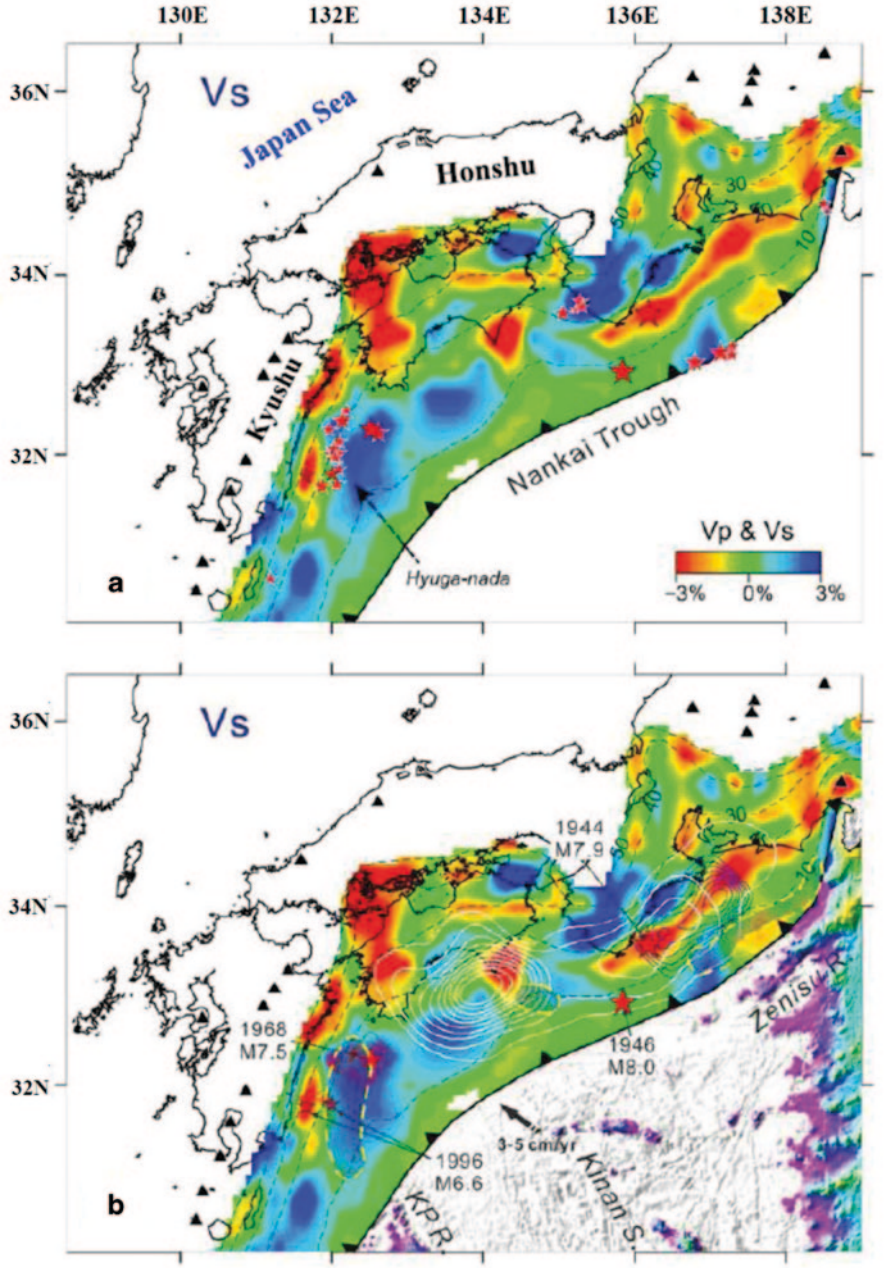

Fig. 4.16 S-wave velocity tomography of the interplate megathrust zone along the upper boundary of the subducting Philippine Sea slab. *Red* and *blue* colors denote low and high velocities, respectively. *Red* stars denote large earthquakes (M≥6.0; 1900–2011) that occurred in the forearc region beneath the Philippine Sea. The *yellow* contour lines in (**b**) denote coseismic slips of large megathrust earthquakes; the *inner contour lines* denote larger coseismic slips. The *black triangles* denote active arc volcanoes. The sawtooth and *dashed lines* indicate the Nankai Trough and the depth contours of the upper boundary of the subducting Philippine Sea plate, respectively. (Modified from Liu et al. 2013b)

strong lateral heterogeneities in the interplate megathrust zone under the Nankai forearc. Similar to the Tohoku and South Kuril arcs, large megathrust earthquakes mainly occurred in, or around, high-V patches in the megathrust zone. Liu et al. (2013b) showed that coseismic slip distributions of some megathrust earthquakes are not limited in the high-V patches (asperities) where the ruptures initiated. Because of weak interplate coupling in the low-V areas, an interplate rupture could pass through the low-V zones and so result in a great megathrust earthquake.

4.2.4 Sumatra

On 12 September 2007, an Mw 8.4 earthquake occurred within the southern section of the Mentawai segment of the Sumatra subduction zone, where the megathrust zone had previously ruptured in 1833 and 1797. Collings et al. (2012) deployed a temporary local seismic network from December 2007 to October 2008 to record the aftershocks of the 2007 event and to determine 2-D and 3-D velocity models of the Mentawai segment. The seismicity distribution revealed significant activity in the megathrust zone and two clusters in the overriding plate either side of the forearc basin. The subducting Australian slab is clearly imaged as a dipping zone of high-Vp (8.0 km/s), which is traced to a depth of 50 km, with an increased Vp/Vs ratio (1.75–1.90) beneath the islands and the western side of the forearc basin, suggesting a hydrated oceanic crust. Above the Australian slab, a shallow continental Moho of < 30 km depth is revealed, suggesting that the intersection of the continental mantle with the subducting slab is much shallower than the down-dip limit of the seismogenic zone, though localized serpentinization takes place at the toe of the mantle wedge. The outer arc islands exhibit low-Vp (4.5–5.8 km/s) and high-Vp/Vs (> 2.0), suggesting that they contain fluid-saturated sediments. The soft outer forearc may have contributed to the slow rupture of the Mw 7.7 Mentawai tsunami earthquake on 25 October 2010 (Collings et al. 2012).

Deep seismic-reflection surveys were conducted along seven profiles covering a 3000-km-long subduction system from Andaman to Southern Sumatra, including zones that ruptured in 2004, 2007 and 2010 (Moeremans et al. 2014). The results show that the frontal zone is characterized by a series of thrusts bounding folded blocks of sediments with preserved layering, showing a northward transition from a dominantly seaward vergence of the frontal thrusts to a dominantly landward vergence of the frontal thrusts. Poor reflection of the seismic energy occurs in the accretionary wedge, possibly because of a high degree of faulting and compaction of the sediments. The oceanic crust contains many faults and topographic reliefs along most of the margin. Landward vergence at the deformation front is associated with a thick incoming sediment section. The segment with a landward vergence corresponds to an area with high near-trench slip during the December 2004 earthquake (Mw 9.2) and the main tsunami source, and it is located just west of the hypocenters of several intraplate events (Mw > 7) in the years after the great 2004 earthquake.

4.2.5 Chile

Travel-time data from the aftershocks of the megathrust Antofagasta earthquake (Mw 8.0) on 30 July 1995 were used to determine detailed 3-D Vp and Vp/Vs images in the source region (Husen et al. 2000). The data were recorded by a dense 44-station seismic network including ocean-bottom hydrophones. The subducting Nazca plate at a depth of 20–50 km was imaged as an eastward dipping high-Vp zone. High Vp/Vs ratios are revealed within the oceanic crust, which may reflect elevated fluid content. Underplating of material eroded close to the trench is found beneath the Mejillones Peninsula. The lower crust of the overlying plate has an average Vp of 6.8–6.9 km/s and an average-to-low Vp/Vs ratio. Large areas of very high-Vp are found in the lower crust south of the city of Antofagasta, which are interpreted as remnants of magmatic intrusions.

A high-Vp/Vs anomaly is revealed within the rupture area of the Antofagasta mainshock, just above the subducting slab. Its location within the zone of highest stress release from the mainshock suggests that the mainshock rupture caused the high Vp/Vs ratio (Husen et al., 2000). The time evolution of the high Vp/Vs ratio after the Antofagasta mainshock was caused by postseismic fluid flow into the overriding plate. The accumulation of high stress may form a permeability barrier in the megathrust zone, capturing the fluids in the subducting plate. This seal is broken only by large megathrust earthquakes that allow the fluids to rapidly migrate into the overlying plate. Postseismic fluid flow implies a relatively high permeability of the overlying lower continental crust (Husen and Kissling 2001).

4.3 Intraslab Earthquakes

The 24 March 2001 Geiyo earthquake (M 6.8) occurred at a depth of 50 km within the subducting PHS slab beneath Southwest Japan (Zhao et al. 2002). This intraslab earthquake was generated by normal faulting under an east-west tensional stress regime. The seismogenic fault is north-south oriented and dips toward the west with a dip angle of 35° from the vertical. The Geiyo aftershocks are distributed along the N–S oriented fault zone with a length of ~30 km. The mainshock hypocenter is located at the northern end of the aftershock zone. It is considered that the Geiyo earthquake was caused by a tensional fracture of the subducted PHS slab. Zhao et al. (2002) determined a detailed Vp tomography of the crust and upper mantle under the Geiyo region, revealing that the Geiyo mainshock hypocenter was located where a mantle wedge low-V zone is nearly connected with the PHS slab, where slab dehydration may take place actively. In addition, very few intermediate-depth earthquakes occur north of the Geiyo mainshock hypocenter, and so the Geiyo hypocenter represents the northern edge of the seismic portion of the PHS slab (Zhao et al. 2012a; Huang et al. 2013), where a change in temperature and/or brittleness takes place in the slab. These features suggest that the 2001 Geiyo earthquake was related to structural anomalies associated with the dehydration and temperature

change of the PHS slab. The strike and dip of the PHS slab change around the Geiyo earthquake area. The slab is nearly flat beneath Shikoku but steeply dips toward the west beneath Kyushu. The local stress regime of east–west extension (the minimum compressional stress) in the Geiyo source area may be associated with the curvature of the PHS slab under the region. The Geiyo earthquake was caused by the joint effects of the local tensional stress regime, structural heterogeneities related to temperature changes within the slab, and the strength weakening and triggering effects due to the PHS slab dehydration (Zhao et al. 2002).

The 26 May 2003 Miyagi-oki earthquake (Mw 7.0) occurred at a depth of 70 km within the subducting Pacific slab beneath the Pacific coast of Tohoku (Okada and Hasegawa 2003). Mishra and Zhao (2004) determined a fine 3-D Vp tomography of the Pacific slab for understanding the genesis of this intraslab earthquake and its aftershock sequence. They found that its mainshock and aftershocks occurred in a distinct zone characterized by a localized lower-velocity anomaly than its surroundings within the Pacific slab. They suggested that the reduced velocity within the slab is attributed to the process of dehydration embrittlement resulting from the dehydration of hydrous minerals in the Pacific slab, which may have induced the mainshock and its aftershock sequence by enhancing pore pressures along a pre-existing fault within the subducting slab beneath the Tohoku forearc.

The 15 January 1993 Kushiro-oki earthquake (M 7.8) took place at a depth of 101 km within the subducting Pacific plate beneath the eastern coast of Hokkaido. Nakajima et al. (2009) determined a detailed tomography in the subducting Pacific slab beneath the region using local-earthquake arrival-time data. They revealed a remarkable low-V layer with a thickness of ~10 km at the uppermost part of the slab, which is interpreted as hydrated oceanic crust. The layer gradually disappears at depths of 70–80 km, reflecting the breakdown of hydrous minerals there. A significant low-V anomaly is imaged along the lower plane of the double seismic zone and above the aftershock area of the 1993 Kushiro-oki earthquake, which may reflect hydrous minerals in the lower plane as well as in the source zone of the Kushiro-oki earthquake. These results suggest that intermediate-depth intraslab earthquakes occur mainly in areas containing hydrous minerals, which support the dehydration embrittlement hypothesis as a cause of intraslab earthquakes.

On 7 April 2011 a strong intraslab earthquake (M 7.2) occurred at a depth of ~60 km within the subducting Pacific slab off Tohoku, which was associated with the great megathrust earthquake (Mw 9.0) of 11 March 2011. Nakajima et al. (2011) determined a detailed tomography in the source zone of this intraslab earthquake. They revealed a low-V zone around its focal area and found that its aftershock activity was limited to the upper 15 km of the mantle portion of the Pacific slab. This low-V zone has a lateral extent comparable to the distribution of aftershocks, suggesting a concentration of fluids in the aftershock area. The angle between the aftershock alignment and the dip of the slab surface is ~60°, being consistent with the dip of an oceanward dipping normal fault observed at the outer-trench slope. These results suggest that this intraslab earthquake may be caused by the reactivation of a buried hydrated fault that formed before subduction. The upper ~15 km of the oceanic mantle may be locally hydrated by bending-related tensional faulting at the outer-rise portion of the Pacific plate (Nakajima et al. 2011).

4.4 Deep Earthquakes

Deep earthquakes (>300 km depth) account for only a few percent of global seismic activity, estimated from either the number of earthquakes or seismic moments (Kirby et al. 1996). Studies of deep earthquakes to date have provided direct information on the thermal, thermodynamic, and mechanical properties inside the subducting slab. However, the mechanism of deep earthquakes is still a matter of debate, and several models have been proposed, including dehydration embrittlement (Raleigh and Paterson, 1965), transformational faulting of olivine (Green and Burnley 1989; Green and Houston 1995; Green 2003), and adiabatic shear instability (Hobbs and Ord 1988; Karato et al. 2001). The second model (i.e., transformational faulting of olivine) seems more popular than the other hypotheses because a majority of deep earthquakes are found to occur at the mantle transition-zone depths within the subducting slab (Green and Houston 1995).

Iidaka and Suetsugu (1992) analyzed travel-time residuals of some deep earthquakes and suggested the presence of a metastable olivine wedge (MOW) with a depth of about 550 km inside the subducting Pacific slab beneath the Izu-Bonin region. They also suggested that the occurrence of deep earthquakes is related to the MOW in the Pacific slab. Koper et al. (1998) used OBS data to investigate this issue for the subducting Pacific slab beneath the Tonga region, but they failed to detect an MOW in the Tonga slab. Kaneshima et al. (2007) and Kubo et al. (2009) revealed an MOW of 5% low-velocity relative to the iasp91 Earth model (Kennett and Engdahl 1991) inside the subducting Pacific slab beneath Mariana. Kawakatsu and Yoshioka (2011) detected an MOW beneath Southwest Japan using teleseismic receiver functions.

Jiang et al. (2008) and Jiang and Zhao (2011) studied the fine structure of the subducting Pacific slab using arrival-time data from deep earthquakes beneath the Japan Sea and the East Asian margin recorded by the dense seismic network on the Japan Islands (Fig. 4.17a). They detected a low-V finger within the subducting Pacific slab in the mantle transition-zone depth under the Japan Sea, which is interpreted to be an MOW (Fig. 4.17b). They relocated the deep earthquakes using the final slab model and found that all the deep earthquakes are located within the MOW or along its edges (Fig. 4.17b), suggesting that the occurrence of deep earthquakes is related to the fine structural heterogeneity and phase changes in the subducting slab, as suggested by earlier studies (e.g., Kirby 1991; Green and Houston 1995).

Recently, a much better data set and a new method have been used to study the precise velocity structure of the subducting Pacific slab under the Japan Sea (Jiang et al. 2015). Travel-time double-residuals, instead of raw travel-time residuals, of 17 well-located deep earthquakes are used in the analysis. A modified double-difference location method is applied to relocate precisely the 17 deep earthquakes which were recorded by both Chinese and Japanese seismic stations, and the relocated hypocenters are accurate to 2 km. As a result, a low-V zone with a P-wave velocity reduction of 5~8% relative to the iasp91 Earth model is revealed within the subducting Pacific slab at the mantle transition-zone depth, which reflects the MOW. The existence of the MOW affects not only the subduction dynamics of the Pacific slab but also the generation of deep earthquakes (Jiang et al. 2015).

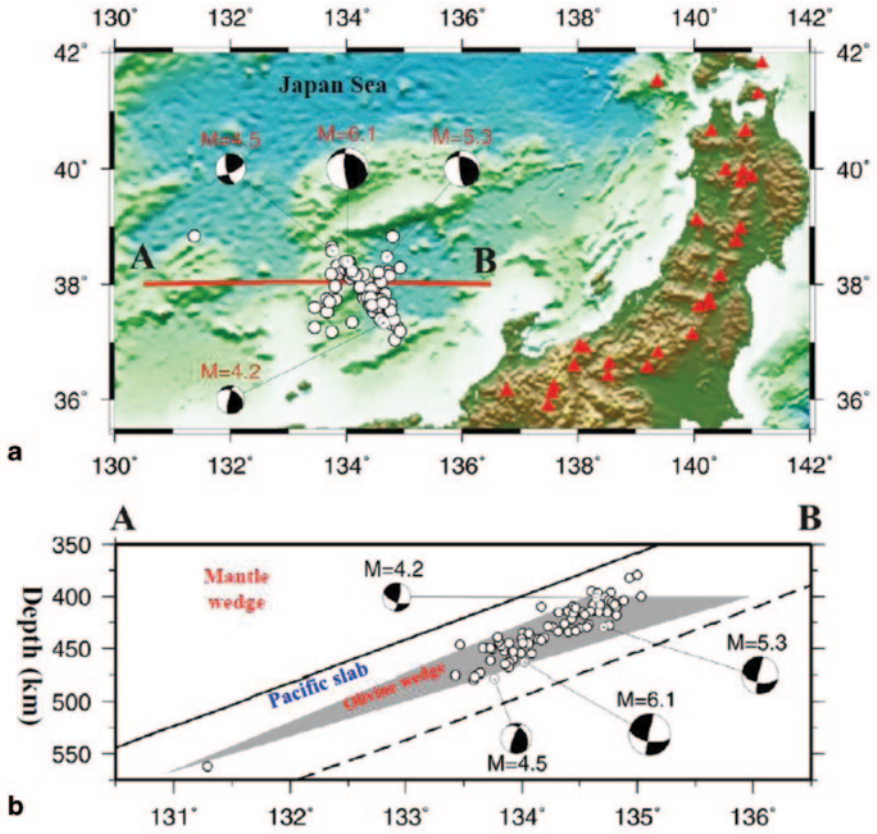

Fig. 4.17 **a** Epicenter locations of the 78 deep earthquakes. Focal mechanism solutions (lower-hemisphere projection) of four deep earthquakes are also shown, whose sizes are proportional to their magnitudes shown above each beach ball. The *black* portions in each beach ball denote the compressional area. The *red triangles* represent active arc volcanoes. **b** Vertical cross-section of the relocated 78 earthquakes and the focal mechanism solutions of four earthquakes in the optimal slab model along line *AB*. The *solid* and *dashed lines* denote the upper and lower boundaries of the Pacific slab. The *grey triangle* in the slab represents the optimal model of the metastable olivine wedge. (Modified from Jiang and Zhao 2011)

The MOW is an important, but less distinguishable, feature in the subducting slab, and the resolution of current tomography under the Japan Sea is still too low to image such a small feature because of the lack of seismic stations in the Japan Sea (e.g., Zhao et al. 2012; Huang et al. 2013). That is why so far seismologists have adopted simple forward-modeling approaches to study the MOW structure. In future studies, it would be ideal to detect the MOW by tomographic imaging when a dense OBS network is installed in the marginal seas (e.g., the Japan Sea, Lau Basin, etc.) above the deep earthquakes.

4.5 Discussion

The majority of the earthquakes occurring on Earth take place in subduction zones where almost every type of earthquakes is observed. The generation of subduction-zone earthquakes is not a pure faulting process, but affected or controlled by subduction dynamics. So far, many researchers have investigated subduction-zone processes using multidisciplinary approaches. These studies indicate that fluids exist widely in the crust and upper mantle, and in particular, in subduction zones (e.g., Tatsumi 1989; Peacock 1990; Iwamori and Zhao 2000; van KeKen et al. 2011; Zhao 2012). Deep subduction of the oceanic lithosphere is accompanied by metamorphic processes which lead to continuous fluid production, which in turn plays a key role in the generation of arc magmas (Fig. 4.5). Slab dehydration takes place continuously down to ~200 km depth through breakdown reactions of hydrous phases in the subducting slab, and fluid inclusion studies of minerals from deep subducted rocks indicate the production of aqueous fluids (e.g., Scambelluri and Philippot 2001). During subduction, hydrous silicates decompose to release metasomatic fluid against the hanging wall which reduces the melting temperature of the mantle wedge, resulting in the formation of arc magmas (Tatsumi, 1989). When the sub-arc mantle produces magma near the Moho discontinuity, two liquid phases are generated: one is arc magma, the other is water-enriched fluid, each of which may move upward independently. Such phase separation has been experimentally demonstrated to occur at ~800–1000 °C near the Moho depth, and low-frequency micro-earthquakes, which often occur near the Moho beneath active arc volcanoes, may be related to the phase separation and fluid activity (e.g., Hasegawa and Zhao 1994; Nakamichi et al. 2003; Zhao et al. 2011a). Understanding the roles of magmatic, metasomatic and metamorphic fluid factories in the subduction environment is very important for clarifying the mechanisms of earthquake generation and rupture propagation.

The interplate megathrust zone is generally overpressured to near-lithostatic values under the forearc hanging wall, and solution migration within the fine-grained material along the slab boundary can contribute to the hydrothermal sealing of fractures, which can reduce bulk permeability (Sibson 2013). Down-dip variations in overpressuring may affect the depth of the peak in frictional shear resistance which may serve as the prime asperity for a megathrust earthquake. To explain the post-seismic changes in the tomographic image of the forearc hanging-wall following the 1995 Antofagasta megathrust earthquake (Mw 8.0), Husen and Kissling (2001) proposed a massive trans-megathrust discharge of fluids across the slab boundary. Such discharges are a form of fault-valve action where the megathrust itself acts as a seal to over-pressured fluids derived from slab dehydration. Brittle failure, or fault reactivation, limits fluid overpressure which is highest at a low differential stress under a compressional stress regime. Following the great 2011 Tohoku-oki earthquake, the stress regime in much of the forearc hanging-wall switched from compressional thrusting to extensional normal faulting (e.g., Yoshida et al. 2012). The overpressure can be reduced by a combination of poroelastic effects and fluid loss through fault–fracture networks, which can increase postfailure permeability in the changing stress field. Local drainage across the slab boundary can greatly increase the frictional strength, resulting in a postfailure distribution of strength

asperities. The time to the next great earthquake is then influenced by the recovery of fluid overpressure and shear stress in the megathrust zone (Sibson 2013).

Fluids in the crust and uppermost mantle in all tectonic settings can affect the long-term structural and compositional evolution of the fault zones, change the strength of the fault zone, and alter the local stress regime (Sibson 1992, 2013; Hickman et al. 1995). These effects can enhance the stress concentration in the seismogenic layer, resulting in mechanical failure. In addition to structural heterogeneities, spatial and temporal changes in the stress field have been detected in the source areas of some large crustal earthquakes (e.g., Katao et al. 1997; Zhao et al. 1997; Huang et al., 2011b) and megathrust earthquakes (e.g., Yoshida et al. 2012), which were related to fluid migrations in the seismogenic zones.

These above-mentioned pieces of geophysical and geological evidence indicate that the occurrence of earthquakes is not entirely a mechanical process, but is closely associated with the physical and chemical properties of rocks in the crust and upper mantle, and in particular, magma, fluids, etc. (Zhao et al. 2002, 2010) The nucleation zone of a large earthquake should have a three-dimensional spatial extent, and not be just limited to a two-dimensional fault plane. In other words, an earthquake volume should exist, as suggested by Tsuboi (1956). Complex physical and chemical reactions may take place in the earthquake volume, resulting in spatial and temporal variations in the material property and stress field, which can be detected and imaged by seismic tomography and other geophysical methods. The rupture zones of M 6 to M 9 earthquakes have spatial extents ranging from ~10 to over 500 km (e.g., Beroza and Kanamori 2007). The resolution of current tomographic models is close to that scale of earthquake sources, which has enabled seismologists to image earthquake-related heterogeneities (i.e., earthquake volumes) in the crust and uppermost mantle in some well-instrumented regions.

Interestingly, recent studies show that even the distribution and generation of deep moonquakes are affected by the structural heterogeneities in the lunar mantle (Zhao et al. 2008, 2012b), suggesting similar seismogenic processes in both the Earth and the Moon.

All these results suggest that large earthquakes do not take place randomly in any regions, but only in anomalous areas having significant lateral (and/or vertical) heterogeneities, which can be detected by high-resolution geophysical imaging. Combining seismic tomography with geological, geochemical and other geophysical investigations would certainly improve our understanding of the earthquake nucleation process and would contribute to the reduction of seismic hazards. For this purpose, permanent or portable seismograph stations should be deployed densely and uniformly in seismogenic zones in future studies.

4.6 Summary

Seismic tomography studies of source areas of large earthquakes carried out to date have shown that structural heterogeneities in the crust and upper mantle strongly affect or control the nucleation of earthquakes in various tectonic environments. In

particular, fluids and magmas play an important role in triggering large earthquakes. The findings of these studies indicate that seismic tomography is a useful and powerful tool for studying earthquakes and seismotectonics.

So far, many tomographic studies have been made for the source areas of large crustal earthquakes and some intraslab earthquakes, because those areas are covered by dense seismic networks. Megathrust earthquakes have been studied using seismic tomography in only a few regions, and none of the source zones of deep earthquakes (>300 km depth) have been imaged by seismic tomography. This is because megathrust earthquakes occur beneath the subduction-zone forearc regions, and deep earthquakes occur in the back-arc regions, both of which are generally covered by oceans. Dense OBS networks are needed to image the detailed structure in the source zones of the megathrust and deep earthquakes using seismic tomography. Future high-resolution geophysical imaging with better data sets and improved methods, and multidisciplinary studies of the seismogenic zones, will reveal more details of the nucleation process of large earthquakes, which will also contribute to the mitigation of seismic hazards.

References

Beroza, G., Kanamori, H.: Comprehensive overview. In: Schubert, G. (ed.) Treatise in Geophysics, vol. 4.01, pp. 1–58. Elsevier, New York (2007)

Chen, C., Zhao, D., Wu, S.: Crust and upper mantle structure of the New Madrid Seismic Zone: insight into intraplate earthquakes. Phys. Earth Planet. Inter. **230,** 1–14 (2014)

Cheng, B., Zhao, D., Zhang, G.: Seismic tomography and anisotropy in the source area of the 2008 Iwate-Miyagi earthquake (M 7.2). Phys. Earth Planet. Inter. **184,** 172–185 (2011)

Cheng, B., Cheng, S., Zhang, G., Zhao, D.: Seismic structure of the Helan-Liupan-Ordos western margin tectonic belt in North-Central China and its geodynamic implications. J. Asian Earth Sci. **87,** 141–156 (2014)

Chiarabba, C., Bagh, S., Bianchi, I., De Gori, P., Barchi, M.: Deep structural heterogeneities and the tectonic evolution of the Abruzzi region (Central Apennines, Italy) revealed by microseismicity, seismic tomography, and teleseismic receiver functions. Earth Planet. Sci. Lett. **295,** 462–476 (2010)

Collings, R., Lange, D., Rietbrock, A., Tilmann, F. et al.: Structure and seismogenic properties of the Mentawai segment of the Sumatra subduction zone revealed by local earthquake traveltime tomography. J. Geophys. Res. **117,** B01312 (2012)

Di Stefano, R., Chiarabba, C., Chiaraluce, L., Cocco, M. et al.: Fault zone properties affecting the rupture evolution of the 2009 (M_w 6.1) L'Aquila earthquake (central Italy): insights from seismic tomography. Geophys. Res. Lett. **38,** L10301 (2011)

Eberhart-Phillips, D., Michael, A.: Seismotectonics of the Loma Prieta, California, region determined from three-dimensional Vp, Vp/Vs, and seismicity. J. Geophys. Res. **103,** 21099–21120 (1998)

Fujie, G., Kasahara, J., Hino, R., Sato, T., Shinohara, M., Suyehiro, K.: A significant relation between seismic activities and reflection intensities in the Japan Trench region. Geophys. Res. Lett. **29,** GL013764 (2002)

Gokalp, H.: Tomographic imaging of the seismic structure beneath the East Anatolian Plateau, Eastern Turkey. Pure Appl. Geophys. **169,** 1749–1776 (2012)

Green, H.: Tiny triggers deep down. Nature **424,** 893–894 (2003)

Green, H., Burnley, P.: A new self-organizing mechanism for deep-focus earthquakes. Nature **341,** 733–737 (1989)
Green, H., Houston, H.: The mechanisms of deep earthquakes. Annu. Rev. Earth Planet. Sci. **23,** 169–213 (1995)
Gupta, S., Zhao, D., Ikeda, M., Ueki, S., Rai, S.: Crustal tomography under the Median Tectonic Line in Southwest Japan using P and PmP data. J. Asian Earth Sci. **35,** 377–390 (2009)
Hasegawa, A., Zhao, D.: Deep structure of island arc magmatic regions as inferred from seismic observations. In: M. P. Ryan (ed.) Magmatic Systems pp. 179–195, Academic Press, Burlington (1994)
Hasegawa, A., Nakajima, J., Umino, N., Miura, S.: Deep structure of the northeastern Japan arc and its implications for crustal deformation and shallow seismicity. Tectonophysics **403,** 59–75 (2005)
Hasegawa, A., Yoshida, K., Asano, Y., Okada, T., Iinuma, T., Ito, Y.: Change in stress field after the 2011 great Tohoku-Oki earthquake. Earth Planet. Sci. Lett. **355,** 231–243 (2012)
Heki, K., Miyazaki, S., Tsuji, H.: Silent fault slip following an interplate thrust earthquake at the Japan trench. Nature **386,** 592–597 (1997)
Hickman S., Sibson, R., Bruhn, R.: Introduction to special section: mechanical involvement of fluids in faulting. J. Geophys. Res. **100,** 12831–12840 (1995)
Hino, R., Yamamoto, Y., Kuwano, A.: Hypocenter distribution of the main- and aftershocks of the 2005 Off Miyagi Prefecture earthquake located by ocean bottom seismographic data. Earth Planets Space **58,** 1543–1548 (2006)
Hirata, N. et al.: Urgent joint observation of aftershocks of the 1995 Hyogo-ken Nanbu earthquake. J. Phys. Earth **44,** 317–328 (1996)
Hobbs, B., Ord, A.: Plastic instabilities: implication for the origin of intermediate and deep focus earthquakes. J. Geophys. Res. **93,** 10521–10540 (1988)
Huang, J., Zhao, D.: Crustal heterogeneity and seismotectonics of the region around Beijing, China. Tectonophysics **385,** 159–180 (2004)
Huang, J., Zhao, D.: Seismic imaging of the crust and upper mantle under Beijing and surrounding regions. Phys. Earth Planet. Inter. **173,** 330–348 (2009)
Huang, Z., Zhao, D.: Relocating the 2011 Tohoku-oki earthquakes (M 6.0–9.0). Tectonophysics **586,** 35–45 (2013a)
Huang, Z., Zhao, D.: Mechanism of the 2011 Tohoku-oki earthquake (Mw 9.0) and tsunami: Insight from seismic tomography. J. Asian Earth Sci. **70,** 160–168 (2013b)
Huang, Z., Zhao, D., Wang, L.: Seismic heterogeneity and anisotropy of the Honshu arc from the Japan Trench to the Japan Sea. Geophys. J. Int. **184,** 1428–1444 (2011a)
Huang, Z., Zhao, D., Wang, L.: Stress field in the 2008 Iwate-Miyagi earthquake (M 7.2) area. Geochem. Geophys. Geosyst. **12,** Q06006 (2011b)
Huang, Z., Zhao, D., Hasegawa, A., Umino, N., Park, J., Kang, I.: Aseismic deep subduction of the Philippine Sea plate and slab window. J. Asian Earth Sci. **75,** 82–94 (2013)
Husen, S., Kissling, E.: Postseismic fluid flow after the large subduction earthquake of Antofagasta, Chile. Geology **29,** 847–850 (2001)
Husen, S., Kissling, E., Flueh, E.: Local earthquake tomography of shallow subduction in north Chile: a combined onshore and offshore study. J. Geophys. Res. **105,** 28183–28198 (2000)
Iidaka, T., Suetsugu, D.: Seismological evidence for metastable olivine inside a subducting slab. Nature **356,** 593–595 (1992)
Ikeda, M., Zhao, D., Ohno, Y.: Crustal structure, fault segmentation and activity of the Median Tectonic Line in Shikoku, Japan. Tectonophysics **412,** 49–60 (2006)
Ito, Y., Tsuji, T., Osada, Y., Kido, M. et al.: Frontal wedge deformation near the source region of the 2011 Tohoku-oki earthquake. Geophys. Res. Lett. **38,** L00G05 (2011)
Iwamori, H., Zhao, D.: Melting and seismic structure beneath the northeast Japan arc. Geophys. Res. Lett. **27,** 425–428 (2000)
Jiang, G., Zhao, D.: Metastable olivine wedge in the subducting Pacific slab and its relation to deep earthquakes. J. Asian Earth Sci. **42,** 1411–1423 (2011)

Jiang, G., Zhao, D., Zhang, G.: Seismic evidence for a metastable olivine wedge in the subducting Pacific slab under Japan Sea. Earth Planet. Sci. Lett. **270,** 300–307 (2008)
Jiang, G., Zhao, D., Zhang, G.: Detection of metastable olivine wedge in the western Pacific slab and its geodynamic implications. Phys. Earth Planet. Inter. **238,** 1–7 (2015)
Kaneshima, S., Okamoto, T., Takenaka, H.: Evidence for a metastable olivine wedge inside the subducted Mariana slab. Earth Planet. Sci. Lett. **258,** 219–227 (2007)
Karato, S., Riedel, M., Yuen, D.: Rheological structure and deformation of subducted slabs in the mantle transition zone: implications for mantle circulation and deep earthquakes. Phys. Earth Planet. Inter. **127,** 83–108 (2001)
Katao, H., Maeda, N., Hiramatsu Y., Iio Y., Nakao, S.: Detailed mapping of focal mechanisms in and around the 1995 Hyogo-Ken Nanbu earthquake rupture zone. J. Phys. Earth **45,** 105–119 (1997)
Kato, A., Kurashimo, E., Hirata, H., Iwasaki, T., Kanazawa, T.: Imaging the source region of the 2004 Mid-Niigata prefecture earthquake and the evolution of the seismogenic thrust related fold. Geophys. Res. Lett. **32,** L07307 (2005)
Kato, A., Igarashi, T., Obara, K., Sakai, S. et al.: Imaging the source regions of normal faulting sequences induced by the 2011 M9.0 Tohoku-Oki earthquake. Geophys. Res. Lett. **40,** 273–278 (2013)
Kawakatsu, H., Yoshioka, S.: Metastable olivine wedge and deep dry cold slab beneath southeast Japan. Earth Planet. Sci. Lett. **303,** 1–10 (2011)
Kawasaki, I., Asai, Y., Tamura, Y.: Space-time distribution of interplate moment release including slow earthquakes and the seismo-geodetic coupling in the Sanriku-oki region along the Japan trench. Tectonophysics **330,** 267–283 (2001)
Kayal, J., Zhao, D., Mishra, O.P., Reena, D., Singh, O.: The 2001 Bhuj earthquake: tomographic evidence for fluids at the hypocenter and its implications for rupture nucleation. Geophys Res. Lett. **29,** GL015177 (2002)
Kirby, S.: Mantle phase changes and deep-earthquake faulting in subducting lithosphere. Science **252,** 216–224 (1991)
Kirby, S., Stein, S., Okal, E., Rubie, D.: Metastable mantle transformations and deep earthquakes in subducting oceanic lithosphere. Rev. Geophys. **34,** 261–306 (1996)
Koper, K., Wiens, D., Dorman, L., Hildebrand, J., Webb, S.: Modeling the Tonga slab: can travel time data resolve a metastable olivine wedge? J. Geophys. Res. **103,** 30079–30100 (1998)
Kubo, T., Kaneshima, S., Torii, Y., Yoshioka, S.: Seismological and experimental constraints on metastable phase transformations and rheology of the Mariana slab. Earth Planet. Sci. Lett. **287,** 12–23 (2009)
Lees J.: Tomographic P-wave velocity images of the Loma Prieta earthquake asperity. Geophys. Res. Lett. **17,** 1433–1436 (1990)
Lees, J., Nicholson, C.: Three-dimensional tomography of the 1992 southern California earthquake sequence: constraints on dynamic earthquake rupture? Geology **21,** 387–390 (1993)
Lei, J., Zhao, D.: Structural heterogeneity of the Longmenshan fault zone and the mechanism of the 2008 Wenchuan earthquake (Ms 8.0). Geochem. Geophys. Geosyst. **10,** Q10010 (2009)
Li, Z., Tian, B., Liu, S., Yang, J.: Asperity of the 2013 Lushan earthquake in the eastern margin of Tibetan Plateau from seismic tomography and aftershock relocation. Geophys. J. Int. **195,** 2016–2022 (2013)
Liu, X., Zhao, D., Li, S.: Seismic heterogeneity and anisotropy of the southern Kuril arc: Insight into megathrust earthquakes. Geophys. J. Int. **194,** 1069–1090 (2013a)
Liu, X., Zhao, D., Li, S.: Seismic imaging of the Southwest Japan arc from the Nankai trough to the Japan Sea. Phys. Earth Planet. Inter. **216,** 59–73 (2013b)
Liu, X., Zhao, D., Li, S.: Seismic attenuation tomography of the Northeast Japan arc: insight into the 2011 Tohoku earthquake (Mw 9.0) and subduction dynamics. J. Geophys. Res. **119,** 1094–1118 (2014)
Michael, A., Eberhart-Phillips, D.: Relations among fault behavior, subsurface geology, and three-dimensional velocity models. Science **253,** 651–654 (1991)

Mishra, O.P.: Crustal heterogeneity in bulk velocity beneath the 2001 Bhuj earthquake source zone and its implications. Bull. Seismol. Soc. Am. **103,** 3235–3247 (2013)
Mishra, O.P., Zhao, D.: Crack density, saturation rate and porosity at the 2001 Bhuj, India, earthquake hypocenter: a fluid driven earthquake? Earth Planet. Sci. Lett. **212,** 393–405 (2003)
Mishra, O.P., Zhao, D.: Seismic evidence for dehydration embrittlement of the subducting Pacific slab. Geophys. Res. Lett. **31,** L09610 (2004)
Mishra, O.P., Zhao, D., Umino, N., Hasegawa, A.: Tomography of Northeast Japan forearc and its implications for interplate seismic coupling. Geophys. Res. Lett. **30,** GL017736 (2003)
Miura, S., Kodaira, S., Nakanishi, A., Tsuru, T.: Structural characteristics controlling the seismicity of southern Japan Trench fore-arc region, revealed by ocean bottom seismographic data. Tectonophysics **363,** 79–102 (2003)
Moeremans, R., Singh, S., Mukti, M., McArdle, J., Johansen, K.: Seismic images of structural variations along the deformation front of the Andaman–Sumatra subduction zone: implications for rupture propagation and tsunamigenesis. Earth Planet. Sci. Lett. **386,** 75–85 (2014)
Mukhopadhyay, S., Mishra, O.P., Zhao, D., Kayal, J.R.: 3-D seismic structure of the source area of the 1993 Latur, India, earthquake and its implications for rupture nucleations. Tectonophysics **415,** 1–16 (2006)
Nakajima, J., Tsuji, Y., Hasegawa, A., Kita, S., Okada, T., Matsuzawa, T.: Tomographic imaging of hydrated crust and mantle in the subducting Pacific slab beneath Hokkaido, Japan: evidence for dehydration embrittlement as a cause of intraslab earthquakes. Gondwana Res. **16,** 470–481 (2009)
Nakajima, J., Hasegawa, A., Kita, S.: Seismic evidence for reactivation of a buried hydrated fault in the Pacific slab by the 2011 M9.0 Tohoku earthquake. Geophys. Res. Lett. **38,** L00G06 (2011)
Nakamichi, H., Hamaguchi, H., Tanaka, S., Ueki, S., Nishimura, T., Hasegawa, A.: Source mechanisms of deep and intermediate-depth low-frequency earthquakes beneath Iwate volcano, northeastern Japan. Geophys. J. Int. **154,** 811–828 (2003)
Nakamura, A., Hasegawa, A., Ito, A. et al.: P-wave velocity structure of the crust and its relationship to the occurrence of the 1999 Izmit, Turkey, earthquake and aftershocks. Bull. Seismol. Soc. Am. **92,** 330–338 (2002)
Obana, K., Fujie, G., Takahashi, T., Yamamoto, Y., Nakamura, Y. et al.: Normal-faulting earthquakes beneath the outer slope of the Japan Trench after the 2011 Tohoku earthquake: implications for the stress regime in the incoming Pacific plate. Geophys. Res. Lett. **39,** L00G24 (2012)
O'Connell, R., Budiansky, B.: Seismic velocities in dry and saturated cracked solids. J. Geophys. Res. **79,** 5412–5426 (1974)
Ohmi, S., Obara, K.: Deep low-frequency earthquakes beneath the focal region of the Mw 6.7 2000 Western Tottori earthquake. Geophys. Res. Lett. **29,** GL014469 (2002)
Okada, T., Hasegawa, A.: Source process and aftershock distribution of May 26, 2003 M7.0 intraslab earthquake off Miyagi Prefecture, NE Japan. Earth Planet Space **55,** 731–739 (2003)
Okada, Y., Kasahara, K., Hori, S., Obara, K.: Recent progress of seismic observation networks in Japan—Hi-net, F-net, K-NET and KiK-net. Earth Planets Space **56,** xv–xxviii (2004)
Okada, T., Umino, N., Hasegawa, A.: Deep structure of the Ou mountain range strain concentration zone and the focal area of the 2008 Iwate-Miyagi Nairiku earthquake, NE Japan—Seismogenesis related with magma and crustal fluid. Earth Planets Space **62,** 347–352 (2010)
Oshiman N.: Electric conductivity structure of western Japan. Earth Monthly **38,** 82–90 (2002)
Padhy, S., Mishra, O.P., Zhao, D., Wei, W.: Crustal heterogeneity in the 2007 Noto-Hanto earthquake area and its geodynamical implications. Tectonophysics **42,** 1381–1393 (2011)
Peacock S.: Fluid processes in subduction zones. Science **248,** 329–345 (1990)
Powell, C., Withers, M., DeShon, H., Dunn, M.: Intrusions and anomalous V_p/V_s ratios associated with the New Madrid seismic zone. J. Geophys. Res. **115,** B08311 (2010)
Qi, C., Zhao, D., Chen, Y.: 3-D P and S wave velocity structures and their relationship to strong earthquakes in the Chinese capital region. Chin. J. Geophys. **49,** 805–815 (2006)

Raleigh, C., Paterson, M.: Experimental deformation of serpentinite and its tectonics implications. J. Geophys. Res. **70,** 3965–3985 (1965)
Reid, H.: The Mechanics of the Earthquake: the California Earthquake of April 18, 1906, Report of the State Investigation Commission, vol. 2, Carnegie Institution of Washington, Washington, D.C, pp. 16–28 (1910)
Salah, M., Zhao, D.: 3-D seismic structure of Kii Peninsula in Southwest Japan: evidence for slab dehydration in the forearc. Tectonophysics **364,** 191–213 (2003)
Salah, M., Sahin, S., Destici, C.: Seismic velocity and Poisson's ratio tomography of the crust beneath southwest Anatolia: an insight into the occurrence of large earthquakes. J. Seismol. **11,** 415–432 (2007)
Salah, M., Sahin, S., Aydin, U.: Seismic velocity and Poisson's ratio tomography of the crust beneath East Anatolia. J. Asian Earth Sci. **40,** 746–761 (2011)
Salah, M., Sahin, S., Topatan, U.: Crustal velocity and Vp/Vs structures beneath central Anatolia from local seismic tomography. Arab. J. Geosci. (2013)
Scambelluri, M., Philippot, P.: Deep fluids in subduction zones. Lithos **55,** 213–227 (2001)
Shibutani T., Katao, H. et al.: High-resolution 3-D velocity structure in the source region of the 2000 Western Tottori earthquake in southwestern Honshu, Japan using very dense aftershock observations. Earth Planets Space **57,** 825–838 (2005)
Sibson R.: Implications of fault-valve behavior for rupture nucleation and recurrence. Tectonophysics **211,** 283–293 (1992)
Sibson, R.: Stress switching in subduction forearcs: Implications for overpressure containment and strength cycling on megathrusts. Tectonophysics **600,** 142–152 (2013)
Tatsumi, Y.: Migration of fluid phases and genesis of basalt magmas in subduction zones. J. Geophys. Res. **94,** 4697–4707 (1989)
Thurber, C., Atre, S., Eberhart-Phillips, D.: Three-dimensional Vp and Vp/Vs structure at Loma Prieta, California, from local earthquake tomography. Geophys. Res. Lett. **22,** 3079–3082 (1995)
Tian, Y., Liu, L.: Geophysical properties and seismotectonics of the Tohoku forearc region. J. Asian Earth Sci. **64,** 235–244 (2013)
Tong, P., Zhao, D., Yang, D.: Tomography of the 1995 Kobe earthquake area: Comparison of finite-frequency and ray approaches. Geophys. J. Int. **187,** 278–302 (2011)
Tong, P., Zhao, D., Yang, D.: Tomography of the 2011 Iwaki earthquake (M 7.0) and Fukushima nuclear power plant area. Solid Earth **3,** 43–51 (2012)
Tsuboi, C.: Earthquake energy, earthquake volume, aftershock area, and strength of the Earth's crust. J. Phys. Earth **4,** 63–66 (1956)
Tsuru, T., Park, J., Miura, S., Kodaira, S., Kido, Y., Hayashi, T.: Along-arc structural variation of the plate boundary at the Japan Trench margin: Implications of interplate coupling. J. Geophys. Res. **107,** 2357 (2002)
Umino, N., Hasegawa, A., Matsuzawa, T.: sP depth phase at small epicentral distances and estimated subducting plate boundary. Geophys. J. Int. **120,** 356–366 (1995)
van KeKen, P., Hacker, B., Syracuse, E., Abers, G.: Subduction factory: 4. Depth-dependent flux H2O from subducting slabs worldwide. J. Geophys. Res. **116,** B01401 (2011)
Wang, Z., Zhao, D.: Seismic imaging of the entire arc of Tohoku and Hokkaido in Japan using P-wave, S-wave and sP depth-phase data. Phys. Earth Planet. Inter. **152,** 144–162 (2005)
Wang, Z., Zhao, D.: Seismic evidence for the influence of fluids on the 2005 west off Fukuoka prefecture earthquake in southwest Japan. Phys. Earth Planet. Inter. **155,** 313–324 (2006a)
Wang, Z., Zhao, D.: Seismic images of the source area of the 2004 Mid-Niigata prefecture earthquake in Northeast Japan. Earth Planet. Sci. Lett. **244,** 16–31 (2006b)
Wang, Z., Zhao, D.: Vp and Vs tomography of Kyushu, Japan: New insight into arc magmatism and forearc seismotectonics. Phys. Earth Planet. Inter. **157,** 269–285 (2006c)
Wang, J., Zhao, D., Yao, Z.: Crustal and uppermost mantle structure and seismotectonics of North China Craton. Tectonophysics **582,** 177–187 (2013)

Wei, W., Zhao, D.: The 2008 Iwate-Miyagi earthquake (M 7.2) and arc volcanism: Insight from irregular-grid tomography. Earth Sci. Frontiers **20,** 155–171 (2013)
Wei, W., Zhao, D., Xu, J.: P-wave anisotropic tomography in Southeast Tibet: new insight into the lower crustal flow and seismotectonics. Phys. Earth Planet. Inter. **222,** 47–57 (2013)
Xia, S., Zhao, D., Qiu, X.: The 2007 Niigata earthquake: Effect of arc magma and fluids. Phys. Earth Planet. Inter. **166,** 153–166 (2008)
Yoshida, K., Hasegawa, A., Okada, T., Iinuma, T., Ito, Y., Asano, Y.: Stress before and after the 2011 great Tohoku-oki earthquake and induced earthquakes in inland areas of eastern Japan. Geophys. Res. Lett. **39,** L03302 (2012)
Yue, H., Lay, T.: Inversion of high-rate (1 sps) GPS data for rupture process of the 11 March 2011 Tohoku earthquake (Mw 9.1). Geophys. Res. Lett. **38**, L00G09 (2011)
Zeng, X., Luo, Y., Han, L., Shi, Y.: The Lushan Ms 7.0 earthquake on 20 April 2013: A high-angle thrust event. Chinese J. Geophys. **56,** 1418–1424 (2013)
Zhan, Y., Zhao, G., Wang, J., Chen, X., Xiao, Q., Huang, Z., Zhen, G.: Deep electric structure in the source area of the 1927 Gulang earthquake and adjacent areas. Chinese J. Geophys. **51,** 511–520 (2008)
Zhang, Q., Sandvol, E., Liu, M.: Lithospheric velocity structure of the New Madrid Seismic Zone: a joint teleseismic and local P tomographic study. Geophys. Res. Lett. **36,** L11305 (2009)
Zhao, D.: New advances of seismic tomography and its applications to subduction zones and earthquake fault zones. Island Arc **10,** 68–84 (2001)
Zhao, D.: Multiscale seismic tomography and mantle dynamics. Gondwana Res. **15,** 297–323 (2009)
Zhao, D.: Tomography and dynamics of Western-Pacific subduction zones. Monogr. Environ. Earth Planets **1,** 1–70 (2012)
Zhao, D., Kanamori, H.: The 1992 Landers earthquake sequence: Earthquake occurrence and structural heterogeneities. Geophys. Res. Lett. **20,** 1083–1086 (1993)
Zhao, D., Kanamori, H.: The 1994 Northridge earthquake: 3-D crustal structure in the rupture zone and its relation to the aftershock locations and mechanisms. Geophys. Res. Lett. **22,** 763–766 (1995)
Zhao, D., Mizuno, T.: Crack density and saturation rate in the 1995 Kobe earthquake region. Geophy. Res. Lett. **26,** 3213–3216 (1999)
Zhao, D., Negishi, H.: The 1995 Kobe earthquake: Seismic image of the source zone and its implications for the rupture nucleation. J. Geophys. Res. **103,** 9967–9986 (1998)
Zhao, D., Kanamori, H., Negishi, H., Wiens, D.: Tomography of the source area of the 1995 Kobe earthquake: Evidence for fluids at the hypocenter? Science **274,** 1891–1894 (1996)
Zhao, D., Kanamori, H., Wiens, D.: State of stress before and after the 1994 Northridge earthquake. Geophys. Res. Lett. **24,** 519–522 (1997)
Zhao, D., Ochi, F., Hasegawa, A., Yamamoto, A.: Evidence for the location and cause of large crustal earthquakes in Japan. J. Geophys. Res. **105,** 13579–13594 (2000)
Zhao, D., Mishra, O.P., Sanda, R.: Influence of fluids and magma on earthquakes: seismological evidence. Phys. Earth Planet. Inter. **132,** 249–267 (2002)
Zhao, D., Tani, H., Mishra, O.P.: Crustal heterogeneity in the 2000 western Tottori earthquake region: effect of fluids from slab dehydration. Phys. Earth Planet. Inter. **145,** 161–177 (2004)
Zhao, D., Todo, S., Lei, J.: Local earthquake reflection tomography of the Landers aftershock area. Earth Planet. Sci. Lett. **235,** 623–631 (2005)
Zhao, D., Wang, Z., Umino, N., Hasegawa, A.: Tomographic imaging outside a seismic network: Application to the northeast Japan arc. Bull. Seismol. Soc. Am. **97,** 1121–1132 (2007)
Zhao, D., Lei, J., Liu, L.: Seismic tomography of the Moon. Chinese Sci. Bull. **53,** 3897–3907 (2008)
Zhao, D., Wang, Z., Umino, N., Hasegawa, A.: Mapping the mantle wedge and interplate thrust zone of the northeast Japan arc. Tectonophysics **467,** 89–106 (2009)
Zhao, D., Santosh, M., Yamada, A.: Dissecting large earthquakes in Japan: role of arc magma and fluids. Island Arc **19,** 4–16 (2010)

Zhao, D., Wei, W., Nishizono, Y., Inakura, H.: Low-frequency earthquakes and tomography in western Japan: insight into fluid and magmatic activity. J. Asian Earth Sci. **42,** 1381–1393 (2011a)

Zhao, D., Z. Huang, Z., Umino. N., Hasegawa, A., Yoshida, T.: Seismic imaging of the Amur-Okhotsk plate boundary zone in the Japan Sea. Phys. Earth Planet. Inter. **188,** 82–95 (2011b)

Zhao, D., Huang, Z., Umino. N., Hasegawa, A., Kanamori, H.: Structural heterogeneity in the megathrust zone and mechanism of the 2011 Tohoku-oki earthquake (Mw 9.0). Geophys. Res. Lett. **38,** L17308 (2011c)

Zhao, D., Yanada, T., Hasegawa, A., Umino, N., Wei, W.: Imaging the subducting slabs and mantle upwelling under the Japan Islands. Geophys. J. Int. **190,** 816–828 (2012a)

Zhao, D., Arai, T., Liu, L., Ohtani, E.: Seismic tomography and geochemical evidence for lunar mantle heterogeneity: comparing with Earth. Global Planet. Change **90,** 29–36 (2012b)

Zhao, D., Kitagawa, H., Toyokuni, G.: A water wall in the Tohoku forearc causing large crustal earthquakes. Geophys. J. Int. **200,** 149–172 (2015)

Chapter 5
Hotspots and Mantle Plumes

Abstract Seismic images under 62 possible hotspots are reviewed for understanding the origin of hotspots and mantle plumes. Plume-like, continuous low-velocity anomalies are visible beneath Hawaii, Tahiti, Louisville, Iceland, Cape Verde, Reunion, Kerguelen, Amsterdam, Afar, Eifel, Hainan, Yellowstone and Cobb hotspots, suggesting that they may be 13 whole-mantle plumes originating from the core-mantle boundary. These plumes exhibit tilted images, suggesting that plumes are not fixed in the mantle but can be deflected by the mantle flow. Upper-mantle plumes seem to exist beneath Cameroon, Easter, Azores, Vema, East Australia and Erebus hotspots. A mid-mantle plume may exist under the San Felix hotspot. Active intraplate volcanoes in Northeast Asia and Southwest China are caused by hot and wet upwelling flows in the big mantle wedge above the stagnant slab in the mantle transition zone. Although low-velocity zones appear at some depth under other hotspots, their plume features are not clear. The complex images under hotspots reflect strong lateral variations in temperature, viscosity and possibly composition of the mantle, which control the generation and ascent of mantle plumes and the flow pattern of mantle convection.

Keywords Hotspots · Mantle plumes · Seismic tomography · Subducting slabs · Intraplate volcanoes

From the viewpoint of plate tectonics, there are basically two kinds of volcanoes on Earth. One is volcanoes which are located at plate boundaries, i.e., mid-ocean ridges and subduction zones. The other is intraplate volcanoes which are located far away from plate boundaries, such as Hawaii and Yellowstone (Fig. 5.1). There are some anomalously large volcanoes which are situated at or very close to mid-ocean ridges, such as Iceland and Azores (Fig. 5.1). The intraplate volcanoes and the anomalously large volcanoes at mid-ocean ridges are generally called hotspots. The origins of the mid-ocean ridge volcanism and arc volcanism at subduction zones have been generally well understood (e.g., Zhao 2001a, 2012; Stern 2002; Dunn and Forsyth 2007), whereas the origin of hotspot volcanism is still a debatable issue (e.g., Campbell 2007; Foulger and Jurdy 2007; Anderson 2011).

Wilson (1963) attributed the Hawaiian and some parallel Pacific island chains to volcanism above rising currents of convection cells in the upper mantle. Morgan

D. Zhao, *Multiscale Seismic Tomography,* Springer Geophysics,
DOI 10.1007/978-4-431-55360-1_5

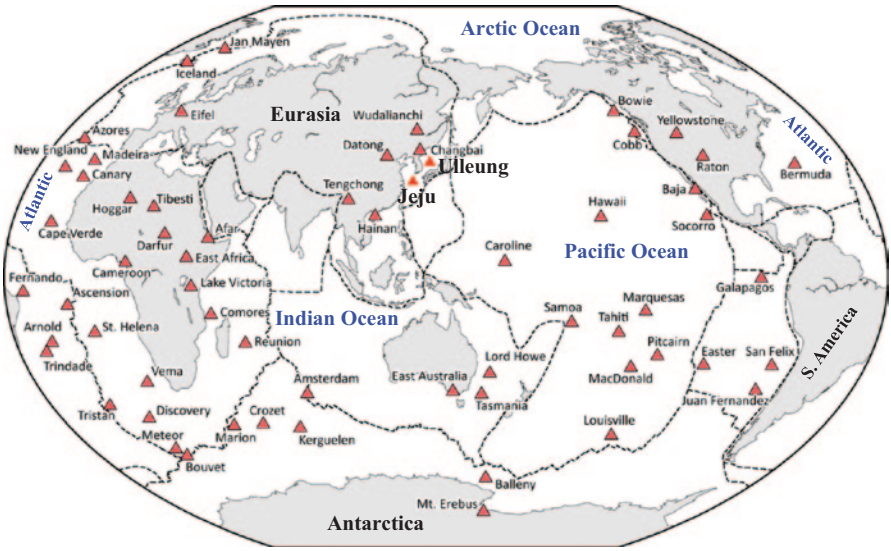

Fig. 5.1 Names and geographic locations of 62 possible hotspots (*red triangles*). The dashed lines show the *plate boundaries*

(1971, 1972) expanded this hypothesis and proposed a plume mechanism for the formation and sustaining of hotspots as sources of anomalous surface volcanism (Figs. 5.2 and 5.3). According to the plume hypothesis, (i) a plume of hot buoyant material forms from a thermal boundary layer in the deep Earth, such as the D" layer at the bottom of the mantle; (ii) the plume rises more rapidly in its conduit than the plume head can push through the viscous mantle, which inflates the head and elevates Earth's surface 1–2 km; (iii) decompression near the surface partially melts the plume head, and the resulting magma fractures the lithosphere and rise through

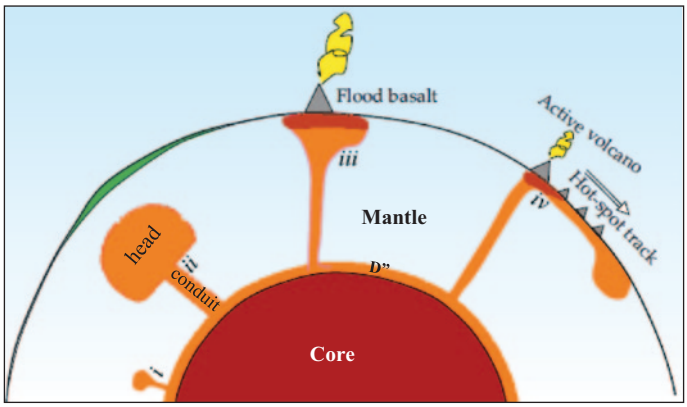

Fig. 5.2 Four stages of formation of a mantle plume (*see text for details*). **(**Modified from Humphreys and Schmandt 2011)

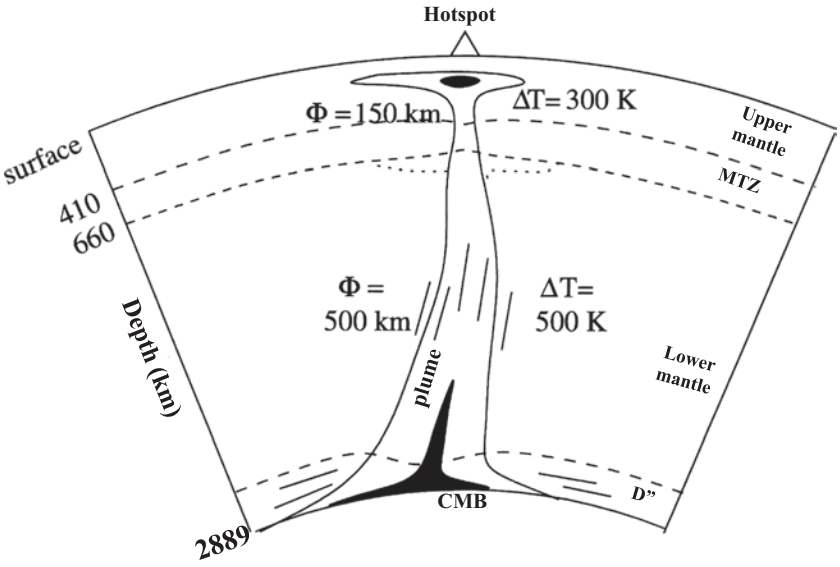

Fig. 5.3 A sketch of what a mantle plume could look like (modified from Nataf 2000). The *dashed* lines show the 410- and 660-km discontinuities and the top of the D" layer above the core-mantle boundary (*CMB*). The *black* parts denote melts. *Short lines* in the mid lower-mantle and the D" layer show the preferential alignment of minerals, which could induce seismic anisotropy. See text for detailed description

it, eventually erupting and forming flood basalt and a large igneous province extending over a wide range around the erupting site; and (iv) the flood basalt is carried away as the plume tail continues to feed a series of volcanoes which become a hot-spot track with ages that progress monotonically (Sleep 2006; Humphreys and Schmandt 2011). On reaching the base of the lithosphere, plume heads may reach diameters of 500–3000 km, while plume tails are typically 100–300 km in diameter (Fig. 5.3). Hence, hotspots are the surface manifestation of mantle plumes and are focused zones of melting. They are characterized by high heat flow, active volcanism, variable topographic highs depending on the plume depth, and hotspot tracks with the age of magmatism and deformation increasing with distance from a hotspot (e.g., Condie 2001; Sleep 2006; Ernst 2007; Ito and van KeKen 2007; Zhao 2007).

Although the plume hypothesis is very attractive and has been widely recognized, direct evidence for actual plumes is still weak, in particular, for lower mantle plumes, and many questions remain unanswered. For example, as Nataf (2000) asked: Do plumes actually exist? What do they look like? How wide are they? How hot are they? Do they really rise from the core-mantle boundary (CMB)? All of them? Are they tilted on their way up? Are there different kinds of plumes? Hotspots and mantle plumes hold the key to some critical issues of Earth sciences, and geologists and geophysicists have been fully aware of their importance.

In the multidisciplinary efforts engaged to understand hotspots, the primary task assigned to seismologists is the determination of fine structure of the crust and mantle beneath hotspots and the detection of mantle plumes, if any (e.g., Nataf 2000; Zhao 2001b, 2007; Boschi et al. 2007; Nolet et al. 2007). This is a challenge for seismologists, because most of the hotspots are located in oceanic regions (Fig. 5.1) where few seismic stations are available, causing difficulty to seismic imaging. However, in the past decade significant progress has been made in seismic imaging of hotspots and mantle plumes, and our knowledge on seismological characteristics of hotspots and plumes has been improved greatly. In this chapter, I review the major findings on this topic obtained during the past decade.

5.1 Main Features of Mantle Plumes and Hotspots

The expected main features of a mantle plume are summarized in Fig. 5.3, with emphasis on the features that can be imaged seismologically (Nataf 2000). In the shallow mantle, there is a wide cushion of plume material ponding beneath the lithosphere. Studies of hotspot swells have shown that this cushion spreads laterally over 1000 km in diameter, and is elongated in the direction of plate motion (e.g., Davies 1988; Sleep 1990; Ito and van KeKen 2007). The maximum temperature in the Hawaiian and Iceland plumes at these depths is about 250 K higher than that of normal mantle (e.g., McKenzie 1984; Watson and McKenzie 1991; Schilling 1991; Li et al. 2000, 2003; Zhao 2001b, 2004; Allen et al. 2002; Shen et al. 2002; Wolfe et al. 2009, 2011). In the uppermost mantle, an excess temperature of 250 K can cause P- and S-wave velocity reductions of 2.25 and 2.75 %, respectively (Nataf and Ricard 1996). Melt occurs down to a depth of ~120 km (e.g., Watson and McKenzie 1991). The radial temperature distribution in the plume can be approximated as Gaussian. The diameter of the plume (Φ) is defined as twice the radius where the temperature excess has dropped to 1/e of its maximum value ΔT. Φ is considered to be on the order of 150–200 km in the upper mantle. A lower-mantle plume passes through two major seismic discontinuities at 410- and 660-km depths, which correspond to phase transitions of mantle minerals (e.g., Ito and Takahashi 1989; Bina and Helffrich 1994; Helffrich 2000). Their Clapeyron slopes could be such that the 410-km discontinuity is depressed in the plume, whereas the 660-km discontinuity is elevated, resulting in a thinner mantle transition zone (MTZ) (e.g., Li et al. 2000, 2003; Shen et al. 2002; Huckfeldt et al. 2013). Ponding may occur beneath the 660-km discontinuity (dotted line in Fig. 5.3). In the lower mantle, the viscosity is ~30 times higher than that in the upper mantle (e.g., Richards and Hager 1984; Ricard et al. 1989; Lambeck et al. 1996; Kido and Cadek 1997). Thus the plume should become thicker in the lower mantle, probably 500 km or greater (Albers and Christensen 1996; Styles et al. 2011; Leng and Gurnis 2012). The temperature increase across the D" layer above the CMB could be as high as 1000 K (Boehler 1993). The temperature excess in the plume could be on the order of 500–600 K in the lower mantle (Albers and Christensen 1996; Farnetani 1997). Melt could be

present both in this bottom thermal boundary layer (Williams and Garnero 1996) and in the conduit of the plume that rises from it. If a discontinuity exists at the top of D" (e.g., Lay and Helmberger 1983; Lay et al. 2004) and it marks the perovskite-postperovskite phase transition, it could be deflected in the hot plume (Sidorin et al. 1999; Murakami et al. 2004; Maruyama et al. 2007). The flow of hot material is nearly vertical everywhere in the plume, except near the top and bottom thermal boundary layers. The flow may cause preferential alignment of mantle minerals, which could induce seismic anisotropy (e.g., Druken et al. 2013). In addition, because the plume ascends in a mantle where large-scale convective motions are present, the plume may be deflected by the mantle wind (e.g., Olson and Singer 1985; Richards and Griffiths 1988; Steinberger 2000; Zhao 2001b, 2007; Lei and Zhao 2006; Zhao et al. 2013). The root of a plume can be offset horizontally up to 1500 km away from its surface expression, according to a mantle convection model (Steinberger 2000).

The number of hotspots on Earth and that of plumes in the mantle are still unclear. Researchers have proposed several hotspot lists, but the number of hotspots included on these lists exhibits large variations, e.g., 19 in Morgan (1972), 66 in Wilson (1973), 42 in Crough and Jurdy (1980), 117 in Vogt (1981), 47 in Richards et al. (1988), 44 in Steinberger (2000), and 60 in Zhao (2007). The hotspots on these lists are not consistent to each other; some hotspots are included on one list but not on another. In most cases, hotspots have well-defined tracks associated with volcanic ridges or lines of volcanic edifices. Some hotspots, and the tracks they have made, appear on all lists, because they have high eruption rates in the recent past, or because they have produced conspicuous traces, such as Hawaii, Iceland, Reunion, Cape Verde, Kerguelen and Azores. Significant volcanic centers in continental regions, such as Yellowstone and some active volcanoes in Africa, are also included in most lists because of their similarity to the oceanic hotspots. Recently, intraplate volcanoes in the East Asian continent and the continental margin have been paid much attention, such as Changbai, Wudalianchi, Datong, Tengchong, Hainan, Jeju and Ulleung, etc. (Zhao et al. 2004, 2009; Lei and Zhao 2005; Lei et al. 2009a, b; Zhao and Liu 2010; Zhao and Tian 2013). Hence, they are also included on the present list of 62 intraplate volcanoes (Table 5.1).

Zhao (2007) presented whole-mantle tomographic images beneath 60 possible hotspots using a global P-wave tomographic model. Four vertical cross-sections of tomographic images were made for each hotspot, which are oriented E-W, N-S, N45°W-S45°E and S45°W-N45°E directions. Considering the possibility of plume deflection by mantle flow (e.g., Zhao 2001b, 2004), among the four cross sections, one that exhibits a plume-like low-velocity (low-V) feature most clearly was adopted. The results (Zhao 2007) are shown in Figs. 5.4, 5.5, 5.6, 5.7 and 5.8. Zhao et al. (2013) used their new global tomography model to examine the seismic structure under the hotspots, and obtained similar results as Zhao (2007). Because of the lower spatial resolution of the global tomographic models as compared with the diameter of the plumes (~100 km in the upper mantle to ~500 km in the lower mantle), low-V anomalies associated with the thermal plumes may not be detected by the global tomography, in particular, in regions where the ray path coverage

Table 5.1 List of 62 hotspots and plume features beneath them according to results of seismic tomography, receiver-functions, geochemistry and petrologically determined mantle potential temperatures

No.	Name	Location	Low-V zone depths	Plume feature
1	Hawaii	19.4°N 155.3°W	whole mantle	1, WM plume
2	Samoa	15.0°S 168.0°W	UM, TZ, ULM	3
3	Tahiti	17.9°S 148.1°W	whole mantle	1, WM plume
4	Pitcairn	25.0°S 130.1°W	MM, D”	3
5	MacDonald	29.0°S 140.2°W	MM, D”	3
6	Easter	27.1°S 109.3°W	UM, LM	2, UM plume
7	Marquesas	11.0°S 138.0°W	whole mantle	1, WM plume
8	Louisville	51.0°S 138.0°W	whole mantle	2, WM plume
9	Caroline	5.0°N 164.0°E	UM, MM, LW, D”	3
10	San Felix	26.0°S 80.0°W	UM, TZ, MM	2, MM plume
11	Juan Fernandez	33.5°S 82.0°W	UM, ULM	3
12	Galapagos	0.4°S 91.5°W	UM, MM	2, LM plume
13	Jan Mayen	71.1°N 8.2°W	whole mantle	1, WM plume
14	Iceland	65.0°N 19.0°W	whole mantle	1, WM plume
15	Azores	38.5°N 28.4°W	UM, TZ, D”	1, UM plume
16	Bermuda	32.0°N 65.0°W	UM, TZ, ULM	3
17	New England	30.0°N 28.0°W	TZ, LM	3
18	Madeira	33.0°N 17.0°W	ULM, D”	4
19	Canary	28.0°N 18.0°W	TZ, ULM, LM	2, WM plume
20	Cape Verde	15.0°N 24.0°W	whole mantle	1, WM plume
21	Fernando	4.0°S 32.5°W	UM, ULM, D”	3
22	Ascension	8.0°S 15.0°W	UM, TZ, LM	3
23	St. Helena	16.0°S 6.0°W	UM. TZ, LM	3
24	Arnold	18.0°S 25.0°W	TZ, MM, LM	3
25	Trindade	20.5°S 28.8°W	MM, LM	3
26	Tristan	37.0°S 14.0°W	TZ, LM	3
27	Discovery	42.0°S 0.0°E	LM, D”	3
28	Vema	31.5°S 8.5°E	UM, TZ, LM	2, UM+MTZ plume
29	Bouvet	54.5°S 3.5°E	LM	3
30	Meteor	52.0°S 1.0°E	LM	3
31	Comores	11.8°S 43.3°E	UM, TZ, ULM	3
32	Reunion	21.2°S 55.7°E	UM, TZ, LM, D”	2, WM plume
33	Kerguelen	49.0°S 69.0°E	whole mantle	1, WM plume
34	Amsterdam	38.0°S 77.5°E	whole mantle	2, WM plume
35	Crozet	47.0°S 52.0°E	MM, LM	4
36	Marion	46.9°S 37.8°E	LM	4

No.	Name	Location	Low-V zone depths	Plume feature
37	Afar	12.0°N 42.0°E	whole mantle	1, WM plume
38	Lake Victoria	3.0°S 36.0°E	UM, TZ	3
39	Cameroon	4.2°N 9.2°E	UM	1
40	Tibesti	21.0°N 17.0°E	TZ, LM, D"	3
41	Darfur	13.0°N 24.0°E	TZ, LM, D"	3
42	Hoggar	23.0°N 6.0°E	MM, LM	4
43	East Africa	6.0°N 34.0°E	UM, TZ, MM, D"	3
44	Lord Howe	32.0°S 159.0°E	UM, TZ, ULM, D"	3
45	East Australia	38.0°S 143.0°E	UM, TZ	2, UM plume
46	Tasmania	39.0°S 156.0°E	UM, TZ	3
47	Eifel	50.0°N 7.0°E	UM, LM, D"	2, WM plume
48	Hainan	20.0°N 110.3°E	UM, TZ, LM	2, WM plume
49	Yellowstone	44.6°N 110.5°W	UM, TZ, LM	1
50	Raton	37.0°N 104.0°W	UM, ULM	3
51	Bowie	53.0°N 135.0°W	UM, ULM, MM, D"	3
52	Cobb	46.0°N 130.0°W	UM, ULM, LM	2, WM plume
53	Baja	27.0°N 113.0°W	UM, ULM, D"	3
54	Socorro	18.7°N 111.0°W	UM, LM	3
55	Balleny	66.8°S 163.3°E	TZ, LM	3
56	Mt. Erebus	78.0°S 167.0°E	UM, TZ	1, UM plume
57	Changbai	42.0°N 128.1°E	UM	1, slab-related
58	Wudalianchi	48.7°N 126.1°E	UM	1, slab-related
59	Datong	40.0°N 113.3°E	UM, MTZ, MM	2, slab-related & MM plume
60	Tengchong	25.3°N 98.5°E	UM	1, slab-related
61	Jeju	33.5°N 126.7°E	UM	1, slab-related
62	Ulleung	37.5°N 130.9°E	UM	1, slab-related

Low-V low-velocity, *UM* upper mantle (<410 km), *TZ* transition zone (410–660 km), *ULM* upper part of the lower mantle, *MM* mid mantle, *LM* lower mantle, *D"* lowermost mantle, *WM* whole mantle
Plume feature: *1* good, *2* fair, *3* poor, *4* bad

is not good enough. Hence, in this chapter I also present high-resolution local or regional tomographic images beneath some hotspots where such high-resolution models are available. Based on these tomographic images and other information, such as seismic receiver-function results (e.g., Li et al. 2003; Deuss 2007; Tauzin et al. 2008) and geochemical and petrologic findings (e.g., Courtier et al. 2007), I discuss the origin of the 62 volcanoes (Table 5.1) and whether mantle plumes exist beneath them, following the general approach of Zhao (2007).

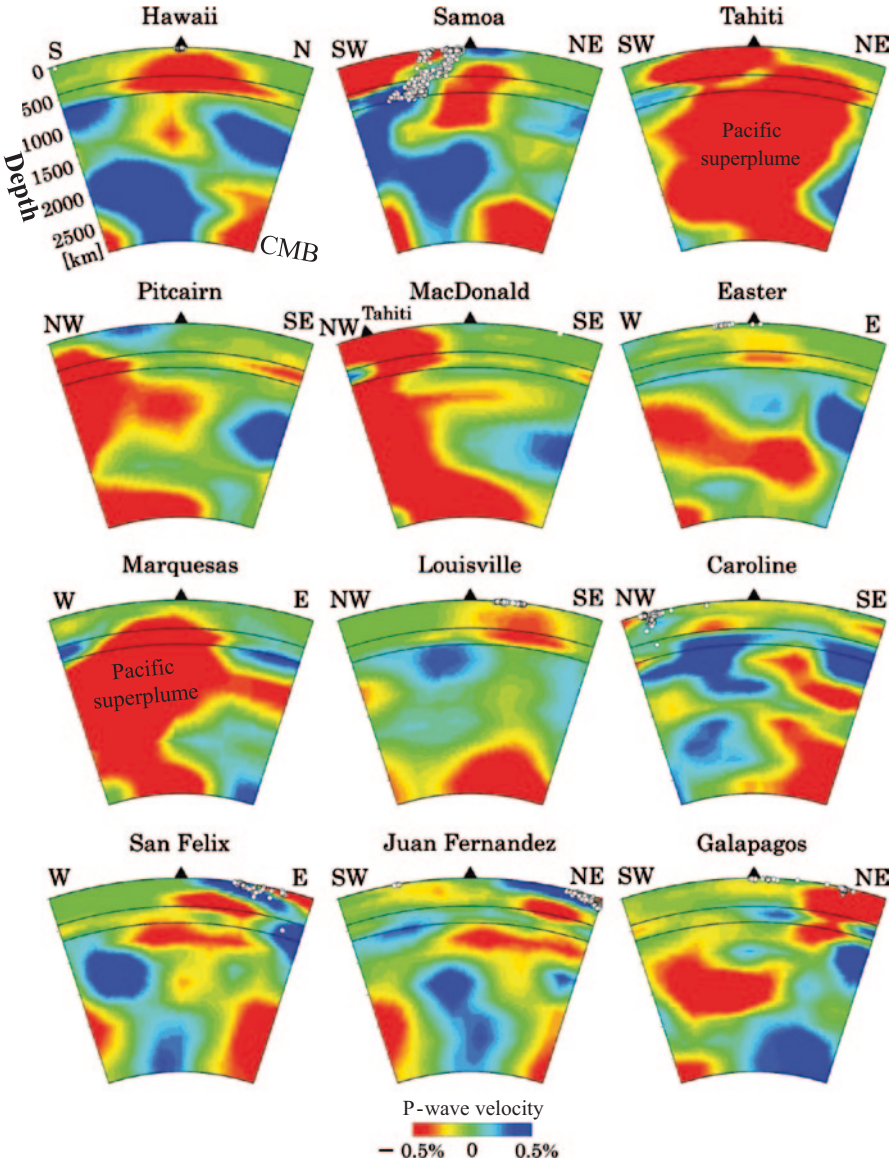

Fig. 5.4 Vertical cross-sections of whole-mantle P-wave tomography from the surface down to the core-mantle boundary (*CMB*) beneath 12 hotspot volcanoes in the Pacific Ocean. Locations of the hotspots are shown in Fig. 5.1. Names of the hotspots (*triangles*) are shown *atop* each cross-section. The *red* and *blue* colors denote slow and fast velocities, respectively. The velocity perturbation scale is shown at the bottom. The *white dots* denote earthquakes (M > 4.0) that occurred within a 100-km width of each profile during 1964 to 1998. (Modified from Zhao 2007)

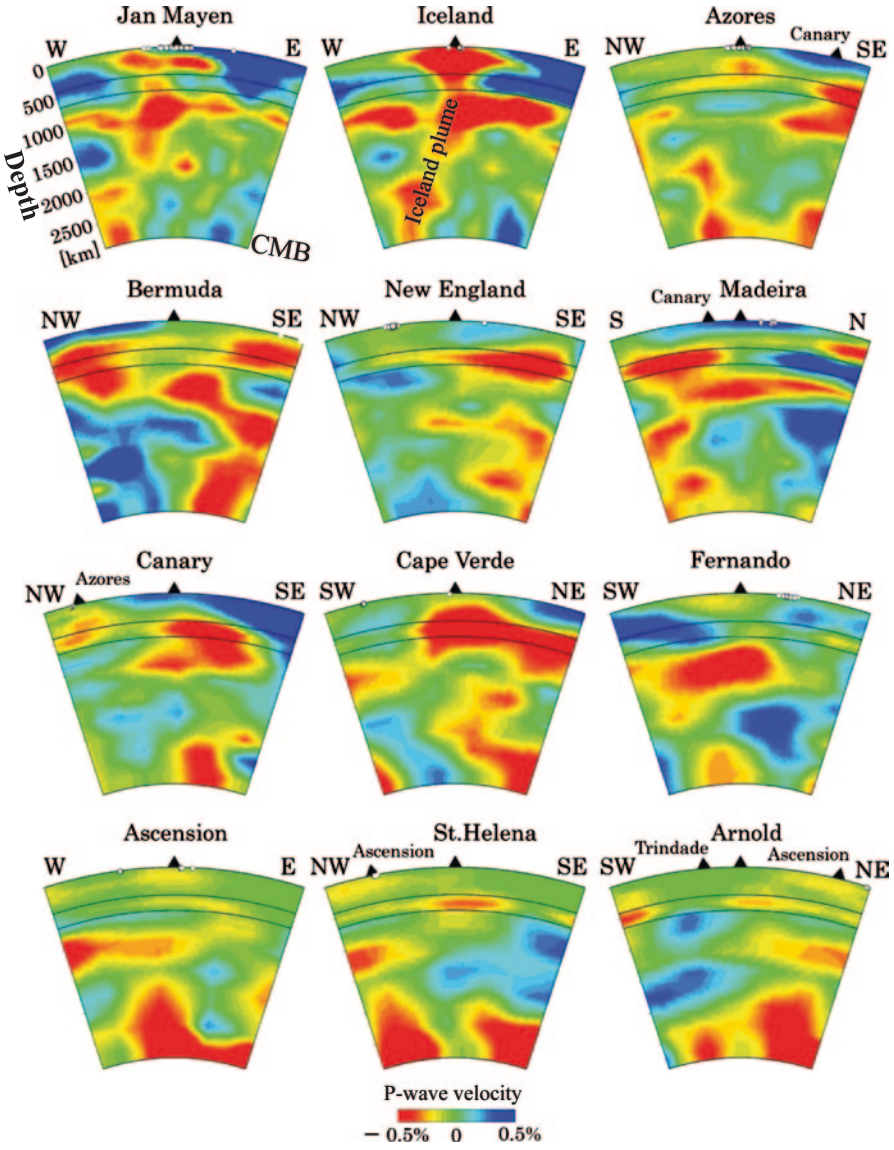

Fig. 5.5 The same as Fig. 5.4 but for 12 hotspot volcanoes in the Atlantic Ocean. (Modified from Zhao 2007)

5.2 Pacific Hotspots

Beneath the classical hotspot, Hawaii, a large low-V zone is visible in the upper mantle (Fig. 5.4). A narrow low-V zone appears at depths of 670–1500 km under Hawaii, and it is connected with a large low-V zone from 2000 km depth to the CMB

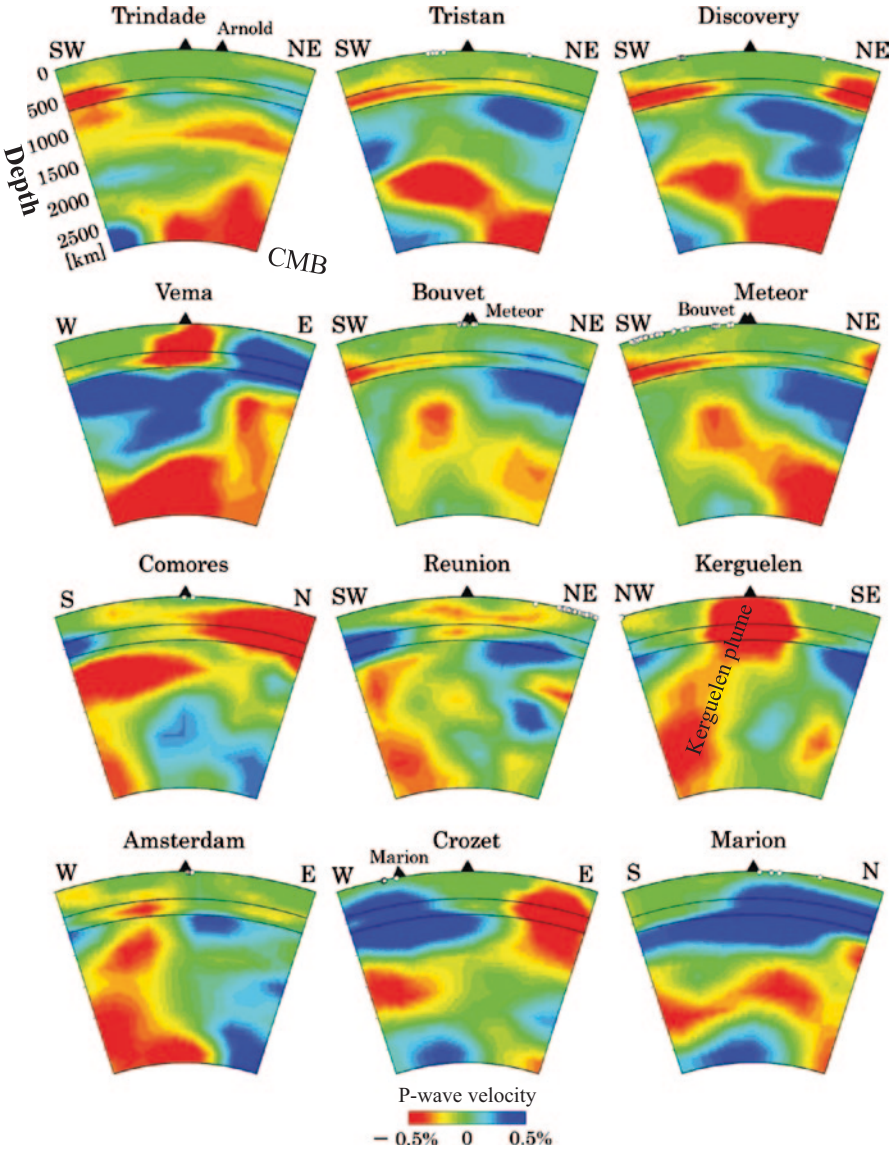

Fig. 5.6 The same as Fig. 5.4 but for 12 hotspot volcanoes in the Atlantic Ocean and the Indian Ocean. (Modified from Zhao 2007)

north of Hawaii, which looks like a tilting plume feeding the Hawaiian hotspot. This result is consistent with a diffraction tomography (Ji and Nataf 1998). The Hawaiian plume is better imaged as a whole-mantle plume using both the mantle and core phase data (Lei and Zhao 2006) (Fig. 5.9). High-resolution local tomography using teleseismic data recorded by a large aperture network of ocean bottom seismome-

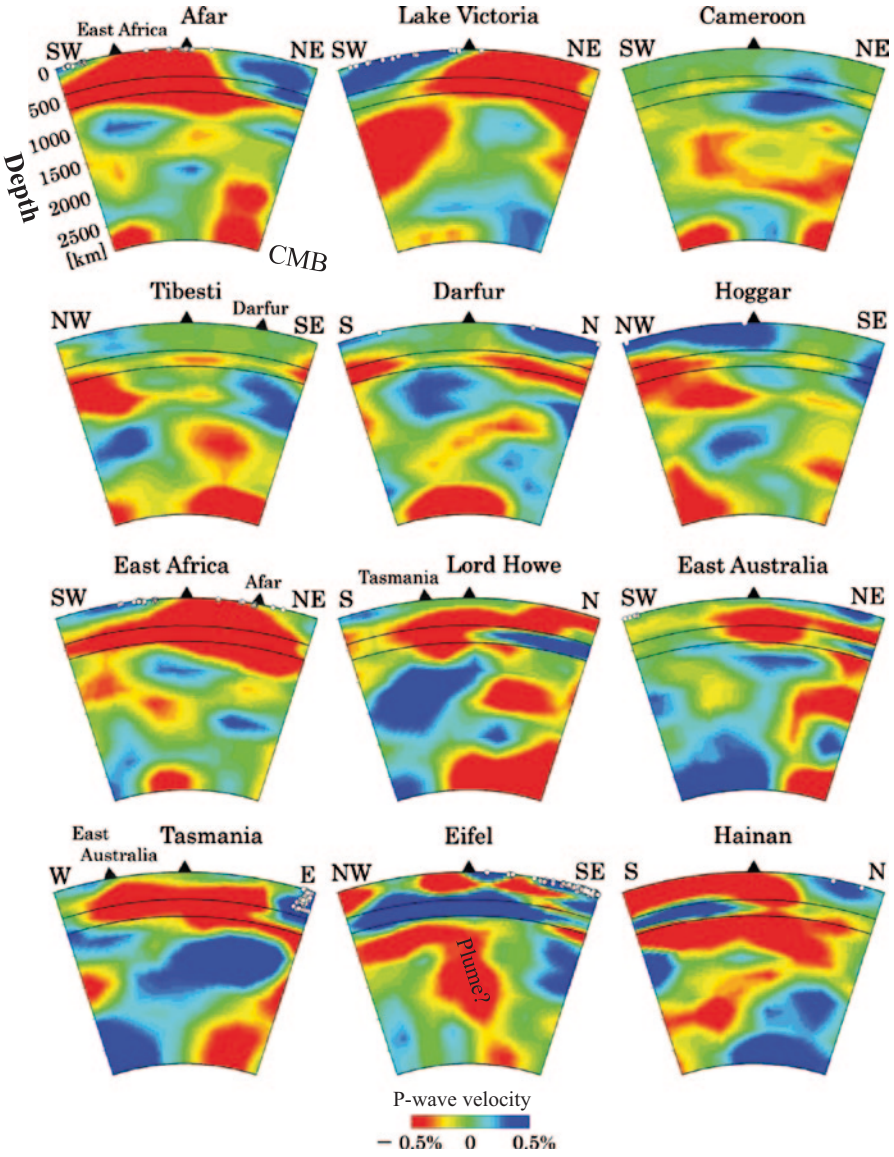

Fig. 5.7 The same as Fig. 5.4 but for 12 hotspot volcanoes in continents or continental margins. (Modified from Zhao 2007)

ters (OBSs) deployed around the Hawaiian Islands has imaged the Hawaiian plume more clearly down to a depth of 1800 km (Wolfe et al. 2009, 2011). Significant thinning of the MTZ also suggests a lower-mantle origin of the Hawaiian plume (e.g., Li et al. 2000; Wolbern et al. 2006; Huckfeldt et al. 2013). Receiver functions have been used to image the base of a melt-rich zone located 110–155 km beneath

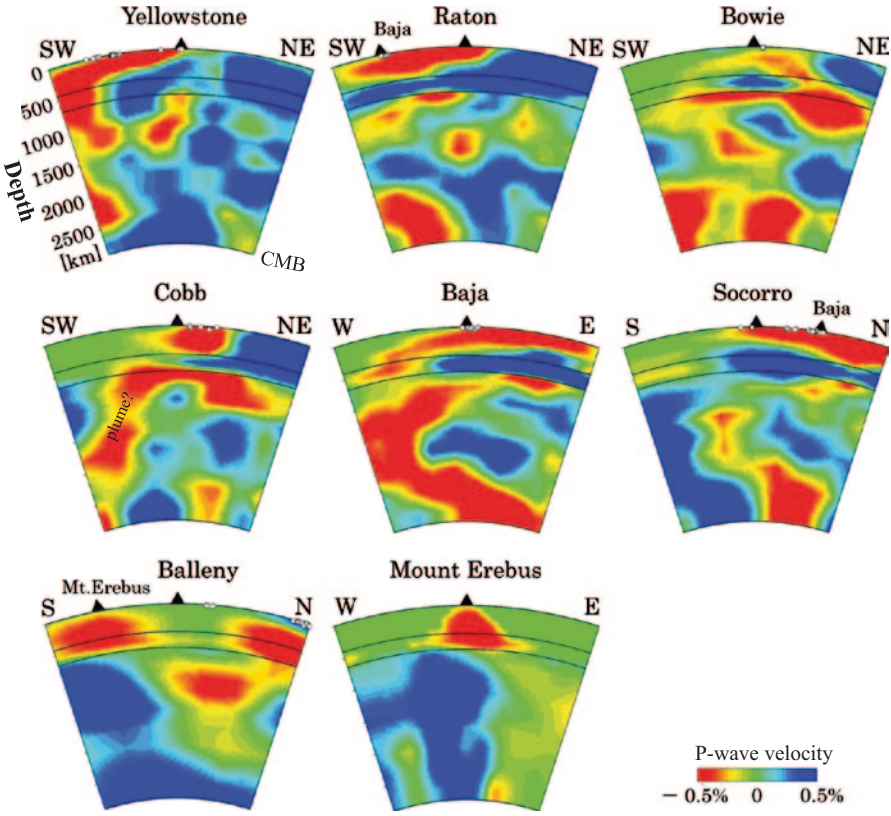

Fig. 5.8 The same as Fig. 5.7 but for another 8 hotspot volcanoes in continents or continental margins. (Modified from Zhao 2007)

Hawaii, and it is found that this melt-rich zone is deepest 100 km west of Hawaii, implying that the plume impinges on the Pacific plate there and causes melting at greater depths in the mantle, rather than directly beneath the island (Rychert et al. 2013). The petrologically determined mantle potential temperature (PMPT) under Hawaii is also higher than that of the global average (Courtier et al. 2007). From these results, it is reasonable to believe that the Hawaiian hotspot is caused by a whole-mantle plume originating from the CMB.

A recent geochemical study found that the mantle sources of Hawaiian volcanoes contain a significant amount of ancient recycled oceanic crust with a factor of ~2 increase from ~8–16% at Loihi and Kilauea to ~15–21% at Mauna Loa and Koolau (Pietruszka et al. 2013). The chemical heterogeneity in the Hawaiian plume results from melting of a package of recycled oceanic crust that was altered by interaction with seawater or hydrothermal fluids prior to being variably dehydrated during subduction. The recycled oceanic crust in the mantle source of Loihi and Kilauea lavas is dominated by the uppermost portion of the residual slab, whereas that of Mauna Loa and Koolau lavas is dominated by the lowermost portion of

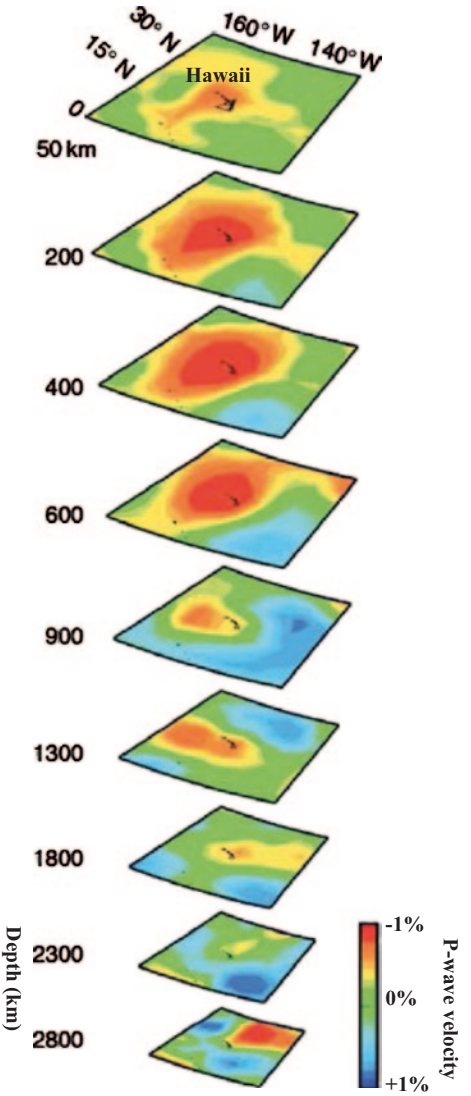

Fig. 5.9 Map views of P-wave tomography at different depths in the mantle beneath Hawaii (modified from Lei and Zhao 2006). The layer depth is shown on the *left* of each map. The *red* and *blue* colors denote slow and fast velocities, respectively. The velocity perturbation scale is shown on the *right*

the residual slab. The present distribution of compositional heterogeneities in the Hawaiian plume cannot be explained by either a large-scale bilateral asymmetry or radial zonation. Instead, the mantle source of the active Hawaiian volcanoes may be heterogeneous on a small scale with a NW-SE oriented spatial gradient in the

amount, type and extent of dehydration of the ancient recycled oceanic crust (Pietruszka et al. 2013).

Farnetani and Hofmann (2009, 2010) conducted high-resolution 3-D numerical simulations to investigate the detailed internal structure of the Hawaiian plume. They linked geochemical observations of surface lavas to fluid dynamic simulations to quantify the flow trajectories of upwelling geochemical heterogeneities and their sampling by volcanoes. Their results suggest that vigorous plumes are able to sample, and to bring side by side, very distant portions of their source region. Using numerical models, Ballmer et al. (2013) predicted that a hot, compositional heterogeneous mantle plume containing a denser eclogite component tends to pool at ~300–410 km depth before rising to feed a shallower sublithospheric layer. They found that this double-layered structure of a thermochemical plume is more consistent with the tomographic images at Hawaii (Wolfe et al. 2009, 2011) than the classic plume model. The thermochemical structure as well as time dependence of plume material rising from the deeper into the shallower layer can further account for the observed long-term fluctuations in volcanic activity and asymmetry in bathymetry, seismic structure, and magma chemistry across the hotspot track (Ballmer et al. 2013).

Six hotspots (Samoa, Tahiti, Pitcairn, MacDonald, Easter, and Marquesas) exist in the South Pacific superswell (McNutt 1998; Fig. 5.1). Under the superswell a huge slow anomaly (>2000 km wide) is visible in the entire mantle (Fig. 5.4), which represents the Pacific superplume (Maruyama 1994; Zhao 2001b, 2004; Montelli et al. 2006; Maruyama et al. 2007; Davies et al. 2012; Zhao et al. 2013). The center of the superplume is located directly beneath Tahiti (Society Island) and Marquesas. Other four hotspots are located at the edges of the superplume (Fig. 5.4). In the upper mantle and the MTZ southwest of the Samoa hotspot, the subducting Tonga slab is clearly imaged as a high-velocity (high-V) zone. Intermediate-depth and deep earthquakes occur actively within the Tonga slab (Fig. 5.4). The seismic structure of the upper and middle mantle under the Pacific superswell has been better imaged using local OBS data (Suetsugu et al. 2009; Tanaka et al. 2009a, b), which indicates that large-scale low-V anomalies (on the order of 1000 km in diameter), reflecting the Pacific superplume, are located from the CMB to 1000 km depth, and small-scaled low-V anomalies (on the order of 100 km in diameter) are present above it. The superplume may be a hot and chemically distinct mantle dome, while the small-scale anomalies may be narrow plumes generated from the top of the dome (Suetsugu et al. 2009). Under the hotspots in the South Pacific superswell, the MTZ is generally thinner than that of the global average (Niu and Inoue 2000; Li et al. 2003; Deuss 2007; Suetsugu et al. 2009), and the PMPT is generally higher (Courtier et al. 2007). A recent receiver-function study has also detected a thinner MTZ beneath the Easter hotspot (Haldar et al. 2014).

Huang et al. (2011) suggested that geochemical zoning is a common feature of mantle plumes beneath the Pacific plate, and the pattern repeats between island chains. They also inferred that isotopically enriched material is preferentially distributed in the lower mantle of the Southern Hemisphere, within the large low-V zone under South Pacific. Geochemical data for submarine lavas from the Samoan

region have suggested that a deep mantle plume generated the shield stage volcanism in Samoa (Jackson et al. 2010). Konter and Jackson (2012) found that their new data obtained on Samoa are unusually enriched isotopically and indicate a relatively voluminous rejuvenated stage compared to other intraplate volcanoes. Their results suggest that the location of Samoa near the Tonga Trench terminus causes plate flexure resulting in upward flow of the shallow mantle driving partial melting. The flexural melting and metasomatism of the Samoan lithosphere may have generated the voluminous and geochemically distinct Samoa rejuvenated lavas, implying that the lithosphere may play an important role during late stage in non-Hawaiian hotspots. Shimoda et al. (2011) also pointed out the importance of tectonic influence on chemical composition of ocean island basalts in the West and South Pacific and the existence of upward flow of material from the deep mantle under the South Pacific superswell.

The Louisville hotspot (Fig. 5.1) has a 4300 km long hotspot track in the South Pacific, consisting of at least 65 major volcanoes, but the exact location of the surface hotspot is still uncertain (Condie 2001). A significant shift occurs between the surface hotspot and plume-like low-V zones in the upper and lower mantle (Fig. 5.4 Louisville). This may suggest that the real location of the Louisville hotspot may be ~700 km southeast of its location shown here (51°S, 138°W) which is taken from the hotspot list of Steinberger (2000).

The seismic image under the Caroline hotspot is complex (Fig. 5.4). The velocity is lower in the upper mantle down to 410 km depth, and two significant low-V zones appear in the lower mantle on the southeastern side, but high-V zones are visible in MTZ and lower mantle on the northwestern side.

The three hotspots close to Australia, Lord Howe, East Australia, and Tasmania, seem to have the same origin (Fig. 5.7). Low-V zones exist in the upper mantle and the MTZ beneath the three hotspots, hence they may be caused by an upper-mantle process.

Similar seismic images appear beneath the San Felix and Juan Fernandez hotspots (Fig. 5.4). The subducting Nazca slab under western South America is clearly imaged as a high-V zone, and intermediate-depth earthquakes occur within the slab. Low-V zones exist under the two hotspots down to about 1000 km depth, which seem to connect with a large low-V zone in the lower mantle beneath the subducting Nazca slab. The MTZ is thicker under San Felix (Deuss 2007). The PMPT is higher under the Juan Fernandez hotspot.

Beneath the Galapagos hotspot, significant low-V zones exist in the upper and lower mantle, but the image is complex and a plume signature is not clear (Fig. 5.4), probably due to the lower resolution of the tomographic model there (Zhao 2007). Villagomez et al. (2014) presented a local tomography of the upper 300 km of the mantle beneath the Galapagos Archipelago. They revealed a low-V anomaly, indicative of an upwelling plume, which tilts towards the mid-ocean ridge at depths well below the lithosphere. This feature of the plume–ridge connection beneath the Galapagos Archipelago is consistent with the presence of multiple stages of partial melting, melt extraction, and melt remixing within the plume and surrounding mantle. These processes affect the viscosity of the asthenosphere, alter the upwelling

plume and influence the compositions of surface lavas. Their results imply that the coupling between the oceanic plate and plume upwelling beneath the Galapagos is weak, and multistage melting may similarly affect the geophysical and geochemical characteristics of other hotspots (Villagomez et al. 2014). Rychert et al. (2014) used teleseismic receiver functions to image the crustal and upper mantle structure under the Galapagos Archipelago. They revealed lateral depth variations of the Moho and the lithosphere–asthenosphere boundary, possibly illuminating multiple plume diversions related to complex plume–ridge interactions. The MTZ is anomalously thin (Hooft et al. 2003) and the PMPT is slightly higher (Courtier et al. 2007) under the Galapagos, suggesting that a lower-mantle plume may exist there.

5.3 Atlantic Hotspots

Similar tomographic images are obtained beneath the Jan Mayen and Iceland hotspots (Fig. 5.5). Plan views and other vertical cross-sections show that the low-V zones under the two hotspots are connected, suggesting that they may be fed by the same plume. Extensive local tomography studies imaged the Iceland plume more clearly in the upper mantle (e.g., Wolfe et al. 1997; Foulger et al. 2000; Allen et al. 2002; Hung et al. 2004). Global tomography suggests that the Iceland plume originates from the CMB (e.g., Bijwaard and Spakman 1999; Zhao 2001b, 2007; Montelli et al. 2006; Zhao et al. 2013). A recent regional S-wave tomography down to 1300 km depth under the North Atlantic region shows a lower-mantle source for the Iceland and Jan Mayen hotspots (Rickers et al. 2013). A lower-mantle or CMB origin of the Iceland plume is also supported by waveform modeling and receiver-function studies (e.g., Helmberger et al. 1998; Shen et al. 2002; Lawrence and Shearer 2006).

A significant low-V zone is revealed in the upper mantle and MTZ beneath the Azores hotspot (Fig. 5.5), which is consistent with local and regional tomography results (Silveira et al. 2006; Yang et al. 2006). However, the connection of the upper-mantle low-V zone to the low-V zones in the lower mantle is not apparent (Fig. 5.5). A recent receiver-function image shows a low-V zone down to ~200 km depth and another low-V zone at 460–500 km depth, which may correspond to the source of a plume which generated the Azores hotspot. Receiver-function studies show an average MTZ thickness under Azores (Li et al. 2003; Deuss 2007; Silveira et al. 2010). These results suggest that the Azores hotspot may be fed by an upper-mantle plume.

Two low-V zones appear in the mantle under the Canary hotspot (Fig. 5.5). One is in the upper mantle and it extends down to ~1500 km depth, the other is visible from ~2200 km depth to the CMB. The two low-V zones seem to be connected by a weak slow anomaly in the mid mantle (Fig. 5.5 Canary). The MTZ is thinner (Li et al. 2003; Deuss 2007) and the PMPT is higher (Courtier et al. 2007) beneath Canary. However, a recent receiver-function study revealed a low-V zone in the upper mantle under the Canary hotspot, without a thermal anomaly perturbing the MTZ discontinuities (410 and 660 km) (Martinez-Arevalo et al. 2013). Another receiver-

function result shows evidence for magmatic underplating and partial melt beneath the Canary Islands (Lodge et al. 2012).

Prominent low-V zones exist in the whole mantle under the Cape Verde hotspot, though the image is a little complex (Fig. 5.5). Crustal and lithospheric structure beneath the Cape Verde archipelago has been investigated using seismic and gravity data (e.g., Lodge and Helffrich 2006; Pim et al. 2008; Wilson et al. 2010). A recent 3-D gravity model shows a high-density volume down to 8 km depth under Maio island of Cape Verde archipelago, which may represent a magma chamber (Represas et al. 2012). Helffrich et al. (2010) find a normal MTZ thickness under the Cape Verde hotspot using receiver functions at eight seismic stations. Vinnik et al. (2012) used receiver functions at tens of seismic stations and find that the MTZ under Cape Verde is thinned by up to ~30 km as compared with that in the ambient mantle, which is a combined effect of a depression of the 410-km discontinuity and an uplift of the 660-km discontinuity, suggesting that the Cape Verde plume has a lower-mantle origin, being consistent with the tomographic image (Fig. 5.5). Recently, Liu and Zhao (2014) determined P and S wave tomography of the upper mantle beneath the Cape Verde hotspot using arrival-time data measured precisely from three-component seismograms of 106 teleseismic events recorded by a local seismic network. Their results show a prominent low-V anomaly imaged as a continuous column of <100 km wide from the Moho down to ~500 km depth under Cape Verde, especially beneath the Fogo active volcano which erupted in 1995 (Fig. 5.10). The low-V anomaly may reflect a hot mantle plume feeding the Cape Verde hotspot (Liu and Zhao 2014).

Complex low-V zones exist in the mantle under the Bermuda hotspot (Fig. 5.5). A whole-mantle tomographic image along a profile passing through the North American continent and the Bermuda hotspot (Fig. 5.11) shows that the old Farallon slab is descending down to the deep lower mantle, and low-V anomalies exist above the slab. Multidisciplinary studies of subduction zones find that, due to the subduction of the oceanic slab, hot upwelling occurs in the mantle wedge above the subducting slab, causing arc and back-arc magmatism and volcanism (e.g., Zhao 2012). Similar processes may have taken place under the Bermuda hotspot which may be caused by hot upwelling from the lower mantle associated with the deep subduction of the Farallon slab (see also Vogt and Jung 2007). The MTZ has a normal thickness under Bermuda (Deuss 2007), but this result was obtained using long-period SS precursors and so has a lower resolution, thus a narrow plume feature might not be detected.

Beneath the other Atlantic hotspots (New England, Madeira, Fernando, Ascension, St. Helena, Arnold, Trindade, Tristan, Discovery, Bouvet, and Meteor), slow anomalies are generally imaged in the lower mantle under the hotspots, but plume-like low-V zones connecting the surface hotspots with the lower-mantle slow anomalies are not well revealed in the upper mantle and/or MTZ by the global tomography (Figs. 5.5 and 5.6). Receiver-function results of Li et al. (2003) show that the MTZ is normal beneath St. Helena, whereas it is thinner and warmer under the Ascension hotspot which is closer to the Mid Atlantic Ridge (Fig. 5.1). A recent receiver-function study also detected a thinner MTZ beneath the Ascension hotspot

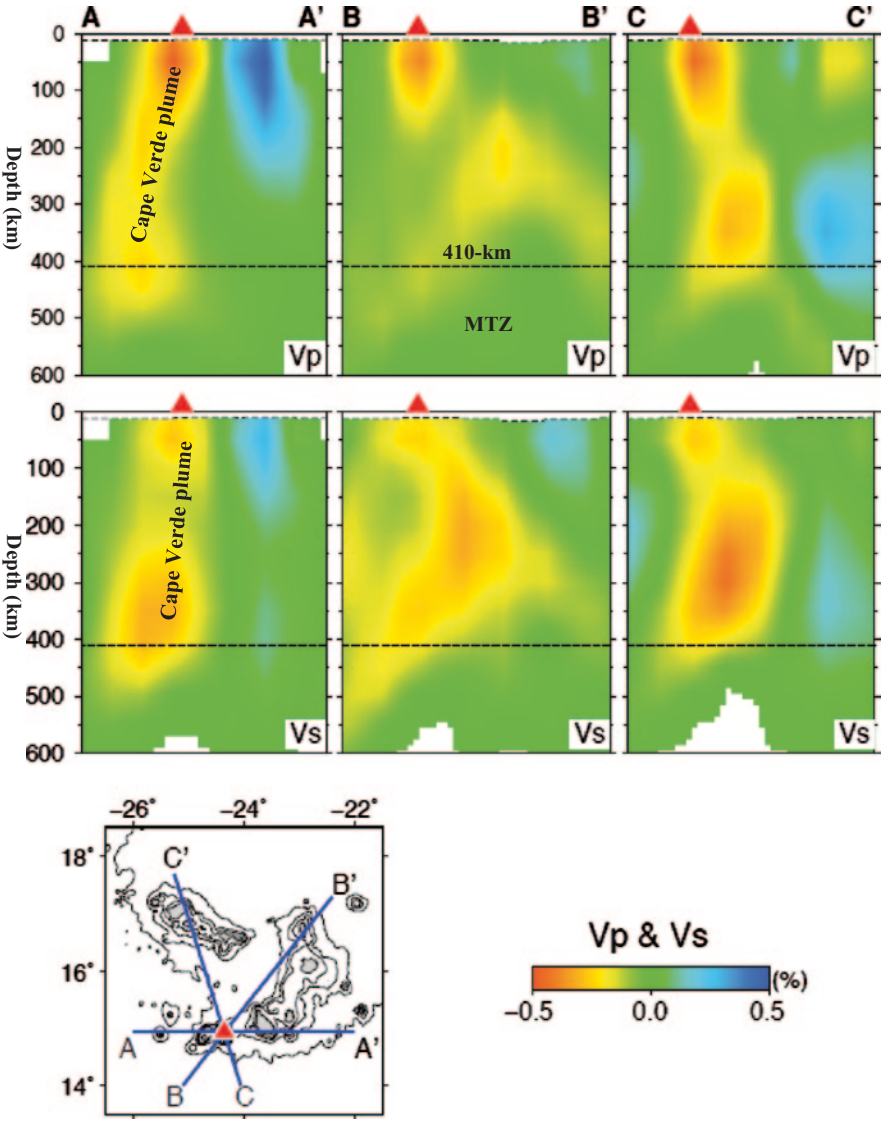

Fig. 5.10 Vertical cross-sections of P- and S-wave tomography along the three profiles shown in the inset map (Liu and Zhao 2014). The *red* and *blue* colors denote *low* and *high* velocities, respectively. The velocity perturbation scale (*in %*) is shown at the *bottom*. The *red triangles* denote the Fogo volcano which erupted in 1995. The two *dashed lines* show the Moho and the 410-km discontinuities

(Haldar et al. 2014). The long-period results of Deuss (2007) show that the MTZ is thinner beneath New England and Discovery, whereas the MTZ is normal beneath Fernando.

Beneath the Vema hotspot which is located close to South Africa, a strong low-V zone is revealed in the upper mantle and MTZ, and another low-V anomaly appears

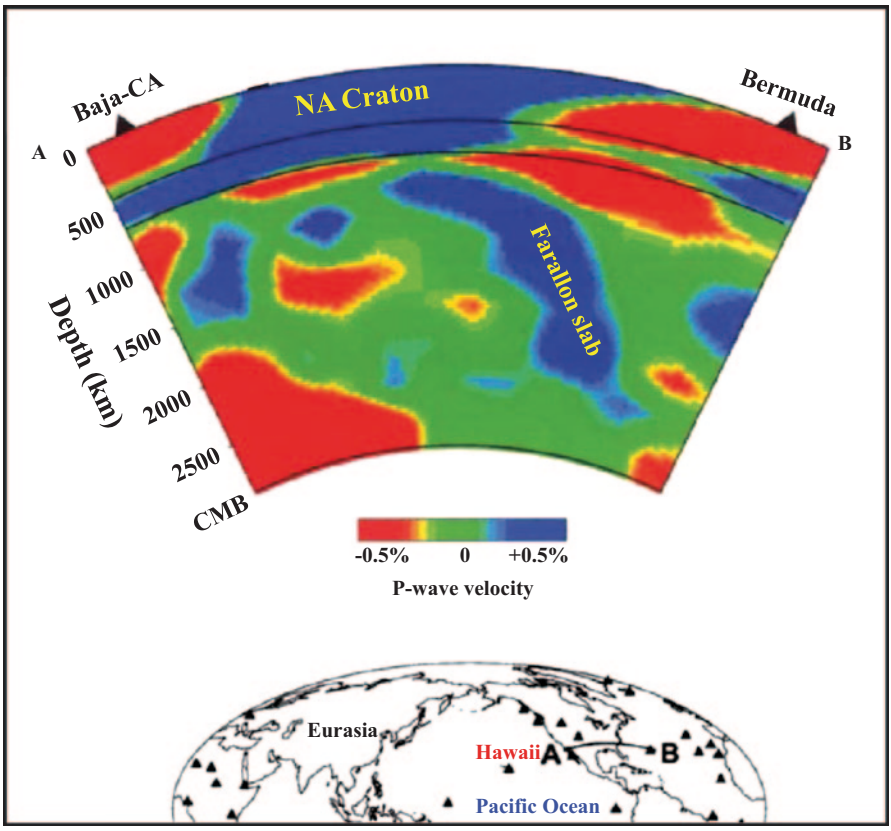

Fig. 5.11 East-west vertical cross-section of whole-mantle P-wave tomography (modified from Zhao 2004). Location of the cross-section is shown in the inset map. The *red* and *blue* colors denote slow and fast velocities, respectively. The velocity perturbation scale is shown above the map. The *triangles* denote the hotspot volcanoes. The *two solid* lines denote the 410- and 660-km discontinuities

in the deep lower mantle, but the two low-V zones are separated by a high-V zone beneath the 660 km discontinuity (Fig. 5.6). The MTZ is quite thin under the Vema hotspot (Deuss 2007).

5.4 Indian Ocean Hotspots

Beneath the Kerguelen hotspot a plume-like low-V zone is clearly visible in the entire mantle (Fig. 5.6). The root of the low-V zone is located at the CMB northwest of the surface hotspot. The Kerguelen hotspot has produced basalt for about 130 Ma, among the longest known volcanic records from a single source. Using radiometric dates and crustal structure determined from geophysical data and drilling

results, Coffin et al. (2002) calculated the magmatic output of the Kerguelen hotspot through time and suggested two possible origins of the Kerguelen magmatism. One is that the magmatism does not arise from a single source, but from multiple plume sources. The other possibility is that a single plume source accounts for the magmatic products attributed to the Kerguelen plume, but the vigorous mantle circulation during Early Cretaceous time resulted in strong mantle shear flow that split the initial Kerguelen plume conduit into several diapirs of varying sizes, buoyancies, and mantle ascent rates. The tomographic image (Fig. 5.6) suggests that the Kerguelen hotspot was caused by a single plume. The MTZ is thinner under Kerguelen (Deuss 2007). Beneath Heard Island which lies on the Kerguelen Plateau, the MTZ is thinner and the PMPT is higher (Courtier et al. 2007). All these results indicate that the Kerguelen plume has a lower-mantle origin.

The Amsterdam hotspot is underlain by a plume-like slow anomaly in the entire mantle west of its surface location (Fig. 5.6).

Beneath the Reunion hotspot, a low-V zone exists in the upper mantle and the MTZ, and two low-V zones are visible in the lower mantle, but the plume signature is not so clear as that beneath the Kerguelen hotspot (Fig. 5.6). The long-period SS reflection results show that the MTZ beneath Reunion is slightly thicker than that of the global average (Deuss 2007).

Widespread low-V anomalies are visible down to the mid mantle beneath the Comores hotspot (Fig. 5.6). The MTZ is slightly thinner under this hotspot (Deuss 2007).

Low-V zones exist in the lower mantle under the Marion and Crozet hotspots, but high-V anomalies appear in the upper 1000 km beneath the two hotspots (Fig. 5.6). The MTZ has a normal thickness under Crozet (Deuss 2007). A recent study revealed geochemical heterogeneities within the Crozet hotspot (Breton et al. 2013). The geochemical variability observed among the Crozet basalts reflects two main processes. The variation in terms of major and trace element concentrations comes from the accumulation and removal of olivine and clinopyroxene to the parental magma, whereas the variation in isotope ratios and trace element ratios reflects the heterogeneity of the deep mantle material feeding the Crozet hotspot (Breton et al. 2013).

5.5 African Hotspots

Significant low-V features are generally revealed in the mantle beneath the African hotspots (Fig. 5.7), which are associated with the African superplume (Maruyama 1994; Ritsema et al. 1999; Zhao 2001b, 2004; Montelli et al. 2006; Chang and Van der Lee 2011; Davies et al. 2012; Hansen et al. 2012; Brandt 2013; Mulibo and Nyblade 2013; Zhao et al. 2013). Large low-V zones are visible from the surface down to about 1000 km under the Afar, Lake Victoria, and East Africa hotspots, which seem to connect with the low-V zones in the lower mantle (Fig. 5.7). Receiver-function analyses revealed a thermal anomaly in the upper mantle under East

Africa which is interpreted as a plume head under the lithospheric keel of the Tanzania craton (Nyblade et al. 2000; Huerta et al. 2009). The MTZ is thinner beneath Comores, Darfur and East Africa (Li et al. 2003; Deuss 2007).

Local tomography revealed upper-mantle low-V zones under the Afar hotspot, the northern Ethiopian rift, and the western branch of the East African rift (Bastow et al. 2005; Benoit et al. 2006; Jakovlev et al. 2013). Pieces of low-V zones exist in the upper and lower mantle under the Tibesti, Cameroon, Darfur, and Hoggar hotspots, whereas high-V zones exist in the upper mantle and the uppermost part of the lower mantle under the Hoggar and Cameroon hotspots (Fig. 5.7). High-resolution local P and S wave tomography shows a low-V zone in the upper mantle extending down to 500 km depth under the Cameroon Volcanic Line (Reusch et al. 2010). The MTZ exhibits a normal thickness beneath Cameroon (Reusch et al. 2011). These results suggest that the Cameroon hotspot is caused by upper-mantle processes such as an edge flow convection cell in the upper mantle along the northwestern side of the Congo Craton lithosphere (Reusch et al. 2011).

Mulibo and Nyblade (2013) determined P and S wave tomography under East Africa down to 1200 km depth (Fig. 5.12). Their images show a low-V anomaly well developed at 100–200 km depths beneath the Eastern and Western branches of the Cenozoic East Africa rift system and northwestern Zambia, and a high-V zone at depths < 350 km beneath the central and northern parts of the East African Plateau and the eastern and central parts of Zambia. At depths > 350 km the low-V zone is most prominent under the central and southern parts of the East African Plateau and dips to the southwest beneath northern Zambia, extending down to ~ 900 km depth. The excess temperature in the low-V zone is ~ 150–300 K. The depth extent of the low-V anomaly indicates that the African superplume is likely a whole mantle structure. A superplume extending from the CMB to the surface implies an origin for the Cenozoic extension, volcanism and plateau uplift in eastern Africa rooted in the dynamics of the lower mantle (Mulibo and Nyblade 2013).

Hilton et al. (2011) reported helium isotope ratios of lavas and tephra of the Rungwe Volcanic Province in southern Tanzania. Values as high as 15 RA far exceed typical upper mantle values, which are attributed to the African superplume (Hilton et al. 2011).

Steinberger (2000) calculated the motion of hotspots in East Africa and the deformation of their underlying plume conduits using models of global mantle flow and suggested the presence of a comparatively broad upwelling rather than localized plumes. This simulation result may explain the large and complex geometry of the low-V zones as imaged beneath the African hotspots (Fig. 5.7).

5.6 European Hotspot

Plume-like low-V zones are clearly visible in the upper and lower mantle under the Eifel hotspot in Europe, though a high-V zone exists in the MTZ (Fig. 5.7). This image is similar to that from other global tomography models (e.g., Goes et al. 1999).

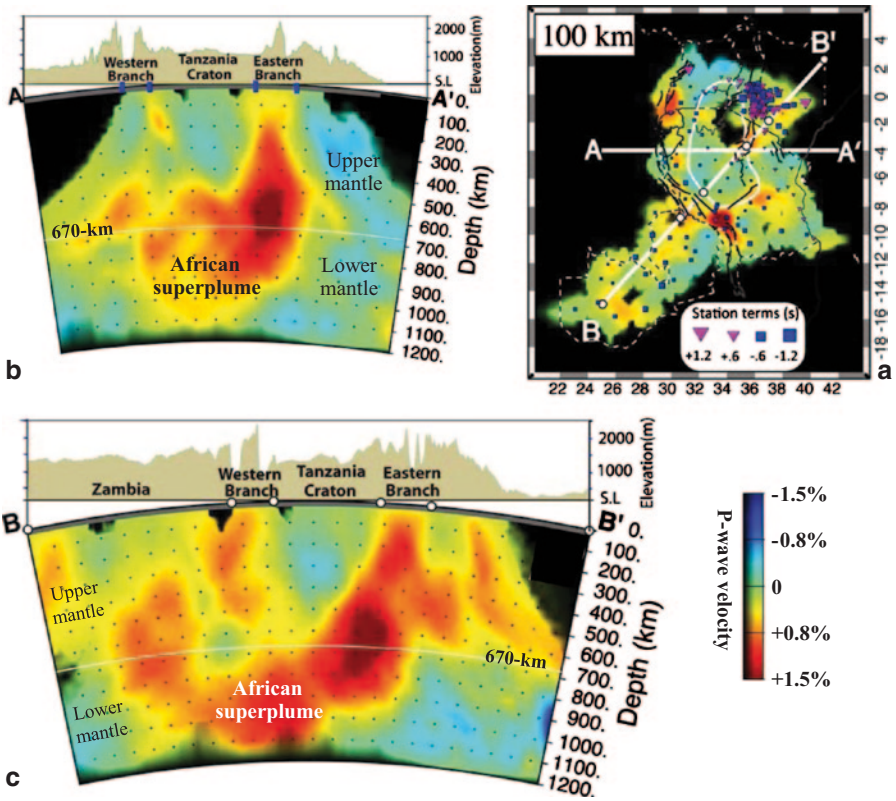

Fig. 5.12 (**a**) Map view of P-wave tomography at a depth of 100 km beneath East Africa. (**b**, **c**) Vertical cross-sections of P-wave tomography. Locations of the cross-sections are shown in (**a**). The *red* and *blue* colors denote slow and fast velocities, respectively. The velocity perturbation scale is shown below (**a**). The surface topography is shown *above* the vertical cross-section. (Modified from Mulibo and Nyblade 2013)

High-resolution local tomography (e.g., Ritter et al. 2001; Keyser et al. 2002; Mathar et al. 2006; Ritter 2007) has imaged the Eifel plume in the upper mantle very clearly, which has a diameter of 50–100 km (Fig. 5.13).

Receiver-function analyses revealed detailed structures of the Moho and the MTZ discontinuities beneath the Eifel hotspot (Budweg et al. 2006; Weber et al. 2007). The average Moho depth is ~30 km in the Eifel region, thinning to ~28 km under the Eifel volcanic fields. The receiver-function images show a low-V zone at depths of 60–90 km under West Eifel, which is consistent with the P and S wave velocity and attenuation tomography results (Ritter 2007). There is a zone of increased velocity near 200 km depth, being consistent with S-wave and attenuation tomographic results. However, this anomaly is invisible in P-wave tomography, which may be caused by S-wave anisotropy that compensates for elevated temperatures. All the three receiver-function anomalies, at the Moho, at 60–90 km and near

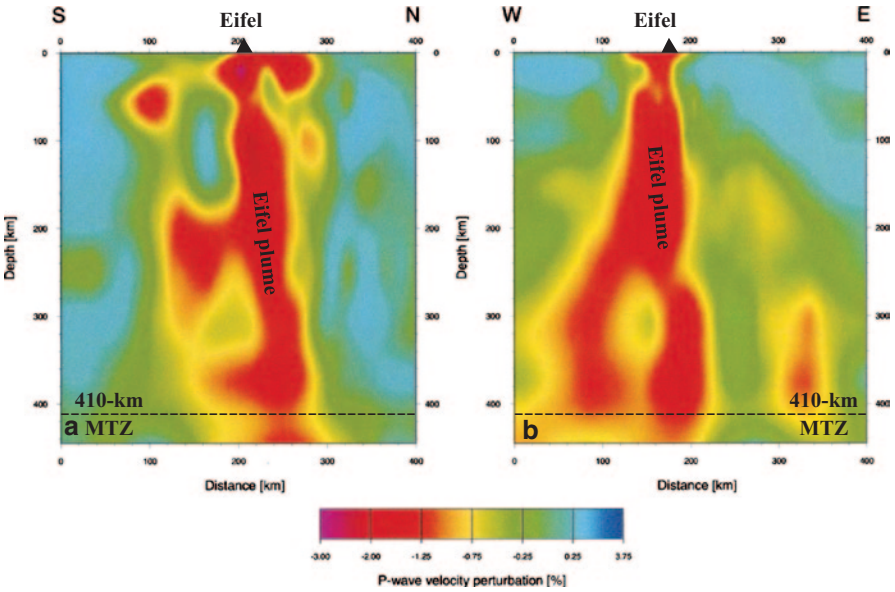

Fig. 5.13 North-south (**a**) and east-west (**b**) vertical cross-sections of P-wave tomography *beneath* the Eifel hotspot (modified from Ritter et al. 2001). The *red* and *blue* colors denote slow and fast velocities, respectively. The velocity perturbation scale is shown at the *bottom*. The *dashed line* denotes the 410 km discontinuity. MTZ, the mantle transition zone

200 km depths, have a lateral extent of ~100 km, possibly reflecting the diameter of the Eifel plume in the upper mantle.

The aperture of the Eifel seismic network limits the resolution of tomography to the upper 400 km depth (Ritter 2007), whereas the receiver-function method can resolve deeper structures (Weber et al. 2007). The 410-km discontinuity under the Eifel is depressed by 15–25 km, which can be explained by a maximum temperature increase of 200–300 K. The receiver-function analysis also revealed two additional seismic wave conversions between 410 and 550 km depth, which may represent remnants of previous subduction or anomalies due to delayed phase changes (Weber et al. 2007). The lateral extent of the two additional conversions and the depression of the 410-km discontinuity is ~200 km. The 660-km discontinuity does not show any depth deviation from its expected value.

Based on the tomography and receiver-function observations, Weber et al. (2007) proposed the following scenario for the Eifel plume. The plume has a temperature 200–300 K higher than the surrounding mantle. The Eifel plume, now residing in the upper mantle, might be originally connected to a larger plume in the lower mantle under Central Europe (Goes et al. 1999; Zhao 2007) and was sheared from its deep root, e.g., by closing of the Tethys ocean.

5.7 North American Hotspots

The global tomography (Zhao 2007) shows that beneath the Yellowstone and Raton hotspots, low-V zones exist in the upper and lower mantle, but not in the MTZ (Fig. 5.8). Slow anomalies under Yellowstone was imaged down to 300 km depth in the upper mantle by earlier local tomography studies (e.g., Saltzer and Humphreys 1997; Waite et al. 2006). In the past a few years, many tomographic models of the western United States (U.S.) have been determined using the data recorded by the dense USArray transportable seismic network, which shed new light on the origin of the Yellowstone hotspot (e.g., Humphreys and Schmandt 2011; Becker 2012; Schmandt et al. 2012; Tian and Zhao 2012 and references therein). Figure 5.14 shows P-wave velocity images under the Yellowstone hotspot from one of the tomographic models determined using the USArray data (Tian and Zhao 2012). Prominent low-V anomalies are imaged at depths of 0 to 200 km beneath the Snake River Plain, which may represent a small-scale convection beneath the western U.S. The low-V structure deviates variably from a narrow vertical plume conduit extending down to ~1000 km depth, suggesting that the Yellowstone plume has a lower-mantle origin. This result is generally consistent with other tomographic models of the western U.S. obtained using the US Array data (see Becker 2012 for a review). Experiments with a laboratory model support the presence of the Yellowstone plume in the northwestern U.S., and also highlight the power of plume-subduction interactions to modify surface geology at convergent plate margins (Kincaid et al. 2013).

The Bowie and Cobb hotspots are located close to the western coast of Canada (Fig. 5.1), and they are not spectacular hotspots. The tomographic image beneath the Bowie hotspot looks complex: low-V zones are visible in the upper mantle and below the 660 km discontinuity, and a large low-V zone exists from 1300 km depth to the CMB (Fig. 5.8). A seismic array study detected a low-V zone beneath Bowie at a depth of ~700 km (Nataf and VanDecar 1993), being consistent with the tomographic image. Low-V zones are also visible in the upper mantle and below the 660 km discontinuity under Cobb, and a dipping low-V zone is revealed from ~500 km depth to the CMB southwest of Cobb, which looks like a plume feeding the Cobb hotspot (Fig. 5.8).

Significant but complex low-V zones are visible in the mantle beneath Baja (Fig. 5.8). Beneath the Socorro hotspot, the seismic velocity is low from the surface to 200 km depth, and a tilted low-V zone exists in the lower mantle. However, the two low-V zones are separated by a high-V anomaly in the MTZ (Fig. 5.8).

The MTZ is generally thinner than the global average beneath the Raton, Baja and Bowie hotspots (Deuss 2007).

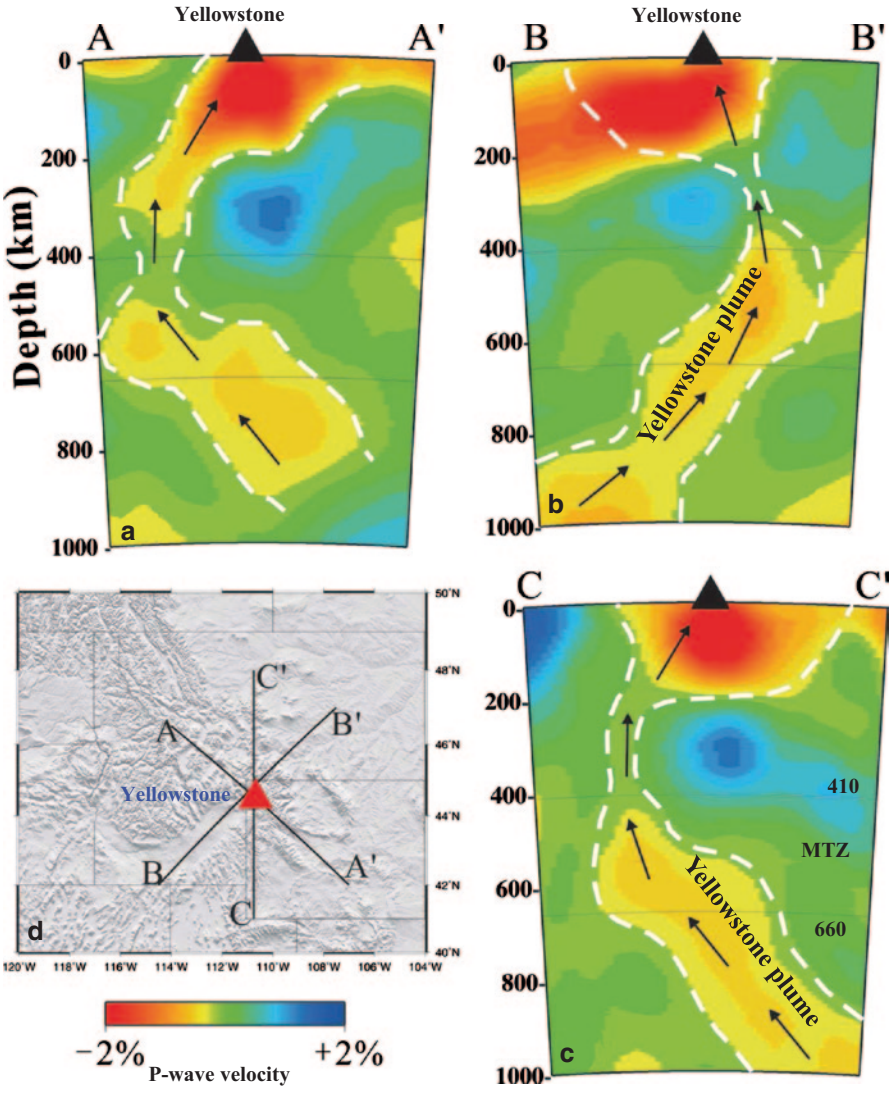

Fig. 5.14 Vertical cross-sections of P-wave tomography beneath the Yellowstone hotspot (modified from Tian and Zhao 2012). Locations of the cross-sections are shown in the inset map. The *red* and *blue* colors denote slow and fast velocities, respectively. The velocity perturbation scale is shown at the *bottom*. The two *thin lines* denote the 410- and 660-km discontinuities. MTZ, the mantle transition zone

5.8 Antarctic Hotspots

Low-V zones are revealed at depths of 700–2000 km under the Balleny hotspot (Fig. 5.8). A prominent low-V zone exists in the upper mantle under Mt. Erebus, which looks like an upper-mantle plume (Fig. 5.8). Kobayashi and Zhao (2004) used surface-wave tomography to study the structure of the Antarctic region and revealed significant low-V anomalies in the upper mantle under the Balleny and Erebus hotspots.

High-resolution local tomography of the upper mantle beneath the Erebus hotspot is determined using teleseismic data recorded by a portable seismic network around the hotspot (Watson et al. 2006; Gupta et al. 2009) (Fig. 5.15). The results show a prominent low-V anomaly of nearly circular symmetry (250–300 km in diameter) to ~200 km depth under the Mount Erebus volcanic region, which further extends down to ~400 km depth as a narrow tilted column. The observed low-V anomaly may reflect a thermal anomaly with its origin in or below the MTZ. Combining the tomographic results with geochemical observations of rift-related volcanism in the region, Mt. Erebus is considered to be a hotspot due to the West Antarctic Rift System linked with a mantle plume. In addition, Gupta et al. (2009) revealed high-V anomalies beneath the East Antarctic Craton, being consistent with other tomographic results of the region (Kobayashi and Zhao 2004; Watson et al. 2006).

Recently, Zandomeneghi et al. (2013) determined a high-resolution (to scale lengths of several hundreds of meters) 3-D P-wave tomography to a depth of ~600 m below the Erebus volcano surface using data recorded by 91 seismometers deployed over an ~4 by 4 km area of the summit region from 12 chemical shots emplaced in shallow snow and ice boreholes. Their results revealed detailed structures of the near-summit magmatic system of the Erebus volcano.

5.9 East Asian Hotspots

Seven major intraplate volcanoes exist in the East Asian region, including Wudalianchi, Changbai, Datong, Ulleung, Jeju, Tengchong and Hainan (Fig. 5.1). Figure 5.16 shows nine east-west vertical cross-sections passing through East Asia from the Japan Trench to central China from a high-resolution regional tomography model (Huang and Zhao 2006). The subducting Pacific slab becomes stagnant in the MTZ under the Korean Peninsula and eastern China, and a big mantle wedge (BMW) has formed in the upper mantle above the stagnant slab (Zhao et al. 2004, 2007; Lei and Zhao 2005; Wei et al. 2012; Zhao and Tian 2013). High-V anomalies are visible in the lower mantle under East Asia, which reflect pieces of slab materials finally collapsing down to the bottom of the mantle (e.g., Zhao 2004; Maruyama et al. 2007; Zhao et al. 2013).

Significant low-V anomalies are visible in the BMW beneath the Wudalianchi, Changbai, Datong, Ulleung and Jeju volcanoes (Figs. 5.16 and 5.17). It is consid-

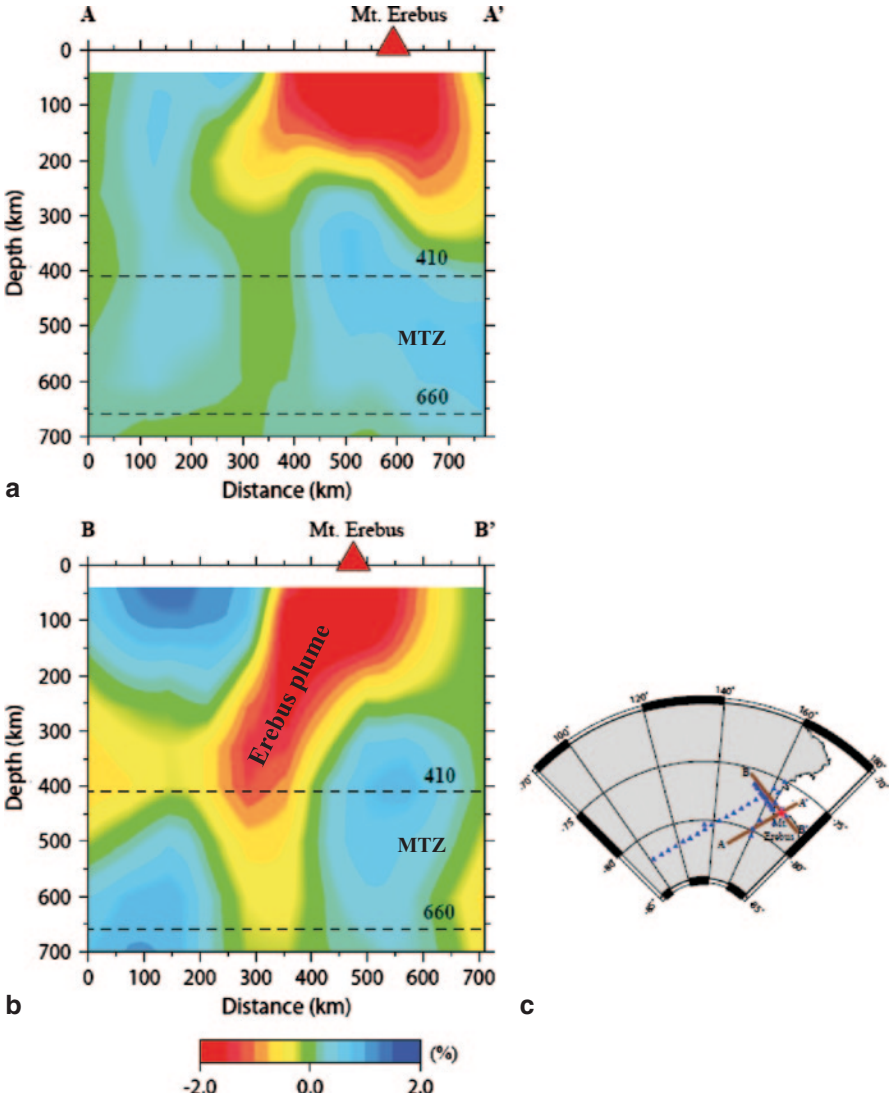

Fig. 5.15 Vertical cross-sections of P-wave tomography beneath the Erebus hotspot (modified from Gupta et al. 2009). Locations of the cross-sections are shown in the inset map. The *red* and *blue* colors denote slow and fast velocities, respectively. The velocity perturbation scale is shown at the *bottom*. The two *dashed lines* denote the 410- and 660-km discontinuities. MTZ, the mantle transition zone. The *blue triangles* in the map denote portable seismic stations used for the tomographic imaging

ered that these five intraplate volcanoes are caused by hot and wet upwelling in the BMW due to the corner flow in the BMW and deep dehydration of the stagnant slab (Zhao et al. 2004, 2009; Lei and Zhao 2005; Huang and Zhao 2006; Duan et al. 2009; Ohtani and Zhao 2009; Zhao and Liu 2010; Kuritani et al. 2011, 2013;

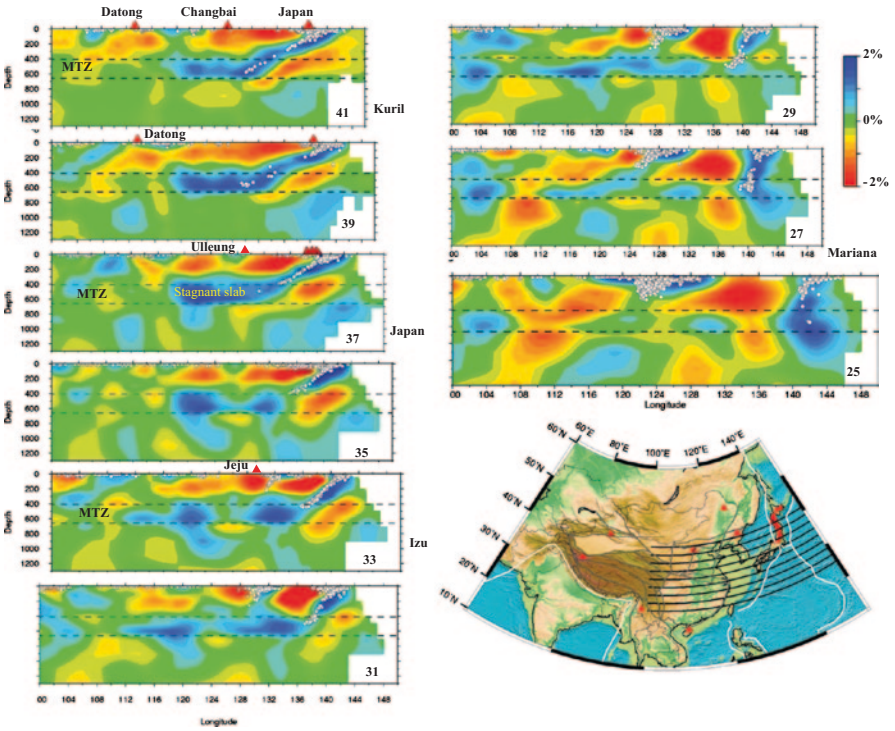

Fig. 5.16 East-west vertical cross-sections of P-wave regional tomography beneath East Asia (modified from Huang and Zhao 2006). Locations of the cross-sections are shown in the inset map. The number at the *lower-right corner* of each panel denotes the north latitude of each profile. The *red* and *blue* colors denote slow and fast velocities, respectively. The velocity perturbation scale is shown on the *right*. The *red triangles* denote the arc or intraplate volcanoes. The *white dots* denote earthquakes that occurred within a 50-km width of each profile. The two *dashed lines* denote the 410- and 660-km discontinuities. MTZ, the mantle transition zone

Wei et al. 2012). A high-resolution local tomography (Zhao et al. 2009) revealed a prominent low-V zone down to ~410 km depth directly beneath the Changbai volcano (Fig. 5.18). Recently, Zhao and Tian (2013) suggest that deep earthquakes in the subducting Pacific slab are related to the origin of the Changbai volcanism. The faulting of large deep earthquakes ($M > 7.0$) may release fluids preserved within the slab to the overlying mantle wedge, which can produce more magmas supplied to the Changbai volcano, making Changbai the largest and most active intraplate volcano in East Asia (Zhao and Tian 2013). The fluids from the deep earthquake faulting may have also contributed to the formation of the Ulleung volcano in the Japan Sea, because large deep earthquakes also occur frequently beneath Ulleung Island (Zhao and Tian 2013).

The Datong volcano is a Quaternary volcano but a potentially active volcano. It is located west of the tip of the stagnant slab. Beneath Datong, a significant low-V zone is visible in the upper mantle, which is connected with a narrow low-V zone in

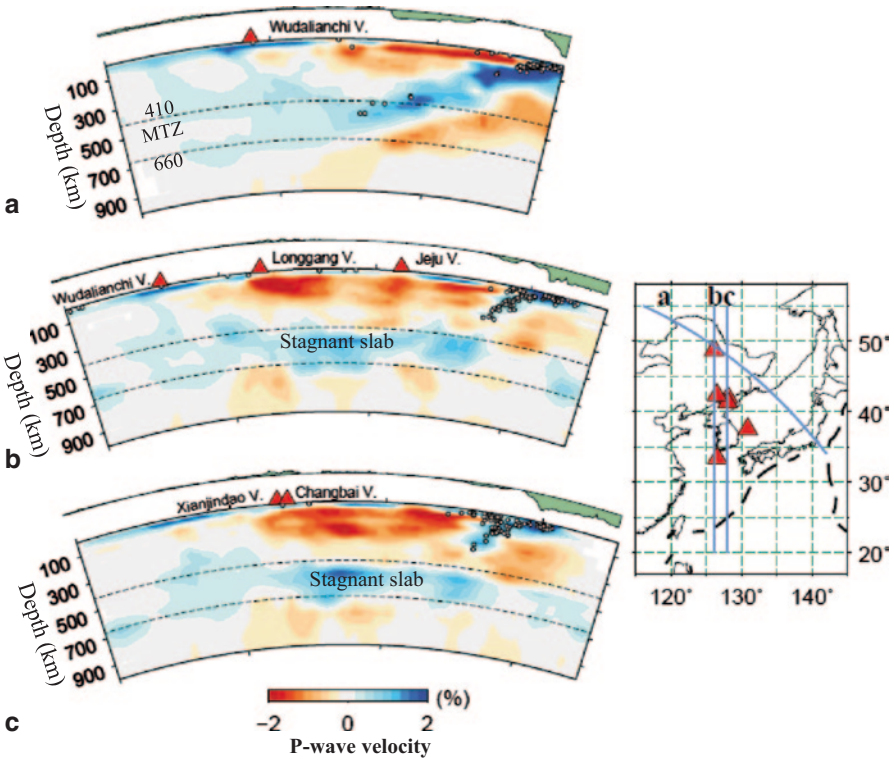

Fig. 5.17 Vertical cross-sections of P-wave regional tomography beneath East Asia (modified from Wei et al. 2012). Locations of the cross-sections are shown in the inset map. The *red* and *blue* colors denote slow and fast velocities, respectively. The velocity perturbation scale is shown at the *bottom*. The *red triangles* denote active intraplate volcanoes. The *white dots* denote earthquakes that occurred within a 30-km width of each profile. The two *dashed lines* denote the 410- and 660-km discontinuities. MTZ, the mantle transition zone

the MTZ and upper part of the lower mantle (Fig. 5.16), suggesting that this volcano may be caused by an upwelling flow in front of the slab edge associated with the slab collapsing down to the lower mantle (Zhao and Tian 2013).

Beneath the Jeju volcano (Fig. 5.17b), a prominent low-V anomaly is revealed in the upper mantle above the Philippine Sea slab which has also subducted down to the MTZ depth (Huang and Zhao 2006; Wei et al. 2012; Zhao et al. 2012; Huang et al. 2013). Longgang and Xianjindao are two minor volcanoes close to Changbai, which are also underlain by significant low-V zones in the BMW above the stagnant slab (Fig. 5.17b, c).

The regional tomography models have a lower resolution in the Wudalianchi volcanic area because there are not many seismic stations there (Huang and Zhao 2006; Duan et al. 2009; Wei et al. 2012). Global tomography shows that the Wudalianchi volcano has a similar origin as the Changbai volcano (Zhao 2004; Zhao and Liu 2010). Wei et al. (2012) suggested that lithospheric delamination has taken

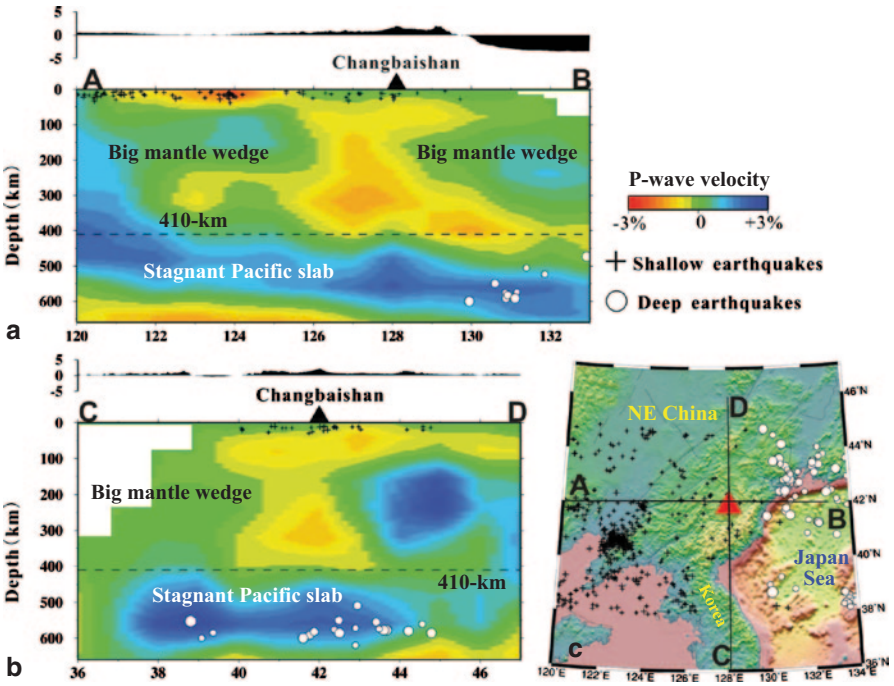

Fig. 5.18 East-west (**a**) and north-south (**b**) vertical cross-sections of local P-wave tomography beneath the Changbai intraplate volcano (modified from Zhao et al. 2009). Locations of the cross-sections are shown in the inset map (**c**). The *red* and *blue* colors denote slow and fast velocities, respectively. The velocity perturbation scale is shown on the *right*. The *black crosses* and *white dots* denote crustal and deep earthquakes, respectively. The *dashed line* denotes the 410-km discontinuity. The surface topography is shown *above* each cross-section

place under Wudalianchi, which caused local upwelling flow producing the volcano (Fig. 5.17a). A dense portable seismic network should be deployed in this region to clarify the origin of this important intraplate volcano whose most recent eruption occurred during 1719–1721 (Liu 1999, 2000).

Figure 5.19a shows an east-west vertical cross-section passing through the Tengchong active volcano in Southwest China from a recent high-resolution regional tomography of East Asia (Wei et al. 2012). A prominent low-V zone is visible under the Tengchong volcano down to ~250 km depth, and the subducting Burma microplate (or the Indian plate) is clearly imaged as a dipping high-V zone which is visible down to the MTZ or even the lower mantle. High-resolution local tomography has imaged the low-V anomaly under the Tengchong volcano in the crust and upper mantle more clearly (Huang et al. 2002; Lei et al. 2009a; Wang et al. 2010; Yang et al. 2014). These results indicate that the Tengchong volcano is not a hotspot associated with a deep mantle plume, it is more likely to be caused by the eastward subduction of the Burma microplate (or the Indian plate) and the hot and wet upwelling in the mantle wedge, similar to a back-arc volcano or the Changbai

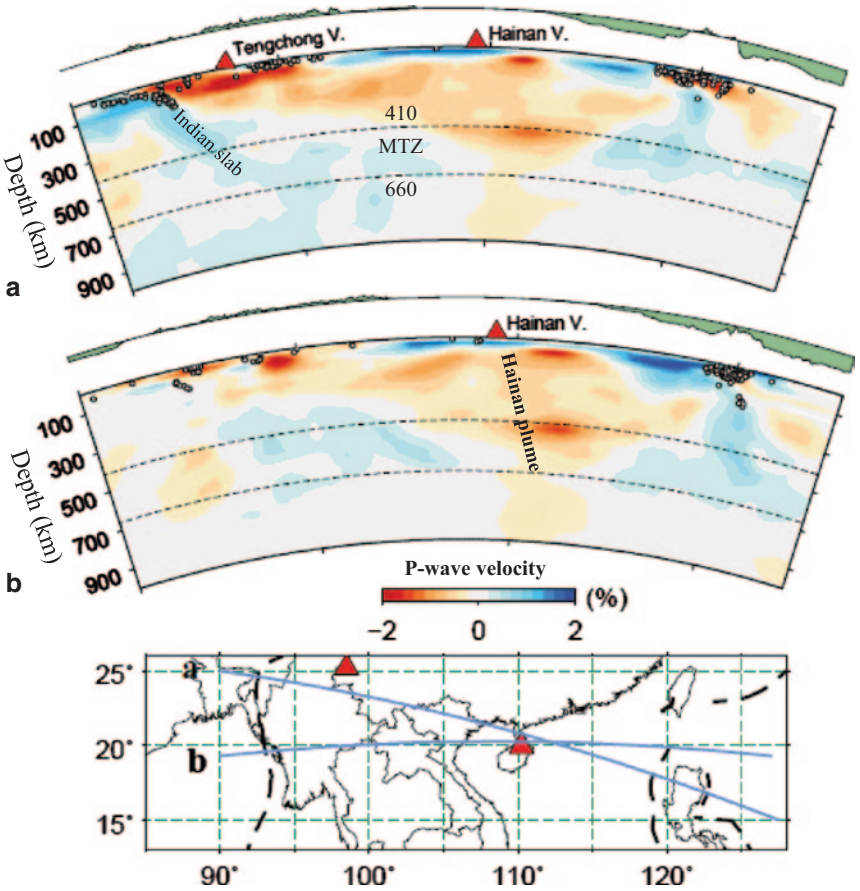

Fig. 5.19 Vertical cross-sections of P-wave regional tomography beneath the active Tengchong and Hainan volcanoes in China (modified from Wei et al. 2012). Locations of the cross-sections are shown in the inset map. The *red* and *blue* colors denote slow and fast velocities, respectively. The velocity perturbation scale is shown *above* the map. The *white dots* denote earthquakes that occurred within a 30-km width of each profile. The two *dashed lines* denote the 410- and 660-km discontinuities. MTZ, the mantle transition zone

intraplate volcano (Lei et al. 2009a; Zhao and Liu 2010). Petrologic and geochemical studies show that the Tengchong volcanics have origin in the upper mantle (Du et al. 2005), supporting the tomographic results.

The Hainan intraplate volcano in southernmost China (Fig. 5.1) is considered to be a hotspot (Liu 1999; Zhao and Liu 2010). The global tomography shows that significant low-V anomalies exist in the upper and lower mantle under Hainan (Fig. 5.7). The Hainan plume was imaged in the upper mantle by a waveform tomography (Lebedev and Nolet 2003). Recent regional tomography of East Asia (Huang and Zhao 2006; Wei et al. 2012) revealed prominent low-V anomalies in the mantle down to ~1000 km depth under Hainan (Fig. 5.19), indicating that the

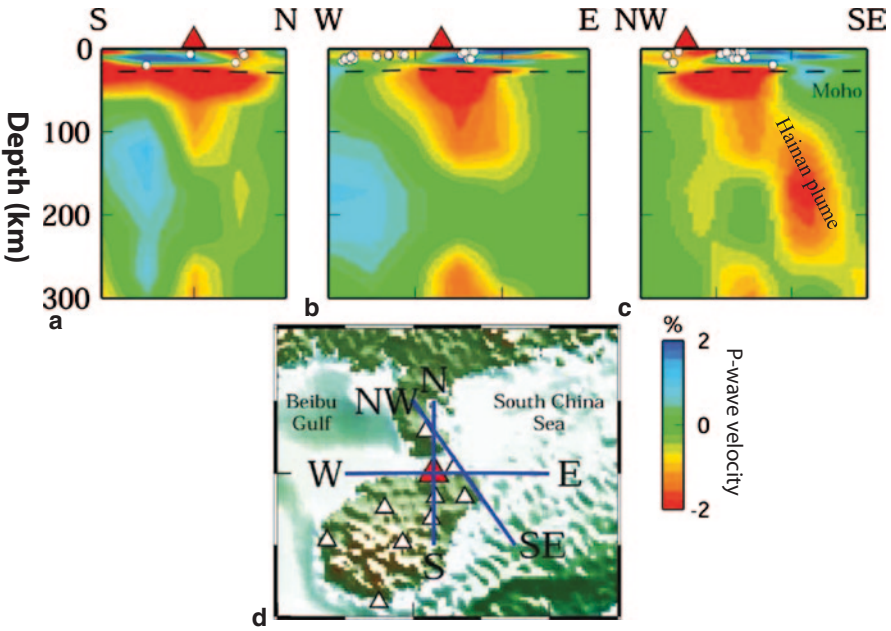

Fig. 5.20 Vertical cross-sections of local P-wave tomography beneath the Hainan hotspot (modified from Lei et al. 2009b). Locations of the cross-sections are shown in the inset map. The *red* and *blue* colors denote slow and fast velocities, respectively. The velocity perturbation scale is shown below (**c**). The *white dots* denote local crustal earthquakes that occurred within a 25-km width of each profile. The *dashed line* denotes the Moho discontinuity. The *white triangles* in the map denote local seismic stations used for the tomographic imaging

Hainan hotspot is fed by a deep mantle plume which may be caused by the deep subduction of the Indian and/or the Burma plate in the west and deep subduction of the Philippine Sea plate in the east (Zhao and Liu 2010; Wei et al. 2012). This interpretation is supported by a recent petrologic study (Wang et al. 2013).

A high-resolution local tomography is determined for the crust and upper mantle under Hainan using arrival-time data of local earthquakes and teleseismic events recorded by a local seismic network (Lei et al. 2009b). A prominent low-V zone is revealed in the upper mantle dipping from the northwest toward the southwest (Fig. 5.20), suggesting that the Hainan plume is deflected by mantle wind, being consistent with the prediction from a mantle convection model (Lei et al. 2009b).

The Baikal rift zone is composed of a branched chain of Late Cenozoic half-grabens extending over a distance of ~1500 km in Siberia (see Zhao et al. 2006 and references therein). It is situated at the boundary of the Siberian platform (craton) to the northwest and the Mongolian fold belt to the southeast. Lake Baikal occupies only about a third of the rift zone. The Baikal rift zone is characterized by high surface heat flow, flanking normal faults, and slower upper-mantle velocity. The 1500 km echelon system of rift depressions is seismically the most active continen-

tal rift in the world (e.g., Radziminovich et al. 2013). The Baikal rift is located over 2000 km away from the closest active plate boundary, and it is probably the most debated of all rifts in terms of its origin. Many scientists support an active rift hypothesis that theorizes an anomalous upper mantle formed beneath the continental lithosphere and led to the development of the rift; whereas a passive hypothesis suggests that the rift began as a result of the India-Asia collision. More recent studies prefer a mixture of several effects, giving a rather complex evolutionary picture (see the many references cited by Zhao et al. 2006 and Radziminovich et al. 2013). A local P-wave tomography of the Baikal rift zone is determined using high-quality arrival time data collected from original seismograms of teleseismic events recorded by a dense portable seismic network (Zhao et al. 2006). A low-V anomaly in the upper mantle with a lateral velocity reduction of up to 2% is revealed under the Baikal rift zone (Fig. 5.21). The low-V zone extends from the surface down to the

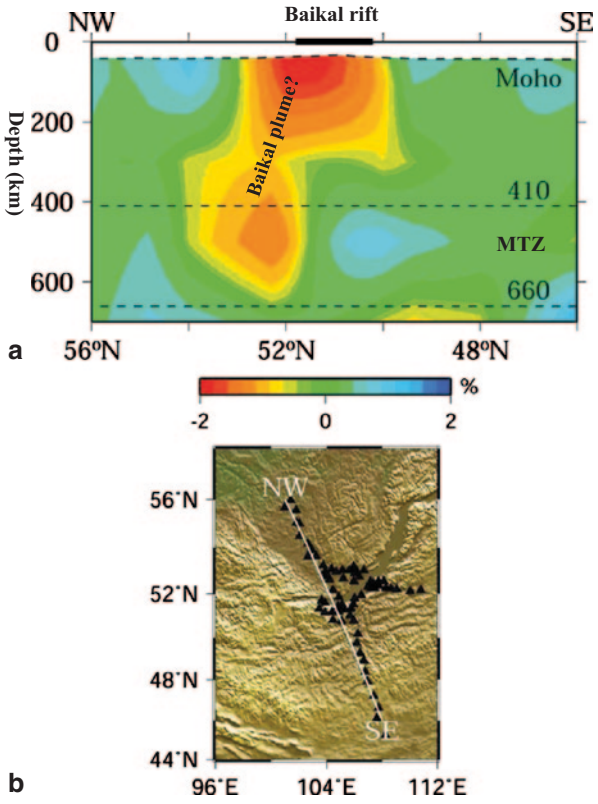

Fig. 5.21 (**a**) Vertical cross-section of local P-wave tomography beneath the Baikal rift zone (modified from Zhao et al. 2006). Location of the cross-section is shown in the inset map (**b**). The *red* and *blue* colors denote slow and fast velocities, respectively. The velocity perturbation scale is shown *below* (**a**). The three *dashed lines* denote the Moho, 410- and 660-km discontinuities. MTZ, the mantle transition zone. The *black triangles* in (**b**) denote portable seismic stations used for the tomographic imaging

MTZ and tilts toward the northwest under the stable Siberian craton. It is interpreted as a mantle upwelling (plume) which has played an important role in the initiation and evolution of the Baikal rift zone. The lithosphere of the stable Siberian craton is imaged as a high-V anomaly having a thickness of 150–180 km. Strong lateral heterogeneity exists in the lithosphere of the complex Mongolian fold belt. In addition to the dominant role of the Baikal mantle plume, the rift formation may be also controlled by other factors such as older (pre-rift) linear lithosphere structures favorably positioned relative to the plume and favorable orientation of the far-field forces caused by the India–Asia collision (Zhao et al. 2006). A recent regional tomography by Koulakov and Bushenkova (2010) shows a similar feature under the Baikal rift. However, a receiver-function result shows that the MTZ is thicker under the Baikal rift and so a mantle plume may not exist there (Liu and Gao 2006). More detailed studies are needed to resolve this issue.

5.10 Discussion and Summary

5.10.1 Types of Hotspots and Mantle Plumes

Based on the above-mentioned multidisciplinary findings, we summarize the main features of the 62 hotspots in Table 5.1. To describe the depth ranges of the low-V anomalies beneath each hotspot, we roughly divide the mantle into the upper mantle (<410 km depth), MTZ (410–660 km depth), upper portion of the lower mantle (660–1000 km depth), mid mantle (1000–1800 km depth), lower mantle (depth 660–2889 km, or 1800–2889 km in some cases), and the D" layer (about 200 km depth range in the lowermost mantle). Depending on the morphology of low-V zones and the MTZ thickness beneath a hotspot, the plume features are roughly divided into four types with grades 1–4 (see Table 5.1).

Thirteen hotspots have seismic structures with Grade 1 or 2 exhibiting plume-like low-V features in both the upper and lower mantle, including Hawaii, Tahiti, Louisville, Iceland, Cape Verde, Reunion, Kerguelen, Amsterdam, Afar, Eifel, Hainan, Cobb and Yellowstone, suggesting that they are probably whole-mantle plumes originating from the CMB feeding these hotspots. Upper-mantle plumes seem to exist under Easter, Azores, Vema, East Australia, Cameroon and Mt. Erebus hotspots. A mid-mantle plume may exist beneath the San Felix hotspot.

Detailed local and regional studies have provided convincing pieces of evidence that the active intraplate volcanoes in NE Asia, including Changbai, Wudalianchi, Jeju, and Ulleung, are caused by hot and wet upwelling flows in the BMW above the Pacific and Philippine Sea slabs which are now stagnant in the MTZ (Zhao et al. 2004, 2007, 2009; Lei and Zhao 2005; Huang and Zhao 2006; Zou et al. 2008; Duan et al. 2009; Kuritani et al. 2011, 2013; Wei et al. 2012; Zhao and Tian 2013). The Datong volcano is underlain by a hot flow ascending from the upper part of the lower mantle in front of the western edge of the stagnant slab. The Tengchong volcano

in Southwest China is related to the deep subduction of the Burma microplate or the Indian slab. The Hainan volcano is a hotspot fed by a whole-mantle plume, but the Hainan plume seems to be caused by deep slab subductions in the west and east (Zhao et al. 2011; Wang et al. 2013).

The seismic features under the other hotspots have grades 3 or 4 (Table 5.1), where low-V anomalies are generally visible in some depth range in the mantle, but their plume features are not very clear, and so their origins are uncertain from the seismological studies so far. In future studies, portable seismic stations should be installed in each of the hotspot areas so as to obtain high-resolution tomographic images and receiver-function results to clarify their origins.

5.10.2 Why are Seismic Images Under Hotspots Complex?

The tomographic images beneath most of the hotspots look complex (Figs. 5.4, 5.5, 5.6, 5.7, 5.8, 5.9, 5.10, 5.11, 5.12, 5.13, 5.14, 5.15, 5.16, 5.17, 5.18, 5.19, 5.20 and 5.21). One or more low-V zones are generally revealed at some depths beneath the surface hotspots, and high-V anomalies are also visible in some cases. Plume-like, continuous low-V columns in the entire mantle appear under only about a dozen hotspots (Table 5.1). In most cases, low-V anomalies are visible at only some depth range beneath a hotspot, rather than in the whole mantle.

The complexity of seismic images beneath the hotspots could be caused by a variety of reasons, which are summarized as follows (Zhao 2007). (1) Some hotspots may simply be not related to mantle plumes, as insisted by the opponents of the plume theory (e.g., Anderson 2000, 2011; Foulger et al. 2000; Foulger and Jurdy 2007). (2) The diameter of a plume ranges from 100–200 km in the upper mantle to 500–600 km in the lower mantle (Fig. 5.3). The thinner portion of the plume may not be detected because of the limited resolution of the current global and regional tomography. Local tomography and some regional tomography have a higher resolution in the upper mantle, but they cannot resolve the lower mantle structure because of the small aperture of the local networks available in most of the hotspots areas. (3) Some plumes may be just shallow mantle (or upper mantle) features and so they do not extend into the MTZ and the lower mantle (Courtillot et al. 2003), such as some of the volcanoes which are located at the edges of continental cratons (King and Ritsema 2000; Reusch et al. 2010, 2011). The other example is the intraplate volcanoes in Northeast Asia which are associated with upper-mantle processes in the BMW above the stagnant slab in the MTZ, as mentioned above. (4) In some cases, the surface location of a hotspot may not be correct (e.g., Louisville in Fig. 5.4). It is also possible that some of the "hotspots" adopted here are simply not a real hotspot. As mentioned above, there are quite several hotspot lists and they are quite different from each other. (5) Beneath many oceanic hotspots, the seismic rays in the data set of global tomography do not crisscross well enough and so the obtained tomography has a very poor resolution. For example, the resolution is very low in the upper mantle under Discovery and Crozet and in the lower mantle

under Fernando, Trindade, Bouvet, Meteor, Marion, Darfur, and Mt. Erebus (see the results of resolution tests in Zhao 2007). The plume signals may be only weakly captured because of the lack of a sufficient number of seismic stations receiving the signals (i.e., delayed arrivals of seismic waves passing through the plumes). The fact is that none or very few seismic stations exist directly above most of the hotspots. (6) Even if there are enough rays passing through the mantle beneath a hotspot and the resolution tests show good recovery of a synthetic plume anomaly, the arrival-time data used in the tomographic inversion may have large picking errors, which would result in a blurred, complex or even wrong image of a plume. (7) Narrow lower-mantle plumes may not be detected due to the wavefront healing effect (Hwang et al. 2011). (8) Some plume may not be detected with seismological methods because it is a chemical plume (Anderson 1975) or a wet spot rather than a hot spot (Newmann 1994). If the wet spot is just hydrated mantle and there is no free water, its seismological features (seismic velocity, attenuation, and anisotropy) may not be very different from those of the surrounding mantle.

5.10.3 Deflection of Mantle Plumes

For those hotspots where a plume-like low-V zone is imaged (Table 5.1), the slow anomalies beneath hotspots usually do not show a simple vertical pillar shape. This suggests that plumes, if any, are not completely fixed in the mantle but can be deflected due to the influences of mantle flow (Griffiths and Richards 1989; Loper 1991; Zhao 2001b, 2004; Shen et al. 2002; Lei et al. 2009b). Computer simulations of mantle convection show that plume conduits can be tilted, with source regions at the D" layer moving in the lowermost mantle flow, generally toward large-scale upwellings under East Africa and South Pacific (Steinberger 2000). The hotspot surface motion often represents the horizontal component of mid-mantle flow, which is frequently opposite to the plate motion (i.e., toward ridges and away from subduction zones) (Steinberger 2000). If the tomographic images of the plumes are precise enough, they may reflect the history of the mantle flow motions beneath each of the hotspot regions, being a good indicator of mantle convection (Zhao 2007).

Because of the deflection of mantle plumes, hotspots would not be fixed during the long geological history but could move on the Earth's surface, as suggested by computer simulation studies, though their relative moving velocities are much smaller than that of the lithospheric plates (Steinberger 2000; Griffiths and Richards 1989; Molnar and Stock 1987). However, results of paleomagnetic studies show that the Hawaiian hotspot may have moved southward continuously at rates of 30–50 mm/yr, which are comparable to those of lithospheric plates in late Cretaceous to early Tertiary times (81–43 Ma), and the bend in the Hawaiian-Emperor chain has recorded primarily differences in motion of the Hawaiian hotspot relative to the Pacific lithosphere (Tarduno et al. 2003, 2009). The tomographic image under Hawaii is well consistent with this scenario (Fig. 5.4). The plume-like low-V zone under Hawaii bends from the north at the CMB to the south at 1500 km depth, and then

it becomes vertical from 1500 km to the surface, which may reflect the southward motion of the Hawaiian hotspot during 81–43 Ma as revealed by paleomagnetic, numerical simulation and geochronological studies (e.g., Tarduno et al. 2003, 2009; Steinberger and Gaina 2007; O'Connor et al. 2013).

5.10.4 Plume Behaviors in and Below Mantle Transition Zone

Tomographic images beneath the hotspots show that low-V zones often become complex around the 660 km discontinuity. Beneath several hotspots such as San Felix, Juan Fernandez (Fig. 5.4), Jan Mayen, Iceland (Fig. 5.5), Eifel, Hainan (Fig. 5.7), Bowie, and Cobb (Fig. 5.8), a thin, laterally spreading, low-V layer appears directly beneath the 660 km discontinuity. The low-V layer may reflect ponding of plume material in the top part of the lower mantle (Fig. 5.3), probably due to the existence of a low-viscosity layer, the so-called "second asthenosphere" lying between 660 and 1000 km depth, as suggested by computer simulation studies (e.g., Kido and Cadek 1997; Cserepes and Yuen 2000; Tosi and Yuen 2011). The second asthenosphere is able to produce mid-mantle plumes which develop from a boundary layer in the middle mantle, in contrast to the upper-mantle plume and lower-mantle plume which develop at the thermal boundary layer at 660 km and 2900 km depth, respectively (Cserepes and Yuen 2000). It is difficult to judge from the current tomographic images if such mid-mantle plumes really exist in the Earth at present. If they exist, the possible candidates are those under San Felix (Fig. 5.4), Tasmania, Lord Howe (Fig. 5.7), and East Africa (Fig. 5.7).

Under some hotspots such as Hawaii, Louisville (Fig. 5.4) and Reunion (Fig. 5.6), low-V zones spread laterally directly above the 660 km discontinuity. The width of the low-V zones is much greater than that in the lower mantle. It is generally considered that the 660 km discontinuity is caused by the endothermic spinel-perovskite phase transition (e.g., Ito and Takahashi 1989; Bina and Helffrich 1994) which can act as a strong, but incomplete barrier to vertical flows, i.e., the subducting slabs and ascending mantle plumes. If this barrier leaks at some relatively small spots, upward directed eruptions of the lower mantle material would take the form of the usual mushroom-shaped plumes in the upper mantle (Cserepes and Yuen 2000). The tomographic images under Hawaii, Reunion and Louisville may reflect such a scenario (Zhao 2007).

5.10.5 Implications for Mantle Dynamics

The complex mantle structures beneath hotspots revealed by the above-mentioned multidisciplinary studies may reflect strong lateral variations in temperature, viscosity and possibly composition of the mantle, which control the generation and ascending of mantle plumes as well as the flow pattern of mantle convection. These results have important implications for the understanding of mantle dynamics and

evolution of the Earth. The hotspots and mantle plumes in the Atlantic and Indian oceans may have contributed to the Gondwana breakup (e.g., Storey 1995), whereas those in the Pacific Ocean may have been associated with the much older opening of the Pacific Ocean (e.g., Maruyama et al. 2007; McNutt and Caress 2007). The hotspots under the continental regions should be the sites of future rifts and will contribute to the future breakup of the continents (e.g., Maruyama et al. 2007; McNutt and Caress 2007). The Afar and other hotspots in East Africa are good examples of this type.

At present we are still in the early stage of imaging mantle plumes because of the sparse distribution of seismometers in the hotspot areas. Because more and more seismographs including OBS stations will be deployed in the non- or less-instrumented regions, and seismic imaging techniques will be further improved, we will be able to image the crust and mantle structure better and better. Geochemical studies (e.g., Courtier et al. 2007; Hilton et al. 2011; Wang et al. 2013), laboratory experiments (e.g., Kumagai et al. 2008; Druken et al. 2013; Kincaid et al. 2013), and numerical simulations (e.g., Leng and Gurnis 2012; Bossmann and van Keken 2013; van Keken et al. 2013) are necessary and important for interpreting the seismological observations. Integrating all the multidisciplinary findings can greatly advance our understanding of the origin of hotspots and mantle plumes as well as deep Earth structure and dynamics.

References

Albers, M., Christensen, U.: The excess temperature of plumes rising from the core-mantle boundary. Geophys. Res. Lett. **23,** 3567–3570 (1996)

Allen, R., Nolet, G., Morgan, W., Vogfjord, K., Bergsson, B., Erlendsson, P. et al.: Imaging the mantle beneath Iceland using integrated seismological techniques. J. Geophys. Res. (2002). doi: 10.1019/2001JB000595

Anderson, D.L.: Chemical plumes in the mantle. Geol. Soc. Am. Bull. **86,** 1593–1600 (1975)

Anderson, D.L.: The thermal state of the upper mantle: no role for mantle plumes. Geophys. Res. Lett. **27,** 3623–3626 (2000)

Anderson, D.L.: Hawaii, boundary layers and ambient mantle—geophysical constraints. J. Petrol. **52,** 1547–1577 (2011)

Ballmer, M., Ito, G., Wolfe, C., Solomon, S.: Double layering of a thermochemical plume in the upper mantle beneath Hawaii. Earth Planet. Sci. Lett. **376,** 155–164 (2013)

Bastow, I., Stuart, G., Kendall, J., Ebinger, C.: Upper-mantle seismic structure in a region of incipient continental breakup: northern Ethiopian rift. Geophys. J. Int. **162,** 479–493 (2005)

Becker, T.: On recent seismic tomography for the western United States. Geochem. Geophys. Geosyst. **13,** Q01W10 (2012)

Benoit, M., Nyblade, A., VanDecar, J.: Upper mantle P-wave speed variations beneath Ethiopia and the origin of the Afar hotspot. Geology **34,** 329–332 (2006)

Bijwaard, H., Spakman, W.: Tomographic evidence for a narrow whole mantle plume below Iceland. Earth Planet. Sci. Lett. **166,** 121–126 (1999)

Bina, C., Helffrich, G.: Phase transition Clapeyron slopes and transition zone seismic discontinuity. J. Geophys. Res. **99,** 15853–15860 (1994)

Boehler, R.: Temperatures in the Earth's core from melting point measurements of iron at high static pressures. Nature **363,** 534–536 (1993)

Boschi, L., Becker, T., Steinberger, B.: Mantle plumes: dynamical models and seismic images. Geochem. Geophys. Geosyst. **8,** Q10006 (2007)
Bossmann, A., van Keken, P.: Dynamics of plumes in a compressible mantle with phase changes: Implications for phase boundary topography. Phys. Earth Planet. Inter. **224,** 21–31 (2013)
Brandt, M: Middle mantle seismic structure of the African superplume. Pure Appl. Geophys. **170,** 845–861 (2013)
Breton, T., Nauret, F., Pichat, S., Moine, B. et al.: Geochemical heterogeneities within the Crozet hotspot. Earth Planet. Sci. Lett. **376,** 126–136 (2013)
Budweg, M., Bock, G., Weber, M.: The Eifel plume—imaged with converted seismic waves. Geophys. J. Int. **166,** 579–589 (2006)
Campbell, I.: Testing the plume theory. Chem. Geol. **241,** 153–176 (2007)
Chang, S., Van der Lee, S.: Mantle plumes and associated flow beneath Arabia and East Africa. Earth Planet. Sci. Lett. **302,** 448–454 (2011)
Coffin, M., Pringle, M., Duncan, R., Gladczenko, T.: Kerguelen hotspot magma output since 130 Ma. J. Petrol. **43,** 1121–1139 (2002)
Condie, K.: Mantle Plumes And Their Record In Earth History. pp. 306. Cambridge University Press, Cambridge (2001)
Courtier, A., Jackson, M., Lawrence, J., Wang, Z., Lee, C. et al.: Correlation of seismic and petrologic thermometers suggests deep thermal anomalies beneath hotspots. Earth Planet. Sci. Lett. **264,** 308–316 (2007)
Courtillot, V., Davaille, A., Besse, J., Stock, J.: Three distinct types of hotspots in the Earth's mantle. Earth Planet. Sci. Lett. **205,** 295–308 (2003)
Crough, S., Jurdy, D.: Subducted lithosphere, hotspots, and the geoid. Earth Planet. Sci. Lett. **48,** 15–22 (1980)
Cserepes, L., Yuen, D.: On the possibility of a second kind of mantle plume. Earth Planet. Sci. Lett. **183,** 61–71 (2000)
Davies, G.F.: Ocean bathymetry and mantle convection: 1. Large-scale flow and hotspots. J. Geophys. Res. **93,** 10467–10480 (1988)
Davies, D., Goes, S., Davies, J., Schuberth, B., Bunge, H., Ritsema, J.: Reconciling dynamic and seismic models of Earth's lower mantle: the dominant role of thermal heterogeneity. Earth Planet. Sci. Lett. **353,** 253–269 (2012)
Deuss, A.: Seismic observations of transition-zone discontinuities beneath hotspot locations. In: Foulger, G., Jurdy, D. (eds.) Plates, Plumes, and Planetary Processes, pp. 121–136. Special Paper 430, Geological Society of America (2007)
Druken, K., Kincaid, C., Griffiths, R.: Directions of seismic anisotropy in laboratory models of mantle plumes. Geophys. Res. Lett. **40,** 3544–3549 (2013)
Du, J., Liu, C., Fu, B., Ninomiya, Y., Zhang, Y.: Variation of geothermometry and chemical-isotopic compositions of hot spring fluids in the Rehai geothermal field, Southwestern China. J. Volcanol. Geotherm. Res. **142,** 243–261 (2005)
Duan, Y., Zhao, D., Zhang, X. et al.: Seismic structure and origin of active intraplate volcanoes in Northeast Asia. Tectonophysics. **470,** 257–266 (2009)
Dunn, R., Forsyth, D.: Crust and lithospheric structure—Seismic structure of mid-ocean ridges. In: Schubert, G. (ed.) Treatise in Geophysics, Vol. 1.12, pp. 419–443. Elsevier, New York (2007)
Ernst, W.: Speculations on evolution of the terrestrial lithosphere-asthenosphere system—plumes and plates. Gondwana Res. **11,** 38–49 (2007)
Farnetani, C.: Excess temperature of mantle plumes: the role of chemical stratification across D". Geophys. Res. Lett. **24,** 1583–1586 (1997)
Farnetani, C., Hofmann, A.: Dynamics and internal structure of a lower mantle plume conduit. Earth Planet. Sci. Lett. **282,** 314–322 (2009)
Farnetani, C., Hofmann, A.: Dynamics and internal structure of the Hawaiian plume. Earth Planet. Sci. Lett. **295,** 231–240 (2010)
Foulger, G., Jurdy, D. (eds): Plates, Plumes, and Planetary Processes. Special Paper 430, Geological Society of America (2007)

Foulger, G., Pritchard, M., Julian, B., Evans, J.: The seismic anomaly beneath Iceland extends down to the mantle transition zone and no deeper. Geophys. J. Int. **142,** F1-F5 (2000)
Goes, S., Spakman, W., Bijwaard, H.: A lower mantle source for central European volcanism. Science **286,** 1928–1931 (1999)
Griffiths, R., Richards, M.: The adjustment of mantle plumes to changes in plate motion. Geophys. Res. Lett. **16,** 437–440 (1989)
Gupta, S., Zhao, D., Rai, S.: Seismic imaging of the upper mantle under the Erebus hotspot in Antarctica. Gondwana Res. **16,** 109–118 (2009)
Haldar, C., Kumar, P., Ravi Kumar, M.: Seismic structure of the lithosphere and upper mantle beneath the ocean islands near mid-oceanic ridges. Solid Earth **5,** 327–337 (2014)
Hansen, S., Nyblade, A., Benoit, M.: Mantle structure beneath Africa and Arabia from adaptively parameterized P-wave tomography: implications for the origin of Cenozoic Afro-Arabian tectonism. Earth Planet. Sci. Lett. **319,** 23–34 (2012)
Helffrich, G.: Topography of the transition zone seismic discontinuities. Rev. Geophys. **38,** 141–158 (2000)
Helffrich, G., Faria, B., Fonseca, J., Lodge, A., Kaneshima, S.: Transition zone structure under a stationary hot spot: cape verde. Earth Planet. Sci. Lett. **289,** 156–161 (2010)
Helmberger, D., Wen, L., Ding, X.: Seismic evidence that the source of the Iceland hotspot lies at the core-mantle boundary. Nature **396,** 251–258 (1998)
Hilton, D., Halldorsson, S., Barry, P., Fischer, T. et al.: Helium isotopes at Rungwe Volcanic Province, Tanzania, and the origin of East African Plateaux. Geophys. Res. Lett. **38,** L21304 (2011)
Hooft, E., Toomey, D., Solomon, S.: 2003. Anomalously thin transition zone beneath the Galapagos hotspot. Earth Planet. Sci. Lett. **216,** 55–64 (2003)
Huang, J., Zhao, D.: High-resolution mantle tomography of China and surrounding regions. J. Geophys. Res. **111,** B09305 (2006)
Huang, J., Zhao, D., Zheng, S.: Lithospheric structure and its relationship to seismic and volcanic activity in southwest China. J. Geophys. Res. **107,** 2000JB000137 (2002)
Huang, S., Hall, P., Jackson, M.: Geochemical zoning of volcanic chains associated with Pacific hotspots. Nature Geosci. **4,** 874–878 (2011)
Huang, Z., Zhao, D., Hasegawa, A., Umino, N., Park, J., Kang, I.: Aseismic deep subduction of the Philippine Sea plate and slab window. J. Asian Earth Sci. **75,** 82–94 (2013)
Huckfeldt, M., Courtier, A., Leahy, G.: Implications for the origin of Hawaiian volcanism from a converted wave analysis of the mantle transition zone. Earth Planet. Sci. Lett. **373,** 194–204 (2013)
Huerta, A., Nyblade, A., Reusch, A.: Mantle transition zone structure beneath Kenya and Tanzania: more evidence for a deep-seated thermal upwelling in the mantle. Geophys. J. Int. **177,** 1249–1255 (2009)
Humphreys, E., Schmandt, B.: Looking for mantle plumes. Phys. Today. **64**(8), 34–39 (2011)
Hung, S., Shen Y., Chiao, L.: Imaging seismic velocity structure beneath the Iceland hot spot: a finite frequency approach. J. Geophys. Res. **109,** B08305 (2004)
Hwang, Y., Ritsema, J., van KeKen, P., Goes, S.: Wavefront healing renders deep plumes seismically invisible. Geophys. J. Int. **187,** 273–277 (2011)
Ito, E., Takahashi, E.: Postspinel transformations in the system Mg2SiO4-Fe2SiO4 and some geophysical implications. J. Geophys. Res. **94,** 10637–10646 (1989)
Ito, G., van Keken, P.: Hot spots and melting anomalies. In: Schubert, G. (ed.) Treatise in Geophysics, Vol. 7, pp. 371–435. Elsevier, New York (2007)
Jackson, M., Hart, S., Konter, J., Koppers, A. et al.: Samoan hot spot track on a "hot spot highway": implications for mantle plumes and a deep Samoan mantle source. Geochem. Geophys. Geosyst. 11**,** Q12009 (2010)
Jakovlev, A., Rumpker, G., Schmeling, H., Koulakov, I., Lindenfeld, M., Wallner, H.: Seismic images of magmatic rifting beneath the western branch of the East African rift. Geochem. Geophys. Geosyst. **14,** 4906–4920 (2013)
Ji, Y., Nataf, H.: Detection of mantle plumes in the lower mantle by diffraction tomography: Hawaii. Earth Planet. Sci. Lett. **159,** 99–115 (1998)

Keyser, M., Ritter, J., Jordan, M.: 3D shear-wave velocity structure of the Eifel plume, Germany. Earth Planet. Sci. Lett. **203,** 59–82 (2002)
Kido, M., Cadek, O.: Inferences of viscosity from the oceanic geoid: Indication of a low viscosity zone below the 660-km discontinuity. Earth Planet. Sci. Lett. **151,** 125–137 (1997)
Kincaid, C., Druken, K., Griffiths, R., Stegman, D.: Bifurcation of the Yellowstone plume driven by subduction-induced mantle flow. Nature Geosci. **6,** 395–399 (2013)
King, S., Ritsema, J.: African hot spot volcanism: small-scale convection in the upper mantle beneath cratons. Science **290,** 1137–1140 (2000)
Kobayashi, R., Zhao, D.: Rayleigh wave group velocity distribution in the Antarctic region. Phys. Earth Planet. Inter. **141,** 167–181 (2004)
Konter, J., Jackson, M.: Large volumes of rejuvenated volcanism in Samoa: evidence supporting a tectonic influence on late-stage volcanism. Geochem. Geophys. Geosyst. **14,** Q0AM04 (2012)
Koulakov, I., Bushenkova, N.: Upper mantle structure beneath the Siberian craton and surrounding areas based on regional tomographic inversion of P and PP travel times. Tectonophysics. **486,** 81–100 (2010)
Kumagai, I., Davaille, A., Kurita, K., Stutzmann, E.: Mantle plumes: thin, fat, successful, or failing? Constraints to explain hot spot volcanism through time and space. Geophys. Res. Lett. **35,** L16301 (2008)
Kuritani, T., Ohtani, E., Kimura, J.: Intensive hydration of the mantle transition zone beneath China caused by ancient slab stagnation. Nature Geosci. **4,** 713–716 (2011)
Kuritani, T., Kimura, J., Ohtani, E., Miyamoto, H., Furuyama, K.: Transition zone origin of potassic basalts from Wudalianchi volcano, northeast China. Lithos **156,** 1–12 (2013)
Lambeck, K., Johnston, P., Smither, C., Nakada, M.: Glacial rebound of the British Isles III. Constraints on mantle viscosity. Geophys. J. Int. **125,** 340–354 (1996)
Lawrence, J., Shearer, P.: A global study of transition zone thickness using receiver functions. J. Geophys. Res. **111,** B06307 (2006)
Lay, T., Helmberger, D.: A lower mantle S wave triplication and the shear velocity structure of D". Geophys. J. R. Astron. Soc. **75,** 799–837 (1983)
Lay, T., Garnero, E., Williams, Q.: Partial melting in a thermo-chemical boundary layer at the base of the mantle. Phys. Earth Planet. Inter. **146,** 441–467 (2004)
Lebedev, S., Nolet, G.: Upper mantle beneath Southeast Asia from S velocity tomography. J. Geophys. Res. **108,** 2000JB000073 (2003)
Lei, J., Zhao, D.: P-wave tomography and origin of the Changbai intraplate volcano in Northeast Asia. Tectonophysics **397,** 281–295 (2005)
Lei, J., Zhao, D.: A new insight into the Hawaiian plume. Earth Planet. Sci. Lett. **241,** 438–453 (2006)
Lei, J., Zhao, D., Su, Y.: Insight into the origin of the Tengchong intraplate volcano and seismotectonics in southwest China from local and teleseismic data. J. Geophys. Res. **114,** B05302 (2009a)
Lei, J., Zhao, D., Steinberger, B., Wu, B., Shen, F., Li, Z.: New seismic constraints on the upper mantle structure of the Hainan plume. Phys. Earth Planet. Inter. **173,** 33–50 (2009b)
Leng, W., Gurnis, M.: Shape of thermal plumes in a compressible mantle with depth-dependent viscosity. Geophys. Res. Lett. **39,** L05310 (2012)
Li, X., Kind, R., Priestley, K., Sobolev, S., Tilmann, F., Yuan, X., Weber, M.: Mapping the Hawaiian plume conduit with converted seismic waves. Nature **405,** 938–941 (2000)
Li, X., Kind, R., Yuan, X.: Seismic study of upper mantle and transition zone beneath hotspots. Phys. Earth Planet. Inter. **136,** 79–92 (2003)
Liu, J.: Chinese Volcanoes. Scientific, Beijing, pp. 219 (1999)
Liu, R.: Active Volcanoes in China. Seismological Publishing, pp. 114 (2000)
Liu, K., Gao, S.: Mantle transition zone discontinuities beneath the Baikal rift and adjacent area. J. Geophys. Res. **111,** B11301 (2006)
Liu, X., Zhao, D.: Seismic evidence for a mantle plume beneath the Cape Verde hotspot. Int. Geol. Rev. **56,** 1213–1225 (2014)

Lodge, A., Helffrich, G.: Depleted swell root beneath the Cape Verde islands. Geology **34,** 449–452 (2006)
Lodge, A., Nippress, S., Rietbrock, A., Garcia-Yeguas, A., Ibanez, J.: Evidence for magmatic underplating and partial melt beneath Canary Islands derived using teleseismic receiver functions. Phys. Earth Planet. Inter. **212,** 44–54 (2012)
Loper, D.: Mantle plumes. Tectonophysics. **187,** 373–384 (1991)
Martinez-Arevalo, C., Mancilla, F., Helffrich, G., Garcia, A.: Seismic evidence of a regional sublithospheric low velocity layer beneath the Canary Islands. Tectonophysics. **608,** 586–599 (2013)
Maruyama, S.: Plume tectonics. J. Geol. Soc. Japan **100,** 24–49 (1994)
Maruyama, S., Santosh, M., Zhao, D.: Superplume, supercontinent, and post-perovskite: Mantle dynamics and anti-plate tectonics on the core-mantle boundary. Gondwana Res. **11,** 7–37 (2007)
Mathar, J., Ritter, J., Friederich, W.: Surface waves image the top of the Eifel plume. Geophys. J. Int. **164,** 377–382 (2006)
McKenzie, D.: The generation and compaction of partial molten rocks. J. Petrol. **25,** 713–765 (1984)
McNutt, M.: Superswells. Rev. Geophys. **36,** 211–244 (1998)
McNutt, M., Caress, D.: Crust and lithospheric structure—Hot spots and hot-spot swells. In: Schubert, G. (ed.) Treatise in Geophysics, Vol. 1, pp. 445–478. Elsevier, New York (2007).
Molnar, P., Stock, J.: Relative motions of hotspots in the Pacific, Atlantic, and India oceans since late Cretaceous time. Nature **327,** 587–591 (1987)
Montelli, R., Nolet, G., Dahlen, F., Master, G.: A catalogue of deep mantle plumes: new results from finite-frequency tomography. Geochem. Geophys. Geosyst. **7,** Q11007 (2006)
Morgan, W.: Convection plumes in the lower mantle. Nature. **230,** 42–43 (1971)
Morgan, W.: Deep motions and deep mantle convection. Geol. Soc. Am. Memo. **132,** 7–22 (1972)
Mulibo, G., Nyblade, A.: The P and S wave velocity structure of the mantle beneath eastern Africa and the African superplume anomaly. Geochem. Geophys. Geosyst. **14,** 2696–2715 (2013)
Murakami, M., Hirose, K., Kawamura, K., Sata, K., Ohishi, Y.: Postperovskite phase transition in MgSiO3. Science. **304,** 855–858 (2004)
Nataf, H.: Seismic imaging of mantle plumes. Ann. Rev. Earth Planet. Sci. **28,** 391–417 (2000)
Nataf, H., VanDecar, J.: Seismological detection of a mantle plume? Nature. **364,** 115–120 (1993)
Nataf, H., Ricard, Y.: 3SMAC: an a priori tomographic model of the upper mantle based on geophysical modeling. Phys. Earth Planet. Inter. **95,** 101–122 (1996)
Newmann, E.: The Oslo Rift: P-T relations and lithospheric structure. Tectonophysics. **240,** 159–172 (1994)
Niu, F., Inoue, H.: Seismic evidence for a thinner mantle transition zone beneath the South Pacific Superswell. Geophys. Res. Lett. **27,** 1981–1984 (2000)
Nolet, G., Allen, R., Zhao, D.: Mantle plume tomography. Chem. Geol. **241,** 248–263 (2007)
Nyblade, A., Owens, T., Gurrola, H., Ritsema, J., Langston, C.: Seismic evidence for a deep upper mantle thermal anomaly beneath east Africa. Geology. **28,** 599–602 (2000)
O'Connor, J., Steinberger, B., Regelous, M., Koppers, A. et al.: Constraints on past plate and mantle motion from new ages for the Hawaiian-Emperor seamount chain. Geochem. Geophys. Geosyst. (2013). doi: 10.1002/ggge.20267
Ohtani, E., Zhao, D.: The role of water in the deep upper mantle and transition zone: dehydration of stagnant slabs and its effects on the big mantle wedge. Russ. Geol. Geophys. **50,** 1073–1078 (2009)
Olson, P., Singer, H.: Creeping plumes. J. Fluid Mech. **158,** 511–531 (1985)
Pietruszka, A., Norman, M., Garcia, M., Marske, J., Burns, D.: Chemical heterogeneity in the Hawaiian mantle plume from the alteration and dehydration of recycled oceanic crust. Earth Planet. Sci. Lett. **361,** 298–309 (2013)
Pim, J., Peirce, C., Watts, A., Grevemeyer, I., Krabbenhoeft, A.: Crustal structure and origin of the Cape Verde Rise. Earth Planet. Sci. Lett. **272,** 422–428 (2008)

Radziminovich, N., Gileva, N., Melnikova, V., Ochkovskaya, M.: Seismicity of the Baikal rift system from regional network observations. J. Asian Earth Sci. **62,** 146–161 (2013)
Represas, P., Catalao, J., Montesinos, F., Madeira, J., Mata, J., Antunes, C., Moreira, M.: Constraints on the structure of Maio Island (Cape Verde) by a three-dimensional gravity model: imaging partially exhumed magma chambers. Geophys. J. Int. **190,** 931–940 (2012)
Reusch, A., Nyblade, A., Wiens, D., Shore, P., Ateba, B., Tabod, C., Nnange, J.: Upper mantle structure beneath Cameroon from body wave tomography and the origin of the Cameroon Volcanic Line. Geochem. Geophys. Geosyst. **11,** Q10W07 (2010)
Reusch, A., Nyblade, A., Tibi, R., Wiens, D., Shore, P., Ateba, B., Tabod, C., Nnange, J.: Mantle transition zone thickness beneath Cameroon: evidence for an upper mantle origin for the Cameroon Volcanic Line. Geophys. J. Int. **187,** 1146–1150 (2011)
Ricard, Y., Vigny, C., Froidevaux, C.: Mantle heterogeneities, geiod and plate motions: a Monte-Carlo inversion. J. Geophys. Res. **94,** 13739–13754 (1989)
Richards, M., Hager, B.: Geoid anomalies in a dynamic Earth. J. Geophys. Res. **89,** 5987–6002 (1984)
Richards, M., Griffiths, R.: Deflection of plumes by mantle shear flow: experimental results and a simple theory. Geophys. J. Int. **94,** 367–376 (1988)
Richards, M., Hager, B., Sleep, N.: Dynamically supported geoid highs over hotspots: observation and theory. J. Geophys. Res. **93,** 7690–7708 (1988)
Rickers, F., Fichtner, A., Trampert, J.: The Iceland-Jan Mayen plume system and its impact on mantle dynamics in the North Atlantic region: evidence from full-waveform inversion. Earth Planet. Sci. Lett. **367,** 39–51 (2013)
Ritsema, J., Jan der Heijst, H., Woodhouse, J.: Complex shear wave velocity structure imaged beneath Africa and Iceland. Science. **286,** 1925–1928 (1999)
Ritter, J.: The seismic signature of the Eifel plume. In: Ritter, J., Christensen, U. (eds.) Mantle Plumes: A Multidisciplinary Approach, pp. 379–404. Springer (2007)
Ritter, J., Jordan, M., Christensen, U., Achauer, U.: A mantle plume below the Eifel volcanic field, Germany. Earth Planet. Sci. Lett. **186,** 7–14 (2001)
Rychert, C., Laske, G., Harmon, N., Shearer, P.: Seismic imaging of melt in a displaced Hawaiian plume. Nature Geosci. **6,** 657–660 (2013)
Rychert, C., Harmon, N., Ebinger, C.: Receiver function imaging of lithospheric structure and the onset of melting beneath the Galapagos Archipelago. Earth Planet. Sci. Lett. **388,** 156–165 (2014)
Saltzer, R., Humphreys, E.: Upper mantle P wave velocity structure of the eastern Snake River Plain and its relationship to geodynamic models of the region. J. Geophys. Res. **102,** 11829–11841 (1997)
Schilling, J.G.: Fluxes and excess temperatures of mantle plumes inferred from their interaction with migrating mid-ocean ridges. Nature **352,** 397–403 (1991)
Schmandt, B., Dueker, K., Humphreys, E., Hansen, S.: Hot mantle upwelling across the 660 beneath yellowstone. Earth Planet. Sci. Lett. **331,** 224–236 (2012)
Shen, Y., Solomon, S., Bjarnason, I., Nolet, G.: Seismic evidence for a tilted mantle plume and north-south mantle flow beneath Iceland. Earth Planet. Sci. Lett. **197,** 261–272 (2002)
Shimoda, G., Ishizuka, O., Yamashita, K. et al.: Tectonic influence on chemical composition of ocean island basalts in the West and South Pacific: Implications for a deep mantle origin. Geochem. Geophys. Geosyst. **12,** Q07020 (2011)
Sidorin, I., Gurnis, M., Helmberger, D.: Dynamics of a phase change at the base of the mantle consistent with seismological observations. J. Geophys. Res. **104,** 15005–15023 (1999)
Silveira, G., Stutzmann, E., Davaille, A., Montagner, J.: Azores hotspot signature in the upper mantle. J. Volcanol. Geotherm. Res. **156,** 23–34 (2006)
Silveira, G., Vinnik, L., Stutzmann, E., Farra, V., Kiselev, S., Morais, I.: Stratification of the Earth beneath the Azores from P and S receiver functions. Earth Planet. Sci. Lett. **299,** 91–103 (2010)
Sleep, N.: Hotspots and mantle plumes: some phenomenology. J. Geophys. Res. **95,** 6715–6736 (1990)
Sleep, N.: Mantle plumes from top to bottom. Earth Sci. Rev. **77,** 231–271 (2006)

Steinberger, B.: Plumes in a convecting mantle: models and observations for individual hotspots. J. Geophys. Res. **105,** 11127–11152 (2000)
Steinberger, B., Gaina, C.: Plate-tectonic reconstructions predict part of the Hawaiian hotspot track to be preserved in the Bering Sea. Geology. **35,** 407–410 (2007)
Stern, R.: Subduction zones. Rev. Geophys. **40,** RG000108 (2002)
Storey, B.: The role of mantle plumes in continental breakup: case histories from Gondwana. Nature. **377,** 301–308 (1995)
Styles, E., Goes, S., van KeKen, P., Ritsema, J., Smith, H.: Synthetic images of dynamically predicted plumes and comparison with a global tomographic model. Earth Planet. Sci. Lett. **311,** 351–363 (2011)
Suetsugu, D., Isse, T., Tanaka, S., Obayashi, M., Shiobara, H.: South Pacific mantle plumes imaged by seismic observation on islands and seafloor. Geochem. Geophys. Geosyst. **10,** Q11014 (2009)
Tanaka, S., Obayashi, M., Suetsugu, D., Shiobara, H.: P wave tomography of the mantle beneath the South Pacific Superswell revealed by joint ocean and island broadband seismic experiments. Phys. Earth Planet. Inter. **172,** 268–277 (2009a)
Tanaka, S., Suetsugu, D., Shiobara, H., Sugioka, H.: On the vertical extent of the large low shear velocity province beneath the South Pacific Superswell. Geophys. Res. Lett. **36,** L07305 (2009b)
Tarduno, J., Duncan, R., Scholl, D., Cottreal, R., Steinberger, B.: The Emperor seamounts: southward motion of the Hawaiian hotspot plume in Earth's mantle. Science **301,** 1064–1069 (2003)
Tarduno, J., Bunge, H., Sleep, N., Hansen, U.: The bent Hawaiian-Emperor hotspot track: Inheriting the mantle wind. Science **324,** 50–53 (2009)
Tauzin, B., Debayle, E., Wittlinger, G.: The mantle transition zone as seen by global Pds phases: no clear evidence for a thin transition zone beneath hotspots. J. Geophys. Res. **113,** B08309 (2008)
Tian, Y., Zhao, D.: P-wave tomography of the Western United States: insight into the Yellowstone hotspot and the Juan de Fuca slab. Phys. Earth Planet. Inter. **200,** 72–84 (2012)
Tosi, N., Yuen, D.: Bent-shaped plumes and horizontal channel flow beneath the 660 km discontinuity. Earth Planet. Sci. Lett. **312,** 348–359 (2011)
Van Keken, P., Davaille, A., Vatteville, J.: Dynamics of a laminar plume in a cavity: the influence of boundaries on the steady state stem structure. Geochem. Geophys. Geosyst. **14,** 158–178 (2013)
Villagomez, D., Toomey, D., Geist, D., Hooft, E., Solomon, S.: Mantle flow and multistage melting beneath the Galapagos hotspot revealed by seismic imaging. Nature Geosci. **7,** 151–156 (2014)
Vinnik, L., Silveira, G., Kiselev, S., Farra, V., Weber, M., Stutzmann, E.: Cape Verde hotspot from the upper crust to the top of the lower mantle. Earth Planet. Sci. Lett. **319,** 259–268 (2012)
Vogt, P.: On the applicability of thermal conduction models to mid-plate volcanism, comments on a paper by Gass et al. J. Geophys. Res. **86,** 950–960 (1981)
Vogt, P., Jung, W.: Origin of the Bermuda volcanoes and the Bermuda Rise: History, observations, models, and puzzles. In: Foulger, G., Jurdy, D. (eds.) Plates, Plumes, and Planetary Processes, pp. 553–591. Special Paper 430, Geological Society of America (2007)
Waite, G., Smith, R., Allen, R.: Vp and Vs structure of the Yellowstone hot spot from teleseismic tomography: evidence for an upper mantle plume. J. Geophys. Res. **111,** B04303 (2006)
Wang, Z., Zhao, D., Wang, J.: Deep structure and seismogenesis of the north-south seismic zone in southwest China. J. Geophys. Res. **115,** B12334 (2010)
Wang, X., Li, Z., Li, X., Li, J., Xu, Y., Li, X.H.: Identification of an ancient mantle reservoir and young recycled materials in the source region of a young mantle plume: implications for potential linkages between plume and plate tectonics. Earth Planet. Sci. Lett. **377,** 248–259 (2013)
Watson, S., McKenzie, D.P.: Melt generation by plumes: a study of Hawaiian mechanism. J. Petrol. **32,** 501–537 (1991)
Watson, T., Nyblade, A., Wiens, D., Anandakrishnan, S., Benoit, M., Shore, P., Voigt, D., VanDecar, J.: P and S velocity structure of the upper mantle beneath the Transantarctic Mountains,

East Antarctic craton, and Ross Sea from travel time tomography. Geochem. Geophys. Geosyst. **7,** Q07005 (2006)
Weber, M., Bock, G., Budweg, M.: Upper mantle structure beneath the Eifel from receiver functions. In: Ritter, J., Christensen, U. (eds.) Mantle Plumes: a Multidisciplinary Approach, pp. 405–415. Springer (2007)
Wei, W., Xu, J., Zhao, D., Shi, Y.: East Asia mantle tomography: new insight into plate subduction and intraplate volcanism. J. Asian Earth Sci. **60,** 88–103 (2012)
Williams, Q., Garnero, E.: Seismic evidence for partial melt at the base of Earth's mantle. Science. **273,** 1528–1530 (1996)
Wilson, J.: A possible origin of the Hawaiian islands. Can. J. Phys. **41,** 863–870 (1963)
Wilson, J.: Mantle plumes and plate motions. Tectonophysics. **19,** 149–164 (1973)
Wilson, D., Peirce, C., Watts, A., Grevemeyer, I., Krabbenhoeft, A.: Uplift at lithospheric swell—I: seismic and gravity constraints on the crust and uppermost mantle structure of the Cape Verde mid-plate swell. Geophys. J. Int. **182,** 531–550 (2010)
Wolbern, I., Jacob, A., Blake, T., Kind, R., Li, X.: Deep origin of the Hawaiian tilted plume conduit derived from receiver functions. Geophys. J. Int. **166,** 767–781 (2006)
Wolfe, C., Bjarnason, I., VanDecar, J., Soloman, S.: Seismic structure of the Iceland mantle plume. Nature. **385,** 245–247 (1997)
Wolfe, C., Solomon, S., Laske, G., Collins, J., Detrick, R., Orcutt, J., Bercovici, D., Hauri, E.: Mantle shear-wave velocity structure beneath the Hawaiian hotspot. Science. **326,** 1388–1390 (2009)
Wolfe, C., Solomon, S., Laske, G., Collins, J., Detrick, R., Orcutt, J., Bercovici, D., Hauri, E.: Mapping P-wave velocity structure beneath the Hawaiian hotspot. Earth Planet. Sci. Lett. **303,** 267–280 (2011)
Yang, T., Shen, Y., van der Lee, S., Soloman, S., Hung, S.: Upper mantle structure beneath the Azores hotspot from finite-frequency seismic tomography. Earth Planet. Sci. Lett. **250,** 11–26 (2006)
Yang, T., Wu, J., Fang, L., Wang, W.: Complex structure beneath the southeastern Tibetan Plateau from teleseismic P-wave tomography. Bull. Seismol. Soc. Am. **104,** 1056–1069 (2014)
Zandomeneghi, D., Aster, R., Kyle, P., Barclay, A., Chaput, J., Knox, H.: Internal structure of Erebus volcano, Antarctica imaged by high-resolution active-source seismic tomography and coda interferometry. J. Geophys. Res. **118,** 1067–1078 (2013)
Zhao, D.: Seismological structure of subduction zones and its implications for arc magmatism and dynamics. Phys. Earth Planet. Inter. **127,** 197–214 (2001a)
Zhao, D.: Seismic structure and origin of hotspots and mantle plumes. Earth Planet. Sci. Lett. **192,** 251–265 (2001b)
Zhao, D.: Global tomographic images of mantle plumes and subducting slabs: Insight into deep Earth dynamics. Phys. Earth Planet. Inter. **146,** 3–34 (2004)
Zhao, D.: Seismic images under 60 hotspots: search for mantle plumes. Gondwana Res. **12,** 335–355 (2007)
Zhao, D.: Tomography and dynamics of Western-Pacific subduction zones. Monogr. Environ. Earth Planets **1,** 1–70 (2012)
Zhao, D., Liu, L.: Deep structure and origin of active volcanoes in China. Geosci. Frontiers. **1,** 31–44 (2010)
Zhao, D., Tian, Y.: Changbai intraplate volcanism and deep earthquakes in East Asia: a possible link? Geophys. J. Int. **195,** 706–724 (2013)
Zhao, D., Lei, J., Tang, R., 2004. Origin of the Changbai volcano in northeast China: evidence from seismic tomography. Chinese Sci. Bull. **49,** 1401–1408 (2004)
Zhao, D., Lei, J., Inoue, T., Yamada, A., Gao, S.: Deep structure and origin of the Baikal rift zone. Earth Planet. Sci. Lett. **243,** 681–691 (2006)
Zhao, D., Maruyama, S., Omori, S.: Mantle dynamics of Western Pacific and East Asia: insight from seismic tomography and mineral physics. Gondwana Res. **11,** 120–131 (2007)

Zhao, D., Tian, Y., Lei, J., Liu, L., Zheng, S.: Seismic image and origin of the Changbai intraplate volcano in East Asia: role of big mantle wedge above the stagnant Pacific slab. Phys. Earth Planet. Inter. **173,** 197–206 (2009)

Zhao, D., Yu, S., Ohtani, E.: East Asia: seismotectonics, magmatism and mantle dynamics. J. Asian Earth Sci. **40,** 689–709 (2011)

Zhao, D., Yamamoto, Y., Yanada, T.: Global mantle heterogeneity and its influence on teleseismic regional tomography. Gondwana Res. **23,** 595–616 (2013)

Zou, H., Fan, Q., Yao, Y.: U-Th systematics of dispersed young volcanoes in NE China: asthenospheric upwelling caused by piling up and upward thickening of stagnant Pacific slab. Chem. Geol. **255,** 134–142 (2008)

Chapter 6
East Asia Structure and Tectonics

Abstract In this chapter, we review seismic tomography studies of the East Asia region and new insights into plate deep subductions, continental seismotectonics, intraplate magmatism, and mantle dynamics. The subducting Pacific slab is stagnant in the mantle transition zone under the Korean Peninsula and East China, and a big mantle wedge (BMW) has formed above the stagnant slab. Hot and wet upwelling flows in the BMW have caused intraplate volcanoes in NE Asia, lithospheric thinning and reactivation of the North China Craton, and large earthquakes in and around East China. Deep earthquakes in the Pacific slab may be related to a metastable olivine wedge in the slab. The deepest earthquakes (~600 km depth) under NE Asia may release more fluids preserved in the slab to the overlying BMW, contributing to the Changbai volcanism. The descending Indian plate beneath the Tibetan Plateau is clearly revealed. The Hainan volcano in South China is a hotspot fed by a deep mantle plume associated with plate deep subductions in the east and the west.

Keywords East Asia · Mantle structure · Tectonics · Intraplate volcanism · Tibetan Plateau

East Asia (Fig. 6.1) is a heterogeneous collage of ancient continental fragments, volcanic arcs, suture belts and accretionary complexes in the convergent zones among the Eurasian, Pacific, Okhotsk, Philippine Sea and Indian plates (Lee and Lawver 1995; Northrup et al. 1995; Li 1998; Metcalfe 2006; and references therein). This broad region has experienced widespread tectonic deformations during the Cenozoic as a result of plate interactions. In the east, the Pacific and Philippine Sea plates are subducting beneath the Okhotsk and Eurasian plates, causing the western Pacific island arcs, marginal seas, and continental rift zones. In the southwest, the India-Asia collision leads to the shortening and elevation of the Tibetan plateau, causing high and great mountain ranges such as the Himalaya, Pamirs, and the Hindu-Kush mountains. The Asian continent has a very complex surface topography, and intensive seismic and volcanic activities (Fig. 6.1). Investigation of seismotectonics, volcanism, mantle dynamics and their relationships in the Asian region is very important from the viewpoint of both scientific research and mitigation of natural hazards. In this region large earthquakes and volcanic eruptions take place

D. Zhao, *Multiscale Seismic Tomography,* Springer Geophysics,
DOI 10.1007/978-4-431-55360-1_6

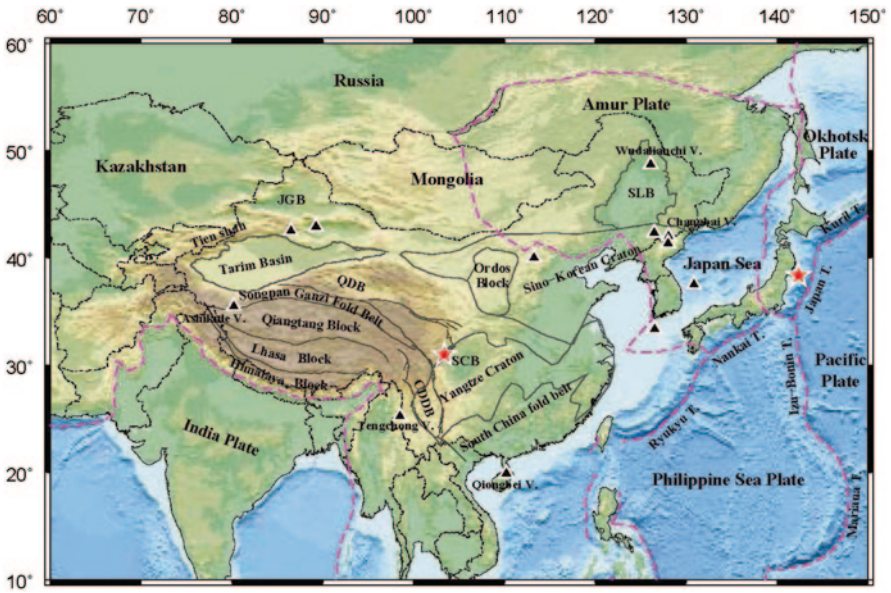

Fig. 6.1 Map showing the surface topography and major tectonic features of East Asia. The *dashed pink* lines show the major plate boundaries, and the *grey thin* lines denote the main tectonic units. The *black triangles* show the active intraplate volcanoes. The two *red stars* denote the 2008 Wenchuan earthquake (M 8.0) and the great 2011 Tohoku-oki earthquake (Mw 9.0). *QDB* Qaidam Basin, *JGB* Jungger Basin, *SLB* Songliao Basin, *SCB* Sichuan Basin, *CDDB* Chuandian Diamond Block. (Modified from Wei et al. 2012)

frequently, which have caused heavy casualties and significant damage in many Asian countries, such as the 1991 explosive eruption of the Pinatubo volcano in the Philippines, the 2004 Sumatra earthquake (M 9.2) in Indonesia and the huge tsunami it caused, the 2008 Wenchuan earthquake (M 8.0) in Southwest China, and the 2011 Tohoku earthquake (Mw 9.0) in Northeast Japan (Zhao et al. 2011). To clarify the mechanism of earthquake generation and volcanic eruptions, it is necessary to study the detailed crust and upper mantle structure in the earthquake and volcanic areas as well as the plate tectonics and mantle dynamics of the broad region, which are the fundamental causes of the seismic and volcanic activities.

In East Asia, there are many intriguing geological and geophysical phenomena which are related to the fundamental scientific issues of Earth sciences, such as the origin of the intraplate volcanoes (e.g., Changbai, Tenchong, Hainan, etc.), the deep structure and fate of subducting slabs, the India-Asia collision and its cause of great earthquakes and fault zones in and around the Tibetan Plateau, lithospheric thinning and reactivation of the North China Craton, and the origin of intracontinental rift zones in central Asia (such as Lake Baikal), etc. (Zhao et al. 2011). Plate tectonics and mantle dynamics are the fundamental causes of seismic and volcanic activities near the Earth's surface, whereas earthquakes and volcanoes are significant aspects of mantle dynamics. Therefore, it is important and necessary to have a consistent

and unified understanding of these scientific issues in the framework of global tectonics and mantle dynamics.

Several seismological methods have been applied to study the crust and mantle structure of East Asia. Teleseismic receiver-functions are effective as detectors of seismic discontinuities, such as the Moho, the lithosphere-asthenosphere boundary, the 410 and 660 km discontinuities, and their lateral depth variations (e.g., Ai et al. 2003; Li and Yuan 2003; Chen 2010; Tian et al. 2010, 2011). Shear-wave splitting measurements are useful for detecting seismic anisotropy in the crust and mantle, though they have no depth resolution (e.g., Liu et al. 2008; Zhao and Xue 2010; Huang et al. 2008, 2011). Surface-wave (including ambient-noise) tomography is effective for studying the 3-D S-wave velocity structure of the crust and shallow mantle, though it generally has a lower spatial resolution compared with body-wave tomography (e.g., Huang et al. 2003; An et al. 2009; Zheng et al. 2010; Li et al. 2012). Pn-wave tomography has been used to determine two-dimensional (2-D) P-wave velocity variation and anisotropy in the uppermost mantle directly beneath the Moho discontinuity (e.g., Hearn et al. 2004; Liang et al. 2004; Pei et al. 2007; Wang et al. 2013a). The waveform modeling approach has been adopted to study the detailed structure of the crust and the subducting slab (e.g., Abdelwahed and Zhao 2005, 2014; Tajima et al. 2009; Ye et al. 2011; Li et al. 2013). Body-wave tomography methods have been applied widely to study 3-D P- and S-wave velocity (Vp, Vs) structures of the crust and mantle down to a depth of ~1300 km beneath East Asia, and they generally have a much higher spatial resolution than surface-wave tomography (e.g., Huang and Zhao 2006, 2009; Lei and Zhao 2005, 2009; Tian et al. 2009; Tian and Zhao 2011; Xu and Zhao 2009; Wang et al. 2006, 2010; Wei et al. 2012). Recently, P-wave anisotropy tomography has been applied to investigate the 3-D distribution of P-wave anisotropy and velocity variations in the crust and upper mantle under East Asia (e.g., Wang and Zhao 2008; 2013; Tian and Zhao 2013; Wei et al. 2013; Wang et al. 2013b). These seismological studies have provided important new insights into interplate and intraplate seismotectonics, volcanism, and mantle dynamics in the East Asia region.

Here, I mainly review seismic tomography studies made for East Asia so far, with emphasis on recent works. First, I review large-scale tomographic models covering the entire East Asian region, then mention local-scale tomography studies in different parts of East Asia, and discuss their tectonic and geodynamic implications. I have attempted to make a complete and balanced review of these studies; however, because of the numerous works published by a great number of researchers and limitations of space here, I consider mainly those studies which I have been involved in or am relatively familiar with.

6.1 East Asian Mantle Tomography

So far, many global tomography models have been determined, which have revealed the large-scale mantle structure under the Western Pacific and East Asia and have found that the Pacific slab is stagnant in the mantle transition zone under NE Asia

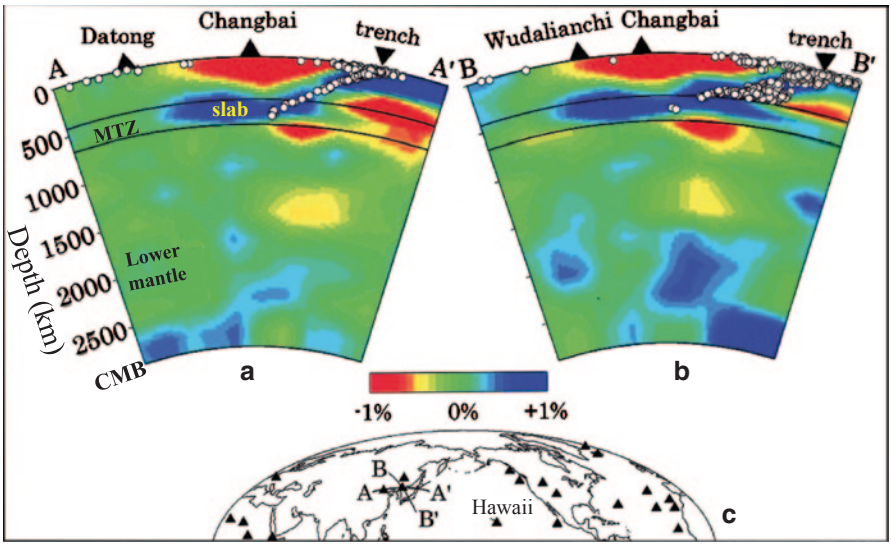

Fig. 6.2 **a, b** Vertical cross-sections of whole-mantle P-wave tomography beneath East Asia. The *red* and *blue* colors denote slow and fast velocity perturbations (*in %*), respectively, from the 1-D iasp91 Earth model. The velocity perturbation scale is shown below the cross-sections. The *white dots* denote earthquakes within a 150 km width of each profile. The two solid lines show the 410 and 670 km discontinuities. *Solid triangles* show the intraplate volcanoes. The *reverse triangles* show the location of the Japan Trench. *CMB* the core-mantle boundary. **c** Map showing locations of the two cross-sections in (**a**) and (**b**). Triangles denote hotspots or intraplate volcanoes on Earth. (Modified from Zhao 2007)

(Fukao et al. 1992) and that a big mantle wedge (BMW) has formed in the upper mantle above the stagnant Pacific slab (Zhao 2001, 2004; Zhao et al. 2004, 2013) (Fig. 6.2). However, all the global models have a low spatial resolution under East Asia and so are not very useful with regard to regional tectonics. Liu et al. (1990) determined the first regional Vp tomography model of the upper mantle beneath China. Later, large-scale Vs tomography models of East Asia were determined (e.g., Friederich 2003; Huang et al. 2003). Inevitably, these early regional tomography models had a low resolution and could only reveal large-scale lateral velocity variations under major tectonic units in East Asia.

Huang and Zhao (2006) determined a high-resolution Vp tomography of the crust and mantle down to a depth of 1300 km beneath East Asia applying the tomography method of Zhao (2001) to about one million arrival-time data of P, pP, PP, and PcP waves from 19,361 earthquakes recorded by 1012 seismic stations (Figs. 5.16 and 6.3). This regional tomography is very consistent with the global tomography under East Asia (e.g., Zhao 2001, 2004), but reveals much more detailed structures in the crust and upper mantle. The subducting Pacific slab is clearly imaged as a high-velocity (high-V) zone from the Japan Trench down to a depth of ~600 km, and intermediate-depth and deep earthquakes are located within the high-V slab (Figs. 5.16 and 6.3). The western edge of the stagnant slab is roughly coincident

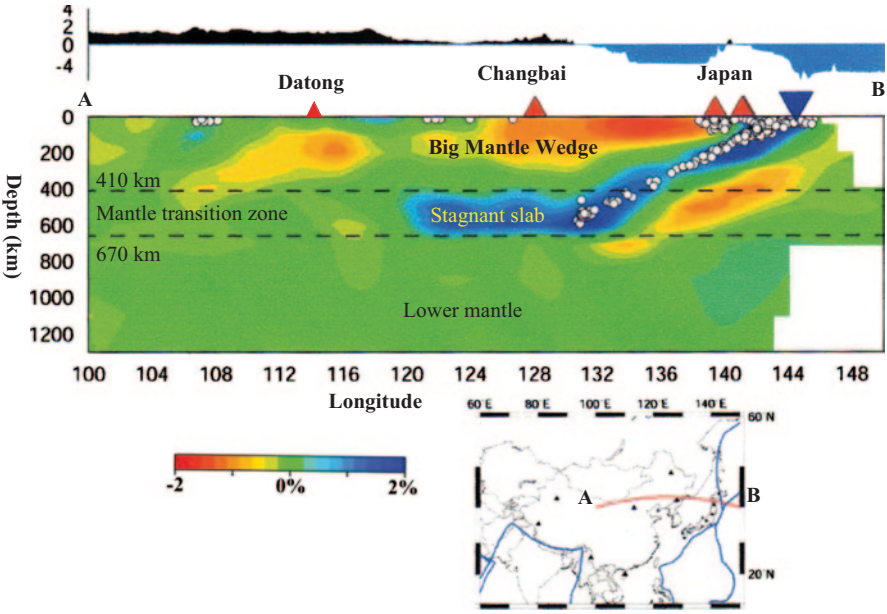

Fig. 6.3 East-west vertical cross-section of P-wave regional tomography from the surface down to 1300 km depth along a profile shown on the insert map. The *red* and *blue* colors denote slow and fast velocity perturbations (*in %*), respectively, from the 1-D iasp91 Earth model. The velocity perturbation scale is shown *below* the cross-section. *White* dots denote earthquakes within a 100 km width of the profile. The two *dashed* lines show the 410 and 670 km discontinuities. The *red* and *black* triangles show the active volcanoes. The *reverse blue* triangle shows the location of the Japan Trench. The surface topography along the profile is shown atop the tomographic image. The *blues* lines on the inset map denote the major plate boundaries. (Modified from Huang and Zhao 2006)

with a surface topographic boundary in East China (Huang and Zhao 2006). The active Changbai and Wudalianchi volcanoes are underlain by significant low-velocity (low-V) anomalies in the BMW. These results suggest that the active intraplate volcanoes in NE Asia are not hot spots like Hawaii but a kind of back-arc volcano associated with hot and wet upwelling flows above the stagnant slab, which have confirmed the BMW model proposed by Zhao et al. (2004) and Lei and Zhao (2005). Beneath the Mariana arc, however, the Pacific slab penetrates directly down to the lower mantle (Fig. 5.16). The active Tengchong volcano in Southwest China is related to the eastward subduction of the Burma microplate. The subducting Indian and Philippine Sea plates are also imaged clearly. The Indian plate has subducted down to a depth of 200–300 km under the Tibetan Plateau with a horizontal range of ~500 km. High-V anomalies are revealed in the upper mantle beneath the Tarim Basin, Ordos, and the Sichuan Basin, which are three stable blocks in China. Li et al. (2006) made a similar study, and the main features of their tomography model are generally consistent with those of Huang and Zhao (2006).

Wei et al. (2012) obtained an updated regional Vp tomography beneath East Asia by applying the tomographic method of Zhao et al. (1992) to a better data set consisting of 1,401,797 arrival-time data of 17,180 local and regional earthquakes recorded by 2247 seismic stations of permanent networks and portable arrays. Their new tomography model (Fig. 6.4) has confirmed the main findings of Huang and Zhao (2006) and revealed some new features, in particular in and around the Tibetan Plateau, because they used many new data recorded by the portable seismic stations in Tibet. Some high-V anomalies atop the 410 km discontinuity are detected beneath the eastern North China Craton and Northeast China, suggesting that lithospheric delamination may have occurred there and greatly affected the thermal state, intraplate magmatism and surface topography of that region. The origin of the Wudalianchi volcano in NE China seems associated with the upwelling of asthenospheric materials caused by the subduction-induced lithospheric delamination (Wei et al. 2012). The Indian lithosphere is imaged more clearly as a high-V anomaly and is subducting nearly horizontally beneath the entire, or most parts of, western Tibet, with a small dipping angle to the southernmost part of eastern Tibet. The active Tengchong volcano is underlain by a prominent low-V anomaly in the shallow mantle, which may be caused by the subduction and dehydration of the Burma microplate plate (or the Indian plate; Fig. 5.19). The Hainan volcano is underlain by a plume-like low-V anomaly that extends down to at least 1000 km depth and seems to be related to the deep subduction of the Burma microplate (or the Indian plate) in the west, and deep subduction of the Philippine Sea plate in the east (Zhao and Liu 2010; Wei et al. 2012; Fig. 5.19).

Zhao et al. (2006) determined a 3-D P-wave tomography of the upper mantle beneath the Baikal rift zone in Siberia using teleseismic data (Fig. 5.21). A prominent low-V anomaly is revealed down to a depth of 650 km under Lake Baikal, reflecting a mantle upwelling (plume) which has played an important role in the initiation and evolution of the Baikal rift zone. High-V anomalies are imaged in the lithosphere under the Siberian craton. The Baikal rift formation may also be affected by other factors, such as older (pre-rift) linear lithosphere structures which are favorably positioned relative to the plume upwelling and a favorable orientation of the far-field forces caused by the India–Asia collision (Zhao et al. 2006; Koulakov and Bushenkova 2010).

6.2 Northeast Asia

The major scientific issues of NE Asia are the origin of intraplate volcanism and the mechanism of deep earthquakes in the subducting Pacific slab. Recent high-resolution seismic studies have shed new light on these issues.

The first local tomography of the crust and upper mantle under the Changbai volcano revealed a prominent low-V zone extending down to a depth of ~400 km beneath the volcano and a high-V anomaly in the mantle transition zone (Zhao et al. 2004; Lei and Zhao 2005). However, this local tomography had a lower lateral

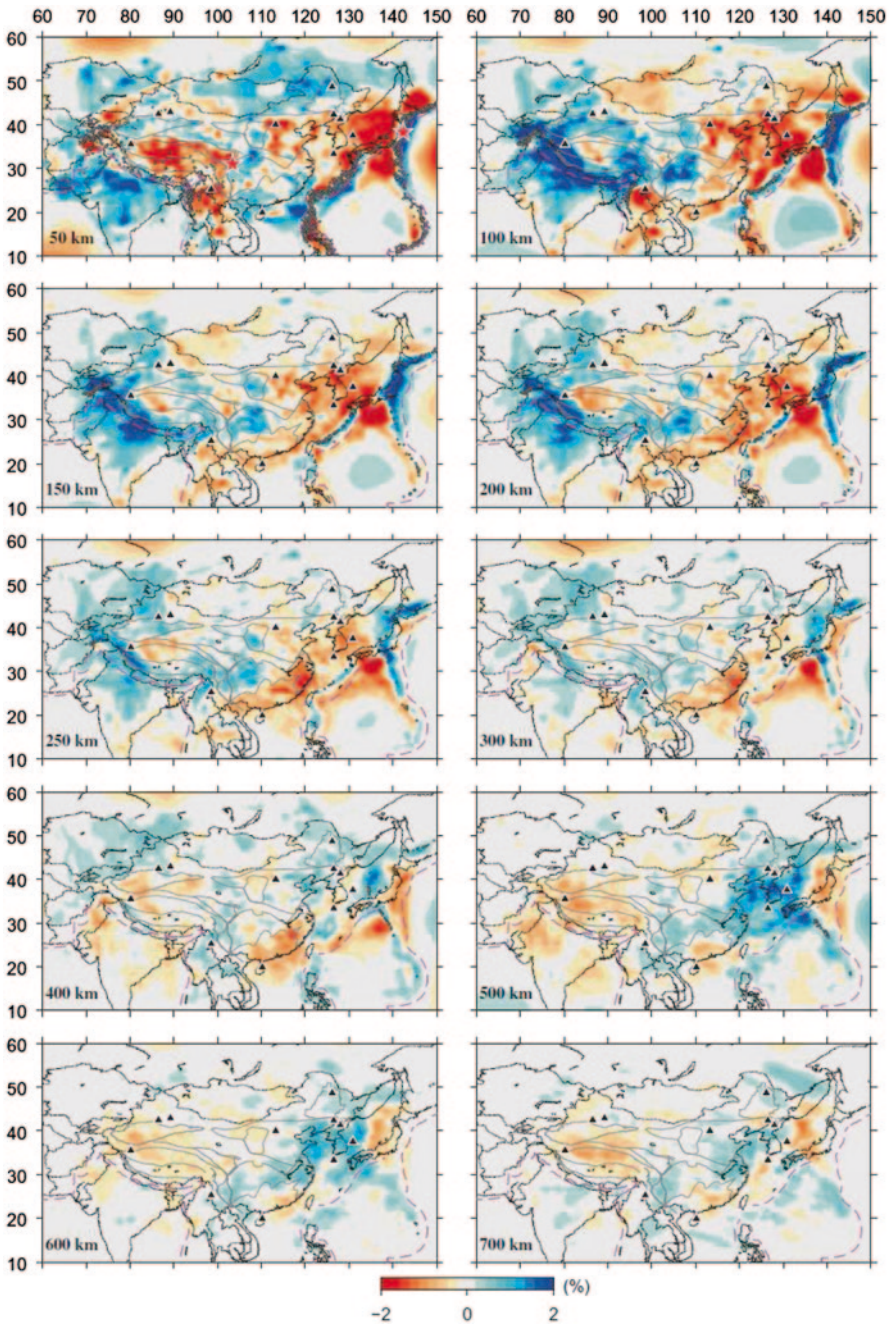

Fig. 6.4 Map views of P-wave tomography beneath East Asia (Wei et al. 2012). The layer depth is indicated at the *lower-left* corner of each map. The *red* and *blue* colors represent slow and fast velocity perturbations, respectively. The velocity perturbation scale is shown at the *bottom*. *White* dots denote earthquakes used in this study that occurred within a depth of 10 km of each layer. The *black* triangles show the active intraplate volcanoes

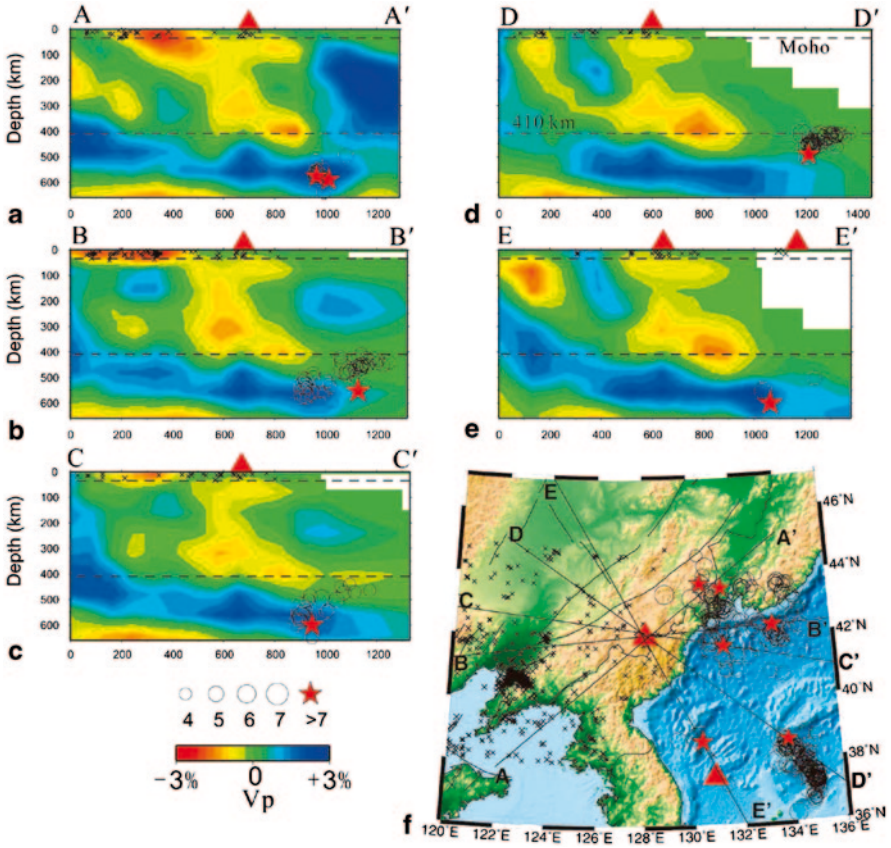

Fig. 6.5 **a-e** Vertical cross-sections of P-wave local tomography along the profiles shown on the inset map (**f**). The *blue* and *red* colors denote high and low velocities, respectively. The *cross* symbols denote crustal earthquakes. Deep earthquakes are shown in open circles ($M < 7.0$) and *red* stars ($M \geq 7.0$). The velocity perturbation and earthquake magnitude scales are shown below (**c**). The two dashed lines denote the Moho and 410 km discontinuities. (After Zhao and Tian 2013)

resolution (~200 km) because of the small data set used which was recorded by only 22 seismic stations.

Zhao et al. (2009) determined a high-resolution (~50 km) local tomography down to a depth of 650 km under the Changbai volcano using a large number of high-quality local and teleseismic data recorded by 645 seismic stations of permanent local seismic networks and 19 portable seismic stations deployed in the Changbai area (Fig. 6.5). A low-V anomaly of ~100 km wide is clearly visible down to a depth of 300 km under the volcano, and the low-V zone extends toward the east in the depth range of 300–480 km. Recent S-wave tomography also shows a prominent low-V anomaly in the crust and upper mantle down to a depth of ~100 km beneath the Changbai volcano (e.g., Zheng et al. 2011; Li et al. 2012). In the lower portion

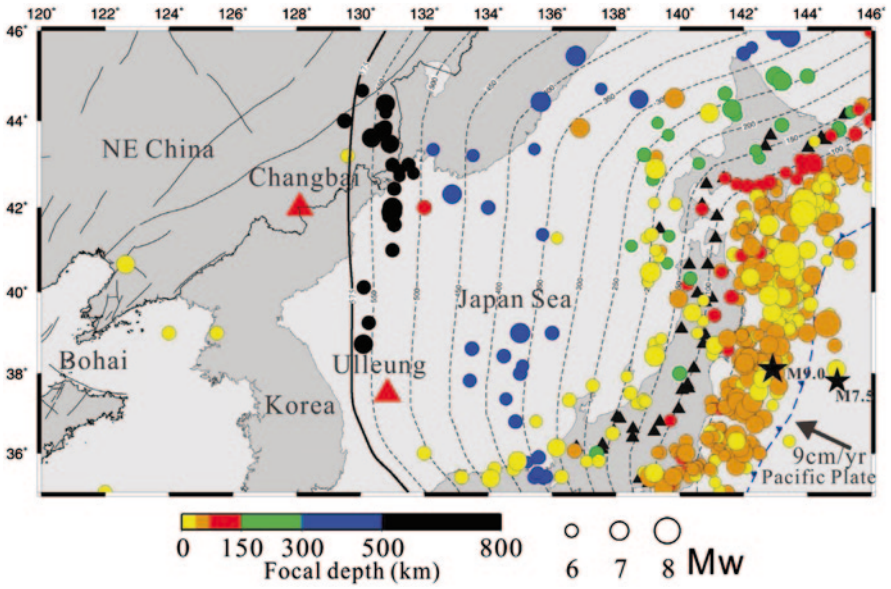

Fig. 6.6 The *dots* show the epicenters of large earthquakes (M ≥6.0) that occurred during the period from 5 January 1900 to 30 September 2009 compiled by the International Seismological Center (ISC). The earthquake magnitude scale is shown at the *bottom*. Different colors of the *dots* denote the focal depths, and the color scale is shown at the *bottom*. The *black stars* represent the great Tohoku-oki earthquake (Mw 9.0) and an outer-rise earthquake (Mw 7.5) which occurred on 11 March 2011. The *contour lines* show the upper boundary of the subducting Pacific slab down to 575 km depth, while toward the west the Pacific slab becomes flat and stagnant in the mantle transition zone. The *blue sawtooth line* denotes the Japan Trench. The *red triangles* denote the active Changbai and Ulleung intraplate volcanoes. The *black triangles* denote the active arc volcanoes on the Japan Islands. The *black lines* in China denote the major active faults. (After Zhao and Tian 2013)

of the mantle transition zone, a continuous high-V anomaly is clearly visible, which represents the stagnant Pacific slab (Fig. 6.5). Zhao and Tian (2013) compared the local tomography with the distribution of earthquakes (M ≥4.0) that have occurred since 1964 in East Asia. Deep earthquakes take place in the subducting Pacific slab at 400–600 km depths. The low-V anomaly under Changbai spreads toward the east to the upper portion of the mantle transition zone above or close to swarms of deep earthquakes in the Pacific slab (Fig. 6.5). Some of the deep earthquakes are greater than M 7.0. A few very deep earthquakes also occurred close to the active Ulleung volcano under the Japan Sea (Fig. 6.6). Unfortunately, the local tomography model has a poor resolution beneath the Ulleung volcano (Fig. 6.5e) because there is no seismic station under the Japan Sea (Zhao et al. 2009).

Of the intraplate volcanoes in NE Asia, Changbai is the largest and most active. Hence, there must be some local causes of the exceptionally significant Changbai volcanism, in addition to the hot upwelling in the BMW. Integrating the findings of geophysical, geochemical and petrological studies so far, Zhao and Tian (2013)

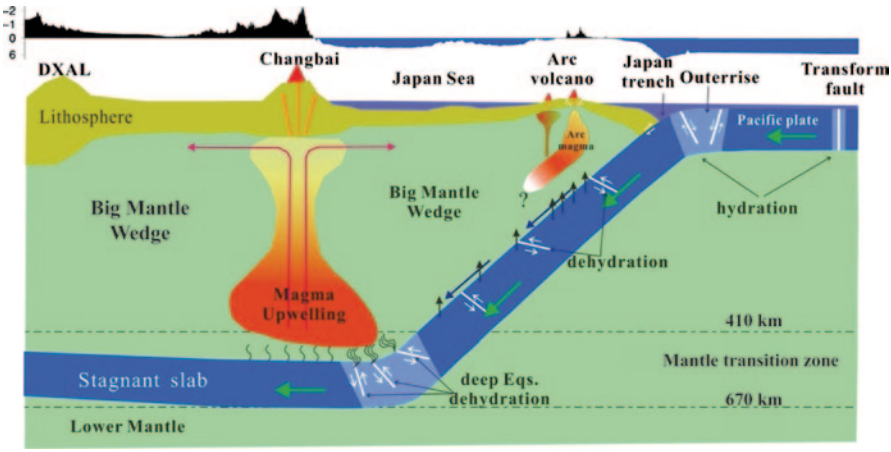

Fig. 6.7 An illustration showing the main features of the upper-mantle structure and dynamics under East Asia, emphasizing the possible relationship between the Changbai intraplate volcanism and deep earthquakes in the Pacific slab (*see text for details*). *DXAL* Daxing-Anling, *MTZ* mantle transition zone. (After Zhao and Tian 2013)

suggest a link between the Changbai volcanism and the deepest earthquakes in the Pacific slab (Fig. 6.7). Many large shallow earthquakes occurred in the Pacific plate in the outer-rise areas close to the Japan Trench (e.g., Kanamori 1971; Hino et al. 2009; Obana et al. 2012), and seawater may enter the deep portion of the oceanic lithosphere through the active normal faults which generated the large outer-rise earthquakes (Peacock 2001; Zhao et al. 2007, 2011). The seawater or fluids may be preserved in the active faults even after the Pacific plate subducts into the mantle. At least some of the large deep earthquakes ($M > 7.0$) are caused by the reactivation of the faults preserved in the subducting slab, and the fluids preserved in the faults within the slab may cause the observed non-double-couple components in the deep earthquake faulting (Frohlich 1994, 2006; Julian et al. 1998; Miller et al. 1998). The fluids preserved in the slab may be released to the overlying mantle wedge through the large deep earthquakes. Because large deep earthquakes occur frequently in the vicinity of the Changbai volcano (Fig. 6.6), much more fluid could be supplied to this volcano than to the other areas in NE Asia, making Changbai the largest and most active intraplate volcano in this region (Zhao and Tian 2013).

It is generally expected, and some studies have shown, that a metastable olivine wedge (MOW) exists in the cold core of the subducting Pacific slab because of a delayed phase transition from olivine to its high-pressure polymorphs (e.g., Iidaka and Suetsugu 1992; Green and Houston 1995; Kirby 1995; Bina et al. 2001; Kaneshima et al. 2007; Kawakatsu and Yoshioka 2011). However, this is still a debatable issue, and even if an MOW exists, its physical properties, such as seismic velocity and density, are still not very clear. Recently, high-quality arrival-time data of deep earthquakes occurring within the Pacific slab under NE China and the Japan Sea are used to study the detailed structure of the slab (Jiang et al. 2008, 2015; Jiang and

Zhao 2011). The deep earthquakes are relocated precisely by applying a modified double-difference location method to arrival-time data recorded at both Chinese and Japanese stations, and travel-time double-residuals are used to estimate seismic velocity within the slab (Jiang et al. 2015). Their results show that an MOW does exist within the Pacific slab under the Japan Sea, and that the MOW has a P-wave velocity 5~8 % lower, and a density 4–7 % lower, than that of the average 1-D Earth model. The MOW in the slab may reduce the speed of plate subduction, and thereby might play an important role in the generation of deep earthquakes (Jiang et al. 2008, 2015).

6.3 North China Craton

In recent years, in China, the mechanism of lithospheric thinning and the reactivation of the North China Craton (NCC) has been a hot topic in many geoscience fields, and a number of researchers have investigated this issue using geological, geophysical and geochemical approaches. Archean cratons generally have a cold, old and thick lithosphere keel, and exhibit low heat flow and lack of volcanism and large earthquakes. However, the NCC is an exception and many large earthquakes have occurred there since historic times up to the present, such as the 1679 Sanhe earthquake (M 8.0) near Beijing, the 1966 Xintai earthquake (M 7.2), the 1975 Haicheng earthquake (M 7.5), and the 1976 Tangshan earthquake (M 7.8), among many others (Huang and Zhao 2004, 2009; Wang et al. 2013b). The NCC is the Chinese part of the Sino-Korean Craton, which contains some of the oldest known continental rocks, being as old as 3.8 Ga (e.g., Liu et al. 1992; Wilde et al. 2002; Kusky and Li 2003; Santosh et al. 2009).

The NCC can be divided into three blocks. Its western and eastern blocks are two major Archean continental nuclei which are separated by a major lithospheric boundary in its central block (e.g., Zhao et al. 2001). Multidisciplinary studies show that the NCC eastern block has experienced significant lithospheric destruction from the Late Mesozoic to the Cenozoic, in contrast to the long-term stabilization of the NCC western block (Fan 1992; Menzies et al. 1993; Xu 2001; Deng et al. 2004; Gao et al. 2004; Wu et al. 2005; Zheng et al. 2007; Yang et al. 2008; Chen 2010). Several major geologic events have affected the NCC reactivation since the late Mesozoic, and compound geological processes, rather than just a single event, caused the NCC reactivation (Menzies et al. 1993; Wu et al. 2005; Zheng et al. 2007; Yang et al. 2008; Tian et al. 2009; Zhao et al. 2009, 2011; Tian and Zhao 2011, 2013).

Concerning the thinning and destruction mechanism of the lithosphere under the eastern NCC, three kinds of models have been proposed: asthenospheric erosion (e.g., Xu 2001; Zheng et al. 2007), hydration weakening (e.g. Niu 2005), and lithospheric delamination (e.g., Deng et al. 2004; Gao et al. 2004; Wu et al. 2005). The role of mantle flow beneath the NCC is an important element of all these models. Zhao and Xue (2010) suggested three end-member models based on the possible mantle flow patterns under the NCC. These were upwelling mantle flow (e.g., Yuan

1999; Xu 2001; Deng et al. 2004; Tian et al. 2009), horizontal mantle flow associated with the westward subduction of the Pacific plate (e.g., Ren et al. 2002; Ai et al. 2003; Zhao et al. 2004, 2009; Tian and Zhao 2011, 2013), and a regional convective flow induced by lithospheric delamination due to gravity instability (e.g., Gao et al. 2004; Wu et al. 2005; Xu and Zhao 2009), which are roughly related to the above-mentioned thinning models. Therefore, studying the mantle flow pattern is very important for understanding the structure and dynamics under the NCC. So far many workers have used the SKS splitting method to study seismic anisotropy and flow patterns beneath the NCC (e.g., Huang et al. 2008, 2011; Zhao and Xue 2010; Chang et al. 2012). Shear-wave splitting, however, reflects an integrated effect along the ray path, which has a poor resolution in the depth direction.

Although many researchers have made tomographic studies of the NCC region (e.g., Huang and Zhao 2004, 2009; Qi et al. 2006; Tian et al. 2009; Xu and Zhao 2009; Tian and Zhao 2011; Wang et al. 2012), they determined only 3-D isotropic velocity variations in the crust and upper mantle. Wang et al. (2013b) determined a 3-D P-wave anisotropic tomography of the crust and uppermost mantle beneath the NCC using arrival times of local earthquakes. Their results show significant lateral heterogeneities beneath the NCC. The lower crust and uppermost mantle beneath the North China Basin show widespread low-V anomalies which may reflect high-temperature materials caused by the late Mesozoic basaltic magmatism. Low-V anomalies also exist beneath the Trans-North China Orogen, which may reflect asthenospheric upwelling since the late Mesozoic. Large crustal earthquakes generally occurred in high-V zones in the upper to middle crust, whereas low-V and high-conductivity anomalies, that may represent fluid-filled, fractured rock matrices, are revealed in the lower crust to the uppermost mantle under source zones of the large earthquakes. The crustal fluids may lead to weakening of the seismogenic layer in the upper and middle crust, and hence cause the large crustal earthquakes. NW–SE P-wave fast velocity directions are revealed in the uppermost mantle under the central parts of the eastern NCC, suggesting that mantle minerals were possibly regenerated but that they have kept the original fossil anisotropy formed before the new lithospheric mantle was produced during the late Mesozoic to the Cenozoic (Wang et al. 2013b).

P-wave anisotropic tomography beneath the NCC is determined using a large number of high-quality arrival-time data from local earthquakes and teleseismic events (Tian and Zhao 2013), which reveals a depth-dependent azimuthal anisotropy in the crust and upper mantle down to a depth of 600 km (Fig. 6.8). In the NCC western block, the fast velocity direction (FVD) varies from east-west in the southern part to NE-SW in the northern part, which may reflect either the interaction between the Yangtze block and the NCC or fossil lithospheric fabrics in the craton. Under the NCC eastern block, a uniform NW-SE FVD is revealed in the lower part of the upper mantle (300–410 km depth) and the mantle transition zone (410–660 km depth), which may reflect horizontal and upwelling flows in the BMW above the stagnant Pacific slab in the mantle transition zone. The NCC central block exhibits a NE-SW FVD, being consistent with the surface tectonic orientation there. These results suggest that the cold and thick (>300 km) cratonic root of the NCC

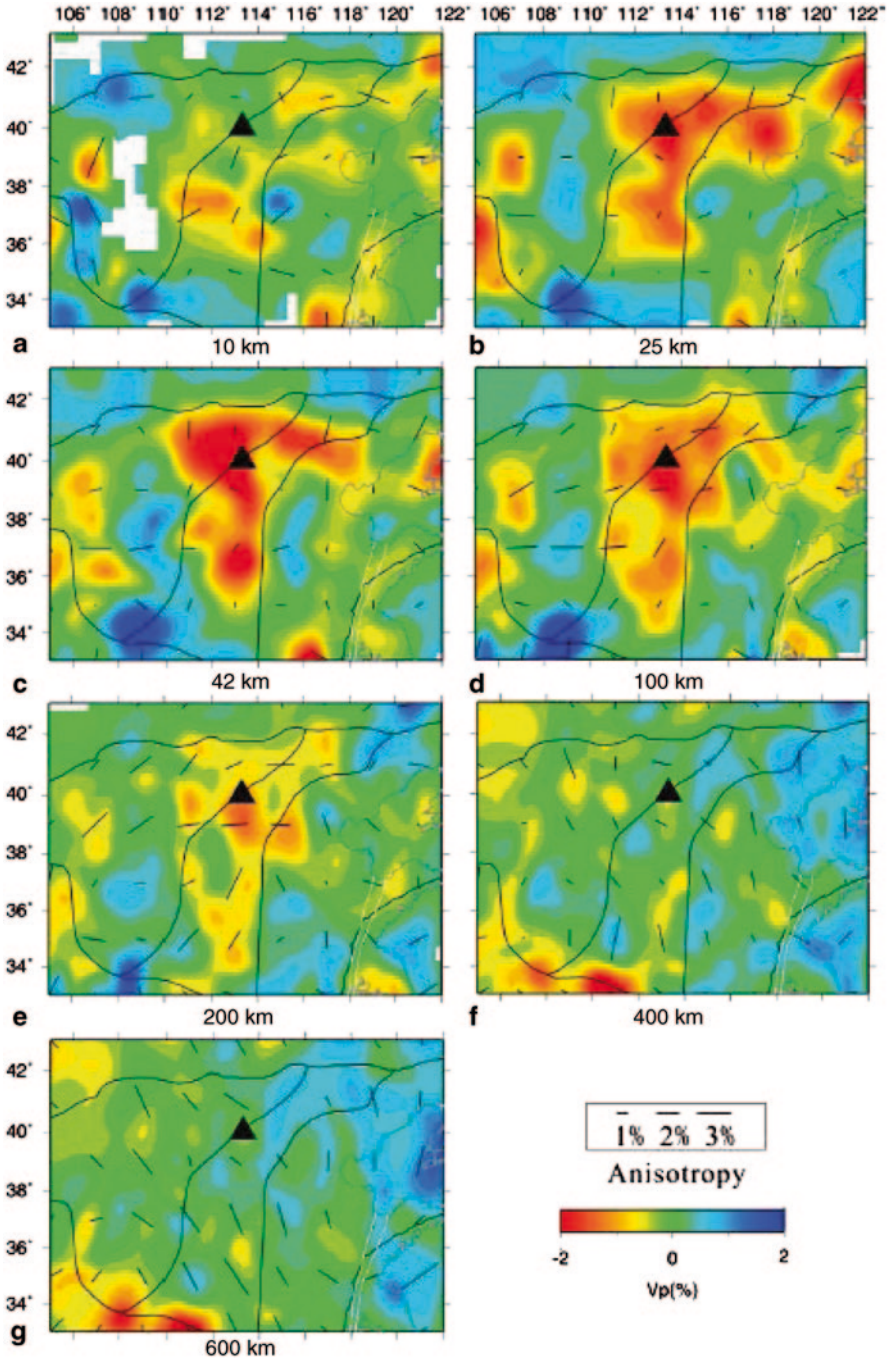

Fig. 6.8 P-wave anisotropy tomography in the crust and *upper* mantle beneath the North China Craton. The layer depth is shown *below* each map. The *blue* and *red* colors denote high and low velocities, respectively. The orientation and length of the short bars represent the fast-velocity direction and anisotropic amplitude, respectively. The scales for the velocity anomaly and the anisotropic amplitude are shown below (f). The *black* triangle denotes the Datong volcano. (After Tian and Zhao 2013)

western block may obstruct the NW-SE trending mantle flow induced by the Pacific plate subduction, resulting in a NE-SW trending mantle flow under the central block. These results indicate that the corner flow in the BMW associated with the deep subduction of the Pacific plate is the main cause of the NCC reactivation and mantle dynamics under East China (Tian and Zhao 2013).

The upper mantle structure beneath the Middle and Lower Yangtze River region in East China has been investigated using teleseismic tomography (Jiang et al. 2013). Two pieces of high-V lithosphere are revealed: one is located at < 100 km depth, while the other is at 250–400 km depth. The two pieces of lithosphere are separated by a low-V asthenosphere. These results suggest that asthenospheric upwelling and lithospheric delamination have taken place in this region, which are caused by the BMW processes above the stagnant Pacific slab (Zhao et al. 2004, 2009). Rich ejections of magmas from the BMW to the surface in the Mesozoic may have caused a mineralization zone in this region (Jiang et al. 2013).

6.4 Southeast China

Southeast (SE) China is located at the southeastern margin of the Eurasian plate which is interacting with the Philippine Sea (PHS) plate along the Nankai Trough, Ryukyu arc, and around Taiwan Island. The PHS plate moves toward the northwest at a rate of ~40 mm/year (e.g., Seno et al. 1993; Yu et al. 1997), resulting in the Taiwan orogen which is one of the youngest and most active orogens in the world (e.g., Sibuet and Hsu 2004). The structure and tectonics around Taiwan and SE China have been of interest to many researchers who have investigated the detailed bathymetry, seismicity, earthquake mechanisms, morphological features, seismogenic structures, and the state of strain and stress in this region (e.g., Kao et al. 1998, 2000; Wang et al. 2006; Chen et al. 2009; Cheng 2009; Wu et al. 2009; Huang et al. 2010; Zheng et al. 2013).

A high-resolution P-wave tomography of the crust and upper mantle in and around Taiwan was determined using local and teleseismic data simultaneously (Wang et al. 2006). A high-V anomaly was revealed from the surface down to a depth of 300 km beneath South Taiwan, which reflects the subducted Eurasian lithosphere (Fig. 3.13). This result indicates that the tectonic framework of Taiwan changes from subduction in the south to collision in the north. The subducted Eurasian lithosphere colliding with the subducted PHS plate may have contributed to mountain building, active seismicity and crustal deformation in and around Taiwan (Wang et al. 2006). Zheng et al. (2013) obtained improved tomographic images in the same region, which have confirmed the early results of Wang et al. (2006).

Huang et al. (2010) applied a tomography method (Zhao et al. 1994) to 5671 relative travel-time residuals from 257 teleseismic events recorded by 69 seismic stations to determine the 3-D P-wave velocity model of the upper mantle under SE China (Fig. 6.9). Their results show prominent low-V anomalies under SE China, which may reflect the remnant magma chambers and channels of the Late Mesozoic

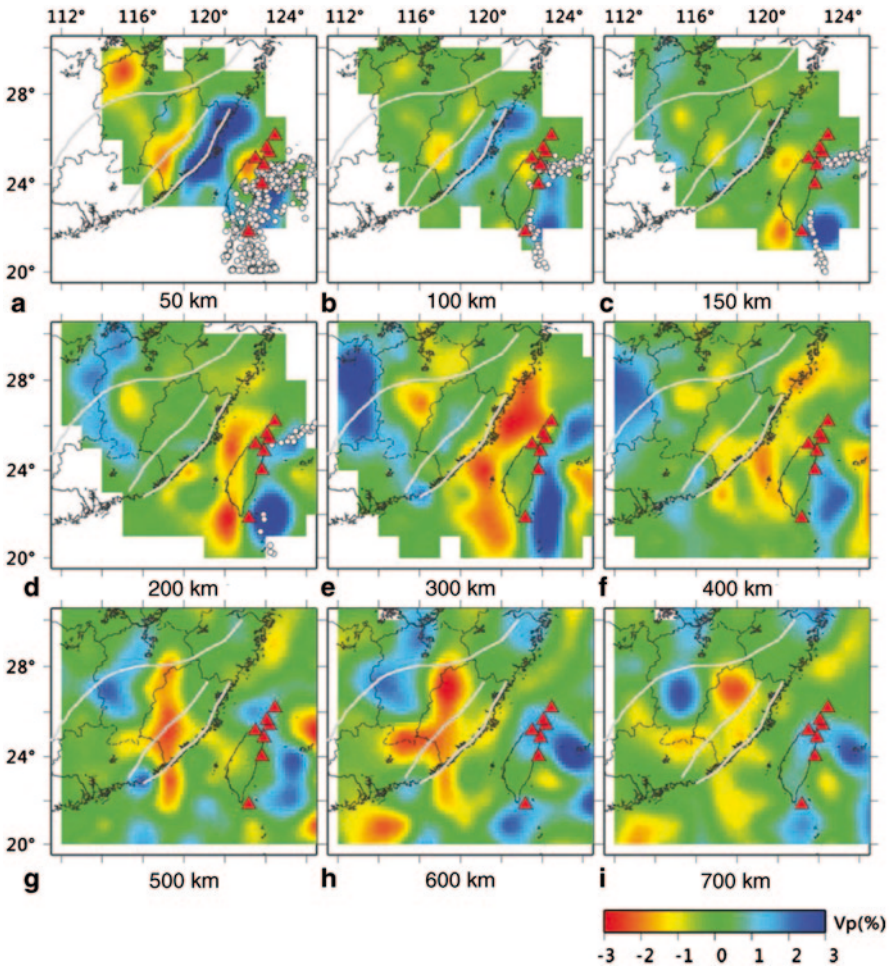

Fig. 6.9 Map views of P-wave tomography beneath Southeast China (Huang et al. 2010). The layer depth is shown below each map. The *red* and *blue* colors denote slow and fast velocities, respectively. The velocity perturbation scale is shown at the *bottom*. The *gray* bold lines and the *black* thin lines denote major faults and province boundaries in Mainland China. The *red* triangles show active arc volcanoes

igneous rocks, which may be reheated by the upwelling mantle flow from the lower mantle driven by the slab deep subductions in East Asia during the Cenozoic. High-V anomalies are revealed in the upper mantle to the east of Taiwan, which represent the subducted Eurasian plate. Their results also suggest that the break-off of the subducted Eurasian plate was caused by its strong interaction with the PHS plate under central and North Taiwan. The slab break-off may have created a mantle window through which the asthenospheric flow arises, resulting in high heat flow and rapid uplift in the Taiwan orogeny (Huang et al. 2010).

Xia and Zhao (2014) have used active source wide-angle seismic data to determine a high-resolution P-wave crustal tomography beneath the onshore-offshore area of Hong Kong at the southern end of a broad belt dominated by the Late Mesozoic intrusive and extrusive rocks in the coastal region of SE China. They revealed a localized high-V anomaly in the lower crust offshore between Hong Kong and Dangan Island, which may reflect basaltic underplating that is closely associated with the formation of voluminous silicic eruptions and granitoid plutons in and around Hong Kong. Tilted high-V zones connecting with the localized high-V anomaly in the lower crust exist in the entire crust beneath Dangan Island and the calderas of Hong Kong. Taking into account previous results of geochemical, petrological and numerical modeling studies, they suggested that the tilted high-V zones reflect mingling of mafic and felsic end members and an extreme degree of crustal partial melt extraction necessary to generate a large amount of extrusive rocks in the calderas, leading to cooled magma conduits as a manifestation of a solidified Late Mesozoic magmatic plumbing system in the crust. Taking into account the petrological and geochemical characteristics of Late Mesozoic granites and basalt in SE China, Xia and Zhao (2014) suggested that the subduction and dehydration of the paleo-Pacific plate might trigger the basaltic magma underplating and result in an extensive crust-mantle interaction, which not only provided necessary heat energy to cause the crustal partial melting, but also added minor mafic materials to the newly-generated granitic melts. This model explains the tomographic results, as well as the intimate mingling of coeval mafic and silicic magmas in Hong Kong. Intersecting faults could play an important role in forming magma conduits and loci of fissure-like volcanic centers (Xia and Zhao 2014).

Hainan Island is located in southernmost China and separated from Mainland China by the Qiongzhou strait (Fig. 6.1). On Hainan Island, there is an active volcano which has erupted many times since the Eocene. Lei et al. (2009a) determined a P-wave tomography of the crust and upper mantle beneath Hainan using both local and teleseismic data recorded by nine permanent seismic stations in Hainan Island and the Leizhou peninsula. They revealed a continuous low-V anomaly from the surface down to a depth of 250 km beneath Hainan, which is NW–SE tilting and has a diameter of ~80 km (Fig. 5.20). This low-V zone is interpreted to be the Hainan plume in the upper mantle (Lei et al. 2009a).

6.5 Tibetan Plateau and Southwest China

The Tibetan Plateau was created by the Indian-Asian continental collision ~50 million years ago (Molnar and Tapponnier 1975; Yin and Harrison 2000). Several models have been proposed to explain its formation mechanism and tectonics, such as rigid block extrusion (Tapponnier et al. 2001), crustal thickening (England and Houseman 1986), and crustal channel flow (Royden et al. 1997), etc. Although many studies have been made using various approaches, controversy still remains regarding some fundamental issues, such as the nature and extent of the northward

subducting Indian plate beneath the Tibetan Plateau, and whether the Asian plate has underthrusted southward beneath the plateau (Zhang et al. 2012; Zhao et al. 2014).

Many findings have been obtained using the data acquired during geophysical experiments conducted by the INDEPTH and Hi-CLIMB projects for studying the Tibetan Plateau (e.g., Kosarev et al. 1999; Chen et al. 2010; Kind et al. 2002; Rapine et al. 2003; Unsworth et al. 2004; Zhao et al. 2010; Zhang et al. 2012). Teleseismic tomography has revealed a high-V zone beneath Tibet, south of the Bangong-Nujiang suture, which reflects the subducting Indian lithosphere (Tilmann et al. 2003). This interpretation is supported by receiver-function studies (e.g., Nabelek et al. 2009). Li et al. (2008) showed that the extending range of the north-dipping Indian plate decreases from the west to the east, whereas other researchers have suggested that the Indian plate underthrusts beneath the whole plateau (e.g., Zhou and Murphy 2005; Priestley et al. 2006). Some authors have suggested that the Asian plate is descending beneath central and eastern Tibet (Kind et al. 2002; Kumar et al. 2006; Nabelek et al. 2009; Chen et al. 2010; Zhao et al. 2010), whereas others have shown that central and northern Tibet is underlain by a hot upper mantle (Rapine et al. 2003; Unsworth et al. 2004; Zhao et al. 2014).

Geological studies have shown that the uplift of eastern Tibet occurred with only slight internal deformation, which has been explained as being due to an influx of lower crustal flow (Royden et al. 1997; Shen et al. 2001). Many geophysical results support this crustal flow model (e.g., Shapiro et al. 2004; Pei et al. 2007; Xu et al. 2007; Li et al. 2008; Lei and Zhao 2009; Fu et al. 2010; Wang et al. 2010; Yang et al. 2012). Although this model has been widely accepted, the detailed flow pattern is still subject to debate. Such a large-scale material flow beneath eastern Tibet, or even the whole plateau, may be interrupted by bodies which are not adaptive for flowing, such as the eclogited Indian crust with a higher density and a lower temperature. The existence of strong lateral heterogeneities in the lower crust (e.g., Yao et al. 2008; Wang et al. 2010) is hard to explain if the flow is not interrupted. GPS and seismic anisotropy results suggest that the extrusion may also occur in the deep Tibetan lithosphere (Wang et al. 2008). A magnetotelluric survey revealed two major zones or channels of high electrical conductivity at a depth of 20–40 km (Bai et al. 2010).

Detailed P-wave tomography down to a depth of 400 km beneath central Tibet was determined using a large number of teleseismic data recorded by portable seismic stations (Zheng et al. 2007; He et al. 2010). The results show that the Indian plate has subducted beneath central Tibet and its frontier has passed through the Bangong-Nujiang Suture and extended northward beneath the Qiangtang Terrane at 34° north latitude (Fig. 6.10). A low-V anomaly is revealed within the Tethyan Himalayan Sequences close to the Yarlung-Zangbo Suture, which is the boundary between the Tethyan Himalayan Sequences and the Lhasa Terrane. The subduction of the Indian plate has caused the east–west extension in central Tibet. The Indian slab beneath the region has not sutured with the Asian lithospheric mantle in the north. This tomographic result can explain many geological and geophysical

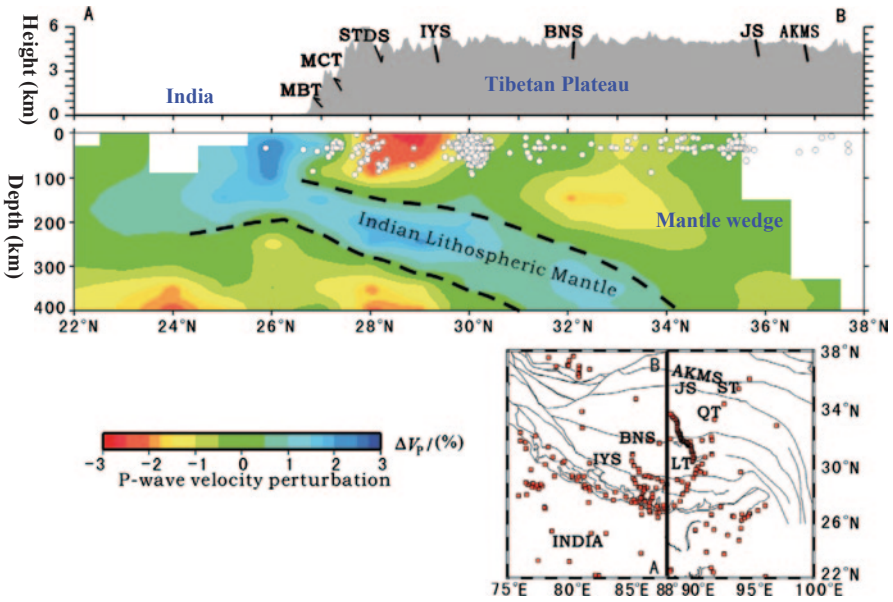

Fig. 6.10 North-South vertical cross-section of P-wave tomography under the Tibetan Plateau along a profile as shown on the inset map. The *red* and *blue* colors denote slow and fast velocities, respectively. The velocity perturbation scale is shown at the *bottom*. *White* dots denote earthquakes that occurred within a 100 km width of the profile. The *red* squares on the map show the portable seismic stations used for the tomographic imaging. (Modified from Zheng et al. 2007).

features, such as the strong seismic anisotropy in the upper mantle and the K-rich and ultra-potassic lavas in northern Tibet (Zheng et al. 2007; He et al. 2010).

A 3-D P-wave velocity model of the crust and upper mantle down to a depth of 400 km beneath eastern Tibet was obtained using many portable seismic stations of the ASCENT project and the Namche Barwa Broadband Seismic Network (Zhang et al. 2012). They collected 16,508 arrival times of P, Pn and Pg phases from 573 local and regional earthquakes and 7450 P-wave arrivals of 435 teleseismic events. Such a high-quality data set enabled a higher-resolution tomography under eastern Tibet to be obtained than in previous studies. Low-V zones were found not to be interconnected well at a shallow depth, suggesting complex material flows in the study region. The Indian plate is underthrusting sub-horizontally under eastern Tibet, and its extent decreases from the west to the east. In the north, the Asian lithospheric mantle is detected under the vicinity of the Qaidam Basin. Between the subducting Indian and Asian slabs, there is an obvious low-V anomaly which may reflect an upwelling mantle flow (Zhang et al. 2012).

P-wave tomography of the crust and upper mantle beneath western Tibet has been obtained using local and teleseismic data recorded by portable seismic stations deployed by the ANTILOPE project (Zhao et al. 2014). This new tomography shows that the Indian plate is currently sub-horizontal and underthrusting to the Jinsha river suture at ~ 100–250 km depths, suggesting that the subduction process has

evolved over time. The Asian plate is also imaged clearly from the surface down to a depth of ~100 km, and it is located under the Tarim Basin north of the Altyn Tagh fault. The Indian and Asian plates are separated by a prominent low-V zone under northern Tibet, which may account for the warm crust and upper mantle beneath that region, and thus explain the different features of magmatism between southern and northern Tibet. High-V zones are revealed beneath the Lhasa terrane, which may reflect the reconstructed Tibetan crust and Lhasa lithosphere which have interrupted the crustal flow under the westernmost Tibetan plateau (Zhao et al. 2014).

Many tomographic studies have been made for the crustal and upper mantle structure beneath the so-called North-South Seismic Belt which is located at the eastern margin of the Tibetan Plateau (e.g., Huang et al. 2002; Wang et al. 2003, 2010; Lei and Zhao 2009; Li et al. 2013b; Wei et al. 2013; Cheng et al. 2014; and the many references therein). Wang et al. (2010) collected a large number of P- and S-wave arrival-time data of both local earthquakes and teleseismic events to invert simultaneously for P- and S-wave velocity tomography in the crust and upper mantle. Their P- and S-velocity images are generally consistent with each other from the crust to the mantle transition zone (Fig. 6.11). The North-South Seismic Belt exhibits significant lateral heterogeneities from the mountainous areas of southeastern Tibet to the Yangtze Platform. Low-V anomalies exist in the upper crust beneath the Sichuan basin, being consistent with the surface geological features that the foreland basin contains primarily Mesozoic and Paleozoic sedimentary rocks with a thickness of several kilometers. The deep part of the Yangtze Platform is characterized by a cratonic lithosphere dipping southwestward down to a depth of 400 km beneath the southeastern margin of the Tibetan Plateau, in sharp contrast to low-V anomalies in the upper mantle beneath the Songpan-Ganzi Fold System and the Northwest Qiangtang Block. In the lower crust and uppermost mantle, a low-V layer is revealed west of the Yangtze Platform, reflecting a lower-crustal flow. The seismotectonics in the North-South Seismic Belt is controlled by the lower-crustal ductile flow and strong heterogeneities in the upper mantle under SW China, in addition to the dominant role of the India-Asia collision (Wang et al. 2010). The detailed 3-D crustal and uppermost mantle structure has been investigated for the source areas of the 2008 Wenchuan earthquake (M 8.0) and the 2013 Lushan earthquake (M 7.0) which occurred in the Longmenshan fault zone of the North-South Seismic Belt, and the results show that the nucleation of the two large earthquakes was affected by fluids in the lower crust flow (Lei and Zhao 2009; Li et al. 2013b).

The active Tengchong volcano is located in the western part of Yunnan Province in SW China. A high-resolution local tomography of the crust and upper mantle beneath Yunnan was determined using a large number of local and teleseismic data (Lei et al. 2009b). A clear low-V column is revealed in a depth range of 0–400 km beneath the Tengchong volcano and high-V anomalies exist in the mantle transition zone. Taking into account the tomographic image and geochemical and geological results, Lei et al. (2009b) suggested that Tengchong is a rift-related volcano caused by a hot upwelling flow associated with deep subduction and dehydration of the Indian plate (or the Burma microplate).

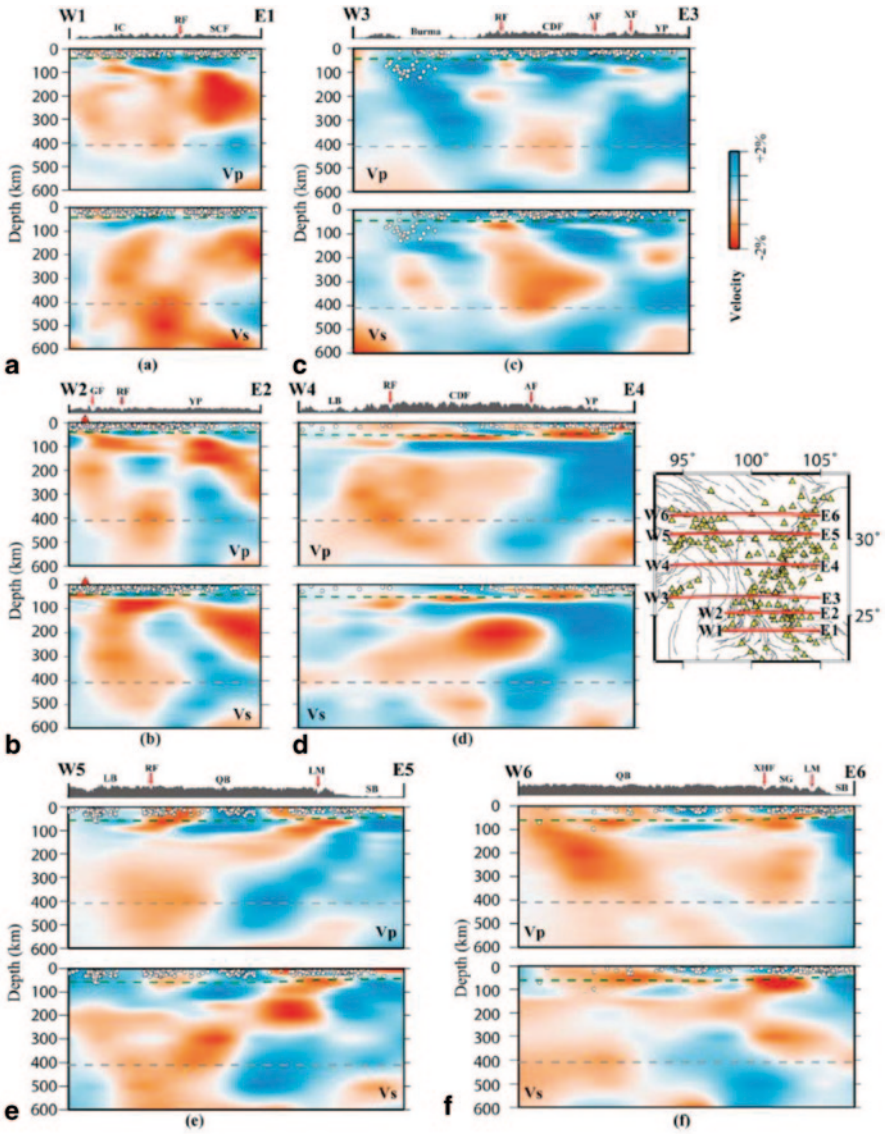

Fig. 6.11 **a–f** Vertical cross-sections of P- and S-wave velocity images along the lines shown on the inset map. The *white* dots denote the background seismicity within a 20 km width of each profile. The *green* and *gray* dashed lines show the Moho and 410 km discontinuities. The *red* and *blue* colors denote low and high velocities, respectively. The velocity perturbation (*in %*) scale is shown beside (**c**). The surface topography is shown atop each profile. The *red* triangles denote the Tengchong volcano. The *arrows* above each section show the locations of active faults. *IC* Indochina, *SCF* South China System, *YP* Yangtze Platform, *CDF* Chuan-Dian Fragment, *LB* Lhasa Block, *QB* Qiangtang Block, *SG* Songpan-Ganzi Fold System, *SB* Sichuan Foreland basin, *RF* Red River fault, *AF* Anninghe fault, *XF* Xiaojiang fault, *GF* Gaoligong fault, *LM* Longmen-Shan fault, *XHF* Xianshuihe fault. (After Wang et al. 2010)

A 3-D P-wave anisotropy tomography beneath SE Tibet and adjacent regions was determined by applying the method of Wang and Zhao (2008, 2013) to a large number of arrival-time data of local and teleseismic events (Wei et al. 2013). A low-V layer of ~20 km thick was revealed in the lower crust, which reflects a mechanically weak zone capable of flow on a geological timescale. This anisotropy tomography shows that the flow direction changes when it encounters the mechanically strong Sichuan basin (Fig. 6.12). Most of the large earthquakes (including the 2008 Wenchuan and the 2013 Lushan earthquakes) took place at the margin of the ductile flow in the lower crust. In the upper mantle the subducting Indian plate is imaged clearly, which has reached near the Jinsha River suture. The seismic anisotropy pattern changes with depth (Fig. 6.12), suggesting that the upper crust and the lithospheric mantle deform separately beneath most parts of eastern Tibet (Wei et al. 2013).

6.6 Summary

Recent high-resolution local and regional tomography results shed new light on the intraplate tectonics, magmatism and mantle dynamics beneath East Asia. The main findings of these studies are summarized as follows.

The subducting Pacific slab is stagnant in the mantle transition zone under East China, and a big mantle wedge (BMW) has formed in the upper mantle above the stagnant slab. The hot and wet upwelling flows in the BMW have caused the intraplate volcanoes in NE Asia, lithospheric thinning and the reactivation of the North China Craton, and large intraplate earthquakes in the region.

Deep earthquakes in the Pacific slab may be related to a metastable olivine wedge in the slab. Large deep earthquakes may release fluids preserved within the inner part of the slab to the overlying BMW, making Changbai the largest and most active intraplate volcano in East Asia.

Prominent low-V anomalies exist beneath SE China, reflecting remnant magma chambers and channels of the Late Mesozoic igneous rocks, which may be reheated by the upwelling mantle flow from the lower mantle driven by deep slab subductions in East Asia during the Cenozoic. The Eurasian plate is subducting beneath South Taiwan. Break-off of the subducted Eurasian plate was caused by its strong interaction with the Philippine Sea plate under central and North Taiwan. The slab break-off may have created a window through which the asthenospheric flow arises, resulting in high heat flow and rapid uplift in the Taiwan orogeny.

The Indian plate is subducting nearly horizontally to the entire or most parts of Western Tibet and with a shallow dipping angle to the southernmost part of Eastern Tibet. Hence, the high elevation and flatness of the Tibetan Plateau are caused by different mechanisms from the west to the east. A plume-like low-V anomaly is revealed beneath central Tibet, which may represent the upwelling of hot asthenospheric materials leading to the post-collisional magmatism of the region.

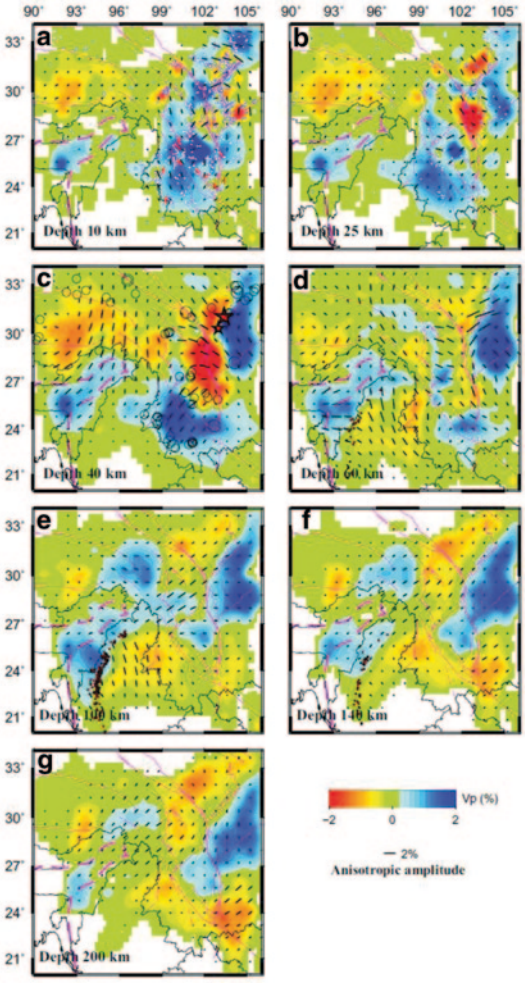

Fig. 6.12 Map views of P-wave anisotropic tomography beneath eastern Tibetan Plateau and Southwest China. The layer depth is shown at the *lower-left* corner of each map. The *red* and *blue* colors denote slow and fast velocity perturbations, respectively. The azimuth and length of each bar represent the fast-velocity direction and anisotropic amplitude, respectively. The *red* bars in (**a**) show the results of S-wave splitting measurements of local earthquakes (Shi et al. 2006). The scales for the velocity perturbation and anisotropic amplitude are shown below (f). The *black* open circles in (**c**) represent the large crustal earthquakes (M > 6.0) that occurred since 1970. The *white* and *red* dots show background seismicity in the crust and the intermediate-depth earthquakes, respectively. The large and small *red* stars in (**c**) represent the 2008 Wenchuan earthquake (M8.0) and the 2013 Lushan earthquake (M7.0), respectively. The *pink* lines show the large active faults and sutures in the study region. The purple dashed lines show the plate boundaries. (After Wei et al. 2013)

The active Tengchong volcanism is caused by an upwelling flow in the (big) mantle wedge above the subducting Indian plate or the Burma microplate. The Hainan volcano in southernmost China is a hot spot fed by a deep mantle plume, whereas the Hainan plume is caused by deep subduction of the Indian plate in the west and deep subduction of the Philippine Sea plate in the east. Interactions between the plate subduction and mantle upwelling (plume) are taking place in the Earth's interior.

References

Abdelwahed, M.F., Zhao, D.: Waveform modelling of local earthquakes in southwest Japan. Earth Planets Space. **57**, 1039–1054 (2005)

Abdelwahed, M.F., Zhao, D.: Genetic waveform modeling for the crustal structure in Northeast Japan. J. Asian Earth Sci. **89**, 66–75 (2014)

Ai, Y., Zheng, T., Xu, W., He, Y., Dong, D.: A complex 660 km discontinuity beneath northeast China. Earth Planet. Sci. Lett. **212**, 63–71 (2003)

An, M., Feng, M., Zhao, Y.: Destruction of lithosphere within the North China Craton inferred from surface wave tomography. Geochem. Geophys. Geosyst. **10**, Q08016 (2009)

Bai, D.H., et al.: Crustal deformation of the eastern Tibetan plateau revealed by magnetotelluric imaging. Nat. Geosci. **3**, 358–362 (2010)

Bina, C., Stein, S., Marton, F., Van Ark, E.: Implications of slab mineralogy for subduction dynamics. Phys. Earth Planet. Inter. **127**, 51–66 (2001)

Chang, L., Wang, C., Ding, Z.: Upper mantle anisotropy beneath North China from shear wave splitting measurements. Tectonophysics. **522**, 235–242 (2012)

Chen, L.: Concordant structural variations from the surface to the base of the upper mantle in the North China Craton and its tectonic implications. Lithos. **120**, 96–115 (2010)

Chen, R., Kao, H., Liang, W., Shin, T., Tsai, Y., Huang, B.: Three-dimensional patterns of seismic deformation in the Taiwan region with special implication from the 1999 Chi-Chi earthquake sequence. Tectonophysics. **466**, 140–151 (2009)

Chen, W.P., Martin, M., Tseng, T., Nowack, R., Hung, S., Huang, B.: Shear-wave birefringence and current configuration of converging lithosphere under Tibet. Earth Planet. Sci. Lett. **295**, 297–304 (2010)

Cheng, W.: Tomographic imaging of the convergent zone in Eastern Taiwan—a subducting forearc sliver revealed? Tectonophysics. **466**, 170–183 (2009)

Cheng, B., Cheng, S., Zhang, G., Zhao, D.: Seismic structure of the Helan-Liupan-Ordos western margin tectonic belt in North-Central China and its geodynamic implications. J. Asian Earth Sci. **87**, 141–156 (2014)

Deng, J., Mo, X., Zhao, H., Wu, Z., Luo, Z., Su, S.: A new model for the dynamic evolution of Chinese lithosphere: continental roots-plume tectonics. Earth Sci. Rev. **65**, 223–275 (2004)

England, P., Houseman, G.: Finite strain calculations of continental deformation: 2. Comparison with the India-Asia collision zone. J. Geophys. Res. **91**, 3664–3676 (1986)

Fan, W., Menzies, M.: Destruction of aged lower lithosphere and accretion of asthenosphere mantle beneath eastern China. Geotect. Metal. **16**, 171–180 (1992)

Friederich, W.: The S-velocity structure of the East Asian mantle from inversion of shear and surface waveforms. Geophys. J. Int. **153**, 88–102 (2003)

Frohlich, C.: Earthquakes with non-double-couple mechanisms. Science. **264**, 804–809 (1994)

Frohlich, C.: Deep Earthquakes (p. 573). Cambridge University Press, Cambridge (2006)

Fu, Y., Li, A., Chen, Y.: Crustal and upper mantle structure of southeast Tibet from Rayleigh wave tomography. J. Geophys. Res. **115**, B12323 (2010)

Fukao, Y., Obayashi, M., Inoue, H., Nenbai, M.: Subducting slabs stagnant in the mantle transition zone. J. Geophys. Res. **97**, 4809–4822 (1992)
Gao, S., Rudnick, R., Yuan, H.: Recycling lower continental crust in the North China craton. Nature. **432**, 892–897 (2004)
Green, H.W., Houston, H.: The mechanics of deep earthquakes. Ann. Rev. Earth Planet. Sci. **23**, 169–213 (1995)
He, R., Zhao, D., Gao, R., Zheng, H.: Tracing the Indian lithospheric mantle beneath central Tibetan Plateau using teleseismic tomography. Tectonophysics. **491**, 230–243 (2010)
Hearn, T., Wang, S., Ni, J., Xu, Z., Yu, Y., Zhang, X.: Uppermost mantle velocities beneath China and surrounding regions. J. Geophys. Res. **109**, B11301 (2004)
Hino, R., et al.: Insight into complex rupturing of the immature bending normal fault in the outer slope of the Japan Trench from aftershocks of the 2005 Sanriku earthquake (Mw = 7.0) located by ocean bottom seismometry. Geochem. Geophys. Geosyst. **10**, Q07O18 (2009)
Huang, J., Zhao, D.: Crustal heterogeneity and seismotectonics of the region around Beijing, China. Tectonophysics. **385**, 159–180 (2004)
Huang, J., Zhao, D.: High-resolution mantle tomography of China and surrounding regions. J. Geophys. Res. **111**, B09305 (2006)
Huang, J., Zhao, D.: Seismic imaging of the crust and upper mantle under Beijing and surrounding regions. Phys. Earth Planet. Inter. **173**, 330–348 (2009)
Huang, J., Zhao, D., Zheng, S.: Lithospheric structure and its relationship to seismic and volcanic activity in southwest China. J. Geophys. Res. **107**, JB000137 (2002)
Huang, Z.X., Su, W., Peng, Y., Zheng, Y., Li, H.: Rayleigh wave tomography of China and adjacent regions. J. Geophys. Res. **108**, 2073 (2003). doi:10.1029/2001JB001696
Huang, Z., Xu, M., Wang, L., Mi, N., Yu, D., Li, H.: Shear wave splitting in southern margin of the Ordos Block, north China. Geophys. Res. Lett. **35**, L19301 (2008)
Huang, Z., Wang, L., Zhao, D., Xu, M., et al.: Upper mantle structure and dynamics beneath Southeast China. Phys. Earth planet. Inter. **182**, 161–169 (2010)
Huang, Z., Wang, L., Zhao, D., Mi, N., Xu, M.: Seismic anisotropy and mantle dynamics beneath China. Earth planet. Sci. Lett. **306**, 105–117 (2011)
Iidaka, T., Suetsugu, D.: Seismological evidence for metastable olivine inside a subducting slab. Nature. **356**, 593–595 (1992)
Jiang, G., Zhao, D.: Metastable olivine wedge in the subducting Pacific slab and its relation to deep earthquakes. J. Asian Earth Sci. **42**, 1411–1423 (2011)
Jiang, G., Zhao, D., Zhang, G.: Seismic evidence for a metastable olivine wedge in the subducting Pacific slab under Japan Sea. Earth Planet. Sci. Lett. **270**, 300–307 (2008)
Jiang, G., Zhang, G., Lu, Q., Shi, D., Xu, Y.: 3-D velocity model beneath the Middle–Lower Yangtze River and its implication to the deep geodynamics. Tectonophysics. **606**, 36–47 (2013)
Jiang, G., Zhao, D., Zhang, G.: Detection of metastable olivine wedge in the western Pacific slab and its geodynamic implications. Phys. Earth Planet. Inter. **238**, 1–7 (2015)
Julian, B., Miller, A., Foulger, G.: Non-double-couple earthquakes 1. Theory. Rev. Geophys. **36**, 525–549 (1998)
Kanamori, H.: Seismological evidence for a lithospheric normal faulting: the Sanriku earthquake of 1933. Phys. Earth Planet. Inter. **4**, 289–300 (1971)
Kaneshima, S., Okamoto, T., Takenaka, H.: Evidence for a metastable olivine wedge inside the subducted Mariana slab. Earth Planet. Sci. Lett. **258**, 219–227 (2007)
Kao, H., Shen, S., Ma, K.: Transition from oblique subduction to collision: earthquakes in the southernmost Ryukyu arc-Taiwan region. J. Geophys. Res. **103**, 7211–7229 (1998)
Kao, H., Huang, G., Liu, C.: Transition from oblique subduction to collision in the northern Luzon arc-Taiwan region: constraints from bathymetry and seismic observations. J. Geophys. Res. **105**, 3059–3080 (2000)
Kawakatsu, H., Yoshioka, S.: Metastable olivine wedge and deep dry cold slab beneath southeast Japan. Earth Planet. Sci. Lett. **303**, 1–10 (2011)
Kind, R., et al.: Seismic images of crust and upper mantle beneath Tibet: Evidence for Eurasian plate subduction. Science. **298**, 1219–1221 (2002)

Kirby, S.H.: Interslab earthquakes and phase changes in subducting lithosphere. Rev. Geophys. **33**, 287–297 (1995)
Kosarev, G., Kind, R., Sobolev, S.V., Yuan, X., Hanka, W., Oreshin, S.: Seismic evidence for a detached Indian lithospheric mantle beneath Tibet. Science. **283**, 1306–1309 (1999)
Koulakov, I., Bushenkova, N.: Upper mantle structure beneath the Siberian craton and surrounding areas based on regional tomographic inversion of P and PP travel times. Tectonophysics. **486**, 81–100 (2010)
Kumar, P., Yuan, X., Kind, R., Ni, J.: Imaging the colliding Indian and Asian lithospheric plates beneath Tibet. J. Geophys. Res. **111**, B06308 (2006)
Kusky, T., Li, J.: Paleoproterozoic tectonic evolution of the North China Craton. J. Asian Earth Sci. **22**, 383–397 (2003)
Lee, T., Lawver, L.: Cenozoic plate reconstruction of Southeast Asia. Tectonophysics. **251**, 85–138 (1995)
Lei, J., Zhao, D.: P-wave tomography and origin of the Changbai intraplate volcano in Northeast Asia. Tectonophysics. **397**, 281–295 (2005)
Lei, J., Zhao, D.: Structural heterogeneity of the Longmenshan fault zone and the mechanism of the 2008 Wenchuan earthquake (Ms 8.0). Geochem. Geophys. Geosyst. **10**, Q10010 (2009)
Lei, J., Zhao, D., Steinberger, B., Wu, B., Shen, F., Li, Z.: New seismic constraints on the upper mantle structure of the Hainan plume. Phys. Earth Planet. Inter. **173**, 33–50 (2009a)
Lei, J., Zhao, D., Su, Y.: Insight into the origin of the Tengchong intraplate volcano and seismotectonics in southwest China from local and teleseismic data. J. Geophys. Res. **114**, B05302 (2009b)
Li, Z.X.: Tectonic history of the major East Asian lithospheric blocks since the mid-Proterozoic—A synthesis. In: Flower, M. et al. (eds.) Mantle Dynamics and Plate Interactions in East Asia, Geodyn. Ser., vol. **27**, pp. 211–243, AGU, Washington, D.C. (1998)
Li, X., Yuan, X.: Receiver functions in northeast China—implications for slab penetration into the lower mantle in Northwest Pacific subduction zone. Earth Planet. Sci. Lett. **216**, 679–691 (2003)
Li, C., van der Hilst, R., Toksoz, N.: Constraining P-wave velocity variations in the upper mantle beneath Southeast Asia. Phys. Earth Planet. Inter. **154**, 180–195 (2006)
Li, C., Van der Hilst, R., Meltzer, A., Engdahl, E.: Subduction of the Indian lithosphere beneath the Tibetan Plateau and Burma. Earth Planet. Sci. Lett. **274**, 157–168 (2008)
Li, Y., Wu, Q., Pan, J., Sun, L.: S-wave velocity structure of northeastern China from joint inversion of Rayleigh wave phase and group velocities. Geophys. J. Int. **190**, 105–115 (2012)
Li, J., Wang, X., Wang, X., Yuen, D.: P and SH velocity structure in the upper mantle beneath Northeast China: evidence for a stagnant slab in hydrous mantle transition zone. Earth planet. Sci. Lett. **367**, 71–81 (2013a)
Li, Z., Tian, B., Liu, S., Yang, J.: Asperity of the 2013 Lushan earthquake in the eastern margin of Tibetan Plateau from seismic tomography and aftershock relocation. Geophys. J. Int. **195**, 2016–2022 (2013b)
Liang, C., Song, X., Huang, J.: Tomographic inversion of Pn travel times in China. J. Geophys. Res. **109**, (2004) doi:10.1029/2003JB002789
Liu, F., Wu, H., Liu, J., Hu, G., Li, Q., Qu, K.: 3-D velocity image beneath the Chinese continent and adjacent regions. Geophys. J. Int. **101**, 379–394 (1990)
Liu, D., Nutman, P., Compston, W., She, Q.: Remnants of >380 Ma crust in the Chinese part of the Sino-Korean craton. Geology. **20**, 339–342 (1992)
Liu, K., Gao, S., Gao, Y., Wu, J.: Shear wave splitting and mantle flow associated with the deflected Pacific slab beneath northeast Asia. J. Geophys. Res. **113**, (2008) doi 10.1029/2007jb005178
Menzies, M., Fan, W., Zhang, M.: Palaeozoic and Cenozoic lithoprobe and the loss of >120 km of Archean lithosphere, Sino-Korean craton, China. In: Prichard, H., Alabaster, T., Harris, N. et al. (eds.). Magmatic Processes and Plate Tectonics, Geol. Soc. Spec. Publ., **76**, 71–81 (1993)
Metcalfe, I.: Palaeozoic and Mesozoic tectonic evolution and palaeogeography of East Asian crustal fragments: the Korean Peninsula in context. Gondwana Res. **9**, 24–46 (2006)

Miller, A., Foulger, G., Julian, B.: Non-double-couple earthquakes 2. Observations. Rev. Geophys. **36**, 551–568 (1998)
Molnar, P., Tapponnier, P.: Cenozoic tectonics of Asia: Effects of a continental collision. Science. **189**, 419–426 (1975)
Nabelek, J., Hetenyi, G., Vergne, J., Sapkota, S., Kafle, B., Jiang, M., Su, H. P., Chen, J., Huang B. S., Team, H.: Underplating in the Himalaya-Tibet collision zone revealed by the Hi-CLIMB Experiment. Science. **325**, 1371–1374 (2009)
Niu, Y.: Generation and evolution of basaltic magmas: some basic concepts and a new view on the origin of Mesozoic- Cenozoic basaltic volcanism in Eastern China. Geol. J. China Uni. **11**, 9–46 (2005)
Northrup, C., Royden, L., Burchfiel, B.: Motion of the Pacific plate relative to Eurasia and its potential relation to Cenozoic extension along the eastern margin of Eurasia. Geology. **23**, 719–722 (1995)
Obana, K., et al.: Normal-faulting earthquakes beneath the outer slope of the Japan Trench after the 2011 Tohoku earthquake: implications for the stress regime in the incoming Pacific plate. Geophys. Res. Lett. **39**, L00G24 (2012)
Panning, M., Cao, A., Kim, A., Romanowicz, B.: Non-linear 3-D Born shear wave form tomography in Southeast Asia. Geophys. J. Int. **190**, 463–475 (2012)
Peacock, S.: Are the lower planes of double seismic zones caused by serpentine dehydration in subducting oceanic mantle? Geology. **29**, 299–302 (2001)
Pei, S., Zhao, J., Sun, Y., Xu, Z., Wang, S., Liu, H., Rowe, C., Toksoz, M., Gao, X.: Upper mantle seismic velocities and anisotropy in China determined through Pn and Sn tomography. J. Geophys. Res. **112**, (2007) doi 10.1029/2006jb004409
Priestley, K., Debayle, E., McKenzie, D., Pilidou, S.: Upper mantle structure of eastern Asia from multimode surface waveform tomography. J. Geophys. Res. **111**, B10304 (2006)
Qi, C., Zhao, D., Chen, Y., Chen, Q., Wang, B.: 3-D P and S wave velocity structures and their relationship to strong earthquakes in the Chinese capital region. Chinese J. Geophys. **49**, 805–815 (2006)
Rapine, R., Tilmann, F., West, M., Ni, J., Rodgers, A.: Crustal structure of northern and southern Tibet from surface wave dispersion analysis. J. Geophys. Res. **108**(B2), 2120 (2003)
Ren, J., Tamaki, K., Li, S., Zhang, J.: Late Mesozoic and Cenozoic rifting and its dynamic setting in eastern China and adjacent areas. Tectonophysics. **344**, 175–205 (2002)
Royden, L., Burchfiel, B., King, R., Wang, E., Chen, Z., Shen, F., Liu, Y.: Surface deformation and lower crustal flow in eastern Tibet. Science. **276**, 788–790 (1997)
Santosh, M., Zhao, D., Kusky, T.: Mantle dynamics of the Paleoproterozoic North China Craton: A perspective based on seismic tomography. J. Geodyn. **49**, 39–53 (2009)
Seno, T., Stein, S., Gripp, A.: A model for the motion of the Philippine Sea plate consistent with NUVEL-1 and geological data. J. Geophys. Res. **89**, 17941–17948 (1993)
Shapiro, N., Ritzwoller, M., Molnar, P., Levin, V.: Thinning and flow of Tibetan crust constrained by seismic anisotropy. Science. **305**, 233–236 (2004)
Shen, F., Royden, L., Burchfiel, B.: Large-scale crustal deformation of the Tibetan Plateau. J. Geophys. Res. **106**, 6793–6816 (2001)
Shi, Y., Gao, Y., Wu, J., Luo, Y., Su, Y.: Seismic anisotropy of the crust in Yunnan, China: polarizations of fast shear-waves. Acta Seismol. Sinica. **19**, 620–632 (2006)
Sibuet, J., Hsu, S.: How was Taiwan created? Tectonophysics. **379**, 159–181 (2004)
Tajima, F., Katayama, I., Nakagawa, T.: Variable seismic structure near the 660 km discontinuity associated with stagnant slabs and geochemical implications. Phys. Earth planet. Inter. **172**, 183–198 (2009)
Tapponnier, P., Xu, Z., Roger, F., Meyer, B., Arnaud, N., Wittlinger, G., Yang, J.: Oblique stepwise rise and growth of the Tibet plateau. Science. **294**, 1671–1677 (2001)
Tian, Y., Zhao, D.: Destruction mechanism of the North China Craton: Insight from P and S wave mantle tomography. J. Asian Earth Sci. **42**, 1132–1145 (2011)
Tian, Y., Zhao, D.: Reactivation and mantle dynamics of North China Craton: Insight from P-wave anisotropy tomography. Geophys. J. Int. **195**, 1796–1810 (2013)

Tian, Y., Zhao, D., Sun, R., Teng, J.: Seismic imaging of the crust and upper mantle beneath the North China Craton. Phys. Earth planet. Inter. **172**, 169–182 (2009)
Tian, X., Zhao, D., Zhang, H., Tian, Y., Zhang, Z.: Mantle transition zone topography and structure beneath the central Tien Shan orogenic belt. J. Geophys. Res. **115**, B10308 (2010)
Tian, X., Teng, J., Zhang, H., Zhang, Z., Zhang, Y., Yang, H., Zhang, K.: Structure of crust and upper mantle beneath the Ordos Block and the Yinshan Mountains revealed by receiver function analysis. Phys. Earth Planet. Inter. **184**, 186–193 (2011)
Tilmann, F., Ni, J., Team, I.: Seismic imaging of the downwelling Indian lithosphere beneath central Tibet. Science. **300**, 1424–1427 (2003)
Unsworth, M., Wenbo, W., Jones, A.G., Li, S., Bedrosian, P., Booker, J., Sheng, J., Ming, D., Handong, T.: T.: Crustal and upper mantle structure of northern Tibet imaged with magnetotelluric data. J. Geophys. Res. **109**, B02403 (2004)
Wang, J., Zhao, D.: P-wave anisotropic tomography beneath Northeast Japan. Phys. Earth Planet. Inter. **170**, 115–133 (2008)
Wang, J., Zhao, D.: P-wave tomography for 3-D radial and azimuthal anisotropy of Tohoku and Kyushu subduction zones. Geophys. J. Int. **193**, 1166–1181 (2013)
Wang, C.Y., Chan, W., Mooney, W.: Three-dimensional velocity structure of crust and upper mantle in southwestern China and its tectonic implications. J. Geophys. Res. **108**, 2442 (2003)
Wang, Z., Zhao, D., Wang, J., Kao, H.: Tomographic evidence for the Eurasian lithosphere subducting beneath South Taiwan. Geophys. Res. Lett. **33**, L18306 (2006)
Wang, C.Y., Flesch, L., Silver, P., Chang, L., Chan, W.: Evidence for mechanically coupled lithosphere in central Asia and resulting implications. Geology. **36**, 363–366 (2008)
Wang, Z., Zhao, D., Wang, J.: Deep structure and seismogenesis of the north-south seismic zone in Southwest China. J. Geophys. Res. **115**, B12334 (2010)
Wang, W., Wu, J., Fang, L.: High resolution Rayleigh wave phase velocity tomography in northern North China. Geophys. J. Int. **189**, 647–658 (2012)
Wang, S., Niu, F., Zhang, G.: Velocity structure of the uppermost mantle beneath East Asia from Pn tomography and its dynamic implications. J. Geophys. Res. **118**, (2013a) doi: 10.1002/jgrb.50085
Wang, J., Zhao, D., Yao, Z.: Crustal and uppermost mantle structure and seismotectonics of North China Craton. Tectonophysics. **582**, 177–187 (2013b)
Wei, W., Xu, J., Zhao, D., Shi, Y.: East Asia mantle tomography: New insight into plate subduction and intraplate volcanism. J. Asian Earth Sci. **60**, 88–103 (2012)
Wei, W., Zhao, D., Xu, J.: P-wave anisotropic tomography in Southeast Tibet: New insight into the lower crustal flow and seismotectonics. Phys. Earth planet. Inter. **222**, 47–57 (2013)
Wilde, S., Zhao, G., Sun, M.: Development of the North China craton during the Late Archean and its final amalgamation at 1.8 Ga: some speculations on its position within a global Palaeoproterozoic supercontinent. Gondwana Res. **5**, 85–94 (2002)
Wu, F., Lin, J., Wilde, S., Zhang, X., Yang, J.: Nature and significance of the Early Cretaceous giant igneous event in eastern China. Earth Planet. Sci. Lett. **233**, 103–119 (2005)
Wu, W., Hsu, S., Lo, C., Chen, H., Ma, K.: Plate convergence at the westernmost Philippine Sea Plate. Tectonophysics. **466**, 162–169 (2009)
Xia, S., Zhao, D.: Late Mesozoic magmatic plumbing system in the onshore-offshore area of Hong Kong: Insight from 3-D active-source seismic tomography. J. Asian Earth Sci. **96**, 46–58 (2014)
Xu, Y.: Thermo-tectonic destruction of the Archean lithospheric, keel beneath the Sino-Korean Cratonin China: evidence, timing and mechanism. Phys. Chem. Earth. **26**, 747–757 (2001)
Xu, L., Rondenay, S., van der Hilst, R.: Structure of the crust beneath the southeastern Tibetan Plateau from teleseismic receiver functions. Phys. Earth Planet. Inter. **165**, 176–193 (2007)
Xu, P., Zhao, D.: Upper-mantle velocity structure beneath the North China Craton: Implications for lithospheric thinning. Geophys. J. Int. **177**, 1279–1283 (2009)
Yang, J., Wu, F., Wilde, S., Belousova, E., Griffin, L.: Mesozoic decratonization of the North China block. Geology. **36**, 467–470 (2008)

Yang, Y., Ritzwoller, M., Zheng, Y., Shen, W., Levshin, A., Xie, Z.: A synoptic view of the distribution and connectivity of the mid-crustal low velocity zone beneath Tibet. J. Geophys. Res. **117**, B04303 (2012)

Yao, H., Beghein, C., van der Hilst, R.: Surface wave array tomography in SE Tibet from ambient seismic noise and two-station analysis– II. Crustal and upper-mantle structure. Geophys. J. Int. **173**, 205–219 (2008)

Ye, L., Li, J., Tseng, T., Yao, Z.: A stagnant slab in a water bearing mantle transition zone beneath northeast China: implications from regional SH waveform modeling. Geophys. J. Int. **186**, 706–710 (2011)

Yin, A., Harrison, T.: Geologic evolution of the Himalayan-Tibetan orogeny. Annu. Rev. Earth Planet. Sci. **28**, 211–280 (2000)

Yu, S., Chen, H., Kuo, L.: Velocity field of GPS stations in the Taiwan area. Tectonophysics. **274**, 41–59 (1997)

Yuan, X.: Velocity structure of the Qinling lithosphere and mushroom cloud model. Sci. China. **39**, 235–244 (1999)

Zhang, H., Zhao, D., Zhao, J., Xu, Q.: Convergence of the Indian and Eurasian plates under eastern Tibet revealed by seismic tomography. Geochem. Geophys. Geosyst. **13**, Q06W14 (2012)

Zhao, D.: Seismic structure and origin of hotspots and mantle plumes. Earth Planet. Sci. Lett. **192**, 251–265 (2001)

Zhao, D.: Global tomographic images of mantle plumes and subducting slabs: Insight into deep Earth dynamics. Phys. Earth Planet. Inter. **146**, 3–34 (2004)

Zhao, D.: Seismic images under 60 hotspots: Search for mantle plumes. Gondwana Res. **12**, 335-355 (2007)

Zhao, D., Liu, L.: Deep structure and origin of active volcanoes in China. Geosci. Frontiers. **1**, 31–44 (2010)

Zhao, L., Xue, M.: Mantle flow pattern and geodynamic cause of the North China Craton reactivation: Evidence from seismic anisotropy. Geochem. Geophys. Geosyst. **11**, (2010) doi:10.1029/2010gc003068

Zhao, D., Tian, Y.: Changbai intraplate volcanism and deep earthquakes in East Asia: A possible link? Geophys. J. Int. **195**, 706–724 (2013)

Zhao, D., Hasegawa, A., Horiuchi, S.: Tomographic imaging of P and S wave velocity structure beneath northeastern Japan. J. Geophys. Res. **97**, 19909–19928 (1992)

Zhao, D., Hasegawa, A., Kanamori, H.: Deep structure of Japan subduction zone as derived from local, regional and teleseismic events. J. Geophys. Res. **99**, 22313–22329 (1994)

Zhao, G., Wilde, A., Cawood, A., Sun, M.: Archean blocks and their boundaries in the North China Craton: lithological, geochemical, structural and P-T path constraints and tectonic evolution. Precambrian Res. **107**, 45–73 (2001)

Zhao, D., Lei, J., Tang, R.: Origin of the Changbai volcano in northeast China: Evidence from seismic tomography. Chinese Sci. Bul. **49**, 1401–1408 (2004)

Zhao, D., Lei, J., Inoue, T., Yamada, A., Gao, S.: Deep structure and origin of the Baikal rift zone. Earth Planet. Sci. Lett. **243**, 681–691 (2006)

Zhao, D., Maruyama, S., Omori, S.: Mantle dynamics of western Pacific to East Asia: New insight from seismic tomography and mineral physics. Gondwana Res. **11**, 120–131 (2007)

Zhao, D., Tian, Y., Lei, J., Liu, L., Zheng, S.: Seismic image and origin of the Changbai intraplate volcano in East Asia: Role of big mantle wedge above the stagnant Pacific slab. Phys. Earth planet. Inter. **173**, 197–206 (2009)

Zhao, J.M., et al.: The boundary between the Indian and Asian tectonic plates below Tibet. Proc. Natl. Acad. Sci. U.S.A. **107**, 11229–11233 (2010)

Zhao, D., Yu, S., Ohtani, E.: East Asia: Seismotectonics, magmatism and mantle dynamics. J. Asian Earth Sci. **40**, 689–709 (2011)

Zhao, D., Yamamoto, Y., Yanada, T.: Global mantle heterogeneity and its influence on teleseismic regional tomography. Gondwana Res. **23**, 595–616 (2013)

Zhao, J.M., Zhao, D., Zhang, H., et al.: P-wave tomography and dynamics of the crust and upper mantle beneath western Tibet. Gondwana Res. **25**, 1690–1699 (2014)

Zheng, J., Griffin, W., O'Reilly, S., Yu, C., Zhang, H., Pearson, N., Zhang, M.: Mechanism and timing of lithospheric modification and replacement beneath the eastern North China Craton: peridotitic xenoliths from the 100 Ma Fuxin basalts and a regional synthesis. Geochim. Cosmochim. Acta. **71**, 5203–5225 (2007)

Zheng, Y., Shen, W., Zhou, L., Yang, Y., Xie, Z., Ritzwoller, M.: Crust and uppermost mantle beneath the North China Craton, northeastern China, and the Sea of Japan from ambient noise tomography. J. Geophys. Res. **116**, B12312 (2011)

Zheng, H., Gao, R., Li, T., Li, Q., He, R.: Collisional tectonics between the Eurasian and Philippine Sea plates from tomography evidences in Southeast China. Tectonophysics. **606**, 14–23 (2013)

Zheng, H., Li, T., Gao, R., Zhao, D., He, R.: Teleseismic P-wave tomography evidence for the Indian lithospheric mantle subducting northward beneath the Qiangtang terrane. Chin. J. Geophys. **50**, 1418–1426 (2007)

Zhou, H., Murphy, M.: Tomographic evidence for wholesale underthrusting of India beneath the entire Tibetan plateau. J. Asian Earth Sci. **25**, 445–457 (2005)

Chapter 7
Global Tomography and Deep Earth Dynamics

Abstract High-resolution global tomography models shed new light on the deep structure and fate of subducting slabs and the origin of hotspots and mantle plumes, as well as deep Earth dynamics. Ray paths of direct and reflected P-waves in a 3-D global velocity model deviate up to 100 km from those in a 1-D Earth model, and the differences in their travel times in the 1-D and 3-D velocity models amount to ~4 s, indicating the necessity of using a 3-D ray tracing technique to calculate ray paths and travel times precisely in global tomographic studies. Ten kinds of later phases transmitted and reflected in the mantle and core are used to conduct global tomographic inversions, and it is found that the later phase data can greatly improve the ray path coverage in the mantle and hence the resolution of mantle tomography. Whole-mantle heterogeneities outside the target volume of a regional tomography can cause significant changes (~0.2–0.4 s) to the observed relative travel-time residuals of a teleseismic event. The pattern of regional tomography remains the same even after correcting for the whole-mantle heterogeneity, but there are some changes in the amplitude of velocity anomalies in regional tomography. Hence, it is necessary to correct for mantle heterogeneity outside the target volume in order to obtain a better regional tomography.

Keywords Global tomography · Geodynamics · Subducting slabs · Mantle plumes · Hotspots

Since the pioneering work of Dziewonski et al. (1977), seismic tomography has been applied to study the three-dimensional (3-D) seismic structure of the crust and mantle of the whole Earth. During the past 3 decades, many global tomographic models have been determined, which have provided deep insights into the basic issues of geodynamics and signify a revolution in Earth sciences (Dziewonski and Anderson 1984). The representative 3-D global models are, e.g., Dziewonski (1984), Inoue et al. (1990), Vasco et al. (1995), Zhou (1996), van der Hilst et al. (1997), Bijwaard et al. (1998), Boschi and Dziewonski (1999, 2000), Fukao et al. (2001), Zhao (2001, 2004), Montelli et al. (2004), Li et al. (2008), Simons et al. (2011), and Zhao et al. (2013) for P-wave velocity tomography, and Woodhouse and Dziewonski (1984), Zhang and Tanimoto (1993), Su et al. (1994), Li and Romanowicz (1996), Ritsema et al. (1999), Megnin and Romanowicz (2000), Grand

D. Zhao, *Multiscale Seismic Tomography,* Springer Geophysics,
DOI 10.1007/978-4-431-55360-1_7

(2002), Takeuchi (2007), Simons et al. (2010), and Schaeffer and Lebedev (2013) for S-wave velocity tomography. Many workers have also determined 3-D global models of seismic attenuation, anisotropy and density in the mantle (e.g., Tanimoto and Anderson 1985; Montagner and Tanimoto 1991; Romanowicz 1995; Ishii and Tromp 1999; Trampert and van Heijst 2002; Becker et al. 2003; Gung and Romanowicz 2004; Simons et al. 2010). Lateral depth variations of major velocity discontinuities in the Earth's interior, such as the Moho, the 410 and 660 km discontinuities, and the core-mantle boundary (CMB), have also been investigated (e.g., Morelli and Dziewonski 1987; Obayashi and Fukao 1997; Mooney et al. 1998; Flanagan and Shearer 1998; Gu et al. 1998, 2012; Sze and van der Hilst 2003; Houser et al. 2008). In addition, many workers have conducted forward modeling of seismic waveforms, which have complemented the tomographic studies and provided details of structural features, as well as small-scale patterns of mantle heterogeneity (e.g., Garnero and McNamara 2008; Lay and Garnero 2010; Kaneshima 2013). These studies using different approaches have shown that structural heterogeneities in the mantle exhibit various scales, which are associated with dynamic processes in the mantle as well as seismic and volcanic activities and other active tectonics in the crust and lithosphere (Zhao 2009; Zhao et al. 2013).

These global tomographic models are well resolved for large spatial scales (>1000 km), whereas smaller-scale anomalies are not so well determined, even though many geological objects with a lateral extent of the order of 100 km, such as subducting slabs and mantle plumes, play a key role in global geodynamics (Becker and Boschi 2002; Montagner 2011). These smaller-scale structural anomalies in the crust and upper mantle are better imaged by local and regional tomographic models which have a higher spatial resolution (~10–50 km) (e.g., Zhao et al. 2011; Zhao 2012 for the recent reviews).

After having worked on local and regional tomography for nearly 10 years, in 1999 I started my studies of global seismic tomography (Zhao 1999), being motivated by the following three factors. Firstly, Engdahl et al. (1998) reprocessed the ISC (International Seismological Center) data set by relocating the world earthquakes using the depth phases (e.g., pP, pwP, sP), resulting in a new ISC data set having much better quality than before. Bijwaard et al. (1998) obtained an impressive P-wave tomography model of the whole mantle using the reprocessed ISC data set. I became used to the high-quality arrival-time data recorded by the dense local and regional seismic networks in Japan and California and disliked the poor-quality ISC data. The improved ISC data set by Engdahl et al. (1998) and the new tomography model of Bijwaard et al. (1998) motivated me to use the new ISC data for a global tomography study. Secondly, Mooney et al. (1998) published a global map of the Moho topography, and Flanagan and Shearer (1998) published global topography maps of the 410 and 660 km discontinuities. One main feature of my tomographic method (Zhao 1991; Zhao et al. 1992) is that it can deal with complex-shaped velocity discontinuities, and our studies of local and regional tomography have shown that a better tomographic model can be obtained if depth variations of velocity discontinuities (e.g., the Conrad, the Moho, and the subducting slab boundary) are taken into account (e.g., Zhao et al. 1992, 1994, 1995). When see-

ing the results of Mooney et al. (1998) and Flanagan and Shearer (1998), I thought to conduct a global tomography considering the topography of the Moho, 410 and 660 km discontinuities. Thirdly, till 1999 almost all the global tomography studies focused on the imaging of subducting slabs, the cold limbs of mantle convection, whereas few studies focused on the hotspots and mantle plumes, the hot limbs of mantle convection. This was mainly because subducting slabs are generally located beneath continental regions which are covered by seismic networks, and so the slabs are relatively easier to image with seismic tomography, whereas most of the hotspots are located in oceanic regions or poorly instrumented continental regions, such as Africa and Antarctica, hence hotspots and mantle plumes are hard to image seismologically. I thought it interesting to challenge this difficulty by detecting and imaging mantle plumes using global tomography.

Because a great number of global tomography studies have been made during the past 3 decades, as mentioned above, it would be impossible to review all of them here. Hence, in this chapter I draw mainly on the global tomographic studies in which I was involved. The interested reader is referred to a few other comprehensive reviews on this topic, e.g., Dziewonski and Romanowicz (2007), Kind and Li (2007), Lay (2007), Romanowicz and Mitchell (2007), Thurber and Ritsema (2007), Rawlinson et al. (2010), and Montagner (2011).

7.1 Global Tomographic Inversion

Zhao (2001) determined a P-wave tomographic model of the whole crust and mantle, which has the following features when compared with the previous models: (1) depth variations of the Moho, 410 and 670 km discontinuities (Mooney et al. 1998; Flanagan and Shearer 1998) were taken into account; (2) the boundary-grid parameterization scheme (Zhao et al. 1992) was adopted to express the 3-D Earth's structure; (3) an efficient 3-D ray-tracing technique (Zhao et al. 1992) was modified to compute travel times and ray paths at the global scale; and (4) a large number of arrival times of first P phase and reflected (pP, PP, PcP) phases (Fig. 7.1) from the reprocessed ISC data set (Engdahl et al. 1998) were used. Zhao (2004) improved the model of Zhao (2001) using an updated ISC data set, in particular, adding the CMB-diffracted (Pdiff) phase data (Fig. 7.1). The tomographic model of Zhao (2004) explains well a new set of high-quality arrival-time data of the first and later P phases manually collected from original seismograms (Zhao et al. 2006), and it was used to examine the detailed mantle structure beneath 60 possible hotspots on the Earth (Zhao 2007).

One problem of the tomographic models of Zhao (2001, 2004) is in the setup of grid nodes for expressing the 3-D mantle structure. The grid nodes were arranged along the latitudinal and longitudinal lines (the geographic grid; Fig. 7.2a), and the number of grid nodes is the same in the east-west direction, thus the grid interval becomes smaller and smaller toward the North Pole and the South Pole. Although the effect of such a gridding was reduced by applying smoothing and damping regu-

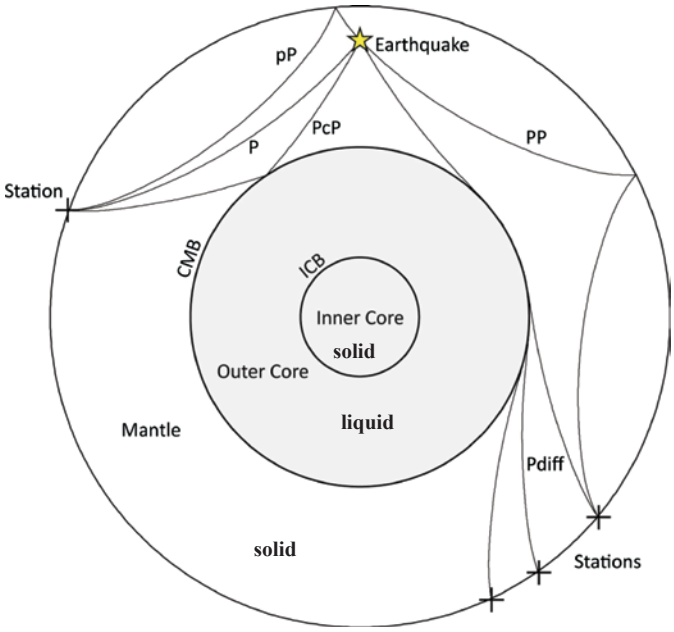

Fig 7.1 Schematic illustration of ray paths of P, pP, PP, PcP and Pdiff waves. The *star symbol* denotes a hypocenter. The *cross symbols* denote seismic stations

larizations to the tomographic inversion, it still affected precise determination of the mantle structure under the polar regions.

To overcome this problem, Zhao et al. (2013) determined a new global P-wave tomography model using the method of Zhao (2004) but adopting a flexible-grid parameterization (Fig. 7.2b, c). In their computer program of the flexible-grid tomography, grid nodes can actually be arranged at any sites rather than along the latitudinal and longitudinal lines as in the geographic-grid approach (Fig. 7.2a). In the model of Zhao et al. (2013), grid nodes are arranged as those shown in Fig. 7.2b, c. In the east-west direction, the number of grid nodes is reduced gradually from the equator toward the North Pole and the South Pole, and the distance between two adjacent grid nodes is nearly the same everywhere in the model (Fig. 7.2b). In the depth direction, 19 layers of grid mesh are set up with intervals of 15–250 km in depth (Fig. 7.2c). The number of nodes in each mesh layer is reduced with depth: it is 10,338 in the mesh layer at a depth of 15 km, while 3301 in the layer at a depth of 2800 km. Thus the distance (in kilometer) between adjacent nodes in the lateral direction is nearly the same for the grid meshes at different depths. This is also different from the geographic-grid adopted by Zhao (2001, 2004) where the number of nodes is the same in every grid meshes at different depths, hence the lateral grid interval becomes smaller with depth in Zhao (2001, 2004). For a lateral grid interval of 2° at the equator (222 km at the surface) and 19 mesh layers in the vertical direction from the crust (15 km depth) to the bottom of the mantle (2800 km depth), there are a total of 138,917 nodes in the flexible grid, whereas the node

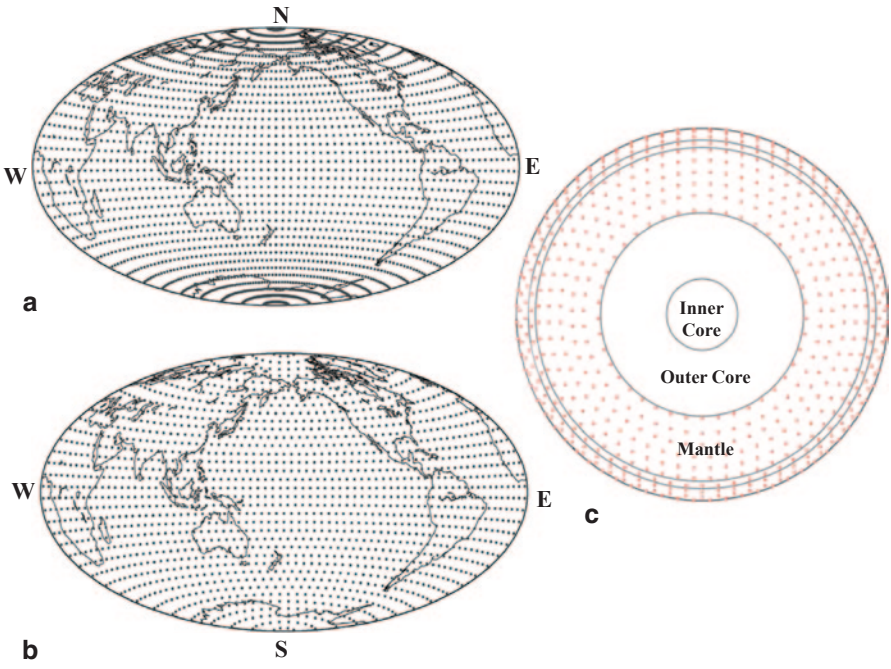

Fig 7.2 **a** Geographic grid and **b** flexible grid adopted for conducting global tomography. **c** Distribution of grid nodes in a vertical cross-section passing through the center of Earth. (Modified from Zhao et al. 2013)

number is $90 \times 180 \times 19 = 307{,}800$ in the geographic grid with the same grid interval at the equator (2°). Hence, the flexible grid (Fig. 7.2b, c) can better express the 3-D mantle structure with less than a half of nodes as in the geographic grid (Fig. 7.2a). P-wave velocity perturbations from the iasp91 1-D Earth model (Kennett and Engdahl 1991) at every grid nodes are taken to be unknown parameters. The velocity perturbation at any point in the model is calculated by linearly interpolating the velocity perturbations at the eight grid nodes surrounding that point. The global 3-D ray tracing technique (Zhao 2001; Zhao and Lei 2004) was used to calculate theoretical travel times and ray paths for the first P-wave and later phase (PP, pP, PcP, and Pdiff) data. The large and sparse system of observation equations was solved using the LSQR algorithm (Paige and Saunders 1982) with damping and smoothing regularizations (Zhao 2001, 2004; Zhao et al. 2013).

Zhao et al. (2013) used the ISC arrival-time data of earthquakes recorded by 6765 seismic stations in the world (see Fig. 1.7), which were reprocessed by Dr. E.R. Engdahl (for details, see Engdahl et al. 1998; Engdahl 2006). The continental regions are generally well covered by the seismic stations (Fig. 1.7b). Although the oceanic regions are still poorly covered, the data set used contains more stations in the oceans than those in previous tomographic studies (e.g., Zhao 2001, 2004). To select a best set of earthquakes for the tomographic inversion, the crust and mantle are divided into cubic blocks with a size of 40 km x 40 km x 20 km. Among the many

earthquakes within each block, only one event was selected that had the maximum number of arrival-time data and the minimum uncertainty in the hypocentral location. As a result, 12,657 earthquakes were selected (Fig. 1.7a), each of which was recorded by over 50 seismic stations. Most of the selected events were actually recorded by hundreds of stations. The hypocentral locations of the selected events were generally well constrained with the depth-phase (pP) data in addition to the direct P-wave data (Engdahl 2006), and the uncertainty in the hypocenter location is generally smaller than 5 km.

Similar to Zhao (2004), Zhao et al. (2013) used five kinds of P-wave data (Fig. 7.1) in their tomographic inversion, which are the direct P-wave, the depth-phase (pP), the surface reflected wave (PP), the reflected wave at the CMB (PcP), and the CMB-diffracted wave (Pdiff) (Fig. 7.1). In total, 1,566,508 P, 65,912 pP, 36,615 PP, 18,712 PcP, and 34,230 Pdiff arrival times from the 12,657 events were used in the tomographic inversion (Zhao et al. 2013). The total number of arrival times used is 1,721,977. The surface topography and bathymetry at the pP and PP bouncing points were considered in the 3-D ray tracing. The arrival times used were corrected for the ellipticity of the Earth (Kennett and Gudmundsson 1996). The ray path coverage is improved greatly by the use of later-phase data, in particular, under oceanic regions (Zhao et al. 2013). Many PP rays pass through the upper mantle under the Pacific, Atlantic and Indian oceans, which are very useful to constrain well the upper-mantle structure under the oceanic regions. The Pdiff data are very important and effective for determining the structure of the D" layer in the lowermost mantle (e.g., Wysession et al. 1992; Sylvander et al. 1997; Zhao 2004). Unfortunately, the distribution of the Pdiff segments at the CMB is still poor in the southern hemisphere due to the sparse distribution of seismic stations there (Fig. 1.7b). The data coverage is very good in the Arctic region, because there are many seismic stations in the continental regions surrounding the Arctic Ocean, and earthquakes occur actively in and around the Arctic (see Fig. 1.7a). Hence, the mantle structure is well constrained under the Arctic region (Zhao et al. 2013). However, the data coverage in the Antarctic region is not very good, because there are not many seismic stations and earthquakes there (Fig. 1.7). Hence, the mantle tomography has a lower resolution under Antarctica (see the results of detailed resolution analyses in Zhao et al. 2013).

Many tomographic inversions were performed with grid intervals of 1–10°, and the obtained 3-D velocity models exhibited nearly the same pattern (Zhao et al. 2013). The optimal model with a grid interval of 2° is shown in Figs. 7.3, 7.4, 7.5 and 7.6. Note that the bottom grid mesh for the inversion was set up at a depth of 2800 km, which represents the average velocity image of the lowermost mantle (the D" layer). One layer of grid mesh was set up at a depth of −200 km, and another grid layer was set up at a depth of 3500 km, which were not included in the inversion but only for calculating the velocity perturbations between −200 and 15 km depths and those between 2800 km depth and the CMB by linear interpolation. The 60 possible hotspots compiled by Zhao (2007) are also shown in the tomographic images (Figs. 7.3–7.6)

The overall pattern of the model of Zhao et al. (2013) is similar to those of Zhao (2001, 2004) and other P-wave tomographic models, but there are some differences in the polar regions, which are caused by the differences between the flexible grid

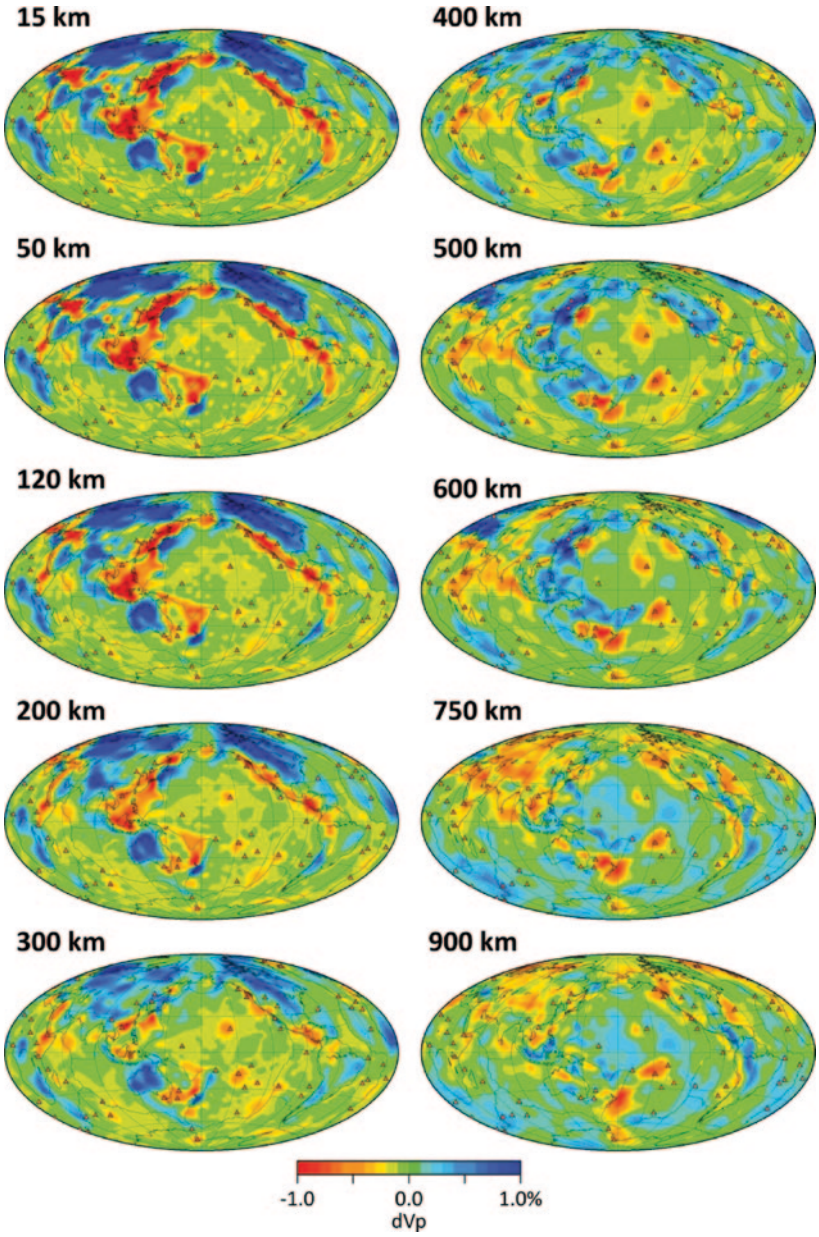

Fig. 7.3 Map views of P-wave tomography at depths of 15–900 km. The *red* and *blue colors* denote low and high velocities, respectively. The velocity perturbation (in %) scale is shown at the *bottom*. The *red triangles* denote the possible hotspots. (After Zhao et al. 2013)

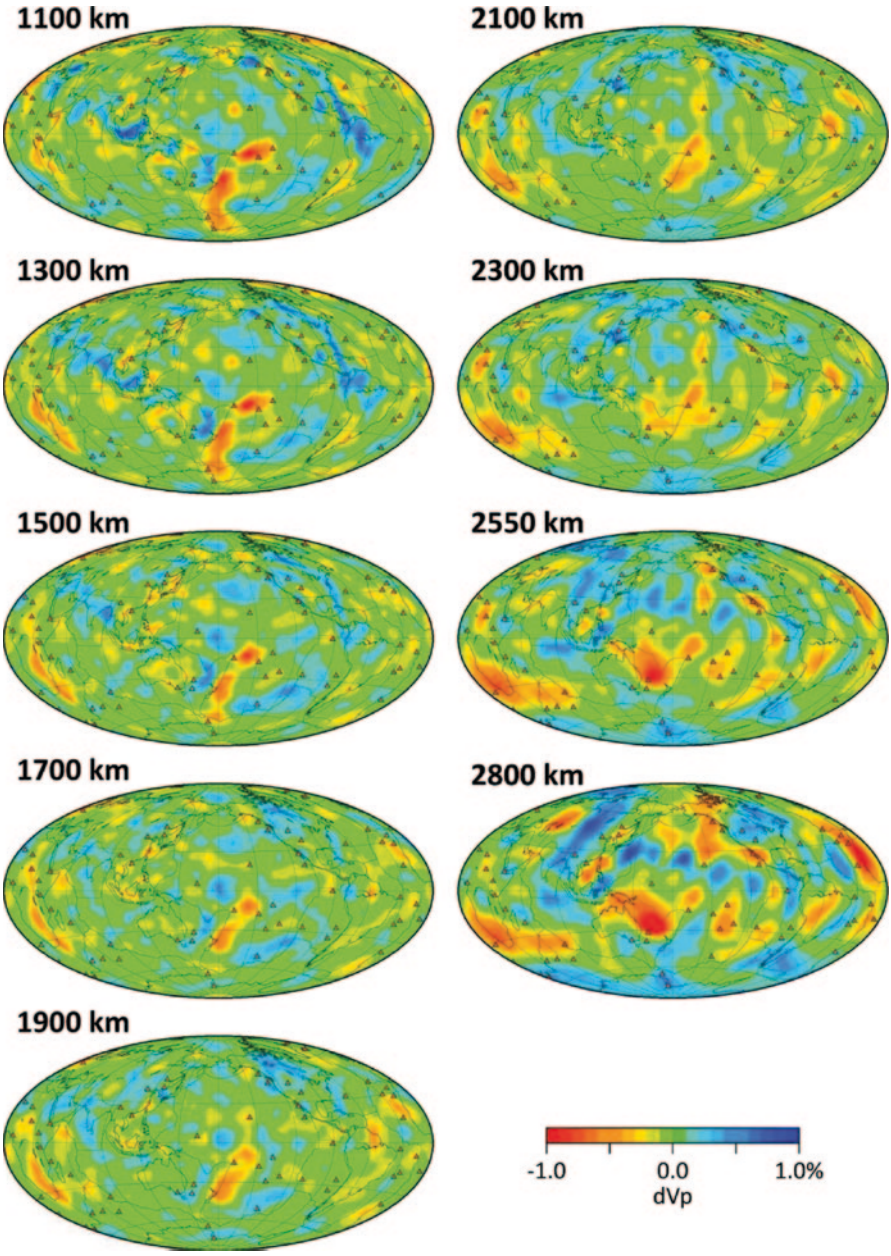

Fig. 7.4 The same as Fig. 7.3 but for P-wave tomography at depths of 1100–2800 km. (After Zhao et al. 2013)

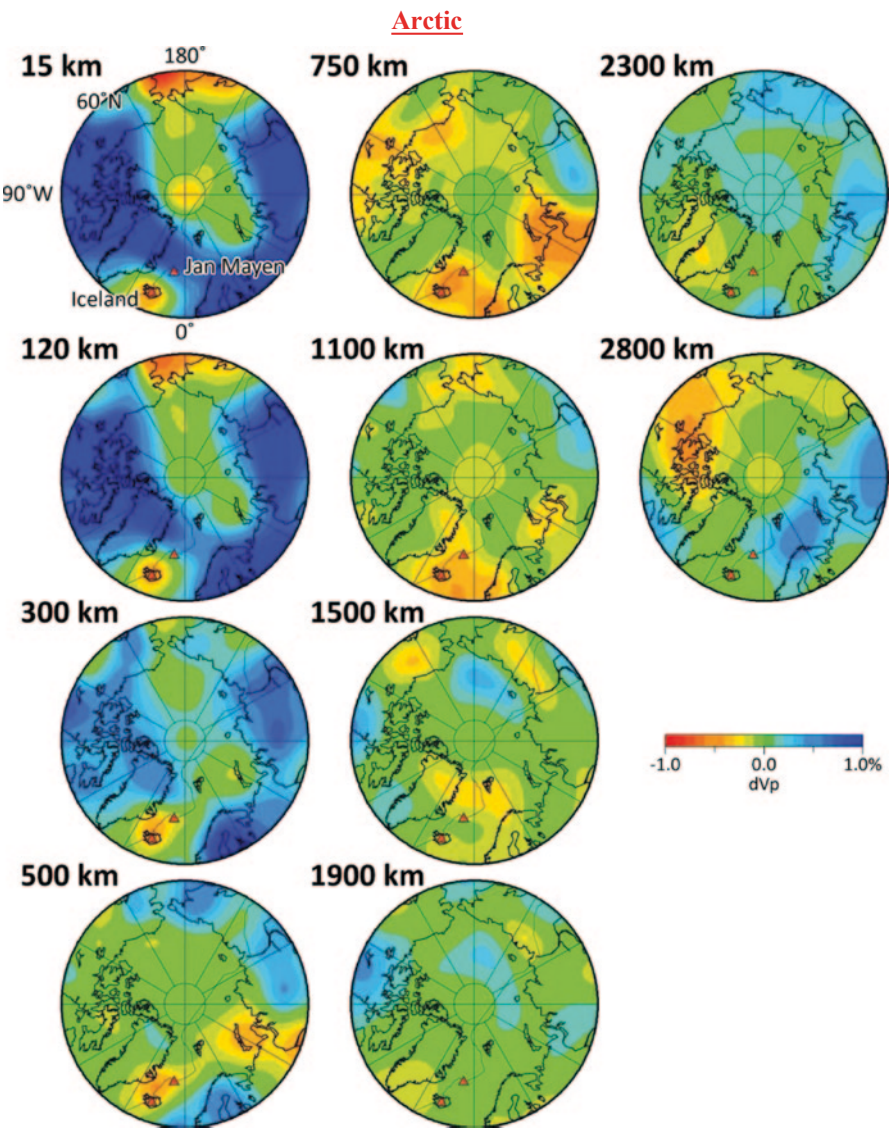

Fig. 7.5 The same as Fig. 7.3 but for P-wave tomography beneath the Arctic region. (After Zhao et al. 2013)

and the geographic grid in both lateral and vertical directions (Fig. 7.2). The new model (Figs. 7.3–7.6) contains the general features observed in the previous global models determined by travel-time tomography. In the crust and shallow part of the mantle (0–300 km depth), a low-velocity (low-V) ring is revealed under the circum-Pacific regions, which corresponds to the belt of active arc volcanoes and hot upper-mantle wedge above subducting slabs under the circum-Pacific subduction

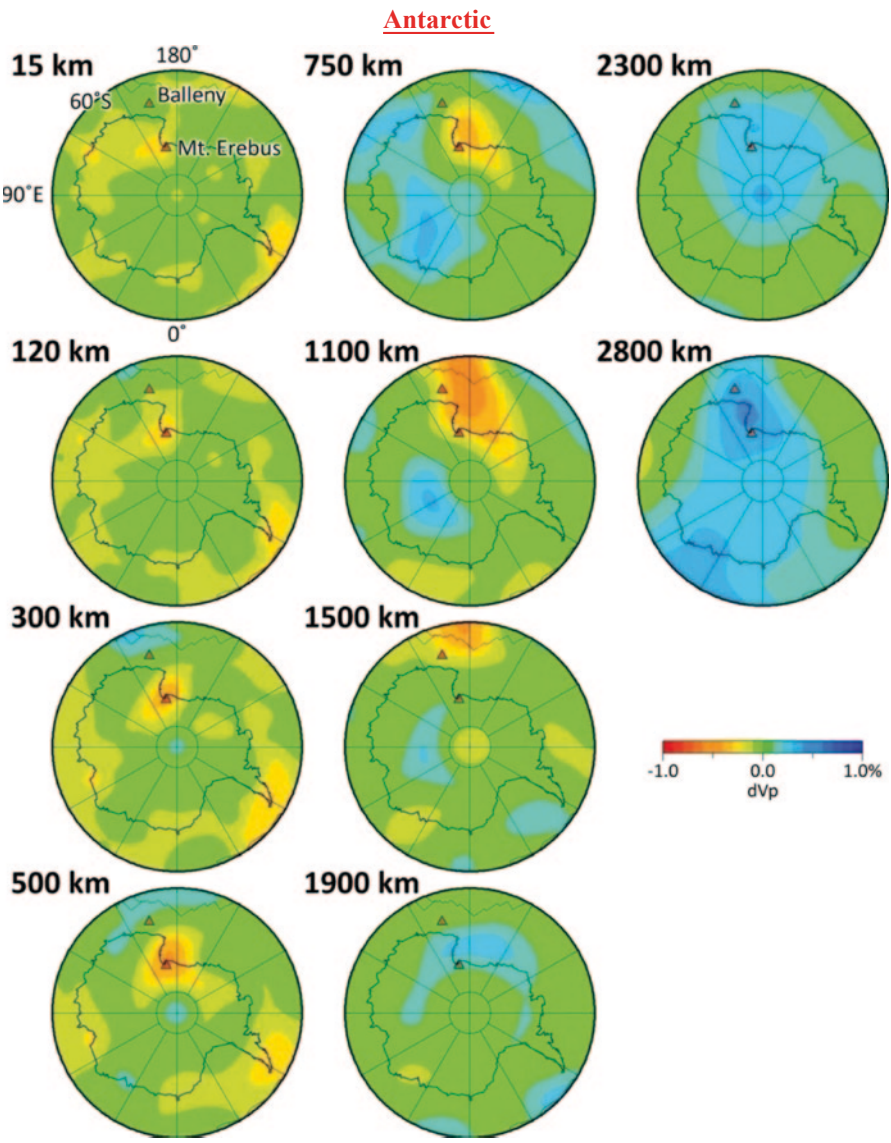

Fig. 7.6 The same as Fig. 7.3 but for P-wave tomography beneath the Antarctic region. (After Zhao et al. 2013)

zones. In contrast, high-velocity (high-V) zones appear under the old and stable continental regions, such as the Eurasian and North American cratons, which indicate that the differences between continents and oceans persist down to a depth of ~300 km. Similar to the previous models (e.g., Zhao 2001, 2004), the new model shows strong and broad high-V anomalies in the mantle transition zone (MTZ, 410–660 km depth) under back-arc regions of the subduction zones, which reflect

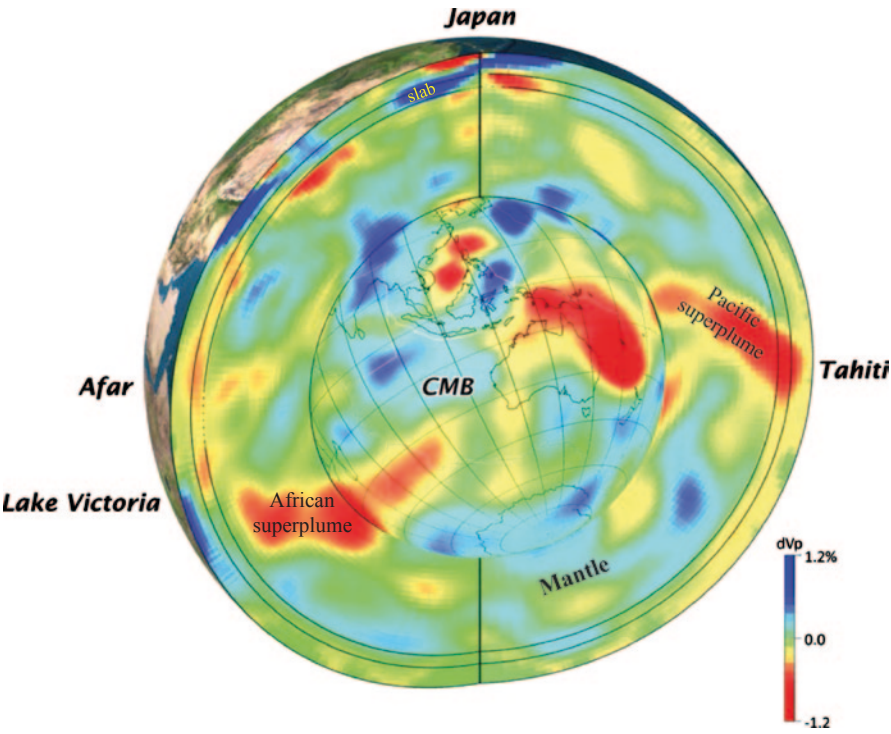

Fig. 7.7 Vertical cross-section of P-wave tomography from the Earth's surface down to the bottom of the mantle passing through Japan, Tahiti and Afar. The *image* in the central circle shows the tomography of the D" layer above the core-mantle boundary. The *red*, *green* and *blue colors* denote lower, average and higher velocities, respectively. The scale of velocity perturbations (in %) is shown beside the image. (Modified from Zhao et al. 2012a)

the subducting slabs stagnant in the MTZ (e.g., Fukao et al. 2001; Zhao 2001, 2004; Zhao et al. 2013).

In the top part of the lower mantle (700–900 km depth), the circum-Pacific high-V zones become less clear or absent (Fig. 7.3). Under the South-Central Pacific and East Africa where two superplumes are considered to exist, low-V zones dominate in the mantle (Figs. 7.3, 7.4 and 7.7–7.10). A long and thin high-V belt is clearly visible in the lower mantle under North and Central America (Figs. 7.4, 7.8 and 7.9), which represents the old Farallon slab that has subducted deeply in the lower mantle (e.g., van der Hilst et al. 1997; Bijwaard et al. 1998; Grand 2002; Zhao 2001, 2004). Detailed resolution analyses were made, which confirmed that these features are reliable and robust (Zhao et al. 2013).

High-V anomalies dominate in the crust and upper mantle (0–300 km depth) beneath the Arctic region, which reflects the thick continental lithosphere of the North American and Eurasian cratons, whereas low-V anomalies dominate at depths of 750–1500 km (Fig. 7.5). In the lowermost mantle under Arctic, a low-V zone appears under North America, while a high-V zone exists under Eurasia. Beneath the

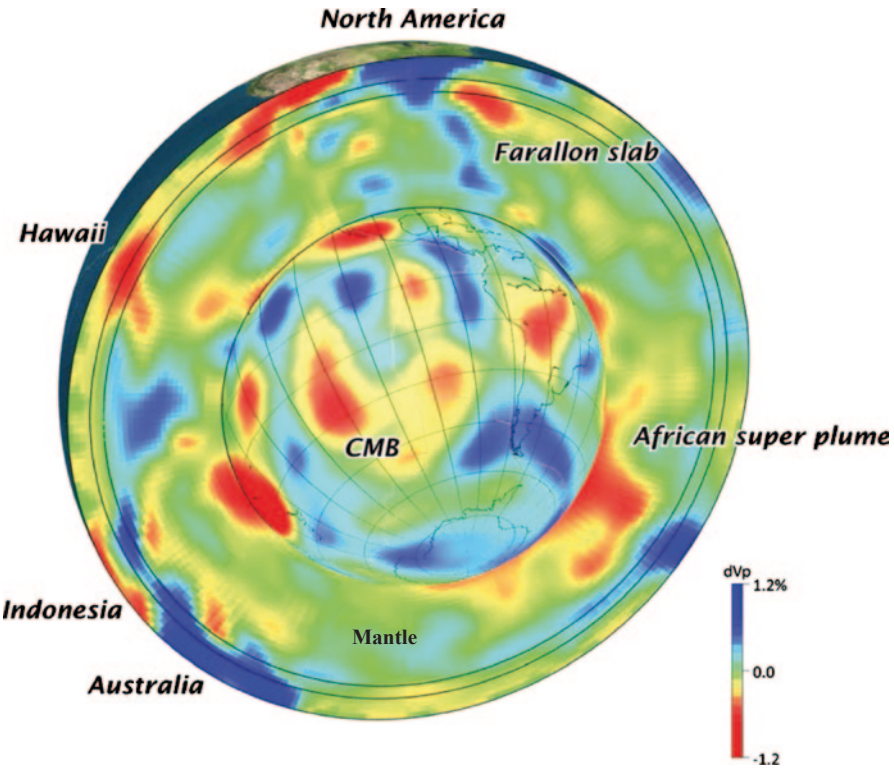

Fig. 7.8 The same as Fig. 7.7 but a vertical cross-section passing through North America, Hawaii and Indonesia. (Modified from Zhao et al. 2013)

Iceland and Jan Mayen hotspots, a localized low-V zone is clearly visible at depths of 0–500 km, whereas it becomes wider at depths of 750–1500 km and less prominent at depths of 2300–2800 km (Fig. 7.5).

Beneath the Antarctic region, the velocity is generally lower in the upper mantle (15–500 km depth), whereas it becomes higher at depths of 1900–2800 km (Fig. 7.6). The velocity is lower under the active West Antarctica than that beneath East Antarctica which is a stable cratonic region (e.g., Kobayashi and Zhao 2004; Gupta et al. 2009). Beneath the Erebus and Balleny hotspots, a prominent low-V zone appears from the crust down to a depth of ~1500 km, which is narrow in the upper mantle but becomes wider in the lower mantle (Fig. 7.6). High-resolution local and regional tomography studies using body-wave and surface-wave data have revealed a clear narrow low-V zone in the upper mantle under the Erebus hotspot, which may be a mantle plume (e.g., Kobayashi and Zhao 2004; Watson et al. 2006; Gupta et al. 2009).

The subducting slab related high-V zones and mantle upwelling related low-V anomalies show up more clearly in the whole-mantle vertical cross-sections (Figs. 7.7–7.10). Many more cross-sections of mantle tomography beneath subduction zones were presented in Zhao et al. (2013). The subducting oceanic slabs are

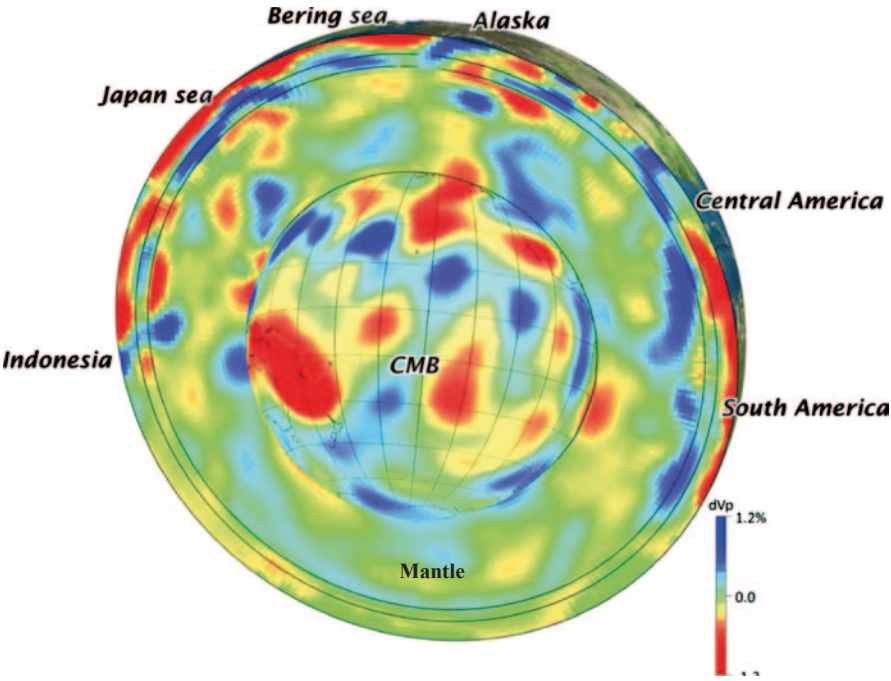

Fig. 7.9 The same as Fig. 7.7 but a vertical cross section passing through Bering Sea, Central America and Indonesia. (Modified from Zhao et al. 2013)

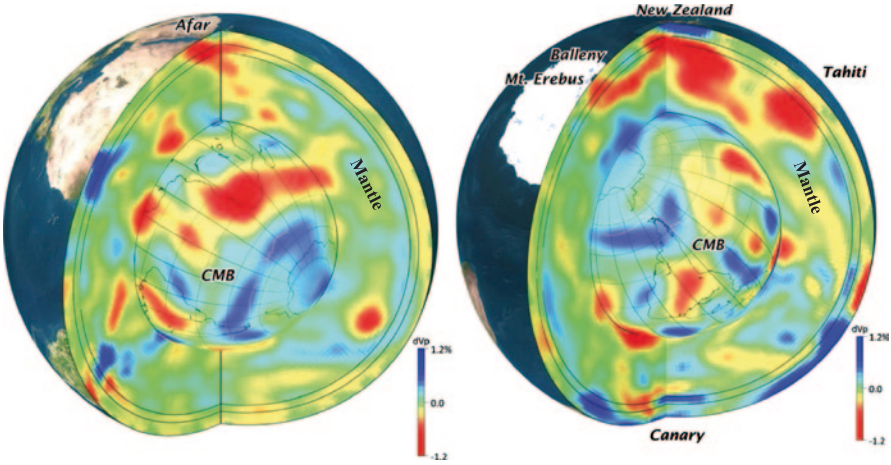

Fig. 7.10 The same as Fig. 7.7 but vertical cross-sections passing through **a** Afar, Central Africa, Antarctic, and **b** New Zealand, Mt. Erebus, and Canary. (Modified from Zhao et al. 2013)

generally well imaged as high-V zones in the upper mantle. The slabs have subducted down to the lower mantle under the Sea of Okhotsk, Mariana, Indonesia, and Central and South America. The Pacific slab becomes stagnant in the MTZ under western Alaska, Bering Sea, and Eastern Eurasia (Zhao et al. 2010, 2013). Whole-mantle P-wave tomographic images under 60 possible hotspots were presented in Zhao et al. (2013), which are generally consistent with those shown in Zhao (2007). Although slow anomalies generally appear under the hotspots, the images are variable and complex. The tomographic images of subducting slabs and hotspots and their implications for deep Earth dynamics are discussed in Sect. 7.5.

7.2 Global 3-D Ray Tracing

Three-dimensional (3-D) seismic ray tracing, i.e., determination of ray paths and travel times in a 3-D seismic velocity model, is one of the key elements in travel-time seismic tomography. Fast and precise 3-D ray tracing is essential for all tomographic studies, because usually a great number of arrival-time data are used and, for each datum, ray tracing is employed several times for earthquake relocation and 3-D velocity model determination. The accuracy of ray tracing dictates the quality of a final tomographic result. Now almost all local and regional tomographic studies are using 3-D ray tracing techniques to compute travel times and ray paths (see Zhao 2012 for the recent review). However, due to a great number of data used, many global tomography studies are still using the 1-D ray tracing method, i.e., ray paths are calculated for a 1-D velocity model where velocity changes with depth alone, and the ray paths are fixed during the inversion process, and ray path variations resulting from the lateral velocity heterogeneity are not considered.

Thanks to significant advances in computer technology, 3-D ray-tracing schemes have been applied to conduct global tomographic inversions during the past decade (e.g., Bijwaard and Spakman 2000; Gorbatov et al. 2001; Zhao 2001, 2004; Simons et al. 2011; Zhao et al. 2013). Bijwaard and Spakman (1999) examined ray path variations of the first P-waves in their 3-D mantle velocity model. They found that for a direct P-wave with an epicentral distance of 87° (note that 1° = 111.2 km), its ray path is displaced by nearly 100 km and its travel-time change is greater than 2 s in their 3-D velocity model, in comparison with those in a 1-D velocity model.

The Moho depth changes from ~10 km under oceans to 40–70 km beneath continental regions (e.g., Mooney et al. 1998). The 410 and 660 km discontinuities exhibit depth variations of up to 36 km at the global scale (e.g., Flanagan and Shearer 1998; Houser et al. 2008). Such large depth variations of the three discontinuities would certainly influence travel times and ray paths of seismic waves propagating in the mantle.

Zhao and Lei (2004) used a 3-D ray-tracing method (Zhao et al. 1992; Zhao 2001) to investigate deviations in ray paths and travel times of P, pP, PP, and PcP phases due to lateral velocity variations in the crust and mantle (Zhao 2001) as well as depth variations of the Moho, 410 and 660 km discontinuities (Mooney et al.

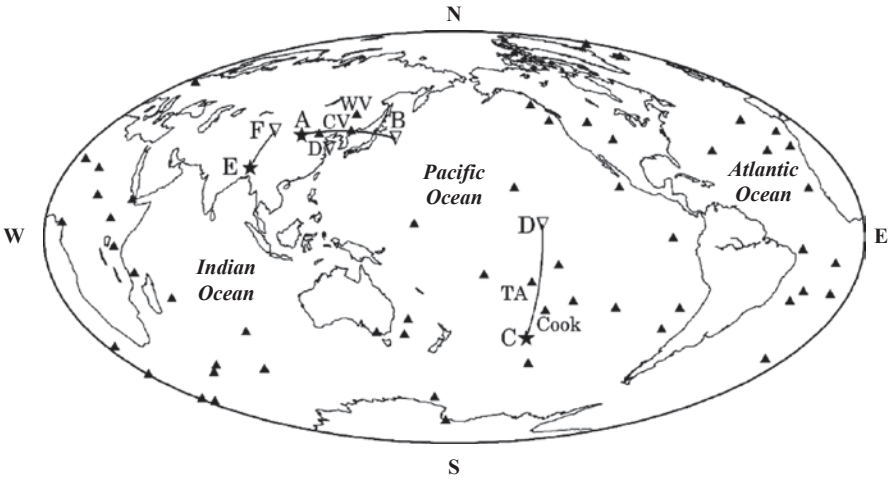

Fig. 7.11 Map showing the locations of three vertical cross-sections (*AB*, *CD* and *EF*) in which seismic ray paths are investigated. The *stars* and *open triangles* denote hypothesized earthquake hypocenters and seismic stations, respectively. The *solid triangles* denote the surface hotspot volcanoes except for those in East China (*WV*, Wudalianchi volcano; *DV*, Datong volcano; *CV*, Changbai volcano). *TA*, Tahiti hotspot. (Modified from Zhao and Lei 2004)

1998; Flanagan and Shearer 1998). The principle of the 3-D ray-tracing technique of Zhao et al. (1992) is to perturb an initial ray estimate iteratively using Snell's law at velocity discontinuities and the pseudo-bending technique (Um and Thurber 1987) in continuous media between discontinuities, until a convergent solution is obtained which gives the minimum travel time. This ray-tracing scheme can deal with a general velocity model including several velocity discontinuities of complex geometry and having 3-D velocity variations everywhere in the model. It is adaptable to tracing the first arrivals as well as reflected and converted waves (for details, see Zhao et al. 1992; Zhao and Lei 2004; Ballard et al. 2009; and Chap. 2 of this book). The modified version of the 3-D ray-tracing algorithm (Zhao 2001, 2004) yields accurate results with computational error in travel times smaller than 0.05 s, which is considered to be accurate enough, because the uncertainty of arrival-time pickings is generally 0.1 s or greater for the mantle rays at the global scale. The 3-D ray-tracing code can deal with not only the first P and S rays but also reflected and converted waves in the mantle and core, such as pP, sP, PP, PcP Pdiff, PKKP, and PKiKP, etc. (Zhao 2001, 2004; Lei and Zhao 2006a, b).

To illustrate the significant changes in ray path and travel time of seismic waves at the global scale, here we show a few examples of 3-D ray tracing for three regions (Fig. 7.11): (1) Western Pacific to East Asia where the high-V subducting Pacific slab exists and the big mantle wedge (BMW) above the slab exhibits significant low-V anomalies (Fig. 7.12a, c); (2) South-Central Pacific where the Pacific superplume exists and exhibits very slow anomalies in the whole mantle (Fig. 7.12b); and (3) the Tibetan Plateau which has a very thick crust (i.e., very deep Moho) and

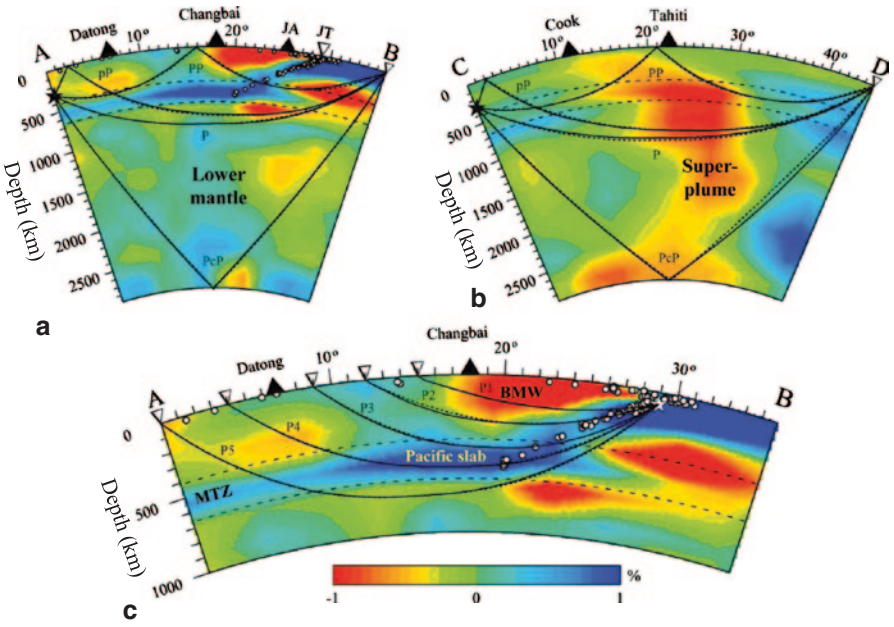

Fig. 7.12 One-dimensional (1-D) and three-dimensional (3-D) ray paths of P, pP, PP and PcP phases and P-wave tomography along the profile *AB* (**a**, **c**) and *CD* (**b**) in Fig. 7.11. The *blue* and *red colors* denote fast and slow velocities, respectively. The *dotted* and *solid lines* denote 1-D and 3-D rays, respectively. The *two dashed lines* show the 410 and 660 km discontinuities. The Moho is taken to be a spherical surface at a depth of 35 km. The *solid triangles* denote active volcanoes, the *small white dots* in (**a**) and (**c**) show earthquakes that occurred within a 150-km width of the profile *AB*. The *stars* and *open triangles* denote hypothesized earthquake hypocenters and seismic stations, respectively. *JA* Japan arc, *JT* Japan trench, *MTZ* the mantle transition zone. (Modified from Zhao and Lei 2004)

complex structures in the crust and upper mantle (e.g., Zheng et al. 2007; He et al. 2010; Zhang et al. 2012).

7.2.1 Effect of Lateral Velocity Variations

The 1-D and 3-D ray paths of P, pP, PP and PcP phases under East Asia and South-Central Pacific are shown in Fig. 7.12. A focal depth of 300 km is assumed, though any other focal depths are feasible. Here the 3-D ray paths mean those which are determined using the 3-D ray tracing scheme (Zhao et al. 1992) for a velocity model with 3-D P-wave velocity variations (Zhao 2001), whereas the Moho (at a depth of 35 km), 410 and 660 km discontinuities are assumed to be spherical interfaces without lateral depth variations. The 1-D ray paths are those determined using the same ray-tracing scheme to a 1-D velocity model which is the average of the 3-D model for each depth. The average 1-D velocity model is nearly the same as the iasp91 Earth model; the difference between them is < 1 % (Zhao 2001).

In addition to the travel time (T11) spent by a 1-D ray path in the 1-D velocity model and that (T33) taken by a 3-D ray path in the 3-D velocity model, we also computed the travel time (T13) of a 1-D ray path with velocities of the 3-D model and that (T31) of a 3-D ray path with velocities of the 1-D model (Zhao and Lei 2004). In most previous global tomographic inversions (e.g., Inoue et al. 1990), ray paths were fixed to those in a 1-D velocity model, whereas travel times were updated using the 3-D velocity distribution obtained after each iteration during the inversion process. The differences among the four travel times (T11, T33, T13, and T31) for the four kinds of mantle phases (P, pP, PP, and PcP) were examined by Zhao and Lei (2004).

For the rays under Western Pacific and East Asia (Fig. 7.12a), the travel-time differences are relatively small (<0.2 s), and the ray-path deviations are generally <33 km. These relatively small differences in both travel time and ray path are due to the alternative low-V and high-V anomalies along the rays (Fig. 7.12a). For the rays under South Pacific, however, the travel-time differences become much greater, amounting to 3.1 s, because of the huge low-V anomaly associated with the Pacific superplume (Fig. 7.12b). The differential times (T13-T33) amount to 0.7 s, which is much greater than the picking error of the arrival-time data recorded by short-period seismometers (0.1–0.3 s), as is the case for the ISC data set. These results suggest that the 1-D ray tracing could cause large computational errors for rays which pass through strong velocity anomalies, such as subducting slabs and mantle plumes. Zhao and Lei (2004) showed that T33 is smaller than T13 for all the cases, indicating that the 3-D ray tracing is always better than the 1-D ray tracing.

Ray trajectories are sensitive to velocity gradients in both lateral and vertical directions, and they are apt to move toward faster areas in a 3-D velocity field, which is clearly visible in Fig. 7.12. Due to the slow anomaly in the BMW under the Changbai volcano and above the Pacific slab, the PP bouncing point at the surface is displaced by 16 km toward the west (Fig. 7.12a). The easternmost segment of PP is elevated by 27 km to escape the slow anomaly under the subducting Pacific slab (Fig. 7.12a). Because of the high-V stagnant slab in the MTZ, the western portion of the long segment of pP is elevated by 12 km (Fig. 7.12a). The PcP bouncing point at the CMB moves by 18 km westward from a low-V zone to a high-V patch in the lowermost mantle (Fig. 7.12a).

The most significant deviation in ray path occurs for the northern segment of PcP under South Pacific (Figs. 7.12b). The horizontal, vertical, and total deviations of the PcP ray are 26, 48, and 77 km, respectively. The PcP ray is displaced from the large low-V Pacific superplume toward a high-V area in the north (Fig. 7.12b). The northern segment of pP is moved by 32 km toward a high-V zone in the north (Fig. 7.12b). In addition, the PP bouncing point at the surface is displaced by 20 km toward the north to escape the slow anomaly under Tahiti.

Most of the PP and pP rays travel long in and around the MTZ and their paths show complex changes because of the existence of high-V slabs and low-V plumes in the region. Hence, computing travel times and ray paths of PP and pP phases precisely using a 3-D ray tracing scheme is particularly important and necessary for global tomography (Zhao and Lei 2004).

Figure 7.12c shows five pairs of 1-D and 3-D rays for the direct P-waves passing through the upper mantle and the MTZ under Western Pacific from an assumed hypocenter at a depth of 75 km within the Pacific slab. The epicentral distances of the five P rays are 14, 17, 20, 25 and 29°, respectively. The high-V Pacific slab and the low-V anomalies in the BMW and below the slab lead to significant changes in travel time and ray path. For the rays P1–P5 (Fig. 7.12c), the differential travel-time (T11-T33) is −0.64, 0.11, 1.58, 2.24 and 1.11 s, respectively, and the maximum displacement in ray path is 6, 19, 10, 9 and 8 km, respectively. It is visible that the rays bend toward the high-V slab and escape from the low-V zones (Fig. 7.12c).

7.2.2 Effect of Discontinuity Topography

Figures 7.13, 7.14 and 7.15 show changes in P, pP and PP ray paths caused by depth variations of the Moho, 410 and 660 km discontinuities revealed by Mooney et al. (1998) and Flanagan and Shearer (1998). The iasp91 Earth model is adopted for

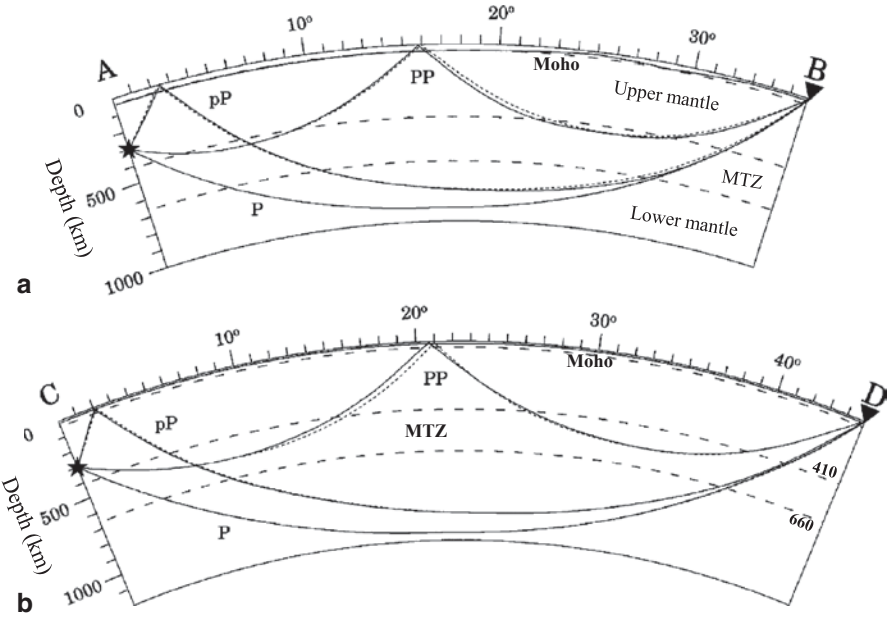

Fig. 7.13 Ray paths of P, pP and PP phases along the profiles *AB* (**a**) and *CD* (**b**) in Fig. 7.11. The *dotted lines* denote rays in the 1-D iasp91 model. The *solid lines* show the rays in a heterogeneous model with lateral depth variations of the Moho discontinuity. The 410 and 660 km discontinuities are assumed to be spherical interfaces without lateral depth variations. The *dashed lines* denote the 410 and 660 km discontinuities and the global-average Moho discontinuity at a depth of 35 km. The Moho depth variations (Mooney et al. 1998) along the profiles *AB* and *CD* are shown in *thin solid lines*. The iasp91 Earth model is used for the 1-D velocities in each layer. Lateral variations in seismic velocity are not considered. (Modified from Zhao and Lei 2004)

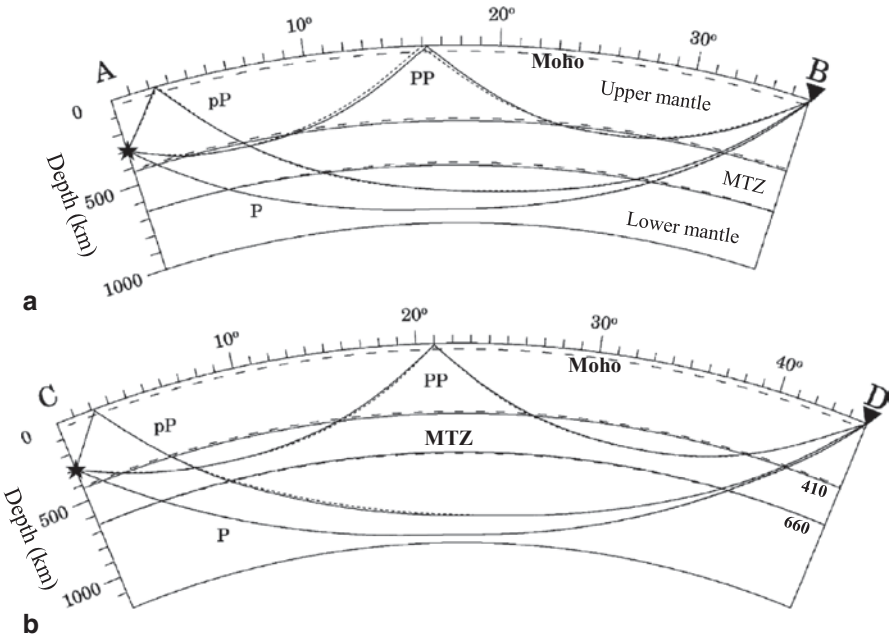

Fig. 7.14 The same as Fig. 7.11 but for rays (*solid lines*) in a velocity model with a flat Moho at a depth of 35 km and with lateral depth variations of the 410 and 660 km discontinuities from the model of Flanagan and Shearer (1998). The *dotted lines* denote rays in the 1-D iasp91 model. (Modified from Zhao and Lei 2004)

the 1-D P-wave velocities in the crust and mantle, whereas lateral velocity variations are not considered. Ray paths in the models with the discontinuity topography are compared with those in the 1-D iasp91 model where the Moho (at a depth of 35 km), 410 and 660 km discontinuities are taken to be spherical interfaces without lateral depth variations (Figs. 7.13–7.15).

Ray path changes due to the Moho topography alone are shown in Fig. 7.13. The Moho depth ranges from 12 to 38 km along the profile AB, and from 11 to 14 km along the profile CD. The PP bouncing point at the surface is displaced by 34 km in Fig. 7.13a and 40 km in Fig. 7.13b, which are caused by the Moho depth variations. The maximum change in the pP ray path is 17 km along the profile AB and 11 km along the profile CD. The P rays are not affected much by the Moho topography, though their travel times have significant changes. The changes in P, pP and PP travel times are 0.91, 0.91, and 1.10 s, respectively, beneath Western Pacific and East Asia (Fig. 7.13a), and their changes under South Pacific (Fig. 7.13b) are 0.91, 3.02, and 3.87 s, respectively. The Moho depth changes from 39 to 60 km along the profile EF passing through the Tibetan Plateau (Fig. 7.11). For the three direct P rays along the profile EF, the travel-time changes are 1.1–2.1 s, and their maximum ray-path deviations are 9–17 km (Zhao and Lei 2004).

Figure 7.14 shows ray-path changes due to depth variations of the 410 and 660 discontinuities under East Asia and South Pacific. The Moho is assumed to be flat

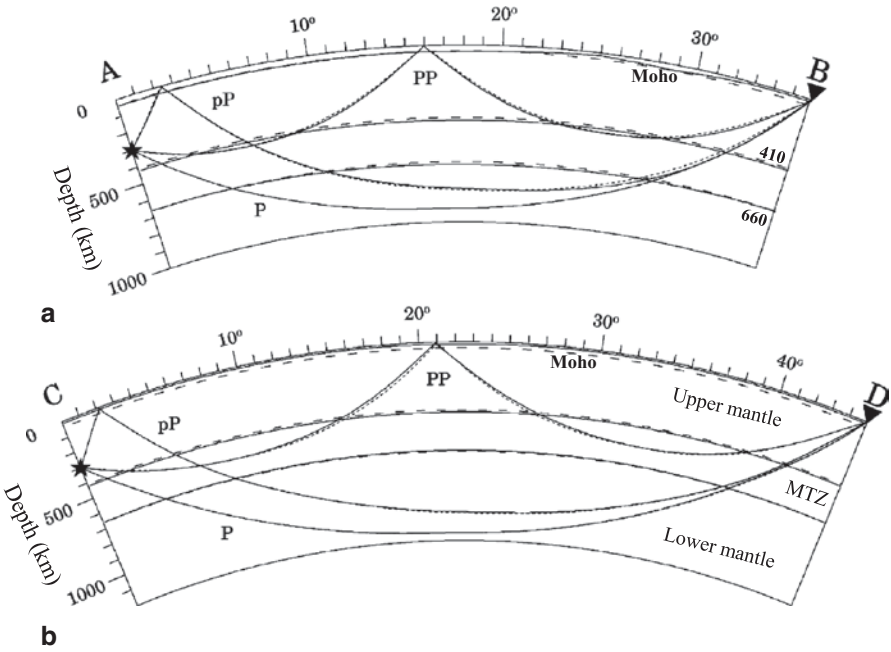

Fig. 7.15 The same as Fig. 7.14 but for rays (*solid lines*) in a velocity model with lateral depth variations of the Moho, 410 and 660 km discontinuities from the models of Mooney et al. (1998) and Flanagan and Shearer (1998). The *dotted lines* denote rays in the 1-D iasp91 model. (Modified from Zhao and Lei 2004)

at a depth of 35 km. The direct P-waves are only slightly affected by the topography of the 410 and 660 km discontinuities, and their maximum ray-path deviations are <6 km in both AB and CD profiles. The maximum changes in pP and PP ray paths are 9 and 34 km under East Asia, and 13 and 11 km under South Pacific, respectively. The P, pP and PP travel-time changes are 0.27, 0.42 and 1.00 s under East Asia, and 0.12, −0.10 and 0.44 s under South Pacific, respectively (Fig. 7.14).

Ray-path changes due to lateral depth variations of all the three discontinuities (the Moho, 410 and 660) are shown in Fig. 7.15. In East Asia, the maximum changes in the P, pP and PP ray paths are 4, 19 and 28 km, and their travel-time changes are 0.64, 0.52 and 0.29 s, respectively (Fig. 7.15a). In South Pacific, The P, pP and PP rays exhibit maximum changes of 6, 6 and 30 km, and their corresponding changes in travel time are 0.80, 2.95 and 3.42 s, respectively (Fig. 7.15b).

7.2.3 Joint Effects of Discontinuity and Velocity Variations

The 3-D velocity model of Zhao (2001) includes both 3-D P-wave velocity variations and lateral depth changes of the Moho, 410 and 660 km discontinuities revealed by Mooney et al. (1998) and Flanagan and Shearer (1998). A few examples

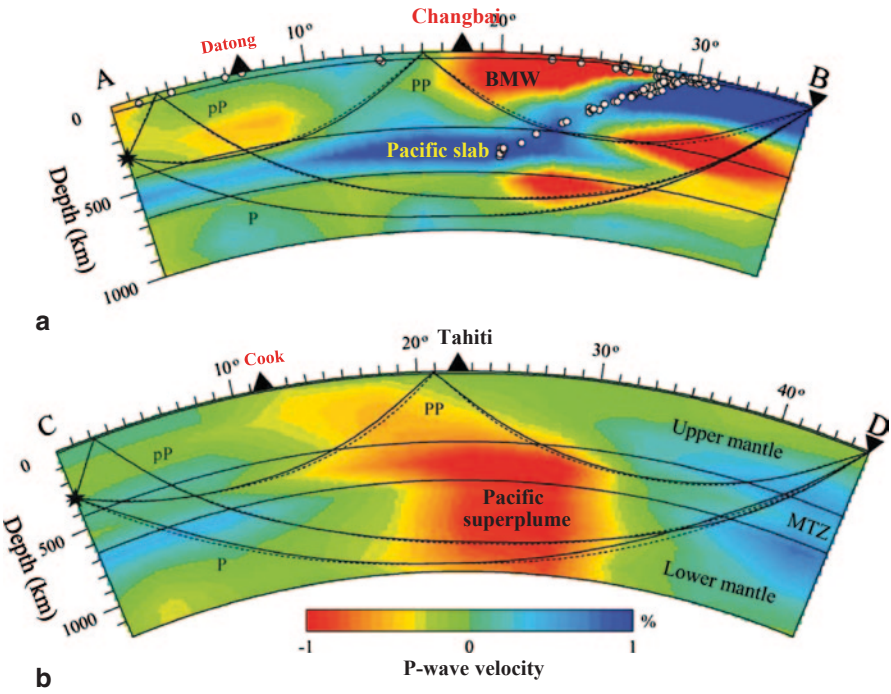

Fig. 7.16 The same as Fig. 7.12 but for rays (*solid lines*) in a velocity model with lateral depth variations of the Moho, 410 and 660 km discontinuities from the models of Mooney et al. (1998) and Flanagan and Shearer (1998) as well as with lateral velocity variations. The *dotted lines* denote rays in the 1-D iasp91 model. (Modified from Zhao and Lei 2004)

of ray-path changes in such a truly 3-D velocity model (Zhao 2001) are shown in Fig. 7.16. The P, pP and PP ray paths in the 3-D model (solid lines in Fig. 7.16) are compared with those in the 1-D iasp91 model (dotted lines in Fig. 7.16). In East Asia, the maximum path differences between the 1-D and 3-D rays for the P, pP and PP phases are 12, 16 and 26 km, and their corresponding travel-time differences are 0.59, 0.73 and 0.14 s, respectively (Fig. 7.16a). In South Pacific, the maximum path changes for the P, pP and PP rays are 46, 38 and 32 km, and their travel-time changes are −0.95, 1.62 and 0.45 s, respectively (Fig. 7.16b).

These 3-D ray-tracing results indicate that, even if the maximal amplitude of velocity anomalies in a 3-D global velocity model is only 1–2 %, seismic rays passing through those very heterogeneous regions (such as subducting slabs and mantle plumes) can deviate up to 100 km from their 1-D ray paths, because of the very long ray trajectories in the global case (Bijwaard and Spakman 1999; Zhao and Lei 2004). The amplitudes of velocity anomalies in the existing tomographic models are generally underestimated, because damping and smoothing regularizations have to be applied in the tomographic inversion in order to obtain a convergent and stable solution. Hence, the actual amplitudes of crustal and mantle heterogeneities may be greater. For example, high-resolution (5–30 km) local and regional tomography

studies have revealed velocity anomalies of up to 6% for P-wave and 10% for S-wave in subduction zones (Zhao et al. 1997, 2009a, 2012b; Tong et al. 2012; Liu et al. 2013). In local or regional scale studies, arrival-time data have better quality and ray paths have a more uniform distribution, hence strong damping and smoothing as for the global tomography can be avoided, enabling the pattern and amplitude of velocity heterogeneities to be recovered better. With the improvement of spatial resolution of global tomography, strong velocity anomalies can be revealed in the crust and mantle, which may cause ray-path and travel-time changes much greater than those shown in Figs. 7.12–7.16. The considerable lateral depth variations of mantle discontinuities together with 3-D velocity variations in the Earth's interior would result in more complicated changes in ray path and travel time.

The existence of complex structural heterogeneities in the Earth's interior requires the use of effective 3-D ray tracing in the global tomographic studies. Although there have been new progresses in the studies of 3-D ray tracing recently (e.g., Ballard et al. 2009; Huang et al. 2013a), continuing efforts are still needed to devise better ray tracing algorithms so that more seismic data can be used to image the 3-D Earth's structure in greater details and in higher resolution by taking advantage of advances in computer technology.

7.3 Role of Later Phases in Mantle Tomography

For conducting global P- or S-wave travel-time tomography, some workers measured arrival times carefully from seismograms (e.g., Woodward and Master 1991; Su et al. 1994; Grand 2002), whereas most seismologists have used the ISC data set to study the 3-D mantle structure, because the ISC bulletins represent the largest collection of arrival-time information available worldwide (see Zhao et al. 2013 for the recent review). The ISC data set has been reprocessed and now its quality has been greatly improved (see Engdahl et al. 1998; Engdahl 2006). With the remarkable advances in computer technology, the spatial resolution of global tomography can be improved by using a huge number of arrival-time data. However, if only direct P-wave data are used, it is still difficult to improve the tomography resolution in the mantle under the oceanic regions and in the southern hemisphere, because there are fewer seismic stations in those regions. Later phases of reflected and converted waves can sample the Earth's interior that is not ordinarily sampled by the direct P rays. Therefore, adding later-phase data is an effective way to improve the tomographic images of the Earth at both local and global scales (e.g., Zhao et al. 1992, 2013; Lei and Zhao 2006a, b; Zhao 2009).

In global P-wave tomography studies, different authors have used different ISC data sets. For example, Inoue et al. (1990) used only the direct P data, while Vasco et al. (1995) added PP phases, van der Hilst et al. (1997) and Bijwaard et al. (1998) used P and pP phases. Vasco and Johnson (1998) used P, PP, PcP, PKPab, PKPbc and PKPdf phases to invert for both the mantle and core structures. Boschi and Dziewonski (2000) also determined both the 3-D mantle and core structures us-

ing P, PcP, PKPbc and PKPdf phases. Gorbatov et al. (2001) used P, PP and Pdiff phases. Karason and van der Hilst (2001) investigated the effects of PKP and Pdiff on the lowermost mantle structure. Zhao (2001, 2004) and Zhao et al. (2013) used five kinds of mantle phases (P, pP, PP, PcP and Pdiff). Montelli et al. (2004) used P and PP waves. Lei and Zhao (2006a, b) investigated the influences of ten kinds of mantle and core phases (P, pP, PP, PcP, Pdiff, PKPab, PKPbc, PKiKP, PKKPab and PKKPbc) on the determination of P-wave tomography of the mantle and the outer core.

Diffraction P-waves (Pdiff) have long paths sampling the D" layer above the CMB than other mantle waves (Fig. 7.17a), hence they are very useful for imaging the lowermost mantle structure (e.g., Wysession et al. 1992; Sylvander et al. 1997). Zhao (2004) conducted detailed resolution tests with and without the Pdiff data (P, pP, PcP, and PP rays were used in the tests) and found that, when the Pdiff data are added, both the pattern and amplitude of velocity anomalies can be improved for the lowermost mantle, in particular, under the southern hemisphere. Figure 7.18 shows P-wave images of the D" layer obtained with and without the Pdiff data (Zhao 2004). Although the two images are quite consistent in the overall pattern of velocity distribution, considerable discrepancy appears in the South Pacific region. In the image determined by P, PP, pP and PcP data (Fig. 7.18a) there is a high-V patch directly beneath the Samoa hotspot which is surrounded by low-V anomalies. When the Pdiff data are added, however, the high-V zone under Samoa disappears (Fig. 7.18b), and the huge low-V zones under South Pacific become more prominent and coherent, which may show the root of the Pacific superplume (Zhao 2004).

Global P-wave tomographic inversions were conducted using a carefully selected ISC data set including 783,024 P, 36,017 pP, 8177 PP, 4644 PcP, 13,401 Pdiff, 5589 PKiKP, 5312 PKPab, 26,768 PKPbc, 157 PKKPab, and 515 PKKPbc arrival times (Lei and Zhao 2006a, b). Figure 7.17 shows a schematic illustration of the ten kinds of rays and the observed travel-time curves of those phases used in the inversions. There are few seismic stations in and around the Hawaiian island chain (Fig. 7.19), and so it is an ideal location to examine the effects of the later-phase data on whole-mantle tomography (Lei and Zhao 2006b).

Figure 7.20 shows distributions of different kinds of rays projected on a north–south vertical cross-section passing through Hawaii. There are much more direct P rays than the other phases, but the P rays have a distribution of a mountain-like shape under Hawaii above a depth of 1000 km and a relatively poor coverage around a depth of 1500 km, and they are almost horizontal below a depth of 2000 km (Fig. 7.20a, d). The pP ray distribution is similar to that of P rays at the global scale. Both P and pP rays are not so useful for imaging the area away from the Hawaiian islands in and above the MTZ (Fig. 7.20a, b, d, e). However, PP rays can fill up the gaps of the P and pP ray coverage above a depth of 1500 km (Fig. 7.20c, f). There are fewer PcP and PKKP rays around the Hawaiian islands (Fig. 7.20g, k). Pdiff and PKP rays cover the lowermost mantle well (Fig. 7.20h, i). There are some Pdiff rays under the Hawaiian islands (Fig. 7.20h), while no PKP arrival times were recorded by the Hawaiian seismic stations in the data set (Fig. 7.20i). Some PKiKP rays exist under the Hawaiian islands (Fig. 7.20j). When all the phases are used, the ray cover-

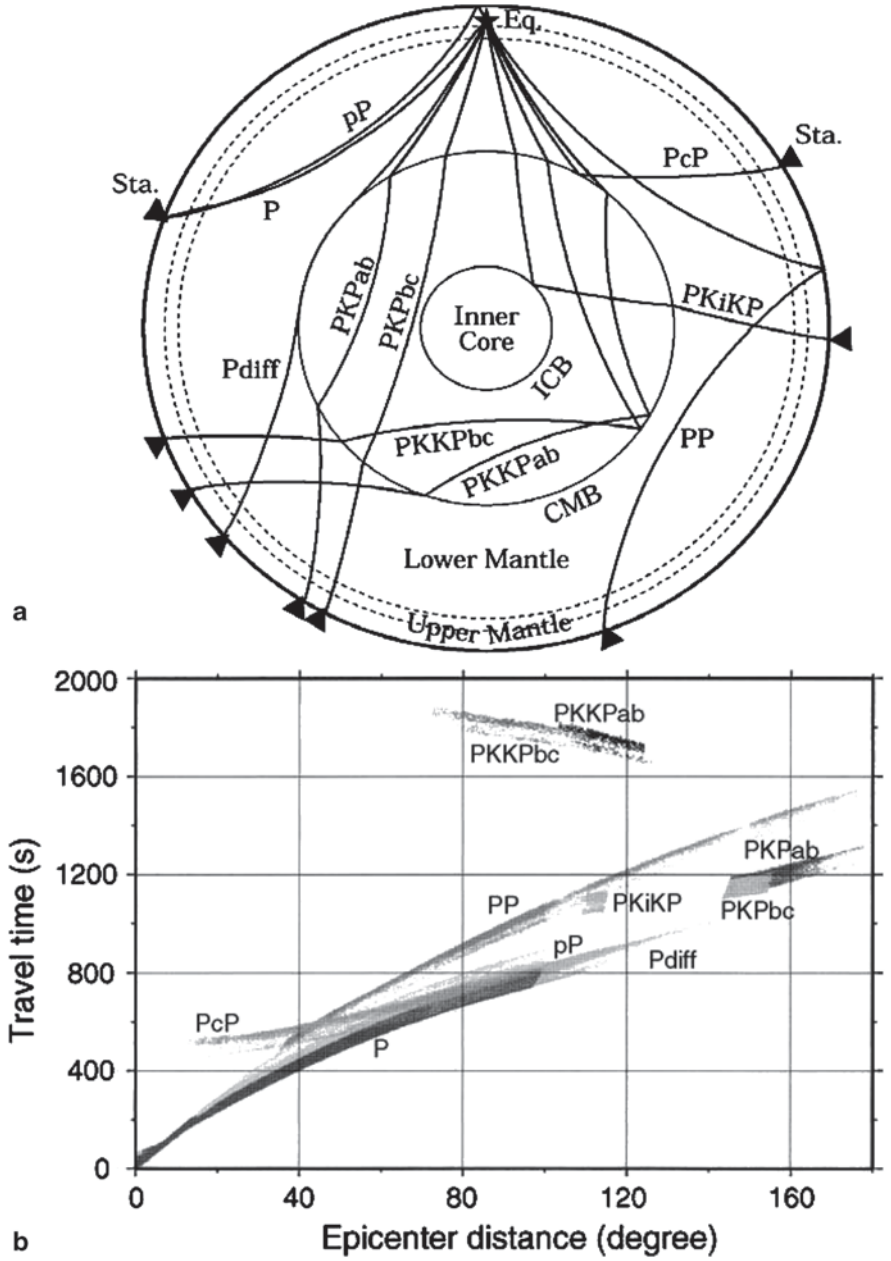

Fig. 7.17 **a** Sketch illustration of ten kinds of P-wave ray paths used in global tomographic inversions. The *star* and *triangles* denote a hypocenter and seismic stations, respectively. The *two dashed lines* denote the 410 and 660 km discontinuities. **b** Observed travel-time curves of the ten kinds of phases shown in (**a**) from the reprocessed ISC data set by Engdahl (2006). (After Lei and Zhao 2006a)

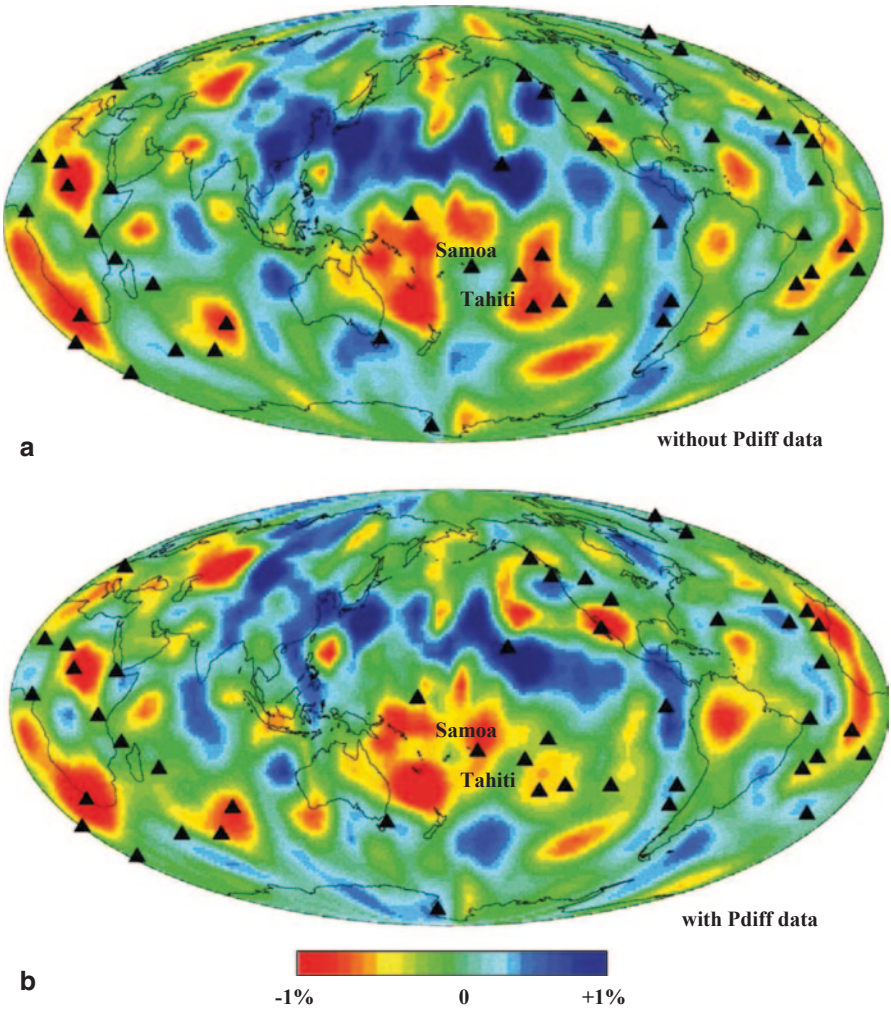

Fig. 7.18 P-wave velocity images at the bottom of the mantle. The result of the inversion using P, pP, PP, and PcP data is shown in (**a**), and that using P, pP, PP, PcP and Pdiff data is shown in (**b**). The *red* and *blue* colors denote slow and fast velocities, respectively. The velocity perturbation scale is shown at the *bottom*. The *solid triangles* denote the surface hotspots. (Modified from Zhao 2004)

age becomes much better in the entire mantle under Hawaii, though it is still sparse in the middle mantle (Fig. 7.20 l).

Figure 7.21a shows a north–south vertical cross-section of P-wave tomography passing through the Hawaiian hotspot when all the ten kinds of data (Fig. 7.17) are inverted for the 3-D structure of both the mantle and the outer core, whereas the CMB is assumed to be a spherical interface without lateral depth variations (Lei and Zhao 2006b). A prominent and continuous low-V zone is clearly visible in the entire

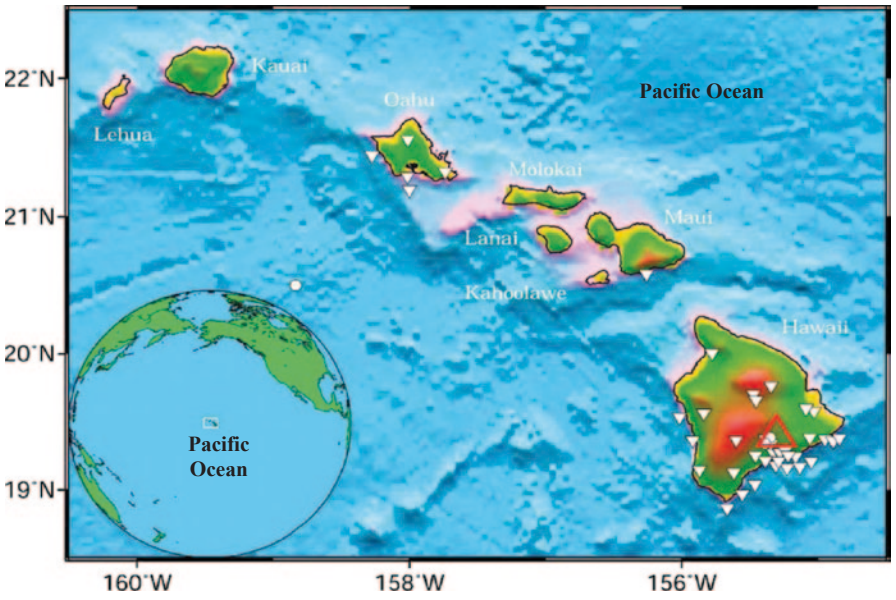

Fig. 7.19 Map of the Hawaiian islands. The *white triangles* and *white dots* denote the seismic stations and earthquakes, extracted from the ISC bulletins. The hotspot (*red triangle*) is currently centered just southeast of Hawaii. The seismic stations are mainly located on the islands of Hawaii, Maui and Oahu. The *inset map* shows the location of the study area. (Modified from Lei and Zhao 2006b)

mantle under Hawaii (Fig. 7.21a). The liquid outer core of the Earth is generally considered to be laterally homogeneous, because active convection is taking place there (e.g., Stevenson 1987). Figure 7.21b shows an image similar to Fig. 7.21a but both the mantle and core phase data (Fig. 7.17) were inverted for the 3-D mantle structure alone assuming that the outer core is laterally homogeneous. The two results (Fig. 7.21a, b) show that the pattern of the mantle tomography remains the same, no matter whether the 3-D outer core structure is inverted or not, though some differences in the amplitude of velocity anomalies appear in the middle and lower mantle, and there are some changes in the image of the D" layer. The tomography without the outer-core structure shows slightly larger amplitude of velocity anomalies (Fig. 7.21b). These results suggest that trade-off may occur between the mantle and the outer-core structures (Lei and Zhao 2006a, b).

The CMB is the most important boundary in the Earth's interior, which exhibits the strongest contrasts in both physical properties (density and seismic velocity) and chemical composition. The CMB may have undulations of up to 10 km due to hot materials pulling up and cold materials depressing in the mantle (Rodgers and Wahr 1993; Sze and van der Hilst 2003). Such large undulations would certainly affect the mantle tomography, because ray paths and travel times of PcP, Pdiff and core phases are sensitive to the CMB topography. However, the obtained CMB topography models exhibit considerable discrepancies, partly because different data sets

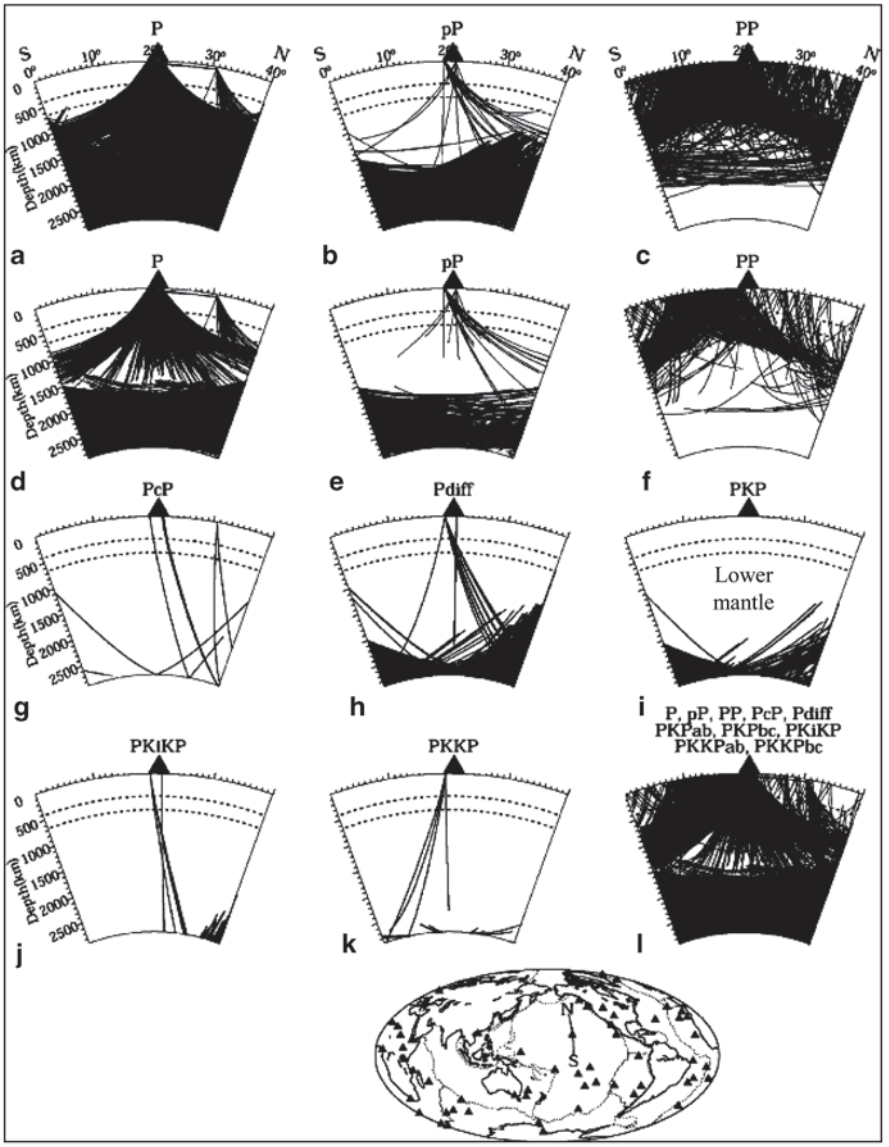

Fig. 7.20 Distribution of seismic rays projected on the north–south vertical cross-section passing through the Hawaiian hotspot. (**a**)–(**c**) and (**g**)–(**k**) show the rays within 20° of the profile, while (**d**)–(**f**) show the rays within 10° of the profile so that the direct P, pP and PP rays under Hawaii can be seen clearly. The rays in (l) are a combination of those in (**d**)–(**k**). Seismic phases are labeled atop each panel. The *two dashed lines* denote the 410 and 660 km discontinuities. The location of the profile is shown in the inset map. The *triangles* in the map denote the hotspot volcanoes. (After Lei and Zhao 2006b)

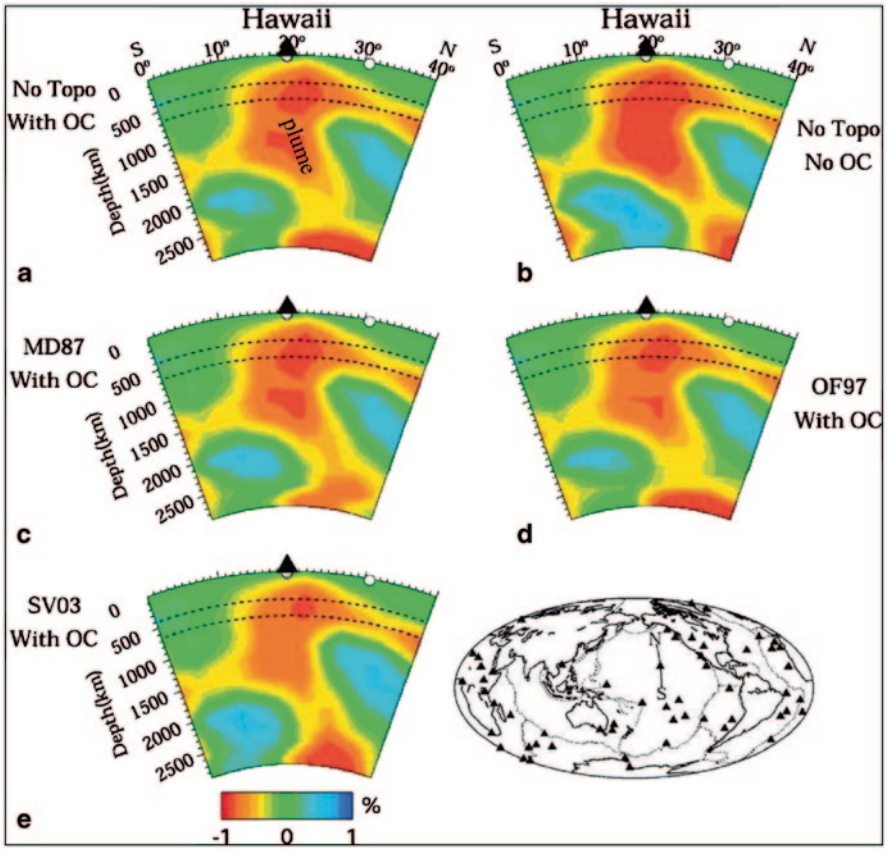

Fig. 7.21 P-wave tomography along the north–south vertical cross-section beneath the Hawaiian hotspot when all the ten kinds of phases are used. **a** The image obtained without the CMB topography and with the outer-core structure included in the inversion. **b** the image obtained without the CMB topography and without the outer-core structure included in the inversion. **c**–**e** the images obtained with the outer-core structure included in the inversion and with three CMB topographic models taken into account. The three CMB models are MD87 (Morelli and Dziewonski 1987), OF97 (Obayashi and Fukao 1997) and SV03 (Sze and van der Hilst 2003). The *two dashed lines* denote the 410 and 660 km discontinuities. The *red* and *blue colors* denote slow and fast velocities, respectively. The velocity perturbation scale (in %) relative to the 1-D iasp91 Earth model is shown at the bottom. The *inset map* shows the location of the cross-section. The *triangles* on the map denote the hotspots. The *white dots* denote earthquakes which occurred within a 250 km width of the profile. (After Lei and Zhao 2006b)

and inversion techniques were used by different authors. Lei and Zhao (2006a, b) used three CMB topographic models (Morelli and Dziewonski 1987; Obayashi and Fukao 1997; Sze and van der Hilst 2003) to investigate the effect of the CMB topography on mantle tomography. The three CMB models show different topography patterns and the CMB topographic peaks are 6, 10 and 3 km, respectively. The model of Morelli and Dziewonski (1987) shows slight depression under the Hawaiian island chain, while that of Sze and van der Hilst (2003) shows elevated

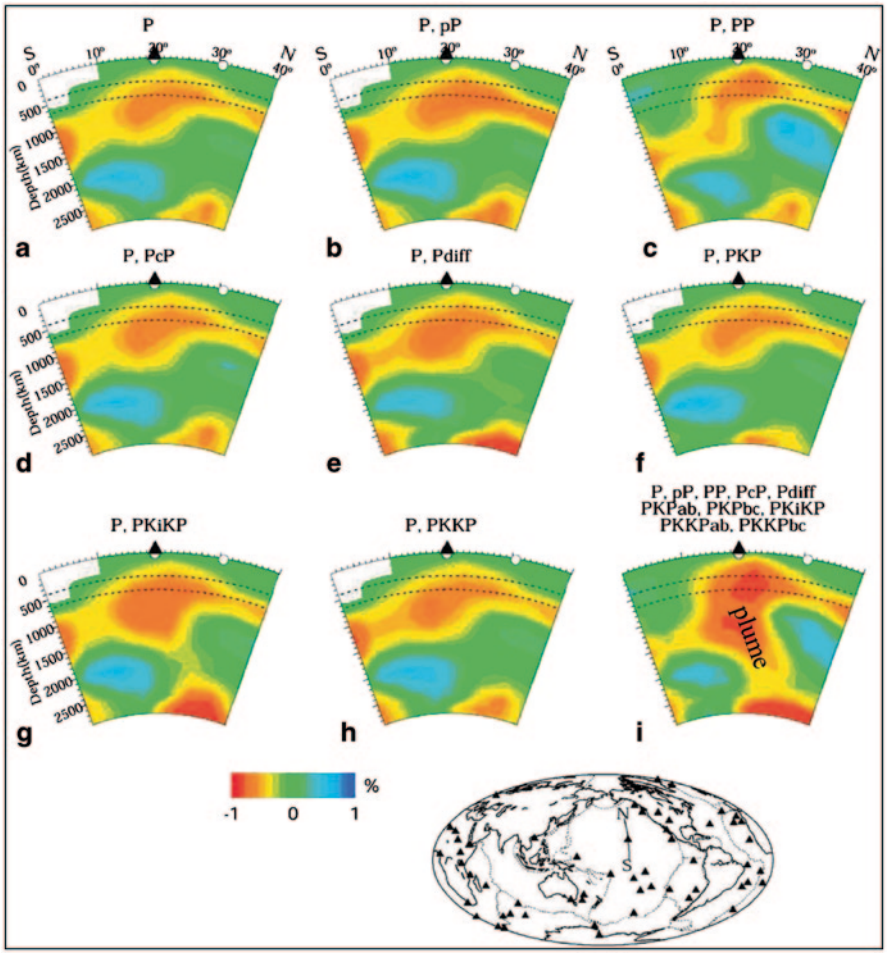

Fig. 7.22 P-wave tomography along the north–south vertical cross-section passing through the Hawaiian hotspot, obtained by using P and one kind of later phases. The mantle and outer-core structures are inverted jointly. The types of the rays used in the inversion are labeled atop each panel. The *red* and *blue colors* denote lower and higher velocities, respectively. The velocity perturbation scale (in %) is shown at the bottom. The *two dashed lines* denote the 410 and 660 km discontinuities. (Modified from Lei and Zhao 2006b)

topography under Hawaii. The tomographic results show that the pattern of mantle tomography remains the same no matter which CMB model is used, and slight differences in tomography occur in the amplitude of velocity anomalies below a depth of 2000 km (Fig. 7.21c, d, e).

To investigate how the mantle and core phases affect the tomographic image, Lei and Zhao (2006a, b) conducted two series of tomographic inversions using different subsets of ISC data. One is to combine the direct P-wave with one kind of later phases in the inversion (Fig. 7.22), the other is to add more kinds of later phases gradually in the inversion (Fig. 7.23). When the pP data are added, the amplitude

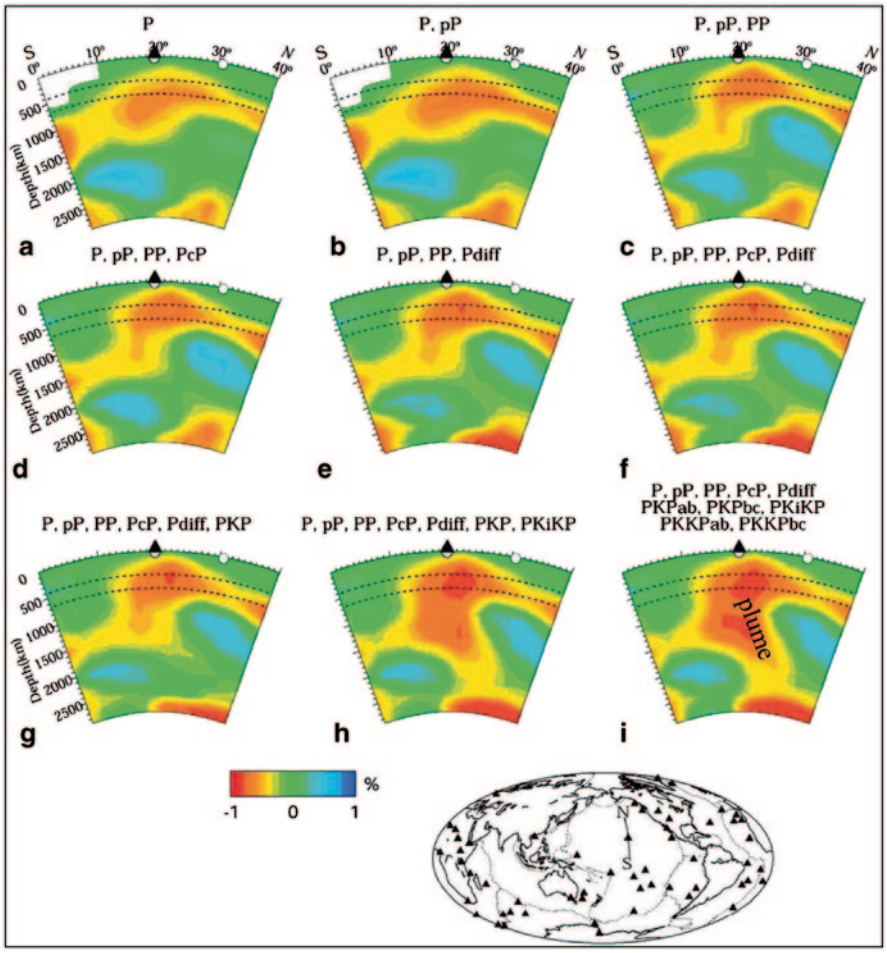

Fig. 7.23 The same as Fig. 7.22 but for P and more kinds of later phases. (Modified from Lei and Zhao 2006b)

of velocity anomalies is changed slightly above the middle mantle and in the lowermost mantle (Figs. 7.22b and 7.23b). The PP rays change the pattern of the image above a depth of 1700 km (Figs. 7.22c and 7.23c), because the PP rays have a good coverage above the middle mantle (Fig. 7.20). When the PcP data are added, both the pattern and amplitude of the low-V anomalies have almost no change (Figs. 7.22d and 7.23d), because there are few PcP rays under Hawaii (Fig. 7.20g). The Pdiff rays enhance the amplitude of slow anomalies above a depth of 1500 km and in the lowermost mantle (Figs. 7.22e and 7.23e). In contrast, the PKP data reduce the amplitude of slow anomalies in the lowermost mantle (Figs. 7.22f and 7.23g). When the PKiKP data are added, the pattern of slow anomalies is changed in the entire mantle (Fig. 7.22g), and their effect is more clearly visible in Fig. 7.23h

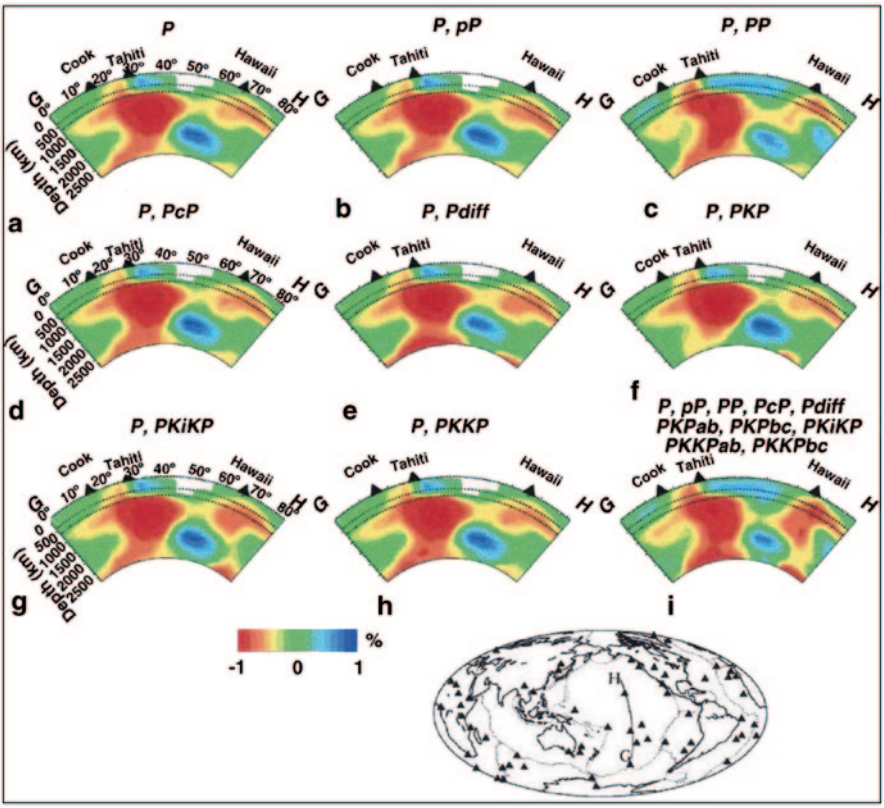

Fig. 7.24 The same as Fig. 7.22 but for the images along a profile shown in the *inset map*. The types of phases used in the inversion are labeled atop each panel. (After Lei and Zhao 2006a)

after the mantle phases and the PKP data are added. The significant contribution of the PKiKP rays to the image of the Hawaiian plume may be due to their quite different take-off angles from those of the other phases (Fig. 7.20j), which improve the ray crisscrossing in the mantle under Hawaii. When only P and PKKP data are used, it is not easy to find the change visually (Fig. 7.22h). However, when all the phases are used, it is clear that the PKKP data affect the amplitude of slow anomalies around a depth of 1500 km beneath Hawaii (Fig. 7.23h, i) and that a continuous low-V anomaly is imaged below the Hawaiian hotspot in the entire mantle.

Figure 7.24 shows effects of the later phases on mantle tomography in a north-south vertical cross-section passing through the Hawaiian and Tahiti hotspots. Similar features of the effects as in Fig. 7.22 show up for this broad region of the Pacific. Prominent low-V anomalies corresponding to both the Pacific superplume and the Hawaiian plume are visible in the whole mantle (Fig. 7.24), which are discussed in detail in Sect. 7.5.

These results (Figs. 7.18 and 7.21, 7.22, 7.23 and 7.24) indicate that later-phase data are very important for improving the ray-path coverage in the mantle, in particular, under the oceanic regions where few seismic stations exist. Although the picking accuracy of later-phase data is generally lower than that of the first P-wave data, they are still very useful for better constraining the 3-D mantle structure. The quality of later-phase arrivals can be improved using the modern technology of waveform processing, thus many kinds of mantle and core phases can be used in future studies of global and regional tomography.

7.4 Influence of Global Mantle Heterogeneity on Regional Tomography

To date, a great number of researchers have used arrival-time data of teleseismic events recorded by local or regional seismic networks in various areas of the world to study the 3-D velocity structure of the crust and upper mantle under the seismic networks applying the ACH method, named after Aki et al. (1977). The great success of the ACH method is attributed to the production of credible and geologically reasonable results from seismic data which are widely available, easily obtained and handled at a relatively low cost (Evans and Achauer 1993). The principle of the ACH tomographic method is to invert a set of relative travel-time residuals of teleseismic events for a 3-D P- or S-wave velocity model of the upper mantle beneath a local seismic network. The final parts of up-going rays under a seismic array are modeled in three-dimensions, whereas a standard 1-D velocity model is adopted for the Earth's structure outside the target volume of the 3-D local tomography (Fig. 7.25a). The selected teleseismic events are usually located in a range of 25–100° from the target area, hence the turning point (i.e., the point with the maximum depth) of every teleseismic P ray is located in the lower mantle (Fig. 7.25a).

For a teleseismic ray, its travel-time residual t_{ij} from the *j*th event to the *i*th seismic station is written as,

$$t_{ij} = T_{ij}^{OBS} - T_{ij}^{CAL} \tag{7.1}$$

where T_{ij}^{OBS} and T_{ij}^{CAL} are observed and calculated travel times, respectively. A relative travel-time residual r_{ij} is defined as,

$$r_{ij} = t_{ij} - \overline{t_j} \tag{7.2}$$

where $\overline{t_j}$ is the average residual for the *j*th event,

$$\overline{t_j} = \frac{1}{m_j} \sum_{i=1}^{m_j} t_{ij} \tag{7.3}$$

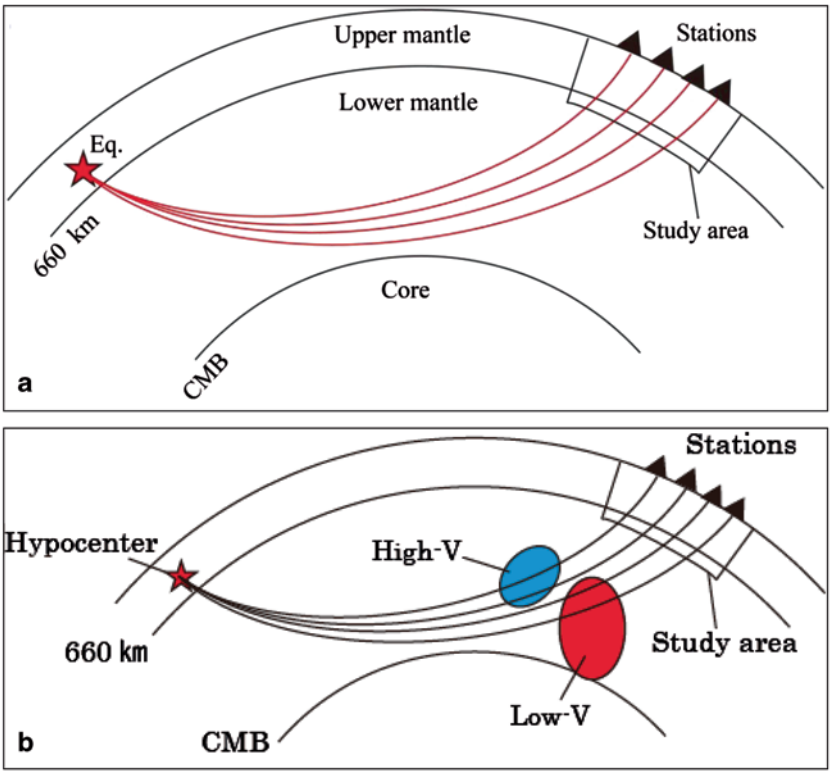

Fig. 7.25 **a** A conceptual diagram of teleseismic local/regional tomography. The *star symbol* denotes a teleseismic event, whereas the *black triangles* denote seismic stations in the target study area. The *red curved lines* show the teleseismic ray paths. A basic assumption underlying the teleseismic regional tomography is that the seismic velocity structure of the entire lower mantle outside of the study region is laterally homogeneous. **b** The same as (**a**) but the *red* and *blue patches* denote low and high velocity anomalies in the lower mantle where the teleseismic rays pass through. (Modified from Zhao et al. 2013)

where m_j is the number of seismic stations in the target area which recorded the *j*th event.

The ACH method uses relative travel-time residuals of teleseismic events to determine local tomography, due to the following two reasons. The first is that the influence of the origin time of a teleseismic event can be removed, and hypocentral mislocations have very small effect on the final tomographic result. The second is that the influence of velocity anomalies in the focal areas of teleseismic events can be removed, because ray paths from a teleseismic event to all the seismic stations in the target area are nearly identical in the crust and upper mantle under the teleseismic event (see Fig. 7.25a). A fundamental assumption of the ACH method is that the effect of velocity anomalies outside the target volume, particularly those in the lower mantle, can be removed by the use of relative travel-time residuals. Thus, all

the relative travel-time residuals of the teleseismic events used are attributed to 3-D velocity variations in the target volume beneath the local seismic array, though the ray paths are actually not identical in the lower mantle, particularly for the segments of the rays close to the target volume (Fig. 7.25a).

To date, many global tomography studies have been made, revealing significant seismic velocity variations in the lower mantle, such as those shown in Figs. 7.7–7.10. Although the average amplitude of velocity anomalies in the lower mantle is much smaller than that in the upper mantle and the MTZ, the velocity heterogeneity in the lower mantle can be very strong beneath some regions (see Fig. 7.32), such as the two superplumes under South-Central Pacific and East Africa, the collapsed slab materials under East Asia, and the deeply subducted Farallon slab under North and Central America (Figs. 7.7–7.10 and 7.21–7.24).

Consider the case shown in Fig. 7.25b: in the lower mantle, some rays pass through a low-V zone, whereas other rays pass through a high-V zone (Zhao et al. 2013). If the ACH method is applied to conduct a tomographic inversion, then these low-V and high-V anomalies in the lower mantle would be mapped into the target volume in the upper mantle. Then a question arises: how valid is the fundamental assumption underlying the ACH method? In other words, how much would the velocity anomalies in the whole mantle imaged by global tomography affect the teleseismic regional tomography obtained with the ACH method?

It seems that so far only two studies have addressed this issue. One is Masson and Trampert (1997) who used a lower-resolution 3-D P-wave global model converted from an S-wave tomography model to investigate the influence of whole-mantle heterogeneity on an essentially 2-D P-wave tomography under a linear seismic array in northern Tibet (Wittlinger et al. 1996). Their linear seismic array was composed of 50 stations with a total length of ~600 km, and their 2-D P-wave tomography model is valid down to a depth of 400 km under the array. Masson and Trampert (1997) found that the relative travel-time residuals caused by the mantle heterogeneity outside the target volume are not negligible and so the fundamental hypothesis underlying the ACH method is not verified.

The other study addressing the issue is Zhao et al. (2013) who used a high-resolution global tomography model (Figs. 7.3–7.10) to investigate the influence of whole-mantle heterogeneity on the determination of 3-D regional tomography of the Japan subduction zone. They used 45,425 high-quality P-wave arrivals of 360 teleseismic events recorded by 779 seismic stations of the High-sensitivity seismic network (Hi-net) and 654 J-Array seismic stations which belong to the Japanese national universities and the Japan Meteorological Agency (Zhao et al. 2012b, 2013). These stations are all equipped with short-period (1 Hz) and high-sensitivity seismometers. The picking accuracy of these teleseismic arrivals is ~0.10 s.

Zhao et al. (2013) calculated precise ray paths and travel times of the 45,425 P-wave data in their 3-D global velocity model and the 1-D iasp91 Earth model using the 3-D ray-tracing technique (Fig. 7.26a). For each ray, they took the difference between the travel times in the 3-D and 1-D velocity models, T3d-T1d, from the teleseismic hypocenter to the bottom or the edge of the 3-D regional tomography model, i.e., the differential travel time outside the target volume of regional

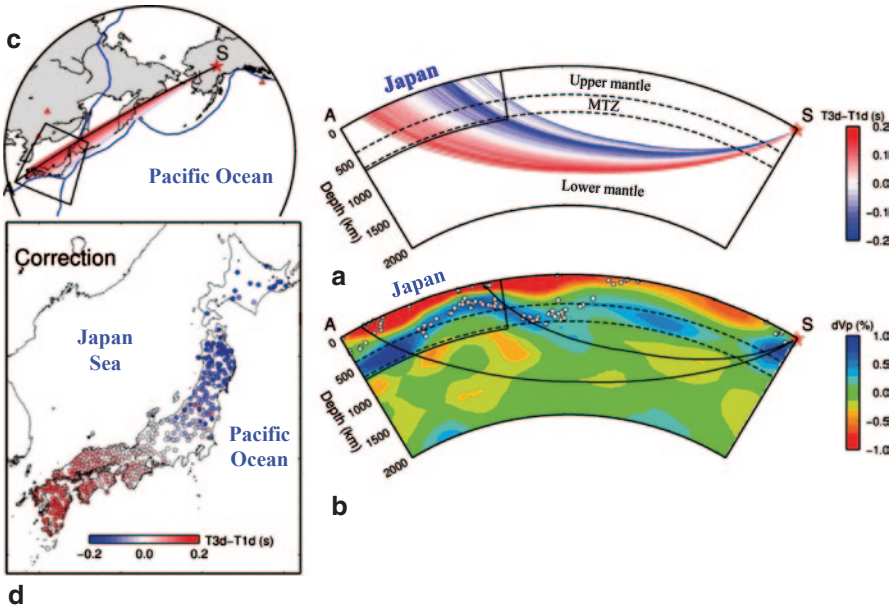

Fig. 7.26 **a** P-wave rays from an earthquake (the *red star*) in Alaska to the seismic stations in Japan. The event (M 6.9) occurred on 11 January 2001 with a focal depth of 25 km. The *color* of rays denotes the outside residuals (see text for details). The *red* and *blue colors* denote slower and faster rays, respectively, with the scale shown on the *right*. **b** Vertical cross-section of P-wave tomography along the profile *A*-*S* as shown in (**c**). The *red* and *blue colors* show low and high velocities, respectively, with the velocity scale shown on the *right*. The *white dots* show earthquakes that occurred within a 50-km width of the profile. The *two dashed lines* in (**a**, **b**) denote the 410 and 670 km discontinuities. The *two black lines* in (**b**) show the rays with the minimum and maximum epicentral distances to the seismic stations in Japan. **c** Map showing the earthquake (*S, red star*), the target study area (*the box*), the location of the profile in (**a**, **b**), and some teleseismic rays (*red lines*). The *blue lines* show the plate boundaries. **d** Distribution of the Hi-net stations that recorded the earthquake in (**c**). The *colors of the dots* denote the outside residuals, the same as in (**a**). (Modified from Zhao et al. 2013)

tomography. Then for a set of *m* rays from a teleseismic event observed by *m* seismic stations in Japan, they calculated the average of the differential times (T3d-T1d) and then subtracted the average from each of the *m* differential times. This procedure is similar to the construction of relative travel-time residuals shown in Eqs. (7.1)–(7.3). Thus, relative travel-time residuals caused by the mantle heterogeneity outside the target volume were obtained, which were called *outside residuals* (Zhao et al. 2013).

Distributions of the outside residuals for a teleseismic event (M 6.9) that occurred in Alaska (Fig. 7.26c) are shown in Figs. 7.26a and d. The outside residuals range from −0.23 to +0.24 s, which are certainly larger than the picking error of the observed P-wave arrivals (~0.10 s). The negative outside residuals are caused by rays passing through the high-V subducting Pacific slab in the MTZ and the up-

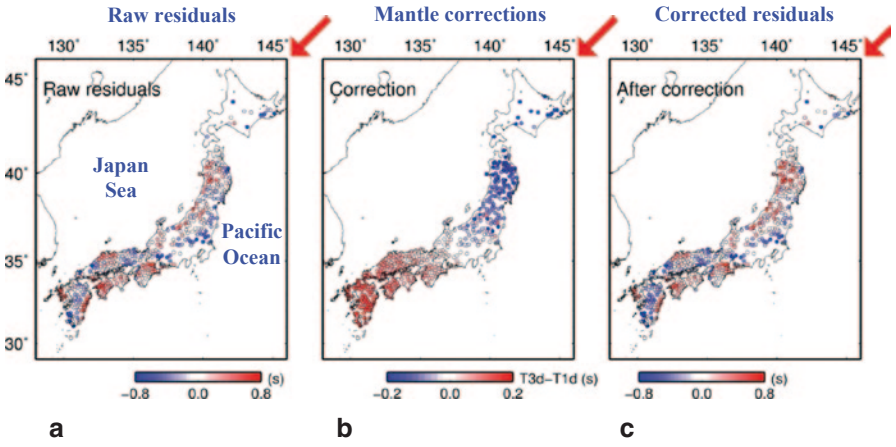

Fig. 7.27 Distribution of the Japanese seismic stations which recorded the earthquake in Fig. 7.26. **a** Observed relative travel-time residuals. **b** Outside residuals (the same as Fig. 7.26d). **c** The same as in (**a**) but after correction, i.e., the difference between those in (**a**) and (**b**). The *scales* are shown below each map. The *red arrows* denote the ray coming direction. Note that the scale in (**b**) is different from those in (**a**, **c**). (Modified from Zhao et al. 2013)

permost lower mantle under the northern and western Pacific regions (Fig. 7.26b), which were observed by the seismic stations in NE Japan (Fig. 7.26d). In contrast, the positive outside residuals correspond to rays passing through a few slow anomalies in the lower mantle (Fig. 7.26b), which were recorded by the seismic stations in SW Japan (Fig. 7.26d).

Figure 7.27a shows the distribution of the observed relative residuals for the Alaskan earthquake (Fig. 7.26c). Figure 7.27c shows the distribution of the observed residuals that were corrected for the whole-mantle heterogeneity, that is, the outside residuals shown in Fig. 7.27b (the same as Fig. 7.26d) were subtracted from the raw relative residuals in Fig. 7.27a. Because the observed relative residuals range from −0.80 to +0.81 s (Fig. 7.27a), whereas the outside residuals vary from −0.23 to +0.24 s, the pattern of the residual distribution remains nearly the same even after the correction, though the amplitudes of the relative residuals exhibit some changes (Figs. 7.27a, c).

Figures 7.28 and 7.29 show another example of the outside residuals and the observed relative residuals for a Sumatra earthquake with a magnitude of 6.6 (Fig. 7.28c). The outside residuals range from −0.29 to +0.24 s. Similar to the case of the Alaskan event (Fig. 7.26), the negative outside residuals of the Sumatra earthquake are caused by the rays passing through the high-V Pacific slab and also the Philippine Sea slab in the MTZ and uppermost lower mantle beneath the Ryukyu back-arc region (Fig. 7.28b), which were observed by the seismic stations in SW Japan (Fig. 7.28d). In contrast, the positive outside residuals correspond to the rays passing through some low-V zones in the lower mantle (Fig. 7.28b), which were observed by the seismic stations in NE Japan (Fig. 7.28d). It seems that the high-V anomalies in the MTZ and the lower mantle beneath the Sumatra earthquake

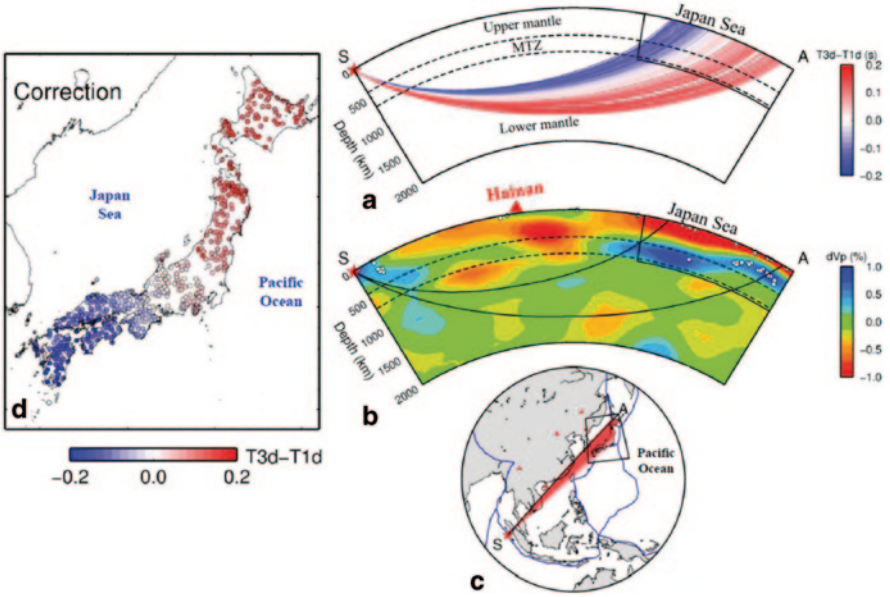

Fig. 7.28 The same as Fig. 7.26 but for an earthquake which occurred in Sumatra as shown in (**c**). The event (M 6.6) occurred on 17 May 2006 with a focal depth of 12 km. (Modified from Zhao et al. 2013)

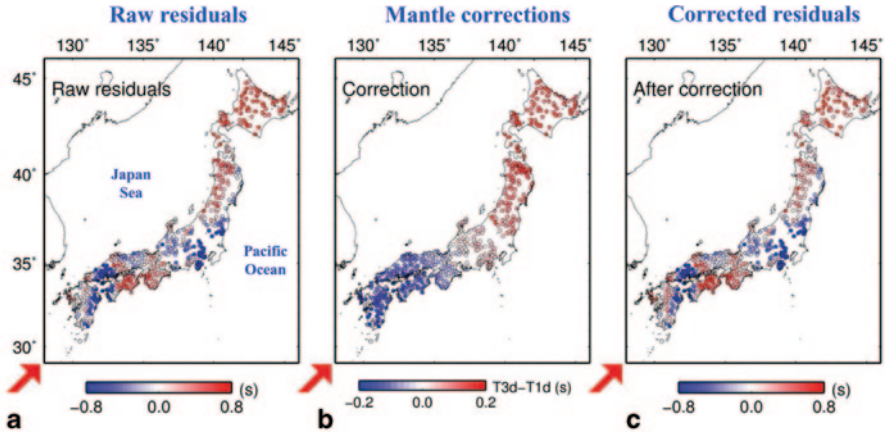

Fig. 7.29 The same as Fig. 7.27 but for the Sumatra earthquake shown in Fig. 7.28. (Modified from Zhao et al. 2013)

hypocenter (Fig. 7.28b), which reflect the subducting Australian plate (Fig. 7.8), have also contributed to the outside residuals (Fig. 7.28b). The pattern of the residual distributions also remains the same after the correction, but there are some changes in the amplitude of the relative residuals (Fig. 7.29a, c).

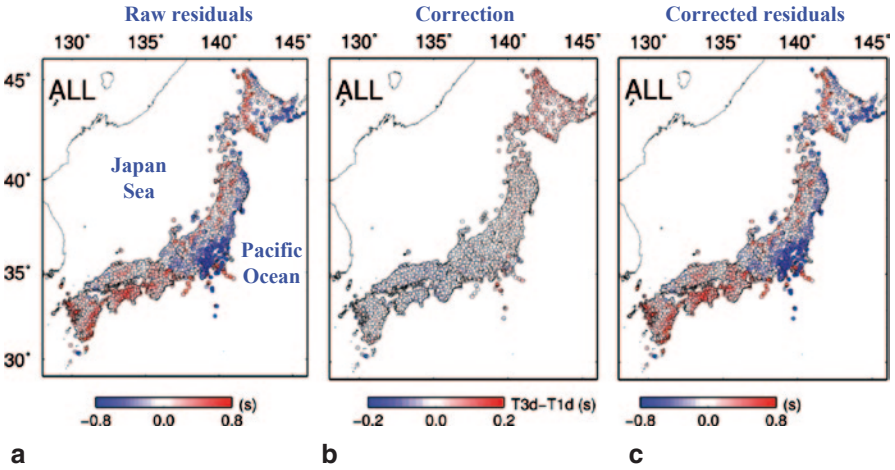

Fig. 7.30 The same as Fig. 7.29 but for 360 teleseismic events in all directions with epicentral distances of 26–99°. (Modified from Zhao et al. 2013)

Zhao et al. (2013) examined the outside residuals for all the 360 teleseismic events. Their results show that the outside residuals vary from −0.25 to +0.25 s for most of the teleseismic events, whereas the outside residuals reach −0.40 to +0.40 s for some events when the teleseismic rays pass through very heterogeneous anomalies in the lower mantle, such as the Pacific and African superplumes and the deeply subducted slabs (Figs. 7.7–7.10). Figure 7.30a shows the distribution of observed relative travel-time residuals of all the 360 teleseismic events recorded by the Japanese stations. Negative residuals are visible at stations on the Pacific coast of eastern Honshu and Hokkaido, whereas positive residuals appear at stations located in the volcanic areas (see the inset map in Fig. 7.31), western Japan, and the western coast of eastern Japan. This distribution pattern of the teleseismic residuals is well consistent with those revealed by the previous studies (Zhao and Hasegawa 1994; Zhao et al. 1994, 2012b; Abdelwahed and Zhao 2007; Huang et al. 2013b). The outside residuals for all the 360 teleseismic events are relatively small, ranging from −0.12 to +0.12 s (Fig. 7.30b), because they are the average of the outside residuals from all the teleseismic events which are situated in different quadrants and so the rays pass through both slow and fast velocity anomalies in the mantle. Hence, the distribution of the corrected residuals (Fig. 7.30c) shows the same pattern as that of the raw residuals (Fig. 7.30a).

Zhao et al. (2012b) determined a high-resolution 3-D P-wave velocity (Vp) model of the Japan subduction zone down to a depth of 700 km (Fig. 7.31a–d) by jointly inverting the 45,425 P-wave relative residuals from the 360 teleseismic events and 274,268 P-wave arrival times from 1180 local shallow and deep earthquakes under the Japan Islands. The local events used have reliable hypocentral parameters, and their mislocation errors are <5 km. A 3-D grid net was set up in the target volume under the Japan Islands with a grid interval of 0.33° in the lateral

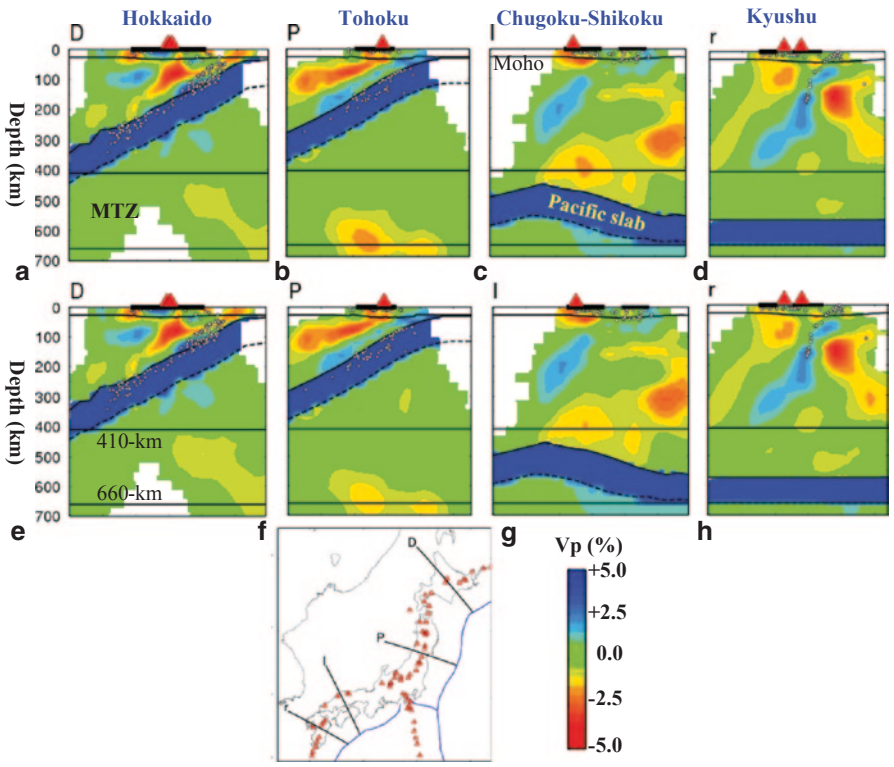

Fig. 7.31 Vertical cross-sections of regional P-wave tomography of the Japan subduction zone. **a**–**d** The 3-D Vp model obtained by using a conventional teleseismic tomography method assuming the mantle structure outside the study area is laterally homogeneous. **e**–**h** The 3-D Vp model obtained after correcting for the global velocity heterogeneity as shown in Figs. 7.3 and 7.4. The locations of the profiles are shown in the *inset map*. The *red* and *blue colors* denote low and high velocities, respectively. The velocity perturbation (in %) scale is shown at the *bottom*. The *white dots* show earthquakes that occurred within a 20-km width of each profile. The *red triangles* denote active arc volcanoes on the Japan Islands. *MTZ*, the mantle transition zone. (Modified from Zhao et al. 2013)

direction 10–30 km in depth. The inversion of the teleseismic data is similar to that of the ACH method. See Zhao et al. (1994, 2012b) for details of the model setup and tomographic inversion for the Japan subduction zone.

The tomographic images in Fig. 7.31a–d were obtained by inverting the local-earthquake arrival times and raw relative residuals of the 360 teleseismic events (Fig. 7.30a), i.e., the crustal and mantle structure outside the target volume was represented by the 1-D iasp91 model. In contrast, the images shown in Fig. 7.31e–h were determined by inverting the local-event data and the corrected relative residuals of the 360 teleseismic events (Fig. 7.30c), i.e., the whole crustal and mantle structure outside the Japan subduction zone was represented by the 3-D global velocity model (Figs. 7.3–7.10). It is clear that the two local 3-D Vp models are quite

similar to each other. The pattern of the images is nearly the same, whereas there are some minor differences in the amplitude of velocity anomalies, in particular, at depths greater than 300 km, both above and below the subducting Pacific slab (Fig. 7.31).

These results (Figs. 7.26–7.30) indicate that the whole-mantle velocity anomalies outside the target volume of a teleseismic local or regional tomography have remarkable effects (~0.2–0.4 s) on the relative travel-time residuals of the individual teleseismic events recorded by the local seismic network in the target area (Zhao et al. 2013). This amount of effects is certainly greater than the picking error of the observed teleseismic P-wave arrivals (~0.1 s). The effects may become more serious and complex for a large-aperture seismic network, such as the USArray (e.g., Tian and Zhao 2012; Huang and Zhao 2013) and ChinaArray (e.g., Huang and Zhao 2006; Wei et al. 2012, 2013; Huang et al. 2014). Therefore, it is necessary and important to make corrections to the observed teleseismic residuals for the whole-mantle velocity heterogeneity using a reliable 3-D global velocity model, enabling a better local or regional tomography to be determined using the ACH-type inversion methods.

Zhao et al. (2013) pointed out that such a correction for the whole-mantle heterogeneity is also necessary for other branches of seismology, such as inverting teleseismic waveforms for the rupture process of large earthquakes (e.g., Shao et al. 2011; Lay et al. 2011), and mapping mantle discontinuities (the Moho, 410 and 660 km) using the teleseismic receiver-function methods (e.g., Ai et al. 2005; Helffrich et al. 2010; Tian et al. 2010). It would be interesting to study how much the global mantle heterogeneity affects teleseismic waveform inversion and receiver-function results.

7.5 Insight into Deep Earth Dynamics

The Earth's interior exhibits a layered structure and is composed of several spherical layers which are separated by major seismic discontinuities such as the Moho, 410, 670 km, CMB and ICB (the inner core boundary). It is important to know the relative strength of lateral heterogeneity in every layers of the Earth, which has important geodynamical implications. Figure 7.32 shows depth distributions of the root-mean-square (RMS) amplitude of velocity heterogeneity for the global mantle and the mantle beneath South Pacific, East Africa, and Western Pacific. The method of calculating the RMS amplitudes is described by Tanimoto (1990) and Zhao (2004). For the global mantle, the strength of velocity heterogeneity (SVH) is much greater in the upper mantle than that in the lower mantle, and it becomes the minimum at a depth of ~1800 km (Fig. 7.32a). This indicates that, as a whole, the seismic structure of the upper mantle is much more inhomogeneous than that of the lower mantle, and the lower mantle contains much less heterogeneity except for the D" layer in the lowermost mantle (e.g., Tanimoto 1990; Zhao 2004). High-V anomalies dominate in the upper mantle, and the SVH becomes smaller suddenly at the 410 and 670 km discontinuities (Fig. 7.32a, d). The high-V SVH becomes the

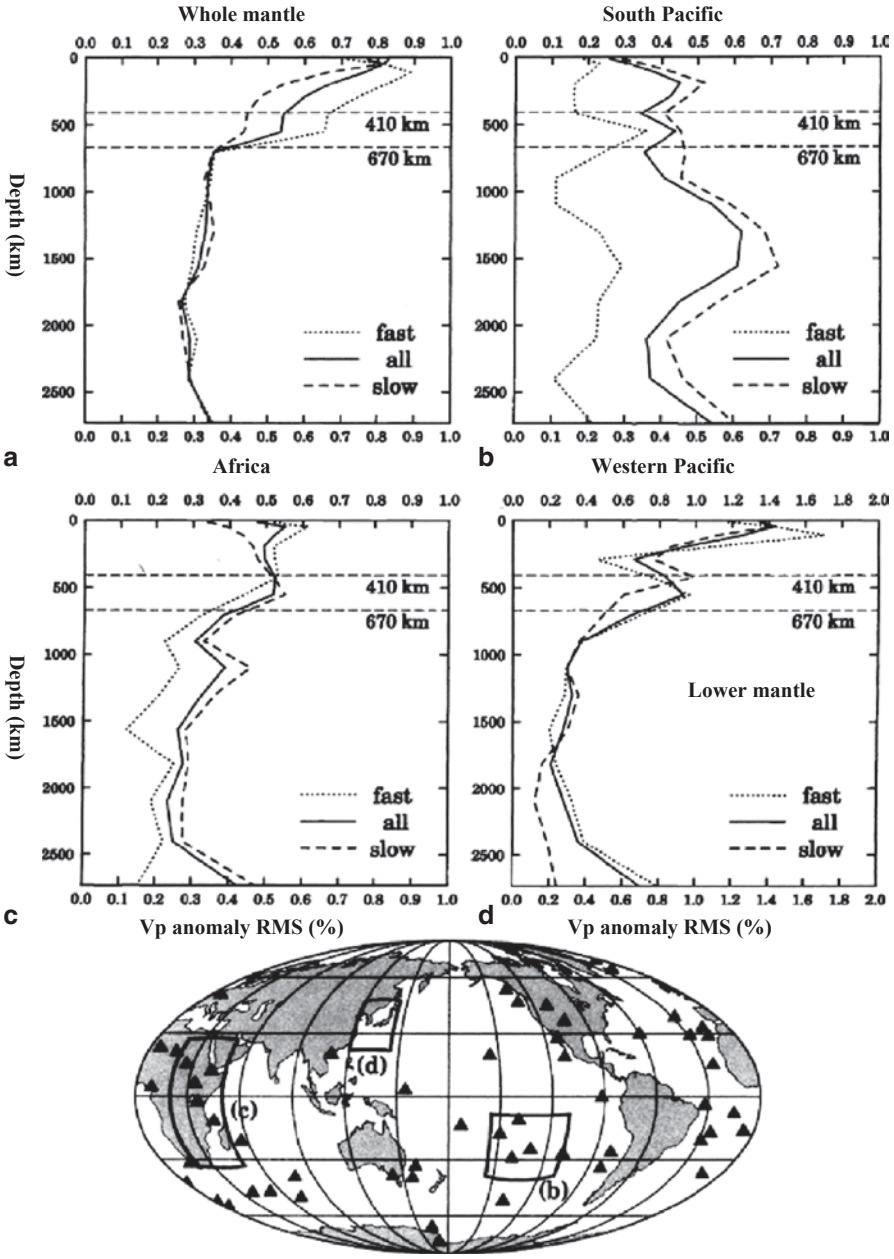

Fig. 7.32 Root-mean-square (RMS) amplitude of velocity heterogeneity versus depth for the global mantle (**a**) and for the mantle under South Pacific (**b**), Africa (**c**), and Western Pacific (**d**). The units are percent perturbation relative to the average velocity at the given depth. The *boxes* in the world map show the ranges of the regions in (**b**–**d**). The *dashed*, *dotted* and *solid lines* denote the results for slow, fast and all velocity anomalies, respectively. (Modified from Zhao 2009)

maximum in the shallow mantle (< 300 km), which reflects the old and stable continental regions including the cratonic areas. The high-V SVH is also large in the MTZ, which reflects stagnant slabs under the back-arc regions of subduction zones (Fig. 7.32a, d). At the 670 km discontinuity, however, the SVH drops suddenly and it remains nearly the same level for most parts of the lower mantle (Fig. 7.32a, d). This result indicates that, from a global point of view, the signatures of plate tectonics and subducting slabs are the most significant in the upper mantle and the MTZ, but such signatures become much smaller in the lower mantle right beneath the 670 km discontinuity. In the D" layer above the CMB, the SVH of both low-V and high-V anomalies becomes large again, which appears in all the global tomographic models (e.g., Tanimoto 1990; Fukao et al. 2001; Zhao et al. 2013).

Under South Pacific and East Africa where two superplumes are considered to exist, low-V anomalies dominate at all depths in the mantle (except for the shallow upper mantle in Africa), whereas high-V anomalies become less significant (Fig. 7.32b, c). The SVH is very large in the lower mantle, unlike the case of the global average (Fig. 7.32a). Two peaks are visible in the SVH under South Pacific: one is at depths of 1200–1700 km, the other is in the D" layer (Fig. 7.32b). The two peaks reflect the major velocity anomalies of the Pacific superplume in the middle and bottom of the mantle (see Fig. 7.24). Under East Africa, the SVH also increases significantly in the D" layer. From the tomographic images and the SVH distribution in the mantle, the Pacific superplume appears to be greater and stronger than the African superplume.

It should be pointed out that the amplitude of velocity anomalies in the mantle revealed by seismic tomography is affected by damping and smoothing regularizations which are required for stabilizing tomographic inversions because of the uneven distribution of seismic rays in the Earth's interior (Zhao 2009). Thus, the SVH in the real Earth is hard to recover completely, and the degree of recovery depends on the scale of the study area, density and homogeneity of the ray path coverage, as well as the resolution scale of a tomographic model. In the local-scale tomography, seismic stations and earthquakes are distributed more uniformly, and so weak damping and smoothing can be applied, leading to better recovery of the amplitude of velocity anomalies which can be up to 6–10% (e.g., Zhao et al. 1992; Huang et al. 2011; Liu et al. 2013). In contrast, strong damping and smoothing have to be applied to the global or large-scale regional tomography because of the very uneven distribution of seismic stations and earthquakes, which leads to velocity anomalies with smaller amplitudes of 1–2% (e.g., Zhao 2001, 2004; Wei et al. 2012; Zhao et al. 2013). Therefore, the SVH features (Fig. 7.32) reflect only relative variations in the strength of mantle heterogeneity in different layers of the Earth's interior and beneath different tectonic settings.

Figure 7.33a shows a representative vertical cross-section of P-wave tomography under Western Pacific and East Asia (Zhao 2009). The subducting Pacific slab becomes stagnant in the MTZ under East Asia, and prominent high-V anomalies are visible in the lower mantle and the D" layer. This tomographic image suggests that the subducting Pacific slab meets strong resistance at the 670-km discontinuity, hence the slab bends horizontally, and accumulates there for a long time (~ 50 m.y.),

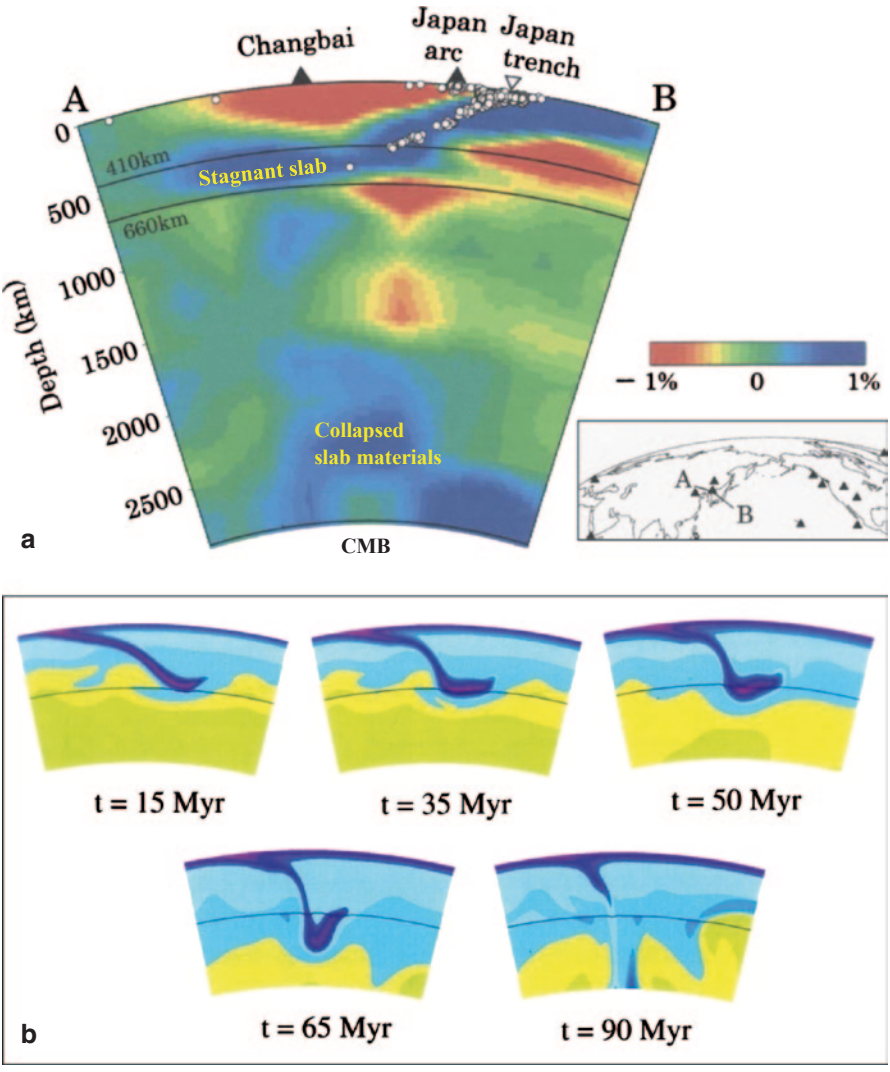

Fig. 7.33 **a** Vertical cross-section of whole-mantle P-wave tomography along a profile passing through Japan and Eastern China (modified from Zhao 2009). The *red* and *blue colors* denote low and high velocities, respectively. The velocity perturbation scale is shown on the *right*. The *two solid lines* denote the 410 and 670 km discontinuities. The *white dots* show earthquakes which occurred within a 100 km width of the profile. **b** A computer simulation result showing the interaction of a subducting slab with the 670 km discontinuity. (Modified from Mitrovica et al. 2000)

and then finally collapses to fall down as blobs onto the D" layer as a result of very large gravitational instability from phase transitions. This scenario has been well explained by the computer simulation results (Mitrovica et al. 2000; Fig. 7.33b). In the western Pacific and East Asian region, high-V anomalies dominate at most parts of the mantle (Fig. 7.32d). The first peak of high-V anomalies is visible at

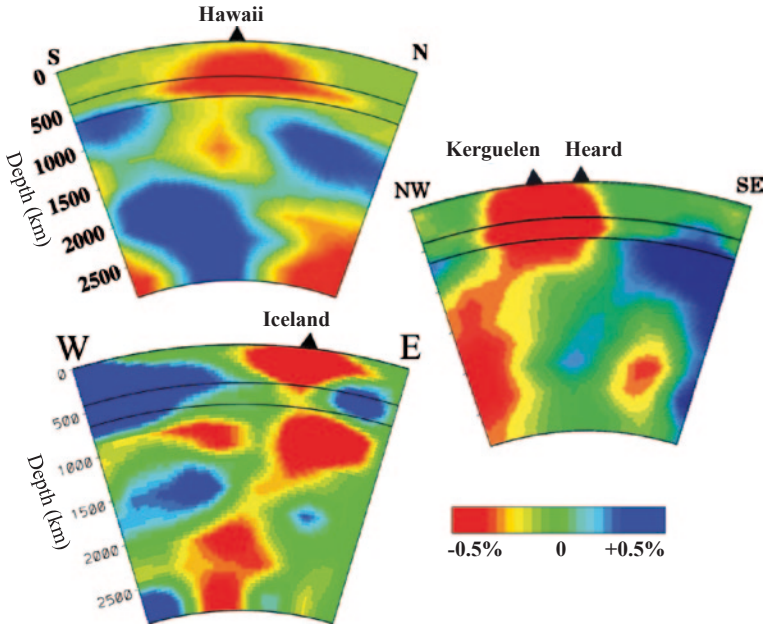

Fig. 7.34 Whole-mantle P-wave tomography under three major hotspot areas. The *black triangles* denote the surface locations of the hotspot volcanoes. The *two thin lines* denote the 410 and 670 km discontinuities. The *red* and *blue colors* denote low and high velocities, respectively. (Modified from Zhao 2001, 2009)

depths shallower than ~200 km, which reflects the old Pacific plate at the surface and its initial stage of subduction. The second peak appears in the MTZ and down to a depth of ~900 km, which reflects the stagnant slab and pieces of old slab materials collapsing down to the lower mantle (Figs. 7.33a). The third peak occurs from a depth of 2000 km to CMB, which is due to the old slab materials collapsed down to the lowermost mantle and piled up in the D" layer (Fig. 7.33a). Low-V anomalies dominate at depths of 200–500 km (Fig. 7.32d), which reflects the arc and back-arc magma and fluids in the BMW above the stagnant Pacific slab (Zhao et al. 2004, 2007, 2009b). At depths of 1200–1700 km, low-V anomalies dominate again (Fig. 7.32d), reflecting the slow feature below the subducting Pacific slab (Fig. 7.33a) which may represent hot mantle upwelling associated with collapsing of the slab materials down to the lower mantle (Zhao 2004; Zhao et al. 2012b, 2013).

Figures 7.34 and 7.35 show whole-mantle tomographic images under the representative hotspots in Hawaii, Iceland, Kerguelen, South Pacific, and East Africa. Huge low-V anomalies are visible under South Pacific and East Africa, which have lateral extents of 1000–3000 km and occur in the whole mantle (Fig. 7.35), reflecting two superplumes existing in the present Earth's mantle. Continuous whole-mantle plumes were also detected under Hawaii, Iceland and Kerguelen hotspots (Fig. 7.34). The general shape of the Pacific superplume in the tomog-

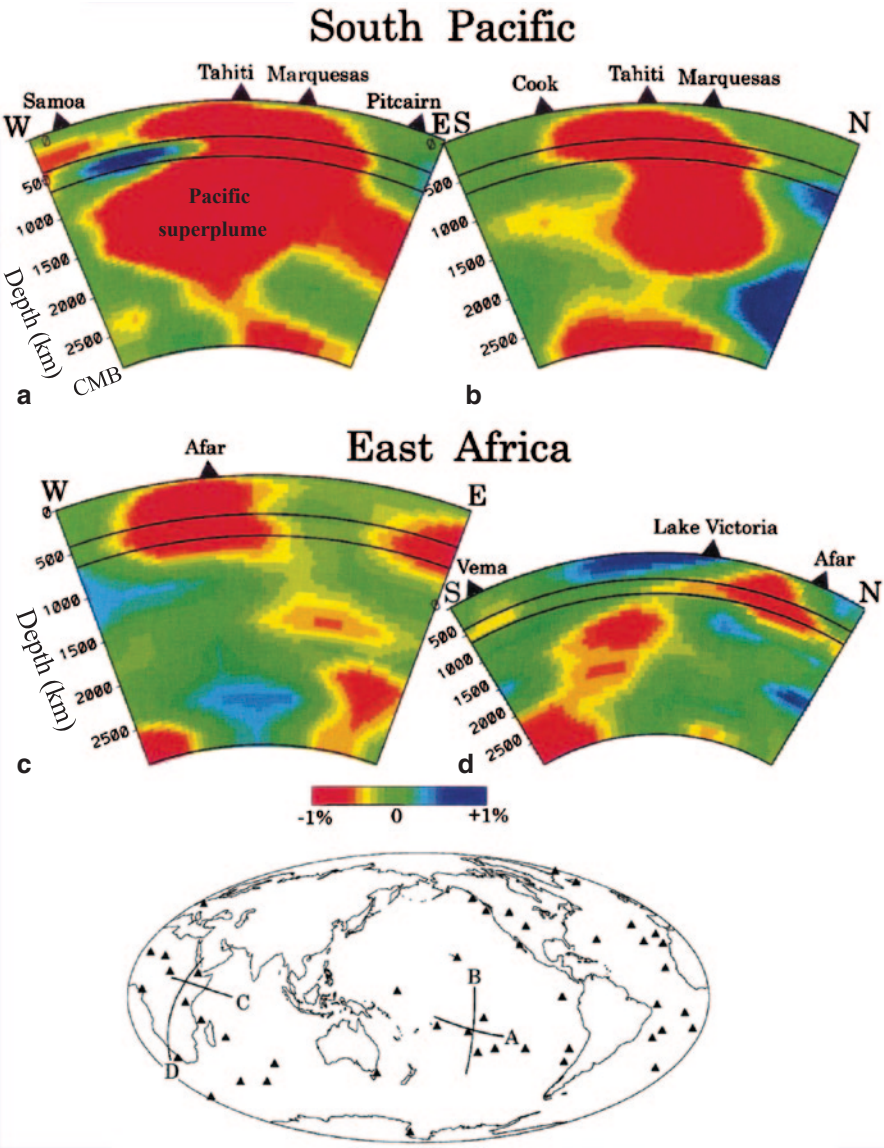

Fig. 7.35 Whole-mantle P-wave tomography under South Pacific (**a**, **b**) and East Africa (**c**, **d**). The locations of the cross-sections are shown in the *inset map*. The *black triangles* denote the surface locations of the hotspot volcanoes. The *two thin lines* denote the 410 and 670 km discontinuities. The *red* and *blue colors* denote low and high velocities, respectively. (Modified from Zhao 2001)

raphy (Fig. 7.35a, b) is coincident with that predicted by a computer simulation of Davies and Pribac (1993) (Fig. 7.36), suggesting that the Pacific superplume is probably made up of a cluster of smaller mantle plumes feeding the several hotspots in South-Central Pacific shown in Figs. 5.1 and 7.37b (see also Schubert et al.

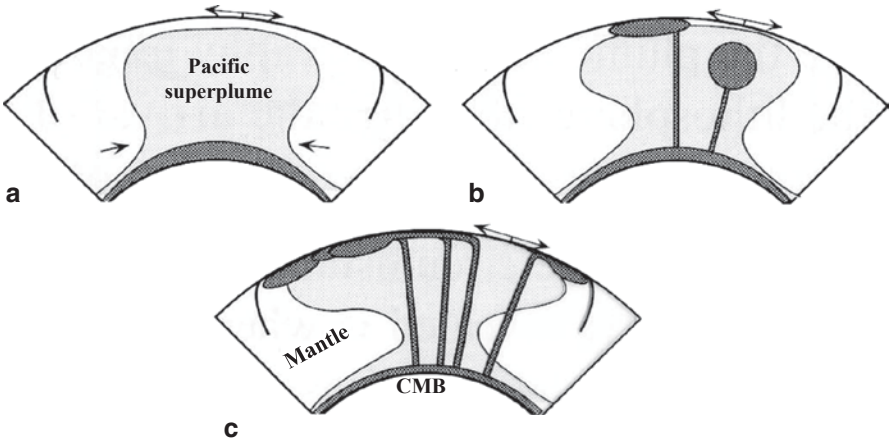

Fig. 7.36 Estimated geometry of the Pacific superplume from computer simulations. (Modified from Davies and Pribac 1993)

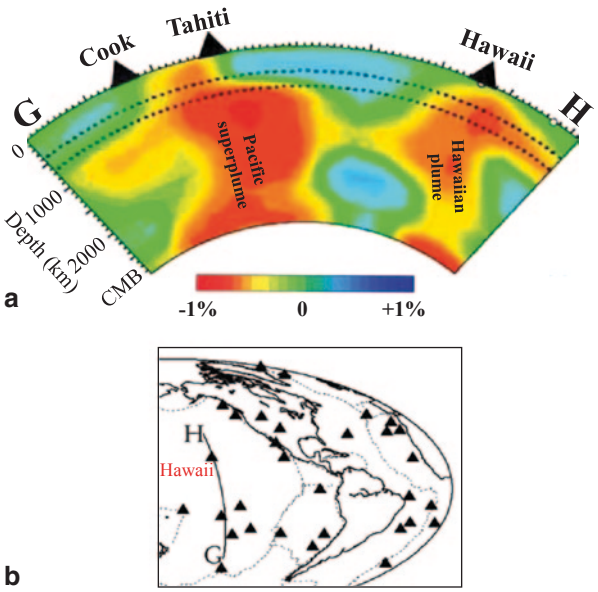

Fig. 7.37 (**a**) A north-south vertical cross-section of P-wave tomography along the profile *GH* shown in the *inset map* (**b**). The *black triangles* show the surface hotspot volcanoes. The *red* and *blue colors* denote slow and fast velocities, respectively. The velocity perturbation scale is shown below (**a**). (Modified from Lei and Zhao 2006b)

2004). In addition to the global tomography, results of seismic waveform modeling and receiver-function studies also suggested a lower-mantle or CMB origin of the Hawaiian plume (e.g., Ji and Nataf 1998; Russell et al. 1999; Li et al. 2003) and the Iceland plume (e.g., Helmberger et al. 1998; Shen et al. 2002).

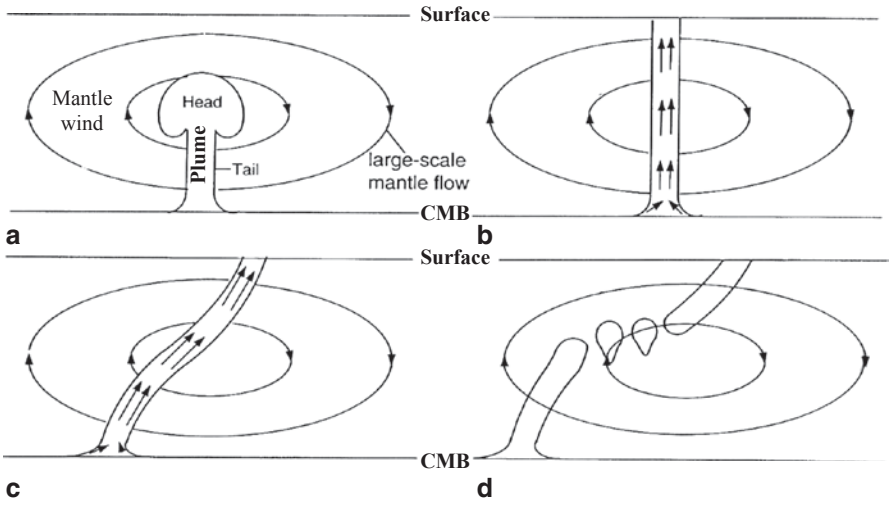

Fig. 7.38 Four potential stages in the evolution of a mantle plume after it impinges on the lithosphere. (Modified from Steinberger and O'Connell 1998)

An important feature revealed by the global tomography of Zhao (2001, 2004) is that low-V anomalies under the major hotspots usually do not show a straight pillar shape, but exhibit winding images (Figs. 7.34 and 7.35), suggesting that plumes are not fixed in the mantle but can be deflected by mantle flow (or mantle wind), as was pointed out by several numerical simulation studies (e.g., Griffiths and Richards 1989; Loper 1991; Steinberger 2000; Fig. 7.38). Other seismic imaging (Bijwaard et al. 1998; Shen et al. 2002) and paleomagnetic studies (Tarduno et al. 2003) have also suggested the deflection of plume tails in the convective mantle. If the hotspots on the Earth's surface are caused by mantle plumes, then the deflection of plumes would cause the hotspots to wander on the Earth's surface instead of being fixed in the long geological history, though the relative moving velocities of the hotspots are much smaller than those of the lithospheric plates (Steinberger 2000; Tarduno et al. 2003; Zhao 2001, 2004, 2007).

The Pacific superplume seems to be the largest mantle plume in the present Earth, whereas the Hawaiian plume seems to be the strongest plume, considering the fact that the Hawaiian hotspot has the largest heat flux among all the hotspots on Earth (Sleep 1990). Then a question arises: what is the relationship between the largest plume and the strongest plume? Some earlier tomographic studies suggested that the Hawaiian plume is part of the Pacific superplume, but recent tomographic results have indicated that this is not true (e.g., Zhao 2001, 2009; Lei and Zhao 2006a; Zhao et al. 2013). The Hawaiian plume is certainly not part of the Pacific superplume but an independent whole-mantle plume (Fig. 7.37a). However, the two low-V zones under Hawaii and Tahiti seem to be connected at depths of 1500–1600 km (Fig. 7.37a), which may suggest that there are some heat or material exchanges between the Hawaiian plume and the Pacific superplume in the mid mantle (Zhao 2004, 2009).

7.6 Summary

1. A novel flexible-grid tomographic inversion resulted in a better global tomographic model (Zhao et al. 2013). Although the general pattern of the new global model is the same as that of the existing models, the mantle tomography under the polar regions is better determined, because the flexible grid can better express the mantle structure under the polar regions. Subducting slabs and mantle plumes have been generally imaged well, which provides new insights into deep Earth dynamics.
2. Seismic ray paths in the 3-D global velocity model deviate considerably from those in the average 1-D Earth model, such as the iasp91 model. For a PcP ray in the mantle under Western Pacific to East Asia where the high-V (1–2 %) Pacific slab is subducting, its ray-path change amounts to 27 km. For a PcP ray in South Pacific where low-V anomalies (the Pacific superplume) exist in the whole mantle, its ray path is displaced by as much as 77 km. Ray paths of other phases (P, pP, and PP) also change by tens of kilometers. The travel-time changes of these waves in the 3-D velocity model amount to 3.9 s. These results suggest that, although the maximal velocity anomaly of the global tomographic model is only 1–2 %, rays passing through regions with strong lateral heterogeneity (in velocity and/or discontinuity topography) can deviate significantly from those in a 1-D model, because the rays have very long trajectories in the global case. If a lower-resolution 3-D velocity model is estimated with larger blocks or grid intervals (3–5°) adopted for inversion, 1-D ray tracing may be feasible. However, if smaller blocks or grid intervals are adopted to determine a higher-resolution model, 3-D ray tracing is necessary and important for global tomography (Zhao and Lei 2004).
3. The use of different kinds of mantle and core phases can improve the mantle tomography. When only the direct P-wave data are used, the resolution is good for most part of the mantle, except for oceanic regions down to a depth of ~1000 km and for most of the D" layer. The PP data can better constrain the structure down to the middle mantle, in particular, for the upper mantle beneath oceans. The PcP data can improve the ray coverage in the middle and lower mantle around the Pacific rim and Europe, whereas the Pdiff data can help improve the tomographic resolution in the lowermost mantle. The outer-core phases (PKP, PKiKP and PKKP) can improve the resolution in the lowermost mantle of the southern hemisphere and beneath oceanic regions. When smaller blocks or grid intervals are adopted to determine a high-resolution model, the pP data are very useful for improving the upper mantle structure. These results suggest that later seismic phases are of great importance in better constraining the mantle structure and dynamics (Zhao 2001, 2004; Lei and Zhao 2006a, b).
4. The global mantle heterogeneities outside the target volume of a local or regional tomography can cause significant changes (0.2–0.4 s) to the observed relative travel-time residuals of a teleseismic event. Although the pattern of regional tomography remains the same even after correcting for the global mantle het-

erogeneity, the amplitude of velocity anomalies in the regional tomography is changed. To obtain a better local or regional tomography, it is necessary to correct for the global mantle heterogeneity outside the target volume (Zhao et al. 2013).

5. Most of the slab materials are stagnant in the mantle transition zone before finally collapsing down to the lower mantle as a result of very large gravitational instability from mantle phase transitions. Plume-like low-V anomalies are visible under the major hotspots in most parts of the mantle, and the low-V zones usually exhibit winding images, suggesting that plumes can be deflected by the mantle flow. As a consequence, hotspots are not really fixed but can wander on the Earth's surface. Broad and strong low-V anomalies have been revealed in the D" layer, which show a good correlation with the hotspot distribution on the surface, suggesting that most of the strong plumes feeding the major hotspots may originate from the CMB. Huge low-V anomalies exist in the entire mantle under East Africa and South-Central Pacific, which represent two superplumes originating from the CMB. The Pacific superplume has a larger spatial extent and stronger low-V anomalies than those of the African superplume. Hawaii, the most active hotspot on Earth, is fed by an isolated whole-mantle plume which deflected toward the south. There may be some heat or material exchanges between the Hawaiian plume and the Pacific superplume at the mid-mantle depth.

References

Abdelwahed, M., Zhao, D.: Deep structure of the Japan subduction zone. Phys. Earth Planet. Inter. **162**, 32–52 (2007)

Ai, Y., Zhao, D., Gao, X., Xu, W.: The crust and upper mantle discontinuity structure beneath Alaska inferred from receiver functions. Phys. Earth Planet. Inter. **150**, 339–350 (2005)

Aki, K., Christofferson, A., Husebye, E.: Determination of the three-dimensional seismic structure of the lithosphere. J. Geophys. Res. **82**, 277–296 (1977)

Ballard, S., Hipp, J., Young, C.: Efficient and accurate calculation of ray theory seismic travel time though variable resolution 3-D earth models. Seismol. Res. Lett. **80**, 990–1000 (2009)

Becker, T., Boschi, L.: A comparison of tomographic and geodynamic mantle models. Geochem. Geophys. Geosyst. **3**, 1003 (2002)

Becker, T., Kellogg, J., Ekstrom, G., O'Connell, R.: Comparison of azimuthal seismic anisotropy from surface waves and finite-strain from global mantle-circulation models. Geophys. J. Int. **155**, 696–714 (2003)

Bijwaard, H., Spakman, W.: Fast kinematic ray tracing of first- and later-arriving global seismic phases. Geophys. J. Int. **139**, 359–369 (1999)

Bijwaard, H., Spakman, W.: Non-linear global P-wave tomography by iterated linearized inversion. Geophys. J. Int. **141**, 71–82 (2000)

Bijwaard, H., Spakman, W., Engdahl, E.: Closing the gap between regional and global travel time tomography. J. Geophys. Res. **103**, 30055–30078 (1998)

Boschi, L., Dziewonski, A.: High- and low-resolution images of the earth's mantle: implications of different approaches to tomographic modeling. J. Geophys. Res. **104**, 25567–25594 (1999)

Boschi, L., Dziewonski, A.: Whole earth tomography from delay times of P, PcP and PKP phases: lateral heterogeneities in the outer core or radial anisotropy in the mantle? J. Geophys. Res. **105**, 13675–13696 (2000)

Davies, G.F., Pribac, F.: Mesozoic seafloor subsidence and the Darwin rise: past and present. In: Pringle, M., Sager, W., Sliter, W., Stein, S. (eds.) The Mesozoic Pacific: Geology, Tectonics, and Volcanism (Geophys. Monogr. **77)**, pp. 39–52. Am. Geophys. Union (1993)

Dziewonski, A.: Mapping the lower mantle: determination of lateral heterogeneity in P velocity up to degree and order 6. J. Geophys. Res. **89**, 5929–5952 (1984)

Dziewonski, A., Anderson, D.: Seismic tomography of the earth's interior. Am. Sci. **72**, 483–494 (1984)

Dziewonski, A., Romanowicz, B.: Overview. In: Schubert, G. (ed.) Treatise in Geophysics, vol. 1, pp. 1–19. Elsevier, New York (2007)

Dziewonski, A., Hager, B., O'Connell, R.: Large-scale heterogeneities in the lower mantle. J. Geophys. Res. **82**, 239–255 (1977)

Engdahl, E.: Application of an improved algorithm to high precision relocation of ISC test events. Phys. Earth Planet. Inter. **158**, 14–18 (2006)

Engdahl, E., van der Hilst, R., Buland, R.: Global teleseismic earthquake relocation with improved travel times and procedures for depth determination. Bull. Seismol. Soc. Am. **88**, 722–743 (1998)

Evans, J., Achauer, U.: Teleseismic velocity tomography using the ACH method: theory and application to continental-scale studies. In: Iyer, H., Hirahara, K. (eds.) Seismic Tomography: Theory and Practice, pp. 319–360. Chapman and Hall, London (1993)

Flanagan, M., Shearer, P.: Global mapping of topography on transition zone velocity discontinuities by stacking SS precursors. J. Geophys. Res. **103**, 2673–2692 (1998)

Fukao, Y., Widiyantoro, S., Obayashi, M.: Stagnant slabs in the upper and lower mantle transition region. Rev. Geophys. **39**, 291–323 (2001)

Garnero, E., McNamara, A.: Structure and dynamics of Earth's lower mantle. Science. **320**, 626–628 (2008)

Gorbatov, A., Fukao, Y., Widiyantoro, S.: Application of a three-dimensional ray-tracing technique to global P, PP and Pdiff traveltime tomography. Geophys. J. Int. **146**, 583–593 (2001)

Grand, S.: Mantle shear-wave tomography and the fate of subducted slabs. Phil. Trans. Royal Soc. A. **360**, 2475–2491 (2002)

Griffiths, R., Richards, M.: The adjustment of mantle plumes to changes in plate motion. Geophy. Res. Lett. **16**, 437–440 (1989)

Gu, Y.J., Dziewonski, A., Agee, C.: Global de-correlation of the topography of transition zone discontinuities. Earth Planet. Sci. Lett. **157**, 57–67 (1998)

Gu, Y.J., Okeler, A., Schultz, R.: Tracking slabs beneath northwestern Pacific subduction zones. Earth Planet. Sci. Lett. **331**, 269–280 (2012)

Gung, Y., Romanowicz, B.: Q tomography of the upper mantle using three-component long period waveforms. Geophys. J. Int. **157**, 813–830 (2004)

Gupta, S., Zhao, D., Rai, S.: Seismic imaging of the upper mantle under the Erebus hotspot in Antarctica. Gondwana Res. **16**, 109–118 (2009)

He, R., Zhao, D., Gao, R., Zheng, H.: Tracing the Indian lithospheric mantle beneath central Tibetan plateau using teleseismic tomography. Tectonophysics. **491**, 230–243 (2010)

Helffrich, G., Faria, B., Fonseca, J., Lodge, A., Kaneshima, S.: Transition zone structure under a stationary hot spot: Cape Verde. Earth Planet. Sci. Lett. **289**, 156–161 (2010)

Helmberger, D., Wen, L., Ding, X.: Seismic evidence that the source of the Iceland hotspot lies at the core-mantle boundary. Nature. **396**, 251–258 (1998)

Houser, C., Masters, G., Flanagan, M., Shearer, P.: Determination and analysis of long-wavelength transition zone structure using precursors. Geophys. J. Int. **174**, 178–194 (2008)

Huang, J., Zhao, D.: High-resolution mantle tomography of China and surrounding regions. J. Geophys. Res. **111**, B09305 (2006)

Huang, Z., Zhao, D.: Mapping P-wave azimuthal anisotropy in the crust and upper mantle beneath the United States. Phys. Earth Planet. Inter. **225**, 28–40 (2013)

Huang, Z., Zhao, D., Wang, L.: Seismic heterogeneity and anisotropy of the Honshu arc from the Japan trench to the Japan sea. Geophys. J. Int. **184**, 1428–1444 (2011)
Huang, G., Bai, C., Greenhalgh, S.: Fast and accurate global multiphase arrival tracking: the irregular shortest-path method in a 3-D spherical earth model. Geophys. J. Int. **194**, 1878–1892 (2013a)
Huang, Z., Zhao, D., Hasegawa, A., Umino, N., Park, J., Kang, I.: Aseismic deep subduction of the Philippine Sea plate and slab window. J. Asian Earth Sci. **75**, 82–94 (2013b)
Huang, Z., Wang, P., Zhao, D., Wang, L., Xu, M.: Three-dimensional P-wave azimuthal anisotropy in the lithosphere beneath China. J. Geophys. Res. **119**, 5686–5712 (2014)
Inoue, H., Fukao, Y., Tanabe, K., Ogata, Y.: Whole mantle P-wave travel time tomography. Phys. Earth Planet. Inter. **59**, 294–328 (1990)
Ishii, M., Tromp, J.: Normal-mode and free-air gravity constraints on lateral variations in velocity and density of earth's mantle. Science. **285**, 1231–1236 (1999)
Ji, Y., Nataf, H.: Detection of mantle plumes in the lower mantle by diffraction tomography: Hawaii. Earth Planet. Sci. Lett. **159**, 99–115 (1998)
Kaneshima, S.: Lower mantle seismic scatters below the subducting Tonga slab: evidence for slab entrainment of transition zone materials. Phys. Earth Planet. Inter. **222**, 35–46 (2013)
Kárason, H., van der Hilst, R.: Tomographic imaging of the lowermost mantle with differential times of refracted and diffracted core phases (PKP, Pdiff). J. Geophys. Res. **106**, 6569–6587 (2001)
Kennett, B., Engdahl, E.: Traveltimes for global earthquake location and phase identification. Geophys. J. Int. **105**, 429–465 (1991)
Kennett, B., Gudmundsson, O.: Ellipticity corrections for seismic phases. Geophys. J. Int. **127**, 40–48 (1996)
Kind, R., Li, X.: Deep earth structure—transition zone and mantle discontinuities. In: Schubert, G. (ed.) Treatise in Geophysics, vol. 1, pp. 571–618. Elsevier, New York (2007)
Kobayashi, R., Zhao, D.: Rayleigh wave group velocity distribution in the Antarctic region. Phys. Earth Planet. Inter. **141**, 167–181 (2004)
Lay, T.: Deep earth structure—lower mantle and D". In: Schubert, G. (ed.) Treatise in Geophysics, vol. 1, pp. 619–654. Elsevier, New York (2007)
Lay, T., Garnero, E.: Deep mantle seismic modeling and imaging. Ann. Rev. Earth Planet. Sci. **39**, 91–123 (2010)
Lay, T., Ammon, C., Kanamori, H., Kim, M., Xue, L.: Outer trench-slope faulting and the 2011 Mw 9.0 off the Pacific coast of Tohoku earthquake. Earth Planet. Space. **63**, 713–718 (2011)
Lei, J., Zhao, D.: Global P-wave tomography: on the effect of various mantle and core phases. Phys. Earth Planet. Inter. **154**, 44–69 (2006a)
Lei, J., Zhao, D.: A new insight into the Hawaiian plume. Earth Planet. Sci. Lett. **241**, 438–453 (2006b)
Li, X.D., Romanowicz, B.: Global mantle shear wave velocity model developed using nonlinear asymptotic coupling theory. J. Geophys. Res. **101**, 22245–22273 (1996)
Li, X.Q., Kind, R., Yuan, X.: Seismic study of upper mantle and transition zone beneath hotspots. Phys. Earth Planet. Inter. **136**, 79–92 (2003)
Li, C., van der Hilst, R., Engdahl, E., Burdick, S.: A new global model for P-wave speed variations in Earth's mantle. Geochem. Geophys. Geosyst. **9**, Q05018 (2008)
Liu, X., Zhao, D., Li, S.: Seismic heterogeneity and anisotropy of the southern Kuril arc: insight into megathrust earthquakes. Geophys. J. Int. **194**, 1069–1090 (2013)
Loper, D.: Mantle plumes. Tectonophysics. **187**, 373–384 (1991)
Masson, F., Trampert, J.: On ACH, or how reliable is regional teleseismic delay time tomography? Phys. Earth Planet. Inter. **102**, 21–32 (1997)
Megnin, C., Romanowicz, B.: The shear velocity structure of the mantle from the inversion of body, surface, and higher modes waveforms. Geophys. J. Int. **143**, 709–728 (2000)
Mitrovica, J., Mound, J., Pysklywec, R., Milne, G.: Sea-level change on a dynamic earth. In: Boschi, E., Esktrom, G., Morelli, A. (eds.) Problems in Geophysics for the New Millennium, pp. 499–529. Editrice Compositori (2000)

Montagner, J.: Earth's structure: global. In: Gupta, H. (ed.) Encyclopedia of Solid Earth Geophysics, pp. 144–154. Springer, Netherlands (2011)
Montagner, J., Tanimoto, T.: Global upper mantle tomography of seismic velocities and anisotropies. J. Geophys. Res. **96**, 20337–20351 (1991)
Montelli, R., Nolet, G., Master, G., Dahlen, F., Hung, S.: Global P and PP traveltime tomography: rays versus waves. Geophys. J. Int. **158**, 637–654 (2004)
Mooney, W., Laske, G., Master, G.: CRUST 5.1: a global crustal model at 5 × 5 degrees. J. Geophys. Res. **103**, 727–747 (1998)
Morelli, A., Dziewonski, A.: Topography of the core–mantle boundary and lateral heterogeneity of the liquid core. Nature. **325**, 678–683 (1987)
Obayashi, M., Fukao, Y.: P and PcP travel time tomography for the core–mantle boundary. J. Geophys. Res. **102**, 17825–17841 (1997)
Paige, C., Saunders, M.: LSQR: an algorithm for sparse linear equations and sparse least squares. ACM Trans. Math. Softw. **8**, 43–71 (1982)
Rawlinson, N., Pozgay, S., Fishwick, S.: Seismic tomography: a window into deep Earth. Phys. Earth Planet. Inter. **178**, 101–135 (2010)
Ritsema, J., Jan der Heijst, H., Woodhouse, J.: Complex shear wave velocity structure imaged beneath Africa and Iceland. Science. **286**, 1925–1928 (1999)
Rodgers, A., Wahr, J.: Inference of core–mantle boundary topography from ISC PcP and PKP travel times. Geophys. J. Int. **115**, 991–1011 (1993)
Romanowicz, B.: A global tomographic model of shear attenuation in the upper mantle. J. Geophys. Res. **100**, 12375–12394 (1995)
Romanowicz, B., Mitchell, B.: Deep earth structure Q of the earth from crust to core. In: Schubert, G. (ed.) Treatise in Geophysics, vol. 1, pp. 731–774. Elsevier, New York (2007)
Russell, S., Lay, T., Garnero, E.: Small scale lateral shear velocity and anisotropy heterogeneity near the core-mantle boundary beneath the central Pacific imaged using broadband ScS waves. J. Geophys. Res. **104**, 13183–13199 (1999)
Schaeffer, A., Lebedev, S.: Global shear speed structure of the upper mantle and transition zone. Geophys. J. Int. **194**, 417–449 (2013)
Schubert, G., Masters, G., Olson, P., Tackley, P.: Superplumes or plume clusters? Phys. Earth Planet. Inter. **146**, 147–162 (2004)
Shao, G., Ji, C., Zhao, D.: Rupture process of the 9 March, 2011 Mw 7.4 Sanriku-Oki, Japan earthquake constrained by jointly inverting teleseismic waveforms, strong motion data and GPS observations. Geophy. Res. Lett. **38**, L00G20 (2011)
Shen, Y., Solomon, S., Bjarnason, I., Nolet, G.: Seismic evidence for a tilted mantle plume and north-south mantle flow beneath Iceland. Earth Planet. Sci. Lett. **197**, 261–272 (2002)
Simons, N., Forte, A., Boschi, L., Grand, S.: GyPSuM: a joint tomographic model of mantle density and seismic wave speeds. J. Geophys. Res. **115**, B12310 (2010)
Simons, N., Myers, S., Johannesson, G.: Global-scale P-wave tomography optimized for prediction of teleseismic and regional travel times for Middle East events: 2. Tomographic inversion. J. Geophys. Res. **116**, B04305 (2011)
Sleep, N.: Hotspots and mantle plumes: some phenomenology. J. Geophys. Res. **95**, 6715–6736 (1990)
Steinberger, B.: Plumes in a convecting mantle: models and observations for individual hotspots. J. Geophys. Res. **105**, 11127–11152 (2000)
Steinberger, B., O'Connell, R.: Advection of plumes in mantle flow: mplications for hotspot motion, mantle viscosity and plume distribution. Geophys. J. Int. **132**, 412–434 (1998)
Stevenson, J.: Limits on lateral density and velocity variations in the earth's outer core. Geophys. J. R. Astron. Soc. **88**, 311–319 (1987)
Su, W., Woodward, R., Dziewonski, A.: Degree 12 model of shear velocity heterogeneity in the mantle. J. Geophys. Res. **99**, 6945–6980 (1994)
Sylvander, M., Ponce, B., Souriau, A.: Seismic velocities at the core-mantle boundary inferred from P-waves diffracted around the core. Phys. Earth Planet. Inter. **101**, 189–202 (1997)

Sze, E., van der Hilst, R.: Core mantle boundary topography from short period PcP, PKP, and PKKP data. Phys. Earth Planet. Inter. **135**, 27–46 (2003)
Takeuchi, N.: Whole mantle SH velocity model constrained by waveform inversion based on three-dimensional Born kernels. Geophys. J. Int. **169**, 1153–1163 (2007)
Tanimoto, T.: Predominance of large-scale heterogeneity and the shift of velocity anomalies between the upper and lower mantle. J. Phys. Earth. **38**, 493–509 (1990)
Tanimoto, T., Anderson, D.: Lateral heterogeneity and azimuthal anisotropy of the upper mantle: Love and Rayleigh waves: 100–250 s. J. Geophys. Res. **90**, 1842–1858 (1985)
Tarduno, J., Duncan, R., Scholl, D., Cottreal, R., Steinberger, B.: The emperor seamounts: southward motion of the Hawaiian hotspot plume in earth's mantle. Science. **301**, 1064–1069 (2003)
Thurber, C., Ritsema, J.: Theory and observation—seismic tomography and inverse methods. In: Schubert, G. (ed.) Treatise in Geophysics, vol. 1, pp. 323–360. Elsevier, New York (2007)
Tian, Y., Zhao, D.: P-wave tomography of the western United States: insight into the Yellowstone hotspot and the Juan de Fuca slab. Phys. Earth Planet. Inter. **200**, 72–84 (2012)
Tian, X., Zhao, D., Zhang, H., Tian, Y., Zhang, Z.: Mantle transition zone topography and structure beneath the central Tien Shan orogenic belt. J. Geophys. Res. **115**, B10308 (2010)
Tong, P., Zhao, D., Yang, D.: Tomography of the 2011 Iwaki earthquake (M 7.0) and Fukushima nuclear power plant area. Solid Earth. **3**, 43–51 (2012)
Trampert, J., van Heijst, H.: Global azimuthal anisotropy in the transition zone. Science. **296**, 1297–1299 (2002)
Um, J., Thurber, C.: A fast algorithm for two-point seismic ray tracing. Bull. Seismol. Soc. Am. **77**, 972–986 (1987)
van der Hilst, R., Widiyantoro, S., Engdahl, E.: Evidence for deep mantle circulation from global tomography. Nature. **386**, 578–584 (1997)
Vasco, D., Johnson, L.: Whole earth structure estimated from seismic arrival times. J. Geophys. Res. **103**, 2633–2671 (1998)
Vasco, D., Johnson, L., Pulliam, R.: Lateral variations in mantle velocity structure and discontinuities determined from P, PP, S, SS, and SS-SdS travel time residuals. J. Geophys. Res. **100**, 24037–24059 (1995)
Watson, T., Nyblade, A., Wiens, D., et al.: P and S wave velocity structure of the upper mantle beneath the Transantarctic Mountains, east Antarctic craton, and Ross Sea from travel time tomography. Geochem. Geophys. Geosyst. **7**, Q07005 (2006)
Wei, W., Xu, J., Zhao, D., Shi, Y.: East Asia mantle tomography: new insight into plate subduction and intraplate volcanism. J. Asian Earth Sci. **60**, 88–103 (2012)
Wei, W., Zhao, D., Xu, J.: P-wave anisotropic tomography in Southeast Tibet: new insight into the lower crustal flow and seismotectonics. Phys. Earth Planet. Inter. **222**, 47–57 (2013)
Wittlinger, G., Masson, F., Poupinet, G., Tapponnier, P., Mei, J., et al.: Seismic tomography of northern Tibet and Kunlun: evidence for crustal blocks and mantle velocity anomalies. Earth Planet. Sci. Lett. **139**, 263–279 (1996)
Woodhouse, J., Dziewonski, A.: Mapping the upper mantle: three-dimensional modeling of earth structure by inversion of seismic waveforms. J. Geophys. Res. **89**, 5953–5986 (1984)
Woodward, R., Master, G.: Lower mantle structure from ScS-S differential travel times. Nature. **352**, 231–233 (1991)
Wysession, M., Okal, E., Bina, C.: The structure of the core-mantle boundary from diffracted waves. J. Geophys. Res. **97**, 8749–8764 (1992)
Zhang, Y., Tanimoto, T.: High-resolution global upper mantle structure and plate tectonics. J. Geophys. Res. **98**, 9793–9823 (1993)
Zhang, H., Zhao, D., Zhao, J., Xu, Q.: Convergence of the Indian and Eurasian plates under eastern Tibet revealed by seismic tomography. Geochem. Geophys. Geosyst. **13**, Q06W14 (2012)
Zhao, D.: A tomographic study of seismic velocity structure in the Japan islands. Ph.D. thesis, Tohoku University, pp. 301 (1991)
Zhao, D.: Whole mantle tomography with grid parameterization, 3-D ray tracing and topography of mantle discontinuities. Eos Trans., Am. Geophys. Union. **80**, 716 (1999)

Zhao, D.: Seismic structure and origin of hotspots and mantle plumes. Earth Planet. Sci. Lett. **192**, 251–265 (2001)
Zhao, D.: Global tomographic images of mantle plumes and subducting slabs: insight into deep earth dynamics. Phys. Earth Planet. Inter. **146**, 3–34 (2004)
Zhao, D.: Seismic images under 60 hotspots: search for mantle plumes. Gondwana Res. **12**, 335–355 (2007)
Zhao, D.: Multiscale seismic tomography and mantle dynamics. Gondwana Res. **15**, 297–323 (2009)
Zhao, D.: Tomography and dynamics of Western-Pacific subduction zones. Monogr. Environ. Earth Planets. **1**, 1–70 (2012)
Zhao, D., Hasegawa, A.: Teleseismic evidence for lateral heterogeneities in the northeastern Japan arc. Tectonophysics **237**, 189–199 (1994)
Zhao, D., Lei, J.: Seismic ray path variations in a 3-D global velocity model. Phys. Earth Planet. Inter. **141**, 153–166 (2004)
Zhao, D., Hasegawa, A., Horiuchi, S.: Tomographic imaging of P and S wave velocity structure beneath northeastern Japan. J. Geophys. Res. **97**, 19909–19928 (1992)
Zhao, D., Hasegawa, A., Kanamori, H.: Deep structure of Japan subduction zone as derived from local, regional, and teleseismic events. J. Geophys. Res. **99**, 22313–22329 (1994)
Zhao, D., Christensen, D., Pulpan, H.: Tomographic imaging of the Alaska subduction zone. J. Geophys. Res. **100**, 6487–6504 (1995)
Zhao, D., Xu, Y., Wiens, D., Dorman, L., Hildebrand, J., Webb, S.: Depth extent of the Lau back-arc spreading center and its relation to subduction processes. Science. **278**, 254–257 (1997)
Zhao, D., Lei, J., Tang, Y.: Origin of the Changbai volcano in northeast China: evidence from seismic tomography. Chin. Sci. Bull. **49**, 1401–1408 (2004)
Zhao, D., Yamada, A., Ohta, Y.: Precisely measured travel times of mantle body waves: implications for mantle heterogeneity and tomography. Earth Sci. Front. **13**, 37–47 (2006)
Zhao, D., Maruyama, S., Omori, S.: Mantle dynamics of western Pacific to East Asia: new insight from seismic tomography and mineral physics. Gondwana Res. **11**, 120–131 (2007)
Zhao, D., Wang, Z., Umino, N., Hasegawa, A.: Mapping the mantle wedge and interplate thrust zone of the northeast Japan arc. Tectonophysics. **467**, 89–106 (2009a)
Zhao, D., Tian, Y., Lei, J., Liu, L., Zheng, S.: Seismic image and origin of the Changbai intraplate volcano in East Asia: role of big mantle wedge above the stagnant Pacific slab. Phys. Earth Planet. Inter. **173**, 197–206 (2009b)
Zhao, D., Pirajno, F., Dobretsov, N.L., Liu, L.: Mantle structure and dynamics under east Russia and adjacent regions. Russ. Geol. Geophys. **51**, 925–938 (2010)
Zhao, D., Yu, S., Ohtani, E.: East Asia: seismotectonics, magmatism and mantle dynamics. J. Asian Earth Sci. **40**, 689–709 (2011)
Zhao, D., Arai, T., Liu, L., Ohtani, E.: Seismic tomography and geochemical evidence for lunar mantle heterogeneity: comparing with earth. Global Planet. Change. **90**, 29–36 (2012a)
Zhao, D., Yanada, T., Hasegawa, A., Umino, N., Wei, W.: Imaging the subducting slabs and mantle upwelling under the Japan islands. Geophys. J. Int. **190**, 816–828 (2012b)
Zhao, D., Yamamoto, Y., Yanada, T.: Global mantle heterogeneity and its influence on teleseismic regional tomography. Gondwana Res. **23**, 595–616 (2013)
Zheng, H., Li, T., Gao, R., Zhao, D., He, R.: Teleseismic P-wave tomography evidence for the Indian lithospheric mantle subducting northward beneath the Qiangtang terrane. Chin. J. Geophys. **50**, 1418–1426 (2007)
Zhou, H.: A high-resolution P-wave model for the top 1200 km of the mantle. J. Geophys. Res. **101**, 27791–27810 (1996)

Chapter 8
Seismic Tomography of the Moon

Abstract Moonquake arrival-time data recorded by the Apollo seismic network operated during 1969 to 1977 have been used to determine P- and S-wave velocity tomography of the crust and mantle beneath the lunar near-side. The results have shown that significant lateral heterogeneities may exist in the lunar interior. A correlation between the S-wave tomography and the thorium abundance distribution is revealed. The area with high thorium abundance exhibits a distinct low shear-velocity which extends down to a depth of ~ 300 km below the Procellarum KREEP Terrane (PKT), which may reflect a thermal and compositional anomaly under the PKT. The distribution of deep moonquakes shows a correlation with the tomography in the deep lunar mantle, similar to earthquakes which are affected by structural heterogeneities in the terrestrial crust and upper mantle. The presence of deep moonquakes and seismic-velocity heterogeneity implies that the interior of the present Moon may still be thermally and dynamically active. Although lunar tomography is still preliminary, it indicates that tomographic imaging of the lunar interior is feasible.

Keywords Moon · Apollo missions · Moonquake · Seismic tomography · Procellarum KREEP Terrane

The Moon is the only planetary body, beside the Earth, which interior structure has been explored using seismological methods. During the United States (U.S.) Apollo missions from July 1969 to December 1972, five seismometers were installed on the near-side lunar surface. Four seismometers had operated during 1969 to 1977, which recorded more than 12,000 moonquakes (Nakamura 2005). Four kinds of moonquakes were detected: shallow moonquakes, deep moonquakes, thermal moonquakes, and meteoroid impacts (Figs. 8.1, 8.2 and 8.3). The deep moonquakes occurred repeatedly at approximately 316 fixed nests in a depth range of 750–1400 km (Nakamura 2005), and they seem to be triggered by tidal deformation of the Moon (e.g., Toksoz et al. 1974; Lammlein 1977). The distribution of deep moonquakes is not uniform (Fig. 8.1), which is one piece of evidence for the existence of lateral heterogeneities in the lunar mantle, because if the lunar mantle structure is laterally homogeneous, then under the tidal stress, the deep moonquakes would occur randomly and their distribution would be uniform. Many seismological

D. Zhao, *Multiscale Seismic Tomography,* Springer Geophysics,
DOI 10.1007/978-4-431-55360-1_8

studies have shown that the generation of earthquakes is influenced by lateral heterogeneities in the terrestrial crust and upper mantle, and so the distribution of both shallow and deep earthquakes reflects and is closely related to the lateral heterogeneities in the Earth, which have been revealed clearly by tomographic imaging (e.g., Zhao et al. 2002, 2010; Jiang et al. 2008; Lei and Zhao 2009; Huang and Zhao 2013a, b; Liu et al. 2013a, b).

To date, many workers have used the moonquake arrival-time data recorded by the Apollo seismic network to estimate one-dimensional (1-D) seismic velocity models of the lunar interior (e.g., Toksoz et al. 1974; Goins et al. 1981; Nakamura 1983; Vinnik et al. 2001; Khan and Mosegaard 2002; Lognonne et al. 2003; Gagnepain-Beyneix et al. 2006; Garcia et al. 2011; Weber et al. 2011). Lateral variations of the lunar crustal thickness were also investigated using the Apollo seismic data set (e.g., Chenet et al. 2006), whereas they have been determined more reliably at a global scale using the lunar gravity and topography data (e.g., Ishihara et al. 2009; Wieczorek et al. 2013). Radar sounding from the Kaguya spacecraft has revealed subsurface layers at an apparent depth of several hundred meters in the nearside maria (e.g., Ono et al. 2009).

Zhao et al. (2008) applied a seismic tomography method to the moonquake arrival-time data to study the three-dimensional (3-D) P- and S-wave velocity and Poisson's ratio structures of the lunar interior. Although it was an experimental work, the results have shown that tomographic imaging of the lunar interior is feasible, and significant lateral heterogeneities may exist in the lunar mantle which may affect the generation of deep moonquakes. Zhao et al. (2012a) compared the lunar seismic tomography with the results of previous geophysical and geochemical studies, and discussed the implications of the lunar tomography for the structure and dynamics of the lunar interior. In this chapter, we review these lunar tomographic studies and related works, and discuss limitations, problems and future perspectives of the lunar tomographic imaging, which may be useful for designing a new seismic network on the lunar surface and lunar exploration in the near future.

8.1 Apollo Seismic Data

The Apollo lunar seismic data are remarkable and unique in that they are the only seismic data set which can be used to infer the internal structure of a planetary body besides the Earth (Lognonne and Johnson 2007; Khan et al. 2013). The four-station lunar seismic network covered a relatively small area on the near side of the Moon and was arranged approximately in an equilateral triangle configuration with Apollo stations 12, 15 and 16 placed ~ 1100 km apart, whereas Apollo stations 12 and 14 were placed on one corner ~180 km apart (Fig. 8.1). Each Apollo seismometer consisted of a three-component long-period (bandwidth 1–15 s) and a short-period sensor unit (bandwidth 0.125–1 s), which was sensitive to vertical motion at high frequencies (for details, see Latham et al. 1973; Toksoz et al. 1974). During the

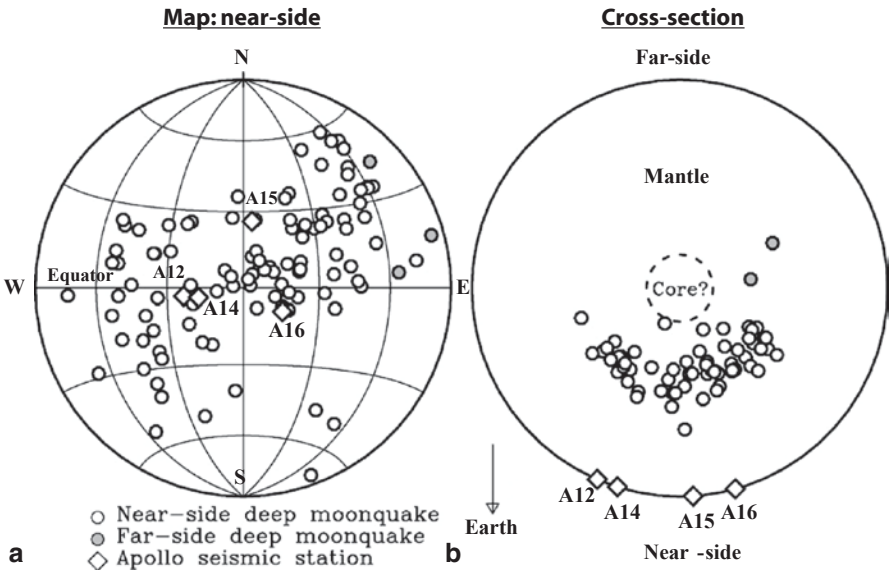

Fig. 8.1 Map of the Moon's near-side (**a**) and equatorial cross-section (**b**) showing deep moonquake nests (*circles*) and the Apollo seismic stations (*diamonds*). Between 1969 and 1977, the four Apollo stations recorded more than 7000 deep moonquakes occurring in about 300 different nests; locations were obtained for about 100 nests. The map includes locations for all nests, including those with undetermined depths, while the cross-section shows only the nests with depths determined. (Modified from Frohlich and Nakamura 2009)

eight-year operation of the Apollo seismic network, over 12,000 seismic events were recorded and catalogued, including 28 shallow moonquakes, 7083 deep moonquakes, 1744 meteoroid impacts, 9 artificial impacts, and 3639 unclassified events, according to the most recent results of the Apollo data processing (Nakamura 2005; Khan et al. 2013).

Most of the moonquakes were very small with equivalent body-wave magnitudes around 1–3 in case of the deep moonquakes, while ranging up to M 5 for a set of shallow events (Goins et al. 1981). Lunar seismic signals were typically of very long duration, of high frequency, and of reverberating nature with small first arrivals and slowly building amplitudes followed by a slow decay (Fig. 8.2). The most prominent feature of the lunar signals is their anomalously long continuance, and they typically continued for 30 min to 2 h (Toksoz et al. 1974; Lammlein 1977; Khan et al. 2013). It is considered that these signals were caused by intense scattering of the waves in the uppermost layers of the lunar crust. Topographic features, lunar regolith, compositional boundaries, and especially joints and cracks in the crust, become very efficient scatters in the absence of water and volatiles and thus absence of damping (Toksoz et al. 1974; Lammlein 1977). The interested reader is referred to Lognonne and Johnson (2007) and Khan et al. (2013) for comprehensive reviews of the lunar seismic network and moonquakes.

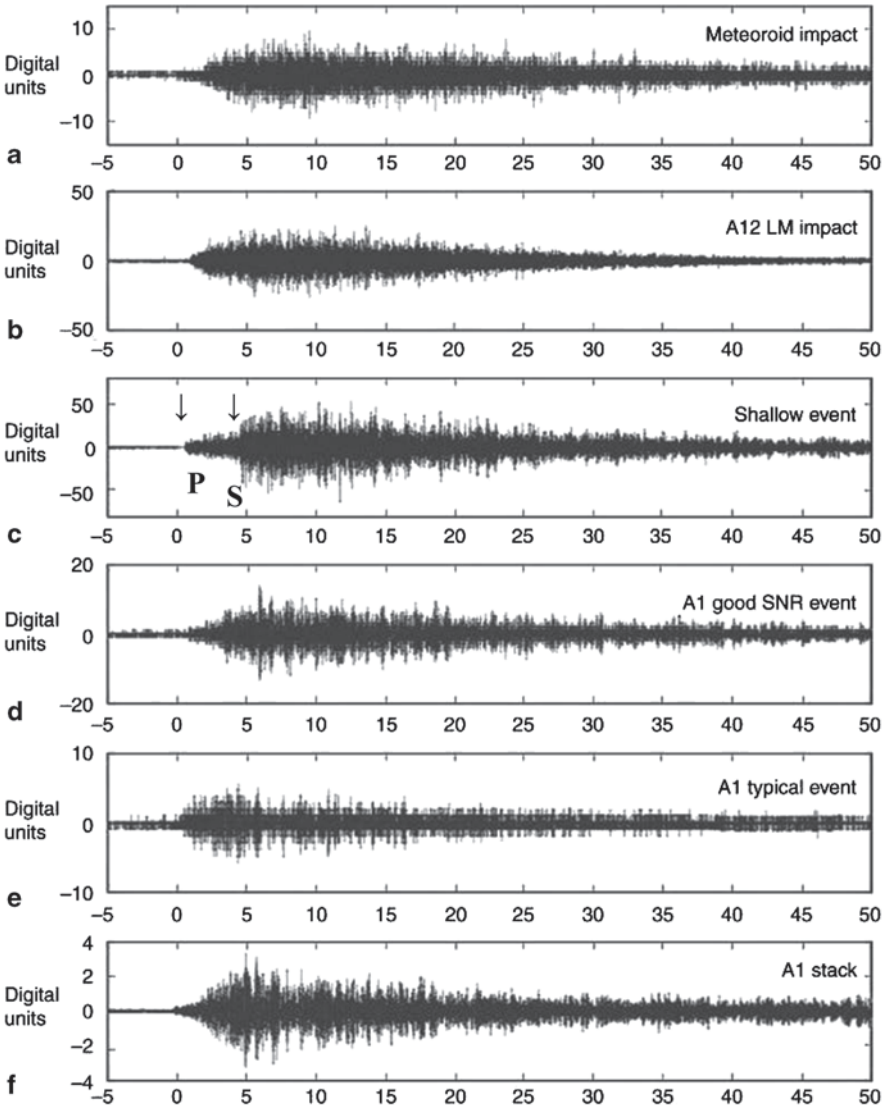

Fig. 8.2 Examples of waveforms for (**a**) natural and (**b**) artificial impacts, (**c**) shallow moonquake, and (**d**–**f**) deep moonquakes recorded on long-period channels by the Apollo lunar seismic network. All records span 55 min; X-axis time is in minutes, Y-axis is in digital units. (Modified from Lognonne and Johnson 2007)

The updated lunar seismic data processed and compiled by Lognonne et al. (2003) and Nakamura (2005) were used for tomographic imaging of the lunar interior by Zhao et al. (2008, 2012a). In the selected data set used in the tomographic studies, there are 221 P-wave arrivals from 80 moonquakes (including 120 arrivals from 46 deep events and 101 arrivals from 34 shallow events) (Fig. 8.4), and

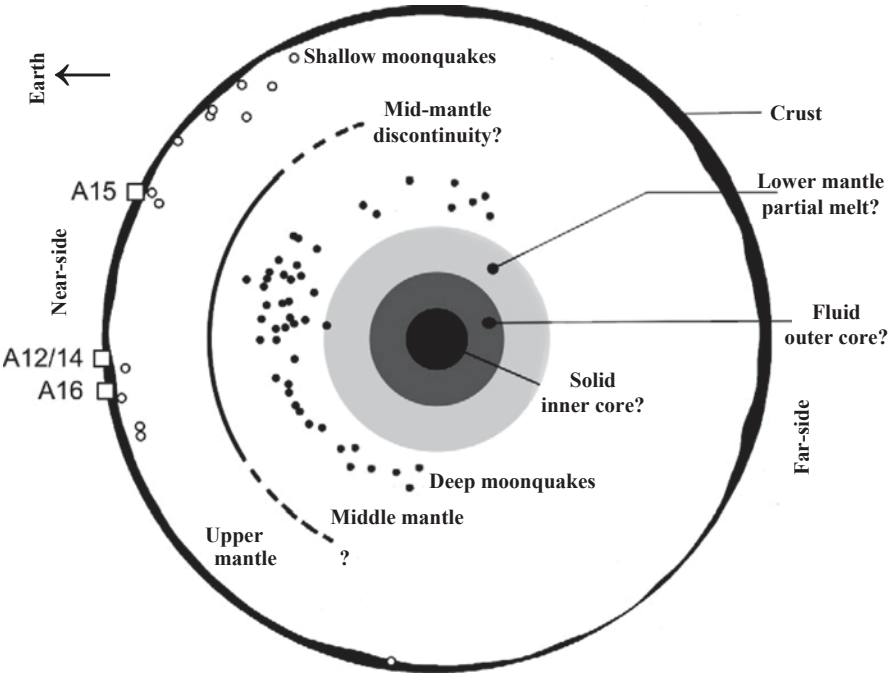

Fig. 8.3 Schematic diagram of the internal structure of the Moon. The structure deeper than the location of deep moonquakes is subject to large uncertainty. A12–A16 denote relative locations of the Apollo lunar seismic stations. (Modified from Wieczorek et al. 2006 and Khan et al. 2013)

381 S-wave arrivals from 123 moonquakes (including 342 arrivals from 102 deep events, and 39 arrivals from 21 shallow events) (Fig. 8.5). In the Apollo data set, there are more S-wave arrivals than P-wave arrivals (Nakamura 2005; Lognonne et al. 2003), which is in contrast to earthquake data. This discrepancy is due to the differences in waveforms between earthquakes and moonquakes (Fig. 8.6). Moonquake waveforms exhibit low attenuation, strong scattering, and long duration (e.g., Nakamura 2005; Lognonne et al. 2003), hence they are quite different from earthquake seismograms.

As shown in Figs. 8.4 and 8.5, some shallow moonquakes had very close hypocenter locations, whereas the deep moonquakes occurred in a depth range of 747–1419 km, which were located by Nakamura (2005) using the 1-D P- and S-wave velocity model of Nakamura (1983) (Fig. 8.7). It was suggested that the lunar interior may be divided into layers with the following depth ranges: the crust (0–58 km), the upper mantle (58–270 km), the middle mantle (270–500 km), and the lower mantle (>500 km) (Nakamura 1983). It is still unclear whether a metallic core exists in the center of the Moon or not, though recent studies on possible core reflected waves in the Apollo lunar seismic data suggested the existence of a small dense lunar core with a radius of <400 km which corresponds to 1–3% of lunar mass (Garcia et al. 2011; Weber et al. 2011).

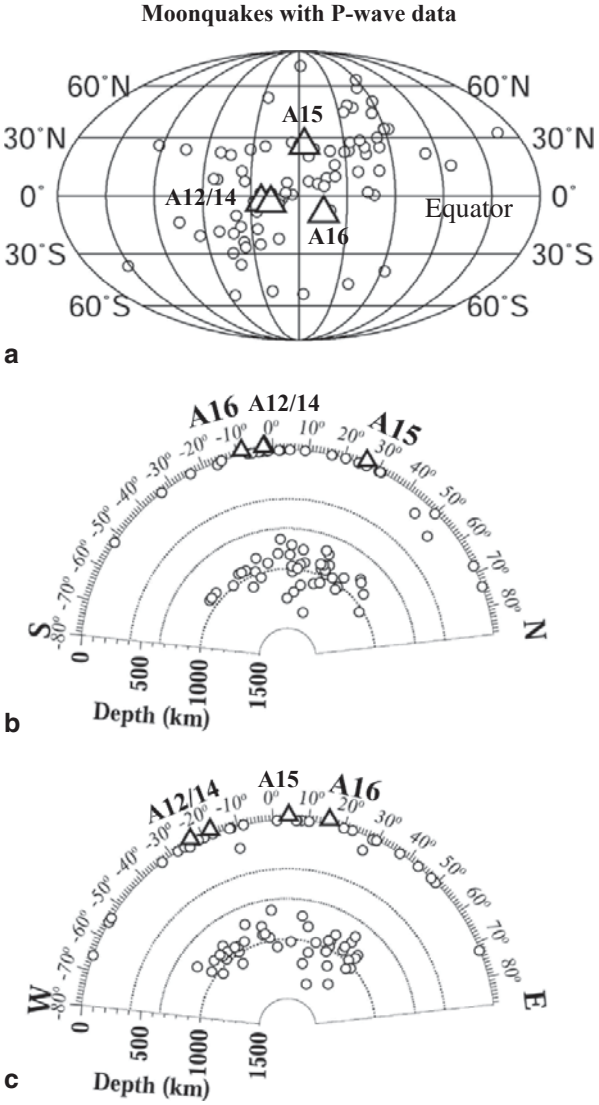

Fig. 8.4 Distribution of moonquakes (*open circles*) that had P-wave arrival-time data used in tomographic inversion in (**a**) map view, and (**b**) north-south and (**c**) east-west vertical cross-sections. The *open triangles* in (**a**) denote the four seismic stations installed during the Apollo missions. The two cross-sections (**b**, **c**) are along the lunar central meridian and the equator, respectively. The *dotted lines* in (**b**) and (**c**) denote depths of 400, 650, and 1000 km for better visualizing the hypocenter distribution of moonquakes. (Modified from Zhao et al. 2008)

The 1-D lunar velocity model shows seismic velocities down to a depth of 1000 km (Fig. 8.7). In the tomographic studies (Zhao et al. 2008, 2012a), the P- and S-wave velocities in the deeper areas are assumed to be the same as those at a depth of 1000 km, which seems reasonable considering the recent 1-D velocity models

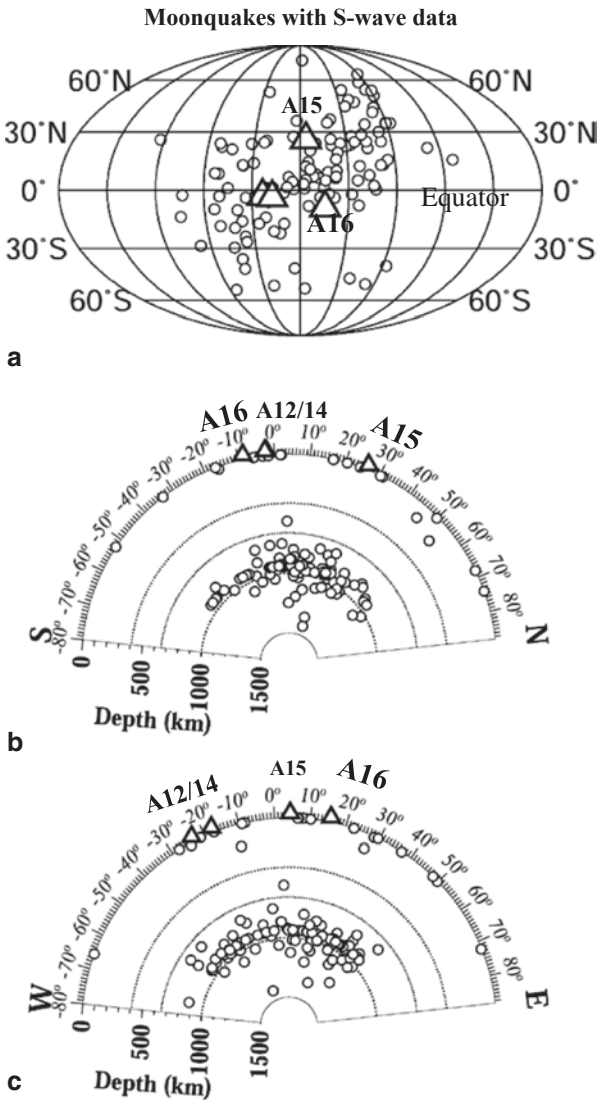

Fig. 8.5 The same as Fig. 8.4 but for the moonquakes with S-wave data used in tomographic inversion. (Modified from Zhao et al. 2008)

of the lunar interior (Garcia et al. 2011; Weber et al. 2011). One moonquake had a focal depth of 559 km (Fig. 8.5b, c), which was not a typo but a result of the moonquake location procedure (Y. Nakamura, personal communication with D. Zhao in November 2007). These invaluable data of the shallow and deep moonquakes recorded by the Apollo seismic network enabled to estimate not only 1-D seismic velocity models but also a 3-D velocity model of the lunar interior (Zhao et al. 2008, 2012a).

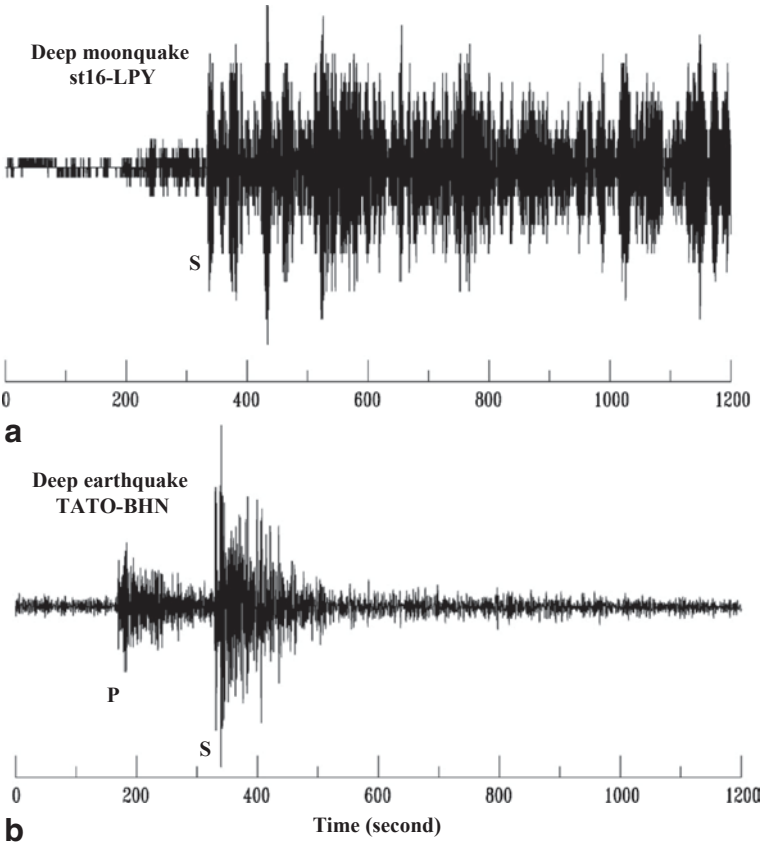

Fig. 8.6 Deep moonquake and deep earthquake seismograms, plotted with probable S arrivals aligned. **a** Horizontal-component displacement seismogram for a deep moonquake occurring on 5 June 1973 at the Apollo lunar station 16, at a source-station epicentral distance of ~1600 km. With a magnitude corresponding approximately to a terrestrial mb of 2.5, this moonquake was among the largest deep moonquakes occurring between 1969 and 1977 in the A1 source region, which had a focal depth estimated to be 870 km. The absence of an impulsive P phase and the long ringing coda are typical of moonquake seismograms. **b** Horizontal-component displacement seismogram for a deep earthquake occurring in the Philippines on 23 May 1998 and recorded at station TATO at a source-station epicentral distance of 1878 km. Harvard reported Mw of 6.0 and a focal depth of 629 km for this earthquake. Here the signal has been narrow-band filtered so that the instrument responses are similar for the two records shown. (Modified from Frohlich 2006)

8.2 Inversion and Synthetic Tests

A seismic tomography method which was developed for studying the 3-D structure of the Earth (Zhao 2001) was applied to the selected lunar data set for determining the 3-D P- and S-wave velocity models of the Moon (Zhao et al. 2008). Although many 1-D velocity models of the lunar interior have been proposed, as mentioned above, the 1-D model by Nakamura (1983; Fig. 8.7) was adopted as the starting

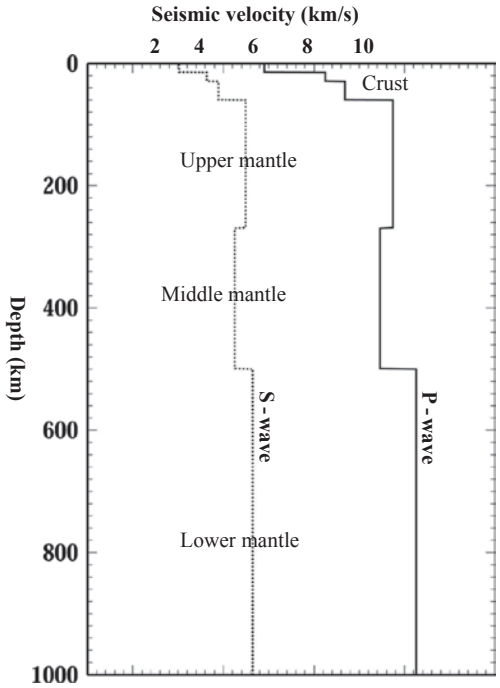

Fig. 8.7 One-dimensional P- and S-wave velocity model of the Moon determined by Nakamura (1983)

model for the 3-D tomographic inversion, because the hypocenter parameters of all the deep moonquakes used were determined with this velocity model (Nakamura 2005). This well-established 1-D velocity model was determined using the complete data set of 5-year simultaneous operation of four Apollo seismometers including many deep moonquake sources (see Nakamura 1983 for details).

Figures 8.8 and 8.9 show the distributions of the 221 P- and 381 S-wave ray paths used, which were calculated for the 1-D velocity model (Fig. 8.7). The P-wave data have a better ray coverage in the upper mantle (Fig. 8.8), because the P-wave data set contains more shallow moonquakes than the S-wave data set. In contrast, the S-wave ray paths have a better coverage in the lower mantle under the Apollo seismic network (Fig. 8.9). Data from a few far-side deep moonquakes (Nakamura 2005) also contributed to the ray coverage (Figs. 8.8 and 8.9).

For expressing the 3-D velocity structure, a 3-D grid was set up in the lunar crust and mantle down to a depth of 1000 km (Fig. 8.10). The grid interval is 10° in the lateral direction (note that 1° = 30.3 km at the lunar equator), which is comparable to the grid interval adopted in global tomography of the Earth (e.g., Zhao 2001, 2004; Zhao et al. 2013). Six layers of grid mesh were set up at depths of 20, 150, 300, 500, 700 and 900 km (Fig. 8.10b). The velocity perturbations at every grid nodes from the 1-D velocity model (Fig. 8.7) were taken as unknown parameters. The velocity perturbation at any point in the model was calculated by linearly interpolating the

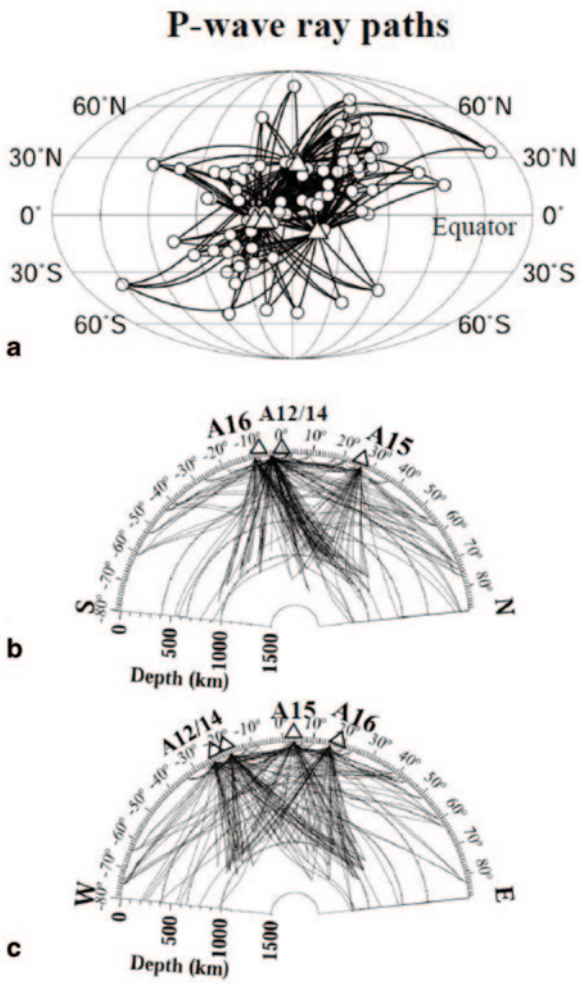

Fig. 8.8 Distribution of ray paths for P-wave arrival-time data used in tomographic inversion in **a** map view, and **b** north-south and **c** east-west vertical cross-sections. The open circles and triangles denote the moonquakes and the four Apollo seismic stations, respectively. (Modified from Zhao et al. 2008).

velocity perturbations at the eight grid nodes surrounding that point. A 3-D ray-tracing technique (Zhao et al. 1992; Zhao 2001) was used to compute travel times and ray paths for every P- and S-wave data. Elevations of the four Apollo seismic stations were taken into account in the 3-D ray tracing. The LSQR algorithm (Paige and Saunders 1982) with damping and smoothing regularizations was used to solve the system of observational equations that relate the arrival-time data to the unknown velocity parameters (Zhao 2001; Zhao et al. 2008, 2012a).

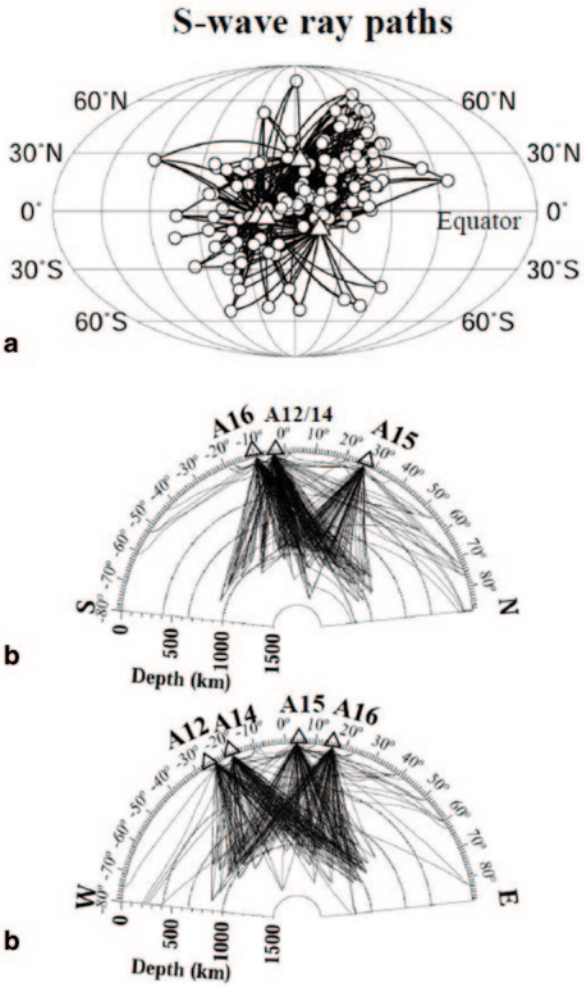

Fig. 8.9 The same as Fig. 8.8 but for the S-wave rays used in tomographic inversion. (Modified from Zhao et al. 2008)

In the tomographic inversions, raw travel-time residuals of the shallow moonquakes were used, because the origin time and hypocenter location of each shallow moonquake were determined (Lognonne et al. 2003). In contrast, relative travel-time residuals of the deep moonquakes were used in the tomographic inversions, because the individual deep moonquakes were small and so their seismic signals were weak, hence Nakamura (2005) used a waveform-stacking technique to measure the P- and S-wave travel times from a group of deep moonquakes which occurred in the same nest. Thus, the origin times of the deep moonquakes were not available in the data set complied by Nakamura (2005). The procedure for the calculation of relative

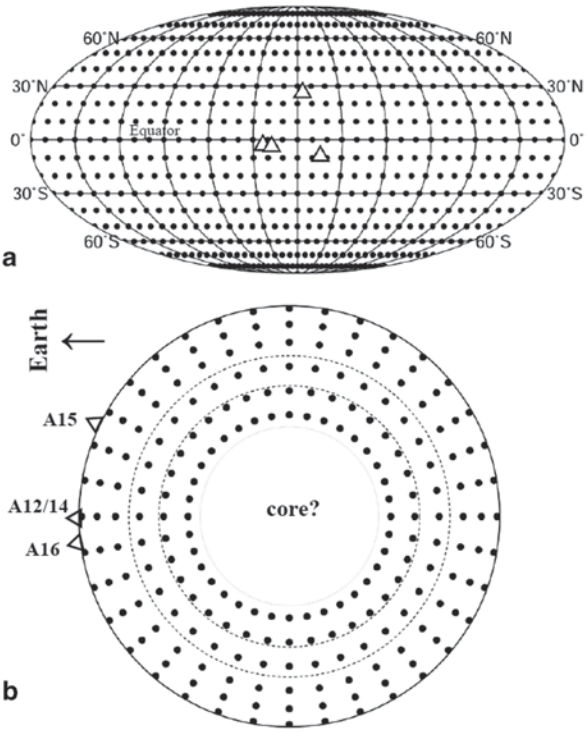

Fig. 8.10 Distribution of the grid nodes adopted for tomographic imaging in map view (**a**) and a vertical cross-section (**b**). The open triangles denote the four Apollo seismic stations. (Modified from Zhao et al. 2008)

travel-time residuals for the deep moonquakes (Zhao et al. 2008) is the same as that for the teleseismic events in the terrestrial tomography (Zhao et al. 1994, 2012b).

Map views and vertical cross-sections of the lunar P- and S-wave tomography obtained by Zhao et al. (2008) are shown in Figs. 8.11, 8.12, 8.13 and 8.14. The lunar seismicity (Lammlein 1977; Lognonne et al. 2003; Nakamura 2005) is also shown in these tomographic images.

Many synthetic tests were conducted to assess the adequacy of the ray coverage and to evaluate the resolution of the lunar tomography (Zhao et al. 2008, 2012a). Some of the test results are shown in Figs. 8.15, 8.16, 8.17 and 8.18. In these synthetic tests, the numbers and locations of seismic stations, moonquakes, as well as the P- and S-wave rays are the same as those in the real data set (Figs. 8.4 and 8.5). An input model was first constructed that contains the main features of velocity anomalies appeared in the obtained tomographic images (Figs. 8.11–8.14). Then theoretical travel times and ray paths for the synthetic input model were computed using the 3-D ray-tracing technique (Zhao et al. 1992), and random errors were added to the theoretical travel times to make a synthetic data set. By inverting the synthetic data using the same algorithm as for the real data, the output model was

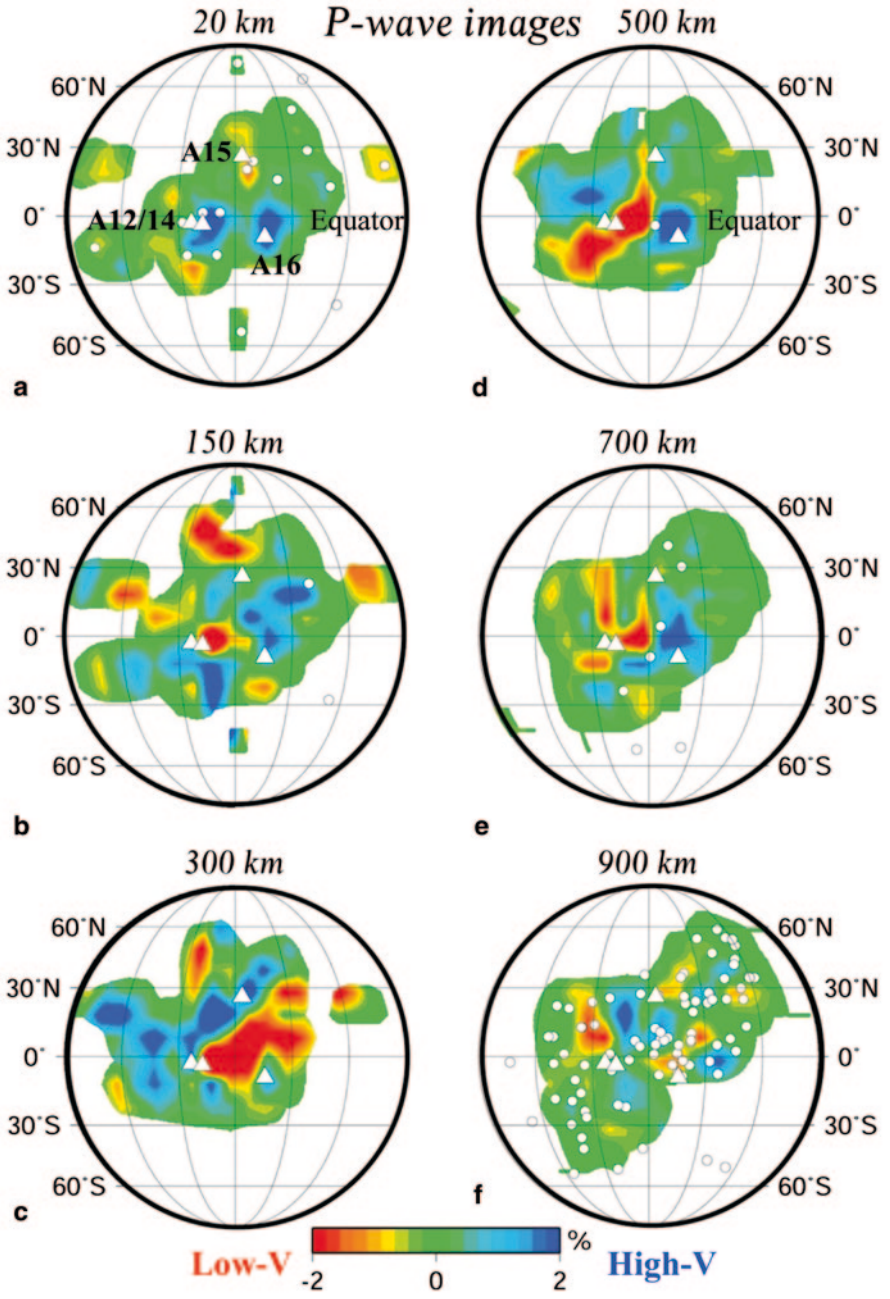

Fig. 8.11 Map views of P-wave tomography at six depth slices under the near-side of the Moon. The depth is shown above each map. The *red* and *blue* colors denote low and high velocities, respectively. The scale of velocity perturbations (in %) relative to the 1-D velocity model (Fig. 8.7) is shown at the bottom. *White* triangles denote the 4 Apollo seismic stations. The *white* dots show the moonquakes which occurred within a depth range of 150 km of each layer. (Modified from Zhao et al. 2008)

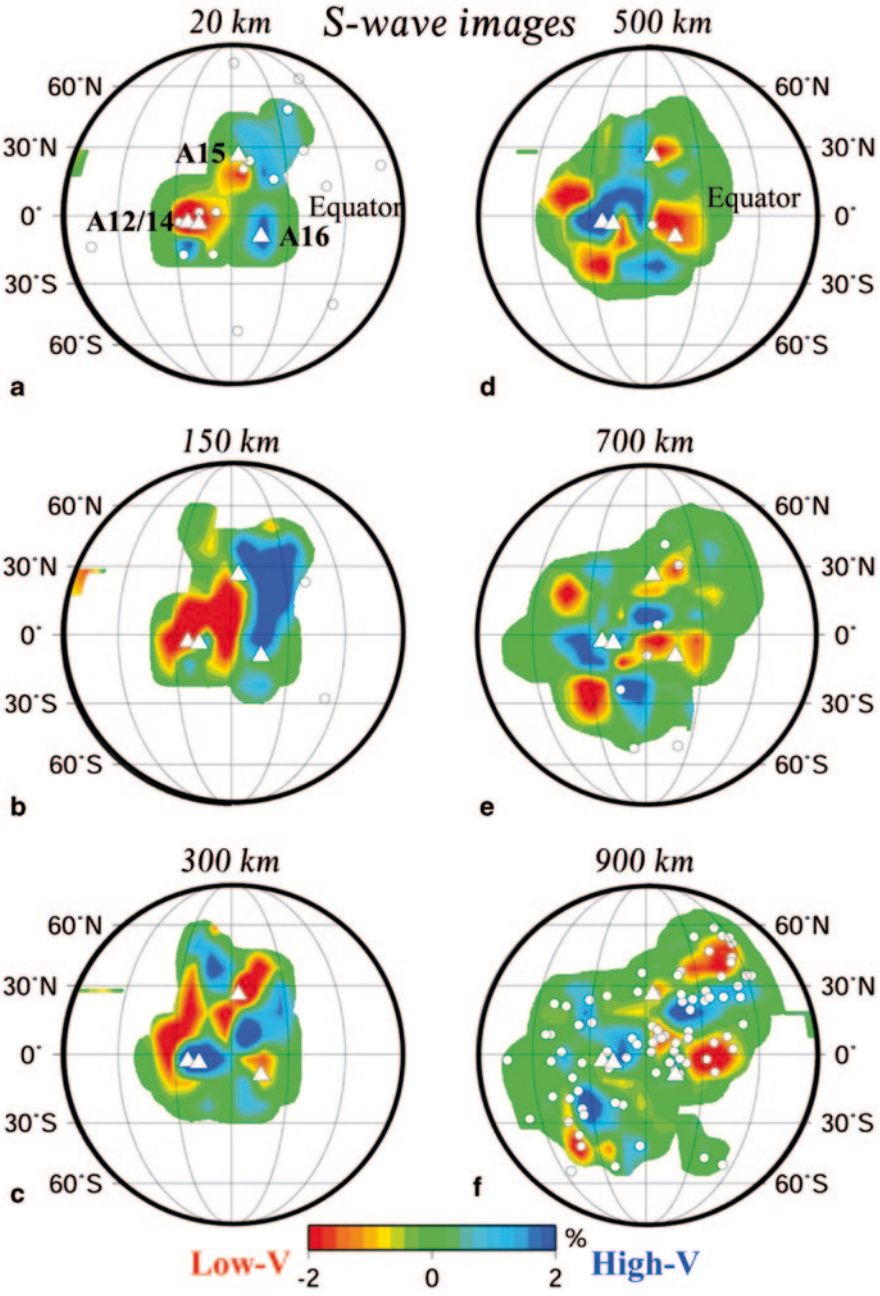

Fig. 8.12 The same as Fig. 8.11 but for S-wave tomography. (Modified from Zhao et al. 2008)

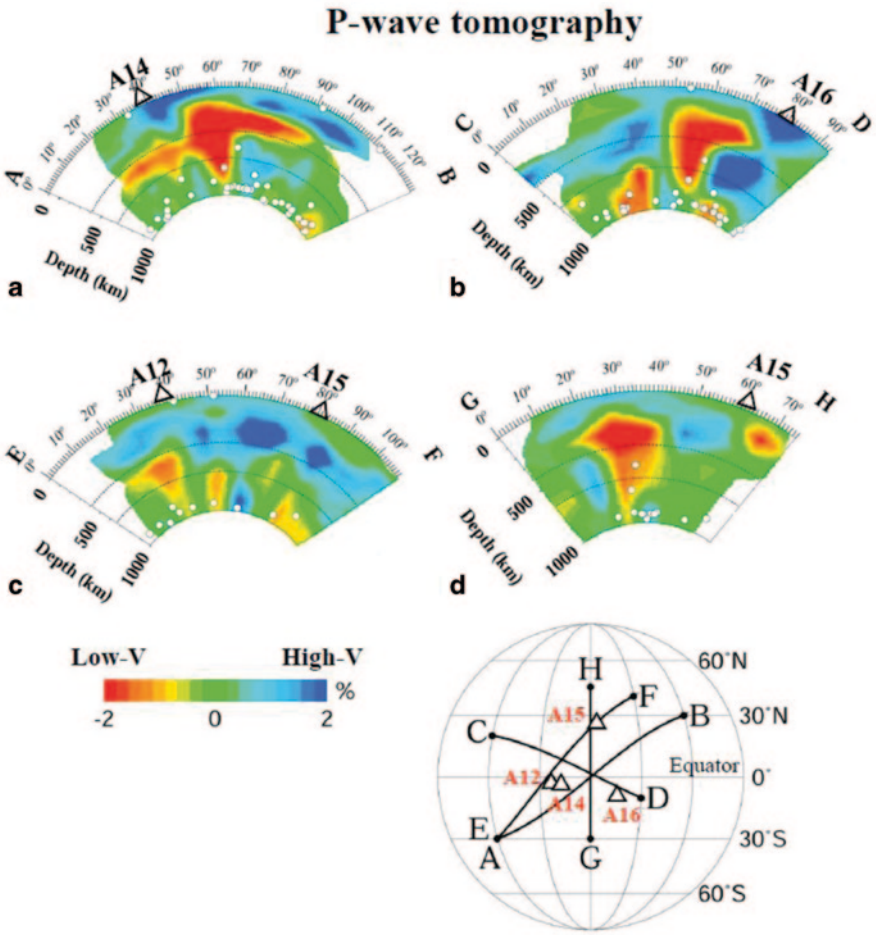

Fig. 8.13 Vertical cross-sections of P-wave tomography along the 4 profiles shown on the insert map. The *red* and *blue* colors denote low and high velocities, respectively. The scale of velocity perturbations (in %) relative to the 1-D velocity model (Fig. 8.7) is shown below (c). The *white* dots denote moonquakes which occurred within a 150 km width of each profile. The open triangles on the inset map denote the 4 Apollo seismic stations. (Modified from Zhao et al. 2008)

obtained which shows the recovered image of the synthetic input model. Comparing the inverted output model with the input synthetic model, we can know whether and how well an anomaly in the input model can be reconstructed or not. Such synthetic tests have been widely used to evaluate the quality and resolution of a tomographic result, and performing the tests has become a standard procedure for tomographic studies (for details, see Chapter 2 of this book).

The uncertainties of the lunar arrival-time data are much larger than those of earthquake data, being estimated to be 1–2 s or even greater (Lognonne et al. 2003;

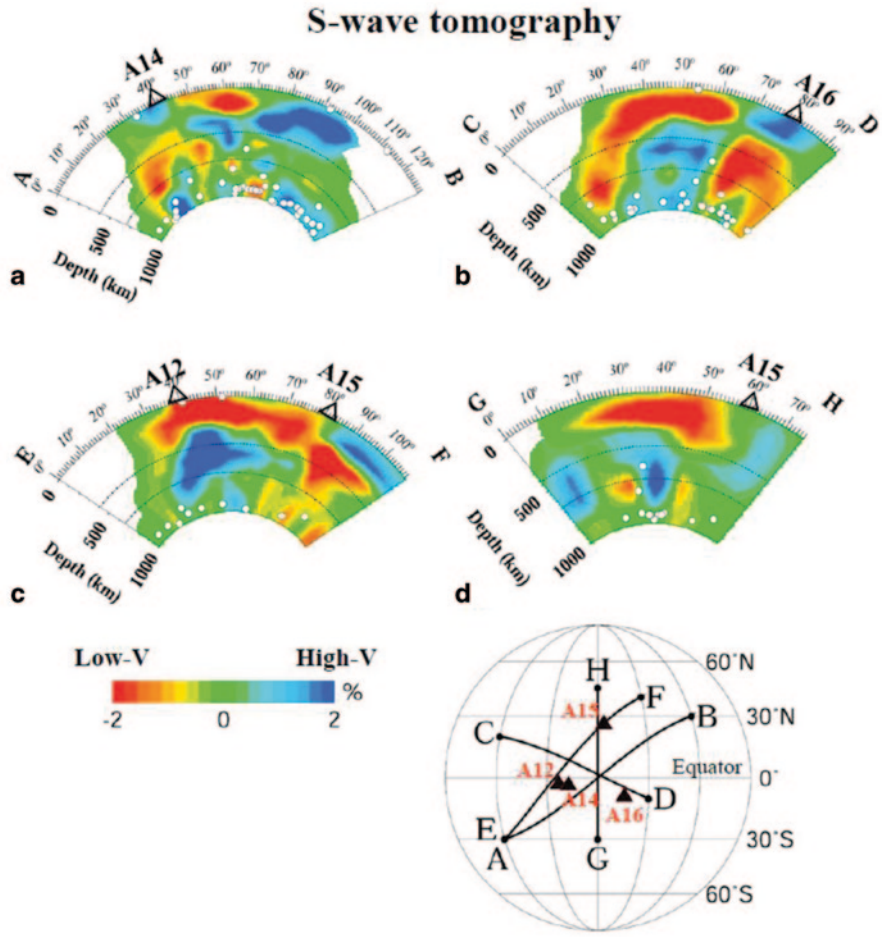

Fig. 8.14 The same as Fig. 8.13 but for S-wave tomography. (Modified from Zhao et al. 2008)

Nakamura 2005). The larger uncertainties of the lunar data are related to the characteristics of the moonquake waveforms as mentioned above (e.g., Figs. 8.2 and 8.6). Many synthetic tests were conducted by adding different levels of random noise to the synthetic data (Zhao et al. 2008). Figures 8.15 and 8.16 show the synthetic test results for P-wave tomography with noise levels of 0.5 and 2.0 s, respectively. The similar synthetic test results for S-wave tomography are shown in Figs. 8.17 and 8.18. These test results indicate that velocity anomalies in the lunar mantle with sizes greater than 300 km beneath the Apollo seismic network can generally be reconstructed, though smearing is visible around the edges of the velocity anomalies (Figs. 8.15–8.18).

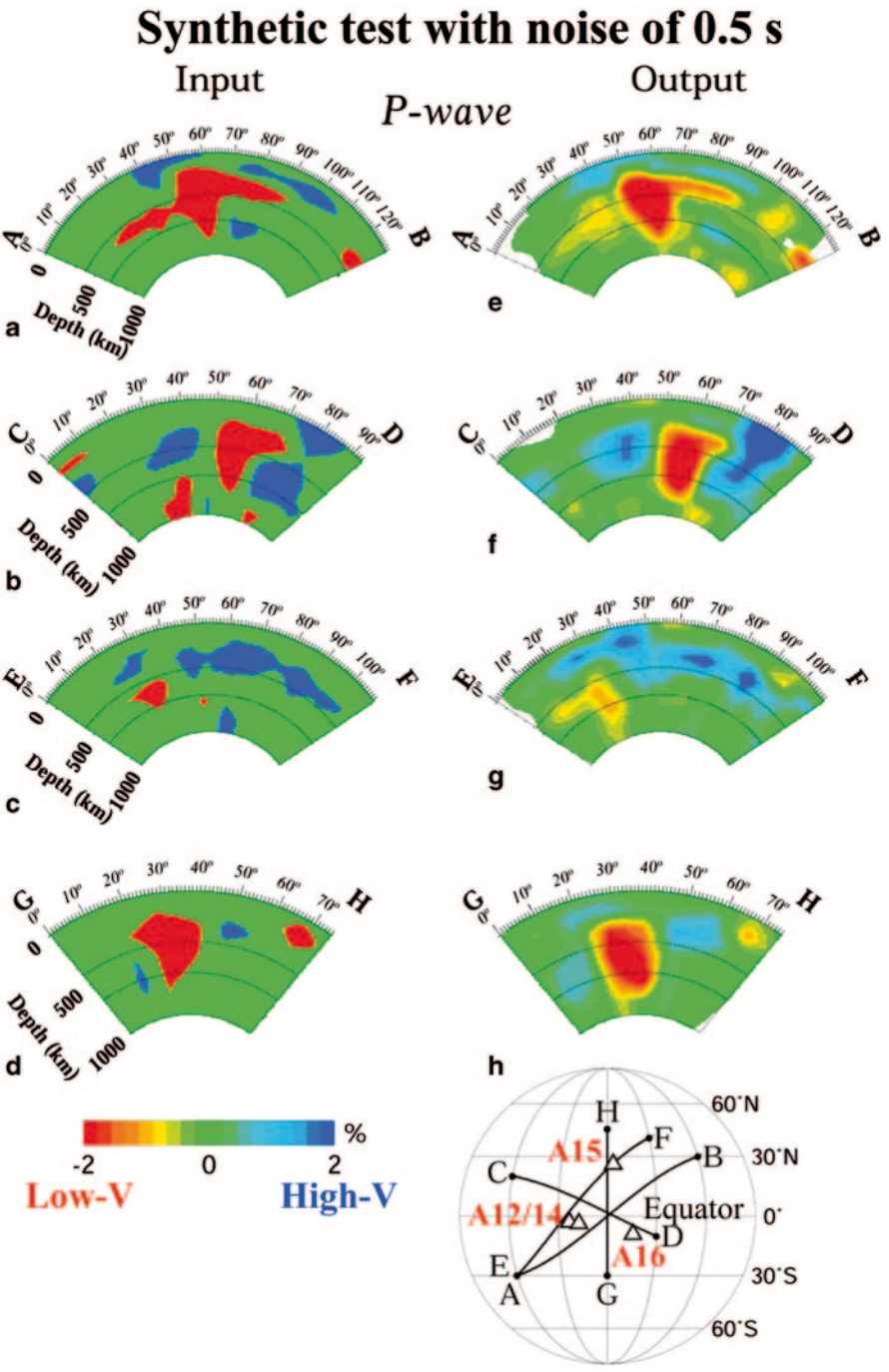

Fig. 8.15 A synthetic test for P-wave tomography. The *left* and *right* panels show the input and output models, respectively. In this test, random errors with a normal distribution having a standard deviation of 0.5 s were added to the theoretical travel times calculated for the input model. (Modified from Zhao et al. 2008)

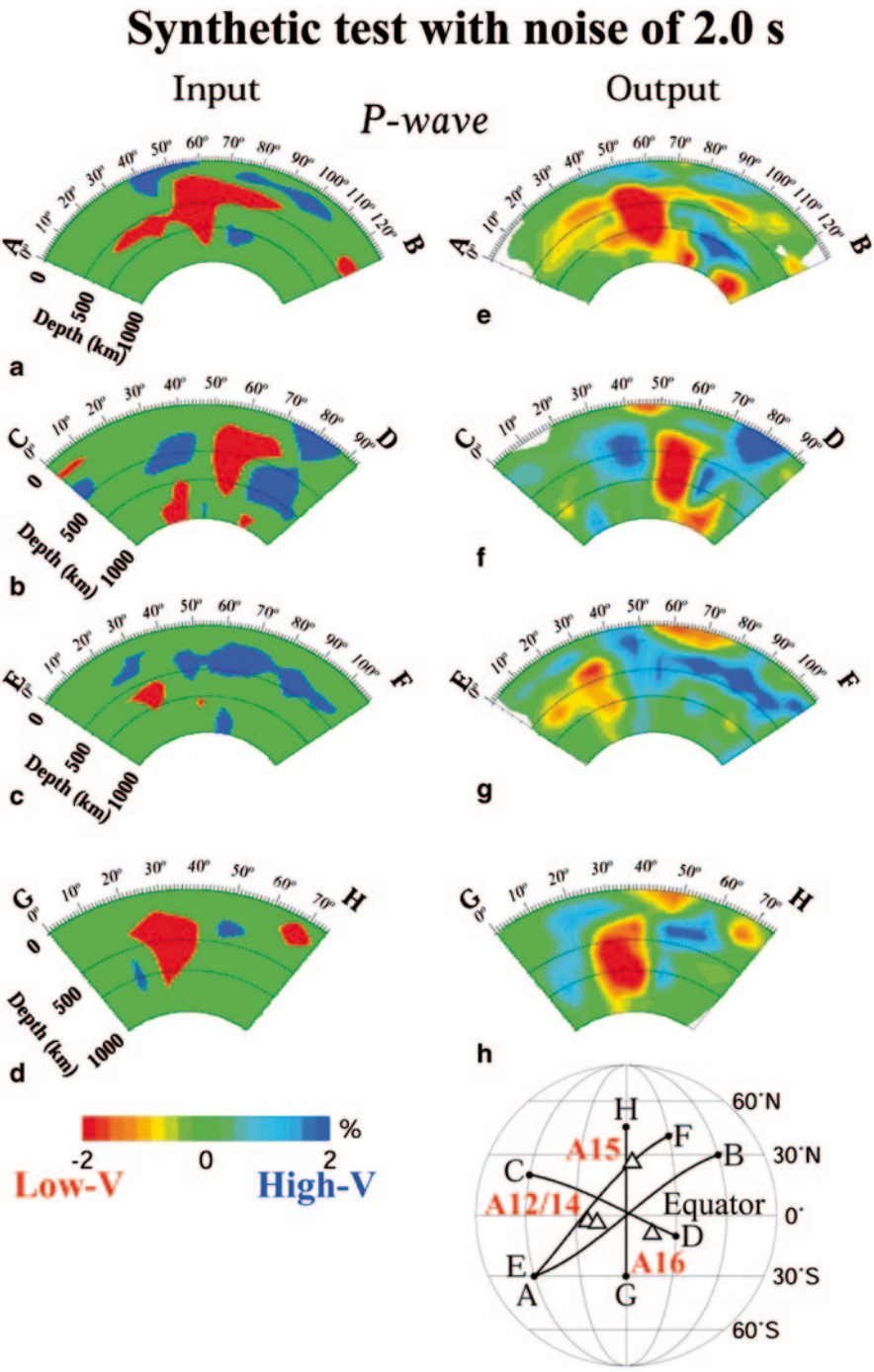

Fig. 8.16 The same as Fig. 8.15 but the standard deviation of the random errors is 2.0 s. (Modified from Zhao et al. 2008)

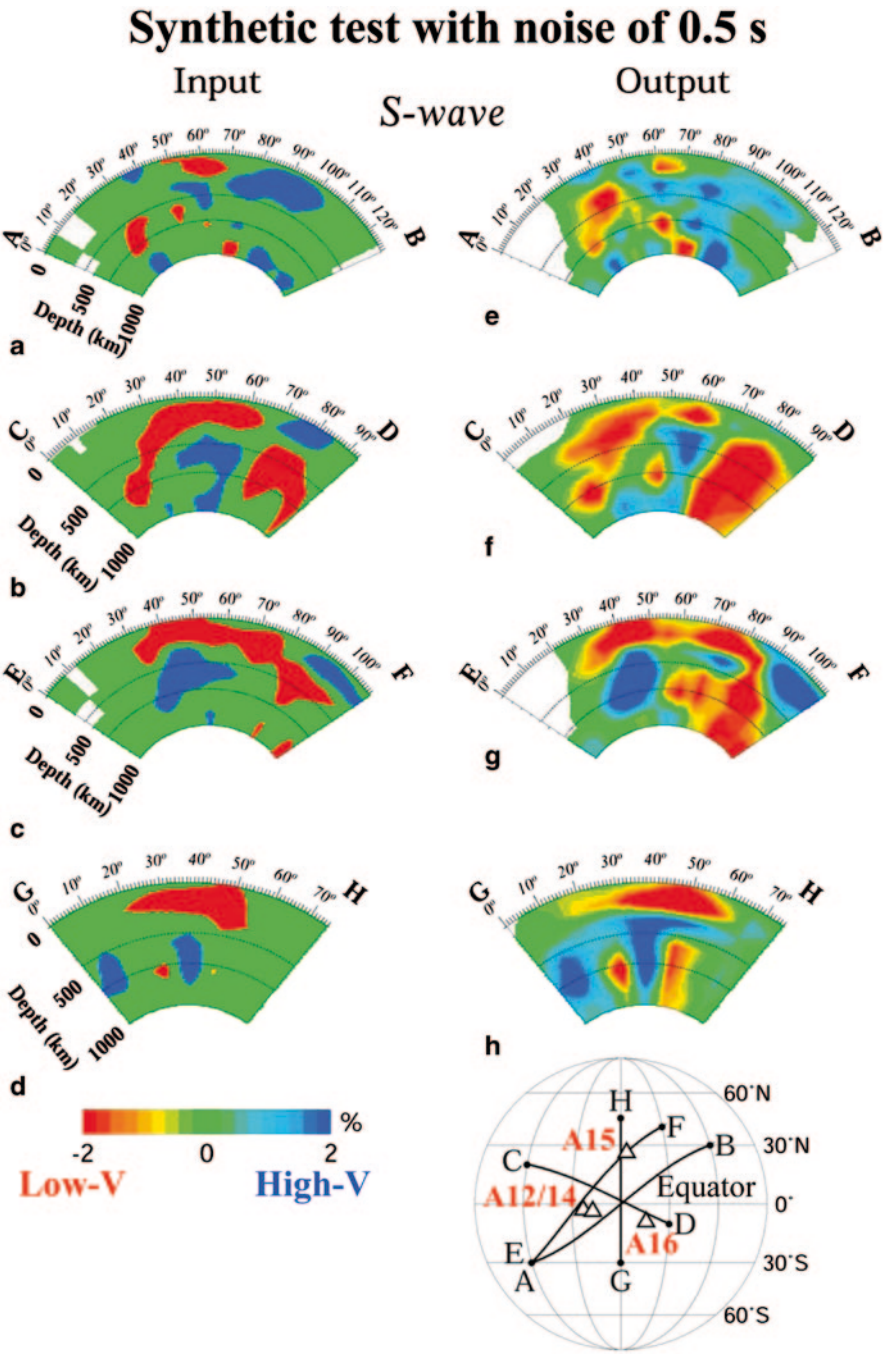

Fig. 8.17 The same as Fig. 8.15 but for S-wave tomography. (Modified from Zhao et al. 2008)

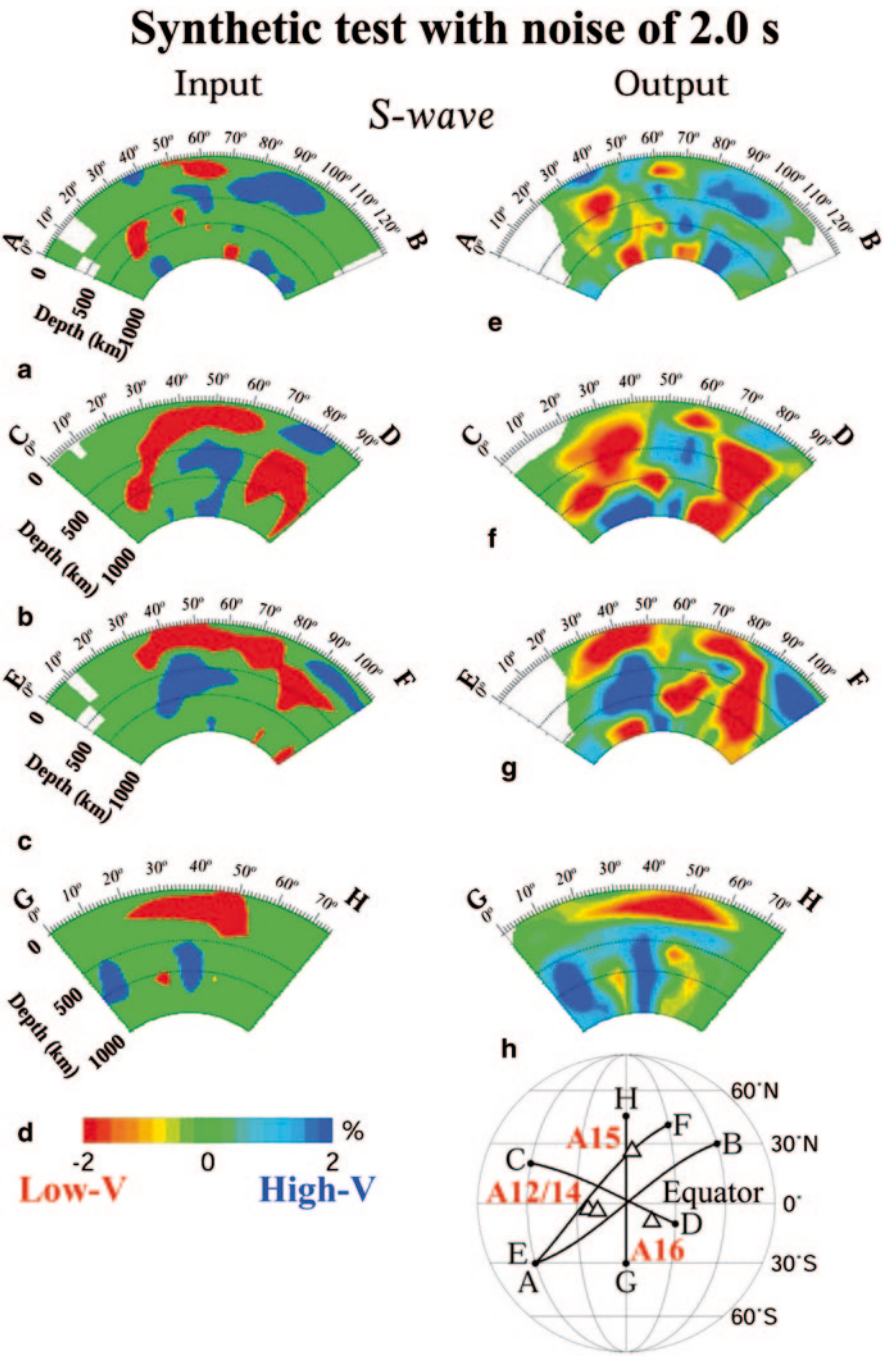

Fig. 8.18 The same as Fig. 8.16 but for S-wave tomography. (Modified from Zhao et al. 2008)

8.3 Lunar Tomographic Images

The obtained lunar tomography shows that significant lateral velocity variations exist in the lunar mantle (Figs. 8.11–8.14). The followings are some of the main features which are recoverable by the synthetic tests (Figs. 8.15–8.18). In the P-wave tomography (Figs. 8.11 and 8.13), a large low-velocity (low-V) anomaly is visible in the depth range of 200–800 km under the Apollo seismic network, and several high-velocity (high-V) zones exist in the upper and middle mantle around the low-V anomaly. A few smaller low-V zones are visible in the lower mantle at depths of 700–1000 km, while average-to-higher velocities prevail in the shallow mantle (Fig. 8.13). The S-wave tomography (Figs. 8.12 and 8.14) exhibits a pattern of velocity variations different from that of the P-wave tomography. Low-V anomalies prevail in the shallow mantle down to a depth of 200–300 km (Fig. 8.14). In contrast, high-V zones prevail in the middle to lower mantle under the Apollo seismic network, and a few low-V anomalies exist around the high-V zones (Fig. 8.14).

After the 3-D P- and S-wave velocity (Vp, Vs) images are obtained, 3-D Poisson's ratio (σ) images were obtained using the relation $(Vp/Vs)^2 = 2(1–\sigma)/(1–2\sigma)$, following the approach of Zhao et al. (1996). By definition, Poisson's ratio is the ratio of the radial contraction to axial elongation, and it is more sensitive to compositional variations and content of fluids and melts than Vp and Vs alone, and so it is a very useful parameter in studying the physical and petrologic properties of the crust and mantle (e.g., Christensen 1996; Zhao et al. 1996). When crustal fluids exist in an earthquake source area or a hot magma chamber exists under an active volcano, they can be detected as low-V and high-σ anomalies by high-resolution local tomography (e.g., Zhao et al. 1996, 2015; Mishra and Zhao 2003; Cheng et al. 2011). Figures 8.19 and 8.20 show the estimated Poisson's ratio images of the lunar interior (Zhao et al. 2008). A prominent high-σ zone is visible in most of the mantle under the Apollo stations A15 and A16 (Fig. 8.20c, d), whereas a low-σ anomaly exists at depths of 400–800 km under the Apollo stations A12 and A14 (Fig. 8.20a, c).

8.4 Discussion

8.4.1 Feasibility of Lunar Seismic Tomography

The Apollo seismic network consisted of only four stations, which were not sufficient to locate the moonquakes precisely. The uncertainty in the moonquake locations ranges from a few to tens of kilometers, which prevents from determining a precise tomography of the lunar interior. As a matter of fact, even the 1-D velocity models determined by different researchers show some discrepancies (see the recent review by Khan et al. 2013).

The lunar tomography, however, has some advantages over the terrestrial tomography (Zhao et al. 2008). The first is that moonquakes occurred down to a depth of

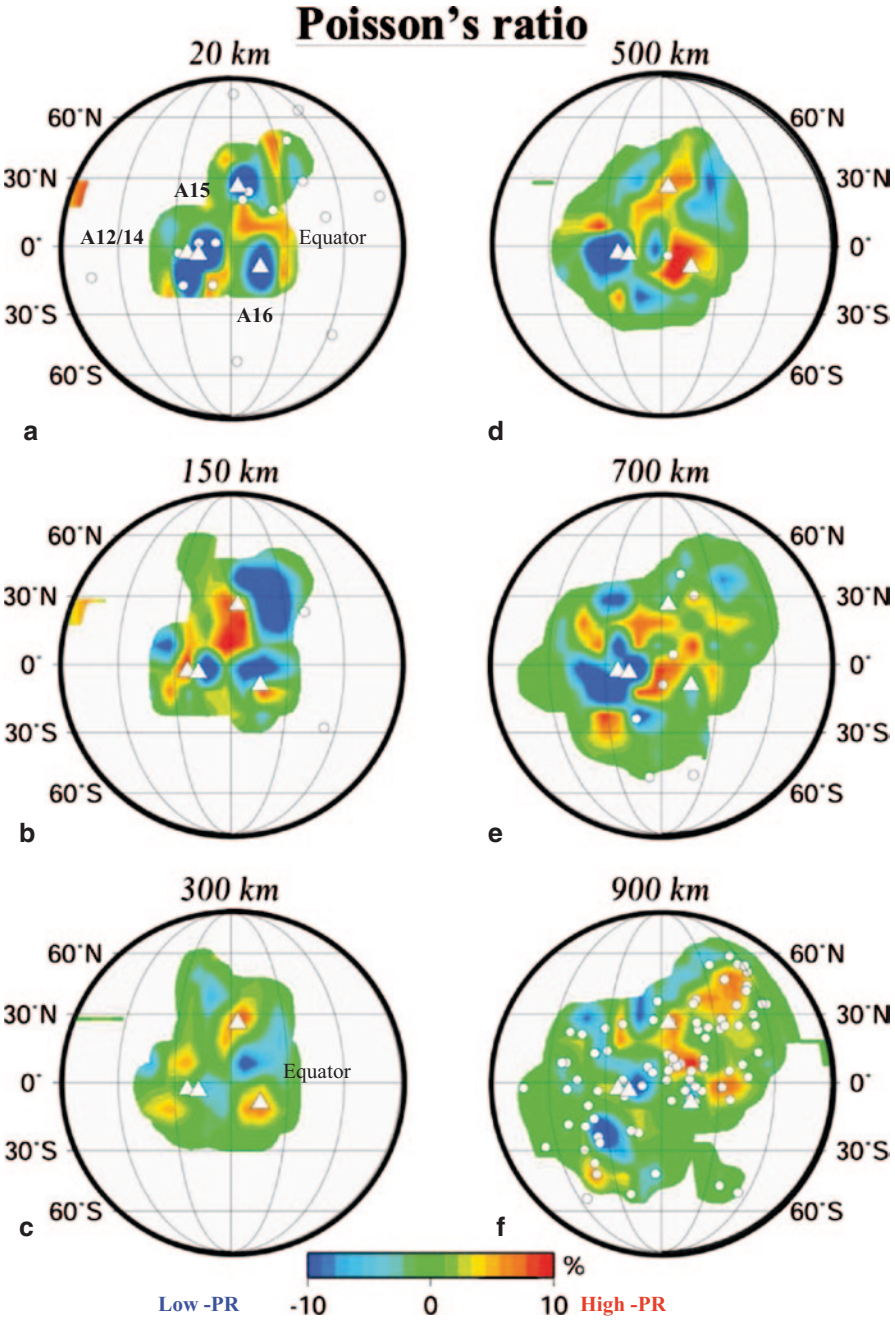

Fig. 8.19 Map views of the Poisson's ratio (*PR*) image at six depth slices. The depth is shown above each map. The *red* and *blue* colors denote high and low values of Poisson's ratio, respectively. The scale of perturbations (in %) relative to the average value (0.25) is shown at the bottom. The open triangles denote the 4 Apollo seismic stations. The *white* dots show the moonquakes which occurred in a depth range of 150 km of each layer. (Modified from Zhao et al. 2008)

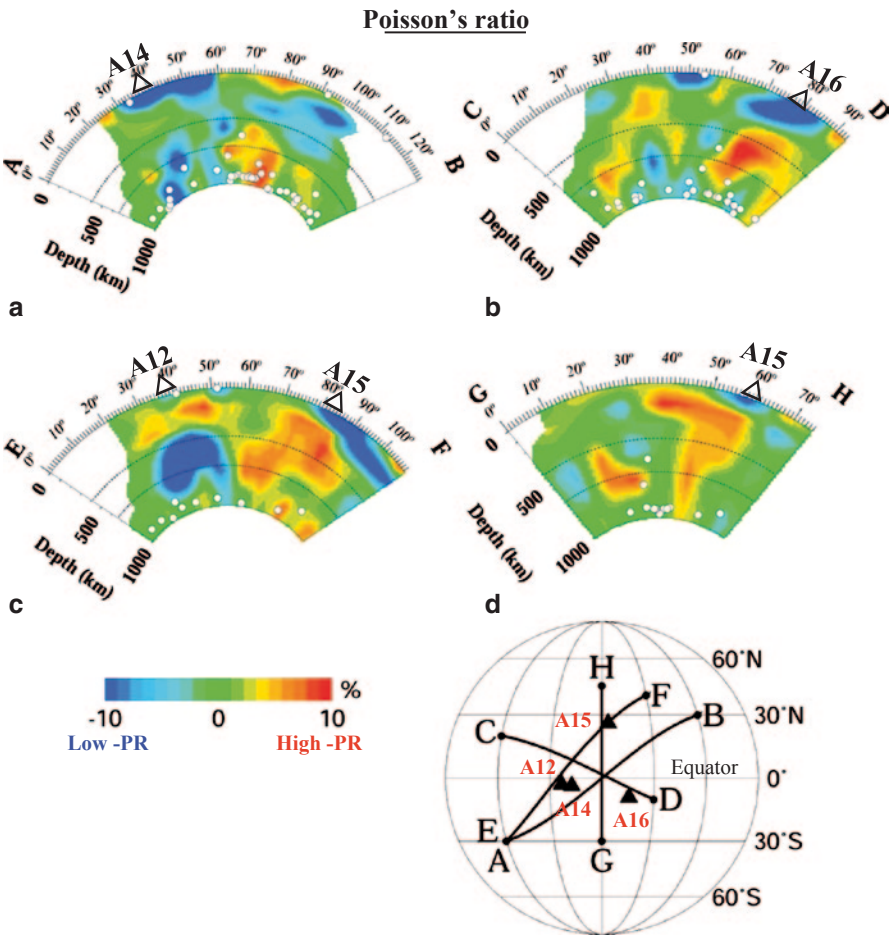

Fig. 8.20 Vertical cross-sections of the Poisson's ratio image along the four profiles shown on the inset map. The *red* and *blue* colors denote high and low values of Poisson's ratio, respectively. The scale of perturbations (in %) relative to the average value (0.25) is shown below (**c**). The *white* dots denote moonquakes which occurred within a 150-km width of each profile. The *black* triangles on the inset map denote the four Apollo seismic stations. (Modified from Zhao et al. 2008).

1400 km (note that the lunar radius is 1738 km), enabling seismic waves from the deep moonquakes to sample a large fraction of the depth range in the lunar interior even with a local seismic array, which is very favorable from the viewpoint of tomographic imaging. In contrast, earthquakes occur down to a depth of 670 km (~1/9 of the Earth's radius), and so deep Earth tomography cannot be determined without a global seismic network. The second advantage is related to the fact that the Moon is much smaller than the Earth. A distance of 10° is 303 km at the lunar equator, whereas it is 1112 km on Earth. As shown in Zhao et al. (2008), lunar tomography can be obtained with a lateral resolution of ~300 km or shorter with a local or regional seismic array consisting of a few stations, if the moonquake hypocenters can

be located reasonably well with the seismic array (hypocenter uncertainty < 10 km). This resolution scale is comparable or even better than that of the current global tomography of the Earth (e.g., Zhao et al. 2013). Therefore, future seismic imaging of the lunar interior with a new seismic network on the Moon is optimistic and feasible.

Two key issues of lunar seismic tomography are: (1) picking up P- and S-wave arrival times precisely, and (2) locating moonquakes accurately. The first issue can be solved using the updated technologies of seismic instrumentation and waveform processing. To resolve the second issue, later phases, i.e., reflected and converted waves at the lunar surface and velocity discontinuities (if any) in the lunar interior, have to be detected and used for locating the moonquakes, because the number of available seismic stations on the lunar surface will be limited. Many previous studies have shown that the later-phase data are very useful for constraining hypocentral locations of earthquakes (e.g., Umino et al. 1995; Zhao et al. 2002, 2011b; Liu et al. 2013a, b) and for improving the ray path coverage for tomographic imaging (e.g., Zhao et al. 1992, 2005; Xia et al. 2007; Sun et al. 2008; Gupta et al. 2009). Zhao et al. (2005) obtained a high-resolution local crustal tomography of the 1992 Landers earthquake (M 7.3) area using only two seismic stations, because they used many reflected waves between the surface and the Moho discontinuity (ScS, sScS) in addition to the first S-wave arrivals (consisting of the direct S-waves and Sn head waves refracted from the Moho), which were detected in the observed seismograms of the Landers aftershocks using waveform modeling techniques (e.g., Helmberger et al. 2001; Abdelwahed and Zhao 2005, 2014).

8.4.2 Lunar Tomography and Thorium Abundance

Many researchers have suggested that a dichotomy in geological processes may have existed between the lunar nearside and farside (e.g., Warren and Wasson 1979; Arai et al. 2008, 2010; Yamashita et al. 2010, and many references therein). The two sides exhibit distinct differences in the surface topography (Araki et al. 2009), gravity field (Namiki et al. 2009; Yan et al. 2012), crustal thickness (Hikida and Wieczorek 2007; Ishihara et al. 2009; Wieczorek et al. 2013), and composition (e.g., Arai et al. 2008, 2010). The dichotomy may be a combined result of asymmetric crystallization of a primordial magma ocean, post-magma-ocean magmatism and resurfacing by basin formation (Arai et al. 2008). The analysis of the returned lunar samples and meteorites revealed that the Moon's evolution was drastically different from that of the Earth (e.g., Warren and Wasson 1979; Arai et al. 2010, and references therein). Returned samples from the Apollo 12, 14 and 15 sites were found to contain highly elevated concentrations of incompatible trace elements, and these rocks were given the name KREEP, because of their high levels of potassium (K), rare earth elements (REE), and phosphorous (P). Although the absolute concentrations of these elements vary among the KREEP-rich samples, their

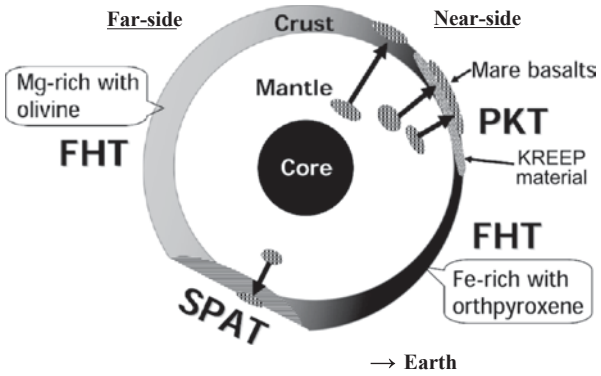

Fig. 8.21 A schematic cross-section of the Moon for illustrating an asymmetric crust composition, stratigraphy and thickness in conjunction with the three terranes and mare basalt distribution. PKT denotes the Procellarum KREEP Terrane; FHT is the Feldspathic Highlands Terrane; and SPAT is the South Pole-Aitken Terrane. (Modified from Arai et al. 2008)

relative concentrations tend to be roughly consistent (Warren and Wasson 1979; Arai et al. 2008, 2010).

Previous studies have shown that the lunar surface can be divided into three major terranes (Fig. 8.21): the Procellarum KREEP Terrane (PKT), the Feldspathic Highlands Terrane (FHT), and the South Pole-Aitken Terrane (SPAT), largely on the basis of geochemical, petrological, and geophysical criteria that indicate each terrane experienced a fundamentally different geological evolution (Jolliff et al. 2000; Arai et al. 2008). The PKT and FHT are likely originated from an early global-scale differentiation. The PKT constitutes only ~15% or less of the crust, but it owes much of its unique character to the sequestration there of a large portion of radioactive heat-producing elements in the Moon (Fig. 8.22c). Mass balance models for thorium (Th) which are based on surface expressions of the terranes indicate that some 75% of lunar Th is located within the crust and that 40% of this occurs within the PKT, hence the PKT is a unique and fundamental geochemical crustal province of the Moon (Jolliff et al. 2000; Lawrence et al. 2000; Saito 2008; Arai et al. 2010; Fig. 8.22c). The spatial distribution of mare volcanism closely parallels the confines of the PKT, suggesting a causal relationship between the two phenomena (Wieczorek and Phillips 2000). The depth extent of the PKT and the vertical distribution of KREEP materials are an important issue concerning the internal structure and evolution of the Moon. However, the issue has remained unconstrained because of the lack of information on the structure of the lunar crust and mantle. The lunar tomography has shed new light on this important issue.

Zhao et al. (2012a) discussed the internal structure in and around the PKT by comparing lunar seismic tomography with the Th surface distribution (Fig. 8.22). A significant low-V anomaly is visible down to a depth of ~150 km under the western side of the Apollo seismic network, i.e., beneath the Apollo stations 12, 14 and 15 (Fig. 8.22a, b), and the low-V anomaly extends down to a depth of ~300 km under the Apollo station A15 (Fig. 8.12c). The lateral extent of the low-V zone is well

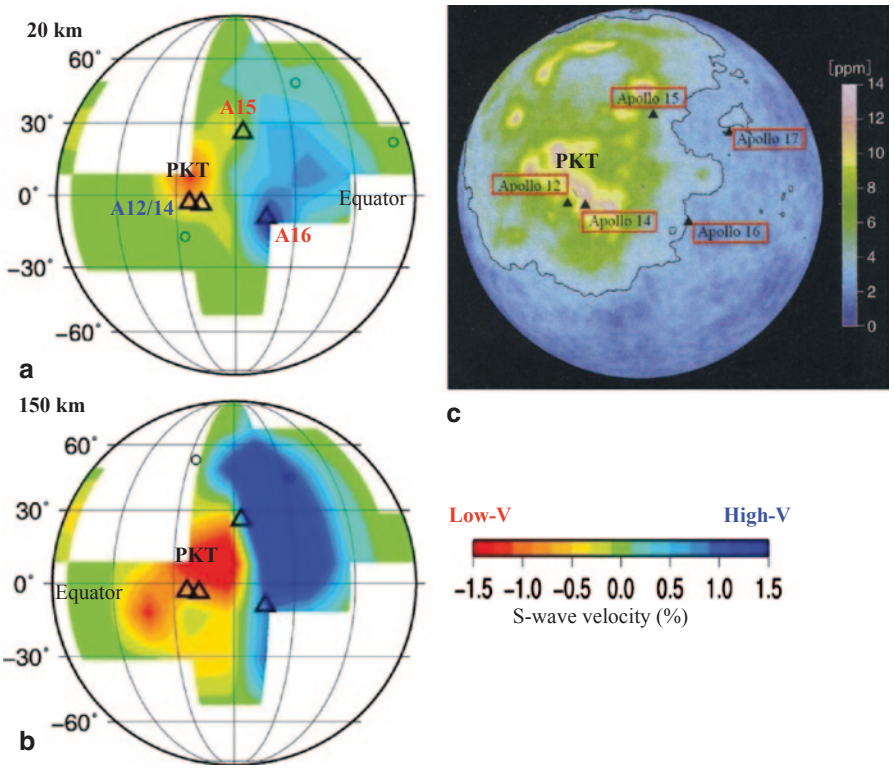

Fig. 8.22 Map views of S-wave tomography at (**a**) 20 km and (**b**) 150 km depths under the near-side of the Moon. The other labeling is the same as that of Fig. 8.12. (**c**) Distribution of the thorium abundance on the lunar surface (modified from Saito 2008 and Lawrence et al. 2000). (Modified from Zhao et al. 2012a)

consistent with the area with significant high Th abundance in the PKT (Fig. 8.22). In contrast, beneath the landing sites of Apollo 16 and 17, the S-wave tomography exhibits distinct high velocity, which corresponds to low Th abundance (Fig. 8.22). The vertical cross-sections of the tomography show that the low-V zone is visible down to a depth of 300–400 km under the Apollo stations 12, 14 and 15 (Fig. 8.14b, c).

Many researchers have attempted to interpret seismic velocity anomalies imaged by seismic tomography, and the results show that velocity anomalies could be the product of thermal anomalies, compositional variations (including volatiles), and the presence of partial melt, cracks, anisotropy, or a combination of these factors (see the reviews by Zhao 2009, 2012). In the Earth's mantle, however, velocity anomalies are mainly affected by lateral variations in temperature. Th is a significant heat-producing radioactive element, and so it is reasonable to consider that the PKT area with high Th abundance has a higher temperature than the surrounding lunar crust and mantle materials, hence it is imaged as a low-V anomaly by lunar seismic tomography (Zhao et al. 2012a). Note that S-wave velocity is much more

sensitive to temperature variations than P-wave velocity, hence the high-Th area in the PKT is better imaged by S-wave tomography than the P-wave tomography (Zhao et al. 2008, 2012a). The composition of the PKT area, such as the KREEP basalt, can certainly affect the seismic velocity. Hence the lower S-wave velocity in the PKT region may reflect both a higher temperature and the KREEP basalt there.

A thermal-conduction modeling study shows that the dramatic enhancement of heat-producing elements within the PKT has had a significant influence on the thermal and magmatic evolution of the PKT (Wieczorek and Phillips 2000). By placing a 10 km layer of KREEP basalt at the base of the crust in the PKT, the modeling results show that this material would remain molten for a few billion years and that it would additionally heat and partially melt the underlying mantle. Partial melting of the mantle may have occurred over most of the lunar history, and the maximum depth of melting may increase with time to a depth of ~600 km. This modeling result is consistent with the long duration of mare magmatism (from at least 4.2 Ga to ~900 Ma) as well as the depth of origin of mare basalts (<540 km) (Longhi 1992).

Zhao et al. (2012a) suggested that the thermal anomaly under the PKT has extended down to a depth of 300–400 km, considering the correlation between the Th abundance distribution and the lunar tomography, as well as the thermal modeling results of Wieczored and Phillips (2000). If we assume temperature to be the only source of the seismic heterogeneity, the S-velocity variations revealed by tomography correspond to a temperature increase of 100–150 K, roughly consistent with that predicted by Wieczorek and Phillips (2000).

8.4.3 Mantle Heterogeneity and Deep Moonquakes

The distribution of deep moonquakes shows a good correlation with the seismic velocity variations in the lunar lower mantle revealed by the lunar tomography (Figs. 8.14 and 8.23). Most of the deep moonquakes are located in areas with an average-to-higher velocity or at the boundary between the low-V and high-V zones, and there are few deep moonquakes in the low-V zones. To confirm this feature, Zhao et al. (2008, 2012a) conducted many tomographic inversions by adopting different values of damping and smoothing parameters, and found that the damping and smoothing affect only the amplitudes of velocity anomalies but do not affect the pattern of velocity variations. They also adopted different grid intervals to conduct tomographic inversions, and found that the pattern of the tomographic image remains the same and the correlation between the deep moonquake distribution and tomography is a reliable feature.

The spatial correlation between the deep moonquakes and lunar tomography suggests that the generation of deep moonquakes was affected by the structural heterogeneity in the lunar deep mantle in addition to the tidal stresses. This feature is very similar to that of shallow and deep earthquakes which take place in the crust and upper mantle of the Earth. All the intermediate-depth and deep earthquakes (60–670 km depth) occur within the subducting oceanic or continental lithosphere (slab) in the upper mantle and the mantle transition zone, and they always form a

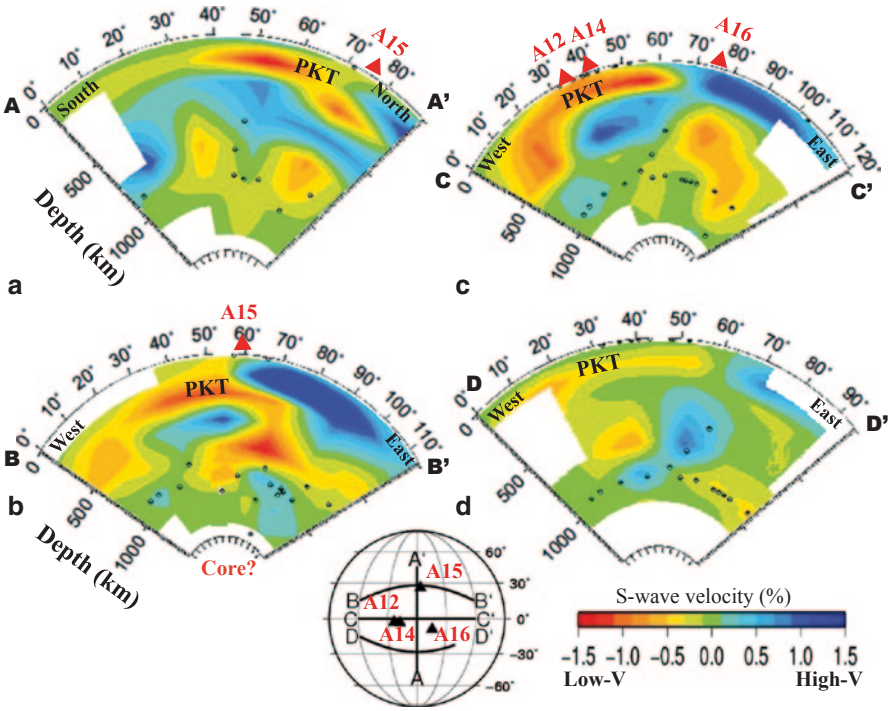

Fig. 8.23 Vertical cross-sections of S-wave tomography along the four profiles shown on the inset map. The *red* and *blue* colors denote low and high velocities, respectively. The scale of velocity perturbations (in %) relative to the 1-D velocity model (Fig. 8.7) is shown at the *bottom*. The *open circles* denote moonquakes which occurred within a 150 km width of each profile. The *black triangles* on the inset map and the *red triangles* atop the *cross-sections* denote the four Apollo seismic stations. (Modified from Zhao et al. 2012a)

clear dipping seismic zone, called the Wadati-Benioff zone. The subducting slabs are colder than the surrounding mantle and so they exhibit a higher seismic velocity and thus can be imaged by seismic tomography (e.g., Zhao 2004; Jiang et al. 2009; Zhao and Ohtani 2009; Wei et al. 2012). Recent seismological studies have shown that the generation of deep earthquakes may be associated with fine structural heterogeneities within the subducting slab, such as the metastable olivine wedge at depths of the mantle transition zone (e.g., Jiang et al. 2008; Jiang and Zhao 2011). The occurrence of intermediate-depth and deep earthquakes may be also affected by the complex dehydration processes in the subducting slab (e.g., Mishra and Zhao 2004; Ohtani and Zhao 2009; Zhao and Ohtani 2009; Wei et al. 2012, 2013; Zhao and Tian 2013). Many workers have investigated the 3-D seismic velocity structure in the source areas of large crustal earthquakes which occurred in various tectonic settings, and the results show that the nucleation of all the large crustal earthquakes was affected (or controlled) by structural heterogeneities in the crust and uppermost mantle (e.g., Mishra and Zhao 2003; Huang and Zhao 2004, 2009; Qi et al. 2006; Lei and Zhao 2009; Xu and Zhao 2009; Wei and Zhao 2013; Chen et al. 2014;

Cheng et al. 2011, 2014). For some large crustal earthquakes in subduction zones, structural heterogeneities in the focal area are associated with arc fluids and magmas caused by dehydration of the subducting slab and corner flow in the mantle wedge (e.g., Ikeda et al. 2006; Wang and Zhao 2006; Xia et al. 2008; Zhao et al. 2010, 2011a, 2015; Cheng et al. 2011; Padhy et al. 2011; Tong et al. 2011, 2012). It is also found that the nucleation of the great 2011 Tohoku-oki earthquake (Mw 9.0) and other megathrust earthquakes (M > 7.0) was affected by structural heterogeneities in the interplate megathrust zone under the fore-arc regions, which may reflect the subducted sediments and seamounts, as well as fluids from the slab dehydration (e.g., Zhao et al. 2011b; Huang and Zhao 2013a, b; Liu et al. 2013a, b, 2014).

Almost all the deep moonquakes are located in the depth range of 750–1400 km (Figs. 8.1, 8.4 and 8.5). A few possible mechanisms have been proposed to explain this feature (Latham et al. 1973), including: (a) Maximum thermo-elastic stresses in a cooling Moon occur in that depth range; (b) Abrupt phase changes of mantle material take place in the active focal zones; (c) A concentration of fluids in that depth range leads to a reduction of effective friction or a weakening of the silicate bond; (d) Weak convective motions at depth beneath a thick, rigid mantle might generate deep moonquakes without the surface manifestations associated with terrestrial plate tectonics; and (e) Radial variations in rigidity of the lunar material may be such as to concentrate the dissipation of tidal energy at great depth. The correlation between the deep moonquake distribution and lunar tomography may be explained by the phase changes, variations in rigidity, and the presence of fluids in the focal zones (Zhao et al. 2012a).

The characteristics of deep moonquakes were compared with those of intermediate-depth earthquakes, and it was suggested that there are partial melts or fluid phases in the lunar mantle that permit deep moonquakes to occur repeatedly (Frohlich and Nakamura 2009). Recent petrological and modeling studies also suggested that the bulk Moon might not be completely depleted in highly volatile elements including water and the presence of water should be taken into account in models constraining the lunar formation and its thermal and chemical evolution (Saal et al. 2008; McCubbin et al. 2010; Elkins-Tanton and Grove 2011). The lateral seismic-velocity variations in the lunar crust and mantle revealed by seismic tomography (Figs. 8.11–8.14) can be better explained by the presence of fluid phases and partial melts in the lunar interior (Zhao et al. 2012a).

8.4.4 Geodynamic Implications

A dense ilmenite-rich layer, which originally crystallized near the top of the lunar magma ocean, may have sunk to the center of the Moon due to the gravitational instability during the late stage of magma ocean crystallization (Parmentier et al. 2002). A dynamic cumulate overturn may have occurred as a result of unstable cumulate density stratification of the magma ocean (Snyder et al. 1992; Hess and Parmentier 1995). Late-stage products of magma ocean solidification should be

enriched in incompatible elements, such as Ti and KREEP. The deeper low-V zones (Fig. 8.23) may reflect the downwelling, ilmenite-rich KREEP materials (Zhao et al. 2012a). In addition, a recent thermo-chemical convection model has shown that hot plumes developing from the hot ilmenite core may rise into the mantle from the core-mantle boundary to accommodate the rapid cooling of the core (de Vries et al. 2010). These plumes have temperatures that exceed the solidus temperature of peridotite and cause melt zones, which spread out well below the crust. These partial-melt zones do not spread out under the full surface, but are localized, which may have been imaged as low-V zones in the upper mantle by the lunar tomography (Figs. 8.11–8.14). Although the timing of the mantle dynamics cannot be constrained, the lunar tomography provides a new line of evidence for the mantle dynamics beneath the near-side of the Moon. The tomographic results may indicate that the Moon experienced nearly global melting down to a depth of ~1000 km, solidification, and subsequent dynamical processes (Zhao et al. 2012a). The non-uniform distribution of deep moonquakes (Figs. 8.1, 8.4 and 8.5) may also reflect the existence of structural heterogeneities in the lower mantle of the Moon.

Sakamaki et al. (2010) measured the density of the Apollo 14 black glass melt, which has the highest TiO_2 content of pristine mare glasses, to 4.8 GPa and 2100 K using an X-ray absorption method. The pressure–density–temperature data were fit to the high-temperature Birch–Murnaghan equation of state, which yielded the isothermal bulk modulus $K_{T0} = 9.0 \pm 1.2$ GPa, its pressure derivative $K_0' = 16.0 \pm 3.4$, and the temperature derivative of the bulk modulus $(\partial K_T/\partial T)_P = -0.0030 \pm 0.0008$ GPa/K at 1700 K. The high-Ti basalt magma has a density lower than the lunar mantle below ~1.0 GPa. Thus, the high-Ti basalt magma produced in the hybridized source (100–200 km depth) can ascend to the lunar surface. The basalt formed at the higher pressure could not ascend but move downwards, and solidify in the lunar mantle. The solidified high-Ti basalt components can cause chemical heterogeneities in the lunar mantle, which may lead to the low-V anomalies revealed by the lunar tomography (Sakamaki et al. 2010).

It should be pointed out that the lunar mantle tomography is only a snapshot of the interior of the present Moon, or more precisely, the time when the lunar seismic data were collected during the Apollo missions. Hence it is difficult to estimate the period of lunar mantle dynamics just from the tomographic images. However, because deep moonquakes occur actively and significant seismic-velocity variations are revealed in the lunar mantle (Figs. 8.11–8.14), it is reasonable to infer that the interior of the present Moon may still be thermally and dynamically active, though much less vigorous as in the Earth's interior. Because there is no volcanic activity at present, it is generally considered that the Moon is no more thermally active. However, recent, probably present, gas release features have been discovered at several locations in and around the PKT (Schultz et al. 2006). Numerical-modeling studies on the lunar thermal history have also suggested that the interior of the present Moon contains both thermal and compositional anomalies (e.g., Konrad and Spohn 1997; Zhong et al. 2000; Stegman et al. 2003; Ziethe et al. 2009; de Vries et al. 2010). All these geophysical and geochemical results indicate that deep magmas and thermal anomalies, as well as compositional variations, coexist in the present

lunar mantle, which have been imaged as seismic-velocity variations by the lunar tomography (Zhao et al. 2008, 2012a).

Because of the limitations of the Apollo seismic data, the tomographic study of the Moon has to be considered as an experimental work. Future lunar explorations, such as the upcoming Japanese Lunar-A mission (Mizutani et al. 2003; Yamada et al. 2009) in which a penetrator-based deployment of seismic stations is planned in both the near-side and far-side of the Moon, are expected to provide better seismic data enabling us to determine a more reliable tomographic image of the lunar interior (Zhao et al. 2008). Fundamental scientific questions concerning the internal structure and dynamics of the Moon, and their implications for the Earth-Moon system, are driving the deployment of a new broadband seismological network on the lunar surface (Yamada et al. 2011). The fundamental but unsolved questions which are driving the design of the new lunar seismic network include: What are the characteristics of long-period seismic signals on the Moon? What are the size and state of the lunar core? How heterogeneous is the lunar mantle? (Yamada et al. 2011). Seismic tomography resulting from new data and waveform modeling of the lunar seismograms using the obtained 3-D velocity model (e.g., Wang et al. 2013) will be able to reveal more detailed features of the lunar interior structure and dynamics.

8.5 Summary

Seismic tomography has been applied to invert the moonquake arrival-time data recorded by the Apollo seismic network operated during 1969 to 1977 to estimate 3-D P- and S-wave velocity and Poisson's ratio variations in the lunar crust and mantle down to a depth of 1000–1300 km under the near-side of the Moon (Zhao et al. 2008, 2012a). The results indicate that tomographic imaging of the lunar interior is feasible, because deep moonquakes occur actively down to a depth of more than 1000 km under the Apollo seismic network. The main findings of the lunar tomographic studies are summarized as follows.

1. Significant structural heterogeneities may exist in the lunar interior, which were mainly produced at the early stage of the Moon formation and evolution and have been preserved till today, because there is no plate tectonics in the Moon.
2. A comparison of the lunar tomography with the distribution of thorium abundance on the lunar surface shows that the area with a high-Th abundance in the PKT exhibits a distinct low S-wave velocity, and the low-velocity zone extends down to a depth of 300–400 km under the PKT. This result suggests that the high abundance of radioactive heat-producing elements has resulted in a high temperature in the PKT, which was imaged as low-velocity anomalies by seismic tomography. The thermal and compositional anomalies under the PKT may extend from the surface down to a depth of 300–400 km in the lunar mantle.
3. Most of the deep moonquakes are located in areas with an average-to-higher velocity or at the boundary between high-velocity and low-velocity zones, whereas few deep moonquakes occur in the low-velocity areas. This feature is

very similar to that of deep and shallow seismicity in the Earth, because many seismological and mineral-physics studies have shown that the distribution and generation of all types of earthquakes are affected, or even controlled, by structural heterogeneities in the terrestrial crust and upper mantle.

4. The existence of deep moonquakes and significant seismic heterogeneities in the lunar mantle suggests that the interior of the present Moon may still be thermally and dynamically active, though much less vigorous as in the Earth's interior. Future lunar explorations are expected to provide better seismic data enabling us to determine a better tomography of the lunar interior.

References

Abdelwahed, M.F., Zhao, D.: Waveform modelling of local earthquakes in Southwest Japan. Earth Planets Space **57,** 1039–1054 (2005)

Abdelwahed, M.F., Zhao, D.: Genetic waveform modeling for the crustal structure in Northeast Japan. J. Asian Earth Sci. **89,** 66–75 (2014)

Arai, T., Takeda, H., Yamaguchi, A., Ohtake, M.: A new model of lunar crust: asymmetry in crustal composition and evolution. Earth Planets Space. **60,** 433–444 (2008)

Arai, T., Hawke, B., Giguere, T., Misawa, K., Miyamoto, M., Kojima, H.: Antarctic lunar meteorites Yamato-793169, Asuka-881757, MIL 05035, and MET 01210 (YAMM): launch pairing and possible cryptomare origin. Geochim. Cosmochim. Acta. **74,** 2231–2248 (2010)

Araki, H., Tazawa, S., Noda, H., Ishihara, Y., Goossens, A., et al.: Lunar global shape and polar topography derived from Kaguya-LALT laser altimetry. Science. **323,** 897–900 (2009)

Chen, C., Zhao, D., Wu, S.: Crust and upper mantle structure of the New Madrid Seismic Zone: insight into intraplate earthquakes. Phys. Earth Planet. Inter. **230,** 1–14 (2014)

Chenet, H., Lognonne, P., Wieczorek, M., Mizutani, H.: Lateral variations of lunar crustal thickness from the Apollo seismic data set. Earth Planet. Sci. Lett. **243,** 1–14 (2006)

Cheng, B., Zhao, D., Zhang, G.: Seismic tomography and anisotropy in the source area of the 2008 Iwate-Miyagi earthquake (M 7.2). Phys. Earth Planet. Inter. **184,** 172–185 (2011)

Cheng, B., Cheng, S., Zhang, G., Zhao, D.: Seismic structure of the Helan-Liupan-Ordos western margin tectonic belt in North-Central China and its geodynamic implications. J. Asian Earth Sci. **87,** 141–156 (2014)

Christensen, N.: Poisson's ratio and crustal seismology. J. Geophys. Res. **101,** 3139–3156 (1996)

de Vries, J., van den Berg, A., van Westrenen, W.: Formation and evolution of a lunar core from ilmenite-rich magma ocean cumulates. Earth Planet. Sci. Lett. **292,** 139–147 (2010)

Elkins-Tanton, L., Grove, T.: Water (hydrogen) in the lunar mantle: results from petrology and magma ocean modeling. Earth Planet. Sci. Lett. **307,** 173–179 (2011)

Frohlich, C.: Deep Earthquakes. Cambridge University Press, London (2006)

Frohlich, C., Nakamura, Y.: The physical mechanisms of deep moonquakes and intermediate-depth earthquakes: how similar and how different? Phys. Earth Planet. Inter. **173,** 365–374 (2009)

Gagnepain-Beyneix, J., Lognonne, P., Chenet, H., Lombardi, D., Spohn, T.: A seismic model of the lunar mantle and constraints on temperature and mineralogy. Phys. Earth Planet. Inter. **159,** 140–166 (2006)

Garcia, R., Gagnepain-Beyneix, J., Chevrot, S., Lognonne, P.: Very preliminary reference Moon model. Phys. Earth Planet. Inter. **188,** 96–113 (2011)

Goins, N., Dainty, A., Toksoz, M.: Lunar seismology: the internal structure of the Moon. J. Geophys. Res. **86,** 5061–5074 (1981)

Gupta, S., Zhao, D., Ikeda, M., Ueki, S., Rai, S.: Crustal tomography under the Median Tectonic Line in Southwest Japan using P and PmP data. J. Asian Earth Sci. **35,** 377–390 (2009)
Helmberger, D., Song, X.J., Zhu, L.: Crustal complexity from regional waveform tomography: aftershocks of the 1992 Landers earthquake. J. Geophys. Res. **106,** 609–620 (2001)
Hess, P., Parmentier, E.: A model for the thermal and chemical evolution of the Moon's interior: Implications for the onset of mare volcanism. Earth Planet. Sci. Lett. **134,** 501–514 (1995)
Hikida, H., Wieczorek, M.: Crustal thickness of the Moon: new constraints from gravity inversions using polyhedral shape models. Icarus. **192,** 150–166 (2007)
Huang, J., Zhao, D.: Crustal heterogeneity and seismotectonics of the region around Beijing, China. Tectonophysics. **385,** 159–180 (2004)
Huang, J., Zhao, D.: Seismic imaging of the crust and upper mantle under Beijing and surrounding regions. Phys. Earth Planet. Inter. **173,** 330–348 (2009)
Huang, Z., Zhao, D.: Mechanism of the 2011 Tohoku-oki earthquake (Mw 9.0) and tsunami: insight from seismic tomography. J. Asian Earth Sci. **70,** 160–168 (2013a)
Huang, Z., Zhao, D.: Relocating the 2011 Tohoku-oki earthquakes (M 6.0–9.0). Tectonophysics. **586,** 35–45 (2013b)
Ikeda, M., Zhao, D., Ohno, Y.: Crustal structure, fault segmentation and activity of the Median Tectonic Line in Shikoku, Japan. Tectonophysics. **412,** 49–60 (2006)
Ishihara, Y., Goossens, S., Matsumoto, K., et al.: Crustal thickness of the Moon: implications for farside basin structures. Geophys. Res. Lett. **36,** L19202 (2009)
Jiang, G., Zhao, D.: Metastable olivine wedge in the subducting Pacific slab and its relation to deep earthquakes. J. Asian Earth Sci. **42,** 1411–1423 (2011)
Jiang, G., Zhao, D., Zhang, G.: Seismic evidence for a metastable olivine wedge in the subducting Pacific slab under Japan Sea. Earth Planet. Sci. Lett. **270,** 300–307 (2008)
Jiang, G., Zhao, D., Zhang, G.: Seismic tomography of the Pacific slab edge under Kamchatka. Tectonophysics. **465,** 190–203 (2009)
Jolliff, B., Gillis, J., Haskin, L., Korotev, R., Wieczorek, M.: Major lunar crustal terranes: surface expressions and crust-mantle origins. J. Geophys. Res. **105,** 4197–4216 (2000)
Khan, A., Mosegaard, K.: An inquiry into the lunar interior: a nonlinear inversion of the Apollo lunar seismic data. J. Geophys. Res. **107**(E6), 2001JE001658 (2002)
Khan, A., Pommier, A., Neumann, G., Mosegaard, K.: The lunar moho and the internal structure of the Moon: a geophysical perspective. Tectonophysics. **609,** 331–352 (2013)
Konrad, W., Spohn, T.: Thermal history of the Moon: implicatioins for an early core dynamo and post-accretional magmatism. Adv. Space Res. **19,** 1511–1521 (1997)
Lammlein, D.: Lunar seismicity and tectonics. Phys. Earth Planet. Inter. **14,** 224–273 (1977)
Latham, G., Ewing, M., Dorman, J., Nakamura, Y., Press, F., Toksoz, N., Sutton, G., Duennebier, F., Lammlein, D.: Lunar structure and dynamics—Results from the Apollo passive seismic experiment. Moon. **7,** 396–420 (1973)
Lawrence, D., Feldman, W., Barraclough, B., Binder et al. Thorium abundances on the lunar surface. J. Geophys. Res. **105,** 20307–20331 (2000)
Lei, J., Zhao, D.: Structural heterogeneity of the Longmenshan fault zone and the mechanism of the 2008 Wenchuan earthquake (Ms 8.0). Geochem. Geophys. Geosyst. **10,** Q10010 (2009)
Liu, X., Zhao, D., Li, S.: Seismic heterogeneity and anisotropy of the southern Kuril arc: insight into megathrust earthquakes. Geophys. J. Int. **194,** 1069–1090 (2013a)
Liu, X., Zhao, D., Li, S.: Seismic imaging of the Southwest Japan arc from the Nankai trough to the Japan Sea. Phys. Earth Planet. Inter. **216,** 59–73 (2013b)
Liu, X., Zhao, D., Li, S.: Seismic attenuation tomography of the Northeast Japan arc: insight into the 2011 Tohoku earthquake (Mw 9.0) and subduction dynamics. J. Geophys. Res. **119,** 1094–1118 (2014)
Lognonne, P., Johnson, C.: Planetary Seismology. In: Schubert, G. (ed.) Treatise in Geophysics, pp. 69–122. Elsevier, New York (2007)
Lognonne, P., Gagnepain-Beyneix, J., Chenet, H.: A new seismic model of the Moon: implications in terms of structure, formation and evolution. Earth Planet. Sci. Lett. **211,** 27–44 (2003)

Longhi, J.: Experimental petrology and petrogenesis of mare volcanics. Geochem. Cosmochim. Acta. **56,** 2235–2251 (1992)
McCubbin, F., Steele, A., Hauri, E., Nekvasil, H., Yamashita, S., Hemley, R.: Nominally hydrous magmatism on the Moon. Proc. Nat. Acad. Sci. **107,** 11223–11228 (2010)
Mishra, O.P., Zhao, D.: Crack density, saturation rate and porosity at the 2001 Bhuj, India, earthquake hypocenter: a fluid driven earthquake? Earth Planet. Sci. Lett. **212,** 393–405 (2003)
Mishra, O.P., Zhao, D.: Seismic evidence for dehydration embrittlement of the subducting Pacific slab. Geophys. Res. Lett. **31,** L09610 (2004)
Mizutani, H., Fujimura, A., Tanaka, S., Shiraishi, H., Nakajima, T.: Lunar-A mission: goals and status. Adv. Space Res. **31,** 2315–2321 (2003)
Nakamura, Y.: Seismic velocity structure of the lunar mantle. J. Geophys. Res. **88,** 677–686 (1983)
Nakamura, Y.: Farside deep moonquakes and deep interior of the Moon. J. Geophys. Res. **110,** E01001 (2005)
Namiki, N., Iwata, T., Matsumoto, K., et al.: Farside gravity field of the Moon from four-way Doppler measurements of SELENE (Kaguya). Science. **323,** 900–905 (2009)
Ohtani, E., Zhao, D.: The role of water in the deep upper mantle and transition zone: dehydration of stagnant slabs and its effects on the big mantle wedge. Russ. Geol. Geophys. **50,** 1073–1078 (2009)
Ono, T., Kumamoto, A., Nakagawa, H., et al.: Lunar radar sounder observations of subsurface layers under the nearside maria of the Moon. Science. **323,** 909–912 (2009)
Padhy, S., Mishra, O.P., Zhao, D., Wei, W.: Crustal heterogeneity in the 2007 Noto-Hanto earthquake area and its geodynamical implications. Tectonophysics. **509,** 55–68 (2011)
Paige, C., Saunders, M.: LSQR: an algorithm for sparse linear equations and sparse least squares. ACM Trans. Math. Softw. **8,** 43–71 (1982)
Parmentier, E., Zhong, S., Zuber, M.: Gravitational differentiation due to initial chemical stratification; origin of lunar asymmetry by the creep of dense KREEP? Earth Planet. Sci. Lett. **201,** 473–480 (2002)
Qi, C., Zhao, D., Chen, Y., Chen, Q., Wang, B.: 3-D P and S wave velocity structures and their relationship to strong earthquakes in the Chinese capital region. Chinese J. Geophys. **49,** 805–815 (2006)
Saal, A., Hauri, E., Cascio, M., Van Orman, J., Rutherford, M., Cooper, R.: Volatile content of lunar volcanic glasses and the presence of water in the Moon's interior. Nature. **454,** 192–195 (2008)
Saito, Y.: Is the lunar composition not similar to the Earth's composition? Kagaku. **78,** 606–609 (2008)
Sakamaki, T., Ohtani, E., Urakawa, S., Suzuki, A., Katayama, Y., Zhao, D.: Density of high-Ti basalt magma at high pressure and origin of heterogeneities in the lunar mantle. Earth Planet. Sci. Lett. **299,** 285–289 (2010)
Schultz, P., Staid, M., Pieters, C.: Lunar activity from recent gas release. Nature. **444,** 184–186 (2006)
Snyder, G., Taylor, L., Neil, C.: A chemical model for generating the sources of mare basalts: combined equilibrium and fractional crystallization of the lunar magma sphere. Geochem. Cosmochem. Acta. **56,** 3809–3823 (1992)
Stegman, D., Jellinek, A., Zatman, S., Baumgardner, J., Richards, M.: An early lunar core dynamo driven by thermochemical mantle convection. Nature. **421,** 143–146 (2003)
Sun, A., Zhao, D., Ikeda, M., et al.: Seismic imaging of southwest Japan using P and PmP data: implications for arc magmatism and seismotectonics. Gondwana Res. **14,** 535–542 (2008)
Toksoz, M., Dainty, A., Solomon, S., Anderson, K.: Structure of the Moon. Rev. Geophys. Space Phys. **12,** 539–567 (1974)
Tong, P., Zhao, D., Yang, D.: Tomography of the 1995 Kobe earthquake area: comparison of finite-frequency and ray approaches. Geophys. J. Int. **187,** 278–302 (2011)
Tong, P., Zhao, D., Yang, D.: Tomography of the 2011 Iwaki earthquake (M 7.0) and Fukushima nuclear power plant area. Solid Earth. **3,** 43–51 (2012)

Umino, N., Hasegawa, A., Matsuzawa, T.: sP depth phase at small epicentral distances and estimated subducting plate boundary. Geophys. J. Int. **120,** 356–366 (1995)
Vinnik, L., Chenet, H., Gagnepain-Beyneix, J., Lognonne, P.: First seismic receiver functions on the Moon. Geophys. Res. Lett. **28,** 3031–3034 (2001)
Wang, Z., Zhao, D.: Seismic evidence for the influence of fluids on the 2005 west off Fukuoka prefecture earthquake in southwest Japan. Phys. Earth Planet. Inter. **155,** 313–324 (2006)
Wang, Y., Takenaka, H., Jiang, X., Lei, J.: Modelling two-dimensional global seismic wave propagation in a laterally heterogeneous whole-Moon model. Geophys. J. Int. **192,** 1271–1287 (2013)
Warren, P., Wasson, J.: The origin of KREEP. Rev. Geophys. **17,** 73–88 (1979)
Weber, R., Lin, P., Garnero, E., Williams, Q., Lognonne, P.: Seismic detection of the lunar core. Science. **331,** 309–312 (2011)
Wei, W., Zhao, D.: The 2008 Iwate-Miyagi earthquake (M 7.2) and arc volcanism: Insight from irregular-grid tomography. Earth Sci. Frontiers **20**(2), 155–171 (2013)
Wei, W., Xu, J., Zhao, D., Shi, Y.: East Asia mantle tomography: new insight into plate subduction and intraplate volcanism. J. Asian Earth Sci. **60,** 88–103 (2012)
Wei, W., Zhao, D., Xu, J.: P-wave anisotropic tomography in Southeast Tibet: new insight into the lower crustal flow and seismotectonics. Phys. Earth Planet. Inter. **222,** 47–57 (2013)
Wieczorek, M., Phillips, R.: The "Procellarum KREEP Terrane": implications for mare volcanism and lunar evolution. J. Geophys. Res. **105,** 20417–20430 (2000)
Wieczorek, M., Joliff, B., Khan, A., et al.: The constitution and structure of the lunar interiors. Rev. Mineral. Geochem. **60,** 221. http://dx.doi.org/10.2138/rmg. 2006.60.3 (2006)
Wieczorek, M., et al.: The crust of the Moon as seen by GRAIL. Science. **339,** 671–675 (2013)
Xia, S., Zhao, D., Qiu, X., et al.: Mapping the crustal structure under active volcanoes in central Tohoku, Japan using P and PmP data. Geophys. Res. Lett. **34,** L10309 (2007)
Xia, S., Zhao, D., Qiu, X.: The 2007 Niigata earthquake: effect of arc magma and fluids. Phys. Earth Planet. Inter. **166,** 153–166 (2008)
Xu, P., Zhao, D.: Upper-mantle velocity structure beneath the North China Craton: implications for lithospheric thinning. Geophys. J. Int. **177,** 1279–1283 (2009)
Yamada, R., Yamada, I., Shiraishi, H., Tanaka, S., et al.: Capability of the penetrator seismometer system for lunar seismic event observation. Planet. Space Sci. **57,** 751–763 (2009)
Yamada, R., Garcia, R., Lognonne, P., et al.: Optimisation of seismic network design: application to a geophysical international lunar network. Planet. Space Sci. **59,** 343–354 (2011)
Yamashita, N., Hasebe, N., Reedy, R., et al.: Uranium on the Moon: Global distribution and U/Th ratio. Geophys. Res. Lett. **37,** L10201 (2010)
Yan, J., Goossens, S., Matsumoto, K., Ping, J., Harada, Y., Iwata, T., Namiki, N., Li, F., Tang, G., Cao, J.: CEGM02: an improved lunar gravity model using Chang'E-1 orbital tracking data. Planet. Space Sci. **62,** 1–9 (2012)
Zhao, D.: Seismic structure and origin of hotspots and mantle plumes. Earth Planet. Sci. Lett. **192,** 251–265 (2001)
Zhao, D.: Global tomographic images of mantle plumes and subducting slabs: insight into deep Earth dynamics. Phys. Earth Planet. Inter. **146,** 3–34 (2004)
Zhao, D.: Multiscale seismic tomography and mantle dynamics. Gondwana Res. **15,** 297–323 (2009)
Zhao, D.: Tomography and dynamics of Western-Pacific subduction zones. Monogr. Environ. Earth Planets. **1,** 1–70 (2012)
Zhao, D., Ohtani, E.: Deep slab subduction and dehydration and their geodynamic consequences: evidence from seismology and mineral physics. Gondwana Res. **16,** 401–413 (2009)
Zhao, D., Tian, Y.: Changbai intraplate volcanism and deep earthquakes in East Asia: a possible link? Geophys. J. Int. **195,** 706–724 (2013)
Zhao, D., Hasegawa, A., Horiuchi, S.: Tomographic imaging of P and S wave velocity structure beneath northeastern Japan. J. Geophys. Res. **97,** 19909–19928 (1992)
Zhao, D., Hasegawa, A., Kanamori, H.: Deep structure of Japan subduction zone as derived from local, regional and teleseismic events. J. Geophys. Res. **99,** 22313–22329 (1994)

Zhao, D., Kanamori, H., Negishi, H., Wiens, D.: Tomography of the source area of the 1995 Kobe earthquake: evidence for fluids at the hypocenter? Science. **274,** 1891–1894 (1996)
Zhao, D., Mishra, O.P., Sanda, R.: Influence of fluids and magma on earthquakes: seismological evidence. Phys. Earth Planet. Inter. **132,** 249–267 (2002)
Zhao, D., Todo, S., Lei, J.: Local earthquake reflection tomography of the Landers aftershock area. Earth Planet. Sci. Lett. **235,** 623–631 (2005)
Zhao, D., Lei, J., Liu, L.: Seismic tomography of the Moon. Chinese Sci. Bull. **53,** 3897–3907 (2008)
Zhao, D., Santosh, M., Yamada, A.: Dissecting large earthquakes in Japan: role of arc magma and fluids. Isl. Arc. **19,** 4–16 (2010)
Zhao, D., Wei, W., Nishizono, Y., Inakura, H.: Low-frequency earthquakes and tomography in western Japan: insight into fluid and magmatic activity. J. Asian Earth Sci. **42,** 1381–1393 (2011a)
Zhao, D., Huang, Z., Umino, N., Hasegawa, A., Kanamori, H.: Structural heterogeneity in the megathrust zone and mechanism of the 2011 Tohoku-oki earthquake (Mw 9.0). Geophys. Res. Lett. **38,** L17308 (2011b)
Zhao, D., Arai, T., Liu, L., Ohtani, E.: Seismic tomography and geochemical evidence for lunar mantle heterogeneity: comparing with Earth. Global Planet. Change. **90,** 29–36 (2012a)
Zhao, D., Yanada, T., Hasegawa, A., Umino, N., Wei, W.: Imaging the subducting slabs and mantle upwelling under the Japan Islands. Geophys. J. Int. **190,** 816–828 (2012b)
Zhao, D., Yamamoto, Y., Yanada, T.: Global mantle heterogeneity and its influence on teleseismic regional tomography. Gondwana Res. **23,** 595–616 (2013)
Zhao, D., Kitagawa, H., Toyokuni, G.: A water wall in the Tohoku forearc causing large crustal earthquakes. Geophys. J. Int. **200**, 149–172 (2015)
Zhong, S., Parmentier, E., Zuber, M.: A dynamic origin for the global asymmetry of lunar mare basalts. Earth Planet. Sci. Lett. **177**, 131–140 (2000)
Ziethe, R., Seiferlin, K., Hiesinger, H.: Duration and extent of lunar volcanism: comparison of 3D convection models to mare basalt ages. Planet. Space Sci. **57**, 784–796 (2009)